Springer Series in Materials Science 200

Ilya V. Shadrivov
Mikhail Lapine
Yuri S. Kivshar *Editors*

Nonlinear, Tunable and Active Metamaterials

Springer

Springer Series in Materials Science

Volume 200

The Springer Series in Materials Science covers the complete spectrum of materials physics, including fundamental principles, physical properties, materials theory and design. Recognizing the increasing importance of materials science in future device technologies, the book titles in this series reflect the state-of-the-art in understanding and controlling the structure and properties of all important classes of materials.

More information about this series at http://www.springer.com/series/856

Ilya V. Shadrivov
Mikhail Lapine
Yuri S. Kivshar
Editors

Nonlinear, Tunable and Active Metamaterials

Springer

Editors
Ilya V. Shadrivov
Yuri S. Kivshar
Nonlinear Physics Centre,
Research School of Physics
and Engineering
Australian National University
Canberra, ACT
Australia

Mikhail Lapine
CUDOS, A28 School of Physics
University of Sydney
Sydney, NSW
Australia

ISSN 0933-033X
ISBN 978-3-319-08385-8
DOI 10.1007/978-3-319-08386-5

ISSN 2196-2812 (electronic)
ISBN 978-3-319-08386-5 (eBook)

Library of Congress Control Number: 2014947657

Springer Cham Heidelberg New York Dordrecht London

Printed on acid-free paper

Springer is part of Springer Science+Business Media (www.springer.com)

Foreword

Metamaterials have seen a huge growth in research activity over the past decade with no sign of letting up. The realisation that new and exotic electromagnetic properties can be achieved by structuring materials on a subwavelength scale has opened new fields in electromagnetic studies, ranging over the entire frequency spectrum from zero to far optical. Indeed the metamaterial concept has been extended beyond electromagnetism to acoustics and other wave phenomena. The latest aspects to be exploited are their nonlinear properties and the introduction of gain, an account of which is the subject matter of this book.

In some ways metamaterials parallel the development of photonic crystals which also rely on structure for their properties. However, the major difference lies in the subwavelength nature of metamaterial structure. This enables us to summarise their properties in terms of permeability and permittivity just as we would for a conventional material. This is an enormous simplification for the design process. Metamaterial design is split into two parts: first define the macroscopic structure of your device in terms of local permeability and permittivity, then locally structure your metamaterial to achieve these properties. In contrast, photonic crystals usually require that the whole structure is designed in one step with changes in one part of the device influencing what happens in another place. The design process is non-local and therefore complex. This underlying simplicity is I think the basis of the success of metamaterials.

Nonlinearity adds greatly to the usefulness of a material but unfortunately in optics it is too often a very weak phenomenon and requires either intensely powerful sources or interaction over a long time period. It has long been realised that metamaterials have the potential to enhance nonlinearity. It is often the case that the sub-wavelength structures deployed in metamaterials concentrate electromagnetic energy into a specific location in the structure. Locating a modestly nonlinear material at this point can give rise to very strong effects. Not only that, the amount of nonlinear material required is greatly reduced.

In this book we find a collection of articles by leading researchers in the field. It will be an invaluable reference for students and researchers alike who are part of this rapidly growing enterprise.

London J.B. Pendry

Preface

The twenty-first century belongs to photonics and harnessing light is the key to life changing technologies, from energy to security, from biotechnology to low-cost precision manufacturing, from high-speed Internet to quantum-level information processing. Many important industries, ranging from integrated-circuit manufacturing, lighting, health care and life sciences, to the space, defence and automotive sectors, rely on the same fundamental mastery of light. Future technologies will demand a steep increase in photonic integration and energy efficiency, far surpassing that of bulk optical components, current silicon photonics, and even innovative plasmonic circuits. Such level of integration can be achieved by embedding the data processing and waveguiding functionalities at the level of the material rather than the chip, and the only possible solution to meet these challenges is to employ the recently emerged concept of metamaterials.

Metamaterials are artificial electromagnetic media structured on the subwavelength scale; they were initially suggested for negative refractive index and superlensing applications, but very soon they became a paradigm for engineering electromagnetic space and controlling the propagation of waves by means of transformation optics. The research agenda is now focusing on the realization of a new generation of metadevices, defined as metamaterial-based devices and structures with novel and useful functionalities achieved by structuring of functional matter on the subwavelength scale.

The fields of metamaterials and metadevices opened technologically important capabilities ranging from subwavelength focusing to unique abilities for controlling electromagnetic waves, by engineering subwavelength structured materials. Research on metamaterials emerged as a new area of physics and engineering, and it is now attracting rapidly growing interest worldwide. Metamaterials not only offer novel possibilities for practical applications and devices but also display unexplored and intriguing properties that challenge fundamental physical concepts. The main hindrance to the use of metamaterials in real-life applications is their absorption of electromagnetic waves and narrow frequency band of operation. The creation of nonlinear, tunable and active metamaterials will solve these problems and will lead to applications.

In particular, nonlinear phenomena are essential for almost all the areas of modern physics, ranging from quantum optics to electronic engineering, and they address a span of questions from fundamental theoretical research to practical engineering applications. Electronics utilizes the nonlinear effects offered by semiconductors through numerous devices. In optics, where nonlinearity originates from the weakly nonlinear atomic response, the key concerns were always related to the relatively high power required to observe useful effects; while electronics, capable of handling strongly nonlinear responses, is limited in speed.

Not surprisingly, the study of nonlinear effects attracted significant attention within the metamaterials research, which has flourished over the past decade. Metamaterials are artificial structures where specific engineered elements play the role of atoms on a macroscopic scale. By offering tremendous opportunities in designing and combining material properties, often reaching phenomena not available in nature, metamaterials are particularly suited to the introduction of nonlinearity. The advantages of the metamaterial paradigm will ensure a remarkable impact on the whole field of nonlinear optics: providing novel solutions to classical problems, on the one hand, and offering new phenomena and applications, on the other.

The aim of this book is to present theoretical, numerical, and experimental expertise in the physics of advanced tunable, nonlinear and active metamaterials and metadevices in different frequency ranges, including microwaves, terahertz and optics, and thereby to unite the fundamental concepts of these different growing fields. More specifically, the book addresses the major methods for creating metamaterials and enabling their tunability, and it presents the latest results on nonlinear, tunable and active metamaterials which are expected to create the background for future optical metadevices with useful applications such as efficient frequency converters, power limiters and parametric amplifiers. In particular, the authors discuss approaches to dynamically manipulate electromagnetic metamaterials in all frequency ranges.

The authors of the chapters are leading experts in the field of metamaterials, they advance the fundamental physics of structured materials and facilitate key experimental observations of many effects predicted theoretically.

The book is aimed at an audience already familiar with the basics of electromagnetic wave propagation. Especially, we address young, advanced scientists as well as scientists in research groups with experimental as well as theoretical expertise. It will offer insights into the basic principles of metamaterial design, homogenization procedures, wave propagation, nonlinear phenomena as well as computational aspects and—most importantly—work out the common ground of these apparently different physical situations where the apparatus is to be applied.

In particular, the chapters collected in this book discuss the fundamental properties and demonstrate control of nonlinear waves and localized excitations, including nonlinear effects in left-handed transmission lines, magnetoelastic interactions, superconducting quantum metamaterials, tunable liquid-crystal-based structures and the possibility of novel nonlinear effects in metamaterial structures that exhibit an optically induced nonlinear magnetic response. Special attention is

paid to the interplay between nonlinear and linear modes, which result in a number of interesting resonant scattering and trapping effects, and active control of the metamaterial parameters. We are confident that the joint gathering of independent contributions of experimentalists and theorists from each sub-field will boost the implementation of ideas and experimental techniques in all fields of research.

A book like this that compiles contributions of different authors is as good as the authors' contributions. Therefore, we thank all authors for their excellent articles as well as their support to the editorial process.

Canberra, Sydney

Ilya V. Shadrivov
Mikhail Lapine
Yuri S. Kivshar

Contents

Contributors

Allan D. Boardman Joule Physics Laboratory, Materials and Physics Research Centre, University of Salford, Greater Manchester, UK

Alexander N. Cartwright University at Buffalo, The State University of New York, Buffalo, NY, USA

Steven A. Cummer Department of Electrical and Computer Engineering, Duke University, Durham, NC, USA

Robert Czaplicki Department of Physics, Tampere University of Technology, Tampere, Finland

Domenico de Ceglia Charles M. Bowden Research Laboratory, National Research Council—AMRDEC, Redstone Arsenal, AL, USA

Timmy Floume Department of Electrical and Electronic Engineering, Imperial College London, London, UK

Ildar R. Gabitov University of Arizona, Tucson, AZ, USA; L.D. Landau Institute for Theoretical Physics, Russian Academy of Sciences, Moscow, Russian Federation

Maxim V. Gorkunov A.V. Shubnikov Institute of Crystallography, Russian Academy of Sciences, Moscow, Russia

Ortwin Hess The Blackett Laboratory, Department of Physics, South Kensington Campus, Imperial College London, London, UK

Hannu Husu Department of Physics, Tampere University of Technology, Tampere, Finland; Centre for Metrology and Accreditation (MIKES), Espoo, Finland

Martti Kauranen Department of Physics, Tampere University of Technology, Tampere, Finland

Neil J. King Joule Physics Laboratory, Materials and Physics Research Centre, University of Salford, Greater Manchester, UK

Yuri S. Kivshar Nonlinear Physics Centre, Research School of Physics and Engineering, Australian National University, Canberra, ACT, Australia

Thomas Koschny Ames Laboratory—U.S. DOE, Iowa State University, Ames, IA, USA; Department of Physics and Astronomy, Iowa State University, Ames, IA, USA

Alexander B. Kozyrev Department of Electrical and Computer Engineering, University of Wisconsin-Madison, Madison, WI, USA

Markku Kuittinen Institute of Photonics, University of Eastern Finland, Joensuu, Finland

Mikhail Lapine School of Physics, CUDOS, The University of Sydney, Sydney, NSW, Australia

Stéphane Larouche Center for Metamaterials and Integrated Plasmonics, Duke University, Durham, NC, USA

Janne Laukkanen Institute of Photonics, University of Eastern Finland, Joensuu, Finland

Nikos Lazarides Department of Physics, Crete Center for Quantum Complexity and Nanotechnology, University of Crete, Heraklion, Greece; Institute of Electronic Structure and Laser, Foundation for Research and Technology-Hellas, Heraklion, Greece

Natalia M. Litchinitser University at Buffalo, The State University of New York, Buffalo, NY, USA

Mingkai Liu Nonlinear Physics Centre, Research School of Physics and Engineering, Australian National University, Canberra, ACT, Australia

Andrei I. Maimistov National Nuclear Research University Moscow Engineering Physics Institute, Moscow, Russian Federation; Moscow Institute for Physics and Technology, Dolgoprudny, Moscow, Russian Federation

Andrey E. Miroshnichenko Nonlinear Physics Centre, Research School of Physics and Engineering, Australian National University, Canberra, ACT, Australia

Rhiannon C. Mitchell-Thomas School of Electronic Engineering and Computer Science, Queen Mary University of London, London, UK

Alexander K. Popov University of Wisconsin-Stevens Point, Stevens Point, WI, USA; Birck Nanotechnology Center, Purdue University, West Lafayette, IN, USA

David A. Powell Nonlinear Physics Centre, Research School of Physics and Engineering, Australian National University, Canberra, ACT, Australia

Yuri G. Rapoport Faculty of Physics, Taras Shevchenko National University, Kiev, Ukraine

Vito Roppo Laboratoire de Photonique et de Nanostructures, CNRS, Route de Nozay, Marcoussis, France

Alec Rose Center for Metamaterials and Integrated Plasmonics, Duke University, Durham, NC, USA

Michael Scalora Charles M. Bowden Research Laboratory, AMRDEC, US Army RDECOM, Redstone Arsenal, AL, USA

Mikhail I. Shalaev University at Buffalo, The State University of New York, Buffalo, NY, USA

David R. Smith Center for Metamaterials and Integrated Plasmonics, Duke University, Durham, NC, USA

Laszlo Solymar Department of Electrical and Electronic Engineering, Imperial College London, London, UK

Costas M. Soukoulis Ames Laboratory—U.S. DOE, Iowa State University, Ames, IA, USA; Department of Physics and Astronomy, Iowa State University, Ames, IA, USA

Richard R.A. Syms Department of Electrical and Electronic Engineering, Imperial College London, London, UK

Philippe Tassin Department of Applied Physics, Chalmers University, Göteborg, Sweden

Kosmas L. Tsakmakidis The Blackett Laboratory, Department of Physics, South Kensington Campus, Imperial College London, London, UK

George P. Tsironis Department of Physics, Crete Center for Quantum Complexity and Nanotechnology, University of Crete, Heraklion, Greece; Institute of Electronic Structure and Laser, Foundation for Research and Technology-Hellas, Heraklion, Greece; Department of Physics, School of Science and Technology, Nazarbayev University, Astana, Kazakhstan

Daniel W. van der Weide Department of Electrical and Computer Engineering, University of Wisconsin-Madison, Madison, WI, USA

Maria Antonietta Vincenti Charles M. Bowden Research Laboratory, National Research Council—AMRDEC, Redstone Arsenal, AL, USA

Xi Wang University at Buffalo, The State University of New York, Buffalo, NY, USA

Ian R. Young Department of Electrical and Electronic Engineering, Imperial College London, London, UK

Alexandre M. Zagoskin Loughborough University, Loughborough, UK

Jinwei Zeng University at Buffalo, The State University of New York, Buffalo, NY, USA

Chapter 1
A Constitutive Description of Nonlinear Metamaterials Through Electric, Magnetic, and Magnetoelectric Nonlinearities

Stéphane Larouche, Alec Rose and David R. Smith

Abstract Nonlinear metamaterials provide a host of interesting phenomena which, like for their linear counterpart, can be described using homogenized, effective properties. Following the convention used in nonlinear optics, the response of nonlinear metamaterials can be expressed as a power series of the incident fields. However, contrarily to most materials used in nonlinear optics that only possess an electric nonlinear response, nonlinear metamaterials often show electric, magnetic, and magnetoelectric nonlinear responses within a single unit cell. In this chapter, we present two complementary approaches to determine all the effective nonlinear susceptibilities of nonlinear metamaterials. First we present a coupled-mode theory that provides insight into the origin of the various nonlinear susceptibilities that arise in nonlinear metamaterials according to the symmetry of the unit cell. This approach also leads to a description of the effect of the finite size of the unit cells, often called spatial dispersion. Second, we present a retrieval approach based on transfer matrices that can be used to determine the effective nonlinear susceptibilities from either simulated or experimental results. We finally demonstrate how to use this approach by applying it to the case of dual-gap varactor-loaded split ring resonators.

1.1 Introduction

Nonlinear metamaterials offer promising opportunities for enhancing and controlling nonlinear response. As discussed in the other chapters of this book, many interesting and unique nonlinear phenomena have been demonstrated using metamaterials, illustrating the potential for structured metamaterials to support novel

S. Larouche (✉) · A. Rose · D.R. Smith
Center for Metamaterials and Integrated Plasmonics, Duke University,
Durham, NC 27708, USA
e-mail: stephane.larouche@duke.edu

A. Rose
e-mail: arose@evolvtechnology.com

D.R. Smith
e-mail: drsmith@ee.duke.edu

I.V. Shadrivov et al. (eds.), *Nonlinear, Tunable and Active Metamaterials*,
Springer Series in Materials Science 200, DOI 10.1007/978-3-319-08386-5_1

nonlinear response not easily realizable in conventional materials. The design of nonlinear metamaterials, as has been the case for their linear counterparts, is greatly facilitated by the introduction of a homogenization scheme, wherein effective nonlinear susceptibilities for a composite are determined, in addition to the linear permittivity and permeability. The homogenization approach allows the anticipated properties of the nonlinear metamaterial to be determined efficiently from simulations of the repeated metamaterial element.

One of the advantages that has propelled the field of linear metamaterials is the expanded palette of available material response, including the capability of implementing electric, magnetic and magnetoelectric properties, even in the absence of inherently magnetic materials. The addition of magnetic response in metamaterials leads to a considerably rich and complex collection of phenomena, especially when magnetic nonlinearity is included. The issue of magnetoelectric coupling, in fact, arises naturally for nonlinear metamaterials, and thus nonlinear homogenization schemes must include and quantify a significantly larger set of nonlinear susceptibilities, the majority of which are negligible for conventional materials.

In this chapter, we present two complementary approaches to determine the homogenized, effective nonlinear susceptibilities of nonlinear metamaterials. First, we present a coupled mode theory that can be used to determine the effective nonlinear susceptibilities of simulated, lossless metamaterials. This method is particularly useful in deriving analytical formulas that provide insight into the origins of the various nonlinear susceptibilities that arise from the metamaterial elements and leads quite naturally to several important symmetry considerations. Second, we present a retrieval approach based on transfer matrices that can be applied to either simulation or experimental results, and is relevant for all scenarios that satisfy the non-depleted pump approximation. The insight provided by the coupled mode theory approach provides a basis for understanding the role that the symmetry of a metamaterial unit cell plays in determining which effective nonlinear susceptibilities can be supported by the homogenized metamaterial. This analysis also incorporates the effects of spatial dispersion due to the finite metamaterial element on the retrieved nonlinear susceptibilities. We illustrate the retrieval approaches using simulations on symmetric and antisymmetric dual-gap varactor-loaded split ring resonators, which have been used over the past several years to form analog nonlinear metamaterials at microwave frequencies.

Following the convention used in nonlinear optics, the nonlinear response of metamaterials can be expressed as a power series in the incident fields. To keep the number of terms tractable, we consider here only second order processes: 3-wave mixing where a field at ω_3 is generated by applying two fields at ω_1 and ω_2. The methods presented here can trivially be expanded to include higher order processes. For the case of 3-wave mixing, the nonlinear polarization and magnetization at ω_3 can depend on either the electric or the magnetic field at ω_1 and ω_2, which we indicate by dividing the nonlinear response in a series of nonlinear susceptibilities $\chi^{(2)}_{ijk}$ where i, j, and k can be either e or m. The first subscript indicates if the nonlinear susceptibility generates a nonlinear polarization or magnetization at ω_3, while the

two other subscripts indicate whether this nonlinear polarization or magnetization is created by the electric or the magnetic field at ω_1 and ω_2. Various nonlinearities generally coexist in a single metamaterial unit cell and it is necessary to devise a method to separate their effects.

It will be seen that for 3-wave mixing there are eight different nonlinear susceptibilities. In general, for an nth order process there are $(n+1)^2$ nonlinearities present. Furthermore, each of these nonlinearities is a rank-3 tensor. By carefully applying the fields at ω_1 and ω_2 in various axes and polarizations, and determining the fields generated at ω_3, it is possible to separately determine each element of these tensors, providing a full description of the nonlinear properties of the metamaterial.

1.2 Effective Nonlinear Susceptibilities: Coupled Mode Theory

In the most general case, the nonlinear properties of a material must take into account not only electric-dipole contributions, but also magnetic-dipole, quadrupole, and so-on. If we assume only dipolar contributions, we can write the second-order polarization through a series of nonlinear susceptibilities,

$$\begin{aligned}\mathbf{P}^{(2)}(\omega_3) = {} & \bar{\bar{\chi}}^{(2)}_{eee}(\omega_3;\omega_1,\omega_2) : \mathbf{E}(\omega_1)\mathbf{E}(\omega_2) + \bar{\bar{\chi}}^{(2)}_{emm}(\omega_3;\omega_1,\omega_2) : \mathbf{H}(\omega_1)\mathbf{H}(\omega_2) \\ & + \bar{\bar{\chi}}^{(2)}_{eem}(\omega_3;\omega_1,\omega_2) : \mathbf{E}(\omega_1)\mathbf{H}(\omega_2) \\ & + \bar{\bar{\chi}}^{(2)}_{eme}(\omega_3;\omega_1,\omega_2) : \mathbf{H}(\omega_1)\mathbf{E}(\omega_2), \end{aligned} \tag{1.1}$$

and the second-order magnetization,

$$\begin{aligned}\mu_0\mathbf{M}^{(2)}(\omega_3) = {} & \bar{\bar{\chi}}^{(2)}_{mmm}(\omega_3;\omega_1,\omega_2) : \mathbf{H}(\omega_1)\mathbf{H}(\omega_2) + \bar{\bar{\chi}}^{(2)}_{mee}(\omega_3;\omega_1,\omega_2) : \mathbf{E}(\omega_1)\mathbf{E}(\omega_2) \\ & + \bar{\bar{\chi}}^{(2)}_{mme}(\omega_3;\omega_1,\omega_2) : \mathbf{H}(\omega_1)\mathbf{E}(\omega_2) \\ & + \bar{\bar{\chi}}^{(2)}_{mem}(\omega_3;\omega_1,\omega_2) : \mathbf{E}(\omega_1)\mathbf{H}(\omega_2), \end{aligned} \tag{1.2}$$

where ':' implies a tensor inner product between the rank-3 second-order susceptibility tensors and the field vectors, and $\omega_3 = \omega_1 + \omega_2$. While the nature of optical magnetism in natural materials usually suppresses all terms except $\chi^{(2)}_{eee}$, this is not the case in metamaterials, whose structurally-induced magnetic moments can be equal in strength, or even stronger, than their electric counterparts. However, relating such a complex series of effective second-order susceptibilities to the microscopic metamaterial structure is not a trivial exercise. Thus, the goal of this section is to find a set of intuitive and general expressions to give insight into this relationship.

Let us consider a typical metamaterial, composed of dielectric and metallic inclusions arranged periodically on a cubic lattice, as conceptually illustrated in Fig. 1.1. The metamaterial itself is thus completely described by a dielectric function $\varepsilon(\mathbf{r})$, periodic along all three cartesian axes with lattice constant a. For the following analysis, it is instructive to take $\varepsilon(\mathbf{r})$ to be purely real, i.e. lossless. While this is

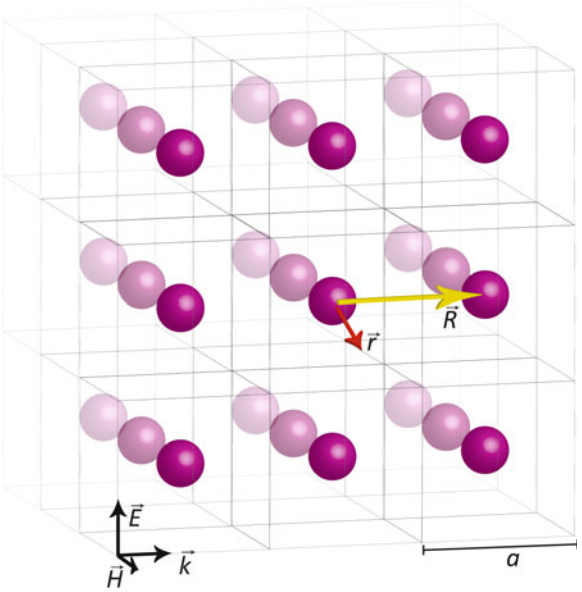

Fig. 1.1 Schematic of a cubic metamaterial lattice, indicating the microscopic position vector **r** and macroscopic lattice vector **R**. By equating coupled mode expressions on the discrete metamaterial lattice to that in a continuous, homogenized medium, we can arrive at a set of eight expressions for the eight effective second-order susceptibilities

clearly a poor approximation for most metamaterials of interest, the expressions that follow are still highly useful for yielding an intuitive understanding of the effective metamaterial properties, as well as probing some typical symmetries. In this limit we are free to decompose the total fields inside the metamaterial into a summation of Bloch modes, such that

$$\mathbf{E} = \sum_{\mu} A_{\mu}\mathbf{e}_{\mu}(\mathbf{r})\mathrm{e}^{\mathrm{i}\mathbf{k}_{\mu}\cdot\mathbf{r}-\mathrm{i}\omega_{\mu}t} \text{ and } \mathbf{H} = \sum_{\mu} A_{\mu}\mathbf{h}_{\mu}(\mathbf{r})\mathrm{e}^{\mathrm{i}\mathbf{k}_{\mu}\cdot\mathbf{r}-\mathrm{i}\omega_{\mu}t}, \tag{1.3}$$

where the μ label includes mode number, frequency, direction, and polarization. Since the repeat distance for elements forming a metamaterial is generally assumed to be much smaller than the wavelengths of interest, propagation is usually dominated by the Bloch mode with the smallest wavevector, often called the fundamental Bloch mode. This situation can be understood conceptually by imagining transmission and reflection from a single plane of the metamaterial, for which all higher order modes beyond the fundamental cannot propagate in free-space; that is, all of the diffractive beams are evanescent. So long as the coupling between adjacent metamaterial elements is relatively weak and is mostly dipolar, only the forward and backward propagating fundamental Bloch modes along a particular axis will contribute significantly to our analysis.

By describing our metamaterial in terms of these fundamental Bloch modes, we can quite naturally describe the perturbative effect of a nonlinear polarization via coupled mode theory, in perfect analogy to nonlinear waveguides [17]. For example, we can describe three waves with frequencies ω_1, ω_2, and $\omega_3 = \omega_1 + \omega_2$ propagating along the z-axis in the unperturbed case according to

$$\mathbf{E}(\omega_n) = A_n \mathbf{e}_n(\mathbf{r}) \mathrm{e}^{\mathrm{i}k_n z} + A_{-n} \mathbf{e}_n^*(\mathbf{r}) \mathrm{e}^{-\mathrm{i}k_n z}, \tag{1.4}$$

$$\mathbf{H}(\omega_n) = A_n \mathbf{h}_n(\mathbf{r}) \mathrm{e}^{\mathrm{i}k_n z} - A_{-n} \mathbf{h}_n^*(\mathbf{r}) \mathrm{e}^{-\mathrm{i}k_n z}, \tag{1.5}$$

for $n = 1, 2, 3$, where we have used Bloch mode symmetries and our freedom in selecting the relative phase of the Bloch functions to impose $\mathbf{e}_n(\mathbf{r}) = \mathbf{e}_{-n}(\mathbf{r})^*$ and $\mathbf{h}_n(\mathbf{r}) = -\mathbf{h}_{-n}(\mathbf{r})^*$. Now, assume that the metamaterial possesses a local second-order electric nonlinearity described by $\bar{\bar{\chi}}^{(2)}_{\mathrm{loc}}(\mathbf{r})$ with the same cubic periodicity. As a first step, consider the nonlinear polarization arising from the product of the *forward* propagating fields at ω_1 and ω_2 and allow the mode amplitude A_3 to vary in space. We can treat the nonlinearity as a perturbation to the fundamental Bloch modes. In the formalism of coupled mode theory, we can expect to find expressions relating the spatial rate of change of one amplitude over one lattice vector $\mathbf{R}$ to the set of driving amplitudes, as in

$$\frac{\partial A_3}{\partial z}(\mathbf{R}) = \mathrm{i}\Gamma A_1(\mathbf{R}) A_2(\mathbf{R}) \mathrm{e}^{\mathrm{i}(k_1 + k_2 - k_3)\hat{z} \cdot \mathbf{R}}, \tag{1.6}$$

through a proportionality constant Γ, called the coupling coefficient. While the formal derivation of this coupling coefficient, given by

$$\Gamma = \frac{\omega_3}{a^3} \iiint_{V_0} \left(\bar{\bar{\chi}}^{(2)}_{\mathrm{loc}}(\mathbf{r}) : \mathbf{e}_1(\mathbf{r}) \mathbf{e}_2(\mathbf{r}) \cdot \mathbf{e}_3^*(\mathbf{r}) \mathrm{e}^{\mathrm{i}(k_1 + k_2 - k_3)z} \right) \mathrm{d}V, \tag{1.7}$$

can be found in [8], it can be simply understood as a volume average over the interacting fields within the nonlinear medium, and is very reminiscent of the coupling coefficients derived for standard nonlinear waveguides. Clearly, for a complete description, we must consider all possible products of forward and backward fields, generating in turn both forward and backward waves at ω_3. However, each contribution will share a similar form to (1.6), and so they are suppressed for brevity.

Analogous expressions can be derived for a homogeneous medium, as a continuous function of position vector $\mathbf{r}$. However, for the sake of generality, the homogeneous medium must take into account all eight nonlinear susceptibilities in (1.1) and (1.2). By equating the discrete and continuous descriptions, three-wave mixing in a metamaterial can be homogenized, yielding expressions for the eight effective nonlinear susceptibility tensors. If we neglect spatial dispersion, i.e. $|k_n a| \ll 1$, then these expressions can be written in closed form, [8]

$$\chi^{(2)}_{eee}(\omega_3;\omega_1,\omega_2) = \frac{1}{a^3}\iiint \mathrm{d}V\left[\bar{\bar{\chi}}^{(2)}_{\mathrm{loc}}(\mathbf{r}) : \theta_1(\mathbf{r})\theta_2(\mathbf{r})\cdot\theta_3(\mathbf{r})\right], \tag{1.8}$$

$$\chi^{(2)}_{emm}(\omega_3;\omega_1,\omega_2) = \frac{-1}{a^3}\iiint \mathrm{d}V\left[\bar{\bar{\chi}}^{(2)}_{\mathrm{loc}}(\mathbf{r}) : \phi_1(\mathbf{r})\phi_2(\mathbf{r})\cdot\theta_3(\mathbf{r})\right], \tag{1.9}$$

$$\chi^{(2)}_{eem}(\omega_3;\omega_1,\omega_2) = \frac{\mathrm{i}}{a^3}\iiint \mathrm{d}V\left[\bar{\bar{\chi}}^{(2)}_{\mathrm{loc}}(\mathbf{r}) : \theta_1(\mathbf{r})\phi_2(\mathbf{r})\cdot\theta_3(\mathbf{r})\right], \tag{1.10}$$

$$\chi^{(2)}_{eme}(\omega_3;\omega_1,\omega_2) = \frac{\mathrm{i}}{a^3}\iiint \mathrm{d}V\left[\bar{\bar{\chi}}^{(2)}_{\mathrm{loc}}(\mathbf{r}) : \phi_1(\mathbf{r})\theta_2(\mathbf{r})\cdot\theta_3(\mathbf{r})\right], \tag{1.11}$$

$$\chi^{(2)}_{mmm}(\omega_3;\omega_1,\omega_2) = \frac{\mathrm{i}}{a^3}\iiint \mathrm{d}V\left[\bar{\bar{\chi}}^{(2)}_{\mathrm{loc}}(\mathbf{r}) : \phi_1(\mathbf{r})\phi_2(\mathbf{r})\cdot\phi_3(\mathbf{r})\right], \tag{1.12}$$

$$\chi^{(2)}_{mee}(\omega_3;\omega_1,\omega_2) = \frac{-\mathrm{i}}{a^3}\iiint \mathrm{d}V\left[\bar{\bar{\chi}}^{(2)}_{\mathrm{loc}}(\mathbf{r}) : \theta_1(\mathbf{r})\theta_2(\mathbf{r})\cdot\phi_3(\mathbf{r})\right], \tag{1.13}$$

$$\chi^{(2)}_{mme}(\omega_3;\omega_1,\omega_2) = \frac{1}{a^3}\iiint \mathrm{d}V\left[\bar{\bar{\chi}}^{(2)}_{\mathrm{loc}}(\mathbf{r}) : \phi_1(\mathbf{r})\theta_2(\mathbf{r})\cdot\phi_3(\mathbf{r})\right], \tag{1.14}$$

$$\chi^{(2)}_{mem}(\omega_3;\omega_1,\omega_2) = \frac{1}{a^3}\iiint \mathrm{d}V\left[\bar{\bar{\chi}}^{(2)}_{\mathrm{loc}}(\mathbf{r}) : \theta_1(\mathbf{r})\phi_2(\mathbf{r})\cdot\phi_3(\mathbf{r})\right], \tag{1.15}$$

where the volume integrals are taken over a single unit-cell. The quantities

$$\theta_n(\mathbf{r}) = \mathrm{Re}\left[\frac{\mathbf{e}_n(\mathbf{r})}{\tilde{e}_n}\mathrm{e}^{\mathrm{i}k_n z}\right] \quad \text{and} \quad \phi_n(\mathbf{r}) = \mathrm{Im}\left[\frac{\mathbf{e}_n(\mathbf{r})}{\tilde{h}_n}\mathrm{e}^{\mathrm{i}k_n z}\right]$$

represent the inhomogeneous local electric fields induced in response to macroscopic, or 'homogeneous', electric fields $\tilde{e}_n$ and magnetic fields $\tilde{h}_n$, respectively. Qualitatively, these expressions imply that any of the eight fundamentally distinct nonlinear tensors, and any of the tensors' individual elements, can be supported in metamaterial composites with no intrinsic magnetic properties, provided that the metamaterial supports sufficient overlap of the induced fields in the nonlinear element. An analogous set of expressions can be derived for the different tensor elements, or for the third-order susceptibilities [8].

1.3 Effective Nonlinear Susceptibilities: Transfer Matrix Method

The previous section presents a method to determine the effective nonlinear susceptibilities of lossless metamaterials by averaging the fields over a simulated unit cell, arriving at closed form solutions that can provide insight for nonlinear metamaterial design. The field averaging approach, however, requires knowledge of the fundamental and harmonic fields at all points throughout the volume of a unit cell of an infinitely periodic medium. An alternative approach uses the waves scattered from a sample of finite thickness to infer the effective linear and nonlinear susceptibilities. The advantage of this scattering (or S-) parameter retrieval is that the wave reflected and transmitted from a finite-thickness sample can be measured

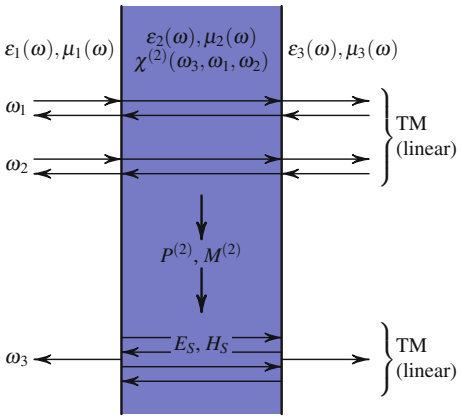

Fig. 1.2 Schematic representation of the calculation of 3 wave mixing in a slab of homogeneous nonlinear material between two semi-infinite linear media: (1) the distribution of waves at ω_1 and ω_2 is calculated using a linear transfer matrix approach; (2) the nonlinear polarization is calculated; and (3) the wave generated at ω_3 is calculated using a linear transfer matrix approach

experimentally, rendering S-parameters retrieval applicable to simulation and experiment alike. Moreover, no restrictions on the geometry or composition of the metamaterial elements are required in the S-parameters method, allowing lossy samples to be investigated.

For linear retrievals, only two complex parameters—the effective permittivity and permeability—need be determined. They can be determined using two independent simulation or experimental complex results, usually the reflection and the transmission of the metamaterial. In the nonlinear case, a larger number of effective parameters must be determined and, therefore, a larger number of independent simulations or experiments must be performed. However, as we will see, the nonlinear retrieval is simpler in some aspects, ultimately involving the solution of a linear system of equations. In this section, we will first summarize how to calculate the nonlinear wave generated by the mixing of two or more waves in a homogeneous nonlinear slab and then we will show how to solve the inverse problem.

We first consider the case of waves normally incident on a slab of homogeneous material with known linear and nonlinear properties, situated between two semi-infinite linear media, as illustrated in Fig. 1.2. In the non-depleted pump approximation, the nonlinear process is sufficiently weak that the generated fields do not significantly impact the incident waves. Therefore, we can first calculate the field distribution of the incident waves by solving the wave equation assuming only the linear properties of the slab. We then calculate the nonlinear polarization, and finally calculate the generated waves [1].

For the transfer matrix formalism, it is useful to form two-element vectors from the complex coefficients of the forward and backward plane waves, which in region i are $E_i^{\pm}(\omega_n, z) = E_i^{\pm}(\omega_n) \exp -\mathrm{i}(\omega_n t \mp kz)$, where the positive and negative superscripts indicate waves propagating in the forward and backward directions, respectively. In region i, the electric and magnetic fields at frequency ω_n can thus be decomposed into the vectors

$$\mathbf{E}_i(\omega_n) = \begin{bmatrix} E_i^+(\omega_n) \\ E_i^-(\omega_n) \end{bmatrix}, \quad \text{or} \quad \mathbf{H}_i(\omega_n) = \begin{bmatrix} H_i^+(\omega_n) \\ H_i^-(\omega_n) \end{bmatrix}. \tag{1.16}$$

In the linear case, the plane wave coefficients for any of the dependent waves can be calculated from the incident waves ($E_1^+(\omega_n)$ and $E_3^-(\omega_n)$, or $H_1^+(\omega_n)$ and $H_3^-(\omega_n)$) by applying the well-established transfer matrix formalism [5]. With all coefficients known, the fields can then be calculated at any position in the system. In particular, we can calculate $\mathbf{E}_2(\omega_{1,2})$ and $\mathbf{H}_2(\omega_{1,2})$, the fields inside the slab, necessary to compute wave-mixing processes.

To keep the number of terms tractable, we will consider the case of a second order nonlinearity, but the approach presented here can easily be extended to arbitrary order nonlinearities. In the present case, the nonlinear polarization and magnetization are representable as a sum of contributions from eight different terms associated with eight nonlinear susceptibilities. Since the fields are decomposed into forward and backward propagating waves, we can seperate the nonlinear polarization and magnetization into two different sums corresponding to the product of waves propagating in the same or in opposite directions and associated with wavevectors $k_{\text{sum}} = k_1 + k_2$ and $k_{\text{diff}} = k_1 - k_2$, respectively. Thus, in the vector notation of (1.16), the nonlinear polarization is the sum of

$$\begin{aligned} \mathbf{P}_{\text{sum}} = {} & \frac{1}{2}\chi^{(2)}_{eee}\mathbf{E}_2(\omega_1)\mathbf{E}_2^{\text{T}}(\omega_2) + \frac{1}{2}\chi^{(2)}_{eem}\mathbf{E}_2(\omega_1)\mathbf{H}_2^{\text{T}}(\omega_2) \\ & + \frac{1}{2}\chi^{(2)}_{eme}\mathbf{H}_2(\omega_1)\mathbf{E}_2^{\text{T}}(\omega_2) + \frac{1}{2}\chi^{(2)}_{emm}\mathbf{H}_2(\omega_1)\mathbf{H}_2^{\text{T}}(\omega_2) \end{aligned} \tag{1.17}$$

and

$$\begin{aligned} \mathbf{P}_{\text{diff}} = {} & \frac{1}{2}\chi^{(2)}_{eee}\mathbf{E}_2(\omega_1)(F\mathbf{E}_2(\omega_2))^{\text{T}} + \frac{1}{2}\chi^{(2)}_{eem}\mathbf{E}_2(\omega_1)(F\mathbf{H}_2(\omega_2))^{\text{T}} \\ & + \frac{1}{2}\chi^{(2)}_{eme}\mathbf{H}_2(\omega_1)(F\mathbf{E}_2(\omega_2))^{\text{T}} + \frac{1}{2}\chi^{(2)}_{emm}\mathbf{H}_2(\omega_1)(F\mathbf{H}_2(\omega_2))^{\text{T}} \end{aligned} \tag{1.18}$$

while the nonlinear magnetization is the sum of

$$\begin{aligned} \mu_0\mathbf{M}_{\text{sum}} = {} & \frac{1}{2}\chi^{(2)}_{mee}\mathbf{E}_2(\omega_1)\mathbf{E}_2^{\text{T}}(\omega_2) + \frac{1}{2}\chi^{(2)}_{mem}\mathbf{E}_2(\omega_1)\mathbf{H}_2^{\text{T}}(\omega_2) \\ & + \frac{1}{2}\chi^{(2)}_{mme}\mathbf{H}_2(\omega_1)\mathbf{E}_2^{\text{T}}(\omega_2) + \frac{1}{2}\chi^{(2)}_{mmm}\mathbf{H}_2(\omega_1)\mathbf{H}_2^{\text{T}}(\omega_2) \end{aligned} \tag{1.19}$$

and

$$\begin{aligned} \mu_0\mathbf{M}_{\text{diff}} = {} & \frac{1}{2}\chi^{(2)}_{mee}\mathbf{E}_2(\omega_1)(F\mathbf{E}_2(\omega_2))^{\text{T}} + \frac{1}{2}\chi^{(2)}_{mem}\mathbf{E}_2(\omega_1)(F\mathbf{H}_2(\omega_2))^{\text{T}} \\ & + \frac{1}{2}\chi^{(2)}_{mme}\mathbf{H}_2(\omega_1)(F\mathbf{E}_2(\omega_2))^{\text{T}} + \frac{1}{2}\chi^{(2)}_{mmm}\mathbf{H}_2(\omega_1)(F\mathbf{H}_2(\omega_2))^{\text{T}}, \end{aligned} \tag{1.20}$$

where

$$F = \begin{bmatrix} 0 & 1 \\ 1 & 0 \end{bmatrix}, \tag{1.21}$$

effectively flipping the vector it multiplies upside down.

In the non depleted pump approximation, the nonlinear polarizations and magnetizations can be treated as source terms at $\omega_3 = \omega_1 + \omega_2$. These are associated with source electric and magnetic fields

$$\mathbf{E}_{s,\text{sum}} = \frac{\mathbf{P}_{\text{sum}}\mu_{r,2}(\omega_3)}{n_{s,\text{sum}}^2 - n_2^2(\omega_3)}, \quad \mathbf{E}_{s,\text{diff}} = \frac{\mathbf{P}_{\text{diff}}\mu_{r,2}(\omega_3)}{n_{s,\text{diff}}^2 - n_2^2(\omega_3)}, \tag{1.22}$$

$$\mathbf{H}_{s,\text{sum}} = \frac{\mathbf{M}_{\text{sum}}\varepsilon_{r,2}(\omega_3)}{n_{s,\text{sum}}^2 - n_2^2(\omega_3)}, \quad \text{and} \quad \mathbf{H}_{s,\text{diff}} = \frac{\mathbf{M}_{\text{diff}}\varepsilon_{r,2}(\omega_3)}{n_{s,\text{diff}}^2 - n_2^2(\omega_3)}. \tag{1.23}$$

Using the method developed by Bethune [1], a series of boundary conditions can be used to derive transfer matrices relating these source fields to the fields at ω_3 generated on both sides of the slab, $E_1^-(\omega_3)$ and $E_3^+(\omega_3)$, or $H_1^-(\omega_3)$ and $H_3^+(\omega_3)$.

At this point, it is important to note that the nonlinear polarizations—and therefore the waves generated at ω_3—depend nonlinearly on the applied fields, but linearly on the nonlinear susceptibilities. Using this to our advantage, we can build a linear system of equations to retrieve the effective nonlinear susceptibilities of a metamaterial. For example, if only one nonlinear susceptibility is present, one can determine it by calculating what would be any of $E_1^-(\omega_3)$, $E_3^+(\omega_3)$, $H_1^-(\omega_3)$, or $H_3^+(\omega_3)$ if the nonlinear susceptibility were unity, and comparing that result with the actual generation from simulation or experiment [4, 7]. When many nonlinear susceptibilities are present, the situation is just slightly more complex [9], leading to a system of linear equations.

To retrieve the effective nonlinear susceptibilities, one must:

1. Determine the effective linear properties of the matematerial at all frequencies involved using the standard retrieval approach.
2. Choose a series of independant simulation or experiment conditions giving as many results as there are effective nonlinear susceptibilities. For 3-wave mixing, if the waves generated in media 1 and 3 are both measured, 4 simulations or experiments are necessary for a total of 8 complex results—Table 1.1 shows two possible series of conditions.
3. Calculate the amplitude of the wave generated at ω_3 in media 1 and 3 using the predetermined linear effective properties and the transfer matrix approach for every susceptibility being separately unity and for all conditions.
4. Simulate or experimentally determine the amplitude of the nonlinearly generated wave in media 1 and 3 for the same series of conditions.
5. Solve the linear system of equations

Table 1.1 Two possible choices of 4 independant simulation or experiment conditions to determine all effective nonlinear susceptibilities for 3-wave mixing

Condition	Choice 1				Choice 2			
	$E_1^+(\omega_1)$ (V/m)	$E_3^-(\omega_1)$ (V/m)	$E_1^+(\omega_2)$ (V/m)	$E_3^-(\omega_2)$ (V/m)	$E_1^+(\omega_1)$ (V/m)	$E_3^-(\omega_1)$ (V/m)	$E_1^+(\omega_2)$ (V/m)	$E_3^-(\omega_2)$ (V/m)
A	1	0	1	0	+1	+1	+1	+1
B	1	0	0	1	+1	+1	+1	−1
C	0	1	1	0	+1	−1	+1	+1
D	0	1	0	1	+1	−1	+1	−1

The first choice might be easier to implement experimentally. The second choice has the advantage of creating standing waves with zeros or maxima in the electric and magnetic fields favoring selected nonlinearities. For experiments the amplitude of the fields should be scaled such that the nonlinear effect produces a good signal to noise ratio, without violating the non-depleted pump approximation

$$\begin{bmatrix} E^-_{1,A}\big|_{\chi^{(2)}_{eee}=1} & E^-_{1,A}\big|_{\chi^{(2)}_{eem}=1} & E^-_{1,A}\big|_{\chi^{(2)}_{eme}=1} & E^-_{1,A}\big|_{\chi^{(2)}_{emm}=1} & \cdots \\ E^+_{3,A}\big|_{\chi^{(2)}_{eee}=1} & E^+_{3,A}\big|_{\chi^{(2)}_{eem}=1} & E^+_{3,A}\big|_{\chi^{(2)}_{eme}=1} & E^+_{3,A}\big|_{\chi^{(2)}_{emm}=1} & \cdots \\ E^-_{1,B}\big|_{\chi^{(2)}_{eee}=1} & E^-_{1,B}\big|_{\chi^{(2)}_{eem}=1} & E^-_{1,B}\big|_{\chi^{(2)}_{eme}=1} & E^-_{1,B}\big|_{\chi^{(2)}_{emm}=1} & \cdots \\ E^+_{3,B}\big|_{\chi^{(2)}_{eee}=1} & E^+_{3,B}\big|_{\chi^{(2)}_{eem}=1} & E^+_{3,B}\big|_{\chi^{(2)}_{eme}=1} & E^+_{3,B}\big|_{\chi^{(2)}_{emm}=1} & \cdots \\ \vdots & \vdots & \vdots & \vdots & \ddots \end{bmatrix} \begin{bmatrix} \chi^{(2)}_{eee} \\ \chi^{(2)}_{eem} \\ \chi^{(2)}_{eme} \\ \chi^{(2)}_{emm} \\ \chi^{(2)}_{mee} \\ \chi^{(2)}_{mem} \\ \chi^{(2)}_{mme} \\ \chi^{(2)}_{mmm} \end{bmatrix} = \begin{bmatrix} E^-_{1,A} \\ E^+_{3,A} \\ E^-_{1,B} \\ E^+_{3,B} \\ E^-_{1,C} \\ E^+_{3,C} \\ E^-_{1,D} \\ E^+_{3,D} \end{bmatrix}, \tag{1.24}$$

where the frequency dependence has been omitted for brevity. The matrix contains the results of the transfer matrix calculations for homogeneous slabs with a single nonlinearity for all conditions, the vector on the right hand side contains the results of the simulations or experiments on the metamaterial in the same conditions, and the vector on the left hand side contains the effective susceptibilities to be determined.

1.4 Symmetries and Spatial Dispersion

At this point, it is useful to consider the effective nonlinear properties from a symmetry standpoint. First, simply by considering the polar and axial natures of the electric and magnetic field vectors, we see that the eight nonlinearities separate naturally into polar and axial tensors. Specifically, the tensors $\bar{\bar{\chi}}^{(2)}_{eee}$, $\bar{\bar{\chi}}^{(2)}_{mme}$, $\bar{\bar{\chi}}^{(2)}_{emm}$, and $\bar{\bar{\chi}}^{(2)}_{mem}$, involving an even number of magnetic fields, are polar, whereas the other four are axial. We would thus expect that certain internal symmetries of a given metamaterial, then, would favor one group of tensors over another.

For example, consider a metamaterial whose linear properties are centrosymmetric, that is, for some choice of origin $\varepsilon(\mathbf{r}) = \varepsilon(-\mathbf{r})$ for all $\mathbf{r}$ within the unit-cell. Such

symmetry is a good approximation for regular arrangements of symmetric nanoparticles and many circuit-based metamaterials like dual-split SRRs and ELCs. It is worth noting that we are not referring to the crystal symmetry of the local materials, at least some of which must be non-centrosymmetric to support a $\chi^{(2)}_{\text{loc}}$, but rather the structural symmetry of the metamaterial unit-cell, which depends on the relative arrangement of the constituent materials and inclusions. As such, even though the anisotropy of the nonlinear elements, as well as the presence of substrates will, strictly speaking, break the inversion symmetry, it is instructive to consider the structural symmetry of the inclusion as the dominant force influencing the effective properties. In any case, for a centrosymmetric unit-cell, we know from Bloch theory that a similar symmetry is enforced in the local fields, or $\mathbf{e}_n(\mathbf{r}) = \mathbf{e}_n(-\mathbf{r})^*$. From the definitions of θ and ϕ, we see that this in turn implies that $\theta(\mathbf{r})$ is an even function of $\mathbf{r}$, while $\phi(\mathbf{r})$ is odd. Clearly, these symmetry properties will have a strong impact on which of the effective nonlinearities are dominant. If the nonlinear properties are similarly centrosymmetric, i.e. $\chi^{(2)}_{\text{loc}}(\mathbf{r}) = \chi^{(2)}_{\text{loc}}(-\mathbf{r})$, then the integrands in the expressions for the axial nonlinear tensors are odd functions of $\mathbf{r}$ and therefore the axial nonlinear tensors vanish identically. If, on the other hand, the material is poled in such a way that the local nonlinear properties are anti-symmetric, $\chi^{(2)}_{\text{loc}}(\mathbf{r}) = -\chi^{(2)}_{\text{loc}}(-\mathbf{r})$, then the polar nonlinear tensors vanish. These cases are illustrated in Fig. 1.3a and b, respectively.

At microwave frequencies, where circuit elements such as varactor diodes are often used as the nonlinear inclusions, it is simple to create metamaterial structures possessing selected symmetries in the nonlinear properties, giving access to any of the eight nonlinear susceptibilities. At optical frequencies, however, local electric nonlinearities are often introduced by using a nonlinear crystal as a substrate

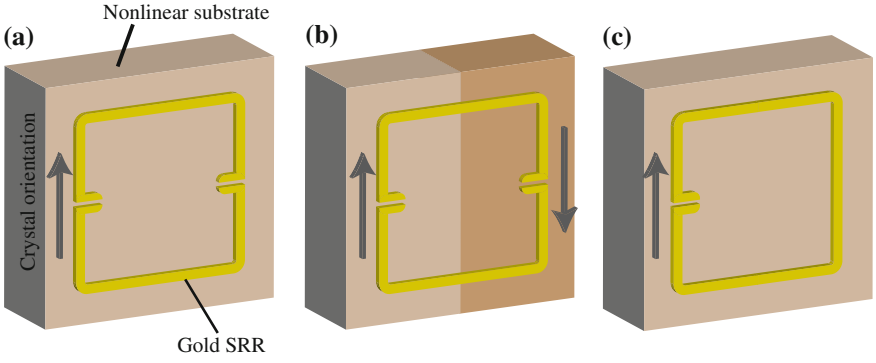

Fig. 1.3 Illustration of symmetries in nonlinear metamaterials. **a** A centrosymmetric inclusion, the double-gap SRR, placed over a uniform nonlinear substrate for maximizing the polar second-order susceptibility tensors. **b** A centrosymmetric inclusion placed over an anti-symmetric nonlinear substrate for maximizing the axial second-order susceptibility tensors. **c** A non-centrosymmetric inclusion placed over a uniform substrate excludes neither polar nor axial second-order susceptibility tensors

or embedding matrix. While a nonlinear crystal as a whole can be aligned along a particular axis, enforcing local directionality in a bulk medium or substrate can be very difficult, especially on the length scales that would be required in a metamaterial. This implies that, at optical frequencies, the class of nonlinear metamaterials composed of centrosymmetric inclusions will tend to support nonlinear processes through effectively polar nonlinear tensors. Accessing the axial tensors requires non-centrosymmetric inclusions, such as the single-gap SRR shown in Fig. 1.3c, which is known to support nonlinearites of the type $\chi^{(2)}_{mmm}$ [3].

Related to these symmetry considerations is the phenomena of spatial dispersion. In the linear properties of metamaterials, it is often the case that spatial dispersion, resulting from the non-negligible lattice dimensions, will lead to artifacts in the effective linear properties other than the principal resonance [13]. Similar effects show up in the nonlinear properties when the lattice constant-to-wavelength ratio is sufficiently large. As an example, let us consider the simple case of a thin slab of nonlinear material possessing only a $\chi^{(2)}_{eee}$ nonlinear susceptibility periodically embedded in dielectric, as in Fig. 1.4. In the long wavelength limit, all nonlinearities vanish with the exception of $\chi^{(2)}_{eee}(\omega_3;\omega_1,\omega_2) = \frac{d}{a}\chi^{(2)}_{\text{loc}}$, in agreement with previous studies of composite nonlinear media [12]. Since the linear and nonlinear properties possess inversion symmetry, the four axial nonlinear susceptibilities are identically zero for *all* wavelengths. This leaves us with a system of four equations and four unknown polar nonlinear susceptibilities. In the limit $d \ll a$, these expressions can be solved to leading order in $k_i a$,

$$\chi^{(2)}_{eee} = \left[1 - \frac{1}{8}a^2\left(k_1^2 + k_2^2 + k_3^2\right)\right]\frac{d}{a}\chi^{(2)}_{\text{loc}} \tag{1.25}$$

$$\chi^{(2)}_{emm} = +Z_1 Z_2\left(\frac{1}{12}a^2 k_1 k_2\right)\frac{d}{a}\chi^{(2)}_{\text{loc}} = +Z_0^2\left(\frac{\pi^2}{3}\frac{a^2}{\lambda_1\lambda_2}\right)\frac{d}{a}\chi^{(2)}_{\text{loc}} \tag{1.26}$$

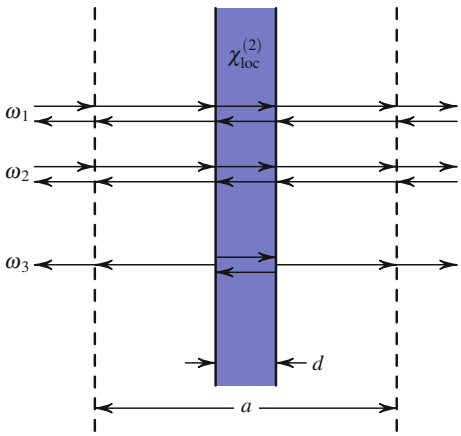

Fig. 1.4 A simple unit cell that can be used to demonstrate the effect of spatial dispersion on the effective nonlinear susceptibilities. This unit cell consists of a slab of thickness d containing an intrinsic nonlinearity centered inside the unit cell of thickness a. For simplicity, all linear properties are considered to be those of vacuum

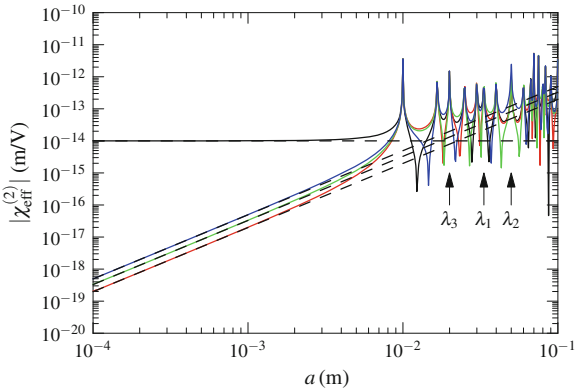

Fig. 1.5 The effective nonlinear susceptibilities, $\chi^{(2)}_{eee}$ (*black*), $\chi^{(2)}_{emm}/Z_0^2$ (*red*), $\chi^{(2)}_{mem}/Z_0^2$ (*green*), and $\chi^{(2)}_{mme}/Z_0^2$ (*blue*) for the unit cell presented in Fig. 1.4, $f_1 = 9\,\text{GHz}$, $f_2 = 6\,\text{GHz}$, and $f_3 = f_1 + f_2 = 15\,\text{GHz}$ determined using the transfer matrix approach. Arrows indicate the wavelengths $\lambda_n = c/f_n$ involved in 3-wave mixing. The *dashed lines* correspond to the prediction of approximate (1.25–1.28)

$$\chi^{(2)}_{mme} = -Z_1 Z_3 \left(\frac{1}{12} a^2 k_1 k_3\right) \frac{d}{a} \chi^{(2)}_{\text{loc}} = -Z_0^2 \left(\frac{\pi^2}{3} \frac{a^2}{\lambda_1 \lambda_3}\right) \frac{d}{a} \chi^{(2)}_{\text{loc}} \tag{1.27}$$

$$\chi^{(2)}_{mem} = -Z_2 Z_3 \left(\frac{1}{12} a^2 k_2 k_3\right) \frac{d}{a} \chi^{(2)}_{\text{loc}} = -Z_0^2 \left(\frac{\pi^2}{3} \frac{a^2}{\lambda_2 \lambda_3}\right) \frac{d}{a} \chi^{(2)}_{\text{loc}} \tag{1.28}$$

where $\lambda_n = 2\pi c/\omega_n$ is the wavelength in free-space, Z_n is the effective impedance of the metamaterial at wavelength λ_n, and Z_0 is the impedance of vacuum. Thus, spatial dispersion manifests itself in the nonlinear susceptibilities of the same polar/axial nature, proportional to the square of the lattice constant-to-wavelength ratio.

Figure 1.5 shows the effect of spatial dispersion on the retrieved parameters as calculated using the transfer matrix approach as well as using the approximate formula just derived. When the unit cell thickness is much smaller than all wavelengths involved, the intrinsic nonlinearity dominates. Nonlinearities of the same polar/axial nature are also present, but tend toward 0 when $a \to 0$ while nonlinearities of the other polar/axial nature are identically 0. Following the same rule of thumb used when determining the linear effective properties, the effect of spatial dispersion can be neglected when the unit cell size is smaller than approximately a tenth of all wavelengths involved.

The unit cell considered here is obviously much simpler than would be expected for any practical metamaterial, but cleanly illustrates the effects of symmetry and spatial dispersion, which will generally impact all nonlinear metamaterial constructs. Moreover, analogous selection rules can be derived for metamaterials belonging to a variety of symmetry classes; for example, the circular polarization selection rules for four-wave mixing in certain chiral metamaterials have been investigated both analytically and experimentally along similar lines of reasoning [10].

1.5 Application to Varactor-Loaded Split-Ring Resonators

The methods developed above can be applied in nonlinear metamaterial design. As an example, in this section we will apply them to varactor-loaded split-ring resonators (VLSRRs), which have been used as nonlinear metamaterials in the microwave range [11, 16]. They are obtained by adding a varactor diode, which has intrinsically large nonlinear response, inside the gap(s) of a SRR. Here, we will consider a SRR with two gaps, like that of Fig. 1.3, but instead of assuming the SRR is patterned on a nonlinear substrate, two varactors are used to introduce the desired nonlinearity. As shown in Fig. 1.6, the varactors can be inserted in the same direction (symmetric case), or in opposite directions (antisymmetric case), to favor different kinds of nonlinear susceptibilities.

Here, we consider the case of second harmonic generation. This is a particular case of 3-wave mixing where ω_1 and ω_2 are degenerate. Because of that, $\chi^{(2)}_{eem}$ and $\chi^{(2)}_{eme}$, as well as $\chi^{(2)}_{mem}$ and $\chi^{(2)}_{mme}$, are also degenerate. The VLSRR has been designed to have a resonance frequency of about 1 GHz. The pump wave is applied around the resonance frequency, while the harmonic is generated at twice that frequency. All simulations were performed using Comsol.

In the previous section, we gained some insight into determining which nonlinear susceptibilities should be favored in such a system using the coupled mode approach. However, for real materials with finite absorption, the assumptions of the coupled mode theory are violated and it cannot be used to provide quantitative evaluations. In this section, we therefore use the transfer matrix approach to obtain quantitative results and compare them to the predictions intuitively obtained from the coupled mode theory.

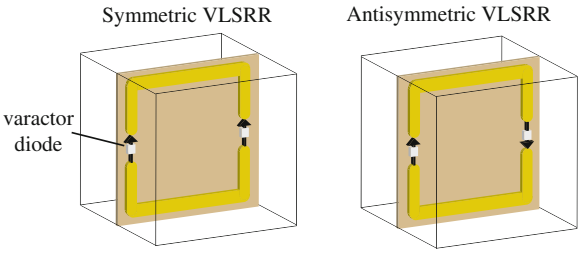

Fig. 1.6 Symmetric and antisymmetric VLSRRs

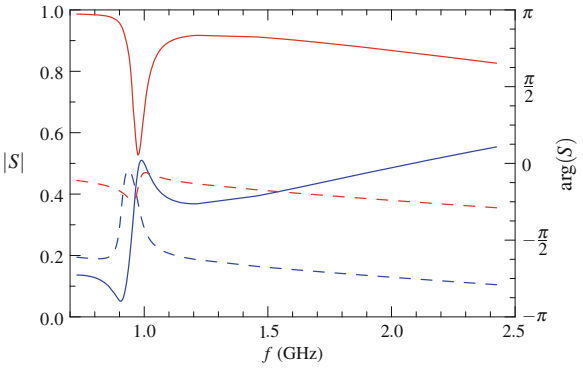

Fig. 1.7 S parameters of a dual gap VLSRR: amplitude (*continuous line*) and phase (*dashed line*) of S_{11} (*blue*) and S_{21} (*red*)

1.5.1 Linear Properties

The first step in the transfer matrix approach is to determine the effective linear properties of the metamaterial unit cell. The only difference between the symmetric and the antisymmetric unit cells is in the nonlinear response, and both therefore have the same linear properties. Figure 1.7 shows the amplitude and phase of the S parameters of the VLSRR determined over a range of frequencies covering both the pump and the harmonic frequencies.

Using the well-established retrieval method [2, 14, 15], the effective linear parameters of this structures were determined, and are shown in Fig. 1.8. It should be observed that this material shows a strong magnetic resonance while the electric response is essentially flat. The small *anti*-resonance in the permittivity is an artifact of spatial dispersion [13]. As shown in Fig. 1.9, it is also interesting to note that applied magnetic fields generate concentration of the electric field inside the gaps of the VLSRR and, therefore, important charges on the varactors. On the contrary, the coupling of the electric field mainly generates field concentration on the sides of the VLSRR, where no nonlinear material is present.

1.5.2 Nonlinear Properties

To determine the nonlinear properties of the VLSRR medium, a series of nonlinear simulations must be performed for various combinations of incident fields. For both the symmetric and antisymmetric VLSRR unit cells, the pump was applied either on the left (condition A), on the right (condition B), or on both sides (condition C) of the unit cell at once. Because of the degeneracy of some of the nonlinear susceptibilities, only three conditions are necessary to determine all six independant susceptibilities.

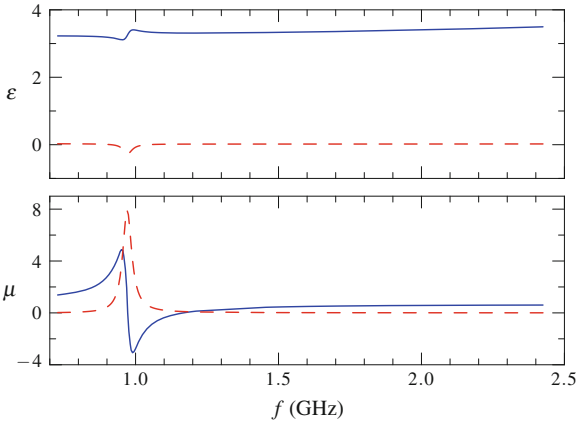

Fig. 1.8 Real (*continuous line*) and imaginary (*dashed line*) parts of the effective linear properties of a dual gap VLSRR

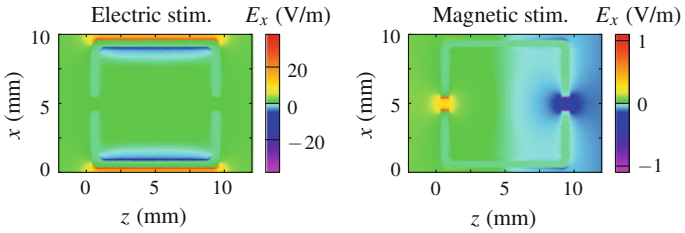

Fig. 1.9 Electric field pattern around the VLSRR for mainly electric (*left*) or magnetic (*right*) stimulation. In both cases, incident fields are applied at the resonance frequency from both sides of the VLSRR with the electric field polarized in the x axis and the magnetic field polarized in the y axis. To stimulate the VLSRR mainly with an electric (magnetic) field, the incident fields on both sides are applied in (anti-)phase creating a maximum (zero) of the electric field and a zero (maximum) of the magnetic field at the center of the unit cell

The applied fields are always 1 V/m. Figure 1.10 shows the amplitude and the phase of the second harmonic generated on the left and the right of the metamaterial.

Many observations can be made directly from these plots, the most obvious being that the symmetric unit cell generates a second harmonic that is almost perfectly in phase on both sides, while the antisymmetric unit cell generates a second harmonic that is approximately π out of phase on both sides of the metamaterial. If the magnetic field were plotted instead of the electric field, the inverse effect would be observed. This symmetry can be explained by the fact that the symmetric unit cell acts as an electric dipole source at the harmonic frequency, while the antisymmetric unit cell acts as a magnetic dipole source [6].

It can also be seen that conditions A and B give identical results, but with the amplitude and phase in the left and right media reversed. This behavior is to be expected for symmetric or antisymmetric unit cells since those two conditions are in fact totally equivalent.

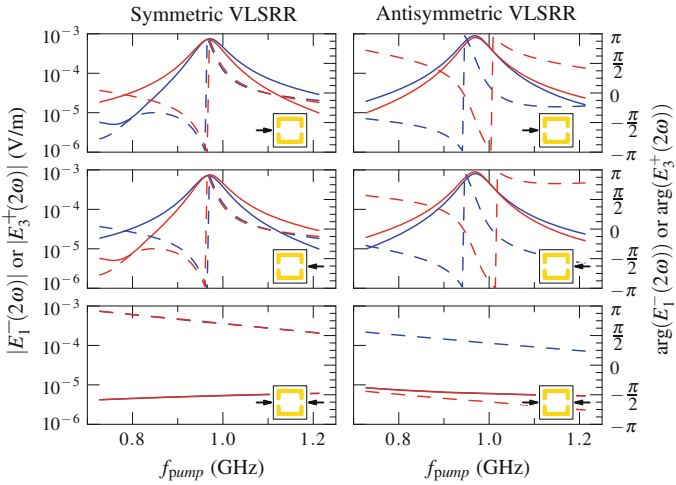

Fig. 1.10 Amplitude (*continuous line*) and phase (*dashed line*) of second harmonic generated on the left (*blue*) and the right (*red*) of the unit cell for symmetric (*left*) and antisymmetric (*right*) VLSRRs in three different conditions. The insets represent the incident fields in conditions A (*top*), B (*middle*), or C (*bottom*)

Finally, it can be seen that when the pump is applied in condition C, the second harmonic generation is suppressed. Since the pump is applied symmetrically in condition C, it creates a standing wave with node in the electric field and a zero in the magnetic field at the center of the unit cell. As shown above in Fig. 1.9, such a combination of incident fields does not generate a concentration of the electric field inside the gaps of the VLSRR, and we expect a weak nonlinear response.

The amplitude and phase of the generated second harmonic can be compared to how much would be generated if the nonlinear susceptibilities were individually unity. Using the transfer matrix approach of Bethune, all the elements of the matrix of (1.24) were calculated and the linear system of equation was solved to obtain the effective nonlinear susceptibilities shown in Fig. 1.11.

The dominant nonlinearity in the symmetric VLSRR is $\chi^{(2)}_{emm}$ while that of the antisymmetric VLSRR is $\chi^{(2)}_{mmm}$. In both cases, it is mainly the applied magnetic field that generates the second harmonic. This is related to the fact that field concentration in the gaps of the VLSRR is mainly generated by the applied magnetic field. When the varactors are in the symmetric orientation the unit cell acts as an electric dipole source at the harmonic frequency, while when the varactors are in the antisymmetric orientation the unit cell acts as a magnetic dipole source. The next two nonlinear susceptibilities in importance for both cases are those of the same symmetry group as the dominant nonlinearity. Their presence is probably for the most part an artifact of spatial dispersion. The three remaining nonlinearities belong to the opposite symmetry group, and are suppressed by several orders of magnitude, in agreement with the conclusions drawn earlier from the coupled mode theory.

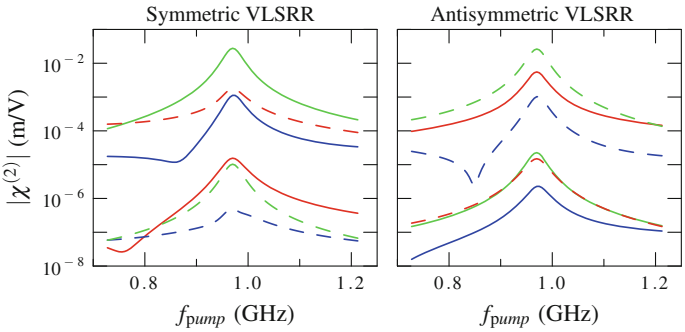

Fig. 1.11 Nonlinear susceptibility for symmetric (*left*) and antisymmetric (*right*) VLSRRs: $\chi^{(2)}_{eee}$ (*blue*), $\chi^{(2)}_{eem}$ (*red*), $\chi^{(2)}_{emm}$ (*green*), $\chi^{(2)}_{mee}/Z_0$ (*blue*, *dashed*), $\chi^{(2)}_{mem}/Z_0$ (*red*, *dashed*), and $\chi^{(2)}_{mmm}/Z_0$ (*green*, *dashed*)

1.6 Conclusion

Metamaterials offer an enormously expanded set of tools for the design of novel nonlinear optical media. With the inclusion of artificial magnetic response, which can readily be realized in artificially structured media, the number of potential nonlinear susceptibilities dramatically increases, allowing much more control over harmonic generation or wave mixing processes, as well as many other nonlinear phenomena. In this chapter, we have presented methods to design and evaluate general magnetoelectric nonlinear metamaterials, and have shown how the various nonlinear susceptibility terms can be understood in terms of symmetry arguments. The simple illustrations we have presented represent only a modest introduction to the subject of nonlinear magnetoelectric metamaterials, which hold great potential for new nonlinear physics and nonlinear device optimization.

Acknowledgments This work was supported by the Air Force Office of Scientific Research (Contract No. FA9550-09-1-0562).

References

1. D.S. Bethune, Optical harmonic generation and mixing in multilayer media: analysis using optical transfer matrix techniques. J. Opt. Soc. Am. B **6**(5), 910–916 (1989)
2. X. Chen, T.M. Grzegorczyk, B.I. Wu, J. Pacheco Jr, J.A. Kong, Robust method to retrieve the constitutive effective parameters of metamaterials. Phys. Rev. E **70**, 016,608 (2004)
3. S. Larouche, A. Rose, E. Poutrina, D. Huang, D.R. Smith, Experimental determination of the quadratic nonlinear magnetic susceptibility of a varactor-loaded split ring resonator metamaterial. Appl. Phys. Lett. **97**, 011,109 (2010)
4. S. Larouche, D.R. Smith, A retrieval method for nonlinear metamaterials. Opt. Commun. **283**, 1621–1627 (2010)

5. P. Markoš, C.M. Soukoulis, *Wave Propagation: From Electrons to Photonic Crystals and Left-Handed Metaamaterials* (Princeton University Press, Princeton, 2008)
6. A. Rose, D. Huang, D.R. Smith, Demonstration of nonlinear magnetoelectric coupling in metamaterials. Appl. Phys. Lett. **101**, 051,103 (2012)
7. A. Rose, S. Larouche, D. Huang, E. Poutrina, D.R. Smith, Nonlinear parameter retrieval from three- and four-wave mixing in metamaterials. Phys. Rev. E **82**, 036,608 (2010)
8. A. Rose, S. Larouche, E. Poutrina, D.R. Smith, Nonlinear magnetoelectric metamaterials: Analysis and homogenization via a microscopic coupled-mode theory. Phys. Rev. A **86**, 033,816 (2012)
9. A. Rose, S. Larouche, D.R. Smith, Quantitative study of the enhancement of bulk nonlinearities in metamaterials. Phys. Rev. A **84**, 053,805 (2011)
10. A. Rose, D.A. Powell, I.V. Shadrivov, D.R. Smith, Y.S. Kivshar, Circular dichroism of four-wave mixing in nonlinear metamaterials. Phys. Rev. B **88**, 195,148 (2013)
11. I.V. Shadrivov, A.B. Kozyrev, D.W. van der Weide, Y.S. Kivshar, Nonlinear magnetic metamaterials. Opt. Express **16**(25), 20,266–20,271 (2008)
12. J.E. Sipe, R.W. Boyd, Nonlinear susceptibility of composite optical materials in the Maxwell Garnett model. Phys. Rev. A **46**(3), 1614–1629 (1992)
13. D.R. Smith, Analytic expressions for the constitutive parameters of magnetoelectric metamaterials. Phys. Rev. E **81**, 036,605 (2010)
14. D.R. Smith, S. Schultz, P. Markoš, C.M. Soukoulis, Determination of effective permittivity and permeability of metamaterials from reflection and transmission coefficients. Phys. Rev. B **65**, 195,104 (2002)
15. D.R. Smith, D.C. Vier, Th. Koschny, C.M. Soukoulis, Electromagnetic parameter retrieval from inhomogeneous metamaterials. Phys. Rev. E **71**, 036,617 (2005)
16. B. Wang, J. Zhou, Th. Koschny, C.M. Soukoulis, Nonlinear properties of split-ring resonators. Opt. Express **16**(20), 16,058–16,063 (2008)
17. A. Yariv, Coupled-mode theory for guided-wave optics. IEEE J. Quantum Electron QE **9**(9), 919–933 (1973)

Chapter 2
Active and Applied Functional RF Metamaterials

Steven A. Cummer

Abstract The concept of electromagnetic metamaterials, defined here as artificial materials that are designed to obtain specific effective electromagnetic material properties, has revolutionized thinking about wave behavior in materials and the design of complex electromagnetic devices. Although originally conceived in passive form, the concept of electromagnetic metamaterials is applicable to more complicated structures. Why not embed into metamaterials circuit behavior that is more complicated than what one can obtain from linear, time-invariant, passive circuit elements? What kinds of new and interesting and potentially useful behavior can one obtain? These are the fundamental questions that have motivated the research described in this chapter. Our focus here is on the integration of complex functionality into metamaterials using powered and/or nonlinear elements.

2.1 Introduction

The concept of electromagnetic metamaterials, defined here as artificial materials that are designed to obtain specific effective electromagnetic material properties, has revolutionized thinking about wave behavior in materials and the design of complex electromagnetic devices. Instead of being limited to the material properties that nature provides, devices and device concepts are being designed using the full range of electromagnetic material properties, electric and magnetic, positive and negative.

This revolution in thinking and materials research has led to many novel properties and device concepts that were simply not possible before metamaterials were conceived, including negative refractive index materials [1], the perfect lens [2], electromagnetic cloaking [3], to name just a few. There remain major challenges in

S.A. Cummer (✉)
Department of Electrical and Computer Engineering, Duke University,
Durham, NC 27708, USA
e-mail: cummer@ee.duke.edu

I.V. Shadrivov et al. (eds.), *Nonlinear, Tunable and Active Metamaterials*,
Springer Series in Materials Science 200, DOI 10.1007/978-3-319-08386-5_2

designing and fabricating metamaterials that exhibit the properties needed for these devices, and there are fundamental physical limits (such as the need for group velocity to remain below the speed of light in a low-loss medium) that may make certain combinations impossible. But the path forward is reasonably well-defined and being aggressively pursued.

Although originally conceived in passive form, the concept of electromagnetic metamaterials is applicable to more complicated structures. The behavior of most passive metamaterial structures, for example the split ring resonator [4], can be derived or estimated from simple circuit analysis. This is because the structures are fundamentally subwavelength in size and thus the lumped circuit element approximation is at least partly valid. But if one now considers a metamaterial unit cell as a circuit, why not embed into metamaterials circuit behavior that is more complicated than what one can obtain from linear, time-invariant, passive circuit elements? What kinds of new and interesting and potentially useful behavior can one obtain?

These are the fundamental questions that have motivated the research described in this chapter. More specifically, our focus here is on the integration of different forms of circuit functionality into metamaterials. Circuits often have adjustable elements like potentiometers, so can adjustable effective material properties be created by integrating adjustable circuit elements into metamaterial cells? Circuits also can have gain so that the output signal is larger than the input signal, so can effective material gain be created by integrating gain into metamaterial cells. Circuits also can exhibit much more complicated behavior, so where are the limits of the complexity of the behavior that can be integrated into metamaterial cells?

The first efforts to embed some sort of functionality into metamaterials focused on dynamically tunable metamaterials. Most passive resonant metamaterial particles can be thought of as lumped electric circuits, at least to first order. By integrating externally tunable circuit elements, one can shift the resonant frequency and thus change the effective material parameters at a fixed frequency. The first demonstrations of this used varactors [5–7], which are diodes designed to behave as voltage tunable capacitors. Other demonstrations of electrically tunable metamaterials include using switchable schottky diodes [8], MEMS switches [9], liquid crystals [10], ferrites [11], and ferroelectric films [12]. And totally different approaches, such as temperature dependence [13] and optical tuning [14], have also been used to realize dynamically tunable metamaterials. These early efforts showed that there were few limits to how one could achieve dynamic tuning of metamaterials.

These broad concepts, and the more specific ones described in this chapter, are examples of trying to integrate specific forms of behavior into metamaterials in order to make them do something useful. As such these can all be considered examples of what we call applied functional metamaterials. The goal of this chapter is to describe some of the different techniques and approaches that have been employed in designing applied functional metamaterials into which circuit-like behavior is integrated. Some of the concepts and research described here overlaps partly with that described by other chapters in this book. However, the circuit-oriented perspective is distinct. We focus herein on two broad classes of functional radio frequency (RF) metamaterials:

- Externally powered active metamaterials, in which external gain is incorporated into unit cells to access effective properties that cannot be obtained with passive structures,
- Applied functional metamaterials, in which complex circuit-inspired behavior, such as nonvolatile memory or amplitude-dependent transmission, is designed into the metamaterial to give it the same application-oriented behavior.

Although these topics span a range of metamaterial concepts, they are linked by the common thread of integrating complex, functional behavior into electromagnetic metamaterials.

2.2 Powered Active RF Metamaterials

It was recognized very early in the modern surge of metamaterials research that passive electromagnetic metamaterials have limitations in the range of achievable effective material parameters. Resonant metamaterial inclusions are unavoidably highly dispersive and lossy. One approach around these limitations is the concept of powered active electromagnetic metamaterials [15] that contain elements that accept outside power and thus can behave internally in ways that are not constrained by passivity.

Although it is straightforward to show theoretically that powered active metamaterials can provide much more extreme material parameters than is possible with passive approaches, such materials are difficult to demonstrate experimentally. Stability is the main hurdle, as adding power and gain to field-sensing elements makes them prone to oscillation [16, 17]. Directly powered active metamaterials have been experimentally demonstrated in several different forms [18–22] and the field is moving forward steadily despite the technical challenges.

We describe here research that builds on the powered active metamaterial architecture first described in [18]. This is by no means the only way one can make powered active metamaterials, but it has some attractive qualities and has been experimentally demonstrated in several different forms. It follows from considering how passive metamaterial structures work, for example an SRR. In an SRR, the loop creates a voltage proportional to the local magnetic field (and to frequency). Then, because of the very small impedance of the loop-gap combination near resonance, this induced voltage drives a large current through the same loop and thereby creates a strong magnetic dipole moment. It is this creation of a magnetic dipole moment proportional to the local magnetic field that mimics the response of naturally magnetic materials.

There are two basic parts to this passive metamaterial response. First is the sensing of a local field, and second is the generation of a strong dipole moment in proportion to that local field. Although in most passive structures these two parts are taken care of by the same structure, there is no reason why they have to be. And this further suggests

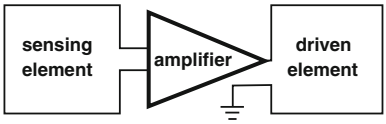

Fig. 2.1 Schematic illustration of one possible powered active metamaterial unit cell architecture. A sensing element produces a voltage signal proportional to some local electromagnetic field component. An active amplifier boosts and perhaps modifies that signal, and the driven element uses that amplified signal to create a large dipole moment proportional to the original local field. Adapted from [18]

a general powered active metamaterial unit cell architecture shown in Fig. 2.1. Let there be one element that senses a local electromagnetic field component—this is the sensing element. This could be a loop, as shown, for sensing the magnetic field, but it could also be a wire or a conducting gap for sensing the electric field. Then let there be a powered amplifier that boosts and perhaps filters or phase-shifts the sensed signal. Finally, let the amplifier drive another element that creates the large dipole moment needed for the metamaterial response—this is the driven element. In this way, the basic physics of a passive metamaterial particle are directly powered controlled by the amplifier. This, in principle, removes some of the constraints imposed by passivity on the possible effective material parameters. That these constraints can be removed through a powered active approach is shown by the examples below.

2.2.1 Zero Loss Active Metamaterials

One clear target for powered active metamaterials is zero-loss metamaterials. Passive metamaterials are unavoidably lossy because of the losses in the materials used to make them (usually due to the resistance of metal traces). These losses can be substantial and are a significant hurdle for realizing some interesting metamaterial applications. The injection of external power into active metamaterials can solve this problem. The critical issue is controlling the *phase* of the particle dipole response relative to the local field. If this phase is not exactly zero or 180°, then there is an imaginary component to the polarizability of the particle. For passive particles, this always means loss. But in active particles this phase can be manipulated to give zero loss and even gain.

This concept was explored and demonstrated experimentally in [20]. The designed and fabricated unit cell is shown in annotated form in Fig. 2.2a. This is an active magnetic metamaterial unit cell, and thus employs loops for the sensing and driven elements. Passive split ring resonators are placed next to both of these loops to amplify the local fields and increase the strength of the cell response. In between the sensing and driven loops is an amplifier, as in Fig. 2.1, connected to an adjustable phase shifter. The adjustable phase gives an important degree of freedom in tuning the material response, as indicated in the discussion above.

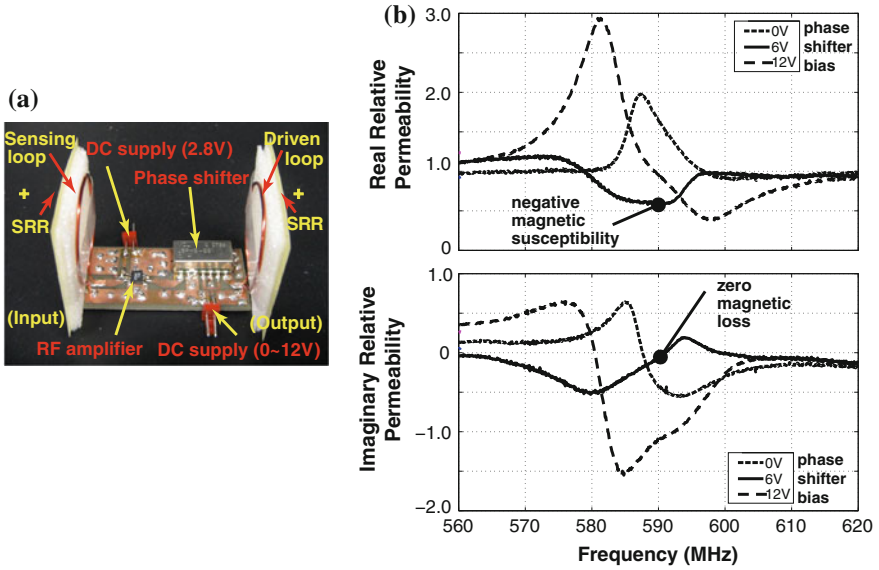

Fig. 2.2 Demonstration of an active magnetic metamaterial unit cell. **a** Annotated photograph showing the fabricated unit cell and its internal components. **b** Experimentally measured real (*top*) and imaginary (*bottom*) parts of the effective magnetic permeability as a function of phase shifter bias. With an appropriate bias and in a narrow range of frequencies, we obtain a response that has a negative magnetic susceptibility and zero loss. Adapted from [20]

The effective magnetic properties of this active unit cell were experimentally measured, and the results are shown in Fig. 2.2b for three different phase shifter bias levels. The frequency dependence of permeability for each bias are all dramatically different. The 12 V bias gives a response that is quite similar to a passive material, with a real part that increases and then decreases, and an imaginary part that is predominantly negative (corresponding to loss for our assumed $\exp(+j\omega t)$ sign convention).

The most interesting results are observed for the 6 V bias level. Here, the effective material properties are completely unlike those in passive materials. The real part of the permeability is essentially at or below unity for all frequencies, and the imaginary part crosses from below zero (loss) to above zero (gain). Therefore there is a frequency at which the real part of the magnetic susceptibility is negative, and the imaginary part is zero implying zero loss. In [20], it was further shown that an array of 3 identical active magnetic unit cells unambiguously result in a negative magnetic permeability and zero loss in a narrow frequency range.

2.2.2 Nonreciprocal Active Metamaterials

The basic powered active unit cell architecture described in Sect. 2.2 presents some interesting possibilities. There is no reason, for example, why the sensing and driven elements need to the same kind of dipole. This means that one could create a metamaterial unit cell that senses the local electric field and thus generates a proportional *magnetic* dipole response. With such a cell one is not controlling permittivity or permeability but instead actively creating and controlling a magneto-electric material response. Some natural media exhibit a magneto-electric material response, but this is uncommon and not usually very strong. Passive metamaterial structures can exhibit magneto-electric coupling [23], but such coupling is always symmetric so that a magnetic field creates an electric response and an electric field creates a magnetic response.

In contrast, an active magneto-electric element easily gives us the ability to make this coupling non-symmetric. With an one-directional amplifier between the sensing and driven elements, only one form of magneto-electric coupling occurs. This has the interesting and unusual effect of making wave propagation highly nonreciprocal, or different in opposite directions [22]. Figure 2.3a shows a schematic layout of such a unit cell, which contains a magnetic field sensing loop, an embedded amplifier, and a driven electric monopole (all with appropriate lumped elements for narrowband matching). This cell produces an electric dipole moment that is proportional to the applied magnetic field, but does not produce the reverse because of the unidirectional nature of the amplifier. An advantage of this mixed-field cell is that the coupling between the driven electric monopole and the sensing loop is small and thus does not contribute much stability-influencing feedback.

Figure 2.3b shows an assembled array of these metamaterial particles of one element thickness. When illuminated at normal incidence with the polarization shown in the figure, this array was designed to be essentially transparent in one direction (S_{12}) while opaque in the other (S_{21}), and thus highly nonreciprocal. The measurements shown in Fig. 2.3c confirm this behavior, with a >25 dB difference in transmission magnitude at the 600 MHz target frequency between these two normal-incidence directions. That such strong nonreciprocity can be created with a metamaterial that is only a small fraction of a wavelength thick speaks to the extreme material properties that can be obtained using powered active metamaterials. To be sure, adding active elements adds complexity to the design and operation, but it enables material properties that cannot be obtained with a passive approach.

2.3 Applied Functional Metamaterials

The final class of metamaterials we will discuss in this chapter is what we call applied functional metamaterials. The term *functional metamaterials* has been applied very broadly to metamaterials that exhibit complex engineered behavior and properties.

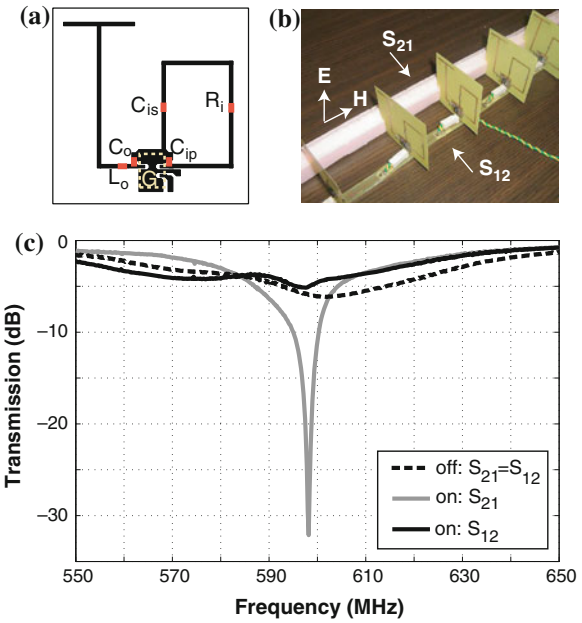

Fig. 2.3 Illustration and demonstration of a nonreciprocal active metamaterial based on magneto-electric coupling. **a** Schematic illustration of the cell and its internal components. **b** Photograph of the fabricated and assembled array of five identical elements. **c** Measurements of transmission with power off, and in the two opposite directions with power on. When powered, this array is nearly transparent in the S_{12} direction but essentially opaque in the S_{21} direction at the target 600 MHz frequency. Adapted from [22]

This includes metamaterials that are designed to mimic *general* complex properties found in natural materials, such as second- and third-order electromagnetic nonlinearities [24, 25]. Careful analysis of such particles can lead to a complete theoretical description of the nonlinear susceptibilities of a bulk metamaterial from the known properties of the components of a single cell [26].

But the concept of functional metamaterials also includes those designed to exhibit specific, rather than general, engineered properties and behavior. This latter class of metamaterials we call *applied* functional metamaterials to distinguish it within the broader context of functional metamaterials. These applied functional metamaterials are the focus of this section of this chapter.

A representative example of an applied functional metamaterial is one that is transparent (or close to it) for low incident power density but becomes less and less transmissive as the incident power density increases [27]. Although this is clearly nonlinear behavior, it is a specific form of nonlinear behavior that is directly tied to an application, namely preventing high power signals from passing through while allowing low power signals to pass (for example, to protect sensitive components from transient high power signals).

In the more detailed descriptions of several examples to follow, the reader will note that the inspiration for many of these application-functional metamaterials is to translate practical electric circuit behavior, which operates on local voltages and currents, to electromagnetic metamaterial behavior, which operates on electromagnetic waves. A circuit-based device that transmits low power signals but blocks high power signals (the example mentioned above) is called a limiter. As described below in Sect. 2.3.2, a way of implementing a circuit limiter guided the strategy for designing that behavior into an electromagnetic metamaterial limiter. In the opinion of the author, this basic idea of translating application-specific circuit behavior to electromagnetic metamaterials is one with substantial future promise.

2.3.1 Individually Addressable and Nonvolatile Tunable Metamaterials

The concept of tunable metamaterials, in which externally controllable elements integrated into metamaterials enable one to change the effective electromagnetic properties, was briefly described above in Sect. 2.1. Most realizations of tunable metamaterials incorporate voltage-tunable elements that are straightforward to control. However, when one removes the control signal, the materials revert to their untuned state, and must be retuned when turned back on. And while tuning a large array of metamaterial particles with a single control signal is straightforward, one might wish to tune each element individually to dramatically increase the reconfigurability of the array. But tuning separately each element in an array of tens or hundreds of elements with a different control signal is a challenge.

One solution to these issues, which we describe in this section and which is based on [28], comes from practical circuit concepts. Electric circuits often incorporate tunable elements, such as potentiometers, so that their behavior can be precisely tuned for a specific application. These elements are usually nonvolatile in that they maintain their tuned state even when power is removed from the system. There are also families of chips that can be individually controlled on a shared bus wire. This means that metamaterial elements can all be connected to a small number of shared wires, and yet be individually tunable.

Individually addressed tuning of elements in a metamaterial array was demonstrated in [28]. The basic design is straightforward. Each split ring resonator element contains a varactor (a voltage-tunable capacitor). Varying the bias voltage on the varactor tunes the resonant frequency of the element and thus tunes its effective magnetic properties as described in Sect. 2.1. The addressable control of each element came through a Maxim DS-2890 digital potentiometer with 1-wire interface. The ends of the potentiometer were connected to 0 and 10 V so that moving the wiper varies the bias voltage on the varactor between these limits (with 256 step resolution).

The individual addressability comes through the Maxim chips' 1-wire interface, which enables each chip to be communicated with individually. Thus the varactor voltage can be set separately on each element through a simple computer-controlled

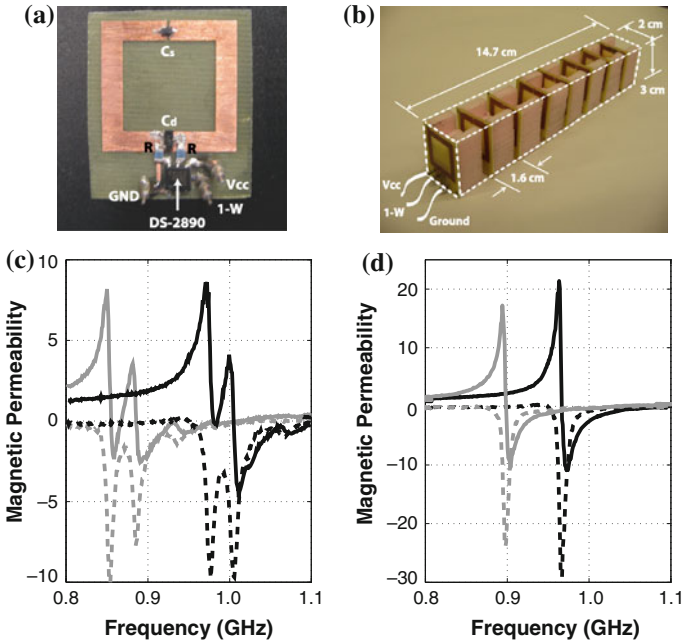

Fig. 2.4 Illustration and demonstration of a tunable metamaterial with individually addressable elements. **a** Photograph of a unit cell and its internal components. **b** Photograph of the fabricated and assembled array of eight identical elements. **c** Measurements of effective magnetic permeability of the 8-element array without individual tuning, for two tuned states. The responses exhibit two distinct resonances because of small variations in the elements, while the goal was for a single resonance. **d** Measurements of effective magnetic permeability after each addressable element was tuned while in the array, showing the desired single tunable resonance. Adapted from [28]

interface between the serial port and the 1-wire bus. As shown by the photo in Fig. 2.4a, each metamaterial element was fabricated with pins that enabled them to be stacked together in a 1D array of arbitrary length with the 1-wire and power connections reaching each one. An annotated photo of an assembled 8-element array is shown in Fig. 2.4b. Unfortunately, the 1-wire chips from Maxim have been discontinued at the time of this writing. But the concept remains valid and the work shows how individual metamaterial element addressability can be implemented in an efficient way.

To experimentally confirm the improvements that come with individual addressability, we performed reflection/transmission measurements of the 8-element array in a waveguide and extracted the effective magnetic permeability of the metamaterial array [28]. Figure 2.4c, d shows the effective magnetic permeability for two different frequency tunings without addressability (c) and with addressability (d). Without addressability and the individual element tuning that comes with it, the variability in the individual varactors means that the particles do not have the same untuned resonant frequency. The material array response contains at least two distinct

resonances, and the resulting effective material parameters are lower in magnitude and more lossy than they need to be. In contrast, the measurements show that with individual element addressing and tuning, each element can be tuned to a give a single, sharp resonance, and this resonance can be shifted without changing shape by more than 10 % in frequency [28]. This provides maximum positive and negative permeabilities that are 2 times larger than without individual addressability, and lower losses at most frequencies as well.

Additional functionality can be added to this addressable material concept through a bit of additional circuitry per unit cell. When the metamaterial array described above is powered down, it reverts back to its untuned state and requires a computer connection to regain the tuned state. One could imagine a scenario in which, after tuning, the array should remain in its tuned state, even when unconnected to the driving computer. This would require a nonvolatile memory chip into each metamaterial element to store the tuned state. A chip that combines a digital potentiometer with a nonvolatile memory, so that the potentiometer reverts to its tuned state simply when power is applied, exists in a commercial product (Intersil X9317). We combined this chip with a 1-wire chip to enable communication to each metamaterial element separately, and confirmed that individual addressability and nonvolatile memory of the tuned state could be implemented in a metamaterial array.

This same addressable metamaterial concept has been extended into a more specific applied functional metamaterial [29]. A reflectarray is an engineered surface designed to have specific electromagnetic reflection properties. By tuning the local reflection phase of individual elements on the surface, one can engineer a surface that reflects signals in non-specular directions. And further, by integrating addressable tunability into the elements of reflectarray, one can reconfigure the surface to change the reflection direction dynamically. In [29] it was shown that this approach can be used to create a thin surface capable of steering the reflection of a normally incident signal continuously by more than 25°.

2.3.2 A Metamaterial Limiter

A final example of integrating application-specific functionality into metamaterials is the metamaterial limiter [27]. RF circuits routinely employ a type of circuit called a limiter that, above a certain threshold input amplitude, begins to clip (or limit) the output amplitude to prevent large input signals from being transmitted through to sensitive components that could be damaged by large signals. A simple circuit implementation of a limiter is shown in Fig. 2.5a. The circuit is based on a PIN diode, which is a nonlinear element that acts as a voltage tunable resistor. At low input power, the PIN diode is a large impedance which does not modify the signal. But at high input power, it becomes a small impedance that shorts some of the signal energy to ground and thus limits the amplitude of the transmitted signal. It is interesting to note that there are also optical limiters that perform the same operation on light-based signals (typically lasers) for the protection of devices or eyes [30].

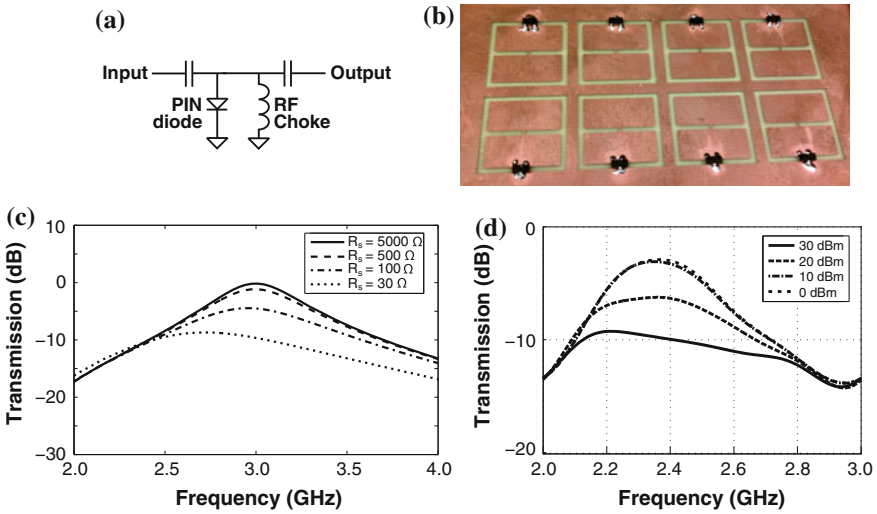

Fig. 2.5 Demonstration of an RF limiter metamaterial. **a** Circuit diagram of a simple limiter. **b** Implementation of CELC surface with PIN diodes integrated into each cell. **c** Simulation of power-dependent transmission through the CELC surface. **d** Measurements of power-dependent transmission through the CELC surface. Adapted from [27]

These optical limiters are usually based on photosensitive chemicals that increase their absorption for higher input power.

One can imagine the need for a thin sheet of material that behaves the same way for incident electromagnetic waves: small input signals are transmitted through, but large signals are attenuated. Integrating this nonlinear circuit functionality into a metamaterial is one way to achieve this goal. The design begins with a baseline passive metamaterial structure that is thin (preferably planar), transmits a relatively broad frequency range, but has a physical structure that can easily be manipulated through the placement of circuit elements. The complementary electric LC resonator (CELC), described in detail in [31] and shown in the photo of Fig. 2.5b, meets these goals with a planar geometry, a relatively broad (in frequency) transmission window, and a physical structure that can be altered by electrical shorting across the two separate conducting regions.

The limiter circuit works by allowing the power-dependent resistance of the PIN diode to short the output when the input power is high. The same behavior can be integrated into the CELC structure by placing a PIN diode across the two conductors that form the metamaterial structure. The transmission through the CELC occurs due to a resonance between these two conductors. A PIN diode placed across them acts as a power-dependent electrical short that weakens the resonance and thus reduces the transmission at higher powers. There are some degrees of freedom in this design, namely the precise placement of the PIN diode to maximally damp the resonance, and the diode characteristics to ensure that the threshold power for the limiter behavior occurs at the desired input power level.

With these parameters chosen, Fig. 2.5c shows simulated transmission versus frequency curves for different PIN diode resistance levels. These indicate that the CELC-PIN structure should behave as a metamaterial limiter, with nearly 100 % transmission near 3 GHz for low incident power (high diode resistance), but with transmission that drops more than 10 dB for higher incident power (low diode resistance). For experimental demonstration, the 2 by 4 CELC array was placed inside a closed metallic waveguide, and the relative transmitted power was measured as a function of input power. As shown in Fig. 2.5d, the relative transmission does not change with power for low incident powers (0 and 10 dBm) and peaks with high relative transmission (−2 dB). But as the incident power increases, the limiter behavior takes over, and the relative transmitted power drops by more than 10 dB for an incident power of 30 dBm.

This example effectively demonstrates both the design approach and the future possibilities for applied functional metamaterials. The desired nonlinear behavior is well-defined and potentially useful in applications, and it is known how to achieve that behavior in lumped circuit form. Metamaterial elements based on that circuit that exhibit that same behavior were designed, and measurements of a fabricated metamaterial surface array confirm the desired behavior. More complex and more useful behaviors can certainly be engineered into metamaterials using the same approach.

2.4 Summary

In this chapter we have reviewed several of the different technical approaches being used to realize active electromagnetic metamaterials. This is a very broad topic, and the term active metamaterials means different things to different people. Our focus has been on two of these approaches. The first is powered active RF metamaterials, in which externally powered elements are used to achieve electromagnetic material parameters not possible in strictly passive materials. The amplifier-based architecture described here has already been used to achieve zero-loss negative permeability materials and also highly non-reciprocal materials that are transparent to waves traveling in one direction but opaque to those traveling in in the opposite direction. There is no question it is challenging to design powered active unit cells that are both robust and stable, but there is no other approach for realizing some of the extreme material parameters needed for some interesting and useful applications.

The second approach is what we call applied functional metamaterials. These are metamaterials into which a specific functionality has been embedded so that a bulk material exhibits a desired appliation-oriented behavior. The examples of addressable tuning of individual elements, nonvolatile memory of that tuned state, and nonlinear power-dependent transmission have shown that complex circuit-inspired behavior can be embedded inside metamaterial elements, resulting in a bulk metamaterial or metasurface that exhibits that same behavior. The surface has just begun to be scratched in all of these aspects of metamaterials, and the coming years should yield significantly more.

References

1. D.R. Smith, W.J. Padilla, D.C. Vier, S.C. Nemat-Nasser, S. Schultz, Phys. Rev. Lett. **84**, 4184 (2000)
2. J.B. Pendry, Phys. Rev. Lett. **85**(18), 3966 (2000)
3. J.B. Pendry, D. Schurig, D.R. Smith, Science **312**, 1780 (2006)
4. J.B. Pendry, A.J. Holden, D.J. Robbins, W.J. Stewart, IEEE Trans. Microw. Theory Tech. **47**(11), 2075 (1999)
5. O. Reynet, O. Acher, Appl. Phys. Lett. **84**, 1198 (2004). doi:10.1063/1.1646731
6. I. Gil, J. Garcia-Garcia, J. Bonache, F. Martyn, M. Sorolla, R. Marques, Electron. Lett. **40**, 20046389 (2004)
7. I.V. Shadrivov, S.K. Morrison, Y.S. Kivshar, Opt. Express **14**, 9344 (2006). doi:10.1364/OE.14.009344
8. H. Chen, W.J. Padilla, J.M.O. Zide, A.C. Gossard, A.J. Taylor, R.D. Averitt, Nature **444**, 597 (2006). doi:10.1038/nature05343
9. T. Hand, S.A. Cummer, IEEE Antennas Wirel. Propag. Lett. **6**, 401 (2007)
10. Q. Zhao, L. Kang, B. Du, B. Li, J. Zhou, H. Tang, X. Liang, B. Zhang, Appl. Phys. Lett. **90**(1), 011112 (2007). doi:10.1063/1.2430485
11. Y. He, P. He, S. Dae Yoon, P.V. Parimi, F.J. Rachford, V.G. Harris, C. Vittoria, J. Magn. Magn. Mater. **313**, 187 (2007). doi:10.1016/j.jmmm.2006.12.031
12. T.H. Hand, S.A. Cummer, J. Appl. Phys. **103**(6), 066105 (2008). doi:10.1063/1.2898575
13. T. Driscoll, S. Palit, M.M. Qazilbash, M. Brehm, F. Keilmann, B.G. Chae, S.J. Yun, H.T. Kim, S.Y. Cho, N.M. Jokerst, D.R. Smith, D.N. Basov, Appl. Phys. Lett. **93**(2), 024101 (2008). doi:10.1063/1.2956675
14. A. Degiron, J.J. Mock, D.R. Smith, Opt. Express **15**, 1115 (2007). doi:10.1364/OE.15.001115
15. S.A. Tretyakov, Microwave Opt. Tech. Lett. **31**, 163 (2001)
16. A.D. Boardman, Y.G. Rapoport, N. King, V.N. Malnev, J. Opt. Soc. Am. B: Opt. Phys. **24**, A53 (2007). doi:10.1364/JOSAB.24.000A53
17. E. Ugarte-Munoz, S. Hrabar, D. Segovia-Vargas, A. Kiricenko, IEEE Trans. Antennas Propagat. **60**, 3490 (2012). doi:10.1109/TAP.2012.2196957
18. B.I. Popa, S.A. Cummer, Microwave Opt. Tech. Lett. **49**(10), 2574 (2007)
19. R.R.A. Syms, L. Solymar, I.R. Young, Metamaterials **2**, 122 (2008)
20. Y. Yuan, B. Popa, S.A. Cummer, Opt. Express **17**, 16135 (2009). doi:10.1364/OE.17.016135
21. S. Hrabar, I. Krois, A. Kiricenko, Metamaterials **4**, 89 (2010). doi:10.1016/j.metmat.2010.07.001
22. B.I. Popa, S.A. Cummer, Phys. Rev. B **85**(20), 205101 (2012). doi:10.1103/PhysRevB.85.205101
23. R. Marques, F. Medina, R. Rafii-El-Idrissi, Phys. Rev. B **65**, 144440 (2002). doi:10.1103/PhysRevB.65.144440
24. M. Lapine, M. Gorkunov, K.H. Ringhofer, Phys. Rev. E **67**(6), 065601 (2003). doi:10.1103/PhysRevE.67.065601
25. A.A. Zharov, I.V. Shadrivov, Y.S. Kivshar, Phys. Rev. Lett. **91**(3), 037401 (2003). doi:10.1103/PhysRevLett.91.037401
26. E. Poutrina, D. Huang, D.R. Smith, New J. Phys. **12**(9), 093010 (2010). doi:10.1088/1367-2630/12/9/093010
27. A.R. Katko, A.M. Hawkes, J.P. Barrett, S.A. Cummer, IEEE Antennas Wirel. Propag. Lett. **10**, 1571 (2011)
28. T.H. Hand, S.A. Cummer, IEEE Antennas Wirel. Propag. Lett. **8**, 262 (2009). doi:10.1109/LAWP.2009.2012879
29. T.H. Hand, S.A. Cummer, IEEE Antennas Wirel. Propag. Lett. **9**, 70 (2010). doi:10.1109/LAWP.2010.2043211
30. L.W. Tutt, T.F. Boggess, Prog. Quantum Elec. **17**(4), 299 (1993)
31. T.H. Hand, J. Gollub, S. Sajuyigbe, D.R. Smith, S.A. Cummer, Appl. Phys. Lett. **93**(21), 212504 (2008). doi:10.1063/1.3037215

Chapter 3
Parametric Amplification of Magneto-Inductive Waves

Richard R.A. Syms, Timmy Floume, Laszlo Solymar and Ian R. Young

Abstract Parametric amplification is a method of low-noise signal amplification of that operates by mixing the signal with a high-frequency, high power pump in a single non-linear reactive component, a varactor diode. Here its application to the amplification of magneto-inductive (MI) waves is demonstrated. MI waves are slow waves that propagate in linear chains of magnetically coupled L-C resonators known as MI waveguides. Such waveguides can be formed into ring resonant structures, and used for signal detection in magnetic resonance imaging (MRI). MI waves and waveguides are first reviewed. The theory of parametric amplification in single resonant elements is then described, and extended to travelling wave structures and ring resonators. Experimental verification is presented for systems designed to operate at 63.85 MHz, the frequency for ^{1}H MRI in a 1.5 T magnetic field.

3.1 Introduction

Magneto-inductive (MI) waves are slow waves of circulating current that, together with their associated magnetic fields, can propagate in arrays of magnetically coupled electrical resonators [1, 2]. The arrays can be constructed in one, two or three dimensions [3], and represent a particularly simple form of metamaterial. Here we will mainly be concerned with the one-dimensional variant, known as a magneto-inductive waveguide. The resonators may be arranged in a plane (the so-called 'planar' configuration) or stacked one behind another (the 'axial' configuration)

R.R.A. Syms (✉) · T. Floume · L. Solymar · I.R. Young
Department of Electrical and Electronic Engineering, Imperial College London,
Exhibition Road, London SW7 2AZ, UK
e-mail: r.syms@imperial.ac.uk

T. Floume
e-mail: timmy@floume.com

L. Solymar
e-mail: laszlo.solymar@hertford.ox.ac.uk

I.R. Young
e-mail: youngimarl@aol.com

I.V. Shadrivov et al. (eds.), *Nonlinear, Tunable and Active Metamaterials*,
Springer Series in Materials Science 200, DOI 10.1007/978-3-319-08386-5_3

and waveguides can be configured as a wide variety of 2-, 3- and 4-port MI devices [4, 5].

Many electrical structures support MI waves. All that is required is resonance and magnetic coupling. At low frequencies, the resonators can be lumped-element circuits based on inductors and capacitors (L-C circuits) [2], which in two dimensions may easily be fabricated on printed circuit boards (PCBs) [6, 7]. Alternatively, they may be three-dimensional structures such as spirals [8] or spiral wound sheets of metal-coated dielectric known as 'Swiss-rolls' [9]. At higher frequencies, components with distributed inductance and capacitance such as split-ring resonators (SRRs) [10–13] may be used. Magneto-inductive waves have even been observed in metamaterials designed for operation at photonic frequencies that simply contain open loops [14].

Because of their ability to confine internal magnetic fields to a defined path, there are obvious applications for MI waveguides in wireless power transfer [15–17] and wireless communications [18, 19]. However, owing to their sensitivity to nearby electrical structures, there are also applications in sensing [20]. Finally, through their ability to couple to external magnetic fields, there is a significant potential for detection of signals in magnetic resonance imaging (MRI). Magneto-inductive devices have been developed to concentrate [21–24] and detect [25, 26] MRI signals, and also to transmit them safely out of the body during internal imaging [27, 28].

MI waveguides must satisfy many conditions before practical systems can be built. To transfer energy at a single frequency over a useful distance, the propagation loss must be inherently low, and bends should have minimal effect. To transfer signals—which are inherently broadband—dispersion should also be low. Efficient transducers are required to inject and recover signals, and components such as splitters to define more complicated paths. Switches, modulators and filters may also be required. Low-cost manufacturing methods must also be developed. Many of these aspects have received attention, and in some cases solutions have already been found. A particularly useful variant is magneto-inductive cable, which can be printed in long lengths on flexible substrates, has the lowest propagation loss of all MI waveguides to date, and can be bent into arbitrary paths [29, 30]. It can easily be connected to a conventional RF system [31], and formed into a range of components [32, 33]. As a result, entire MI systems can be printed on a single flexible substrate.

Because MI waves are slow, the current spends a relatively long time circulating in each loop as it propagates. Unfortunately, the ability to construct a low-loss metallic resonator has improved very little over the last century. At room temperature, the most easily available material with high conductivity is still copper, and its ability to carry current at radio frequency is limited by the skin effect. Compared with dielectric resonators, metallic resonators are therefore relatively lossy, with quality factors typically in the range 100–1,000. As a result, the propagation loss of MI waveguides remains stubbornly high. One solution is distributed amplification, and elements containing conventional amplifiers have already been developed [34, 35]. However, because of their resonant arrangement, parametric amplifiers are strong candidates for gain elements.

Before the advent of metamaterials, the parametric amplifier was largely consigned to history. It was developed in the late 1950s, just after the development of the PN junction diode but before the widespread introduction of the transistor [36]. Its particular virtue is low noise amplification, which is achieved by mixing signals in a set of resonators that are coupled by a single non-linear reactance, a variable capacitor (or varactor). Because voltage-dependent capacitance is inherent to the reverse-biased diode, a high-performance amplifier can be constructed using a single diode, a significant advantage in the early days of microelectronics when active components were scarce.

Many configurations were investigated, including circuits involving mixing of two, three and four different frequencies (see e.g., [37, 38]). The simplest—the two-frequency or degenerate amplifier—is often an explanatory example in textbooks. Unfortunately, it is not useful, since it provides gain only when the two frequencies are phase-locked together, and this cannot be the case for realistic signals [39, 40]. The four-frequency amplifier is the most versatile. However, because of its complexity, attention has concentrated on the three-frequency amplifier, which can provide phase-independent amplification using a simple circuit [41].

Three-frequency amplification is a two-step process. First, the weak signal (at angular frequency ω_S) is mixed with a strong pump (at a higher frequency ω_P) to create a so-called 'idler' (at an intermediate frequency ω_I), which is larger than the original signal. The three signals are kept separate by circulating them in appropriately resonant loops, which share the non-linear element. The idler is then mixed with the pump, to create an additional (and now very much larger) signal term, which adds in-phase to the original signal to give the same effect as amplification. In fact, the net effect of the pump is equivalent to insertion of a negative resistance into the signal resonator.

Unfortunately, the three-frequency amplifier suffers from easily identifiable limitations. Firstly, its gain-bandwidth product is fixed, and it cannot provide high gain over a wide bandwidth, an essential feature for a communications amplifier. Secondly, it provides low-noise amplification at room temperature only if $\omega_I \gg \omega_S$. Both aspects posed problems as signal bandwidths rose in the 1970s. Although frequencies were successfully raised using waveguide components [42, 43], it became increasingly difficult to obtain low noise without cryogenic cooling [44], making it hard for parametric amplifiers to compete with a device with inherently large gain-bandwidth and very high power: the travelling wave tube [45, 46]. The parametric amplifier was therefore subsequently confined to instrument applications, typically in radio astronomy [47, 48].

The efforts made to increase gain-bandwidth largely involved more complicated filters, often arranged as ladder networks and supporting travelling waves [49–51]. Structures of this type should rightly be regarded as the precursors of amplified metamaterials, and may provide the solution to the problem of high propagation loss. A number of attempts have been made to introduce the principles of both two- and three-frequency parametric amplification to metamaterials [52–54]. The aim of this Chapter is to describe the use of parametric amplification of magneto-inductive systems designed for MRI signal detection [55–57].

3.2 Magneto-Inductive Waves and Ring Resonators

We begin by describing simple passive magneto-inductive systems. Figure 3.1a shows a one-dimensional MI waveguide, which consists of a set of capacitively loaded loops, each coupled magnetically to its nearest neighbours. The array has lattice spacing 'a' and is infinitely long.

Figure 3.1b shows the equivalent circuit. The elements are modelled as resonant circuits consisting of a capacitor C, an inductor L and a resistor R (which accounts for loss). Magnetic coupling is modelled as a mutual inductance M. The current I_n in the nth element can be related to the currents I_{n-1} and I_{n+1} in the $n-1$th and $n+1$th elements at angular frequency ω using Kirchhoff's voltage law. In the absence of sources, the result is the recurrence relation [1]:

$$(R + j\omega L + 1/j\omega C)\, I_n + j\omega M(I_{n-1} + I_{n+1}) = 0 \tag{3.1}$$

Equation (3.1) may be solved by assuming travelling wave solutions, in the form $I_n = I_0 \exp(-jnka)$, where k is the propagation constant. These are magneto-inductive current waves. Substitution into 3.1 and cancellation of exponential terms then leads to the MI dispersion equation [2]:

$$\{1 - \omega_0^2/\omega^2 - j/Q\} + \kappa \cos(ka) = 0 \tag{3.2}$$

Here $\omega_0 = 1/\sqrt{LC}$ is the angular resonant frequency of the isolated loops, and $Q = \omega Q_0/\omega$ where $Q_0 = \omega_0 L/R$ is their quality factor. The constant $\kappa = 2M/L$ is the coupling coefficient, and may be positive or negative, depending on whether the loops are arranged in the axial or the planar configuration. In the former case,

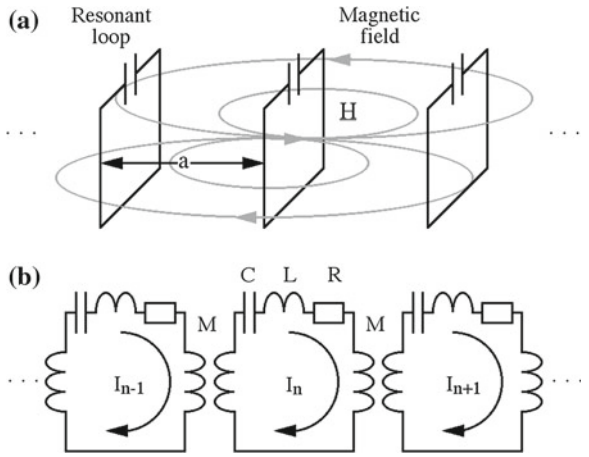

Fig. 3.1 **a** Linear magneto-inductive waveguide, and **b** its equivalent circuit

a forward wave is obtained, and in the latter a backward wave. The propagation constant is generally complex, and can be written as $k = k' - jk''$, where $k'a$ and $k''a$ are the phase shift and attenuation per element, respectively. Equation (3.2) may of course be solved exactly. However when losses are low, we may write:

$$\begin{aligned}(1 - \omega_0^2/\omega^2) + \kappa \cos(k'a) &\approx 0 \\ k''a &\approx 1/\{\kappa Q \sin(k'a)\}\end{aligned} \tag{3.3}$$

The upper equation implies that MI waves can exists over the frequency band $1/(1 + |\kappa|) \leq (\omega/\omega_0)^2 \leq 1/(1 - |\kappa|)$ whose extent depends on the value of κ, and hence on M. The lower equation implies that low losses require Q_0 and κ both to be high. However, the losses are only low near the resonant frequency ω_0 (when $k'a \approx \pi/2$), and they rise rapidly as the band edges ($k'a = 0$ or π) are approached. Higher losses, which require full solution of (3.2), result in lossy propagation outside the band. For backward waves, $k''a$ is negative, and $k''a$ is the attenuation per element.

In practice, the assumption of nearest-neighbour coupling is obeyed only weakly, and non-nearest neighbour coupling is often significant [7]. Such effects may be modelled by introducing additional coupling terms κ_m into (3.2) to obtain the modified dispersion relation

$$\{1 - \omega_0^2/\omega^2 - j/Q\} + \sum_m \kappa_m \cos(mka) = 0 \tag{3.4}$$

Here κ_m is the coupling coefficient between mth nearest neighbours. The primary effect of non-nearest neighbour coupling is clearly to change the dispersion characteristic, although a secondary effect is to introduce higher-order modes. In addition, it significantly complicates design.

In practice, MI waveguides cannot be infinite. However, guides of finite length may be terminated with signal sources and receivers, or connected together to form device structures. One of the simplest MI devices is the ring resonator, shown in Fig. 3.2 [25]. Here a set of N resonant elements (here, 8) is arranged in a polygon. The elements are rectangular, and have their edges placed close together to maximise the magnetic coupling. The ring again supports travelling magneto-inductive waves, which can clearly run around it in either direction. If the phase accumulated in a round trip is a whole number of multiples of 2π, the wave will arrive back at its starting point with its original phase, and the ring will resonate. Under these circumstances we would expect the current to become large if energy is continually injected from an external source.

A suitable source is a magnetic dipole that rotates at the same rate, so that its excitation remains in phase with the MI wave as it propagates around the ring. Precessing nuclear magnetic dipoles in MRI provide exactly suitable sources, and the magneto-inductive ring is clearly analogous to the 'birdcage' body or head coil [58]. The main advantage of the magneto-inductive ring is the lack of rigid connections, which allows it to be flexed to accommodate different imaging subjects [26].

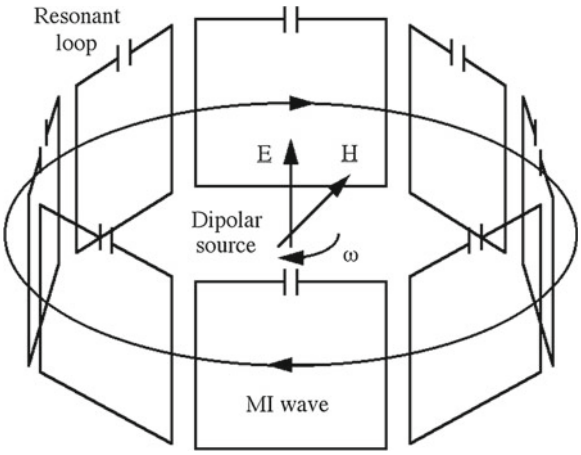

Fig. 3.2 Magneto-inductive ring resonator coupled to a rotating dipole source

Resonant operation requires the wave to satisfy the phase condition:

$$k'Na = 2\mu\pi \tag{3.5}$$

Here μ is an integer known as the mode number. The total number of modes in system of N coupled resonators is nominally also N. However, in a ring, some modes are degenerate and the observable total is therefore lower [59, 60]. For an even number of elements, there are $N/2 + 1$ distinct resonances, whose propagation constants k'_μ are given by:

$$k'_\mu a = 2\mu\pi/N \ (\mu = 0, 1...N/2) \tag{3.6}$$

Once these values of $k'_\mu a$ are known, the corresponding angular frequencies ω_μ may be obtained from the dispersion equation. For low losses, the resonant frequencies may be estimated as:

$$\omega_\mu = \omega_0 / \sqrt{\left\{1 + \sum_m \kappa_m \cos(mk'_\mu a)\right\}} \tag{3.7}$$

In a ring configuration, there will be non-nearest neighbour coupling to the extent that each element is actually coupled to all the others. Furthermore, the signs of the coupling coefficients will alter, depending on the relative orientation and position of the elements concerned. However, the largest coefficient will be between nearest neighbours, and the resonances may therefore be estimated to a reasonable approximation by neglecting all terms except κ_1. For an eight-element ring (for example), the primary resonance ($\mu = 1$) is at $k'_1 a = \pi/4$, and hence has the normalised resonant

frequency $\omega_1 = \omega_0/\sqrt{\left\{1 + \kappa_1/\sqrt{2}\right\}}$. Because the configuration is quasi-planar, κ_1 must be negative and ω_1 therefore lies slightly above ω_0. This resonance may be coupled to a magnetic dipole rotating at the same angular frequency, and hence can be used for detection in MRI. Higher-order resonances require excitation by rotating quadrupoles, hexapoles and so on.

3.3 Parametric Amplification

We now consider how the signal may be amplified, starting with a single resonant element. Figure 3.3 shows a lumped-element three-frequency circuit. Here three L-C resonators operating at signal, idler and pump angular frequencies ω_S, ω_I and ω_P are linked by a non-linear capacitor C. The signal varies harmonically at ω_S, and is assumed to come from a source with output impedance R_{SO}. The pump voltage V_P varies at ω_P and is taken from a source with output impedance R_{P0}. The idler frequency ω_I is assumed to satisfy the mixing law $\omega_P = \omega_S + \omega_I$. The signal resonator contains a capacitor C_S and an inductor L_S with a resistance R_S. The idler and pump resonators are similar L-C-R circuits and their components are subscripted 'I' and 'P'. The varactor capacitance is assumed to follow the first order approximation to a Taylor series expansion of its true C-V characteristic, namely $C = C_1(1 + \beta V_C)$.

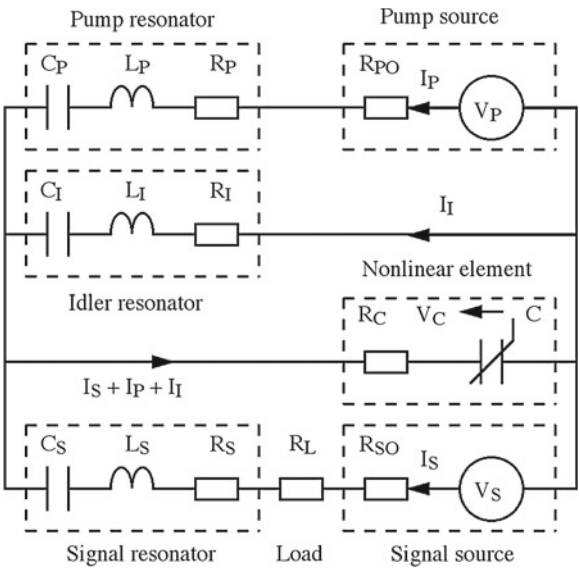

Fig. 3.3 Equivalent circuit of a three-frequency parametric amplifier

Here C_1 and β are constants and V_C is the voltage across C, which has a series resistance R_C. The output signal is measured across a load R_L.

The current in each resonator is assumed only to contain terms oscillating near its resonance while the varactor voltage contains all three frequencies. It is convenient to write the time variation of the signal in the form $V_S = \{v_S \exp(j\omega_S t) + c.c.\}/2$, where 'c.c.' denotes complex conjugate. Writing the other voltages and currents in the same form, we have:

$$\begin{aligned} I_S &= \{i_S \exp(j\omega_S t) + c.c.\}/2 \\ I_I &= \{i_I \exp(j\omega_I t) + c.c.\}/2 \\ I_P &= \{i_P \exp(j\omega_P t) + c.c.\}/2 \\ V_C &= \{v_{CS} \exp(j\omega_S t) + c.c.\}/2 + \{v_{CI} \exp(j\omega_I t) + c.c.\}/2 \\ &\quad + \{v_{CP} \exp(j\omega_P t) + c.c.\}/2 \end{aligned} \tag{3.8}$$

Applying Kirchhoff's voltage law around each of the loops containing the non-linear capacitor and neglecting signals at any other frequencies yields:

$$\begin{aligned} \{1 - \omega_{S0}^2/\omega_s^2 - j/Q_S\} i_S + v_{CS}/j\omega_S L_S &= v_S/j\omega_S L_S \\ \{1 - \omega_{I0}^2/\omega_I^2 - j/Q_I\} i_I + v_{CI}/j\omega_I L_I &= 0 \\ \{1 - \omega_{P0}^2/\omega_P^2 - j/Q_P\} i_P + v_{CP}/j\omega_P L_P &= v_P/j\omega_P L_P \end{aligned} \tag{3.9}$$

Here $\omega_{S0}^2 = 1/L_S C_S$, $\omega_{I0}^2 = 1/L_I C_I$ and $\omega_{P0}^2 = 1/L_P C_P$ are nominal resonant frequencies for the signal, idler and pump resonators. Similarly, $Q_S = \omega_S L_S/R'_S$, $Q_I = \omega_I L_I/R'_I$ and $Q_P = \omega_P L_P/R'_P$ are the corresponding Q-factors, where $R'_S = R_S + R_C + R_{SO} + R_L$, $R'_I = R_I + R_C$ and $R'_P = R_P + R_C + R_{PO}$ are resistances around the three loops. The current through the varactor must obey the relation:

$$I_{Sn} + I_{In} + I_{Pn} = d(CV_C)/dt = C_1(1 + 2\beta V_C) dV_C/dt \tag{3.10}$$

Equating coefficients of exponential terms at frequencies ω_S, ω_I and ω_P separately, making use of the mixing law, and ignoring signals at other frequencies, we obtain:

$$\begin{aligned} i_S &= j\omega_S C_1 \{v_{CS} + \beta v_{CI}^* v_{CP}\} \\ i_I &= j\omega_I C_1 \{v_{CI} + \beta v_{CS}^* v_{CP}\} \\ i_P &= j\omega_P C_1 \{v_{CP} + \beta v_{CS} v_{CI}\} \end{aligned} \tag{3.11}$$

If the signal and idler are weak, the product $v_{CS} v_{CI}$ in the lowest equation may be neglected, so that $v_{CP} \approx i_P/j\omega_P C_1$. Substituting into the lower of (3.9), we obtain:

$$\{1 - \omega_{P0}'^2/\omega_P^2 - j/Q'_P\} i_P = v_P/\omega_P L_P \tag{3.12}$$

Here $\omega'^2_{P0} = (1/L_P)\{1/C_P + 1/C_1\}$ is a modified pump resonant frequency, effectively derived from the inductor L_P and the series combination of C_P and C_1. If the pump frequency is such that $\omega_P = \omega'_{P0}$, we obtain $i_P = v_P/R'_P$ and $v_{CP} \approx v_P/j\omega_P C_1 R'_P$.

Considering now the signal and idler, the upper pair of (3.11) can be re-arranged as:

$$\begin{aligned} v_{CS} &= i_S\alpha/j\omega_S C_1 - i_I^*\alpha\beta v_P/\omega_I\omega_P C_1^2 R'_P \\ v_{CI} &= -i_S^*\alpha\beta v_P/\omega_S\omega_P C_1^2 R'_P + i_I\alpha/j\omega_I C_1 \end{aligned} \tag{3.13}$$

Here $\alpha = 1/[1-\beta^2 v_{CP}v_{CP}^*]$ is of order unity. The upper pair of (3.9) then becomes:

$$\begin{aligned} \{1 - \omega'^2_{S0}/\omega_s^2 - j/Q_S\}i_S - i_I^*\alpha\beta v_P/j\omega_S\omega_I\omega_P L_S C_1^2 R'_P &= v_S/j\omega_S L_S \\ \{1 - \omega'^2_{I0}/\omega_I^2 - j/Q_I\}i_I - i_S^*\beta v_P/j\omega_S\omega_I\omega_P L_I C_1^2 R'_P &= 0 \end{aligned} \tag{3.14}$$

Here $\omega'^2_{S0} = (1/L_S)\{1/C_S + \alpha/C_1\}$ is a modified signal resonant frequency, and $\omega'^2_{I0} = (1/L_I)\{1/C_I + \alpha/C_1\}$ is a similar term for the idler. If the signal and idler frequencies are correctly chosen we can have $\omega_S = \omega'_{S0}$ and $\omega_I = \omega'_{I0}$ and hence

$$i_I = i_S^*\alpha\beta v_P/\omega'_{S0}\omega'_{P0}C_1^2 R'_I R'_P \quad \text{and} \quad i_S = v_S/(R'_S - R_A) \tag{3.15}$$

where R_A is an effective negative resistance, given by:

$$R_A = \alpha^2\beta^2 v_P v_P^*/\omega'_{S0}\omega'_{I0}\omega'^2_{P0}C_1^4 R'_I R'^2_P \tag{3.16}$$

The circuit is therefore a negative resistance amplifier, which uses the power of the pump to decrease the effective resistance of the signal circuit. Since the load voltage is $i_S R_L$, the voltage gain is

$$G = 1/(1 - R_A/R'_S) \tag{3.17}$$

Because R_A contains $v_P v_P^*$, there is no dependence on pump phase. However, low idler and pump resistances are required to achieve useful gain at low pump power.

A reduction in the effective signal resistance will clearly increase the Q-factor of the signal loop. The circuit then becomes extremely sensitive to variations in signal frequency so parametric amplifiers are essentially narrow-band. This is unimportant in MRI. However, because the gain becomes infinite when $R_A = R'_S$, self-oscillation will occur if the device is pumped hard enough. Care must therefore be taken to operate below the oscillation threshold. Pumping may also be viewed as a way to overcome losses in the signal loop. In practice, there are other ways to lose signal than resistive heating. For example, if the component values in the idler and pump loops are poorly chosen, a non-zero current will flow round these loops at the signal frequency. Similarly, some of the pump and idler currents may be diverted from their respective loops. The net effect is to make the previous estimate of R_A inaccurate.

As a result, the gain is often rewritten in terms of the pump power P (which is proportional to $v_P v_P^*$), as:

$$G = 1/(1 - P/P_{osc}) \tag{3.18}$$

Here P_{osc} is the oscillation threshold, which must be determined experimentally.

3.4 Amplification of Magneto-Inductive Waves

We now consider how three-frequency amplification may be introduced into a MI waveguide [55]. All that is required is to alter the circuit of Fig. 3.3 to allow magnetic coupling between elements in a linear array. Figure 3.4a shows one possible unit cell. Here the signal, idler and pump loops have mutual inductances M_S, M_I and M_P to nearest neighbours. This arrangement will clearly allow propagation of signal, idler and pump as separate MI waves, which can mix in varactors. Note that the signal and pump sources have been omitted, together with the load and the varactor resistance.

Analysis can proceed as before. If the signal, pump and idler currents in the nth section are labelled I_{Sn}, I_{In} and I_{Pn} and the voltages across the varactor at the three frequencies are labeled v_{CSn}, v_{CIn} and v_{CPn}, Kirchhoff's law gives:

$$\begin{aligned}
\{1 - \omega_{S0}^2/\omega_s^2 - j/Q_S\}i_{Sn} + (\kappa_s/2)\{i_{Sn-1} + i_{Sn+1}\} + v_{CSn}/j\omega_S L_S &= 0 \\
\{1 - \omega_{I0}^2/\omega_I^2 - j/Q_I\}i_{In} + (\kappa_I/2)\{i_{In-1} + i_{In+1}\} + v_{CIn}/j\omega_I L_I &= 0 \\
\{1 - \omega_{P0}^2/\omega_P^2 - j/Q_P\}i_{Pn} + (\kappa_P/2)\{i_{Pn-1} + i_{Pn+1}\} + v_{CPn}/j\omega_P L_P &= 0
\end{aligned} \tag{3.19}$$

Here $\kappa_S = 2M_S/L_S$, $\kappa_I = 2M_I/L_I$ and $\kappa_P = 2M_P/L_P$ are the magnetic coupling coefficients for the signal, idler and pump. Similarly, for the varactor we now have:

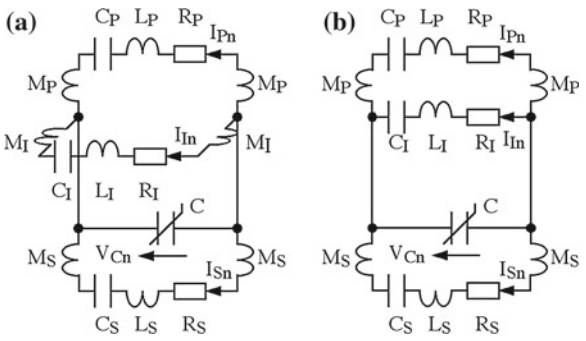

Fig. 3.4 Unit cells for magneto-inductive parametric amplifiers **a** with and **b** without idler coupling

$$
\begin{aligned}
i_{Sn} &= j\omega_S C_1\{v_{CSn} + \beta v_{CIn} * v_{CPn}\} \\
i_{In} &= j\omega_I C_1\{v_{CIn} + \beta v_{CSn} * v_{CPn}\} \\
i_{Pn} &= j\omega_P C_1\{v_{CPn} + \beta v_{CSn} v_{CIn}\}
\end{aligned} \tag{3.20}
$$

If the signal and idler waves are weak, the voltage product in the lowest equation may be neglected as before, so that $v_{CPn} \approx i_{Pn}/j\omega_P C_1$. Substituting into the lowest of 3.19, we obtain a recurrence equation for the pump currents:

$$
\{1 - \omega_{P0}'^2/\omega_P^2 - j/Q_P\} i_{Pn} + (\kappa_P/2)\{i_{Pn-1} + i_{Pn+1}\} = 0 \tag{3.21}
$$

Equation (3.21) simply implies that the pump will propagate as a MI wave. Considering now the signal and idler, the upper pair of 3.20 reduces to:

$$
\begin{aligned}
v_{CSn} &= i_{Sn}\alpha/j\omega_S C_1 - i_{In}^*\alpha\beta i_{Pn}/\omega_I\omega_P C_1^2 \\
v_{CIn} &= -i_{Sn}^*\alpha\beta i_{Pn}/\omega_S\omega_P C_1^2 + i_{In}\alpha/j\omega_I C_1
\end{aligned} \tag{3.22}
$$

Substituting into the upper pair of 3.19 we then get:

$$
\begin{aligned}
&\{1 - \omega_{S0}'^2/\omega_s^2 - j/Q_S\} i_{Sn} + (\kappa_s/2)\{i_{Sn-1} + i_{Sn+1}\} \\
&\quad - i_{In}^*\alpha\beta i_{Pn}/j\omega_S\omega_I\omega_P L_S C_1^2 = 0 \\
&\{1 - \omega_{I0}'^2/\omega_I^2 - j/Q_I\} i_{In} + (\kappa_I/2)\{i_{In-1} + i_{In+1}\} \\
&\quad - i_{Sn}^*\alpha\beta i_{Pn}/j\omega_S\omega_I\omega_P L_I C_1^2 = 0
\end{aligned} \tag{3.23}
$$

If we now assume the signal, idler and pump currents are all MI waves, and can be written as $i_{Sn} = i_S \exp(-jk_S na)$, $i_{In} = i_I \exp(-jk_I na)$ and $i_{Pn} = i_P \exp(-jk_P na)$ where i_S, i_I and i_P are amplitudes and k_S, k_I and k_P are propagation constants, we obtain:

$$
\begin{aligned}
&\left[\{1 - \omega_{S0}'^2/\omega_s^2 - j/Q_S\} + \kappa_s \cos(k_S a)\right] i_S \\
&\quad - i_I^*\alpha\beta i_P \exp\{j(k_S + k_I - k_P)na\}/j\omega_S\omega_I\omega_P L_S C_1^2 = 0 \\
&\left[\{1 - \omega_{I0}'^2/\omega_I^2 + j/Q_I\} + \kappa_I \cos(k_I a)\right] i_I \\
&\quad - i_S^*\alpha\beta i_P \exp\{j(k_S + k_I - k_P)na\}/j\omega_S\omega_I\omega_P L_I C_1^2 = 0
\end{aligned} \tag{3.24}
$$

The exponentials above clearly vanish if $k_P = k_S + k_I$. This relation is a phase matching condition, which always occurs in travelling wave parametric interactions [49]. If the system can be designed so that it holds—by no means an easy matter—and there is also no loss, we get:

$$
\begin{aligned}
&\left[\{1 - \omega_{S0}'^2/\omega_s^2\} + \kappa_s \cos(k_S a)\right] i_S - i_I^*\alpha\beta i_P / j\omega_S\omega_I\omega_P L_S C_1^2 = 0 \\
&[\{1 - \omega_{I0}'^2/\omega_I^2\} + \kappa_I \cos(k_I a)] i_I - i_S^*\alpha\beta i_P / j\omega_S\omega_I\omega_P L_I C_1^2 = 0
\end{aligned} \tag{3.25}
$$

Uncoupling 3.25 we then get

$$\left[\{1-\omega_{S0}'^2/\omega_s^2\}+\kappa_s\cos(k_S a)\right]\left[\{1-\omega_{I0}'^2/\omega_I^2\}+\kappa_I\cos(k_I a)\right]-\gamma^2=0 \quad (3.26)$$

Here $\gamma^2=\alpha^2\beta^2 i_P i_P^*/\omega_S^2\omega_I^2 L_I L_P C_1^4$. To solve this equation, we assume that $k_S=k_{S0}+\Delta k_S$ and $k_I=k_{I0}-\Delta k_S$, where k_{S0} and k_{I0} are the propagation constants obtained in the absence of pumping ($\gamma=0$). Assuming that Δk_S is small, and eliminating terms using the dispersion equations of the signal and idler waves, we get:

$$\Delta k_S=j\gamma/\{\kappa_s\kappa_I\sin(k_{S0}a)\sin(k_{I0}a)\}^{1/2} \quad (3.27)$$

Because Δk_S is imaginary, (3.27) describes a gain coefficient for exponential growth of the signal and idler, the conventional result. Here we have implicitly assumed that κ_S and κ_I have the same sign, so that the group velocities of the two waves are in the same direction. Loss and lack of phase matching both complicate the analysis. For simplicity we omit the details, and simply point out that the results above are typical of standard travelling wave parametric amplifiers.

Instead, we note that the conditions $\omega_P=\omega_S+\omega_I$ and $k_P=k_S+k_I$ will be difficult to satisfy simultaneously, and even more so in a ring when the three waves must be simultaneously resonant. To relax these constraints, we return to (3.23), and consider the case when the idler resonators are uncoupled as shown in Fig. 3.4b, so that $\kappa_I=0$. Now, the lower equation becomes:

$$i_{In}=i_{Sn}^*\alpha\beta i_{Pn}/[j\omega_S\omega_I\omega_P L_I C_1^2\{1-\omega_{I0}'^2/\omega_I^2-j/Q_I\}] \quad (3.28)$$

Assuming now that the idler matches its resonance, so that $\omega_I^2=\omega_{I0}'^2$, the idler currents are simply given by $i_{In}=i_{Sn}^*\alpha\beta i_{Pn}/\omega_S\omega_P R_I' C_1^2$ and the upper equation in (3.23) reduces to:

$$\{1-\omega_{S0}'^2/\omega_s^2-j/Q_{Seff}\}i_{Sn}+(\kappa_s/2)\{i_{Sn-1}+i_{Sn+1}\}=0 \quad (3.29)$$

Here the effective Q-factor of the signal resonators is now $Q_{Seff}=\omega_S L_S/(R_S'-R_B)$, where R_B is again an effective negative resistance, given by:

$$R_B=\alpha^2\beta^2 i_{Pn}i_{Pn}^*/\omega_S'\omega_{I0}'\omega_P'^2 C_1^4 R_I' \quad (3.30)$$

Equation (3.29) is again a recurrence equation for a MI wave, while (3.30) implies that the result of pumping is to decrease the loop resistance, so propagation losses must reduce. The overall system therefore again corresponds to a travelling-wave negative resistance amplifier.

The requirement that $\omega_I=\omega_{I0}'$ clearly renders the Fig. 3.4b less versatile than Fig. 3.4a, in which the idler can exist over a band. However, for a ring detector of MRI signals (whose bandwidths are small) it offers many advantages. The signal and pump need merely be resonant on the lowest ring mode, and the idler operating on

its resonant frequency. Because the amplification is determined by $i_{Pn}i^*_{Pn}$, there is again no dependence on pump phase. There is no need for phase matching, and the group velocities of the pump and signal waves need not even have the same sign.

3.5 Experimental Verification

The theory above has been verified experimentally, using non-magnetic eight-element rings approximately two-thirds the size of a conventional head-coil and designed for detection of ^{1}H MRI signals in a 1.5 T field (at a signal frequency of $f_0 = 63.85$ MHz) [26, 56]. For passive rings, each element is a separate PCB carrying a single-turn rectangular loop inductor measuring 60 mm × 180 mm and formed using 1 mm wide Cu tracks on a FR-4 substrate. The elements are made resonant using surface mount capacitors and mounted in a Perspex frame. Capacitor values (16.5 pF) are established by iteration, to place the individual resonances at $f_0 = \omega_0/2\pi = 53$ MHz and the primary ring resonance at 63.85 MHz. The Q-factor of isolated elements was 130. Mounts are provided for inductive transducers (similar non-resonant loops) to inject and recover signals using an Agilent E50601A electronic network analyser (ENA).

Two transducer arrangements are used, as shown in Fig. 3.5. Using transducers on either side of the ring, as shown in Fig. 3.5a, standing waves may be excited and detected. Here, all modes are probed approximately equally, allowing the spectrum of ring resonances to be identified. Using a rotating dipole source and quadrature taps, as shown in Fig. 3.5b, the important primary travelling mode may be preferentially excited and detected, mimicking signal detection in MRI.

The source is centrally mounted, and constructed from two small inductors at right angles to each other, fed with signals of equal amplitude but 90° phase difference using a quadrature hybrid coupler. The taps are a pair of non-resonant elements, mounted on the ring at right angles with their signals combined using a second quadrature hybrid. In each case, adjustment of the tap spacing allows impedance

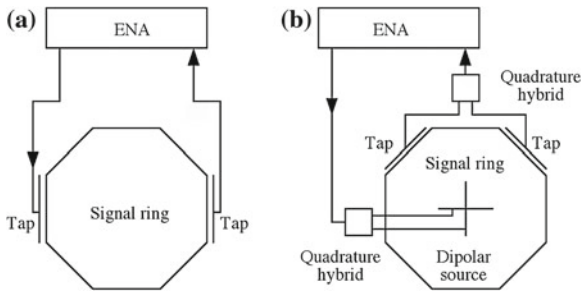

Fig. 3.5 Arrangements for **a** standing-wave and **b** travelling-wave excitation, for an eight-element ring

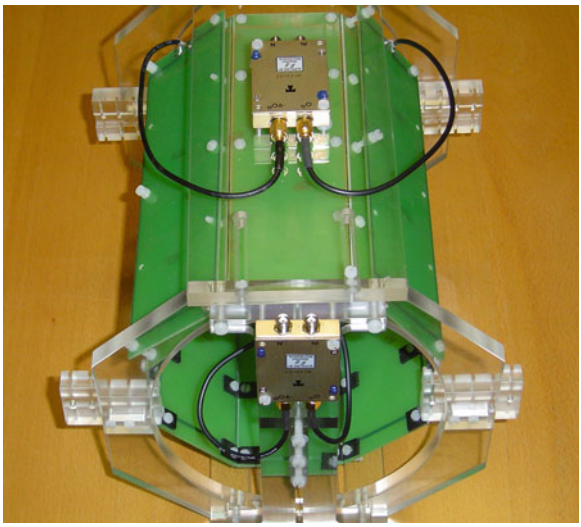

Fig. 3.6 Experimental eight-element ring with quadrature taps and an internal rotating dipole source

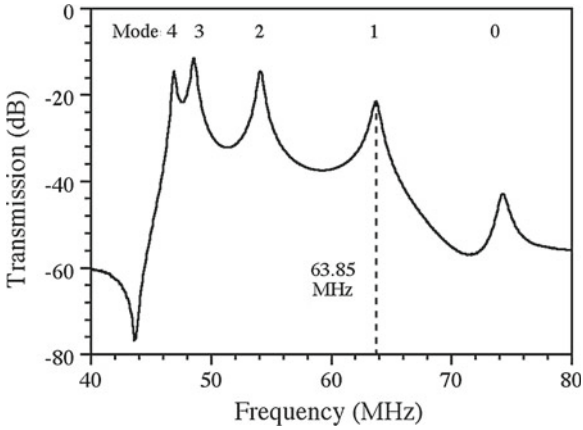

Fig. 3.7 Frequency spectrum of transmission in an eight-element ring, obtained using standing-wave excitation

matching. Figure 3.6 shows the experimental ring, with the rotating dipole source fitted.

Figure 3.7 shows the frequency variation of transmission across the ring using standing-wave excitation. Five sharp resonances may be identified, corresponding to modes with $\mu = 0,1\ldots4$, and the mode with $\mu = 1$ lies at 63.85 MHz as required.

Since the value of $k'a$ for the μth mode is $2\mu\pi/N$, the dispersion diagram may be constructed from the frequency values as shown in Fig. 3.8. Here the discrete

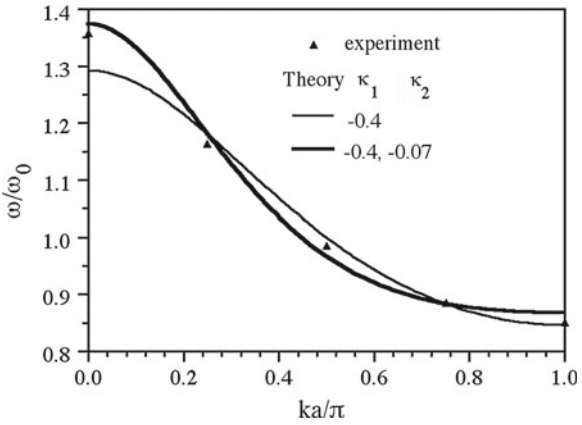

Fig. 3.8 Dispersion characteristic of an eight-element ring. Points are experimental; lines are theoretical, based on 1st neighbour (*thin line*) and 1st and 2nd neighbour (*thick line*) interaction

data points are experimental, while the two lines are theoretical predictions made by inserting the values of f_0 and a set of coupling coefficients κ_m into (3.7). The coefficients may be measured experimentally, by measuring the splitting of resonant frequencies obtained when two elements are mounted together at the correct angle and separation and probed with inductive transducers. In this case nearest- and second-nearest-neighbour coupling coefficients were established as $\kappa_1 = -0.4$ and $\kappa_2 = -0.07$. The thin line (which only takes κ_1 into account) is a poor fit to the data. However the thick line (derived from κ_1 and κ_2) is clearly a more accurate model.

Figure 3.9 shows the corresponding frequency variation with travelling-wave excitation and detection. Now only a single resonance (the primary mode) has significant amplitude, highlighting the modal discrimination inherent in this arrangement.

However, the other modes may still be seen in the frequency variation of reflection, as shown in Fig. 3.10. Thus, a variety of methods may be used to identify the different resonant modes and adjust the circuit parameters to place them in the correct frequency bands.

^{1}H magnetic resonance imaging was demonstrated at 1.5 T using a GE Signa Excite clinical scanner at St Mary's Hospital, Paddington, London. The system body coil was used for excitation, and the MI ring for detection, with quadrature taps. However, modifications were first carried out to de-couple the ring from the large RF magnetic field used for excitation. Firstly, the inductive taps were replaced with capacitive taps. Impedance matching was then carried out, by splitting the capacitors into three components (two for tuning and one for matching). Finally, passive decoupling was introduced by placing an inductor and a pair of crossed diodes across one of the tuning capacitors, to form a diode-switched tank filter designed to block large currents at a set threshold.

One imaging subject was a pomelo (citrus maximus, a sweet grapefruit with a thick pith layer native to South-East Asia) mounted at the centre of the ring, as

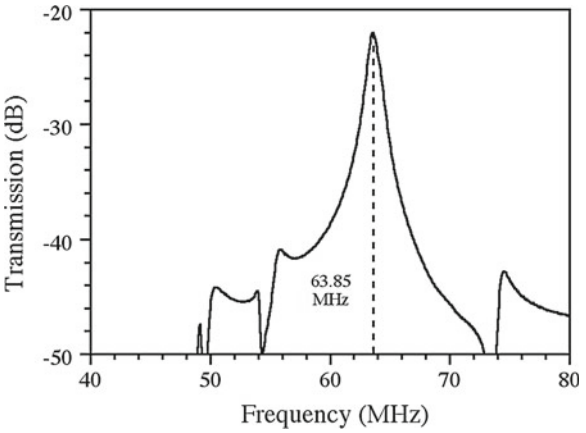

Fig. 3.9 Frequency spectrum of transmission in an eight-element ring obtained using travelling-wave excitation

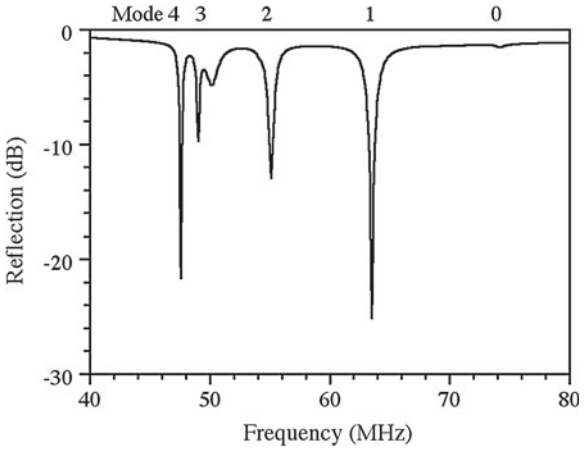

Fig. 3.10 Frequency spectrum of reflection in an eight-element ring obtained using travelling-wave excitation

shown in Fig. 3.11. Imaging was carried out using a fast spin echo sequence, with a repetition time TR = 800 ms, an echo time TE = 90 ms, an echo train length ETL = 15 and a flip angle $\varphi = 90°$. A slice thickness of 4 mm and a slice spacing of 5 mm were used, and the field-of-view was FOV = 200 mm. The number of excitations used to improve signal-to-noise-ratio was NEX = 2. Slice images were obtained with a signal-to-noise ratio of around 30, demonstrating that the MI ring can offer good imaging performance.

Figure 3.12 shows a three-dimensional image of the pomelo reconstructed from a set of axial slices. The outer skin and the inner segmented structure may both be

Fig. 3.11 Eight-element MI ring with a pomelo imaging subject in a clinical MRI scanner

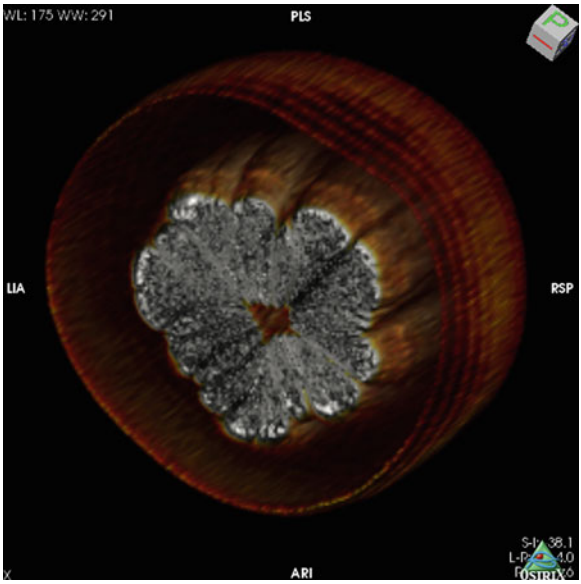

Fig. 3.12 Three-dimensional MR image of a pomelo, reconstructed from two-dimensional slices

clearly seen, while the thick pith (which is largely dry and devoid of signal) appears as a transparent spacer layer between.

The passive MI ring was then converted into a parametrically amplified detector based on the unit cell of Fig. 3.4b. Several major modifications were required. Firstly, the PCBs were modified to add a second inductor measuring 90 mm × 60 mm and an associated tuning capacitor for the pump resonator, so that a pump could also propagate as a MI wave when the ring was assembled. A separate circuit was provided

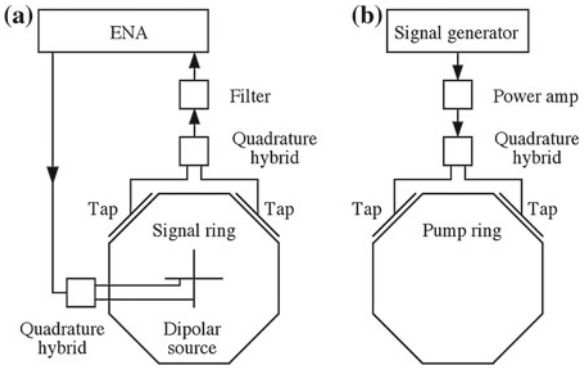

Fig. 3.13 Arrangements for **a** travelling-wave signal excitation and detection and **b** travelling-wave pump excitation, for an eight-element parametrically amplified MI ring

for the idler loop, which used a very small spiral inductor to avoid magnetic coupling between neighbouring elements. The signal, idler and pump loops were arranged to share a varactor (ZC832C, a silicon diode from Zetex Semiconductors), and circuits were provided to reverse-bias each varactor. Separate inductive taps were provided for the signal and pump loops. Figure 3.13a shows the arrangement for insertion and detection of travelling waves into the signal loop and Fig. 3.13b the arrangement for injection of a travelling pump wave using an Agilent N5181A signal generator and a power amplifier.

Figure 3.14 shows the prototype parametrically amplified MI ring. The signal ring is on the left, the pump ring on the right, and the idler and varactor bias circuits lie between. Technical difficulties (parasitic capacitance of individual inductors and unwanted mutual inductance between inductors) made it difficult to adjust the circuit so that the signal, idler and pump were all resonant at appropriate frequencies, without the signal and pump bands overlapping. Compromises were therefore required to obtain a functioning circuit. Particularly, the idler frequency f_I was actually smaller than the signal frequency f_S (a sub-optimal choice for a low noise system). With $f_I \approx 36\,\text{MHz}$, the pump frequency was $f_P = 36 + 63.85 \approx 100\,\text{MHz}$.

Figure 3.15 shows the frequency variation of transmission across the ring, measured using standing-wave excitation. Two sets of data are shown. The thick line shows transmission across the signal ring. Here the signal band resonances previously shown in Fig. 3.7 can again be seen, together with an additional single low-frequency resonance for the idler. Additional features can be seen at high frequency. From the thin line, which shows transmission across the pump ring, it is clear that these are pump band resonances. The nature of these resonances implies that the signal and pump are MI waves, while the idler is not a propagating wave.

Figure 3.16 shows the frequency variation of signal transmission with travelling wave excitation and detection. Two sets of data are shown. The thick line (without pumping) is clearly similar to the passive ring response of Fig. 3.9. The thin line (with a pump signal applied) shows a significant increase in transmission near the

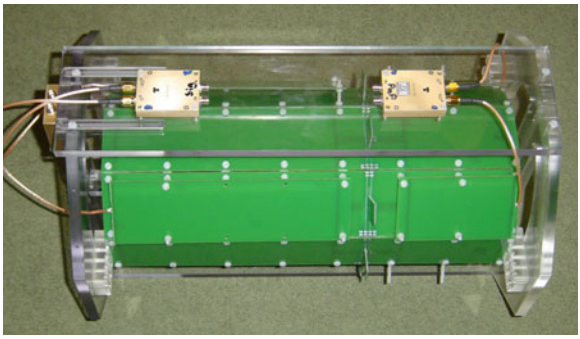

Fig. 3.14 Experimental eight-element parametrically amplified MI ring with quadrature taps

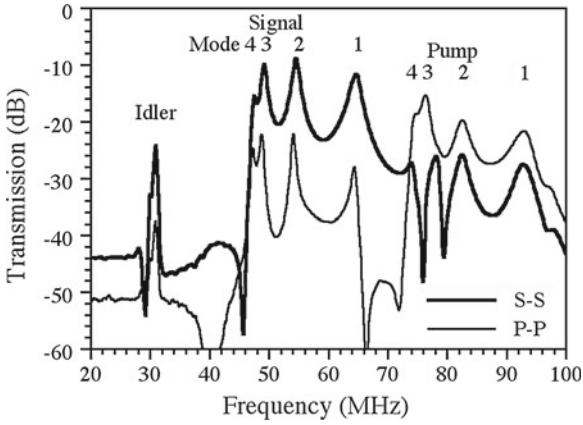

Fig. 3.15 Frequency spectrum of transmission in an eight-element parametrically amplified ring, obtained using standing-wave excitation across the signal (*S*-*S*) and pump rings (*P*-*P*)

important primary resonance. To obtain this data without also detecting the powerful pump, the signal was passed through a band-pass filter centred on the MRI detection frequency. Despite this, some breakthrough of the pump signal can be seen. Crosstalk of this type is a characteristic problem of parametric amplifiers, and some effort must be made to prevent broadcasting of both the pump and idler in a practical system.

Figure 3.17 shows more detailed frequency variations near the primary resonance, at different pump powers. The effect of increasing pump power is clearly to raise the Q-factor of this mode, amplifying the detected signal but reducing the bandwidth in the process. This inherent linkage implies a fixed gain-bandwidth product, a key limitation for parametric amplifiers that was largely responsible for their eventual demise.

Figure 3.18 shows the variation of signal gain with pump power, which shows a rapid rise in power gain from 0 to around 28 dB (corresponding to a linear gain of $G = 25$) near an oscillation threshold of 26.5 mW. These data clearly imply high-gain

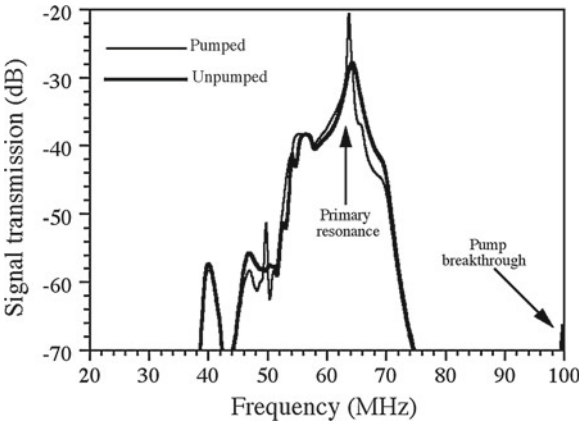

Fig. 3.16 Frequency spectrum of transmission in an eight-element parametrically amplified ring, obtained using travelling-wave excitation, with filtering to suppress the pump

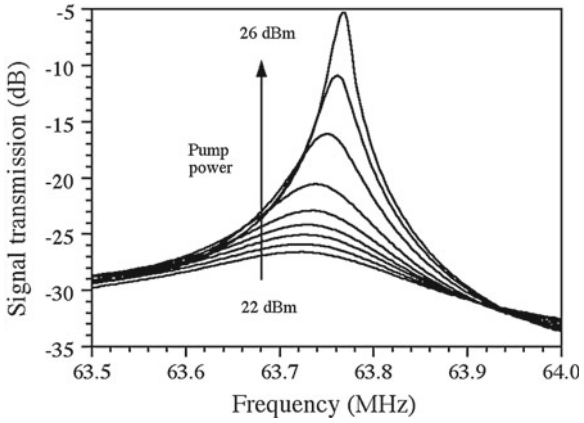

Fig. 3.17 Frequency dependence of signal transmission in eight-element parametrically amplified MI ring, at different pump powers

parametric amplification of a travelling MI signal wave by a similar MI pump wave. The system requires modification to allow decoupling before it can be evaluated in a scanner; however, MR images have already been amplified using single amplifier cells [57] and the necessary work is in progress.

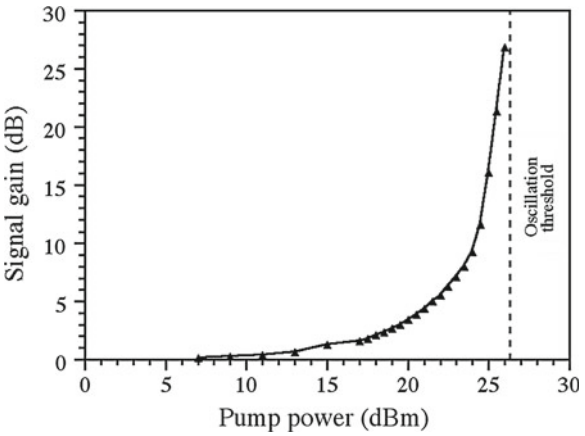

Fig. 3.18 Variation of signal gain with pump power, for an eight-element parametrically amplified ring

3.6 Conclusions

Magneto-inductive waves are slow waves of current that propagate in magnetically coupled L-C resonators. The open structure of MI waveguides makes them particularly suitable for detection of RF magnetic signals in magnetic resonance imaging. However, the low Q-factors of metallic resonators at room temperature limit propagation loss and detection sensitivity. Parametric amplification may provide one answer, and preliminary demonstrations of amplification of MI waves have been carried out using a ring resonator configuration.

The results point the way to more general application of parametric amplification in metamaterials. The main limitations are the design complexity of parametrically amplified networks, the difficulty of obtaining suitable performance from passive components such as inductors at high frequency, the need for very high frequency pumping to obtain low noise, and coupling of the powerful pump into the signal circuit. The last aspect is especially important, since it effectively broadcasts the pump signal. Many of these limitations may be overcome by replacing the simple lumped-element circuits used here with equivalent waveguide components, the solution adopted in the 1960s.

Acknowledgments The Authors are grateful to Dr. Marc Rea for carrying out the MR imaging and Prof. Wady Gedroyc for scanner access, and acknowledge many useful discussions with Dr. Katya Shamonina, Dr. Oleksiy Sydoruk and Dr. Mike Wiltshire.

References

1. E. Shamonina, V.A. Kalinin, K.H. Ringhofer, L. Solymar, Magneto-inductive waveguide. Elect. Lett. **38**, 371–373 (2002)
2. M.C.K. Wiltshire, E. Shamonina, I.R. Young, L. Solymar, Dispersion characteristics of magneto-inductive waves: comparison between theory and experiment. Elect. Lett. **39**, 215–217 (2003)
3. E. Shamonina, V.A. Kalinin, K.H. Ringhofer, L. Solymar, Magnetoinductive waves in one, two, and three dimensions. J. Appl. Phys. **92**, 6252–6261 (2002)
4. E. Shamonina, L. Solymar, Magneto-inductive waves supported by metamaterial elements: components for a one-dimensional waveguide. J. Phys. D Appl. Phys. **37**, 362–367 (2004)
5. R.R.A. Syms, E. Shamonina, L. Solymar, Magneto-inductive waveguide devices. IEE Proc. Microw. Antennas Propag. **153**, 111–121 (2006)
6. R.R.A. Syms, I.R. Young, L. Solymar, Low-loss magneto-inductive waveguides. J. Phys. D Appl. Phys. **39**, 3945–3951 (2006)
7. R.R.A. Syms, O. Sydoruk, E. Shamonina, L. Solymar, Higher order interactions in magneto-inductive waveguides. Metamaterials **1**, 44–51 (2007)
8. S. Maslovski, P. Ikonen, I. Kolmakov, S. Tretyakov, Artificial magnetic materials based on the new magnetic particle: metasolenoid. PIER **54**, 61–81 (2005)
9. M.C.K. Wiltshire, E. Shamonina, I.R. Young, L. Solymar, Experimental and theoretical study of magneto-inductive waves supported by one-dimensional arrays of "Swiss rolls". J. Appl. Phys. **95**, 4488–4493 (2004)
10. A. Radkovskaya, M. Shamonin, C.J. Stevens, G. Faulkner, D.J. Edwards, E. Shamonina, L. Solymar, An experimental study of the properties of magnetoinductive waves in the presence of retardation. J. Magn. Magn. Mater. **300**, 29–32 (2006)
11. I.V. Shadrivov, A.N. Reznik, Y.S. Kivshar, Magnetoinductive waves in arrays of split-ring resonators. Physica B **394**, 180–183 (2007)
12. H. Liu, Y.M. Liu, S.M. Wang, S.N. Zhu, X. Zhang, Coupled magnetic plasmons in metamaterials. Phys. Status Solidi B **246**, 1397–1406 (2009)
13. M. Decker, S. Burger, S. Linden, M. Wegener, Magnetization waves in split-ring resonator arrays: evidence for retardation effects. Phys. Rev. B **80**, 193102 (2009)
14. G. Dolling, M. Wegener, A. Schädle, S. Burger, S. Linden, Observation of magnetization waves in negative-index photonic metamaterials. Appl. Phys. Lett. **89**, 231118 (2006)
15. A. Kurs, A. Karalis, R. Moffatt, J.D. Joannopoulos, P. Fisher, M. Soljacik, Wireless power transfer via strongly coupled magnetic resonances. Science **317**, 83–86 (2007)
16. A.P. Sample, D.A. Meyer, J.R. Smith, Analysis, experimental results, and range adaptation of magnetically coupled resonators for wireless power transfer. IEEE Trans. Industr. Electron. **58**, 544–554 (2011)
17. W.X. Zhong, C.K. Lee, S.Y.R. Hui, Wireless power domino-resonator systems with non-coaxial axes and circular structures. IEEE Trans. Power Electron. **27**, 4750–4762 (2012)
18. Z. Sun, I.F. Akyildiz, Magnetic induction communications for wireless underground sensor networks. IEEE Trans. Antennas Propag. **58**, 2426–2435 (2010)
19. C.J. Stevens, C.W.T. Chan, K. Stamatis, D.J. Edwards, Magnetic metamaterials as 1-D data transfer channels: an application for magneto-inductive waves. IEEE Trans. Microw. Theory Tech. **58**, 1248–1256 (2010)
20. T. Floume, Magneto-inductive conductivity sensors. Metamaterials **5**, 206–217 (2011)
21. M.C.K. Wiltshire, J.B. Pendry, I.R. Young, D.J. Larkman, D.J. Gilderdale, J.V. Hajnal, Microstructured magnetic materials for RF flux guides. Science **291**, 849–851 (2001)
22. M.C.K. Wiltshire, J.V. Hajnal, J.B. Pendry, D.J. Edwards, C.J. Stevens, Metamaterial endoscope for magnetic field transfer: near field imaging with magnetic wires. Opt. Express **11**, 709–714 (2003)
23. M.J. Freire, R. Marques, Planar magnetoinductive lens for three-dimensional subwavelength imaging. Appl. Phys. Lett. **86**, 182505 (2005)

24. M.J. Freire, R. Marques, L. Jelinek, Experimental demonstration of a $\mu = -1$ metamaterial lens for magnetic resonance imaging. Appl. Phys. Lett. **93**, 231108 (2008)
25. L. Solymar, O. Zhuromskyy, O. Sydoruk, E. Shamonina, I.R. Young, R.R.A. Syms, Rotational resonance of magnetoinductive waves: basic concept and application to nuclear magnetic resonance. J. Appl. Phys. **99**, 123908 (2006)
26. R.R.A. Syms, T. Floume, I.R. Young, L. Solymar, M. Rea, Flexible magnetoinductive ring MRI detector: design for invariant nearest neighbour coupling. Metamaterials **4**, 1–14 (2010)
27. R.R.A. Syms, L. Solymar, I.R. Young, Periodic analysis of MR-safe transmission lines. IEEE J. Sel. Top. Quantum Electron. **16**, 433–440 (2010)
28. R.R.A. Syms, I.R. Young, M.M. Ahmad, M. Rea, Magnetic resonance imaging with linear magneto-inductive waveguides. J. Appl. Phys. **112**, 114911 (2012)
29. R.R.A. Syms, I.R. Young, L. Solymar, T. Floume, Thin-film magneto-inductive cables. J. Phys. D Appl. Phys. **43**, 055102 (2010)
30. R.R.A. Syms, L. Solymar, Bends in magneto-inductive waveguides. Metamaterials **4**, 161–169 (2010)
31. R.R.A. Syms, L. Solymar, I.R. Young, Broad-band coupling transducers for magneto-inductive cable. J. Phys. D Appl. Phys. **43**, 285003 (2010)
32. O. Sydoruk, Resistive power divider for magneto-inductive waveguides. Elect. Lett. **47**, 549–550 (2011)
33. R.R.A. Syms, L. Solymar, Magneto-inductive phase shifters and interferometers. Metamaterials **5**, 155–161 (2011)
34. Y. Yuan, B.-I. Popa, S.A. Cummer, Zero loss magnetic metamaterials using powered active unit cells. Opt. Express **17**, 16135–16143 (2009)
35. K.Z. Rajab, Y. Hao, D. Bao, C.G. Parini, J. Vazquez, M. Philippakis, Stability of active magnetoinductive metamaterials. J. Appl. Phys. **108**, 054904 (2010)
36. W.W. Mumford, Some notes on the history of parametric transducers. Proc. IRE **48**, 848–853 (1960)
37. L.A. Blackwell, K.L. Kotzebue, *Semiconductor-Diode Parametric Amplifiers* (Prentice Hall, Englewood Cliffs, 1961)
38. D.P. Howson, R.B. Smith, *Parametric Amplifiers* (McGraw-Hill, New York, 1970)
39. G.A. Klotzbaugh, Phase considerations in degenerate parametric amplifier circuits. Proc. IRE **57**, 1782–1783 (1959)
40. G.L. Matthaei, Experimental verification of the phase relationships in parametric amplifiers. IEEE Trans. Microw. Theory Tech. **MTT–12**, 365–367 (1964)
41. H. Heffner, G. Wade, Gain, bandwidth and noise characteristics of a variable parameter amplifier. J. Appl. Phys. **29**, 1332–1331 (1958)
42. C.S. Aitchison, R. Davies, P.J. Gibson, A simple diode parametric amplifier design for use at S, C and X band. IEEE Trans. Microw. Theory Tech. **MTT–15**, 22–31 (1967)
43. Y. Kinoshita, M. Maeda, An 18 GHz single-tuned parametric amplifier with large gain bandwidth product. IEEE Trans. Microw. Theory Tech. **18**, 409–410 (1970)
44. S. Takahashi, M. Nojima, T. Fukuda, A. Yamada, K-band, cryogenically cooled, wideband nondegenerate parametric amplifier. IEEE Trans. Microw. Theory Tech. **18**, 1176–1178 (1970)
45. J.R. Pierce, Traveling-wave tubes. Proc. IRE **35**, 108–111 (1947)
46. D. Schiffler, J.A. Nation, G.S. Kerslick, A high-power, traveling wave tube amplifier. IEEE Trans. Plasma Sci. **18**, 546–552 (1990)
47. J.T. De Jager, Parametric amplifiers for radio astronomy. Solid State Electron. **4**, 266–270 (1962)
48. M.P. Hughes, E. Moley, D.R. Parenti, J.J. Whelehan, A 5 Gc/s parametric receiver for radio astronomy. IEEE Trans. Antennas Propag. **13**, 432–436 (1965)
49. P.K. Tien, Parametric amplification and frequency mixing in propagating circuits. J. Appl. Phys. **29**, 1347–1357 (1958)
50. P.P. Lombardo, E.W. Sard, Low-frequency prototype traveling-wave reactance amplifier. Proc. IRE **47**, 995–996 (1959)

51. R.C. Honey, F.M.T. Jones, A wide-band UHF traveling-wave variable reactance amplifier. IRE Trans. Microw. Theory Tech. **MTT–8**, 351–361 (1960)
52. M. Lapine, M. Gorkunov, Three-wave coupling of microwaves in metamaterials with nonlinear resonant conductive elements. Phys. Rev. E **70**, 66601 (2004)
53. A.B. Kozyrev, H. Hongjoon Kim, D.W. van der Weide, Parametric amplification in left-handed transmission line media. Appl. Phys. Lett. **88**, 264101 (2006)
54. O. Sydoruk, E. Shamonina, L. Solymar, Parametric amplification in coupled magnetoinductive waveguides. J. Phys. D: Appl. Phys. **40**, 6879–6887 (2007)
55. R.R.A. Syms, I.R. Young, L. Solymar, Three-frequency parametric amplification in magneto-inductive ring resonators. Metamaterials **2**, 122–134 (2008)
56. T. Floume, R.R.A Syms, L. Solymar, M.R. Young, A practical parametric magneto-inductive ring detector, in *Proceedings of the 3rd International Congress on Advanced Electromagnetic Materials in Microwaves and Optics*, London, UK, 30 Aug–4 Sept 2009, pp 132–134
57. R.R.A. Syms, T. Floume, I.R. Young, L. Solymar, M. Rea, Parametric amplification of magnetic resonance images. IEEE Sens. J. **12**, 1836–1845 (2012)
58. C.E. Hayes, W.A. Edelstein, J.F. Schenck, O.M. Mueller, M.J. Eash, An efficient, highly homogeneous radiofrequency coil for whole-body nmr imaging at 1.5T. Magn. Reson. **63**, 622–628 (1985)
59. J. Tropp, The theory of the bird cage resonator. J. Magn. Reson. **82**, 51–62 (1989)
60. M.C. Leifer, Resonant modes of the birdcage coil. J. Magn. Reson. **124**, 51–60 (1997)

Chapter 4
Coupled Electromagnetic and Elastic Dynamics in Metamaterials

David A. Powell, Mingkai Liu and Mikhail Lapine

Abstract Metamaterials are well established in the field of electromagnetism, where they have demonstrated a wide variety of exotic material properties. More recently, mechanical metamaterials have also been shown to be quite promising in achieving exotic properties for acoustic waves. Here we discuss an emerging class of metamaterials with both electromagnetic and elastic properties, which are *coupled to each other*, giving rise to a new range of metamaterial properties. In particular, this can yield a very strong nonlinear response, including bistable states and self-oscillations. We present several structures which exhibit these properties, and experimentally demonstrate their feasibility.

4.1 Introduction

It is now well established that metamaterials can be engineered to provide a wide variety of linear electromagnetic properties, as well as to demonstrate an impressive range of nonlinear effects [1]. Additionally, the idea of metamaterials has also been implemented successfully in acoustic waves [2–10], exploiting the universal physics common to many types of wave propagation. Furthermore, metamaterial concepts have been applied in mechanics, also allowing static mechanical properties to be engineered in new ways [11].

D.A. Powell (✉) · M. Liu
Nonlinear Physics Centre, Research School of Physics and Engineering,
Australian National University, Canberra, ACT 0200, Australia
e-mail: david.a.powell@anu.edu.au

M. Liu
e-mail: Mingkai.Liu@anu.edu.au

M. Lapine
CUDOS, School of Physics, The University of Sydney, Sydney, NSW 2006, Australia
e-mail: mlapine@physics.usyd.edu.au

I.V. Shadrivov et al. (eds.), *Nonlinear, Tunable and Active Metamaterials*,
Springer Series in Materials Science 200, DOI 10.1007/978-3-319-08386-5_4

Here we consider a class of metamaterials which encompasses both electromagnetic and mechanical functionalities. More importantly, these degrees of freedom are coupled to each other, such that the electromagnetic response is sensitive to the mechanical conformation of the structure, and the electromagnetic field also induces significant forces on the structure. This coupling can give rise to two distinct effects. First, manipulation of micro or nano scaled devices by electromagnetic waves can be greatly enhanced. Second, by incorporating some elastic restoring force into the structure, the conformation of the device changes, and this changed conformation modifies the electromagnetic response.

To clarify this, consider the block diagram shown in Fig. 4.1, which compares three different classes of metamaterials. Ordinary materials and the vast majority of electromagnetic metamaterials reported to date fall into the first category (Fig. 4.1a), as they have a response which can be described using only electromagnetic degrees of freedom. This category also includes many nonlinear and tunable metamaterials, where the polarisability may be nonlinear, but can ultimately be reduced to a particular form of material constitutive relations.

The simplest form of coupled electromagnetic and mechanical dynamics is where the electromagnetic forces induce some motion on the structure, Fig. 4.1b. This case is represented by optical tweezers [12], optical motors [13] and wrenches [14]; applications where the ultimate aim is to manipulate mechanical degrees of freedom. In most examples, the external fields dominate the electromagnetically induced forces, although modification of the trapping potential through interaction with a substrate has been reported [15]. We note that in such systems the motion of the structure does effect the electromagnetic response, however the resultant scattered field is not normally considered. While these systems can show a time-varying electromagnetic response due to the mechanical motion, typically the response does not have any of the interesting stationary points which will be shown here.

For the fully coupled case, Fig. 4.1c, an elastic restoring force is introduced into the system. This force opposes the electromagnetic force, allowing the system to reach an equilibrium position. This equilibrium position is determined by the frequency, polarisation and power of the incident field. It also has a strong influence on the electromagnetic response of the structure, with the result that the electromagnetic response of the structure depends on the incident field. Thus the system does not obey superposition with respect to the incident field, and is clearly nonlinear.

Such a nonlinearity arising from coupled dynamics presents an alternative to more conventional methods of introducing nonlinearity through a lumped circuit element or nonlinear optical material. See [16–18] for reviews and other chapters of this book for detailed descriptions of such approaches.

This chapter will give an overview of several metamaterial systems which allow such coupled nonlinear dynamics to occur. Such systems share several similarities with the field of opto-mechanics [19, 20], particularly the interaction between the optical and mechanical degrees of freedom. However the metamaterial approach allows this interaction to be controlled at wavelengths much longer than in optics, and allows the stored energy in near-fields to be manipulated through geometric structuring [21].

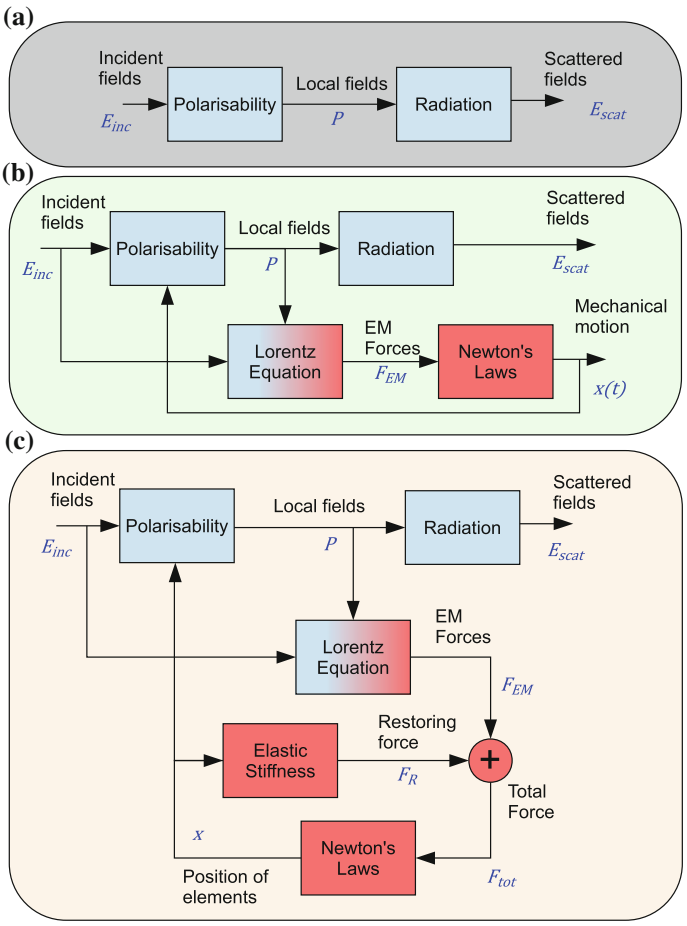

Fig. 4.1 A schematic representation of different physical processes in metamaterials: **a** Those which have a purely electromagnetic response; **b** those which undergo motion due to optical forces and **c** structures where electromagnetic forces are balanced by elastic restoring forces to yield nonlinear coupled dynamics. The quantities in *blue* are representative of those which could be involved in these processes

4.2 Magneto-Elastic Metamaterials

The first conceptual demonstration of coupled electromagnetic and mechanical interactions in metamaterials was with *magneto-elastic metamaterials* [22], as shown in Fig. 4.2. In this configuration, a dense uniaxial array of split ring resonators is immersed into an elastic supporting material. The structure is designed to be excited with an incident plane wave having its magnetic field $\mathbf{H}_0$ perpendicular to the plane of the rings.

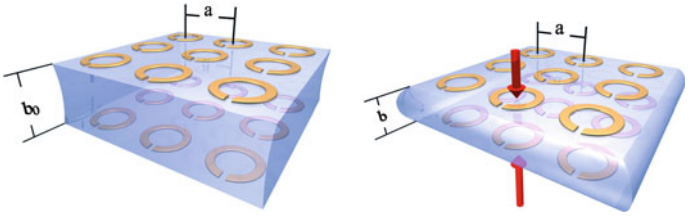

Fig. 4.2 Schematic of anisotropic magnetic metamaterial combined with an elastic medium (reproduced from [22]). Two layers of the bulk sample are shown. *Left* metamaterial before the electromagnetic field is applied. *Right* metamaterial is compressed by the electromagnetic forces acting between the elements. Dimensionless lattice parameters a and b are normalized to the resonator radius r

It is well known that in such a system a substantial fraction of the electromagnetic energy is stored in the fields between the rings, and the response has an essentially collective nature [23] imposed via mutual inductance. The mutual interaction leads to a remarkable shift of the resonance towards lower frequencies, depending on the lattice constants in the array. In addition, there are Ampère forces *between* the rings, being attractive if they are excited in phase. This attractive force is opposed by the stiffness of the material between the rings.

For reasonable levels of input power, the elastic response of the structure must be quite weak in order to observe nonlinear effects. However by utilising metamaterial concepts, not only the electromagnetic, but also the elastic properties of the meta-atoms may be controlled by using an appropriate geometry. Structures such as small springs, wires and filaments can give the necessary compliance. On the basis of theoretical estimates, it seems likely that the required stiffness is not reduced as the structure is scaled to smaller wavelengths, thus leaving open the possibility of observing the effects in THz and optical frequencies.

Since the mechanical response time is many orders of magnitude longer than the electromagnetic response time, it is appropriate to model the electromagnetic response for a slow-varying separation between the rings, without needing to account for the mechanical dynamics. The magnetic interaction force is calculated exactly the same way as for DC currents, and the electric interaction can be suppressed by either the use of small gaps in the rings, utilising a pair of broadside coupled resonators, or by orienting the rings with their gaps perpendicular. To describe the system in metamaterial terms, it is also desirable to have the operating wavelength as large as possible compared to the unit cell size.

An alternative implementation of such a structure has also been demonstrated using a gravitational restoring force [24], where a fine tuning of the mechanical balance of the resonators can provide very high sensitivity. The theoretical basics of the operation of that system are, generally, the same.

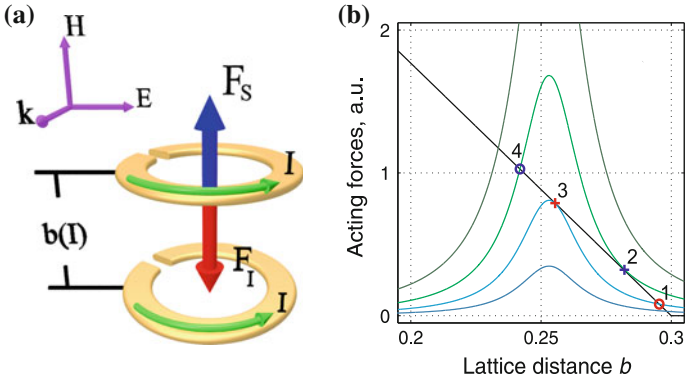

Fig. 4.3 General explanation of magnetoelastic behaviour (reproduced from [22]). **a** Schematic of the forces acting on a ring within a metamaterial, where the total compressing force resulting from current attraction, F_I, is countered by the elastic force F_S, both being dependent on the lattice distance b which varies with the current amplitude; **b** An example of force magnitudes depending on the lattice distance, where attraction forces F_I for several current amplitudes are shown with coloured peaks and the counter-acting spring force F_S with a *black straight line*. Stable equilibrium points are shown with *circles* while unstable ones with *crosses*

4.2.1 Theory

The mechanism for the self action is the mutual interaction between the rings, which depends on the normalised lattice constants a and b. In the quasi-static limit, mutual inductance between all rings in an array can be taken into account via the lattice sum Σ, which depends on the lattice parameters [23]. We then seek the steady-state solution for b which satisfies the balance between the Ampère's force (F_I) and the restoring Hooke force (F_S), with the direction conventions for each force being shown in Fig. 4.3a.

The axially-oriented interaction force between two isolated rings on the same axis can be calculated as [25, 26]

$$F_\mathrm{i} = \frac{\mu_0 I^2}{2\sqrt{4+b^2}} \left(\mathbb{E}(\kappa)\, \frac{2+b^2}{b^2} - \mathbb{K}(\kappa) \right), \tag{4.1}$$

where $\mathbb{E}$ and $\mathbb{K}$ are the complete elliptic integrals of first and second kind with parameter $\kappa^2 = 4/(4+b^2)$ and I is the current amplitude. If the inter-layer lattice constant b is small compared to the lateral lattice constant a, then only rings stacked directly above or below each other need to be taken into account when calculating the total compression force. This greatly simplifies the calculation for any two rings in bulk media, leading to:

$$F_\mathrm{I}(b) \approx \sum_{n=1}^{N} n \cdot F_\mathrm{i}(nb) \approx \frac{\pi}{2}\, \frac{1}{b}\, F_\mathrm{i}. \tag{4.2}$$

In the absence of the external field, the lattice constant will have some initial value b_0. The elastic force will oppose any deviation from this configuration, according to Hooke's law

$$F_{\mathrm{S}}(b) = kr(b - b_0), \tag{4.3}$$

with stiffness constant k and radius r. In practice the force will be linear only over a certain range of positions. For simplicity, we represent this effect in the model by imposing a threshold value $b_{\min}$ which sets a lower limit on the value of b.

The electromagnetic response of the system is determined by the following impedance equation, which includes the electromagnetic interaction between rings, and depends on the lattice constant b and self impedance Z:

$$\left[Z + \mathrm{j}\omega\mu_0 r\,\Sigma(a, b)\right] \cdot I = -\mathrm{j}\omega\pi r^2 \mu_0 H_0. \tag{4.4}$$

This must be combined with the balance condition $F_{\mathrm{I}}(b, I) = F_{\mathrm{S}}(b)$, substituting the expressions for the forces given by (4.2) and (4.3). The solution of these equations yields the lattice constant b and current in the rings I as a function of the amplitude H_0 and frequency ω of the incident magnetic field.

Figure 4.3b gives a graphical picture of the forces as a function of the lattice constant b, with the different curves for F_{I} corresponding to different levels of excitation current. Clearly, the balance condition of the forces corresponds to intersections of F_{I} and F_{S}. However, not all such equilibrium points b_0 are stable. In particular, if there is some perturbation in position δb, we required that the resultant total force is directed towards b_0 in order to have stability. This is equivalent to requiring

$$\frac{\mathrm{d}F_{\mathrm{I}}}{\mathrm{d}b} > \frac{\mathrm{d}F_{\mathrm{S}}}{\mathrm{d}b}. \tag{4.5}$$

From (4.4), we see the resonant behaviour of F_{I} and its dependence on b, which is clearly reflected in Fig. 4.3b.

It is clear that there can either be a single stable state, or three states, one of which will be unstable. Once the current amplitude exceeds a threshold level (shown by cross "2" in Fig. 4.3b), the initial "right-side" equilibrium (such as at circle "1") cannot be achieved, so the lattice constant b will reduce. This changes the mutual interaction dramatically, leading to a significant shift of the resonance frequency, so the current magnitude drops, enabling the system to enter the other equilibrium state (Fig. 4.3, circle "4"), corresponding to the same force curve.

However, if the current amplitude is decreasing, the balance at circle "4" remains stable as long as the peak attractive force is sufficient to counter the elastic force (down to a threshold point, cross "3"), from where the system jumps back to the corresponding "right-side" solution (circle "1").

The magnetisation of the entire metamaterial $M(H_0, \omega)$ can be then calculated as

$$M = I\nu\pi r^2 = \frac{\pi}{ra^2}\,\frac{I}{b}, \tag{4.6}$$

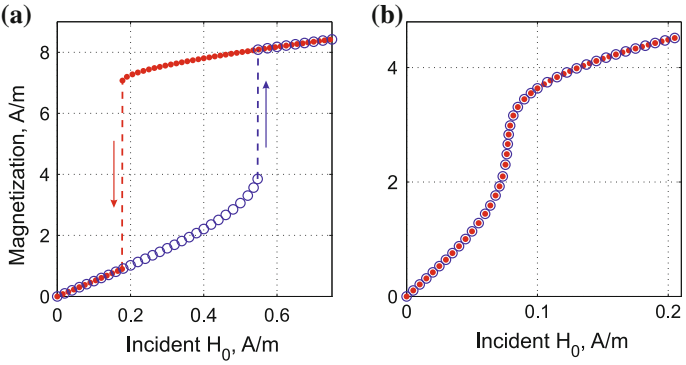

Fig. 4.4 Examples of power dependence of the metamaterial response (reproduced from [22]). Magnetization $M(H_0, \omega)$ in the metamaterial vs. incident amplitude H_0, observed at $\omega = 0.55\omega_0$ (**a**) and $\omega = 0.60\omega_0$ (**b**), for increasing (*blue circles*) and decreasing (*red bullets*) amplitudes. The rings have radius $r = 5\,\text{mm}$, individual resonant frequency of 1 GHz and quality factor of 100. Metamaterial parameters are $a = 4$, $b_0 = 0.3$, $b_{\min} = 0.1$, with a stiffness coefficient $k = 0.44\,\text{mN/m}$

and shows a stronger dependence on the lattice constant b compared to that of the current I, thanks to the explicit effect of the volumetric density $\nu = 1/(r_0^3 a^2 b)$.

Thus, the nonlinear magnetisation can be characterised as a function of the amplitude and frequency of the incident field (Fig. 4.4). Here the case of fixed frequency is discussed, noting that even more exotic regimes can be found, including inaccessible regimes of bistability, if the incident field amplitude is fixed while the frequency is varied [27].

At frequencies lower than the eigenfrequency of the initial state, a slightly nonlinear $M(H_0)$ dependence is observed as the amplitude grows, until the metamaterial abruptly switches to a stronger compression. However, when the amplitude is decreased, the metamaterial remains in the compressed state until much lower magnitudes, exhibiting a hysteresis-like behaviour (Fig. 4.4a). But close to the original resonance, the hysteresis disappears while the nonlinearity is quite strong (Fig. 4.4b).

4.2.2 Experimental Demonstration

To demonstrate that these nonlinear effects are realistic, experiments were conducted for three pairs of elastically coupled resonators, where there is coupling within pairs but not between them. The governing equations for such a system are the similar to those for the bulk, except that the lattice sum Σ is replaced with the mutual coupling over the finite-sized sample, and the volumetric enhancement as in (4.2) is not available.

Each ring is attached to a thin layer of cellulose acetate to ensure mechanical stability and to prevent thermal expansion. A control experiment with a single ring

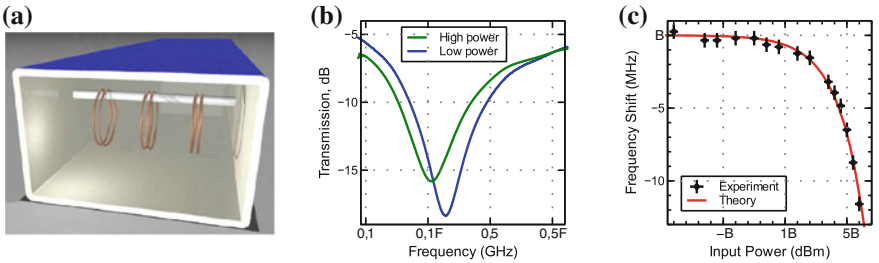

Fig. 4.5 Experimental observation of the magnetoelastic nonlinearity in a system of three elastic pairs within a WR229 rectangular waveguide (reproduced from [22]). **a** experimental layout; **b** measured transmission spectra at low (−12.3 dBm) and high (29 dBm) power; **c** dependence of the resonance frequency on the incident power, showing the experimental (*circles with error bars*) and theoretical (*solid line*) results. The rings are made from 0.18 mm-thick copper wire and have 3 mm radius and ∼1 mm gap

(not shown) detected no noticeable change in response with incident power. Thus it is safe to assume that the measured response is entirely due to interaction between the rings.

The rings are suspended from a dielectric rod with grooves to control their initial spacing with $b_0 = 0.3r$, Fig. 4.5a. When the attractive Ampère force is induced, the rings are able to swing towards each other. The opposing Hooke's force is created by thin keratin filaments placed between the rings within each pair.

Figure 4.5b shows the spectra measured in the linear regime (−12.3 dBm incident power), and near the maximum (29 dBm incident power). It is seen that the resonance experiences a shift which is comparable to the width of the resonance. Figure 4.5c shows the shift of the resonant frequency as a function of the applied power, achieving a maximum frequency shift of 13 MHz. For comparison purposes the theoretical curve is also shown, obtained with the corresponding parameters and assuming a stiffness coefficient of 0.13 ± 0.01 N/m. The contribution of gravity to the restoring force (due to the inclination of the rings) is also taken into account, amounting to around 20 % at the maximum power level.

4.3 Torsional System

While the magneto-elastic system is very promising for showing strong nonlinearity due to coupled electromagnetic and mechanical degrees of freedom, achieving a sufficiently compliant mechanical restoring force is a significant challenge. To overcome this disadvantage, it was proposed that instead of utilising compressional forces between rings, rotational forces are utilised. We denote these torsional structures as *nonlinear metamaterials with intrinsic rotation* [28].

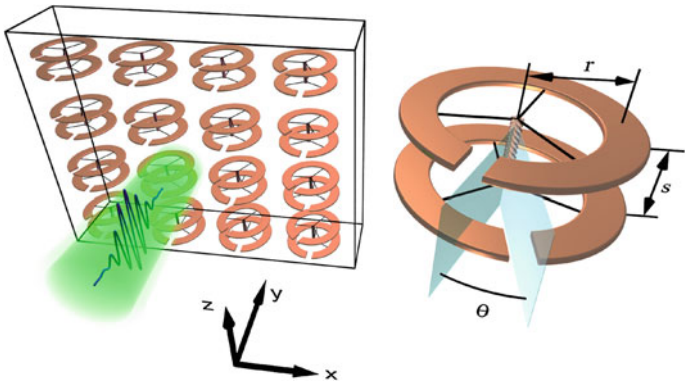

Fig. 4.6 Conceptual layout of a new metamaterial and its rotational "meta-atom" (reproduced from [28]). The incident wave propagates along the y direction, having a linear polarisation with the electric field along x and magnetic field along z. The induced electromagnetic torque between the resonators changes the mutual twist angle θ between the rings, connected by an elastic wire

The idea here is to employ a rotational degree of freedom, having two or more non-symmetric resonators free to rotate around a common axis against an elastic feedback. Such rotation will affect the electromagnetic modes of the system and therefore change the distribution and amplitudes of the induced charges and currents, altering the electromagnetic forces which drive the mutual rotation.

An example of experimental realisation is shown in Fig. 4.6: a pair of split rings is arranged coaxially and allowed to rotate about a common axis. The elastic feedback is provided by a thin elastic wire connecting the two rings. The electromagnetic *torque* is used to drive the meta-atom, modulating the resonant frequencies by changing the internal rotation of the system. The major advantage of this system is that the effective lever arm of the electromagnetic force can be much stronger than that of the restoring force. Compared to collinear forces, this can lead to deformation which is enhanced by several orders of magnitude.

For simplicity, it is assumed that one of the rings is fixed to a substrate, and the other is suspended from above by a wire. This ring is connected to the wire by three shorter wires, arranged to provide a stable orientation of the suspended ring and prevent it from tilting. The result is that only rotation of the ring about its axis is permitted, and all other motional degrees of freedom can be neglected.

As we see from Fig. 4.6, the rings start out with some angle between their slits, which is a design parameter of the system. An incoming electromagnetic wave then induces charges and currents on the rings, and the angle between the rings and the spacing between them will determine the hybridised resonant frequencies of the meta-atom [29]. For fixed excitation strength, the energy stored in this system varies with the angle of twist, and the rings will tend to seek the equilibrium angles with

minimum energy. At any non-equilibrium angle, the rings will experience a torque, with magnitude and direction dependent on the angle, the mode(s) excited in the ring and the incident field strength [30].

The addition of the elastic wire introduces a restoring torque which opposes the electromagnetic torque, and the equilibrium twist angle then depends on the balance between the two. The design has an additional degree of freedom in choosing the initial angle between the rings of the unexcited system. This will determine which electromagnetic mode dominates the response of the system, which then determines the strength and direction of the torque.

This torsional design therefore offers a tunable approach to achieving strong nonlinearity in metamaterials, with a response much stronger than that provided by lumped nonlinear circuit elements. We will show that this leads to a very strong bistable response which can be observed experimentally.

4.3.1 Theoretical Treatment

For a single isolated meta-atom a semi-analytical model is utilised. Figure 4.6 shows the two coaxial SRRs, separated by a distance s in the z direction, with angle θ between the gaps. The incident wave propagates along y, with the electric field polarised along x. The angle Φ describes the orientation of the gap of the bottom ring relative to the electric field.

The currents on each ring are approximated by a single mode, and the near-field interaction between them is calculated by integrating the Green's function over both rings to find the mutual impedance between them [29]. This model gives quite good accuracy for the electromagnetic properties of such meta-atoms [30]. For simplicity, the simulation is done with perfect electric conductor as the material for the SRRs, so only the radiative component of the electromagnetic force is taken into account.

The current $\mathbf{J}$ and charge ρ on a meta-atom can be represented by a spatial distribution $\mathbf{j}(\mathbf{r})$, the magnitude and phase of which is described by a frequency dependent scalar $Q(\omega)$, with an assumed $\exp(-i\omega t)$ time dependence [31]

$$\mathbf{J}(\mathbf{r},\omega) = -i\omega Q(\omega)\mathbf{j}(\mathbf{r}), \quad \rho(\mathbf{r},\omega) = Q(\omega)q(\mathbf{r}), \quad q(\mathbf{r}) = -\nabla\cdot\mathbf{j}(\mathbf{r}). \tag{4.7}$$

For a pair of rings this leads to coupled equations for the mode amplitudes $Q_{1,2}$:

$$Q_1 = (\mathscr{E}_2 Z_\mathrm{m} - \mathscr{E}_1 Z_\mathrm{s})/(Z_\mathrm{s}^2 - Z_\mathrm{m}^2), \quad Q_2 = (\mathscr{E}_1 Z_\mathrm{m} - \mathscr{E}_2 Z_\mathrm{s})/(Z_\mathrm{s}^2 - Z_\mathrm{m}^2), \tag{4.8}$$

where $\mathscr{E}_1$ and $\mathscr{E}_2$ represent the overlap of the incident electric field with the mode of each ring, which for plane-wave incidence can be quite accurately calculated as

$$\mathscr{E}_1 = -\mathbf{E}_{\text{ext}} \cdot \mathbf{l}_{\text{e}} \cdot e^{ik_0 a_{\text{E}} \cos \Phi} + j\omega \mathbf{B}_{\text{ext}} \cdot \mathbf{u}_{\text{e}} \cdot e^{ik_0 a_{\text{M}} \cos \Phi}, \tag{4.9}$$

$$\mathscr{E}_2 = -\mathbf{E}_{\text{ext}} \cdot \mathbf{l}_{\text{e}} \cdot e^{ik_0 a_{\text{E}} \cos(\Phi+\theta)} + j\omega \mathbf{B}_{\text{ext}} \cdot \mathbf{u}_{\text{e}} \cdot e^{ik_0 a_{\text{M}} \cos(\Phi+\theta)}, \tag{4.10}$$

where a dipole approximation is used with the normalised electric $\mathbf{l}_{\text{e}}(\theta, \Phi) = \int_V q(\mathbf{r})\mathbf{r}\mathrm{d}V$, and magnetic $\mathbf{u}_{\text{e}}(\theta, \Phi) = \frac{1}{2}\int_V \mathbf{r} \times \mathbf{j}(\mathbf{r})\mathrm{d}V$ dipole moments.

The effective central positions of the electric and magnetic dipoles are

$$a_{\text{E}} = \frac{\int_V [q(\mathbf{r}_1)\mathbf{r}_1 \cdot \hat{\mathbf{x}}](\mathbf{r}_1 \cdot \hat{\mathbf{y}})\mathrm{d}V_1}{\left|\int_V q(\mathbf{r}_1)\mathbf{r}_1 \mathrm{d}V_1\right|}, \quad a_{\text{M}} = \frac{\int_V [\mathbf{r}_1 \times \mathbf{j}(\mathbf{r}_1) \cdot \hat{z}](\mathbf{r}_1 \cdot \hat{\mathbf{y}})\mathrm{d}V_1}{\left|\int_V \mathbf{r}_1 \times \mathbf{j}(\mathbf{r}_1)\mathrm{d}V_1\right|}, \tag{4.11}$$

similar to the definition of centre of mass, and they are calculated based on the charge and current distributions of the lower SRR when $\Phi = 0$.

The phase term in coupling to the external field is due to the retardation experienced by the wave before reaching the SRRs. The self impedance Z_{s} and mutual impedance Z_{m} are given by

$$Z_{\text{s}} = \mathrm{i}/\omega C_{\text{s}} - \mathrm{i}\omega L_{\text{s}}, \quad Z_{\text{m}} = \mathrm{i}/\omega C_{\text{m}} - \mathrm{i}\omega L_{\text{m}}, \tag{4.12}$$

where the effective capacitances C and inductances L can be calculated from the modal current $\mathbf{j}(\mathbf{r})$ and charge $q(\mathbf{r})$ distributions (see [31]).

After the mode amplitudes Q are found, the torque between the meta-atoms can be calculated. Since the bottom ring is fixed, while the top ring is allowed to rotate about the z axis, the torque on the top ring is of interest:

$$\mathbf{M}_{\text{EM}} = \int_{V_2} \rho(\mathbf{r}_2)\mathbf{r}_2 \times \mathbf{E} + \mathbf{r}_2 \times [\mathbf{J}(\mathbf{r}_2) \times \mathbf{B}]\mathrm{d}V_2, \tag{4.13}$$

where the integration is performed over the volume V_2 of the top SRR.

It is convenient to split the torque into two physically distinct components, being the external torque $\mathbf{M}_{\text{ext}}$ due to the impinging field [30] and the internal torque $\mathbf{M}_{\text{int}}$ which the excited rings exert upon each other. When the ring rotates about the geometry centre, the magnetic part of the torque does not contribute to the torque in the z direction. The explicit expressions for the external and internal torque are:

$$\begin{aligned}\mathbf{M}_{\text{ext},2} &= \frac{1}{2}\mathrm{Re}\left[\int_{V_2} \rho^*(\mathbf{r}_2)\mathbf{r}_2 \times \mathbf{E}_{\text{ext}}\mathrm{d}V_2\right] \\ &= -\frac{1}{2}\mathrm{Re}\left[Q_2^*(\omega, \Phi)e^{jk_0 a_{\text{E}} \cos(\Phi+\theta)}\right]\mathbf{E}_{\text{ext}} \cdot \mathbf{l}_{\text{e}} \sin(\Phi + \theta) \cdot \hat{z}, \end{aligned} \tag{4.14}$$

$$\mathbf{M}_{\text{int},2} = \frac{1}{2}\mathrm{Re}\left[\int_{V_2} \rho^*(\mathbf{r}_2)\mathbf{r}_2 \times \mathbf{E}_{\text{int}}(\mathbf{r}_2)\mathrm{d}V_2\right], \tag{4.15}$$

with the internal field component given by

$$\begin{aligned}\mathbf{E}_{\text{int}}(\mathbf{r}_2) &= -\nabla\phi(\mathbf{r}_2) - \frac{\partial}{\partial t}\mathbf{A}(\mathbf{r}_2) \\ &= -\int_{V_1} \nabla\frac{\rho(\mathbf{r}_1)e^{ik|\mathbf{r}_2-\mathbf{r}_1|}}{4\pi\epsilon_0|\mathbf{r}_2-\mathbf{r}_1|} + \frac{\partial}{\partial t}\frac{\mathbf{J}(\mathbf{r}_1)e^{ik|\mathbf{r}_2-\mathbf{r}_1|}}{4\pi c^2\epsilon_0|\mathbf{r}_2-\mathbf{r}_1|}\mathrm{d}V_1. \end{aligned} \tag{4.16}$$

This yields the following expression for the internal torque

$$\begin{aligned}\mathbf{M}_{\text{int},2} = \frac{1}{2}\text{Re}\Bigg\{ &\frac{Q_1(\omega)Q_2^*(\omega)}{4\pi\epsilon_0}\int\int\frac{q^*(\mathbf{r}_2)e^{ik|\mathbf{r}_1-\mathbf{r}_2|}}{|\mathbf{r}_1-\mathbf{r}_2|} \\ &\times\left[\frac{1-ik|\mathbf{r}_1-\mathbf{r}_2|}{|\mathbf{r}_1-\mathbf{r}_2|^2}q(\mathbf{r}_1)\mathbf{r}_1\times\mathbf{r}_2 + k^2\mathbf{r}_2\times\mathbf{j}(\mathbf{r}_1)\right]\mathrm{d}V_1\mathrm{d}V_2\Bigg\}. \end{aligned} \tag{4.17}$$

The elastic wire on which the SRR is suspended provides a restoring torque

$$M_{\text{R}} = -\pi a^4 G(\theta-\theta_0)/(2d), \tag{4.18}$$

where a and d are the radius and the length of the wire, respectively, G is the shear modulus and θ_0 is the initial twist angle of the structure. The system will be at equilibrium when the total torque is zero

$$M_{\text{EM}}(\theta, P_{\text{I}}) + M_{\text{R}}(\theta, \theta_0) = 0. \tag{4.19}$$

4.3.2 Numerical Results

To illustrate the rotational nonlinearity, the above model was applied to a specific pair of twisted SRRs, with radius $r = 6\,\text{mm}$ and vertical spacing $s = 2\,\text{mm}$. The gap in each ring is expressed in angular form as $\alpha_0 = 10°$. The elastic coupling is provided with a wire of radius $a = 50\,\mu\text{m}$ and of length $d = 100\,\text{mm}$, made from rubber with a shear modulus of $G = 0.6\,\text{MPa}$.

The resulting mode amplitude Q_2 and the total electromagnetic torque $\mathbf{M}_{\text{EM}} = \mathbf{M}_{\text{ext}} + \mathbf{M}_{\text{int}}$ experienced by the top SRR as functions of frequency and twist angle θ, are plotted in Fig. 4.7a, b respectively. A complication is that the angle Φ between the bottom ring and the external field polarisation changes the strength of excitation of the meta-atoms. However, physically important quantities such as the direction of the electromagnetic torque are independent of Φ, since they depend only on the mode profile and symmetry, thus we only consider the case $\Phi = 0$.

The model takes into account radiation losses [31], thus the line shapes of the mode amplitudes and their resonances are well described. This structure supports

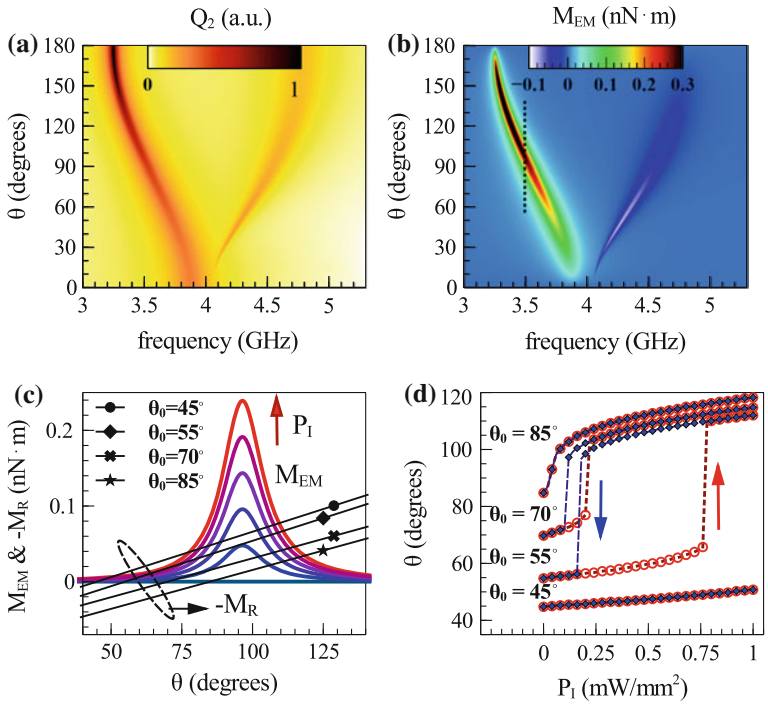

Fig. 4.7 Nonlinear response in rotatable meta-atoms (reproduced from [28]). **a** The mode amplitude Q_2 and **b** the electromagnetic torque $\mathbf{M}_{\mathrm{EM}}$ of the top rotatable ring. **c** The electromagnetic torque at 3.5 GHz for different pump powers from 0 to 1 mW/mm^2 in 0.2 mW/mm^2 steps, and the restoring torque for different initial twist angle θ_0; **d** the corresponding paths of power-dependent twist angles under different θ_0

two hybridised resonances, which are denoted the symmetric $Q_1 = Q_2$ and anti-symmetric $Q_1 = -Q_2$ modes [29] (in terms of fields we can consider this to be the symmetry of the magnetic dipole moments). The phase difference between these two modal excitations results in opposite directions of the electromagnetic torque.

If the rings are excited symmetrically, the configuration $\theta = 0°$ corresponds to the electric dipole moments being parallel to each other, thus they tend to repel, with the lowest energy state being $\theta = 180°$ in the absence of mechanical restoring torque. For the anti-symmetric mode, the opposite orientations of the currents mean that $\theta = 180°$ becomes unstable and $\theta = 0°$ is stable. The evaluated external torque is about one order of magnitude smaller than the internal torque, and the total torque is of the order of 10^{-10} Nm when the structure is pumped with a power density $P_{\mathrm{I}} = 1\,\mathrm{mW/mm^2}$. These modelling results are validated by numerical solution of Maxwell's equations (using CST Microwave Studio), followed by a surface integral of the Maxwell stress tensor to find the induced torque.

Figure 4.7c shows the electromagnetic and mechanical torques which oppose each other to yield the equilibrium. The chosen pump frequency of 3.5 GHz (denoted by the black dashed line in Fig. 4.7b) corresponds to excitation of the symmetric mode.

Analogous to the balance of forces within the magneto-elastic system, shown in Fig. 4.3a, $\mathbf{M}_{\mathrm{EM}}$ is a Lorentz-like function of the twist angle, while the restoring torques $\mathbf{M}_{\mathrm{R}}$ under different initial twist angles θ_0 are approximated by linear functions. The intersections of these two functions given by (4.19) correspond to the equilibrium angles θ_e. However, stable solutions for the angles must satisfy

$$\frac{\partial}{\partial\theta}\left[\mathbf{M}_{\mathrm{EM}}(\theta)+\mathbf{M}_{\mathrm{R}}(\theta)\right]\Big|_{\theta=\theta_e}<0. \tag{4.20}$$

The twist angle as a function of pump power is depicted in Fig. 4.7d, where the power is increased then decreased to reveal bistable behaviour. We see the evolution from smooth nonlinear to bistable response as θ_0 departs from the angle of maximum electromagnetic torque. In principle, as θ_0 moves further away from the resonance, more noticeable rotation and hysteresis effects are expected, but higher pump power is required (see the case for $\theta_0 = 45°$). Such evolution of the power-dependent nonlinear response can also be observed by fixing the initial twist angle but changing the pump frequency, as will be demonstrated by experiments.

4.3.3 Experimental Verification

The nonlinear response of these torsional structures is verified by performing pump-probe experiments at microwave frequencies. The critical parameter to allow a strong response to be observed is the restoring torque provided by the wire, which must be small enough to allow strong rotation of the structure for a reasonable level of input power.

The experimental confirmation was performed with the split rings having inner radius $r = 3.2$ mm, track width 1 mm, copper thickness 0.035 μm and slit width $g = 0.2$ mm and are printed on Rogers R4003 substrates with $\epsilon_{\mathrm{r}} = 3.5$, loss tangent 0.0027, substrate thickness 0.5 mm. The pair of SRRs is placed within WR229 rectangular waveguide, with the lower SRR in the centre, fixed at the angle $\Phi = 0°$, and the upper SRR suspended 0.75 mm above the lower by the rubber wire (radius $a = 50$ μm, length $d = 20$ mm) such that it is free to rotate. Care is taken to ensure that the SRRs are aligned with each other, and the twist angle of the unexcited structure is fixed at approximately 70°. The shear modulus of the material $G \approx 0.69$ MPa was assessed by measuring the Young's modulus, estimated as 2.06 MPa through the elongation of the wire due to loading by the sample.

The difference between the pump frequency and the linear resonance is a critical parameter in determining the nonlinear behaviour observed. The pump power is swept in 1 dB steps, with the system allowed to reach steady state before measurement. This takes approximately 30 s due to the low mechanical damping of the system, and if the

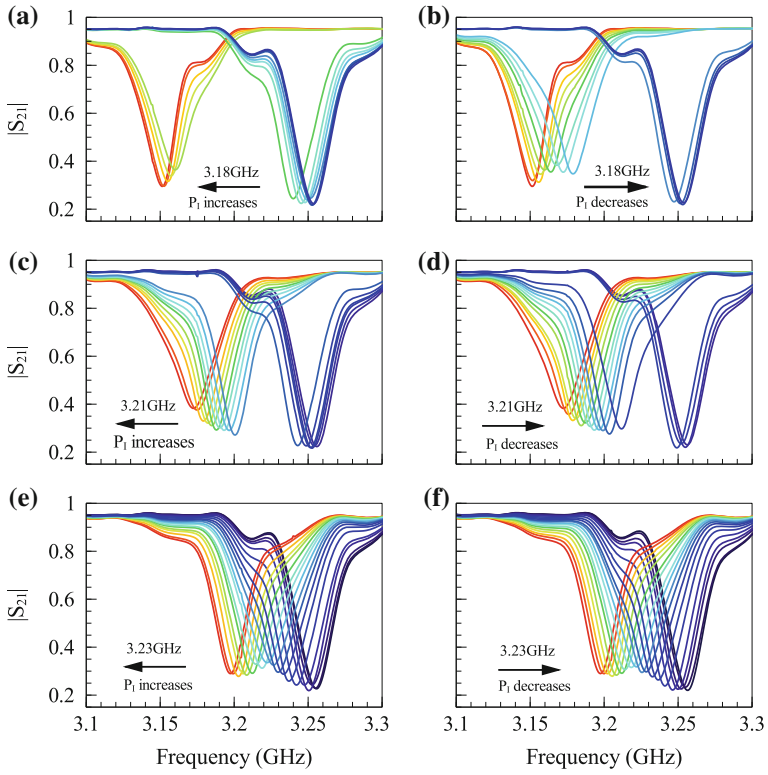

Fig. 4.8 Experimental transmission coefficients $|S_{21}|$ for different pump frequencies and powers (reproduced from [28]). The initial resonance locates around 3.256 GHz and the pump power is swept in 1 dB steps. **a** and **b** pump at 3.18 GHz, power changes from 15.2 to 27.2 dBm; **c** and **d** pump at 3.21 GHz, power changes from 12.2 to 27.2 dBm; **d** and **e** pump at 3.23 GHz, power changes from 15.2 to 27.2 dBm

system is opened it is possible to observe the oscillating rotation of the structure due to the change in incident power. This rules out other mechanisms for the observed nonlinear behaviour, such as thermal expansion.

Figure 4.8 shows the transmission spectra found in experiment, with the extracted resonant frequencies shown in Fig. 4.9a, c and e. It can be clearly seen that the system changes from bistable behaviour to a smooth nonlinearity. The initial resonance (symmetric mode) without the pump is located around 3.256 GHz, and it red-shifts as the pump power increases, which indicates that the twist angle is increased. When the pump frequency is at the red tail of the resonance, a large spectral "jump" (about three times the resonance linewidth) is observed when the pump power passes a certain threshold (Fig. 4.9a). The thresholds are different for increasing and decreasing pump powers. As the pump frequency approaches the initial resonance, the spectral "jump" becomes smaller (Fig. 4.9c) and finally disappears (Fig. 4.9e). Similar effects

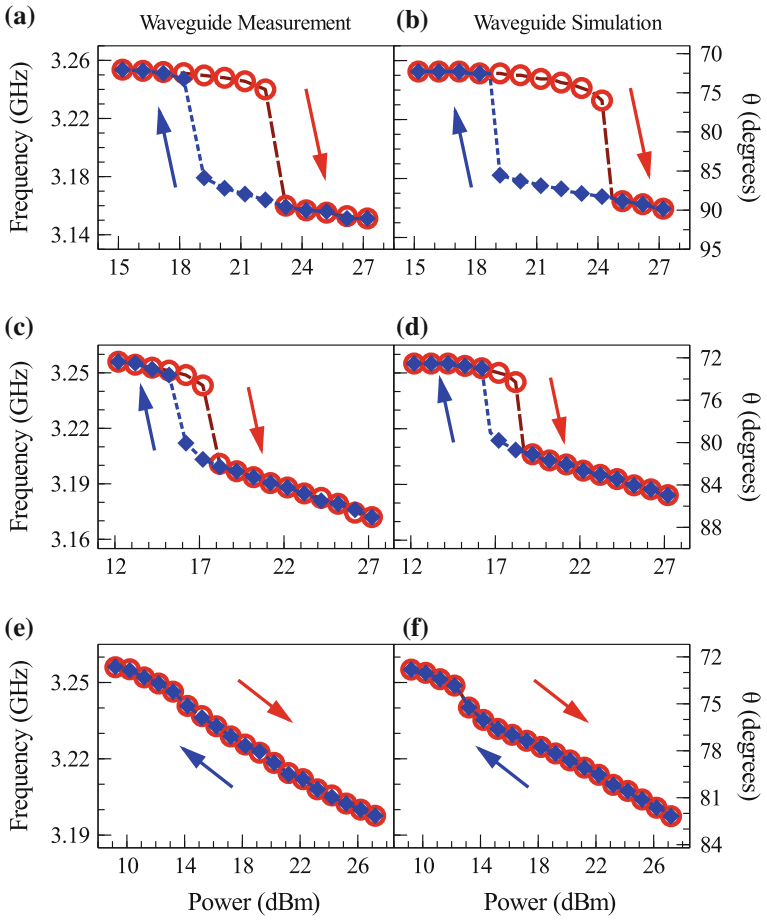

Fig. 4.9 Comparison of experimentally measured (**a**), (**c**), (**e**) and numerically calculated (**b**), (**d**), (**f**) resonant frequency sweeps for identical geometry (adapted from [28]). The corresponding stable twist angles are shown on the right axes. **a** and **b** pump at 3.18 GHz; **c** and **d** pump at 3.21 GHz; **e** and **f** pump at 3.23 GHz

were also observed (not shown) when the pump frequency is at the red tail of the antisymmetric mode, in which case the two resonances approach each other due to the opposite direction of the electromagnetic torque.

Although these simulations and experiments are conducted for a single element in a waveguide, it should be noted that the mirror images on the waveguide walls make this system qualitatively similar to an array. This has been verified numerically, and it has been shown that the dynamics in a dilute array are qualitatively similar to those shown in the waveguide system [28].

4.4 Dynamic Response

Nonlinear dynamic phenomena, such as self-oscillations and chaos, have been widely studied in different types of systems [32, 33]. Recent research in optomechanics also demonstrated exotic coupling effects between optical resonance and mechanical vibration [34, 35]. In optomechanical systems, the excitation of self-oscillation requires a phase lag between the optical force and mechanical vibration. This phase lag can be introduced by either retarded radiation pressure or bolometric force [36, 37]; the former mechanism requires the spectral linewidth of the optical resonance to be comparable with the mechanical oscillation frequency; while the latter arises from the photo-thermal effect, with a typical response time at the sub-millisecond scale, which can be significant for micro-nano mechanical oscillators [37, 38].

With regards to torsional metamaterials, it was demonstrated [39] that the system of three elastically coupled rings supports self-oscillations, and in contrast to most previously studied optomechanical systems this oscillation can be supported even with very strong damping.

4.4.1 Model of the System

Figure 4.10 shows the torsional structure, consisting of three coaxial split-ring resonators connected by wires. The twist angles with respect to the y axis are θ_m, $m \in \{1, 2, 3\}$. We fix the first ring at $\theta_1 = 0°$ so that the structure as a whole cannot rotate, only the second and third rings. Since this system has an additional mechanical degree of freedom introduced, we can consider it as a "meta-molecule" made from elastically and electromagnetically coupled meta-atoms.

In contrast to a pair of rings, the eigenmodes of the three ring system have a more complicated distribution. However, these hybridised modes can be found using our semi-analytical method [31], which we extend to account for higher order eigenmodes of the individual rings. The frequencies of these hybrid modes are shown in Fig. 4.10 as a function of the two twist angles θ_2 and θ_3. The radius of each SRR is 6 mm, the slit width is 1 mm, and the inter-ring distance is 3 mm. The incident wave propagates along the z direction, and excites some combination of the resonant modes which depends on their overlap with the incoming field.

The SRRs are connected with cylindrical thin elastic wires, and the restoring torques are approximated by Hooke's law:

$$M_{\mathrm{R},2} = -\kappa[2(\theta_2 - \breve{\theta}_2) - (\theta_3 - \breve{\theta}_3)], \quad M_{\mathrm{R},3} = -\kappa[(\theta_3 - \breve{\theta}_3) - (\theta_2 - \breve{\theta}_2)], \quad (4.21)$$

with $\kappa = \pi a^4 G/(2d)$; a and d are the radius and the length of the wires, respectively; G is the shear modulus and $\breve{\theta}$ are the initial twist angles. The dynamic equation of the m-th SRR ($m \in \{2, 3\}$) can then be expressed as

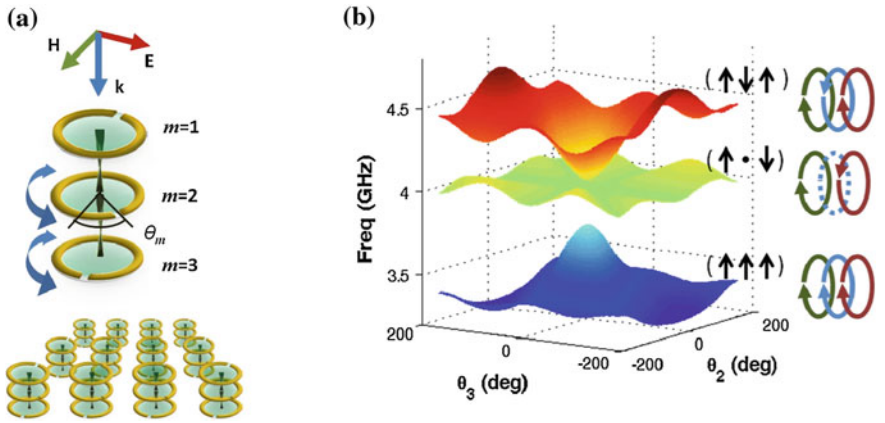

Fig. 4.10 **a** Schematic of the torsional metamaterials and **b** the three eigenfrequencies supported by the hybridised meta-molecule (reproduced from [39]). Each meta-molecule consists of three coaxial split-ring resonators connected elastically. The first ring is fixed, while the second and the third rings are free to rotate about the common axis z. The twist angles θ strongly modify the eigenfrequencies and are defined as the angle between the slit and the y axis

$$\ddot{\theta}_m + \Gamma\dot{\theta}_m = \frac{M_m}{\mathfrak{I}}, \quad \text{where} \quad M_m = (\mathbf{M}_{\mathrm{EM},m} + \mathbf{M}_{\mathrm{R},m}) \cdot \hat{z}. \tag{4.22}$$

Here, $\mathfrak{I}$ is the moment of inertia, Γ is the damping coefficient, and M_m is the total torque experienced by the m-th SRR.

As with the two ring system, the mechanical response time is many orders of magnitude slower than the lifetime of the electromagnetic resonant modes. Therefore the electromagnetic torque can be considered as a function of the ring angles without the need to account for their angular velocities. For a pair of rings with one angle fixed, there is only a single mechanical degree of freedom, and the total work done by the external field over each period of oscillation is zero. This means that the system will undergo damped oscillations, and will eventually become stable. In contrast, the three ring system has two mechanical degrees of freedom, and in particular it is possible for the oscillations of the two free rings to have some phase delay between them. This can enable the electromagnetic field to do non-zero work on the system over an oscillation cycle, which can compensate for the mechanical losses and can also lead to dynamic steady-state solutions.

In Fig. 4.11 we show the torque on each ring for the angles $\theta_2 = -\theta_3 = 30°$. These results were also confirmed by comparison with full wave simulation. For the pair of rings studied in Sect. 4.3, the direction of the torque on the rings is related directly to the symmetry of the mode which is excited. However, for the meta-molecule with three or more resonators, the torque must be summed over the contributions from each ring, whose direction also depends on the relative strength of the modes of the hybridised system. This creates a complex frequency-dependence of the torque in

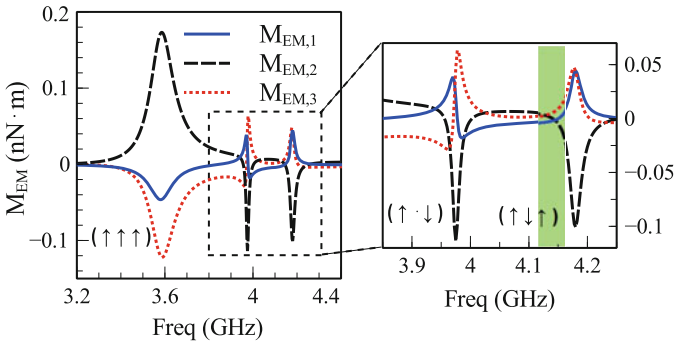

Fig. 4.11 Electromagnetic torques M_{EM} experienced by the three rings with configuration $\theta_2 = -\theta_3 = 30°$ (reproduced from [39]). The incident wave propagates along the z direction, with its electric field component in the x direction ($\Phi = 0°$). The torques are normalised to a power density of 1 mW/mm^2. The inset on the right magnifies the details within the *dashed rectangle*, and the *green shading* shows the regime where self-oscillations can exist

the system, including the highly asymmetric Fano type resonance shapes, such as that shown in the inset of Fig. 4.11.

It is assumed that each ring is placed within a polyurethane foam package which enables connection of the elastic wires, but which has a permittivity near unity and is thus transparent to electromagnetic waves. This results in a calculated moment of inertia for each ring as $\mathfrak{I} \approx 3.755 \times 10^{-10}$ kg · m^2, and the elastic wire is assumed to have radius 50 μm and shear modulus 1 MPa.

4.4.2 Self-Oscillations

The system of coupled equations can be solved to find the dynamics of the meta-molecule as a function of pump frequency and power. The pump frequency is assumed fixed, and the incident wave intensity is swept from zero to a maximum of 60 mW/mm^2 in 1 mW/mm^2 steps, then swept along the reverse path to reveal any regimes of bistable behaviour.

The twist angles θ_2 and θ_3 undergo damped oscillations as the power is changed, and in most cases they converge to a stable angle. Near the resonances a very strong nonlinear response can be found, which can show bistability similar to that in a pair of rings, and can even exhibit tristability. But the most interesting behaviour, which occurs for a limited range of input power and frequency, is that the system becomes unstable, and the rings continue to oscillate indefinitely, with the energy lost to mechanical damping being compensated by energy from the pump.

Due to its role in balancing the energy gain from the pump, the mechanical damping plays a critical role in the dynamics of the system. In Fig. 4.12 a and b we show the nonlinear response of this meta-molecule for two different values of damping, using

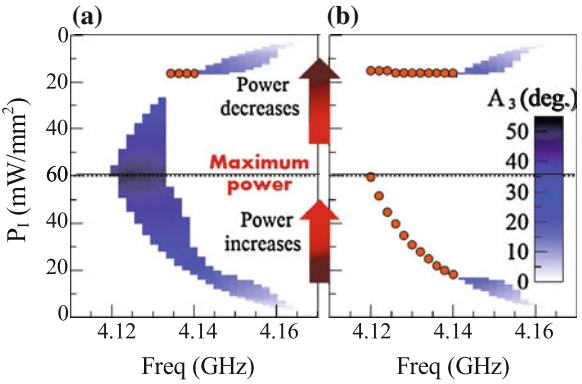

Fig. 4.12 Nonlinear behaviour as a function of pump frequency and power density (reproduced from [39]). Regime and amplitude of self-oscillations are denoted with colour scale. A_3 is defined as the peak amplitude of the oscillations of θ_3. The arrows denote the direction of power change, which increases from zero to 60 mW/mm^2 and then decreases back to zero. The *orange circles* show the threshold power densities of bistable hopping. Results with different damping coefficients are compared, **a** $\Gamma = 0.71$ Hz and **b** $\Gamma = 1.42$ Hz

the same initial twist angles as in Fig. 4.11. On the vertical axis we plot the incident power, with the lower part of the scale showing the results for increasing power, and the upper part showing the results as power is decreased. The coloured regions correspond to the regimes of self-oscillation, with the colour corresponding to the magnitude of the oscillation in degrees. This self oscillation region corresponds to the green shaded area of Fig. 4.11, which is on the red side of the resonance denoted ($\uparrow\downarrow\uparrow$) in Fig. 4.10.

In Fig. 4.12b the mechanical damping has been increased drastically to $\Gamma = 1.42$ Hz, which corresponds to the viscous damping which would occur in water. This high level of damping eliminates the self oscillatory behaviour for many pump frequencies, with the system instead reverting to a bistable stationary response. The orange circles plotted in Fig. 4.12 show the threshold power levels for bistable hopping. However, it is interesting to note that the regime of self-oscillation from 4.14 to 4.16 GHz is preserved.

4.4.3 Stability Analysis

We now investigate further why some regimes of self oscillation are highly robust even to very strong damping, while other regimes are quenched quite easily. This difference can be understood by analysing the local stability about the equilibrium points. The equilibrium positions of the structure clearly require the total torques $M_{2,3}$ to be zero. These points can be found from the intersection of the curves $M_2(\theta_2, \theta_3, f_P, P_I) = 0$ and $M_3(\theta_2, \theta_3, f_P, P_I) = 0$. Fixing the pump frequency, we

can calculate these torques as a function of θ_2, θ_3 and study how the equilibrium points change with increasing input power P_1. Since at equilibrium $\dot{\theta}_2 = \dot{\theta}_3 = 0$, we need only consider the projection of the full phase diagram onto (θ_2, θ_3) to show the dynamic trajectory. The key to understanding this trajectory is to study the local stability of the equilibria.

The local stability of the system around equilibria is estimated by analysing the eigenvalues of its linear variational dynamic equations [33], where the coefficients can be written in a compact matrix form:

$$\begin{bmatrix} \frac{\partial F_2}{\partial \theta_2} & \frac{\partial F_2}{\partial \Omega_2} & \frac{\partial F_2}{\partial \theta_3} & \frac{\partial F_2}{\partial \Omega_3} \\ \frac{\partial G_2}{\partial \theta_2} & \frac{\partial G_2}{\partial \Omega_2} & \frac{\partial G_2}{\partial \theta_3} & \frac{\partial G_2}{\partial \Omega_3} \\ \frac{\partial F_3}{\partial \theta_2} & \frac{\partial F_3}{\partial \Omega_2} & \frac{\partial F_3}{\partial \theta_3} & \frac{\partial F_3}{\partial \Omega_3} \\ \frac{\partial G_3}{\partial \theta_2} & \frac{\partial G_3}{\partial \Omega_2} & \frac{\partial G_3}{\partial \theta_3} & \frac{\partial G_3}{\partial \Omega_3} \end{bmatrix} = \begin{bmatrix} 0 & 1 & 0 & 0 \\ C_1 & -\Gamma & C_2 & 0 \\ 0 & 0 & 0 & 1 \\ C_3 & 0 & C_4 & -\Gamma \end{bmatrix}, \tag{4.23}$$

with $F_{2,3} = \Omega_{2,3} = \dot{\theta}_{2,3}$, and $G_{2,3} = \dot{\Omega}_{2,3} = \ddot{\theta}_{2,3} = M_{2,3}/\mathfrak{I} - \Gamma\Omega_{2,3}$, and C_n being determined by numerical differentiation of the total torque terms. The eigenvalues of the matrix have explicit expressions

$$\lambda_{1,2,3,4} = \frac{-\Gamma}{2} \pm \left\{ \frac{(C_1 + C_4)}{2} + \frac{\Gamma^2}{4} \pm \frac{1}{2}\left[(C_1 - C_4)^2 + 4C_2C_3\right]^{1/2} \right\}^{1/2}, \tag{4.24}$$

For an equilibrium point to be stable, all four eigenvalues must have negative real parts, otherwise it is unstable. For any finite mechanical damping, all four eigenvalues have finite real parts. This makes the equilibria hyperbolic, and allows the variational equations to model the local behaviour of the nonlinear system [33]. From this analysis, we can show that the difference in robustness of the self-oscillation to damping seen in Fig. 4.12 is due to the difference in stability of the equilibria.

By analysing the evolution of the equilibria, we found that the distinct behaviour of self-oscillations shown above corresponds to two different mechanisms. The difference between these two regimes is demonstrated in Fig. 4.13a, b for pump frequencies of 4.134 and 4.15 GHz. θ_3 is plotted as a function of power, with red indicating increasing and blue indicating decreasing power. The dashed lines show the amplitude of the oscillation when $\Gamma = 0.71$ Hz, while the circles show the stable positions.

4.4.3.1 Self-Oscillations Resulting from Limited Local Stability

The case shown in Fig. 4.13a, with the 4.134 GHz pump, corresponds to self oscillations induced by the limited local stability of the equilibria. Once the input power exceeds $\sim$25 mW/mm^2, the stable equilibrium terminates and the system enters a region of unstable oscillation, which continues until the power reaches $\sim$55 mW/mm^2. However, strong damping can change this dynamic behaviour, and cause the system to

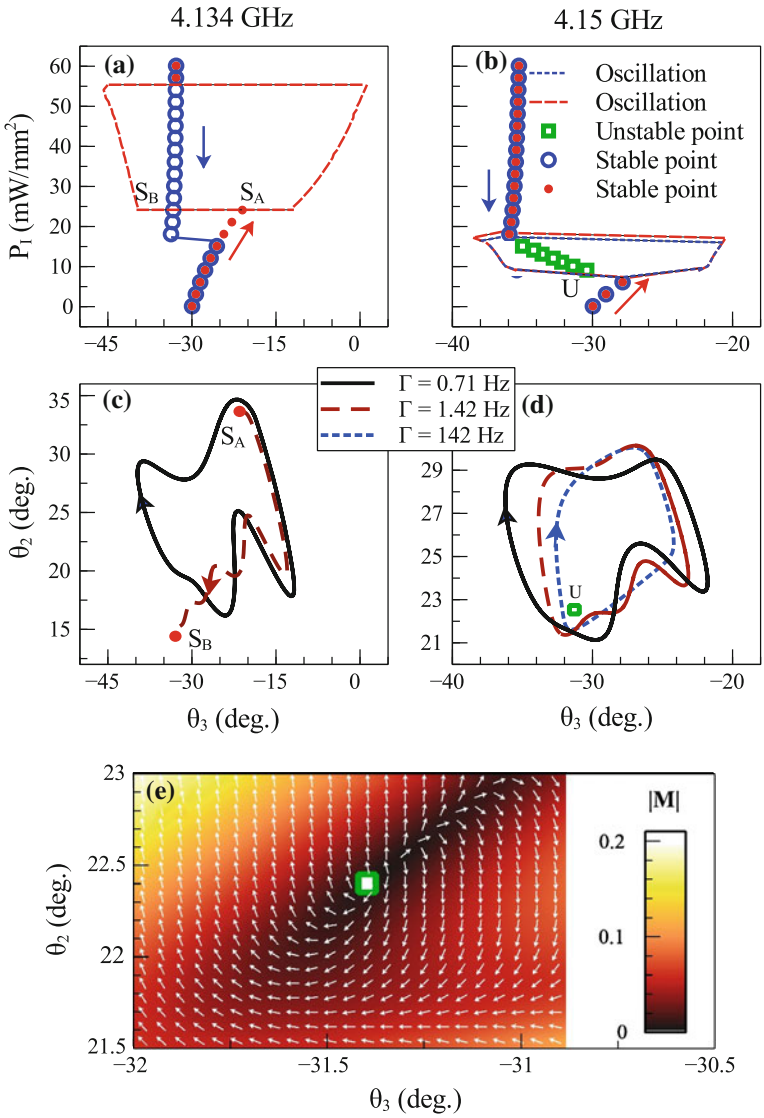

Fig. 4.13 Evolution of the system at two different pump frequencies: **a** 4.134 GHz and **b** 4.15 GHz (reproduced from [39]). The *red solid circles* and *blue empty circles* denote the stable equilibria during the process of increasing and decreasing power density, respectively. *Green squares* are the unstable equilibria. The *red dashed curves* and *blue dotted curves* show the boundaries of self-oscillation under the damping factor $\Gamma = 0.71$ Hz. The trajectories at the threshold power density of transition: **c** 4.134 GHz, $P_I = 25\,\mathrm{mW/mm^2}$ and **d** 4.15 GHz, $P_I = 9\,\mathrm{mW/mm^2}$. Damping factor $\Gamma = 1.42$ Hz is calculated based on the viscosity of water. S_A, S_B and U correspond to the equilibria denoted in (**a**) and (**b**). **e** The diagram of torque $\mathbf{M} = M_2\hat{\boldsymbol{e}}_{\theta 2} + M_3\hat{\boldsymbol{e}}_{\theta 3}$ near the equilibrium U shown in (**d**). The vectors show the direction of **M**

be attracted to another stable equilibrium point. This is exactly the case in Fig. 4.12b, and is further illustrated by the dashed line in Fig. 4.13c, showing the trajectory from stable equilibrium S_A to S_B, which are the points labelled in Fig. 4.13a.

For sufficiently low damping, instead of terminating at S_B, the trajectory is able to create a limit cycle, show by the black curve in Fig. 4.13c. This occurs because the system has sufficient kinetic energy to overcome the attraction to the equilibrium point, which is only locally stable. The limit cycle occurs when the mechanical damping exactly compensates the energy coupled into the system from the torque induced by the electromagnetic wave.

As the power further increases, the equilibria become more strongly attracting, until the trajectory is no longer able to escape and falls into a stable state. If the power is subsequently decreased, the state remains stable, as sufficient kinetic energy is not developed to enable self oscillations. The trajectory follows a stable branch, until a power of $\sim$18 mW/mm^2, where it undergoes a bistable jump back to the original state shown by the blue circles. This gives rise to the the features observed in Fig. 4.12 which depend on whether the power is increasing or decreasing.

4.4.3.2 Self-Oscillations Resulting from Local Instability

For the pump frequency of 4.15 GHz, in Fig. 4.13b we also see two branches of the stable nonlinear response. However, when the first branch ends at input power of $\sim$9 mW/mm^2, it is replaced by a series of locally unstable equilibria, which are shown by the green squares. This results in a different mechanism of self-oscillations, with the amplitudes again shown by the lines. At an input power of $\sim$17 mW/mm^2 the equilibria again become stable. The key difference is that the local instability means that additional kinetic energy is not required, thus when reducing the input power, a very similar regime of self-oscillations occurs. Note that the equilibrium point and its local stability remain the same if M_{EM} and M_R are increased by the same factor; this indicates that self-oscillations due to local instability are still observable at the same regime of pump frequency and power density, and the speed of oscillation will increase accordingly.

In Fig. 4.13 d the projected phase diagram is shown as a function of the damping coefficient. It can be seen that the oscillations remains extremely robust against very high values of damping, as shown in the dotted lines. The blue dotted line indicates the trajectory which the system approaches as damping is increased, although the increasing damping does change the frequency of oscillation. To understand this, we visualise the torques M_2 and M_3 in a two dimensional vector form: $\mathbf{M} = M_2\hat{\boldsymbol{e}}_{\theta 2} + M_3\hat{\boldsymbol{e}}_{\theta 3}$, where $\hat{\boldsymbol{e}}_{\theta 2}$ and $\hat{\boldsymbol{e}}_{\theta 3}$ denote the unit vectors in the θ_2 and θ_3 directions. Figure 4.13e shows this distribution of torques about the unstable equilibrium point (marked by the green square). It can be seen that the torque always pushes the system away from this equilibrium point, and will develop into a limit cycle if there is no stable equilibrium point which will attract the system. This feature is distinct from many previously studied optomechanical systems, in which self-oscillations can not survive strong damping. Although the regime of self-oscillations

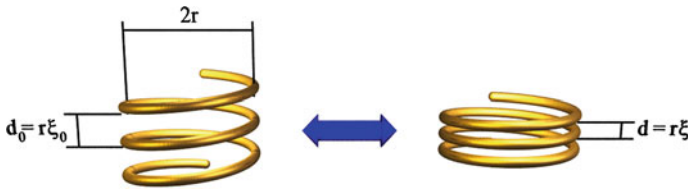

Fig. 4.14 Conceptual schematic and geometrical parameters of nonlinear flexible helices. (Adapted from [40])

varies when the configuration changes, the two mechanisms shown above are general. For meta-molecules with more than three rings, self-oscillations can also be observed.

4.5 Nonlinear Chirality of Helical Resonators

An alternative approach which exploits mechanical compression for elastic feedback, is implemented with metallic helices [40, 41]. The idea is that the helix is at once a chiral electromagnetic resonator and a mechanical spring. The currents induced in the windings by an incident electromagnetic wave, will impose attractive forces between them, so mechanical compression occurs until the Ampère forces are balanced by the spring forces. However, this compression changes the pitch of the helix, altering the effective capacitance and shifting the resonant frequency. Furthermore, as the helix is a chiral electromagnetic resonator [42, 43] and its chirality is related to the pitch, the response of the helix manifests itself with nonlinear chirality.

The arising nonlinear feedback is qualitatively similar to that observed in magnetoelastic metamaterials, but the difference is that in the magnetoelastic system the mutual interaction between different elements is affected, whereas in helices the effect occurs within each resonator individually, providing an intrinsic structural nonlinearity. We note that, similar to magnetoelastic behaviour, the acting electromagnetic forces in flexible helices are time-averaged with respect to electromagnetic oscillations, and that any mechanical dynamics occurs at a time scale incomparably slow with respect to that of electromagnetic response.

The resonant frequency of a helix is determined by its geometry (Fig. 4.14). Consider a helix with winding radius r, and dimensionless parameters ξ for the ratio of the pitch to r, and w for the ratio of the wire radius to r. For two turns, electromagnetic resonance can be described with a simple circuit model [44], with the same inductance L and resistance R as that of a single turn, and the capacitance C taken as a sum of the parallel capacitances between the cylindrical wire turns:

$$\omega_2 = \frac{1}{\sqrt{LC}} \quad \text{with} \quad L = \mu_0 r\left(\ln\frac{8}{w} - 2\right), \quad C = \frac{2\pi\varepsilon_0 \cdot \pi r}{\cosh^{-1}(\xi/2w)}. \tag{4.25}$$

The resulting resonance frequency ω_2 was confirmed to be an exact match to the results of numerical simulations for a wide range of $0.022 < \xi < 0.1$ [40].

For multi-turn ($N > 2$) helices, this simple circuit model is not applicable, however the same functional form for the resonant frequency can be extrapolated:

$$\omega_{\mathrm{s}} = \frac{c}{\pi r}\left(\frac{\cosh^{-1}(\xi/2w)}{2(N-1)\psi\big(\ln(8/w)-2\big)}\right)^{1/2}, \tag{4.26}$$

where it is assumed that with the increase in the number of windings either capacitance or inductance must be multiplied with $(N-1)$, and an additional factor ψ stands for the discrepancy with the exact results. Indeed, a comparison of the analytical expression (4.26) with the results of full-wave numerical simulations (CST Microwave Studio) for various ξ and N up to 9, demonstrated good agreement [41]; the correction factor ψ slightly increases from $\psi \approx 1$ at $N = 2$ to $\psi \approx 1.36$ at $N = 9$. This said, it is important to emphasise that a multi-turn helix cannot be directly described with the localised L and C circuit parameters, and the (4.26) fails to describe long helices.

The mechanical properties of the helix are described by the stiffness coefficient, which equals to $k = Grw^4/4$ for one turn, where G is the shear modulus of the material which makes the wire of the helix. Note that the characteristic frequency of mechanical oscillations, $\omega_{\mathrm{M}} = w\sqrt{3G/2\rho}/(2\pi rN)$ is many orders of magnitude smaller than the electromagnetic frequencies involved, so the analysis of the spiral geometrical reconfiguration is essentially static and is determined by time-averaged amplitudes of the current. The spring response is then described with the Hooke's law, so the compression force linearly increases with the deviation from the initial pitch value ξ_0: $F_{\mathrm{s}} = kr(\xi - \xi_0)$. This compression balances the attractive force F_{c}, induced by the current excited in the helix.

For small ξ, the Ampère force acting between the windings of the helix can be calculated as that between the two parallel wires of the corresponding length. Generally, it is $F_{\mathrm{c}} = \mu_0 I^2/2\xi$ between two windings. For multiple turns, it is reasonable to neglect the effect on the edges, and write the force balance in each turn as

$$Gr^2w^4(\xi - \xi_0)\xi + 2\Xi\mu_0 I^2 = 0, \tag{4.27}$$

where an additional enhancement factor Ξ is due to the interaction of multiple windings; for 9 turns, for instance, $\Xi \approx 2$ [41]. However, for a helix with two turns, the actual current distribution [44] results in a smaller net total force, $F_2 = \mu_0 I^2/12\xi$, so for a short helix the (4.27) is modified by letting $\Xi = 1/3$. Thus, a 9-turn helix experiences a 6 times stronger compression for a given current magnitude.

Equation (4.27) may seem to be a quadratic equation for ξ, however it is in fact more complicated as the current I also depends on ξ and r through the impedance equation. The latter depends on the type of experiment to be conducted. In a pump-probe experiment, as in [40], a complete impedance equation should be used, which in the case of two-turn helix can be explicitly written as

$$\left(R + \mathrm{i}\omega L - \frac{\mathrm{i}}{\omega C}\right) \cdot I = -\mathrm{i}\omega\mu_0 \pi r^2 H_0. \tag{4.28}$$

As in (4.4), H_0 is the amplitude of the magnetic field of the incident wave (we imply that the incident polarization with $\mathbf{H_0}$ is parallel to the spiral axis), but the difference is that the dependence on geometric parameters manifests itself in the self-capacitance rather than in mutual inductance as in (4.4).

When, instead, a frequency scan at variable power is adopted, and sufficient time is allowed for the frequency sweep, the helix should be at the equilibrium position while at resonance (whereas the frequency of the resonance changes depending on the power), in which case the impedance is reduced to the resistance and the equation takes the form

$$\frac{1}{w}\sqrt{\frac{\omega_s \mu_0}{2\sigma}} I = \mathfrak{E}(\omega, P), \tag{4.29}$$

where $\mathfrak{E}(\omega, P)$ is the effective electro-motive force acting per turn of the helix depending on the frequency and power of the incident wave.

Taken together, the (4.25) [or (4.26)], (4.27), and (4.28) [or (4.29)], form a system of coupled equations, which can be numerically solved for ξ and I for a given frequency ω and amplitude H_0 of the incident field.

Note that an additional effect on the nonlinear response of the helices is provided by its thermal expansion (so that r depends on temperature, affecting the self-inductance and resistance) as well as by the temperature dependence of metal conductivity. The thermal effect also shifts the resonant frequency, leading to even more complicated nonlinear feedback (see [40] for details).

In accordance with this analysis, nonlinear self-action has been predicted to occur in a way, similar to magnetoelastic metamaterials, with nonlinear or even bistable response in the power-dependence of the resonance frequency and chirality [40].

The first experimental attempt to observe the intrinsic structural nonlinearity [40] was performed with two-turn helices and revealed a thermal contribution dominating over the mechanical response. To overcome this problem, an improved fabrication approach was employed with multi-turn helices [41], manufactured with high geometrical precision and thermal annealing of the helices to improve their stability. As a result, a remarkable power-dependent shift of the resonant frequency was observed in the arrays of multi-turn helices, which was mostly due to mechanical compression: it is estimated that the thermal contribution did not exceed 12 %.

The outcome of the measurements on the multi-turn helices [41] are presented in Fig. 4.15, where the change in the helix pitch is recalculated from the experimental data based on the measured resonant frequencies, and compared with the theoretical fit in accordance with the above analysis. Chiral properties of the helix are directly proportional to its pitch, and can be characterised [45] with the normalised (dimensionless) ratio between the electric p and magnetic m dipole moments along its axis,

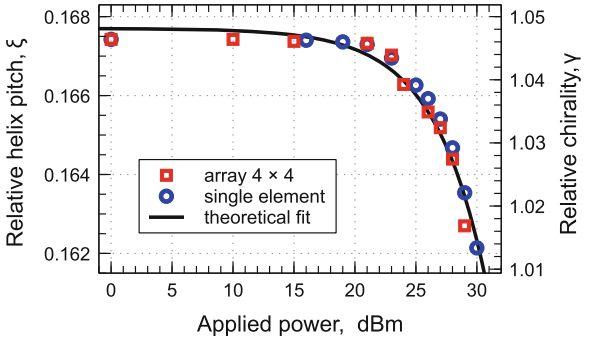

Fig. 4.15 Change of the relative helix pitch ξ with power, recalculated from the experimental data on the resonance shift with power (adapted from [41]). *Blue circles* represent the data obtained for a single resonator, and *red squares* for the lattice; the size of the symbols commensurate with the measurement errors. *Black solid curve* shows the theoretical fit to the presented data The axis on the right indicates γ as a measure of chirality

$$\gamma = \frac{|p|}{|m|} \cdot c = \frac{c\xi}{\omega\pi r} = \frac{\xi}{\pi} \cdot \frac{\lambda}{2\pi r}, \tag{4.30}$$

where λ is the wavelength and c is the light velocity. The auxiliary axis on the right of Fig. 4.15 indicates the magnitude of γ for the data presented in the figure, calculated at the initial frequency of the resonance in the array.

By choosing an appropriate arrangements of helices, either anisotropic or isotropic lattices can be assembled, and also non-chiral (but still nonlinear) arrays be realised using a racemic mixture of helices with opposite chirality. At the same time, a more rigorous analysis should be developed to account for the effects of non-uniform compression and thermal expansion, taking actual current distribution into account. Such calculations however are not likely to be analytically plausible and must involve numerical simulations. It would be particularly interesting to study wave propagation in large chiral arrays, where polarisation rotation over the course of wave propagation through the sample will eventually impose a kind of dynamic grating of domains with different chirality, resulting in weird patterns of wave dynamics.

4.6 Conclusion and Outlook

We have presented several metamaterial structures which couple electromagnetic and elastic dynamics within the elements. The magnetoelastic metamaterial undergoes compression in response to an electromagnetic force, which results in strong nonlinear behaviour including a bistable response. This is a rare example of nonlinear mutual interaction of the elements with linear self-response.

Alternatively, it is possible to combine the functionality of electromagnetic resonator and mechanical spring into a single structure, by utilising self-compressing helices. This approach has been also demonstrated experimentally, whereby the undesirable thermal side effects can be overcome by using compact multi-turn helices.

The meta-atoms with intrinsic rotation utilise an alternative degree of freedom. They rely on electromagnetic torque, which can be balanced by a very soft mechanical restoring torque, leading to a much stronger nonlinear response. The system exhibits similar qualitative features to the magneto-elastic structure, and has a strong bistable response which was demonstrated experimentally.

Extending the rotational system to a three-ring meta-molecule leads to the possibility of self-oscillations. Furthermore, it turned out that these self-oscillations occur due to two distinct physical mechanisms. The system with local instability has the remarkable property of being extremely insensitive to damping, with mechanical self-oscillations being undisturbed even for strong damping.

The structures outlined here rely on the dynamics of an individual meta-atom or meta-molecule to achieve their physical properties. This means that the analysis and experimental results presented here are directly applicable to dilute arrays, whereby neighbouring elements do not exert significant electromagnetic forces on each other. The densely packed array regime is expected to show further complexity of behaviour, and thus a bulk metamaterial based on these principals is an intriguing possibility. Another direction of great interest is to extend such structures to shorter wavelength regimes. The optical regime is naturally promising due to the high power density available in lasers, however the fabrication of analogous structures at these length scales would be a significant challenge.

Acknowledgments We acknowledge the contributions of Alexey P. Slobozhanyuk, Yue Sun, Ilya V. Shadrivov, Ross C. McPhedran, Pavel Belov, and Yuri S. Kivshar, to the work reported in this chapter.

References

1. M. Lapine, I.V. Shadrivov, Y.S. Kivshar, Rev. Mod. Phys. **86**, 1093 (2014)
2. J. Li, C.T. Chan, Phys. Rev. E **70**, 055602 (2004)
3. S. Guenneau, A. Movchan, G. Patursson, S. Ramakrishna, New J. Phys. **9**, 399 (2007)
4. A.N. Norris, Proc. Royal Soc. A **464**, 2411 (2008)
5. D. Torrent, J. Sanchez-Dehesa, New J. Phys. **10**, 063015 (2008)
6. A. Baz, New J. Phys. **11**, 123010 (2009)
7. S. Zhang, L. Yin, N. Fang, Phys. Rev. Lett **102**, 194301 (2009)
8. J. Zhu, J. Christensen, J. Jung, L. Martin-Moreno, X. Yin, L. Fok, X. Zhang, F. Garcia-Vidal, Nat. Phys. **7**, 52 (2011)
9. G. D'Aguanno, K. Le, R. Trimm, A. Alu, N. Mattiucci, A. Mathias, N. Akozbek, M. Bloemer, Sci. Rep. **2**, 340 (2012)
10. J. Christensen, F. Garcia de Abajo, Phys. Rev. Lett. **108**, 124301 (2012)
11. J.H. Lee, J.P. Singer, E.L. Thomas, Adv. Mater. **24**, 4782 (2012)
12. K.C. Neuman, S.M. Block, Rev. Sci. Instrum. **75**, 2787 (2004)

13. P. Galajda, P. Ormos, Appl. Phys. Lett. **78**, 249 (2001)
14. A. La Porta, M. Wang, Phys. Rev. Lett. **92**, 190801 (2004)
15. E.R. Dufresne, D.G. Grier, Rev. Sci. Instrum. **69**, 1974 (1998)
16. A. Boardman, V. Grimalsky, Y. Kivshar, S. Koshevaya, M. Lapine, N. Litchinitser, V. Malnev, M. Noginov, Y. Rapoport, V. Shalaev, Laser Photonics Rev. **5**, 287 (2011)
17. M. Kauranen, A.V. Zayats, Nat. Photonics **6**, 737 (2012)
18. N.I. Zheludev, Y.S. Kivshar, Nat. Mater. **11**, 917 (2012)
19. T.J. Kippenberg, K.J. Vahala, Opt. Express **15**, 17172 (2007)
20. F. Marquardt, S.M. Girvin, Phys. **2**, 40 (2009)
21. D.A. Powell, M. Lapine, M.V. Gorkunov, I.V. Shadrivov, Y.S. Kivshar, Phys. Rev. B **82**, 155128 (2010)
22. M. Lapine, I.V. Shadrivov, D.A. Powell, Y.S. Kivshar, Nat. Mater. **11**, 30 (2012)
23. M.V. Gorkunov, M. Lapine, E. Shamonina, K. Ringhofer, Eur. Phys. J. B **28**, 263 (2002)
24. I.E. Khodasevych, I.V. Shadrivov, D.A. Powell, W.S.T. Rowe, A. Mitchell, in *Metamaterials 2012 Congress* (Saint Petersburg, 2012), pp. 113–115
25. L.D. Landau, E.M. Lifshitz, *Electrodynamics of Continuous Media*, 2nd edn. (Pergammon Press, 1984)
26. K.B. Kim, E. Levi, Z. Zabar, L. Birenbaum, IEEE Trans. Magn. **32**, 478 (1996)
27. M. Lapine, L. Jelinek, R. Marqués, Opt. Express **20**, 18297 (2012)
28. M. Liu, Y. Sun, D.A. Powell, I.V. Shadrivov, M. Lapine, R.C. McPhedran, Y.S. Kivshar, Phys. Rev. B **87**, 235126 (2013)
29. D.A. Powell, K.E. Hannam, I.V. Shadrivov, Y.S. Kivshar, Phys. Rev. B **83**, 235420 (2011)
30. M. Liu, D.A. Powell, I.V. Shadrivov, Appl. Phys. Lett. **101**, 031105 (2012)
31. M. Liu, D.A. Powell, I.V. Shadrivov, Y.S. Kivshar, Appl. Phys. Lett. **100**, 111114 (2012)
32. S. Strogatz, *Nonlinear Dynamics and Chaos: with Applications to Physics, Biology, Chemistry and Engineering* (Perseus Books Group, USA, 2001)
33. S. Wiggins, *Introduction to Applied Nonlinear Dynamical Systems and Chaos* (Springer, New York, 2003)
34. C.H. Metzger, K. Karrai, Nat. **432**, 1002 (2004)
35. T.J. Kippenberg, K.J. Vahala, Sci. **321**, 1172 (2008)
36. H. Rokhsari, T. Kippenberg, T. Carmon, K.J. Vahala, Opt. Express **13**, 5293 (2005)
37. C. Metzger, M. Ludwig, C. Neuenhahn, A. Ortlieb, I. Favero, K. Karrai, F. Marquardt, Phys. Rev. Lett. **101**, 133903 (2008)
38. S. Zaitsev, A.K. Pandey, O. Shtempluck, E. Buks, Phys. Rev. E **84**, 046605 (2011)
39. M. Liu, D.A. Powell, I.V. Shadrivov, M. Lapine, Y.S. Kivshar, New J. Phys. **15**, 073036 (2013)
40. M. Lapine, I.V. Shadrivov, D.A. Powell, Y.S. Kivshar, Sci. Rep. **1**, 138 (2011)
41. A.P. Slobozhanyuk, M. Lapine, D.A. Powell, I.V. Shadrivov, Y.S. Kivshar, R.C. McPhedran, P.A. Belov, Adv. Mater. **25**, 3409 (2013)
42. K.F. Lindman, Öfversigt af Finska Vetenskaps-Societetens förhandlingar, A LVII, 1 (1914)
43. I.V. Lindell, A.H. Sihvola, S.A. Tretyakov, A.J. Viitanen, *Electromagnetic Waves in Chiral and Bi-Isotropic Media* (Artech House, Boston, 1994)
44. J.D. Baena, R. Marqués, F. Medina, J. Martel, Phys. Rev. B **69**, 014402 (2004)
45. P.A. Belov, C.R. Simovski, S.A. Tretyakov, Phys. Rev. E **67**, 056622 (2003)

Chapter 5
Nonlinear and Tunable Left-Handed Transmission Lines

Alexander B. Kozyrev and Daniel W. van der Weide

5.1 Introduction

Metamaterials are artificial structures that are designed to exhibit specific electromagnetic properties required for different applications but not commonly found in nature. The methodology of synthesizing materials composed of micro- and nano-structured components that mimic the electromagnetic response of individual atoms and molecules (meta-atoms and meta-molecules) has proven to be very productive and resulted in the development of metamaterials exhibiting strong magnetic response at microwave and optical frequencies and so-called left-handed metamaterials (LHMs) (both impossible in conventional real-world materials).

LHMs are designed to exhibit simultaneously negative permittivity and permeability [1, 2]. In 2000, Smith et al. developed the first experimental left-handed (LH) structure, which was composed of metallic split-ring resonators and thin metal wires [3, 4]. An alternative transmission line approach for left-handed materials was proposed, almost simultaneously, by several different groups [5–7]. This approach, based on nonresonant components, allows for low-loss left-handed structures with broad bandwidth. The unique electrodynamic properties of these materials, first postulated by Veselago in 1968, include the reversal of Snell's law, the Doppler effect, Vavilov-Cherenkov radiation, and negative refractive index, making these materials attractive for new types of RF and microwave components [1, 2, 8]. The range of applications for LHMs is extensive, and opportunities abound for development of new and powerful imaging and communication techniques.

Most studies of LHMs have been concerned with linear wave propagation, and have inspired many applications that were unthinkable in the past [1, 9] such as LH phase shifters [10], LH directional couplers [11, 12], and leaky-wave antennas

A.B. Kozyrev (✉) · D.W. van der Weide
Department of Electrical and Computer Engineering, University of Wisconsin-Madison, Madison, WI 53706, USA
e-mail: alexander.kozyrev@gmail.com

I.V. Shadrivov et al. (eds.), *Nonlinear, Tunable and Active Metamaterials*,
Springer Series in Materials Science 200, DOI 10.1007/978-3-319-08386-5_5

[13–15] to name just a few. Materials that combine *nonlinearity* with the anomalous dispersion exhibited by LH media [16–19], however, give rise to a new class of phenomena and promising applications [20–22]. Here we present a review of the basic *nonlinear* wave propagation phenomena in LH media. We consider left-handed nonlinear transmission lines (LH NLTL) as the simplest systems that would allow us to combine anomalous dispersion with nonlinearity in a controlled fashion. Understanding the nonlinear phenomena in LH NLTL media is important for both the development of new devices and improvement of the performance of recent devices based on LH NLTLs like harmonic generators, phase shifters [23], tunable leaky-wave antennas [9, 24] and notch filters [25].

5.2 Comparison of Conventional Right-Handed and Left-Handed Nonlinear Transmission Lines

The transmission line approach proves to be a useful description of LH media. It provides insight into the physical phenomena of LH media and is an efficient design tool for LH applications [9]. A LH NLTL is the dual of a conventional right-handed nonlinear transmission line (RH NLTL) shown in Fig. 5.1b, where inductors are replaced with capacitors and capacitors with inductors. The effective permeability and permittivity of one-dimensional transmission line metamaterials in the lossless case are expressed as follows:

$$\mu_{eff} = -\frac{2d}{\omega^2 C_L}; \quad \varepsilon_{eff} = -\frac{d}{\omega^2 L_L}, \tag{5.1}$$

where d is the period of the LH NLTL and ω is the radian frequency. In contrast with RH NLTL where capacitance gives rise to electric nonlinearity, nonlinear capacitances C_L introduce magnetic-type nonlinearity into the LH NLTL (i.e. effective magnetic permeability becomes nonlinear).

Although both the RH and LH NLTLs use the same components arranged in a similar way, the performance of this two circuits is dramatically different. This difference primarily comes from the difference in their dispersion characteristics (see Fig. 5.1c).

A conventional (right-handed) nonlinear transmission line has normal dispersion and frequency increases with the wavenumber. In contrast to the RH NLTL, the LH transmission line exhibits anomalous dispersion and frequency decreases with the wave number (see Fig. 5.1c). The waves propagating in such media are also known as backward waves because the direction of group velocity v_g is opposite to phase velocity ($v_p \cdot v_g < 0$).

Nonlinear transmission lines first drew attention in connection with the idea of distributed parametric amplification. It had been predicted that a distributed parametric amplifier or oscillator circuit could exhibit superior stability of operation and efficiency over lumped parametric circuits [26, 27]. Lumped parametric amplifiers

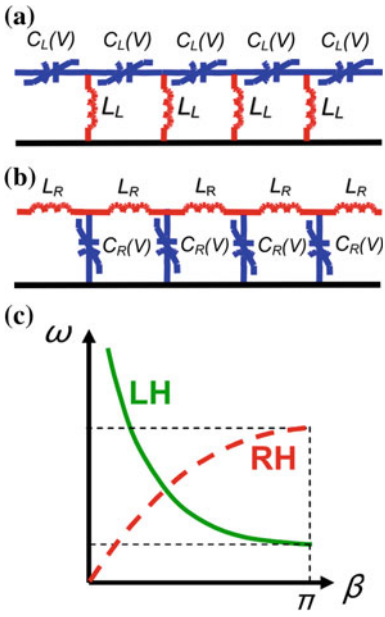

Fig. 5.1 **a** Equivalent circuit of a LH NLTL; **b** Equivalent circuit of a dual RH NLTL; **c** Typical dispersion curves of LH NLTL (*solid line*) and RH NLTL (*dashed line*)

were popular as very low-noise alternatives to vacuum tubes prior to the widespread use of semiconductor amplifiers [28]. (Parametric resonance responsible for amplification in lumped circuits is similar to the physical mechanism playing on a swing which allows large amplitudes by alternately raising and lowering the center of mass at a certain relation between the frequency of the swing and the frequency of external force.) Their complexity (they require external resonators and matching circuits) and low efficiencies however made them less attractive for widespread use. Conventional NLTLs were thought to be very promising candidates for use in distributed amplifiers because they do not require external resonant circuits and conversion efficiency was claimed to be very high due to accumulative effect of parametrically interacting waves propagating along NLTLs.

It turned out that parametric interactions (such as three- and four-wave mixing of phase matched waves) in RH NLTLs typically compete with shock wave formation [29, 30] and generation of temporal solitons [31]. For instance, parametric generation and amplification in dispersionless RH transmission lines is entirely suppressed by shock wave formation [32, 33]. In contrast to conventional NLTLs, both nonlinearity and dispersion present in LH NLTLs (see Fig. 5.1) lead to waveform spreading [34], consequently making shock wave and electronic soliton formation impossible. Anomalous dispersion makes sharp field transients in left-handed NLTL unstable. Once created, they decompose very quickly during propagation of the waveform due to substantial difference in the phase velocities of the propagating waves. This inability to form shock waves enables a variety of parametric processes to occur

instead [35, 36]. Furthermore, since the parametric interactions no longer compete with shock wave formation, it is possible to use stronger nonlinearities, consequently achieving considerable gain in shorter transmission lines [37].

Both theoretical [36, 38] and experimental [35, 37] investigations demonstrate that nonlinear wave form evolution in a LH NLTL can be understood in terms of competition between harmonic generation, subharmonic generation, frequency down conversion and parametric instabilities.

5.3 Parametric Generation and Amplification

5.3.1 Theory

Effective parametric interaction in medium exhibiting a second-order nonlinearity generally requires phase matching of three waves. The anomalous dispersion of a LH NLTL system enables effective parametric interactions of the type:

$$f_1 + f_2 = f_3, \quad \beta_1 - \beta_2 = \beta_3. \tag{5.2}$$

In the "parametric oscillator configuration", a high-frequency backward pump wave having a frequency f_3 and wavenumber β_3 is excited by the voltage source connected at the input port of a LH NLTL. It generates two other waves having frequencies f_1 and f_2, such that $f_1 < f_2$ and $f_1 + f_2 = f_3$. The wave having frequency f_2 propagates in the opposite direction relative to the pump wave and the wave having frequency f_1 (this is emphasized in the (5.2) with the minus sign). We therefore have a similar situation to backward wave parametric generation [38, 39]. The backward-propagating parametrically generated wave f_2 enables internal feedback that results in a considerable energy transfer from the pump wave to the parametrically excited waves.

If the amplitude of a high-frequency pump wave exceeds a certain threshold value, it may parametrically generate two other waves. This threshold value depends on the loss present in the LH NLTL, its length and the boundary conditions (matching) at the input and output. No parametric generation occurs when the amplitude of the voltage source is below this value. However, when a weak signal wave is fed into the LH NLTL together with a pump wave having an amplitude below the threshold value, a parametric amplification is observed. In this case, we have two input waves: an intense pump wave and a weak signal wave [40]. The power from the pump wave is transferred to the signal wave, thus amplifying it. A third parasitic idler wave is generated which provides phase matching. From a previous analysis [38], for the lossless case, the frequencies and powers of these waves also obey the nonlinear Manley-Rowe relations.

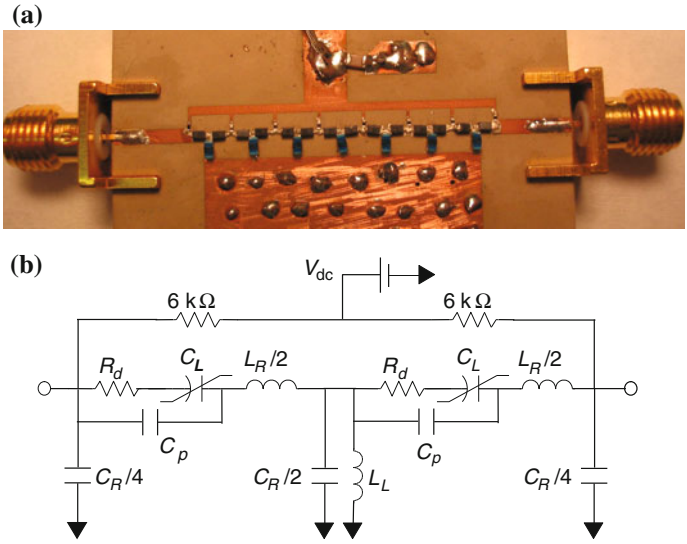

Fig. 5.2 **a** Fabricated 7-section LH NLTL; **b** equivalent circuit of one stage

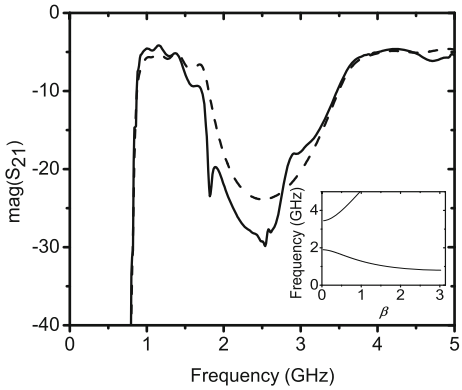

Fig. 5.3 Measured (*solid*) and simulated (*dashed*) magnitudes of S_{21} parameter for 7-section LH NLTLs for the reverse bias voltage $V_B = 3.823$ V. Inset shows dispersion curve of the LH NLTL (dependence of the frequency versus relative wave number β)

5.3.2 Experiment

We observed efficient parametric amplification in 7-section LH NLTL having identical sections [37] shown in Fig. 5.2a.

The circuit was realized on a Rogers RT/Duroid 3010 board with $\varepsilon = 10.2$ and thickness $h = 1.27$ mm. The entire circuit has been implemented using a microstrip geometry. Series nonlinear capacitance in each section is formed by two back-to-back Skyworks Inc. SMV1233 silicon hyperabrupt junction varactors with DC bias applied between them. Shunt inductances were implemented using high-Q 10 nH chip inductors (Murata LQW18A_00). The pads on the board surface, together with

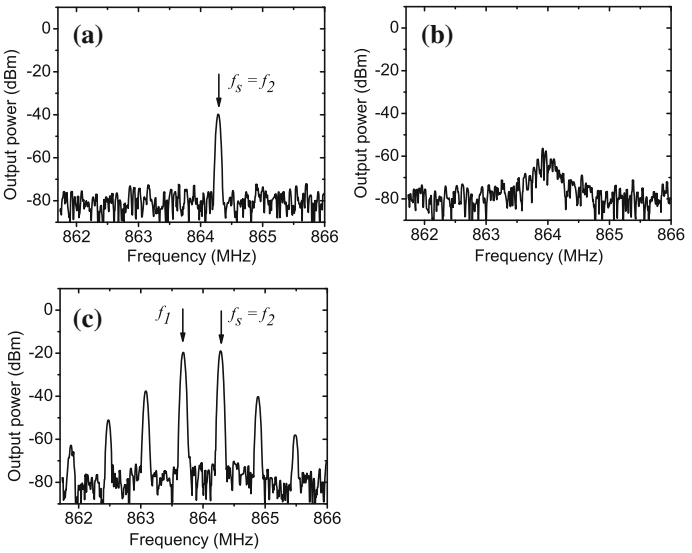

Fig. 5.4 Spectra of the output waveforms generated by a 7-section LH NLTL fed by: **a** only weak signal source 864.252 MHz, −28 dBm; **b** only pump source 1.7279 GHz, 13.96 dBm; **c** simultaneously signal and pump sources specified in **a** and **b**. Reverse bias voltage is 3.87 V

inherent parasitics introduce unavoidable series inductance and shunt capacitance, making the whole circuit a composite right/left-handed transmission line having the equivalent circuit shown in Fig. 5.2b. Figure 5.3 shows measured and simulated magnitude of the linear wave transmission (S_{21}) of this 7-section LH NLTL. The circuit model of Fig. 5.2b with component values extracted from measured S-parameters has also been used to calculate the dispersion curve of the LH transmission line as shown in the inset in Fig. 5.3. The dispersion characteristic of a composite right/left-handed transmission line has two passbands divided by the stop band. The low frequency passband exhibits anomalous dispersion (left-handed passband from 800 MHz to 1.9 GHz) while the high-frequency one is right-handed.

Figure 5.4 demonstrates the effect of the intensive pump wave, having frequency $f_p = f_3$, on a weak signal wave ($f_s = f_2$). Figure 5.4b shows the spectrum at the output of the 7-section LH NLTL when only a 1.7279 GHz, 13.96 dBm intensive pump wave is applied at the input. The magnitude of the pump wave was chosen so as to be 0.1 dB below the threshold value required for the occurrence of parametric generation, which manifests itself in distinct, narrow peaks corresponding to the parametrically generated frequencies.

Figure 5.4a shows the spectrum at the output when only the 864.252 MHz, −28 dBm signal wave is applied at the LH NLTL input (no pump wave). The graph shows 11.7 dB attenuation of the weak signal wave at the output due loss in the NLTL and power conversion to higher harmonics. And finally, Fig. 5.4c shows the spectrum at the output when the signal and the pump wave are both applied concurrently at the

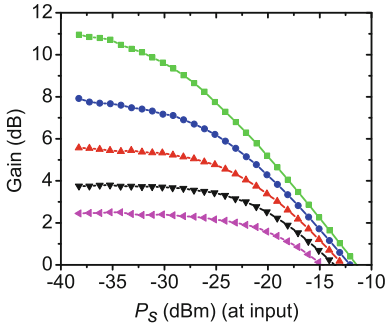

Fig. 5.5 Measured gain versus power of the signal at the input of LH NLTL for different values of the power of the pump wave at the input $P_{p,in}$: squares – $P_{p,in} = 13.96$ dBm; circles – $P_{p,in} = 13.86$ dBm; up triangles – $P_{p,in} = 13.76$ dBm; down triangles – $P_{p,in} = 13.66$ dBm; left triangles – $P_{p,in} = 13.56$ dBm

input of the 7-section LH NLTL. In this spectrum, the components corresponding to the signal wave ($f_s = f_2$), idler wave (f_1), as well as many difference frequencies generated due to the strong nonlinearity in LH NLTL, are evident. Thus, the application of the intensive pump wave results in amplification of the weak signal by 9 dB.

Figure 5.5 represents the measured gain of a weak 864.252 MHz signal stimulated by an intense 1.7279 GHz pump wave versus the power of the signal at the input, for fixed values of the pump power. The gain was calculated as the difference between the power of the signal at the output and the power at the input when both are expressed in dBm. Thus, we measured a greater than 10 dB amplification of the signal with power of −32 dBm and below for the power of the pump wave at the input of 13.96 dBm. The measured dependencies of gain versus input signal power becomes flatter with decreasing pump power, thus revealing the potential for amplification in a broad band of the signal power. The results of our measurements in Fig. 5.5 are in a good agreement with the results of simulations reported in [41].

5.3.3 Motivation for Considering Parametric Generation and Amplification

Parametric amplification can be of interest for building "active" or "amplifying" metamaterials and for providing a means to compensate for inherent LH media loss, as suggested in [37, 41, 42]. The primary drawback of current negative-index metamaterials (NIMs) (for example those composed of the arrays of metallic wires and split-ring resonators) is their considerable loss, which renders the results ambiguous and the materials all but useless for practical applications. These losses have been overcome to some extent by careful fabrication and assembly techniques [43], but still remain the primary obstacle to using NIMs in imaging applications. It was shown [44] that due to causality requirements, the use of conventional composite NIMs (based on arrays of metallic wires and arrays of split-ring resonators) does not

allow for the realization of low-loss NIMs without the incorporation of some active components (transistor amplifiers, etc.) in a composite NIM. The idea of using parametric amplification to compensate for inherent loss in optical left-handed systems has been also discussed in [45].

5.4 Higher Harmonic Generation

In short LH NLTLs, harmonic generation dominates over parametric instabilities [36]. We observed very efficient 2nd harmonic generation in a 4-section LH NLTL. The design of this transmission line is similar to the design of 7-section LH NLTL described in the previous section. However, this time, the nonlinear capacitance in each section is formed by two back-to-back M/A-COM hyperabrupt junction GaAs flip-chip varactor diodes (MA46H120) and shunt inductances were implemented with 0.12 mm diameter copper wires connecting the pads to the ground plane on the back side of the board.

The measured value for the second harmonic conversion efficiency in this 4-section LH NLTL was 19 % at 2.875 GHz, using a +17.9 dBm input signal and a reverse bias voltage of 6.4 V (Fig. 5.6). The second harmonic power delivered into a 50 Ω load was +10.72 dBm. The fundamental wave is close to the Bragg cutoff frequency while the second harmonic wave is close to the transmission maximum, which is located in the middle of the left-handed passband. A fundamental of 2.875 GHz generates numerous higher harmonics, with the second harmonic dominating over the fundamental and the other harmonics. Thus, the LH NLTL combines the properties of both a harmonic generator and a bandpass filter, and under certain conditions may provide an almost pure higher harmonic at its output.

The conversion efficiency observed in the LH NLTL is comparable with the per-stage efficiency of a hybrid Schottky-diode RH NLTL operated in a lower frequency range [46]. The fundamental wave propagating in the left-handed media is badly mismatched with its higher harmonics due to inherent anomalous dispersion, yet the generation of higher harmonics can still be very effective in LH NLTLs and the discrete nature of the NLTL plays a crucial role in it. The detailed analysis indicates that, within the range of parameters of the pump wave where the 2nd harmonic conversion efficiency has maximum, the amplitude of the voltage oscillations across the nonlinear capacitors varies periodically with the period equal to 2 sections. This self-induced periodicity of the voltage amplitude across the nonlinear capacitors leads to a periodic variation of the capacitance along the line. Due to strong nonlinearity (large capacitance ratio), this periodicity results in a considerable change of the dispersion characteristics and enables quasi-phase matching of the fundamental wave and its second harmonics. Simulations have also shown that, under certain conditions, the self-induced periodicity may provide quasi-phase matching of the fundamental wave with some other higher harmonics in such a way that a particular higher harmonic will dominate over other higher harmonics in the spectrum of the waveform at the LH NLTL output.

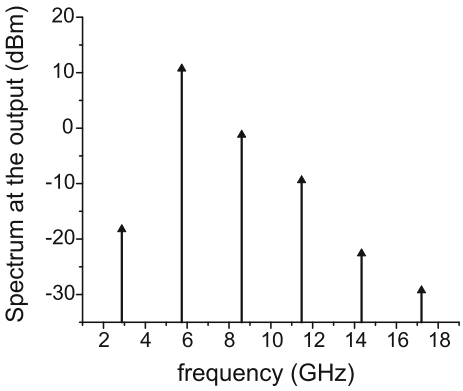

Fig. 5.6 Spectrum of the output waveform generated by a -section LH NLTL fed by 2.875 GHz, +17.9 dBm input signal at reverse bias voltage of 6.4 V

Efficient 2nd harmonic generation can be also achieved in dual band LH NLTLs that allow phase-matching between two zero phase velocity waves, as well as between two backward propagating modes [47].

5.5 Envelope Solitons in LH NLTLs

Besides the nonlinear evolution of a waveform itself, another class of phenomena involving evolution of amplitude and phase of continuous waves is also possible. This type of nonlinear wave propagation phenomena arise in NLTLs having strong frequency dispersion with respect to the average amplitude for amplitude-modulated wave containing a carrier of relatively high frequency. This dispersion may lead to amplitude instability as well as to formation of envelope solitons and periodic modulation of a carrier wave propagating in a stationary manner. The observation of amplitude instability and envelope soliton generation in conventional (RH) NLTLs has already been the subject of many publications [48–50]. The experimental observation of the generation of the trains of envelope solitons in LH NLTLs arising from the self-modulational instability was first reported in [51].

The analysis of LH NLTLs is straightforward when the equations governing envelope evolution can be reduced to the one-dimensional cubic nonlinear Schrödinger equation (NSE), which provides a canonical description for the envelope dynamics of a quasi-monochromatic plane wave (the carrier) propagating in a weakly nonlinear dispersive medium when dissipative processes (including nonlinear damping due to higher harmonic generation and nonlinear wave mixing) are negligible [52, 53]. However, in most of the practical situations the parametric decay instabilities and higher harmonic generation can be very significant [35, 37, 38, 54]. The threshold for parametric generation is known to be very low (lower then in conventional RH NLTLs). In order to realize the scenario described by the NSE, the LH NLTL should be operated below this threshold so that the nonlinearity should be very

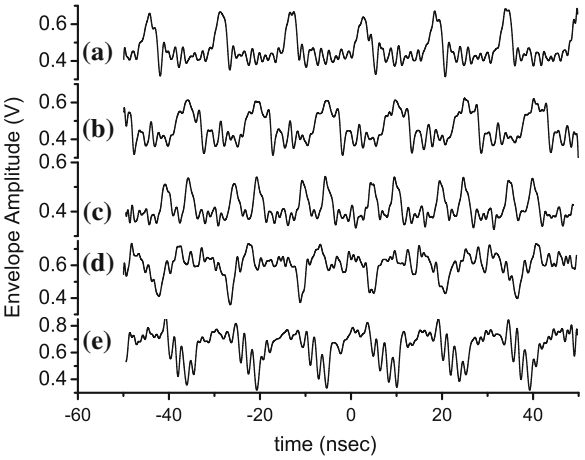

Fig. 5.7 Measured trains of envelope solitons for different power P_{inp} and the frequency f_{inp} of the input signal. **a** $f_{inp} = 1.3723\,\text{GHz}$, $P_{inp} = 24.66\,\text{dBm}$; **b** $f_{inp} = 1.3125\,\text{GHz}$, $P_{inp} = 21.60\,\text{dBm}$; **c** $f_{inp} = 1.321596\,\text{GHz}$, $P_{inp} = 19.34\,\text{dBm}$; **d** $f_{inp} = 1.2974\,\text{GHz}$, $P_{inp} = 24.64\,\text{dBm}$; **e** $f_{inp} = 1.102\,\text{GHz}$, $P_{inp} = 23.62\,\text{dBm}$

weak and the NLTL impractically long. In contrast, we performed an experimental study of nonlinear envelope evolution and envelope soliton generation in relatively short LH NLTLs and when nonlinear damping is very strong. We are also taking advantage of a fast nonlinearity introduced by Schottky diodes when nonlinear capacitance is a function of the instantaneous value of voltage along the line rather then its amplitude, a type of nonlinearity not described in the framework of the NSE and its modifications developed for slow (retarding) nonlinearity.

Depending on the amplitude and frequency of the input signal, trains of envelope solitons of different shape and types can be generated. Figure 5.7 shows envelopes of the measured waveforms at the output of 7-section LH NLTL. These envelopes' functions have been obtained by applying the Hilbert transform to the original voltage waveforms. Traces (a), (b) and (c) in Fig. 5.7 show trains of bright envelope solitons of different shapes while traces (d) and (e) show periodic trains of dark-like solitons (dips in the cw background). The envelope shape is not smooth since strong nonlinearity gives rise to numerous higher harmonics and subharmonics of carrier frequency. In the spectral domain, generation of envelope solitons manifests itself in the appearance of spectral regions with numerous closely spaced spectral harmonics. The interval between adjacent spectral components is $\Delta f = 1/\tau$, where τ is the period of the train of solitons.

A small variation of the parameters of the input signal leads to switching between the generation of bright and dark solitons [compare traces (a) and (b)] in contrast to the scenario described by the NSE. The observed switching is enabled by the counterplay of the significant nonlinear damping (due to strong and fast nonlinearity) and strong spatial dispersion exhibited by the periodic LH NLTLs. Neither is taken

into account by standard NSE yet both are known to lead to co-existence of bright and dark solitons in other physical systems [54, 55]. For example, somewhat similar processes have recently been observed in the system of an in-plane magnetized single crystal yttrium-iron-garnet (YIG) film in the magnetostatic backward volume wave configuration [55]. In contrast to this work, we applied non-modulated sine wave at the input.

Furthermore, efficient envelope soliton generation has been observed in active resonant rings based on LH NLTLs. Stable regimes corresponding to one, two and three solitons circulating in the ring has been enabled without any special mode selection arrangements and has been explained as the interplay of anomalous dispersion and discreteness resulting in formation of spatially localized structures [56].

5.6 Pulse Formation in LH NLTL Media

Here we discuss another type of envelope evolution resulting in generation of RF pulses of limited duration with stable amplitude and very short rise/fall times (sharp transients). This type of envelope evolution is primarily enabled by the amplitude-dependent higher harmonic generation rather than self-modulation instability leading to generation of the envelope solitons [57].

Figure 5.8 shows a typical dependence of the magnitude of the second harmonics at the output of 7-section LH NLTL shown in Fig. 5.2 versus magnitude of the input sinusoidal signal. This dependence has three distinct regions. In the first region the power of the generated second harmonic follows a square law as predicted by the small signal analysis. When the power of the fundamental wave reaches certain threshold level the second harmonic power jumps by almost 5 dB indicating a bifurcation (multistability region) followed by the saturation region where second harmonic amplitude changes insignificantly with the input power. Step-like dependence of the second harmonic power indicates a bifurcation-type change in the field distribution along the line and formation of field patterns that change dispersion properties of the line (quasi-phase matching) resulting in significant increase of the generation efficiency.

The step-like dependence of the second harmonic power on the power of the fundamental signal may impact significantly the output waveform if the amplitude in the fundamental wave is modulated around the threshold value. Figure 5.9 shows voltage waveforms at the input and output port and spectrum at the output of 7-section LH NLTL. The voltage waveform at the input is a sinusoidal wave modulated by another sinusoidal signal at 100 MHz. The envelope of the output waveform is dramatically different from the one of the input wave. It represents itself a series of pulses with the shape approaching a rectangular. Furthermore, the carrier frequency of the output signal is the second harmonic of the fundamental signal as revealed by the spectrum presented in Fig. 5.9c. Modulated signal switches second harmonic generation on and off thus enabling generation of a train of RF pulses at the output. Since the fundamental frequency is chosen below the cut-off frequency, it is heavily

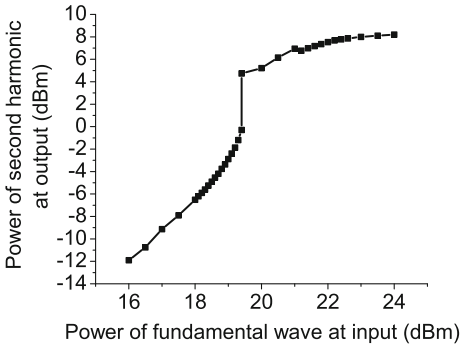

Fig. 5.8 Dependence of the power of the 2nd harmonic at the output on the power of the fundamental signal at the input in 7-section LH NLTL shown in Fig. 5.2 and measured at 783 MHz and the reverse bias voltage $V_B = -4.1$ V

attenuated in transmission line and only second harmonic is present at the output. Some asymmetry of the shape of the RF pulses at the output is related to the existence of hysteresis and narrow multistability region. The experimental results presented

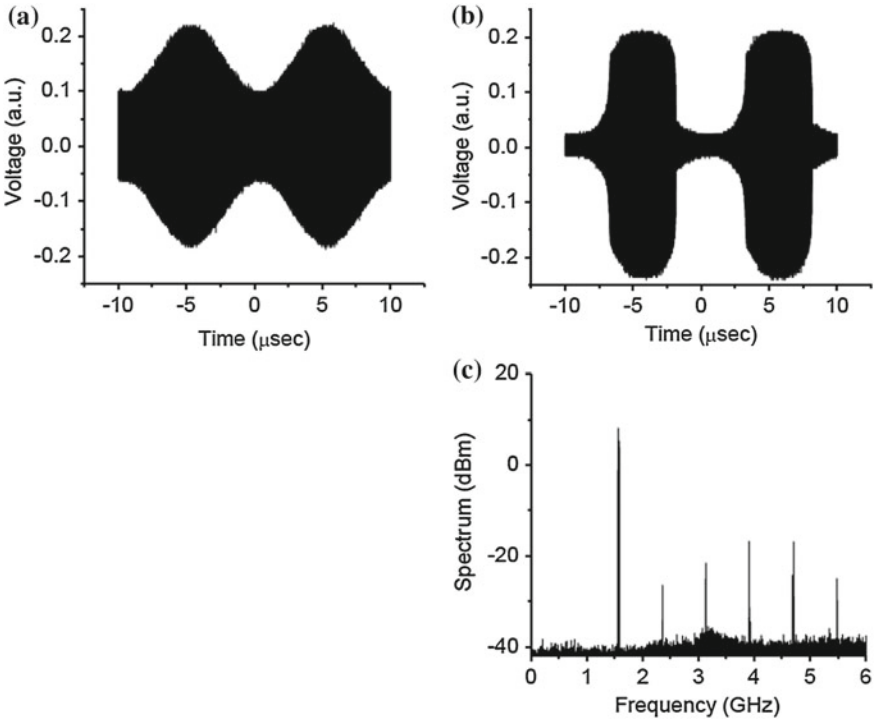

Fig. 5.9 Voltage waveforms at the input (**a**) and output (**b**) port and spectrum at the output (**c**) of 7-section LH NLTL. Voltage was measured at the coupled output of directional couplers connected at the input and output ports of NLTL

in Fig. 5.9 clearly demonstrate that a small modulation signal can be used to control the shape, duration and repetition rate of the RF pulses at the output which is very promising to numerous applications.

Our experimental results correlate very well with speculations in [58] where authors predicted that the shape of pulses at the output of LH media can be drastically different from those expected from an ordinary nonlinear medium.

5.7 Conclusion

We have reviewed several nonlinear wave phenomena in LH NLTL media, including harmonic generation, parametric amplification as well as generation of the trains of envelope solitons and their competition. Furthermore, LH NLTLs which were considered as a model system in this paper, can be also of interest from the design perspective for development of various compact and robust applications for wireless communications and imaging. LH NLTLs have already been used as the key counterparts of recently designed and implemented tunable phase-shifters, tunable band-pass filters, and the arbitrary waveform generator [23, 59–61]. Moreover, extending the results for 1-D LH NLTL to higher dimensions would enable combining harmonic generation in LH NLTL media with focusing [15], due to the negative refractive index of 2-D or 3-D LH transmission line media. This may lead to the development of highly efficient and powerful frequency multipliers, as well as to building "active" or "amplifying" super lenses. Furthermore, our approach can be also scaled from its current microwave form into terahertz, infrared, and, ultimately, visible form [62, 63]. Potential applications may include pulse forming circuits, optical comb generators (in optical metrology systems), amplifiers of digital signals as well as very efficient modulators at power levels or in frequency ranges not attainable by conventional semiconductor devices.

This work was supported under the Air Force Office of Scientific Research, MURI Grant No F49620-03-1-0420, 'Nanoprobe Tools for Molecular Spectroscopy and Control'.

References

1. N. Engheta, R.W. Ziolkowski, *Metamaterials: Physics and Engineering Explorations* (Wiley, New York, 2006)
2. V.G. Veselago, Sov. Phys. Uspekhi **10**, 509 (1968)
3. R.A. Shelby, D.R. Smith, S. Schultz, Science **292**, 77 (2001)
4. D.R. Smith, W.J. Padilla, D.C. Vier, S.C. Nemat-Nasser, S. Schultz, Phys. Rev. Lett., **84**, 4184 (2000)
5. A.M. Belyantsev, A.B. Kozyrev, Tech. Phys. **47**, 1477 (2002)
6. C. Caloz, T. Itoh, IEEE Antennas Propag. Soc. Int. Symp. Dig. **2**, 412 (2002)
7. A.K. Iyer, G.V. Eleftheriades, IEEE MTT-S Int Symp. Dig., **2**, 1067 (2002)

8. J.B. Pendry, Phys. Rev. Lett. **85**, 3966 (2000)
9. A. Lai, C. Caloz, T. Itoh, IEEE Microw. Mag. **5**, 34 (2004)
10. M. Anioniades, G.V. Eleftheriades, IEEE Antenna Wirel. Prop. Lett. **2**, 103 (2003)
11. C. Caloz, A. Sanada, T. Itoh, IEEE Trans. Microw. Theory Tech. **52**, 980 (2004)
12. L. Liu, C. Caloz, C.-C. Chang, T. Itoh, J. Appl. Phys. **92**, 5560 (2002)
13. S. Lim, C. Caloz, T. Itoh, IEEE Trans. Microw. Theory Tech. **53**, 161 (2005)
14. L. Liu, C. Caloz, T. Itoh, Electron. Lett. **38**, 1414 (2002)
15. A. Grbic, G.V. Eleftheriades, J. Appl. Phys. **92**, 5930 (2002)
16. M. Lapine, M. Gorkunov, Phys. Rev. E **70**, 066601 (2004)
17. M. Lapine, M. Gorkunov, K.H. Ringhofer, Phys. Rev. E **67**, 065601 (2003)
18. D.A. Powell, I.V. Shadrivov, Y.S. Kivshar, M.V. Gorkunov, Appl. Phys. Lett. **91**, 144107 (2007)
19. I.V. Shadrivov, S.K. Morrison, Y.S. Kivshar, Opt. Exp. **14**, 20 (2006)
20. A.A. Zharov, I.V. Shadrivov, Y.S. Kivshar, Phys. Rev. Lett. **91**, 037401 (2003)
21. I.V. Shadrivov, Y.S. Kivshar, J., Opt. A Pure Appl. Opt. **7**, 68 (2005)
22. V.M. Shalaev, Nature Photon. **1**, 41 (2007)
23. H. Kim, A.B. Kozyrev, D.W. van der Weide, IEEE Microw. Wirel. Comp. Lett. **15**, 366 (2005)
24. D.F. Sievenpiper, IEEE Trans. Antennas Prop. **53**, 236 (2005)
25. I. Gil, J. Garcia-Garcia, J. Bonache, F. Martin, M. Sorolla, R. Marques, Electron. Lett. **40**, 1347 (2004)
26. A.L. Cullen, Nature **181**, 332 (1958)
27. P.K. Tien, J. Appl. Phys. **29**, 1347 (1958)
28. W.H. Louisell, *Coupled Mode and Parametric Electronics* (Wiley, New York, 1960)
29. A.V. Gaponov, L.A. Ostrovskii, G.I. Freidman, Radiophys. Quant. Electron. **10**, 772 (1967)
30. I.G. Kataev, *Electromagnetic Shock Waves* (Illife, London, 1966)
31. R. Hirota, K. Suzuki, Proc. IEEE **61**, 1483 (1973)
32. R. Landauer, IBM J. **4**, 391 (1960)
33. R. Landauer, J. Appl. Phys. **31**, 479 (1960)
34. C. Caloz, I.H. Lin, T. Itoh, Microw. Opt. Tech. Lett. **40**, 471 (2004)
35. A.B. Kozyrev, H. Kim, A. Karbassi, D.W. van der Weide, Appl. Phys. Lett. **87**, 121109 (2005)
36. A.B. Kozyrev, D.W. van der Weide, IEEE Trans. Microw. Theory Tech. **53**, 238 (2005)
37. A.B. Kozyrev, H. Kim, D.W. van der Weide, Appl. Phys. Lett. **88**, 264101 (2006)
38. A.S. Gorshkov, G.A. Lyakhov, K.I. Voliak, L.A. Yarovoi, Physica D **122**, 161 (1998)
39. S.E. Harris, Appl. Phys. Lett. **9**, 114 (1966)
40. A. Yariv, *Quantum Electronics* (Wiley, New York, 1988)
41. A.B. Kozyrev, D.W. van der Weide, IEEE Antennas Prop. Soc. Int. Symp. Dig. 672 (2005)
42. A.B. Kozyrev, D.W. van der Weide, US Patent 7,135,917 B2 (2006)
43. A.A. Houck, J.B. Brock, I.L. Chuang, Phys. Rev. Lett. **90**, 137401 (2003)
44. S.A. Tretyakov, Microw. Opt. Tech. Lett. **31**, 163 (2001)
45. A.K. Popov, V.M. Shalaev, Opt. Lett. **31**, 2169 (2006)
46. J.-M. Duchamp, P. Ferrari, M. Fernandez, A. Jrad, X. Melique, J. Tao, S. Arscott, D. Lippens, R.G. Harrison, IEEE Trans. Microw. Theory Technol. **51**, 1105 (2003)
47. W.R.C. Somerville, D.A. Powell, I.V. Shadrivov, Appl. Phys. Lett. **98**, 161111 (2011)
48. K.E. Lonngren, A. Scott, *Solitons in Action* (Academic Press, New York, 1978)
49. L.A. Ostrovskii, L.V. Soustov, Izvestiya Vysshikh Uchebnykh Zavedenii. Radiofizika **15**, 242 (1972)
50. T. Yagi, A. Noguchi, Electron. Commun. Japan **59**, 1 (1976)
51. A.B. Kozyrev, D.W. van der Weide, Appl. Phys. Lett. **91**, 254111 (2007)
52. S. Gupta, C. Caloz, IEEE MTT-S Int. Symp. Dig. **18**, 979–982 (2007)
53. K. Narahara, T. Nakamichi, T. Suemitsu, T. Otsuji, E. Sano, J. Appl. Phys. **102**, 024501 (2007)
54. Y.S. Kivshar, W. Krolikowski, O.A. Chubykalo, Phys. Rev. E **50**, 5020–32 (1994)
55. M.M. Scott, M.P. Kostylev, B.A. Kalinikos, C.E. Patton, Phys. Rev. B **71**, 174440 (2005)
56. A.B. Kozyrev, I.V. Shadrivov, Yu.S. Kivshar, Appl. Phys. Lett. **104**, 084105 (2014)
57. A.B. Kozyrev, D.W. van der Weide, Appl. Phys. Lett. **96**, 104106 (2010)
58. V.M. Agranovich, Y.R. Shen, R.H. Baughman, A.A. Zakhidov, Phys. Rev. B **69**, 165112 (2004)

59. H. Kim, A.B. Kozyrev, S.-J. Ho, D.W. van der Weide, Microwave Symp. Dig. P. **4** (2005)
60. H. Kim, S.-J. Ho, M.K. Choi, A.B. Kozyrev, D.W. van der Weide, IEEE Trans. MTT **54**, 4178 (2006)
61. H. Kim. A.B. Kozyrev, D.W. van der Weide, IEEE Trans. MTT, **55**, 571 (2007)
62. C. Qin, A.B. Kozyrev, A. Karbassi, D.W. van der Weide, Metamaterials **2**, 26 (2008)
63. N. Engheta, A. Salandrino, A. Alu, Phys. Rev. Lett. **95**, 95504 (2005)

Chapter 6
Optimization Strategies for Second-Order Nonlinear Metamaterials

Robert Czaplicki, Hannu Husu, Janne Laukkanen, Markku Kuittinen and Martti Kauranen

Abstract We summarize our recent results regarding the control and optimization of the second-order nonlinear response of plasmonic metamaterials. Such materials consist of arrays of metal nanoparticles, where the plasmonic resonances of individual particles depend on the size, shape, and dielectric environment of the particles. The resonances are further influenced by the coupling of the particles through the array. We first show that the second-order response, as determined by second-harmonic generation is significantly enhanced by the state-of-the-art sample quality and the resulting narrow plasmonic resonance lines. We then show that the response can depend on subtle details of the ordering of the particles in the array, with apparently similar orderings resulting in second-harmonic generation responses that differ by a factor of 50. Finally, we show that the response can be enhanced by complementing the second-harmonic active particles with passive elements that have no nonlinear response as such. Our results are important in developing metamaterials with tailorable nonlinear properties.

R. Czaplicki (✉) · M. Kauranen · H. Husu
Department of Physics, Tampere University of Technology, P.O. Box 692,
33101 Tampere, Finland
e-mail: robert.czaplicki@tut.fi

M. Kauranen
e-mail: martti.kauranen@tut.fi

H. Husu
Centre for Metrology and Accreditation (MIKES), P.O. Box 9,
FI-02151 Espoo, Finland
e-mail: hannu.husu@mikes.fi

J. Laukkanen · M. Kuittinen
Institute of Photonics, University of Eastern Finland,
P.O. Box 111, 80101 Joensuu, Finland
e-mail: janne.laukkanen@uef.fi

M. Kuittinen
e-mail: markku.kuittinen@uef.fi

I.V. Shadrivov et al. (eds.), *Nonlinear, Tunable and Active Metamaterials*,
Springer Series in Materials Science 200, DOI 10.1007/978-3-319-08386-5_6

6.1 Introduction

The collective oscillations of electrons, known as plasmons, play an important role in the optical response of metal nanoparticles. The properties of the particle plasmons are determined by the particle dimensions and shape, and are further influenced by the surrounding medium [1]. Individual particles are often arranged in arrays, as is the case for metamaterials. As a result, the plasmons are affected by the coupling between particles.

The plasmon resonances are associated with "hot spots", which are strong electromagnetic fields in the proximity of the particles [2]. The hot spots can significantly enhance nonlinear optical interactions, which scale with high powers of the fundamental field [3]. For example, second-harmonic generation (SHG) scales with the second power of the local field. SHG was observed in metal nanostructures already a few decades ago [4]. Since then a lot of SHG studies have been performed on different kinds of nanostructures, such as hole arrays [5–7], sharp metallic tips [8–10], split-ring resonators [11–13], L-shaped [14–19] and G-shaped [20, 21] nanoparticles, nanoprisms [22], spherical nanoparticles [9, 23, 24], T-nanodimers [25, 26], nanoantennas [27–29] and nanocups [30].

Second-order nonlinear effects are particular because of their symmetry rules, which forbid such effects in centrosymmetric materials. This property, on the other hand, can be used to probe symmetry breaking in the material structure. In the early studies of the nonlinear properties of metal nanoparticles, the symmetry breaking due to defects and shape distortions played a significant role in the responses of real fabricated structures [31].

In this chapter, we focus on summarizing our recent results regarding the various factors that need to be considered when one attempts to optimize the second-order nonlinear response of plasmonic metamaterials consisting of arrays of metal nanoparticles. In order to achieve the necessary noncentrosymmetry, our basic building unit (metamolecule) is an anisotropic, L-shaped gold nanoparticle. The SHG response of the samples is shown to depend sensitively on the sample quality, detailed particle ordering in the array, as well as the presence of centrosymmetric passive elements in the array.

6.2 Samples and Techniques

Our samples are fabricated by standard electron-beam lithography and lift-off techniques. All samples are fabricated on fused silica substrates. The 20 nm thick nanoparticles are separated from the substrate by a chromium adhesion layer (3–5 nm) and are also covered by 20 nm protective layer of fused silica. The dimensional parameters (l—length of arm, w—width of arm and d—array period) vary between different samples (Table 6.1 and Fig. 6.1).

Table 6.1 The dimensional parameters of L-shaped nanoparticles from studied samples

	Arm length (l)[nm]	Arm width (w)[nm]	Array period (d)[nm]
Low-quality sample [18]	200	100	400
High-quality sample [32]	250	100	500
Samples A and B [33]	250	100	500
Nanoantenna [34]	175, 275	100	1,000

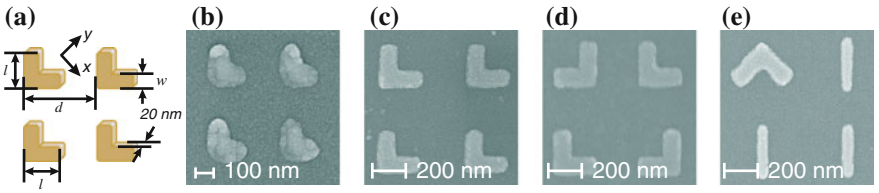

Fig. 6.1 **a** The geometry and coordinate system of L-shaped nanoparticles in standard array (l—length of arm, w—width of arm, d—spacing between particles, thickness 20 nm). The scanning electron microscope images of **b** low-quality L-shaped nanoparticles, **c** high-quality L-shaped nanoparticles (standard array), **d** high-quality L-shaped nanoparticles with different orientations in array and **e** high-quality active L-shaped nanoparticles and passive bars

The L-shape is strongly dichroic with plasmon resonances at distinct wavelengths for x- and y-polarized light, where y is along the symmetry axis and x orthogonal to that. This was confirmed by measuring the extinction spectra of the samples. The measurements were performed at normal incidence with a fiber-coupled halogen light source and two spectrometers as detectors, which cover a total range from 400 to 1,700 nm.

In order to address the nonlinear properties of the samples, polarization-dependent SHG measurements are performed (Fig. 6.2). Infrared radiation from a pulsed Nd:glass laser (Time-Bandwidth Products GLX-200; 200 fs, 1,060 nm, 150 mW, 82 MHz) is the source of fundamental light. The polarization state of fundamental beam is cleaned with a high-quality Glan polarizer and further modulated by rotating a half- (HWP) or quarter-wave plate (QWP). The polarization of the SHG signal is selected by another Glan polarizer as an analyzer before the detector. A long pass filter before the sample blocks the SHG radiation from optical components. The SHG light is isolated from the laser beam with a short pass filter and is measured with a photomultiplier tube combined with a photon counting system.

6.3 Tailoring Nonlinear Optical Response

We have been working on the nonlinear properties of the arrays of metal nanoparticles for several years. The work has been based on systematic testing of the various concepts, and has recently been facilitated by significant improvements in nanofabrication, which gives rise to samples of very high quality.

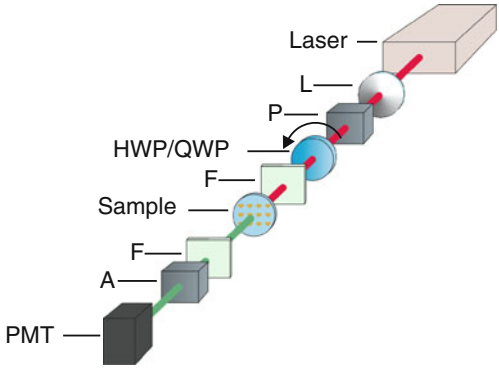

Fig. 6.2 Experimental setup for second-harmonic generation measurements. *L*—lens, *P*—polarizer, *HWP*—half-wave plate, *QWP*—quarter-wave plate, *F*—filter, *A*—analyzer, *PMT*—photomultiplier tube

6.3.1 Sample Quality

All even-order nonlinear processes, including SHG, are extremely sensitive to symmetry and consequently to the details of the local-field distribution in the sample. Fabrication-related defects can give rise to additional hot spots that attract strong local fields. Small deviations of the actual sample from the design as well as the defects also break the structural symmetry of the sample. This can lead to SHG responses that can be interpreted in terms of multipolar contributions to the nonlinear response [16–18]. The imperfections in the fabrication process lead also to variations in the dimensions of the particles in the array. As a consequence the resonance peaks are inhomogeneously broadened, which also reduces the nonlinear response [14, 32]. All the above factors make it difficult to design nanostructures with controlled nonlinear responses. The recent vast improvement in fabrication methods overcomes these problems. Such improvement is evident in the case of our samples (cf. Fig. 6.1b, c). This improvement in sample quality is already visible in linear extinction spectra of the samples, where the plasmonic peaks are greatly enhanced and linewidths narrowed compared to the low quality samples (cf. Fig. 6.3a, b) [32]. The resonances with less inhomogeneous broadening also allow high-order resonances to be observed [35, 36].

Our experimental technique allows the samples to be characterized for polarization-dependent SHG. In order to address the various multipolar contributions to the response, it is necessary to detect SHG radiation in transmission and reflection and for particle- and substrate-side incidence of the fundamental beam [18, 32]. In essence, the four signals should behave in the same way when the response has dipolar origin, whereas higher-multipole contributions lead to differences in the signals. The results for low-quality ($l = 200\,\text{nm}$, $w = 100\,\text{nm}$, $d = 400\,\text{nm}$) and high-quality ($l = 250\,\text{nm}$, $w = 100\,\text{nm}$, $d = 500\,\text{nm}$) L-shaped gold nanoparticles are shown in Fig. 6.3c, d, respectively. The symmetry breaking of the low-quality sample due to defects results in strong differences in second-harmonic signals (Fig. 6.3c), which is interpreted as a multipolar character of the SHG response [16–18]. The

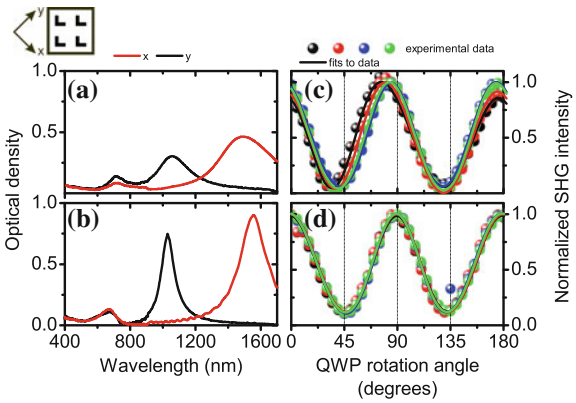

Fig. 6.3 Extinction spectra of **a** low-quality (cf. Fig. 6.1b) and **b** high-quality nanoparticles (cf. Fig. 6.1c). SHG signals from an array of L-shaped gold nanoparticles as a function of rotation angle of QWP for **c** low-quality and **d** high-quality nanoparticles. Adapted with permission from [18], Copyright Institute of Physics 2011 and [32], Copyright Optical Society of America 2011

respective SHG signals for the high-quality sample, on the other hand, overlap very well (Fig. 6.3d). Furthermore, a detailed tensor analysis of these signals suggests that multipolar tensor components for SHG are suppressed to below 2 % of the dominant dipolar component. In addition to that, the sample with improved quality gives rise to the enhancement of SHG by a factor of ten compared to the low-quality sample.

6.3.2 Particle Ordering

When the shape and dimensions of the nanoparticles are optimized to the desired parameters, the next natural step is to play with the ordering of the particles in the array. At the same time, the changes in the ordering lead to changes in the dimensions of the unit cells of the arrays. The unit cell size in turn determines whether the unit cells can or cannot be coupled to each other through diffractive effects. Such coupling occurs in the resonance domain where the array period is close to the wavelength of incident light outside the sample or in the substrate. It has been shown earlier that such effects can lead to spectral narrowing and enhancement of plasmonic resonances [27, 37–42].

For our samples, the size of the unit cell is controlled by the orientation of the L-shaped particles ($l = 250\,\text{nm}$, $w = 100\,\text{nm}$, $d = 500\,\text{nm}$) in the array [33, 43]. The modifications in the sample layout from the standard (Fig. 6.3) lead to the doubling of the period of the array in one (sample A) or two (sample B) directions (cf. insets in Fig. 6.4a, b). Note that such modifications in the sample structure also lead to changes in their proper eigenpolarizations, which are denoted as u and v (Fig. 6.4). The first observation is that the linear properties of the samples are modified resulting

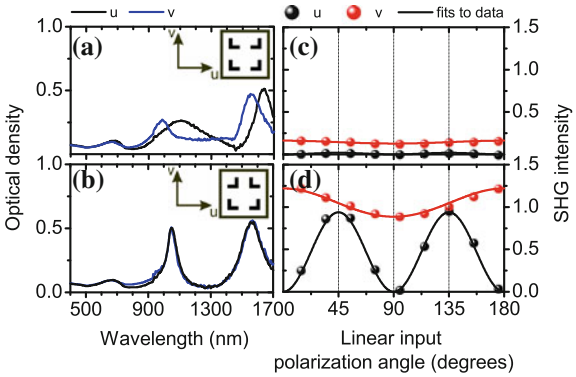

Fig. 6.4 The linear spectra of **a** Sample A and **b** Sample B (Fig. 6.1d). Insets show the layouts of the samples and coordinate systems. Second-harmonic intensity from **c** Sample A and **d** Sample B as a function of the linear input polarization state for *u*- and *v*-polarized outputs. The polarization rotation starts from *u* polarization reaching the *v*-polarized input at 90°. Adapted with permission from [33]. Copyright American Chemical Society 2012

in narrower (Fig. 6.4b) or broader (Fig. 6.4a) plasmon resonances compared to the resonances for reference sample (Fig. 6.3b).

This approach thus opens new directions in the design of plasmonic arrays, in general, but also influences their nonlinear properties. Sample B with very narrow resonances enhances SHG (Fig. 6.4d) whereas sample A with broad resonances, decreases SHG (Fig. 6.4c). The SHG signals from the two modified samples differ from each other by a factor of 50. This is mostly due to the fact that the efficiency of SHG depends on the location and the width of resonances close to the fundamental wavelength (in our case 1,060 nm) [33]. In addition to that, the modification of the particle orientations modifies the tensorial properties of SHG radiation.

These results show that minor changes in the sample layout can be used to tailor both linear and nonlinear properties of the samples. Such approaches therefore provide additional degrees of freedom in tailoring the optical properties of metamaterials.

6.3.3 Passive Elements

So far we used only one type of particles in our sample arrays. However, combining particles of different shapes in the same array will provide additional opportunities where each particle is designed for a particular purpose. Our concept is based on the combination of SHG active L-shaped particles with centrosymmetric passive nanobars (cf. Fig. 6.1e) [34]. The bars are passive in the sense that they are centrosymmetric and thus do not produce SHG as such. However, when the nano-

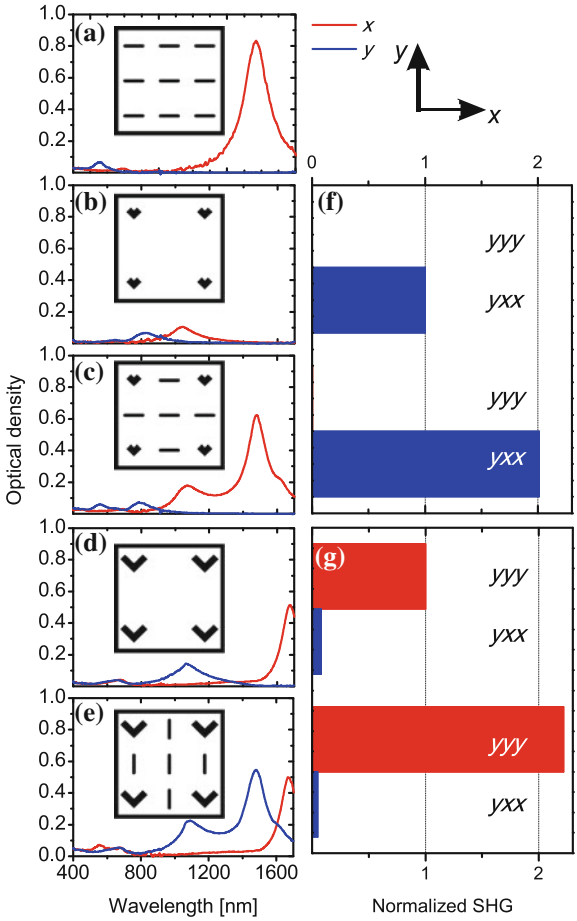

Fig. 6.5 **a–e** Polarized extinction spectra of studied samples (layouts shown as *insets*). **f** and **g** SHG signals from the samples normalized to the strongest signals of the reference L sample (*yxx* for small L's and *yyy* for big L's). Adapted with permission from [34]. Copyright (2013) by The American Physical Society

bars are placed in the same array as SHG active L's, they modify linear responses and subsequently the local electromagnetic fields.

We prepared two series of samples: reference samples consisting of an array of SHG active L-shaped nanoparticles ($l = 175\,\text{nm}$, $w = 100\,\text{nm}$, $d = 1,000\,\text{nm}$, inset in Fig. 6.5b and $l = 275\,\text{nm}$, $w = 100\,\text{nm}$, $d = 1000\,\text{nm}$, inset in Fig. 6.5d), array of passive bars ($l = 300\,\text{nm}$, $w = 50\,\text{nm}$, $d = 500\,\text{nm}$, inset in Fig. 6.5a) and samples combining active and passive elements (insets in Fig. 6.4c, e). In the latter case, the bars are oriented in x or y directions. The resonant polarizations of the L particles were also chosen to be x or y for smaller or bigger L's, respectively.

For the samples combining the two types of particles, the bars modify the resonances of the L's in a way that the entire spectrum is more than simple superposition of spectra of the L's and bars (Fig. 6.4c, e). As previously mentioned, the SHG efficiency depends on position of the plasmon peak with respect to the laser wavelength and also on the magnitude of the resonance. In the samples combining active and passive particles, the plasmon peaks close to the laser wavelength are enhanced by about a factor of two when the long axis of the bars is oriented along the polarization of the corresponding resonance. This enhancement is due to coupling between two types of particles although their resonances occur at different wavelengths. In contrast, for the samples containing bars oriented orthogonally, the plasmon peaks at the laser wavelength remain almost unchanged [34].

Such modification of the linear properties has strong influence on the nonlinear response of the samples. Compared to the respective reference samples, the SHG signals of the samples combining the two types of particles are enhanced by about a factor of two when the bars are oriented along the resonant polarization of the L's (Fig. 6.5f, g). In the case of small L's the tensor component *yxx* is enhanced, whereas the component *yyy* is enhanced in the case of large L's. Note also that, due to centrosymmetry, SHG from the bars is very close to the background noise. Furthermore, similarly to linear results, when the bars are oriented orthogonally to the resonant polarization of L's, the SHG signals are modified only little [34].

The results, particularly the strong correlation between linear data and SHG response, suggest that the enhancement of second-order nonlinear radiation arises from the modification by passive elements of the plasmon resonances and associated local-field distributions at the fundamental wavelength.

The results can be explained by using coupled-dipole model [44]. In terms of this model we treat each particle as a point dipole with anisotropic polarizability, where the total field acting on an individual particle includes the incident field and the sum of the retarded fields scattered by the other particles. The effective polarizability of the L's is thus modified by their coupling to the bars [34].

6.4 Towards Optimized Response

The optimization of the nonlinear optical responses of metal nanostructures and metamaterials has been gathering more and more attention during the last decade [3, 29, 45–49]. In order to enhance SHG from plasmonic surfaces, a variety of structures and ideas have been studied.

The resonance enhancement of SHG from split-ring resonators has been addressed and interpreted through a favorable effect from resonances at the fundamental wavelength but a detrimental loss mechanism at the harmonic frequency [13]. Losses are thus an obstacle for further enhancement of the second-order response. One way to overcome such problems is to use diffractive coupling between particles,which leads

to narrow resonances [41, 42]. Another approach to enhance the nonlinear response without increasing losses may be to use high-order resonances.

Using multiple resonances at the fundamental and second-harmonic wavelengths is another idea to boost the SHG response from nanostructures [28]. The latter was presented for double-resonant plasmonic antennas, which already use the idea of combining several particles into a more complex structure.

Typical examples of structures consisting of several particles are dimers which involve two nanoparticles placed closely to each other. Such adjacent location results in nanogap where the local-field is enhanced. We have shown this for T-shaped nanodimers formed from two bars, vertical and horizontal, separated by a few nm gap [25]. Our results suggested that the local-field distribution is affected by the coupling between the bars. Also, even very small differences in the structure of dimer significantly affect the local-field distribution and thus the SHG response [25].

More complicated oligomers show also strong coupling between particles [50, 51]. Recently, such oligomeric system has been studied in terms of enhancing second-harmonic response through Fano resonances [49].

6.5 Conclusions

We have addressed several issues that need to be considered in order to tailor and enhance the second-order nonlinear response from structured plasmonic surfaces. Although we have already obtained very promising results and demonstrated several new concepts, most of the presented ideas are not optimized yet. Furthermore, we have not yet combined these approaches into one in order to obtain the most efficient SHG plasmonic structure.

There are still many open questions concerning the nonlinearity from metal nanostructures. For example the role of surface and bulk effects in origin of the local SHG response is not clear yet. Some theoretical results emphasize the bulk contribution [52], while experimental results on flat metal films suggest the dominance of the surface effects [53]. Other ideas connect the importance of surface and bulk effects with experimental details [54] or emphasize the role of particle shape [55, 56].

We believe that our work is only the beginning of designing metamaterials with fully controllable nonlinear optical properties what will lead to various plasmonic applications.

Acknowledgments We thank B. K. Canfield, G. Genty, J. Lehtolahti, K. Koskinen, S. Kujala, J. Mäkitalo, H. Pietarinen, R. Siikanen, S. Suuriniemi, Y. Svirko, J. Turunen and M. Zdanowicz for fruitful discussions and/or help in measurements. This work was supported by the Academy of Finland (132438 and 134980) and by the Graduate School of the Tampere University of Technology.

References

1. K. Kelly, E. Coronado, L. Zhao, G. Schatz, The optical properties of metal nanoparticles: the influence of size, shape, and dielectric environment. J. Phys. Chem. B **107**, 668–677 (2003)
2. M. Stockman, D. Bergman, C. Anceau, S. Brasselet, J. Zyss, Enhanced second-harmonic generation by metal surfaces with nanoscale roughness: nanoscale dephasing, depolarization, and correlations. Phys. Rev. Lett. **92**, 057402 (2004)
3. M. Kauranen, A.V. Zayats, Nonlinear plasmonics. Nat. Photon. **6**, 737–748 (2012)
4. A. Wokaun, J.G. Bergman, J.P. Heritage, A.M. Glass, P.F. Liao, D.H. Olson, Surface second-harmonic generation from metal island films and microlithographic structures. Phys. Rev. B **24**, 849–856 (1981)
5. J.A.H. van Nieuwstadt, M. Sandtke, R.H. Harmsen, F.B. Segerink, J.C. Prangsma, S. Enoch, L. Kuipers, Strong modification of the nonlinear optical response of metallic subwavelength hole arrays. Phys. Rev. Lett. **97**, 146102 (2006)
6. T. Xu, X. Jiao, G.-P. Zhang, S. Blair, Second-harmonic emission from sub-wavelength apertures: effects of aperture symmetry and lattice arrangement. Opt. Express **15**, 13894–13906 (2007)
7. F. Eftekhari, R. Gordon, Enhanced second harmonic generation from noncentrosymmetric nanohole arrays in a gold film. IEEE J. Sel. Top. Quant. Electron. **14**, 1552–1558 (2008)
8. S. Takahashi, A.V. Zayats, Near-field second-harmonic generation at a metal tip apex. Appl. Phys. Lett. **80**, 3479–3481 (2002)
9. A. Bouhelier, M. Beversluis, A. Hartschuh, L. Novotny, Near-field second-harmonic generation induced by local field enhancement. Phys. Rev. Lett. **90**, 013903 (2003)
10. J.M. Kontio, H. Husu, J. Simonen, M.J. Huttunen, J. Tommila, M. Pessa, M. Kauranen, Nanoimprint fabrication of gold nanocones with 10 nm tips for enhanced optical interactions. Opt. Lett. **34**, 1979–1981 (2009)
11. M. Klein, C. Enkrich, M. Wegener, S. Linden, Second-harmonic generation from magnetic metamaterials. Science **313**, 502–504 (2006)
12. N. Feth, S. Linden, M. Klein, M. Decker, F. Niesler, Y. Zeng, W. Hoyer, J. Liu, S. Koch, J. Moloney, M. Wegener, Second-harmonic generation from complementary split-ring resonators. Opt. Lett. **33**, 1975–1977 (2008)
13. F.B.P. Niesler, N. Feth, S. Linden, M. Wegener, Second-harmonic optical spectroscopy on split-ring-resonator arrays. Opt. Lett. **36**, 1533–1535 (2011)
14. H. Tuovinen, M. Kauranen, K. Jefimovs, P. Vahimaa, T. Vallius, J. Turunen, N.-V. Tkachenko, H. Lemmetyinen, Linear and second-order nonlinear optical properties of arrays of noncentrosymmetric gold nanoparticles. J. Nonlinear Opt. Phys. Mater. **11**, 421–432 (2002)
15. B. Canfield, S. Kujala, K. Jefimovs, T. Vallius, J. Turunen, M. Kauranen, Polarization effects in the linear and nonlinear optical responses of gold nanoparticle arrays. J. Opt. A **7**, S110–S117 (2005)
16. S. Kujala, B. Canfield, M. Kauranen, Y. Svirko, T. Turunen, Multipole interference in the second-harmonic optical radiation from gold nanoparticles. Phys. Rev. Lett. **98**, 167403 (2007)
17. S. Kujala, B. Canfield, M. Kauranen, Y. Svirko, J. Turunen, Multipolar analysis of second-harmonic radiation from gold nanoparticles. Opt. Express **16**, 17196–17208 (2008)
18. M. Zdanowicz, S. Kujala, H. Husu, M. Kauranen, Effective medium multipolar tensor analysis of second-harmonic generation from metal nanoparticles. New J. Phys. **13**, 023025 (2011)
19. M. Gentile, M. Hentschel, R. Taubert, H. Guo, H. Giessen, M. Fiebig, Investigation of the nonlinear optical properties of metamaterials by second harmonic generation. Appl. Phys. B **105**, 149–162 (2011)
20. V.K. Valev, N. Smisdom, A.V. Silhanek, B. De Clercq, W. Gillijns, M. Ameloot, V.V. Moshchalkov, T. Verbiest, Plasmonic ratchet wheels: switching circular dichroism by arranging chiral nanostructures. Nano Lett. **9**, 3945–3948 (2009)
21. V.K. Valev, A.V. Silhanek, N. Verellen, W. Gillijns, P. Van Dorpe, O.A. Aktsipetrov, G.A.E. Vandenbosch, V.V. Moshchalkov, T. Verbiest, Asymmetric optical second-harmonic generation from chiral G-shaped gold nanostructures. Phys. Rev. Lett. **104**, 127401 (2010)

22. G. Hajisalem, A. Ahmed, Y. Pang, R. Gordon, Plasmon hybridization for enhanced nonlinear optical response. Opt. Express **20**, 29923–29930 (2012)
23. J. Butet, J. Duboisset, G. Bachelier, I. Russier-Antoine, E. Benichou, C. Jonin, P.-F. Brevet, Optical second harmonic generation of single metallic nanoparticles embedded in a homogeneous medium. Nano Lett. **10**, 1717–1721 (2010)
24. J. Butet, G. Bachelier, I. Russier-Antoine, C. Jonin, E. Benichou, P.-F. Brevet, Interference between selected dipoles and octupoles in the optical second-harmonic generation from spherical gold nanoparticles. Phys. Rev. Lett. **105**, 077401 (2010)
25. B. Canfield, H. Husu, J. Laukkanen, B. Bai, M. Kuittinen, J. Turunen, M. Kauranen, Local field asymmetry drives second-harmonic generation in noncentrosymmetric nanodimers. Nano Lett. **7**, 1251–1255 (2007)
26. H. Husu, B. Canfield, J. Laukkanen, B. Bai, M. Kuittinen, J. Turunen, M. Kauranen, Chiral coupling in gold nanodimers. Appl. Phys. Lett. **93**, 183115 (2008)
27. K.D. Ko, A. Kumar, K.H. Fung, R. Ambekar, G.L. Liu, N.X. Fang, K.C. Toussaint, Nonlinear optical response from arrays of Au bowtie nanoantennas. Nano Lett. **11**, 61–65 (2011)
28. K. Thyagarajan, S. Rivier, A. Lovera, O.J.F. Martin, Enhanced second-harmonic generation from double resonant plasmonic antennae. Opt. Express **20**, 12860–12865 (2012)
29. J. Butet, K. Thyagarajan, O.J.F. Martin, Ultrasensitive optical shape characterization of gold nanoantennas using second harmonic generation. Nano Lett. **13**, 1787–1792 (2013)
30. Y. Zhang, N.K. Grady, C. Ayala-Orozco, N.J. Halas, Three-dimensional nanostructures as highly efficient generators of second harmonic light. Nano Lett. **11**, 5519–5523 (2011)
31. B. Canfield, S. Kujala, K. Laiho, K. Jefimovs, J. Turunen, M. Kauranen, Chirality arising from small defects in gold nanoparticle arrays. Opt. Express **14**, 950–955 (2006)
32. R. Czaplicki, M. Zdanowicz, K. Koskinen, J. Laukkanen, M. Kuittinen, M. Kauranen, Dipole limit in second-harmonic generation from arrays of gold nanoparticles. Opt. Express **19**, 26866–26871 (2011)
33. H. Husu, R. Siikanen, J. Mäkitalo, J. Lehtolahti, J. Laukkanen, M. Kuittinen, M. Kauranen, Metamaterials with tailored nonlinear optical response. Nano Lett. **12**, 673–677 (2012)
34. R. Czaplicki, H. Husu, R. Siikanen, J. Mäkitalo, J. Laukkanen, J. Lehtolahti, M. Kuittinen, M. Kauranen, Enhancement of second-harmonic generation from metal nanoparticles by passive elements. Phys. Rev. Lett. **110**, 093902 (2013)
35. H. Husu, J. Mäkitalo, J. Laukkanen, M. Kuittinen, M. Kauranen, Particle plasmon resonances in L-shaped gold nanoparticles. Opt. Express **18**, 16601–16606 (2010)
36. R. Czaplicki, M. Zdanowicz, K. Koskinen, H. Husu, J. Laukkanen, M. Kuittinen, M. Kauranen, Linear and nonlinear properties of high-quality L-shaped gold nanoparticles. Nonl. Opt. Quant. Opt. **45**, 71–83 (2012)
37. S. Linden, J. Kuhl, H. Giessen, Controlling the interaction between light and gold nanoparticles: selective suppression of extinction. Phys. Rev. Lett. **86**, 4688–4691 (2001)
38. L. Zhao, K.L. Kelly, G.C. Schatz, The extinction spectra of silver nanoparticle arrays: influence of array structure on plasmon resonance wavelength and width. J. Phys. Chem. B **107**, 7343–7350 (2003)
39. A. Christ, S.G. Tikhodeev, N.A. Gippius, J. Kuhl, H. Giessen, Waveguide-plasmon polaritons: strong coupling of photonic and electronic resonances in a metallic photonic crystal slab. Phys. Rev. Lett. **91**, 183901 (2003)
40. A. Christ, T. Zentgraf, J. Kuhl, S.G. Tikhodeev, N.A. Gippius, H. Giessen, Optical properties of planar metallic photonic crystal structures: experiment and theory. Phys. Rev. B **70**, 125113 (2004)
41. Y. Chu, E. Schonbrun, T. Yang, K.B. Crozier, Experimental observation of narrow surface plasmon resonances in gold nanoparticle arrays. Appl. Phys. Lett. **93**, 181108 (2008)
42. B. Auguié, W.L. Barnes, Collective resonances in gold nanoparticle arrays. Phys. Rev. Lett. **101**, 143902 (2008)
43. H. Husu, J. Mäkitalo, R. Siikanen, G. Genty, H. Pietarinen, J. Lehtolahti, J. Laukkanen, M. Kuittinen, M. Kauranen, Spectral control in anisotropic resonance-domain metamaterials. Opt. Lett. **36**, 2375–2377 (2011)

44. García de Abajo, F.J. Colloquium, Light scattering by particle and hole arrays. Rev. Mod. Phys. **79**, 1267–1290 (2007)
45. C.M. Soukoulis, M. Wegener, Past achievements and future challenges in the development of three-dimensional photonic metamaterials. Nat. Photon. **5**, 523–530 (2011)
46. N.J. Halas, S. Lal, W.-S. Chang, S. Link, P. Nordlander, Plasmons in strongly coupled metallic nanostructures. Chem. Rev. **111**, 3913–3961 (2011)
47. M. Navarro-Cia, S.A. Maier, Broad-band near-infrared plasmonic nanoantennas for higher harmonic generation. ACS Nano **6**, 3537–3544 (2012)
48. H. Aouani, M. Navarro-Cia, M. Rahmani, T.P.H. Sidiropoulos, M. Hong, R.F. Oulton, S.A. Maier, Multiresonant broadband optical antennas as efficient tunable nanosources of second harmonic light. Nano Lett. **12**, 4997–5002 (2012)
49. K. Thyagarajan, J. Butet, O.J.F. Martin, Augmenting second harmonic generation using Fano resonances in plasmonic systems. Nano Lett. **13**, 1847–1851 (2013)
50. J. Ye, F. Wen, H. Sobhani, J.B. Lassiter, P. Van Dorpe, P. Nordlander, N.J. Halas, Plasmonic nanoclusters: near field properties of the Fano resonance interrogated with SERS. Nano Lett. **12**, 1660–1667 (2012)
51. J.A. Fan, K. Bao, L. Sun, J. Bao, V.N. Manoharan, P. Nordlander, F. Capasso, Plasmonic mode engineering with templated self-assembled nanoclusters. Nano Lett. **12**, 5318–5324 (2012)
52. Y. Zeng, W. Hoyer, J. Liu, S.W. Koch, J.V. Moloney, Classical theory for second-harmonic generation from metallic nanoparticles. Phys. Rev. B **79**, 235109 (2009)
53. F. Wang, F. Rodríguez, W. Albers, R. Ahorinta, J. Sipe, M. Kauranen, Surface and bulk contributions to the second-order nonlinear optical response of a gold film. Phys. Rev. B **80**, 233402 (2009)
54. A. Benedetti, M. Centini, M. Bertolotti, C. Sibilia, Second harmonic generation from 3D nanoantennas: on the surface and bulk contributions by far-field pattern analysis. Opt. Express **19**, 26752–26767 (2011)
55. C. Cirací, E. Poutrina, M. Scalora, D.R. Smith, Second-harmonic generation in metallic nanoparticles: clarification of the role of the surface. Phys. Rev. B **86**, 115451 (2012)
56. C. Cirací, E. Poutrina, M. Scalora, D.R. Smith, Origin of second-harmonic generation enhancement in optical split-ring resonators. Phys. Rev. B **85**, 201403 (2012)

Chapter 7
Nonlinear Optical Interactions in ε-Near-Zero Materials: Second and Third Harmonic Generation

Maria Antonietta Vincenti, Domenico de Ceglia, Vito Roppo and Michael Scalora

Abstract Second and third harmonic generation in materials that display near-zero permittivity values are discussed. The enormous field enhancement due to the continuity of the longitudinal component of the displacement field enhances the nonlinear response drastically. Nonlinear surface terms due to symmetry breaking and phase-locked harmonic components should not be neglected in such extreme environments.

7.1 Introduction

Although the first demonstration of artificial media exhibiting near-zero permittivity values occurred more than 50 years ago [1, 2], in more recent years the study of the linear properties of these media has enjoyed renewed interest: near-zero-permittivity (NZP) or ε-near-zero (ENZ) materials may be used to control antenna directivity [3, 4], or to realize perfect coupling through electromagnetic tunneling in sub-wavelength low-permittivity regions [5, 6]. Moreover, since the component of the (TM-polarized) electric field normal to the interface becomes singular when a material exhibits permittivity values close to zero [7], these materials may also be exploited to boost nonlinear processes such as harmonic generation [8–10], optical

M.A. Vincenti (✉) · D. de Ceglia
Charles M. Bowden Research Laboratory, National Research Council—AMRDEC, Redstone Arsenal, AL 35898, USA
e-mail: vincentiantonella@gmail.com

V. Roppo
Laboratoire de Photonique et de Nanostructures, CNRS,
Route de Nozay 91460, Marcoussis, France

M. Scalora
Charles M. Bowden Research Laboratory, AMRDEC, US Army RDECOM,
Redstone Arsenal, AL 35898, USA
e-mail: michael.scalora@us.army.mil

I.V. Shadrivov et al. (eds.), *Nonlinear, Tunable and Active Metamaterials*,
Springer Series in Materials Science 200, DOI 10.1007/978-3-319-08386-5_7

bistability [11], and soliton excitation [12]. Zero permittivity values may be obtained either naturally or artificially: all natural materials exhibit electronic resonances at wavelengths that vary from the far infrared (LiF, CaF_2, MgF_2 or SiO_2) to the visible (Au, Ag, Cu) and ultraviolet (GaAs, GaP) frequency range [13]. However, in most cases absorption plays a major role by abating local field enhancement and frustrating both linear and nonlinear optical properties. In contrast, artificial media may provide a more effective path to overcome nature's limitations. For example, active materials may be introduced into metal-based composites by tailoring the electric properties of metamaterials to decrease losses [14–16]. Similarly, losses may be reduced for materials having both electric and magnetic resonances [17]. An alternative approach to achieve effective zero permittivity is to exploit waveguides operating near their cut-off. The introduction of nonlinear media inside such waveguides has been shown to help attain tunneling control [18] and switching [19].

The inclusion of metals in artificial structures with effective ENZ properties can have additional implications thanks to nonlinear processes that arise directly from the metal [10]. In fact, although metals are centrosymmetric and do not possess intrinsic, quadratic nonlinear terms, they display an effective second-order response that arises from symmetry breaking at the surface, magnetic dipoles (Lorentz force), inner-core electrons, convective nonlinear sources, and electron gas pressure [20]. In addition, metals also display an unusually large third-order nonlinearity that, together with effective second-order nonlinear sources, may significantly contribute to the generated signals especially under circumstances where the electric field is dramatically enhanced [21–27], including ENZ materials.

In what follows we present a brief overview of the key linear properties that may be exploited to enhance second (SH) and third harmonic (TH) generation in materials with permittivity values close to zero, and show how losses influence their linear and nonlinear optical properties. Then we will compare the efficiency of nonlinear processes arising from bulk and surface contributions and evaluate the importance of phase-locked harmonic components in scenarios where absorption at the harmonic frequency is not negligible.

7.2 Nonlinear Processes in ε-Near-Zero Materials

When a monochromatic plane wave impinges on an interface between a generic medium and a material with relative permittivity that *tends to zero* ($\mathrm{Re}(\varepsilon(\omega)) \to 0^+$), the continuity requirement for the displacement field component normal to the interface implies that the normal component of the electric field inside the ENZ material is singular. This occurs at Brewster or critical angle conditions [7]. In finite slabs (see Fig. 7.1a) singular behavior of the normal electric field component may be achieved by reducing the thickness d of the slab; approaching normal incidence ($\vartheta_\mathrm{i} \to 0$), or both [7]. If on the other hand one fixes $\mathrm{Re}(\varepsilon(\omega))$ to a near-zero value, it suffices to reduce slab thickness to exploit tunneling of evanescent waves and multiple reflections to enhance the local field [28]. Any natural material displays regions where the

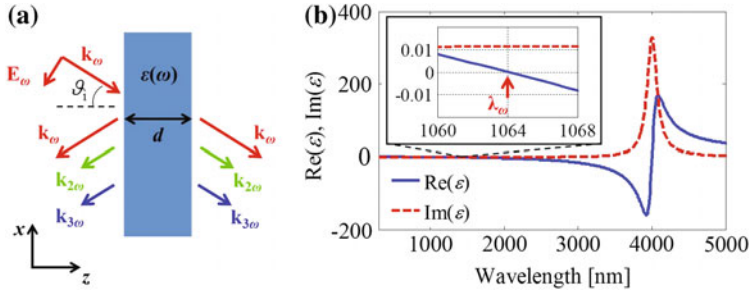

Fig. 7.1 **a** Sketch of the system under investigation: a TM-polarized pump with electric field $\mathbf{E}_\omega$ and wavevector $\mathbf{k}_\omega$ impinges on a slab of thickness d with angle of incidence ϑ_i. **b** Material dispersion of the slab in **a**, modeled with a single species of Lorentz oscillators; (inset) Detail of the short-wavelength zero-crossing region

permittivity value crosses zero. For example, the permittivity of a medium may be described as a superposition of Lorentz oscillators:

$$\varepsilon(\omega) = 1 - \sum_j \frac{\omega_{\mathrm{p}j}^2}{\omega^2 - \omega_{0j}^2 + i\omega\gamma_j}. \tag{7.1}$$

The plasma frequencies are denoted by $\omega_{\mathrm{p}j}$, γ_j are damping coefficients, ω_{0j} are resonance frequencies, and $i = \sqrt{-1}$. From (7.1) one may infer that for each resonance $\mathrm{Re}(\varepsilon(\omega))$crosses zero twice. The spectral positions of the crossing points depend on ω_{pj} and ω_{0j}. However, the values of $\mathrm{Im}(\varepsilon(\omega))$ at the crossing points are substantially different from each other, as absorption tends to diminish at the short-wavelength tail (Fig. 7.1b).

For simplicity we now assume the slab in Fig. 7.1a is modeled by a single species of Lorentz oscillators. As an example, choosing Lorentz oscillator parameters as follows: $\omega_{p1} = 0.91\,\omega_\mathrm{r}$, $\omega_{01} = 0.25\,\omega_\mathrm{r}$, and $\gamma_1 = 0.010\,\omega_\mathrm{r}$, where the reference frequency is $\omega_\mathrm{r} = 2\pi c/(1\,\mu\mathrm{m})$ and c is the speed of light *in vacuo*, ensures an ENZ condition in the vicinity of $\lambda_\omega = 1064\,\mathrm{nm}$ (Fig. 7.1b). The same parameters also yield small values for the imaginary part of the permittivity at the second ($\lambda_{2\omega} = 532\,\mathrm{nm}$) and third ($\lambda_{3\omega} = 354.6\,\mathrm{nm}$) harmonic wavelengths. We note that this choice of parameters is by no means unique, and other parameters may be used to obtain similar values for the permittivities at the same frequencies. We set slab thickness to $d = 200\,\mathrm{nm}$. In the vicinity of the pump wavelength the linear properties of the slab are strongly related to both $\mathrm{Re}(\varepsilon(\omega))$ and $\mathrm{Im}(\varepsilon(\omega))$. For example, on the one hand transmission and reflection (Fig. 7.2a, b) frequency selectivity and asymmetry are dictated by the slope and change in sign of $\mathrm{Re}(\varepsilon(\omega))$, respectively. On the other hand, both angular and spectral selectivity of the slab's absorption (Fig. 7.2c) are strongly related to the oscillator's damping coefficient γ_1 and, as a consequence, to the value of $\mathrm{Im}(\varepsilon(\omega))$.

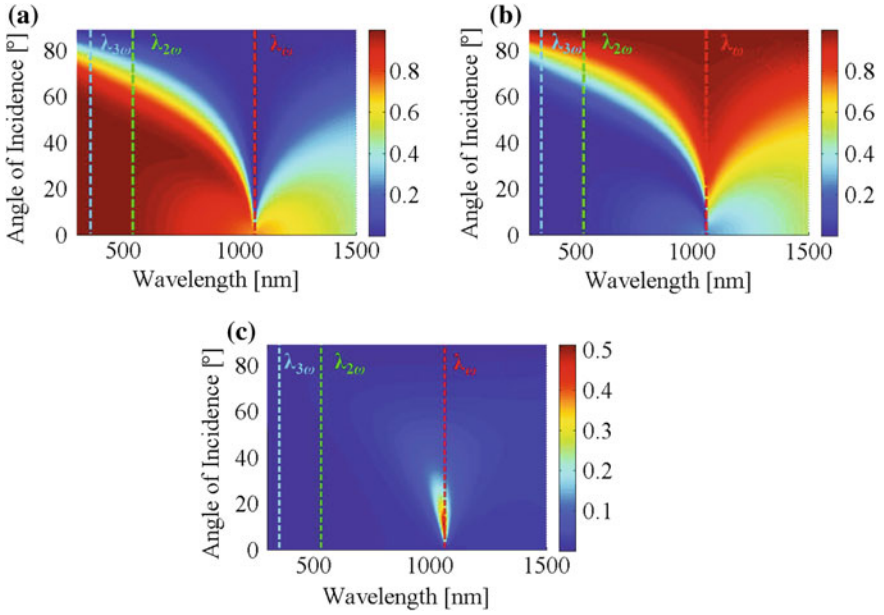

Fig. 7.2 **a** Transmission, **b** reflection and **c** absorption versus wavelength and incident angle ϑ_i for a slab $d = 200\,\text{nm}$ thick and a singly-resonant oscillator species. Fundamental (*red, dashed line* marked λ_ω), second (*green, dashed line* marked $\lambda_{2\omega}$) and third (*blue, dashed line* marked $\lambda_{3\omega}$) harmonic wavelengths are shown on the maps

No other relevant spectral and angular features may be identified far from the pump wavelength, i.e., where $\text{Re}(\varepsilon(\omega)) = 0$. Absorption is practically zero at both second (green, dashed lines marked $\lambda_{2\omega}$ in Fig. 7.2) and third harmonic wavelengths (blue, dashed lines marked $\lambda_{3\omega}$ in Fig. 7.2). This implies that the homogeneous solution of the nonlinear wave equation [29] is generated and propagates freely inside the slab. The influence of absorption at the harmonic wavelengths is discussed in Sect. 2.3.

In order to understand the potential of this system for nonlinear applications one can evaluate the electric field enhancement, $\max\left(|E_z|/|\text{E}_\omega|\right)$, inside the slab. Indeed electric field enhancement (Fig. 7.3a) is related to the absorption profile (Fig. 7.2c) and thus linked to the choice of the damping coefficient of the oscillator γ_1.

Maximum absorption values in the slab depend weakly on $\text{Im}(\varepsilon(\omega))$: since absorption is proportional to the product $\text{Im}(\varepsilon(\omega))|\mathbf{E}|^2$, a decreasing $\text{Im}(\varepsilon(\omega))$ is associated with an increase of the electric field enhancement. For this reason nonlinear optical interactions are expected to increase by decreasing γ_1 [30]. The electric field enhancement maps for different values of γ_1 as a function of wavelength and angle of incidence are shown in Fig. 7.3: although electric field enhancement may increase by

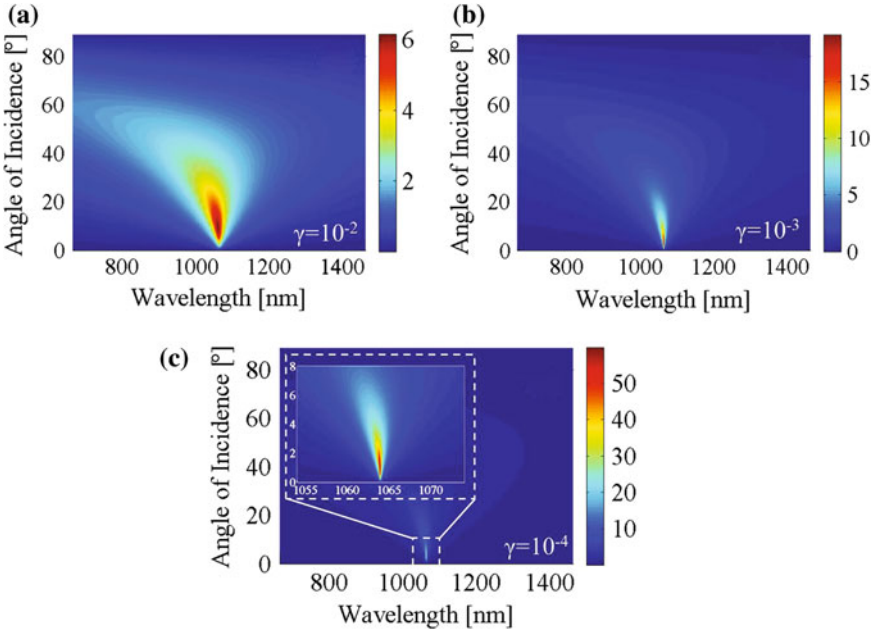

Fig. 7.3 Electric field enhancement, $\max\left(|E_z|/|\mathrm{E}_\omega|\right)$, as a function of wavelength and angle of incidence for a slab $d = 200\,\mathrm{nm}$ thick, modeled with one species of Lorentz oscillators, with $\omega_{\mathrm{p1}} = 0.91\omega_{\mathrm{r}}$, $\omega_{01} = 0.25\omega_{\mathrm{r}}$ and **a** $\gamma_1 = 0.01\omega_{\mathrm{r}}$, **b** $\gamma_1 = 0.001\omega_{\mathrm{r}}$ and **c** $\gamma_1 = 0.0001\omega_{\mathrm{r}}$

reducing $\mathrm{Im}(\varepsilon(\omega))$, we emphasize that similar results may be achieved by reducing slab thickness, thus favoring the buildup of the electric field by increased tunneling of evanescent waves. This condition may be achieved only for incident angles ϑ_i greater than the critical angle ϑ_C ($\vartheta_C = \sin^{-1}\sqrt{\varepsilon(\omega)}$) [7].

7.2.1 Second and Third Harmonic Generation Arising from Bulk Nonlinearities

In a scenario where the pump intensity may be dramatically enhanced thanks to a vanishing $\mathrm{Re}(\varepsilon(\omega))$, nonlinear processes become exceptionally favored even in sub-wavelength structures and for relatively low pump irradiance values. To account for second and third order nonlinear effects we express the leading contributions of the nonlinear polarization densities in the k direction at the second ($P_{2\omega,k}$) and third ($P_{3\omega,k}$) harmonic frequencies as [31]:

$$P_{2\omega,k} = \varepsilon_0 \sum_{l,m=1}^{3} \chi^{(2)}_{klm}(2\omega, \omega, \omega) E_{\omega,l} E_{\omega,m}, \tag{7.2}$$

$$P_{3\omega,k} = \varepsilon_0 \sum_{l,m,n=1}^{3} \chi^{(3)}_{klmn}(3\omega, \omega, \omega, \omega) E_{\omega,l} E_{\omega,m} E_{\omega,n}, \tag{7.3}$$

where k, l, m, n are Cartesian coordinates, ε_0 is the vacuum electric permittivity, $\chi^{(2)}_{klm}$ and $\chi^{(3)}_{klmn}$ are the instantaneous second, and third order susceptibility tensor components, respectively. Since the efficiency of the nonlinear processes depend on the values of $\chi^{(2)}_{klm}$ and $\chi^{(3)}_{klmn}$, one can expect significantly different results depending on the materials used to achieve the ENZ condition. For example, in metamaterials composed of core-shell nanoparticles [10, 32] high effective $\chi^{(3)}_{klmn}$ that derive mostly from the metal are expected, whereas the values of the effective $\chi^{(2)}_{klm}$ will vary according to the dielectrics present.

In what follows we assume $\chi^{(2)}_{xxx} = \chi^{(2)}_{yyy} = \chi^{(2)}_{zzz} = 10\,\text{pm/V}$, $\chi^{(3)}_{xxxx} = \chi^{(3)}_{yyyy} = \chi^{(3)}_{zzzz} = 10^{-20}\,\text{m}^2/\text{V}^2$, typical for dielectric materials [31]. Slab thickness and Lorentz oscillator parameters are as in Sect. 2. The resulting material dispersion is shown in Fig. 7.1b.

In the undepleted pump approximation the total (forward plus backward) SH and TH conversion efficiencies, $I_{2\omega}/I_\omega$ and $I_{3\omega}/I_\omega$, are of the order of 10^{-5} and 10^{-7}, respectively, and are shown in Fig. 7.4a, b. The input irradiance is $I_\omega = 100\,\text{MW/cm}^2$. Harmonic efficiency maps are similar to the field enhancement map (Fig. 7.3b) in both spectral and angular features. The results in Fig. 7.4 were acquired assuming a continuous wave pump. Similar results may be obtained by using incident pulses at least 200 fs in duration, because of the non-resonant nature of the field enhancement in ENZ slabs [32]. We note that although forward and backward conversion efficiencies have almost identical spectral and angular shapes for homogeneous sub-wavelength slabs and homogeneous bulk nonlinearities, they may exhibit different spectral and angular features whenever resonant modes are excited, or if nonlinear contributions are not uniformly distributed inside the slab [10].

7.2.2 Harmonic Generation from Surface and Volume Sources

In Sect. 2.1 we saw that under circumstances where electric field enhancement is limited by either the finite thickness of the slab or losses, the nonlinear response in the presence of bulk nonlinearities can be significant even for relatively low input irradiance values. In that case surface sources, magnetic dipoles [20], and electric quadrupole contributions may be neglected. If, on the other hand, $\chi^{(2)} = \chi^{(3)} = 0$, these sources become the sole contributors to harmonic generation. It is generally not possible to separate surface from volume contributions, as their relative weights depend on a number of factors, such as material dispersion, thickness and geometrical

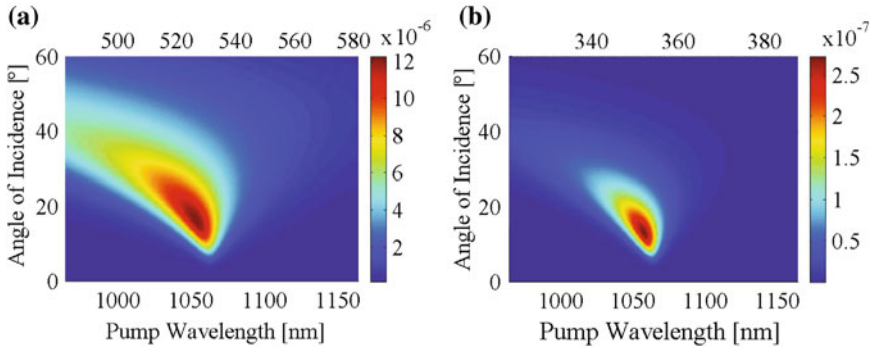

Fig. 7.4 Total (forward plus backward) **a** SH and **b** TH conversion efficiencies for a slab of ENZ $d = 200\,\text{nm}$ thick as a function of incident angle and pump wavelength

features like corrugations and/or presence of slits, and should be evaluated on a case-by-case basis.

We consider a classical, local oscillator model in order to provide physical insight into how second and third harmonic generation may come about in a medium where dipolar nonlinearities are absent, i.e., $\chi^{(2)} = \chi^{(3)} = 0$. One may argue that an incident field tends to distort the electronic cloud of an atom, consisting mostly of outermost, more loosely bound electrons. While this picture suffices to explain most linear optical phenomena, the explanation of nonlinear optical phenomena like harmonic generation from centrosymmetric materials requires us to look more intimately at the details of the atom. As the outer electronic cloud becomes slightly distorted, inner core electrons that occupy lower orbitals interact just a little more strongly with the nucleus, giving way to small imbalances in the charge distribution which in turn interacts weakly with the externally applied fields in the form of quadrupolar transitions. One may then begin with an equation of motion for a multipolar charge distribution assumed to be under the action of internal forces (damping, harmonic and anharmonic restoring forces) and external forces due to the applied electromagnetic fields. With reference to Fig. 7.5, a possible, quite simplistic way to describe nonlinear optical processes is then to modify the Lorentz model of the atom by introducing external electric and magnetic forces on a charge e as follows [33, 34]:

$$\mathbf{F}(\mathbf{r}_0 + \mathbf{r}, t) = e\mathbf{E}(\mathbf{r}_0 + \mathbf{r}, t) + e\dot{\mathbf{r}} \times \mathbf{B}(\mathbf{r}_0 + \mathbf{r}, t). \tag{7.4}$$

The fields at the electron position $\mathbf{r}_0 + \mathbf{r}$ may be expanded about the origin $\mathbf{r}_0$, so that:

$$\mathbf{E}(\mathbf{r}_0 + \mathbf{r}, t) = \mathbf{E}(\mathbf{r}_0, t) + (\mathbf{r} \cdot \nabla_\mathbf{r})\,\mathbf{E}(\mathbf{r}_0, t) \; + \frac{1}{2}\nabla_\mathbf{r}\,(\mathbf{r}\,\mathbf{r} \cdot \nabla_\mathbf{r}\mathbf{E}(\mathbf{r}_0, t)\,) + \cdots \tag{7.5}$$

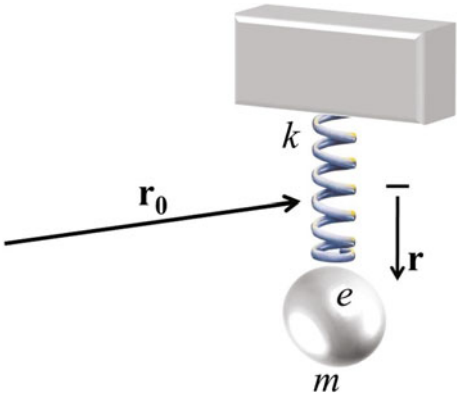

Fig. 7.5 Lorentz model of the atom. A charge e is attached to a spring of constant k, subject to external electric and magnetic forces, and to internal linear and nonlinear restoring forces. The origin is at $\mathbf{r}_0$; r is the displacement from equilibrium

and

$$\mathbf{B}(\mathbf{r}_0+\mathbf{r},t)=\mathbf{B}(\mathbf{r}_0,t)+(\mathbf{r}\cdot\nabla_{\mathbf{r}})\,\mathbf{B}(\mathbf{r}_0,t)\;+\frac{1}{2}\nabla_{\mathbf{r}}\left(\mathbf{r}\,\mathbf{r}\cdot\nabla_{\mathbf{r}}\mathbf{B}(\mathbf{r}_0,t)\right)+\cdots \tag{7.6}$$

Collecting lowest order terms, the force in (7.4) becomes:

$$\begin{aligned}m^*\ddot{\mathbf{r}}(t)+\gamma m^*\dot{\mathbf{r}}(t)+k\mathbf{r}(t)=e\mathbf{E}(\mathbf{r}_0,t)+e\,(\mathbf{r}\cdot\nabla_{\mathbf{r}})\,\mathbf{E}(\mathbf{r}_0,t)+\frac{e}{4}\nabla_{\mathbf{r}}\left(\mathbf{r}\mathbf{r}{:}\nabla_{\mathbf{r}}\mathbf{E}(\mathbf{r}_0,t)\right)\\+e\dot{\mathbf{r}}\times\left(\mathbf{B}(\mathbf{r}_0,t)+(\mathbf{r}\cdot\nabla_{\mathbf{r}})\,\mathbf{B}(\mathbf{r}_0,t)+\cdots\right)\end{aligned} \tag{7.7}$$

where one may recognize $\mathbf{p}=e\mathbf{r}$ and $\mathbf{Q}=\frac{e}{2}\mathbf{r}\mathbf{r}$ as the electric dipole and (intrinsically nonlinear) quadrupole contributions, respectively; $m^*$is the effective mass of the oscillator (we assume $m^*=m_e$); k is the spring constant; γ is the damping coefficient. The magnetic field expansion is truncated at its dipole term. Equation (7.7) is a nonlinear equation capable of generating harmonics even in the absence of dipolar nonlinearities. Then, assuming a solution of the type

$$\mathbf{r}=\mathbf{r}_\omega\,e^{-i\omega t}+\mathbf{r}_{2\omega}e^{-2i\omega t}+\mathbf{r}_{3\omega}e^{-3i\omega t}+\text{c.c.}, \tag{7.8}$$

the equation for the polarizations at the pump, SH and TH frequencies read as follows [35]:

$$\begin{aligned}\ddot{\mathbf{P}}_\omega+\gamma\dot{\mathbf{P}}_\omega+\omega_0^2\mathbf{P}_\omega=\frac{e}{m^*}\Bigg\{n_0e\mathbf{E}_\omega-\frac{1}{2}\left(\nabla\cdot\mathbf{P}_{2\omega}\right)\mathbf{E}^*_\omega+2\left(\nabla\cdot\mathbf{P}^*_\omega\right)\mathbf{E}_{2\omega}\\+\left(\dot{\mathbf{P}}^*_\omega+i\omega\mathbf{P}^*_\omega\right)\times\mathbf{H}_{2\omega}+\left(\dot{\mathbf{P}}_{2\omega}-2i\omega\mathbf{P}_{2\omega}\right)\times\mathbf{H}^*_\omega+\frac{1}{4}\mathbf{F}_\omega\Bigg\}\end{aligned} \tag{7.9}$$

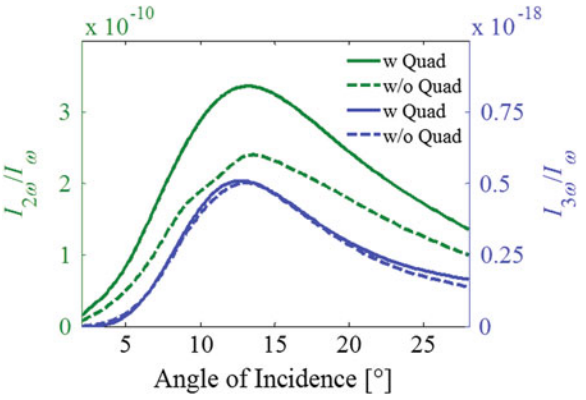

Fig. 7.6 Total SH (*blue, solid line*—with quadrupoles; *blue dashed line*—without quadrupoles) and TH (*green, solid line*—with quadrupoles; *green dashed line*—without quadrupoles) efficiencies versus angle for a slab $d = 200\,\text{nm}$ thick modeled with a Lorentz oscillators with parameters in Sect. 2. Pump irradiance is $I_\omega = 100\,\text{MW/cm}^2$ and second and third order bulk susceptibilities are zero

$$\ddot{\mathbf{P}}_{2\omega} + \gamma\dot{\mathbf{P}}_{2\omega} + \omega_0^2\mathbf{P}_{2\omega} = \frac{e}{m^*}\left\{n_0 e\mathbf{E}_{2\omega} + (\nabla\cdot\mathbf{P}_\omega)\,\mathbf{E}_\omega - \frac{1}{3}(\nabla\cdot\mathbf{P}_{3\omega})\,\mathbf{E}_\omega^* - 3\left(\nabla\cdot\mathbf{P}_\omega^*\right)\mathbf{E}_{3\omega} + \left(\dot{\mathbf{P}}_\omega - i\omega\mathbf{P}_\omega\right)\times\mathbf{H}_\omega + \frac{1}{4}\mathbf{F}_{2\omega}\right\} \tag{7.10}$$

$$\ddot{\mathbf{P}}_{3\omega} + \gamma\dot{\mathbf{P}}_{3\omega} + \omega_0^2\mathbf{P}_{3\omega} = \frac{e}{m^*}\left\{n_0 e\mathbf{E}_{3\omega} + \frac{1}{2}(\nabla\cdot\mathbf{P}_{2\omega})\,\mathbf{E}_\omega + 2(\nabla\cdot\mathbf{P}_\omega)\,\mathbf{E}_{2\omega} + \left(\dot{\mathbf{P}}_{2\omega} - i\omega\mathbf{P}_{2\omega}\right)\times\mathbf{H}_\omega + \left(\dot{\mathbf{P}}_\omega - i\omega\mathbf{P}_\omega\right)\times\mathbf{H}_{2\omega} + \frac{1}{4}\mathbf{F}_{3\omega}\right\}, \tag{7.11}$$

where n_0 is the electron density and $\omega_0 = \sqrt{k/m^*}$. $\mathbf{E}_\omega$, $\mathbf{E}_{2\omega}$, $\mathbf{E}_{3\omega}$, $\mathbf{H}_\omega$, $\mathbf{H}_{2\omega}$ and $\mathbf{H}_{3\omega}$ are the electric and magnetic field envelope functions at each harmonic, and $\mathbf{F}_\omega$, $\mathbf{F}_{2\omega}$ and $\mathbf{F}_{3\omega}$ are the lowest-order, quadrupolar contributions at the pump, SH and TH frequencies [35]. Only lowest-order magnetic contributions have been retained.

We solve (7.9), (7.10) and (7.11) in the time domain together with Maxwell's equations assuming $n_0 = 5.8\times10^{28}\ \text{m}^{-3}$, $\gamma = \gamma_1$ and $\omega_0 = \omega_{01}$ as in Sect. 2. With these parameters one obtains total SH conversion efficiency maximum of approximately 10^{-10}, and a TH efficiency maximum of approximately 10^{-18}, shown in Fig. 7.6 as a function of incident angle for $I_\omega = 100\,\text{MW/cm}^2$ and pulses $\sim$200 fs in duration. In the figure, blue and green dashed curves show SH and TH responses without quadrupolar contributions, thus revealing their importance for the SH generation process, in contrast to TH generation. Even if the SH efficiency appears to be

small, one should compare the efficiency shown in Fig. 7.6 with other systems where bulk second order contributions are absent. For example, the SH response from the ENZ slab is still ∼100 times more efficient than the SH response of a silver grating where surface plasmons or resonant cavity modes are excited [20, 22].

7.2.3 Phase-Locked Second Harmonic Generation in ε-Near-Zero Media

In a situation where pump electric field enhancement is maximized, harmonic efficiencies may be penalized by either a reduction of the nonlinear susceptibility values or by the presence of absorption. The case of vanishing bulk $\chi^{(2)}$ and $\chi^{(3)}$ has been analyzed in Sect. 2.2, while the presence of absorption losses and the dynamics of phase-locking in the ENZ medium is discussed in this section.

Evidence of a phase-locking process, which is produced by the inhomogeneous solutions of the wave equation [36–39], may be found in experimental works, where large phase and group velocity mismatches between the fundamental frequency (FF) and the SH waves allow the observation of two distinct SH pulses traveling at different phase and group velocities [40–42]. The homogeneous solution propagates with the phase and group velocity dictated by material dispersion, and walks off from the pump. The inhomogeneous solution is trapped by the pump and propagates with the pump's phase and group velocity. This peculiar behavior occurs in negative index [42, 43] and absorbing materials [44, 45] alike, thus allowing the generation and propagation of harmonic signals in materials or structures where propagation is ordinarily forbidden [22].

In order to obtain ENZ at $\lambda_\omega = 1064\,\text{nm}$ and significant absorption losses at the SH wavelength one may consider a different set of Lorentz oscillator parameters that describe the medium. For example, an ENZ condition at the pump with absorption at the SH wavelength may be obtained using two species of Lorentz oscillators having the following parameters: $\omega_{\text{p1}} = 0.95\omega_\text{r}$, $\omega_{01} = 0.25\omega_\text{r}$, $\gamma_1 = 10^{-4}\omega_\text{r}$, $\omega_{\text{p2}} = 0.50\omega_\text{r}$, $\omega_{02} = 1.92\omega_\text{r}$, $\gamma_2 = 0.05\omega_\text{r}$. Figure 7.7a shows the dispersion of a medium modeled with this particular set of parameters. Differently from the case shown in Sect. 2.1, the medium is now strongly absorptive at the SH wavelength. This implies that the homogeneous solution of the nonlinear wave equation is absorbed in the medium. In contrast, the phase-locked (PL) SH component, i.e., the inhomogeneous solution of the nonlinear wave equation, will experience the same dispersion as the pump.

This suggests that in this case SH generation strongly depends on slab thickness, as the amount of the homogeneous SH signal that is eventually absorbed is greater for thicker slabs. For example, assuming a slab $d = 200\,\text{nm}$ thick, an input irradiance of $I_\omega = 100\,\text{MW/cm}^2$, and bulk second order susceptibilities $\chi^{(2)}_{xxx} = \chi^{(2)}_{yyy} = \chi^{(2)}_{zzz} = 10\,\text{pm/V}$, SH efficiency decreases by about one order of

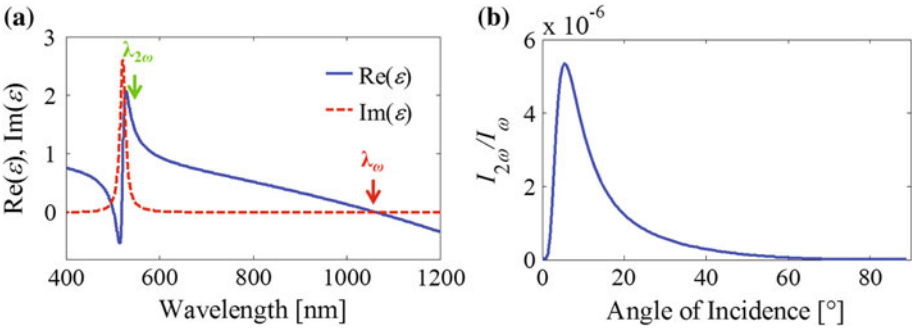

Fig. 7.7 **a** Dispersion of a material modeled with two species of Lorentz oscillators. **b** Total (forward plus backward) SH efficiency from a slab $d = 200\,\text{nm}$ thick of material with the dispersion in **a**, $I_\omega = 100\,\text{MW/cm}^2$ and $\chi^{(2)}_{xxx} = \chi^{(2)}_{yyy} = \chi^{(2)}_{zzz} = 10\,\text{pm/V}$

magnitude ($\sim 10^{-6}$) when compared to the case shown in Sect. 2.1. For this thickness ($d = 200\,\text{nm}$) absorption limits harmonic generation only partially since the homogeneous component of the SH is not completely absorbed. Figure 7.7b shows total (forward plus backward) SH efficiency as a function of the angle of incidence for $\lambda_\omega = 1064\,\text{nm}$. If the thickness of the slab increases, total second harmonic generation suffers because more of the homogeneous signal is absorbed. However, while the total conversion efficiency decreases when compared to the absorption-less case, the phase-locked component manages to survive and still contribute to the conversion process. For example, SH conversion efficiency for a slab $d = 2\,\mu\text{m}$ thick slab is still a respectable $\sim 10^{-7}$.

Another interesting aspect of the nonlinear dynamics is the possibility to monitor the refraction of the two harmonic components as they propagate in the medium [44, 46]. In order to immediately visualize the decay of the homogeneous SH signal and the refraction angles of all the fields during propagation, we illuminate a semi-infinite slab of ENZ medium with a spatio-temporal, Gaussian shaped pulse. This scenario helps us avoid interference effects that arise in the presence of multiple reflections caused by a second interface. The fundamental frequency (FF) pulse is $\sim 20\,fs$ in duration, has a beam waist $\sim 4\,\lambda_\omega$, and it is incident at an angle $\vartheta_\text{i} = 1.6°$. In the limit of monochromatic, homogeneous, plane-wave pump signal, the angle of refraction for the FF and phase-locked SH components is $\vartheta_\omega = \vartheta_{2\omega,PL} = 30.48° + i\ 38.45°$, while the homogeneous SH component refracts at $\vartheta_{2\omega} = 1.1° + i\ 0.19°$. The imaginary part of the refraction angle is associated with attenuation of the inhomogeneous, refracted, plane-wave signals in the ENZ medium. However, the use of a finite, broad-band beam modifies the angles of refraction of all components because of chromatic dispersion around the FF. In fact, since the FF is tuned at the plasma frequency, the red-side of the pulse tends to refract negatively, while the blue-side of the pulse tends to refract positively (see material dispersion in Fig. 7.7a). We distinguish between refraction of the phase front and refraction of energy, as

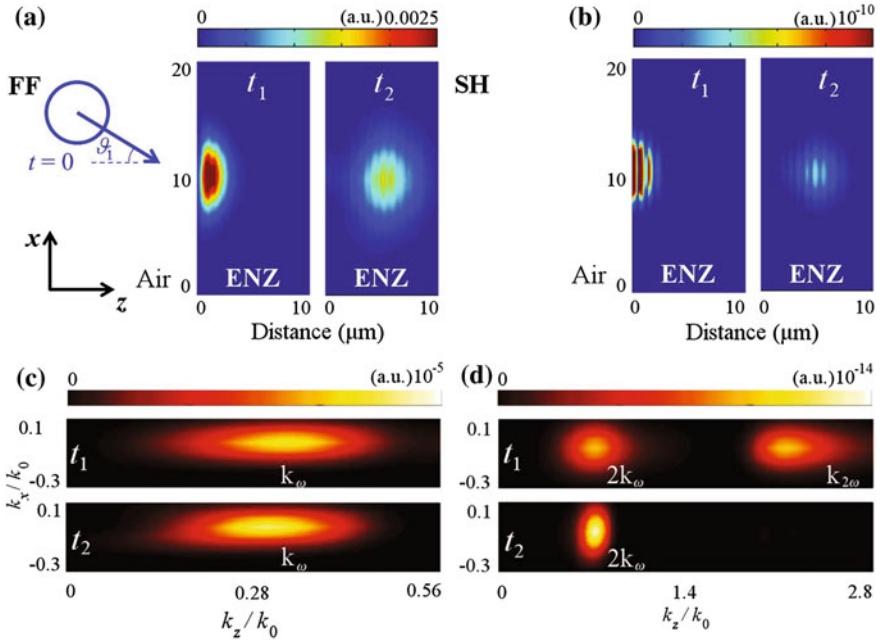

Fig. 7.8 **a** Temporal snapshots of the FF Gaussian beam, incident at 1.6°, and propagating in an ENZ medium. **b** Same temporal snapshots in **a** showing the SH components generated in the ENZ medium. **c** Two-dimensional Fourier transform of panels t_1 and t_2 in **a** showing the effective phase refraction angle of the FF in the ENZ medium **d** Two-dimensional Fourier transform of panels t_1 and t_2 in **b** showing the effective phase refraction angles of the homogeneous and phase-locked SH components in the ENZ medium

the two directions can be quite different. Figure 7.8a shows two different temporal snapshots (t_1 and t_2) of the pump pulse, as it enters the ENZ medium (panel labeled t_1 in Fig. 7.8a) and after it has propagated ∼5 μ m inside the medium (panel labeled t_2 in Fig. 7.8a). Figure 7.8c shows the pump pulse in the ENZ medium at instants t_1 and t_2 (same as in Fig. 7.8a) in the spatial frequency domain. The pump pulse is centered at $\mathbf{k}_\omega/k_0 = (0.027,\ 0.32)$, which indicates a phase-front refraction angle of ∼5°. The momentum refraction angle [47, 48], which indicates the actual direction of energy flow, is approximately 7°. Propagation of the SH signal is visualized in Fig. 7.8b. Snapshots are taken for the same instants t_1 and t_2 of Fig. 7.8a. Visualization of the SH signals in the spatial frequency domain (Fig. 7.8d) clearly reveals both homogeneous and PL components, which are centered at $\mathbf{k}_{2\omega}/k_0 = (0.056,\ 2.159)$ and $2\mathbf{k}_\omega/k_0$, respectively. For these components effective phase refraction angles ∼1.5° (homogeneous) and ∼5° (PL SH component) are calculated.

7.3 Conclusions

The unique properties of ENZ or NZP materials may be exploited to enhance SH and TH generation. Although absorption losses limit electric field enhancement and frustrate both linear and nonlinear optical processes, either the introduction of active materials or the exploitation of tunneling of evanescent waves that occurs above the critical angle of incidence reveal a path to overcome such limits.

Nonlinear optical processes can be significant both in the presence of bulk nonlinearities and in regimes where only surface sources, magnetic dipoles, and electric quadrupole contributions are present.

Finally, high absorption losses at the harmonic frequencies limit only partially the efficiency of nonlinear processes thanks to the relevance of phase-locked harmonic components and strong field enhancement at the pump frequency.

References

1. J. Brown, Artificial dielectrics having refractive indices less than unity. Proc. IEE - Part IV: Inst. Monogr. **100**(5), 51–62 (1953)
2. W. Rotman, Plasma simulation by artificial dielectrics and parallel-plate media. IRE Trans. Antennas Propag. **10**(1), 82–95 (1962)
3. S. Enoch, G. Tayeb, P. Sabouroux, N. Guérin, P. Vincent, A metamaterial for directive emission. Phys. Rev. Lett. **89**(21), 213902 (2002)
4. G. Lovat, P. Burghignoli, F. Capolino, D.R. Jackson, D.R. Wilton, Analysis of directive radiation from a line source in a metamaterial slab with low permittivity. IEEE Trans. Antennas Propag. **54**(3), 1017–1030 (2006)
5. A. Alù, M.G. Silveirinha, A. Salandrino, N. Engheta, Epsilon-near-zero metamaterials and electromagnetic sources: Tailoring the radiation phase pattern. Phys. Rev. B **75**(15), 155410 (2007)
6. M. Silveirinha, N. Engheta, Tunneling of electromagnetic energy through subwavelength channels and bends using ϵ-near-zero materials. Phys. Rev. Lett. **97**(15), 157403 (2006)
7. S. Campione, D. de Ceglia, M.A. Vincenti, M. Scalora, F. Capolino, Electric field enhancement in ϵ-near-zero slabs under TM-polarized oblique incidence. Phys. Rev. B **87**(3), 035120 (2013)
8. M.A. Vincenti, D. de Ceglia, A. Ciattoni, M. Scalora, Singularity-driven second- and third-harmonic generation at ϵ-near-zero crossing points. Phys. Rev. A **84**(6), 063826 (2011)
9. A. Ciattoni, E. Spinozzi, Efficient second-harmonic generation in micrometer-thick slabs with indefinite permittivity. Phys. Rev. A **85**(4), 043806 (2012)
10. M.A. Vincenti, S. Campione, D. de Ceglia, F. Capolino, M. Scalora, Gain-assisted harmonic generation in near-zero permittivity metamaterials made of plasmonic nanoshells. New J. Phys. **14**(10), 103016 (2012)
11. A. Ciattoni, C. Rizza, E. Palange, Extreme nonlinear electrodynamics in metamaterials with very small linear dielectric permittivity. Phys. Rev. A **81**(4), 043839 (2010)
12. C. Rizza, A. Ciattoni, E. Palange, Two-peaked and flat-top perfect bright solitons in nonlinear metamaterials with epsilon near zero. Phys. Rev. A **83**(5), 053805 (2011)
13. E.D. Palik, G. Ghosh, *Handbook of Optical Constants of Solids* (Academic press, USA, 1998)
14. S. Campione, M. Albani, F. Capolino, Complex modes and near-zero permittivity in 3D arrays of plasmonic nanoshells: loss compensation using gain. Opt. Mater. Express **1**(6), 1077–1089 (2011)

15. S. Campione, F. Capolino, Composite material made of plasmonic nanoshells with quantum dot cores: loss-compensation and epsilon-near-zero physical properties. Nanotechnol. **23**(23), 235703 (2012)
16. A. Ciattoni, R. Marinelli, C. Rizza, E. Palange, |\epsilon|-Near-zero materials in the near-infrared. Appl. Phys. B **110**(1), 23–26 (2013)
17. S. Xiao, V.P. Drachev, A.V. Kildishev, X. Ni, U.K. Chettiar, H.-K. Yuan, V.M. Shalaev, Loss-free and active optical negative-index metamaterials. Nat. **466**(7307), 735–738 (2010)
18. D.A. Powell, A. Alù, B. Edwards, A. Vakil, Y.S. Kivshar, N. Engheta, Nonlinear control of tunneling through an epsilon-near-zero channel. Phys. Rev. B **79**(24), 245135 (2009)
19. C. Argyropoulos, P.-Y. Chen, G. D'Aguanno, N. Engheta, A. Alù, Boosting optical nonlinearities in ϵ-near-zero plasmonic channels. Phys. Rev. B **85**(4), 045129 (2012)
20. M. Scalora, M.A. Vincenti, D. de Ceglia, V. Roppo, M. Centini, N. Akozbek, M.J. Bloemer, Second- and third-harmonic generation in metal-based structures. Phys. Rev. A **82**(4), 043828 (2010)
21. D.T. Owens, C. Fuentes-Hernandez, J.M. Hales, J.W. Perry, B. Kippelen, A comprehensive analysis of the contributions to the nonlinear optical properties of thin Ag films. J. Appl. Phys. **107**(12), 123114–123118 (2010)
22. M. Vincenti, D. de Ceglia, V. Roppo, M. Scalora, Harmonic generation in metallic, GaAs-filled nanocavities in the enhanced transmission regime at visible and UV wavelengths. Opt. Express **19**(3), 2064–2078 (2011)
23. N.N. Lepeshkin, A. Schweinsberg, G. Piredda, R.S. Bennink, R.W. Boyd, Enhanced nonlinear optical response of one-dimensional metal-dielectric photonic crystals. Phys. Rev. Lett. **93**(12), 123902 (2004)
24. M. Airola, Y. Liu, S. Blair, Second-harmonic generation from an array of sub-wavelength metal apertures. J. Opt. A: Pure Appl. Opt. **7**(2), S118 (2005)
25. A. Lesuffleur, L.K.S. Kumar, R. Gordon, Enhanced second harmonic generation from nanoscale double-hole arrays in a gold film. Appl. Phys. Lett. **88**(26), 261104–261104-3 (2006)
26. R. Nikifor, E.R. Francisco, X. Mufei, Strong second-harmonic radiation from a thin silver film with randomly distributed small holes. J. Phys.: Condens. Matter **15**(23), L349 (2003)
27. T. Xu, X. Jiao, S. Blair, Third-harmonic generation from arrays of sub-wavelength metal apertures. Opt. Express **17**(26), 23582–23588 (2009)
28. M.A. Vincenti, D. de Ceglia, J.W. Haus, M. Scalora, Harmonic generation in multiresonant plasma films, Phys. Rev. A **88**, 043812 (2013)
29. J.A. Armstrong, N. Bloembergen, J. Ducuing, P.S. Pershan, Interactions between Light Waves in a Nonlinear Dielectric. Phys. Rev. **127**(6), 1918–1939 (1962)
30. M.A. Vincenti, D. de Ceglia, M. Scalora, Nonlinear dynamics in low permittivity media: the impact of losses. Opt. Express **21**(24), 29949–29954 (2013)
31. R.W. Boyd, *Nonlinear Optics* (Academic Press, USA, 2003)
32. D. de Ceglia, S. Campione, M.A. Vincenti, F. Capolino, M. Scalora, Low-damping epsilon-near-zero slabs: Nonlinear and nonlocal optical properties. Phys. Rev. B **87**(15), 155140 (2013)
33. J.D. Jackson, *Classical Electrodynamics* (Wiley, New York, 1999)
34. N. Bloembergen, R.K. Chang, S.S. Jha, C.H. Lee, Optical second-harmonic generation in reflection from media with inversion symmetry. Phys. Rev. **174**(3), 813–822 (1968)
35. M. Scalora, M. Vincenti, D. de Ceglia, N. Akozbek, V. Roppo, M. Bloemer, J. Haus, Dynamical model of harmonic generation in centrosymmetric semiconductors at visible and UV wavelengths. Phys. Rev. A **85**(5), 053809 (2012)
36. N. Bloembergen, P.S. Pershan, Light waves at the boundary of nonlinear media. Phys. Rev. **128**(2), 606–622 (1962)
37. W. Glenn, Second-harmonic generation by picosecond optical pulses. IEEE J. Quantum Electron. **5**(6), 284–290 (1969)
38. J.T. Manassah, O.R. Cockings, Induced phase modulation of a generated second-harmonic signal. Opt. Lett. **12**(12), 1005–1007 (1987)
39. S.L. Shapiro, Second harmonic generation in $linbo_3$ by picosecond pulses. Appl. Phys. Lett. **13**(1), 19–21 (1968)

40. L.D. Noordam, H.J. Bakker, M.P. de Boer, HBvL Heuvell, Second-harmonic generation of femtosecond pulses: observation of phase-mismatch effects: reply to comment. Opt. Lett. **16**(12), 971–971 (1991)
41. N.C. Kothari, X. Carlotti, Transient second-harmonic generation: influence of effective group-velocity dispersion. J. Opt. Soc. Am. B **5**(4), 756–764 (1988)
42. V. Roppo, M. Centini, C. Sibilia, M. Bertolotti, D. de Ceglia, M. Scalora, N. Akozbek, M.J. Bloemer, J.W. Haus, O.G. Kosareva, Role of phase matching in pulsed second-harmonic generation: Walk-off and phase-locked twin pulses in negative-index media. Phys. Rev. A **76**(3), 033829 (2007)
43. V. Roppo, M. Centini, D. de Ceglia, M. Vicenti, J. Haus, N. Akozbek, M. Bloemer, M. Scalora, Anomalous momentum states, non-specular reflections, and negative refraction of phase-locked, second-harmonic pulses. Metamater. **2**(2–3), 135–144 (2008)
44. M. Centini, V. Roppo, E. Fazio, F. Pettazzi, C. Sibilia, J.W. Haus, J.V. Foreman, N. Akozbek, M.J. Bloemer, M. Scalora, Inhibition of linear absorption in opaque materials using phase-locked harmonic generation. Phys. Rev. Lett. **101**(11), 113905 (2008)
45. V. Roppo, C. Cojocaru, F. Raineri, G. D'Aguanno, J. Trull, Y. Halioua, R. Raj, I. Sagnes, R. Vilaseca, M. Scalora, Field localization and enhancement of phase-locked second- and third-order harmonic generation in absorbing semiconductor cavities. Phys. Rev. A **80**(4), 043834 (2009)
46. V. Roppo, N. Akozbek, D. de Ceglia, M.A. Vincenti, M. Scalora, Harmonic generation and energy transport in dielectric and semiconductors at visible and UV wavelengths: the case of GaP. J. Optical Soc. Am. B **28**(12), 2888–2894 (2011)
47. M. Scalora, G. D'Aguanno, N. Mattiucci, M.J. Bloemer, J.W. Haus, A.M. Zheltikov, Negative refraction of ultra-short electromagnetic pulses. Appl. Phys. B **81**(2–3), 393–402 (2005)
48. M. Scalora, G. D'Aguanno, N. Mattiucci, M.J. Bloemer, D. de Ceglia, M. Centini, A. Mandatori, C. Sibilia, N. Akozbek, M.G. Cappeddu, M. Fowler, J.W. Haus, Negative refraction and sub-wavelength focusing in the visible range using transparent metallo-dielectric stacks. Opt. Express **15**(2), 508–523 (2007)

Chapter 8
Nonlinear Optical Effects in Positive-Negative Refractive Index Materials

Andrei I. Maimistov and Ildar R. Gabitov

Abstract The parametric interaction of electromagnetic waves in a medium with a negative index of refraction is considered. Two cases of Kerr and quadratic nonlinearities are investigated. The properties of nonlinear coupler, channels of which made of material with opposing signs of refraction index, are studied. Dynamics of extremely short pulses in the homogeneous doubly-resonant medium is analyzed in the framework of Maxwell-Duffing-Lorentz model. The new type of quasi-solitons is presented.

8.1 Introduction

In recent years the new materials with unusual properties have evolved. Among such materials refereed as metamaterials special attention is given to "left-handed material" [1–3]. These media are characterized by a negative refraction index (NRI) when the real parts of the dielectric permittivity and the magnetic permeability are simultaneously negative in a certain frequency range. Negative sign of the index of refraction leads to the left-hand orientation of the fundamental triplet **E**, **H**, **k**. For the current state of technology the losses in the NRI materials are considerable. Therefore problem of loss reduction and compensation is the focus of intensive research worldwide [4–8]. Most impressive experiential achievement of loss

A.I. Maimistov
National Nuclear Research University Moscow Engineering Physics Institute, Kashirskoe Sh. 31, Moscow 115409, Russian Federation

A.I. Maimistov(✉)
Moscow Institute for Physics and Technology, Institutskii Lane 9, Dolgoprudny, Moscow 141700, Russian Federation
e-mail: aimaimistov@gmail.com

I.R. Gabitov
University of Arizona, 617 North Santa Rita Avenue, Tucson, AZ 85721, USA

I.R. Gabitov
L.D. Landau Institute for Theoretical Physics, Russian Academy of Sciences, 2 Kosygin Street, Moscow 119334, Russian Federation
e-mail: gabitov@math.arizona.edu

I.V. Shadrivov et al. (eds.), *Nonlinear, Tunable and Active Metamaterials*,
Springer Series in Materials Science 200, DOI 10.1007/978-3-319-08386-5_8

compensation was reported in [9]. These results offer hope that the low-loss materials with a negative index of refraction will be fabricated in the foreseeable future. A linear electrodynamics of metamaterials is well described in a number of review papers both in the specialized journals [10–13], and in the books [14–17].

It is well known that the unusual properties of negative refractive index materials manifest themselves when the wave passes through the interface between such medium and a conventional dielectric. On the other hand, the refractive index for the same medium can be positive in one spectral region and negative in another. This media can be referred to as *negative-positive refractive index materials*. The new features of the wave propagation phenomena in negative-positive refractive index materials where considered in [18, 19].

Second harmonic generation is one of the first examples of the nonlinear phenomena where unusual property of a negative-positive refractive index material was identified [18, 20–22]. It should be noted that the effect of second- and third-harmonic generation in metamaterials was observed experimentally [23, 24] (see also [25, 26]).

Hereafter we will discuss several kinds of the nonlinear phenomena in negative-positive refractive index materials.

The parametric interaction of the waves under the slowly varying envelope pulses approximation in a quadratic or cubic nonlinear medium that is characterized by NRI is considered. Second and third harmonic generation is discussed comprehensively in [27] and in [28, 29].

The novel kind of nonlinear interaction of the forward and backward waves can be realized in a nonlinear oppositely-directional coupler. This coupler consist of two tightly spaced nonlinear/linear waveguides. The sign of the index of refraction of one of these waveguides is positive and the index of refraction of other waveguide is negative. The opposite directionality of the phase velocity and the energy flow in the NRI waveguide facilitates an effective feedback mechanism that leads to optical bistability [30] and gap soliton formation [31–33]. Steady state solitary waves (i.e., gap solitons) in the nonlinear oppositely-directional coupler is considered in detail.

The combination of the metal nano-rods and split ring resonators can be viewed as a model for doubly-resonant medium [34]. The linear electrodynamics of the metamaterials is based on the Maxwell equations and the Lorentz models for the magnetic and electric resonances. We take into account nonlinearity in the leading order of polarization using the Duffing oscillator model. It results in the Maxwell-Duffing-Lorentz model [35]. Here we consider extremely short steady state pulse propagation in doubly-resonant medium. New type of solitons are presented.

8.2 Parametric Interaction of the Backward and Forward Waves

Parametric processes are well known examples of nonlinear optics. In general case of the parametric processes one multi-frequency wave transforms to another multi-frequency wave: $\omega_1 + \omega_2 + \cdots \to \omega_1' + \omega_2' + \cdots$. The three waves and four waves parametric interactions are the most studied cases.

Second harmonic generation (SHG) is a special case of three wave interaction ($\omega_1 + \omega_1 = \omega_2$) in a $\chi^{(2)}$-medium. Third harmonic generation (THG) is a special case of four wave interaction ($\omega_1 + \omega_1 + \omega_1 = \omega_3$) in a $\chi^{(3)}$-medium. In both cases ω_1 denotes the fundamental (pump) wave frequency. The $\omega_{2,3}$ are named as harmonic wave frequency.

8.2.1 Second Harmonic Generation

Original system of the equation describing the SHG in nonlinear metamaterials has been considered in [18–22].

$$-E_{1,z} + v_1^{-1} E_{1,t} + i(D_1/2)E_{1,tt} = ig_1 E_2 E_1^* \exp(-i\Delta kz), \tag{8.1}$$

$$E_{2,z} + v_2^{-1} E_{2,t} + i(D_2/2)E_{2,tt} = ig_2 E_1^2 \exp(+i\Delta kz), \tag{8.2}$$

where E_1 and E_2 are slowly varying envelopes of the electric field for fundamental and second harmonic waves. $\Delta k = 2k_1 - k_2$ is phase mismatch. The coupling constants g_1 and g_2 are proportional to the non-linear susceptibility of second order $\chi^{(2)}$. The group-velocity dispersion is taken into account by the coefficients D_1 and D_2.

The normalized form of the equations describing the SHG is as follows

$$iq_{1,\zeta} + (\sigma/2)q_{1,\tau\tau} - q_2 q_1^* = 0, \tag{8.3}$$

$$iq_{2,\zeta} + i\delta q_{2,\tau} - (\beta/2)q_{2,\tau\tau} - \Delta q_2 + q_1^2/2 = 0. \tag{8.4}$$

Here q_1 and q_2 represent the normalized fundamental and harmonic waves envelopes. δ is normalized group velocity mismatch, Δ is normalized phase mismatch, σ and β are parameters of the group-velocity dispersion. The all functions $q_{1,2}(\zeta, \tau)$, independent variables ζ, τ and otherwise parameters are expressed in terms of the physical values are represented in [19].

It should be pointed out that in contrast to the case of positive refractive index medium, parameter δ here can not be zero. This parameter takes into account the walk-off effect for pump and harmonic pulses that is due to the difference of the group velocities' directions for the interacting waves.

8.2.1.1 Continuous Wave Limit for SHG

It is convenient to start study of SHG by representing (8.3)–(8.4) in terms of real functions (amplitudes and phases). The real variables for interacting waves are defined by formulae $q_{1,2} = e_{1,2}\exp(i\varphi_{1,2})$. For continuous waves, (8.3)–(8.4) can be reduced to following equations

$$e_{1,\zeta} = e_1 e_2 \sin\Phi, \quad e_{2,\zeta} = (1/2)e_1^2 \sin\Phi, \tag{8.5}$$

$$\Phi_{,\zeta} = (e_1^2/2e_2 + 2e_2)\cos\Phi + \Delta, \tag{8.6}$$

where $\Phi = \varphi_2 - 2\varphi_1$.

There are two integrals of motion for the system of equations (8.5) and (8.6):

$$e_1^2/2 - e_2^2 = c_0^2, \tag{8.7}$$

$$e_1^2 e_2 \cos\Phi + \Delta e_2^2 = c_1. \tag{8.8}$$

The boundary conditions for a nonlinear plate of a finite width l are as follows: $e_1(0) = e_{10}$, $e_2(l) = 0$. Hence, the constant c_1 is zero, and constant $\sqrt{2}c_0$ is the fundamental wave amplitude at $\zeta = l$. In this case the (8.7) and (8.8) lead to

$$\cos\Phi = -\frac{\Delta e_2}{2(e_2^2 + c_0^2)}. \tag{8.9}$$

Substitution of the (8.9) into second equation of (8.5) results in equation for e_2:

$$(e_{2,\zeta})^2 = (e_2^2 + c_0^2)^2 + (\Delta/2)^2 e_2^2.$$

The solution of this equation can be represented in terms of elliptic functions, either $\wp$-function by Weierstrass, or Jacobi sine function [27]. We use the following expression

$$e_2(\zeta) = c_0(s_1 + is_2)\mathrm{sn}[c_0(s_1 - is_2)(l - \zeta);\ m_0], \tag{8.10}$$

where $s_1 = \Delta/4c_0$, $s_2^2 = 1 - s_1^2$ and modulus of the Jacobi function m_0 is

$$m_0 = \frac{\Delta + i\sqrt{(4c_0)^2 - \Delta^2}}{\Delta - i\sqrt{(4c_0)^2 - \Delta^2}}.$$

If the phase mismatch is zero, then (8.10) results in expression [20, 21]

$$e_2(\zeta) = \frac{\sqrt{2}c_0}{\cos[c_0(l - \zeta)]}.$$

When $\Delta \neq 0$ (8.9) defines the function $F(e_2) = \cos\Phi$ depending on e_2. The function $F(e_2)$ has extremum at $e_* = c_0$ and $F(e_*) = -\Delta/4c_0$. Since $|\cos\Phi| \leq 1$ then there is critical value of mismatch $|\Delta_{cr}| = 4c_0$ such that $\cos\Phi$ is defined for arbitrary values of e_2 if $|\Delta| \leq \Delta_{cr}$. If $|\Delta| \geq \Delta_{cr}$, then there is prohibited gap for values of e_2:

$$0 \leq e_2 \leq e_m = \frac{1}{4}\left(|\Delta| - \sqrt{\Delta^2 - \Delta_{cr}^2}\right), \quad e_2 \geq \frac{1}{4}\left(|\Delta| + \sqrt{\Delta^2 - \Delta_{cr}^2}\right), \tag{8.11}$$

As value of $e_2(\zeta)$ is fixed on the right side of the sample ($\zeta = l$) to be zero, the conversion efficiency of fundamental wave to second harmonic $|e_2(0)/e_{10}|^2$ is limited by the value $|e_m/e_{10}|^2$. At $\Delta = \Delta_{cr}$ the spatial distribution of the second harmonic amplitude follows from (8.10):

$$e_2(\zeta) = (\Delta_{cr}/4)\tanh[s_1(\zeta - l)].$$

At $\Delta > \Delta_{cr}$ the parameter s_2 in (8.10) is equal to $i[(\Delta/4c_0)^2 - 1]^{1/2}$ and the modulus of elliptic function in (8.10) is

$$m_0 = \frac{\Delta - \sqrt{\Delta^2 - \Delta_{cr}^2}}{\Delta + \sqrt{\Delta^2 - \Delta_{cr}^2}} < 1,$$

Expression (8.10) results in following one

$$e_2(\zeta) = -\frac{1}{4}\left(\Delta - \sqrt{\Delta^2 - \Delta_{cr}^2}\right)\mathrm{sn}\left[\frac{1}{4}\left(\Delta + \sqrt{\Delta^2 - \Delta_{cr}^2}\right)(l - \zeta); m_0\right]. \tag{8.12}$$

The Jacobi sine function oscillates with period $4\mathrm{K}(m_0)$, where K—the complete elliptic integral of the first kind. According to (8.12) normalized electric field of second harmonic is the periodic function. The distance between neighbor zeros of harmonic wave amplitude $\Delta\zeta$ is defined by following formula

$$\Delta\zeta = \frac{8\mathrm{K}(m_0)}{\Delta + \sqrt{\Delta^2 - \Delta_{cr}^2}}.$$

At some value of Δ the size of the interval $\Delta\zeta$ can be equal to l. Thus, under this conditions second harmonic wave is totally confined inside nonlinear material and does not escape outside. In this case material is transparent for fundamental wave.

The solutions describing SHG contain parameter Δ_{cr}. This parameter depends on the initial value of the fundamental wave amplitude e_{10}. The first integral of motion (8.7) represents transcendental equation for Δ_{cr} as an implicit function of e_{10} and l:

$$e_{10}^2 = 2e_2^2(0) + \Delta_{cr}^2/8,$$

where $e_2^2(0)$ is determined by expression (8.12) at $\zeta = 0$.

The behavior of the second harmonic wave amplitude for different values of phase mismatch Δ is shown in Fig. 8.1. It has been shown that increase of phase mismatch leads to reduction of the energy transfer from the first to second harmonic. When Δ reaches critical value $\Delta = \Delta_{cr}$ the energy transfer becoming zero in some point inside the sample. In this case the conversion efficiency sharply drops up to some value. If $\Delta \geq \Delta_{cr}$ then energy transfer is changing direction at some points inside the sample. Inside the interval, where transfer of energy becoming negative, energy

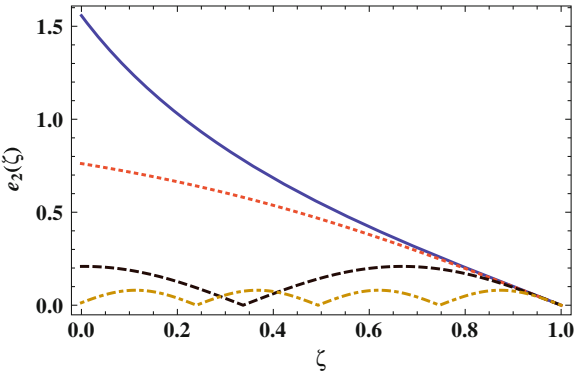

Fig. 8.1 The dependence of second harmonic's amplitude $e_2(\zeta)$ on the ζ with different values of phase mismatch (the *solid blue curve*: $\Delta = 0$, *dashed red curve*: $\Delta_{cr} = 4$, *dashed black curve*: $\Delta = 10$, *dot-dashed brown curve*: $\Delta = 25$)

"flow" from second harmonic wave to fundamental harmonic. In this case monotonic decay of both amplitudes with growth of ζ switches to periodic fields oscillations along the sample.

It is important to emphasize that in the case of conventional harmonic generation the critical value of mismatch Δ_{cr} is equal to zero. In the case under consideration the monotonic regime of harmonic generation is robust relative to variations of phase mismatch. The influence of losses on the second harmonic generation process in negative index materials in presence of phase mismatch Δk was considered in [27]. It was shown that in the presence of losses there is $\Delta_{cr} \neq 0$. Therefore, monotonic regime persists within the interval of phase mismatch values $-\Delta_{cr} \leq \Delta \leq \Delta_{cr}$.

8.2.1.2 Solitary Wave Solutions

The propagation of the fundamental and second harmonic solitary waves under the slowly varying envelope pulses approximation in a quadratic nonlinear medium that characterized by negative refraction index at the frequency of fundamental wave and by positive refractive index at the second harmonic frequency is governed by the system of equations (8.3)–(8.4). Dynamics of the interacting wave packets propagating in negative index materials in this case was considered in [36]. It was shown that in contrast to a weak intensity of fundamental wave, at high intensities pulse of second harmonics can be trapped by the fundamental wave pulse and forced to propagate in the same direction. This kind of coupled waves is refereed as simulton. The cnoidal waves, the bright and dark simultons and two-hump simulton are represented in [36] as examples of the coupled steady state waves.

To do comparison of the solitons in quadratic NRI material with solitons in PRI material it is suitable to represent the appropriate expressions for second case. If one sets the dispersion parameters as follows $\sigma = \beta = -1$ in the case of PRI medium, the solution for bright simulton reads as

$$e_1(\xi) = \frac{3\sqrt{2}(\Delta + \delta^2)}{2\cosh^2[\sqrt{(\Delta + \delta^2)/2}\xi]}, \qquad e_2(\xi) = \frac{3(\Delta + \delta^2)}{2\cosh^2[\sqrt{(\Delta + \delta^2)/2}\xi]},$$

where $\xi = \tau - \zeta/v_s - \tau_0$, v_s—simulton group velocity, τ_0—position of the simulton amplitude maximum. This simulton exists under condition $\Delta + \delta^2 > 0$. In the case of NRI medium bright simulton reads as

$$e_1(\xi) = \frac{\sqrt{2}(3\Delta - \delta^2)}{6\cosh^2[\sqrt{(3\Delta - \delta^2)/2}\xi/3]}, \qquad e_2(\xi) = \frac{(3\Delta - \delta^2)}{6\cosh^2[\sqrt{(3\Delta - \delta^2)/2}\xi/3]}.$$

This solution exists under condition $\Delta > \delta^2/3$. Thus the NRI simultons and PRI simultons exist in different regions of parameters plane (δ, Δ).

The numerical simulation of the SHG and simulton propagation in the negative refractive materials with quadratic nonlinearity was done in [37–39]. It was found that under certain conditions the second-harmonic pulse can be trapped and dragged along by the fundamental wave pulse. The case that a fundamental beam is tuned in a positive index region and generates second and/or third harmonics in a negative index region was considered in [40]. Phase matching condition, phase locking, inhibition of absorption at the harmonic wavelengths, and second and third harmonic lenses are investigated.

8.2.1.3 Second Harmonic Amplification

An important case of three wave interaction broadly used for practical applications is parametric amplification. We consider particular degenerated case of three wave interaction which involves interaction of fundamental and second harmonic. System of equations describing spatial distribution of interacting fields is reads as follows

$$e_{1,\zeta} = e_1 e_2 \sin\Phi - \alpha_1 e_1, \qquad e_{2,\zeta} = (1/2)e_1^2 \sin\Phi + \alpha_2 e_2, \tag{8.13}$$

$$\Phi_{,\zeta} = (e_1^2/2e_2 + 2e_2)\cos\Phi + \Delta, \tag{8.14}$$

Boundary conditions corresponding to second harmonic amplification have following form:

$$e_1(0) = e_{10}, \quad e_2(l) = e_{2l}\exp(i\varphi_0). \tag{8.15}$$

Here e_{10} is the amplitude of incident pump field at the point $\zeta = 0$; e_{2l} and φ_0 are the amplitude and initial phase of the second harmonic field (signal) launched at the opposite end of the sample $\zeta = l$; $\alpha_{1,2}$ are coefficients describing material losses.

Output amplitude of the second harmonic $e_2(0)$ depends on both values of e_{2l} and φ_0. Optimization of the amplification efficiency is equivalent to maximization of the output value of $e_2(0)$ at the fixed values of e_{10} and e_{2l}. This maximization can be achieved by varying of the value of φ_0.

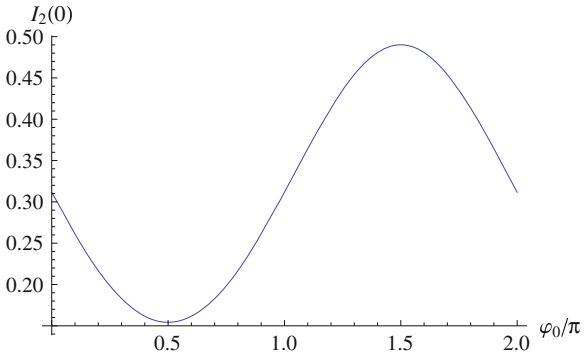

Fig. 8.2 The output intensity of the second harmonic field as function of the phase of the incident second harmonic field $e_2(L) = 0.5 \times \exp(i\varphi_0)$, here $\Delta = \alpha_1 = \alpha_2 = 0$ and incident pump field is $e_{10} = 1$

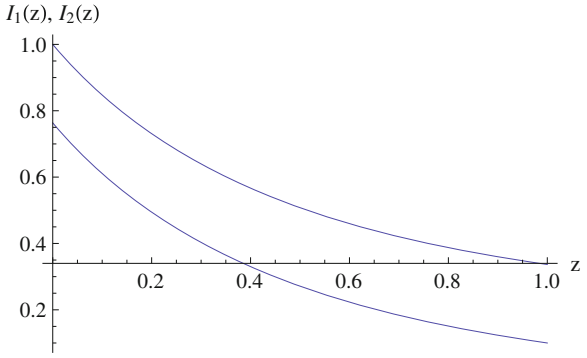

Fig. 8.3 Field intensities as functions of ζ, here $e_2(L) = 0.5 \times \exp(-i\pi/2)$, $e_{10} = 1$, $\Delta = \alpha_1 = \alpha_2 = 0$

Results of numerical simulations illustrating dependence of intensity of $I_2(0) = e_2^2(0)$ on φ_0 are shown in Fig. 8.2. In this case incident fields amplitudes are chosen to be $e_{10} = 1$ and $e_{2l} = \sqrt{0.1}$. The length of the sample is $l = 1$. Output field intensity $I_2(0)$ has maximum, corresponding to the maximum of energy conversion efficiency from fundamental harmonic to second harmonic, when input phase $\varphi = -\pi/2$ (see Fig. 8.2). Figure 8.3 illustrates corresponding spatial intensity profiles $I_1(\zeta)$ and $I_2(\zeta)$. Both intensities are monotonically decreasing with ζ. Dependance of output intensity $I_2(0)$ as function of $I_2(l)$ for optimal value of $\varphi_0 = -\pi/2$ is shown on Fig. 8.4. On the interval $0 \leq I_2(l) \leq\sim 0.2$ output field intensity is rapidly growing. Growth of the output field outside of this interval is almost linear. Presence of losses $\alpha_{1,2}$ and phase mismatch Δ are changing the value of optimal phase φ_0 and other characteristics of second harmonic amplification. Results of numerical simulations for $\alpha_1 = 0.2$, $\alpha_2 = 0.3$ and $\Delta = 3$ are shown on Figs. 8.5, 8.6, 8.7, and 8.8. Note that if $\Delta = 0$, then the most intensive energy transfer from fundamental

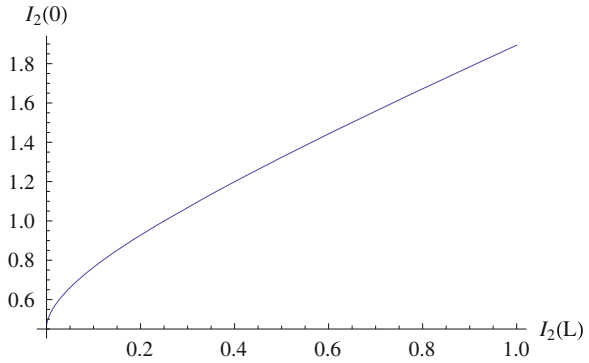

Fig. 8.4 Output intensity $I_2(0)$ as function of $I_2(l)$ for optimal value of $\varphi_0 = -\pi/2$, here $e_2(L) = 0.5 \times \exp(-i\pi/2)$, $e_{10} = 1$, $\Delta = \alpha_1 = \alpha_2 = 0$

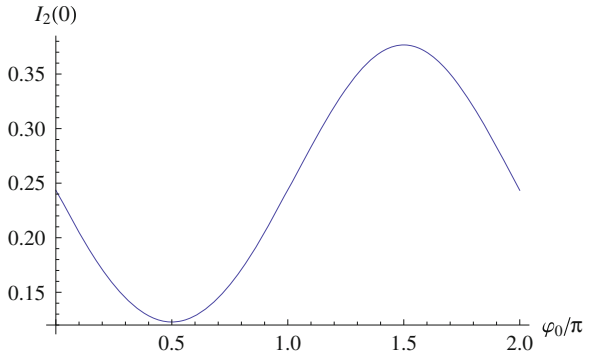

Fig. 8.5 Output intensity $I_2(0)$ as function of φ_0 for $\alpha_1 = 0.3$, $\alpha_2 = 0.5$ here $e_2(L) = 0.5 \times \exp(-i\pi/2)$, $e_{10} = 1$, $\Delta = 0$. The optimal value of φ_0 is found to be $\varphi_0 = -\pi/2$

to second harmonics takes place when $\Phi = -\pi/2$ in (8.5), (8.6). This conclusion is in an excellent agreement with numerical simulations portrayed in Fig. 8.3. Optimal value of φ_0, calculated for $\alpha_1 = 0.3$, $\alpha_2 = 0.5$ and $\Delta = 0$ with high accuracy is found to be $\varphi_0 = -\pi/2$. Corresponding dependence of output intensity versus input value of input phase is plotted in Fig. 8.5. Group of the numerical simulations illustrating second harmonic generation, when value of parameters are chosen as $\alpha_1 = 0.3$, $\alpha_2 = 0.5$ and $\Delta = 3$ are presented in Fig. 8.6, 8.7 and 8.8. Figure 8.6 shows an impact of incident phase φ_0 on output intensity of second harmonic. The optimal value of φ_0 for energy transfer in this case is $\varphi_0/\pi \approx 0.922496$.

Intensity profiles is this case are shown in Fig. 8.7. Intensity of pump field in this case is insufficient for amplification of second harmonic field.

Figure 8.8 demonstrates how intensity of output field $I_2(0)$ is changing with increase of the intensity of pump field. In this case amplification takes place only

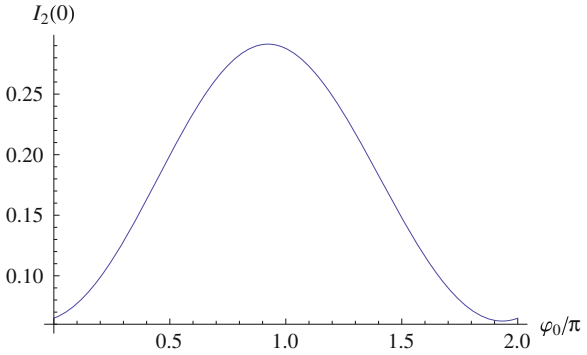

Fig. 8.6 An impact of incident phase φ_0 on output intensity of second harmonic $I_2(0)$. The optimal value of φ_0 for energy transfer in this case is $\varphi_0/\pi \approx 0.922496$. Here $\alpha_1 = 0.3$, $\alpha_2 = 0.5$, $\Delta = 3$

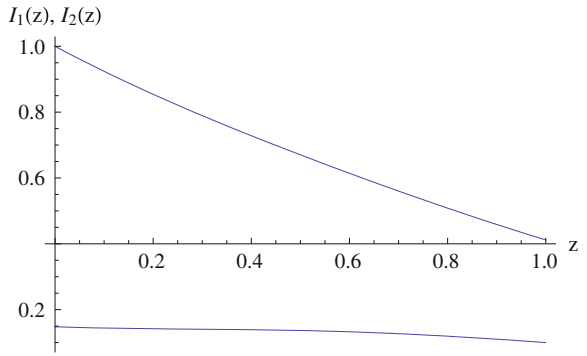

Fig. 8.7 Intensity profiles $I_1(\zeta)$ and $I_2(\zeta)$ for optimal value of $\varphi_0/\pi \approx 0.922496$. Here $\alpha_1 = 0.3$, $\alpha_2 = 0.5$, $\Delta = 3$, $e_2(L) = 0.5 \times \exp(-i\pi/2)$, $e_{10} = 1$

inside the interval $0 \leq I_2(l) \leq\sim 0.2$. There is no amplification outside of this interval.

Problem of second harmonic amplification, in contrast to second harmonic generation, requires optimization with respect to relative phase of incident pump and second harmonic fields. The value of incident field amplitude is zero ($e_2(l) = 0$) in case of second harmonic generation. To eliminate singularity in the right-hand side of the (8.6), the value of $\Phi(l)$ must be $\Phi(l) = -\pi/2$. Therefore in case of SHG phase value at the point $\zeta = 0$ is the result of self-selecting process. In case of second harmonic amplification both entry phases of the fundamental and second harmonics are fixed by the external sources. In presence of losses, when phase mismatch is zero, this relative phase is also equal to $-\pi/2$ and does not depends on loss values. Presence of phase mismatch changes the value of optimal relative phase.

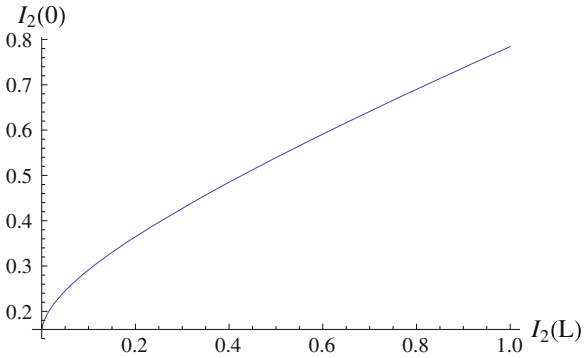

Fig. 8.8 Output intensity $I_2(0)$ as function of input intensity $I_2(L)$. Here optimal value of $\varphi_0/\pi \approx 0.922496$, $\alpha_1 = 0.3$, $\alpha_2 = 0.5$, $e_{10} = 1$, $\Delta = 3$

8.2.2 Third Harmonic Generation

Now we will consider the third harmonic generation (THG). The TGH is due to $\chi^{(3)}$-nonlinearity of material. Contrary to the SHG the self-modulation and cross-modulation take place in this case in addition to the transfer of energy from one wave to another. The normalized form of the basic equations is following one [19, 28, 29]

$$iq_{1,\zeta} + (\sigma/2)q_{1,\tau\tau} - q_3 q_1^{*2} - \alpha_{11}|q_1|^2 q_1 - \alpha_{13}|q_3|^2 q_1 = 0, \tag{8.16}$$

$$iq_{3,\zeta} + i\delta q_{3,\tau} - (\beta/2)q_{3,\tau\tau} - \Delta q_3 + q_1^3 + \alpha_{31}|q_1|^2 q_3 + \alpha_{33}|q_3|^2 q_3 = 0. \tag{8.17}$$

Here α_{jl} is the self-modulation and cross-modulation coefficients.

8.2.2.1 Continuous Wave Limit for THG

As above let us consider THG in the case of continuous waves. Equations (8.16) and (8.17) can be reduced to following equations

$$e_{1,\zeta} = e_1^2 e_2 \sin\Phi, \qquad e_{3,\zeta} = e_1^3 \sin\Phi, \tag{8.18}$$

$$\Phi_{,\zeta} = (e_1^3/e_3 + 3e_1 e_3)\cos\Phi + \Delta + a_0 e_1^2 + b_0 e_3^2, \tag{8.19}$$

where $\Phi = \varphi_3 - 3\varphi_1$. Parameters $a_0 = \alpha_{31} + 3\alpha_{11}$ and $b_0 = \alpha_{33} + 3\alpha_{31}$ take account self-modulation and cross-modulation effects.

As in the case of SHG we can find two integrals of motion

$$e_1^2 - e_3^2 = c_0^2, \tag{8.20}$$

$$e_1^3 e_3 \cos\Phi + \frac{1}{2}\left(\Delta + a_0 c_0^2\right) e_1^2 + \frac{1}{4}(a_0 + b_0) e_3^2 = C_1. \tag{8.21}$$

We will consider nonlinear plate of a finite width l. With allowance for the boundary condition $e_3(l) = 0$, one can see that the constant C_1 is zero. Substituting $y = e_3/c_0$ and using expression (8.20), we will rewrite (8.21) as follows:

$$\cos\Phi = -\frac{\kappa_1 y + \kappa_3 y^3}{(1+y^2)^{3/2}},$$

where $\kappa_1 = (\Delta + a_0 c_0^2)/2c_0^2$ and $\kappa_3 = (a_0 + b_0)/4$.

Condition $|\cos\Phi| \le 1$ is restriction on permissible variation of the harmonic wave amplitude. However, total analysis of that is very cumbersome. This analysis was done in [29] by means of the numerical calculation. It was shown that regions of monotonic transformation of the fundamental wave to third harmonic wave in parametric space (κ_1, κ_3) are akin to islands. The main part of parametric space corresponds to a periodic regime of transformation.

8.2.2.2 Steady State Pulse Propagation

Steady state solitary bounded waves can be found by solving system of equations (8.16) and (8.17) under several assumptions: (1) there is no chirp; (2) there are no self- and cross interaction, i.e., $\alpha_{jl} = 0$; (3) the real envelopes and phases of the coupled waves are dependant on $\xi = \tau - \zeta/v_s$, where v_s is simulton group velocity; (4) $\Phi = \varphi_3 - 3\varphi_1 = 0$ for any ξ; (5) the steady state waves for both frequencies must be propagating as single one. These assumptions allow us to reduce the (8.16) and (8.17) to a single equation for the real envelope e_1 [19]. If we put dispersion parameters as follows $\sigma = \beta = -1$, the bright simulton reads as

$$e_1(\xi) = e_3(\xi) = \frac{\sqrt{4\Delta - 3\delta^2}}{4\cosh[\sqrt{4\Delta - 3\delta^2}\,\xi]}. \tag{8.22}$$

Steady state cnoidal waves solutions for system of equations (8.16) and (8.17) have been found in [28], by taking into account all above-listed assumptions.

It is interesting to remark that walk-off effect, which is accounted by parameter δ in (8.17), is liable to frustrate coupling between fundamental and harmonic waves. In this case the waves will propagate independently according to following equations

$$iq_{1,\zeta} + (\sigma/2)q_{1,\tau\tau} - \alpha_{11}|q_1|^2 q_1 = 0,$$
$$iq_{3,\zeta} + i\delta q_{3,\tau} - (\beta/2)q_{3,\tau\tau} - \Delta q_3 + \alpha_{33}|q_3|^2 q_3 = 0.$$

Either of the two equations is the Nonlinear Schrödinger-type equation. Hence, the fundamental wave pulse and/or third harmonic wave pulse can be transformed into soliton (or solitons), propagating with own velocity. That was observed in numerical simulation of the THG in [28].

8.3 Oppositely Directional Nonlinear Coupler

A directional coupler that is widely used in integral optics consists of two waveguides so closely spaced that the radiation from one waveguide can leak into the other; the direction of the energy flow in this case is preserved. However, if one of the waveguides is made of PRI material, while the other is made of NRI material, the directions of the phase velocities must be the same, whereas the Poynting vectors will have opposite directions. Because of this coupler can be referred as the oppositely directional coupler. In what follows the nonlinear oppositely directional coupler will be considered.

8.3.1 Nonlinear Waveguide Array

Let us suppose that waveguides marked by $J = 2n$ ($J = 2n + 1$) are produced from PRI (NRI) medium. The system of equations describing the electromagnetic wave propagation in this structure have been represented in [19]. The slowly varying complex envelopes obey the following equations

$$i\left(E_{2n,z} + v_{g2n}^{-1}E_{2n,t}\right) + K_{12}(E_{2n+1} + E_{2n-1})e^{i\Delta\beta z} + \mathscr{R}_{2n}|E_{2n}|^2E_{2n} = 0, \tag{8.23}$$

$$i\left(-E_{2n+1,z} + v_{g2n+1}^{-1}E_{2n+1,t}\right) + K_{21}(E_{2n} + E_{2n+2})e^{-i\Delta\beta z} + \mathscr{R}_{2n+1}|E_{2n+1}|^2E_{2n+1} = 0, \tag{8.24}$$

where K_{12} and K_{21} are coupling constants, E_J is a slowly varying envelope of the electric field in Jth waveguide. Linear properties of the waveguides is defined by dielectric permittivity $\varepsilon_J(\omega_0)$ and magnetic permeability $\mu_J(\omega_0)$. These values are assumed to be real, that corresponds to lossless materials. Nonlinear properties of the Jth waveguide are determined by parameters

$$\mathscr{R}_J = \frac{2\pi\omega_0^2\mu(\omega_0)\chi_{eff}^{(J)}}{c^2\beta^{(J)}}.$$

Here parameters $\beta^{(J)}$ are propagation constant, $\chi_{eff}^{(J)}$ is the effective nonlinear susceptibility for Jth waveguide.

Introduce the normalized variables for envelopes

$$q_{2n} = \sqrt{K_{21}} A_0 E_{2n} e^{-i\Delta\beta z/2}, \quad q_{2n+1} = \sqrt{K_{12}} A_0 E_{2n+1} e^{+i\Delta\beta z/2},$$

and the parameters

$$\zeta = z/L_c, \quad \tau = t_0^{-1}(t - z/V_0), \quad L_c = (K_{12}K_{21})^{-1/2},$$

$$t_0 = \frac{v_{g2} + v_{g1}}{2v_{g1}v_{g2}} L_c, \quad V_0 = \frac{v_{g2} - v_{g1}}{2v_{g2}v_{g1}}.$$

Here we assumed that wave group velocity doesn't depend on number of the PRI and NRI waveguides, i.e., $v_{g2n} = v_{g1}$, $v_{g2n+1} = v_{g2}$. The system of equations (8.23)–(8.24) takes the form

$$i\left(\frac{\partial q_{2n}}{\partial \zeta} + \frac{\partial q_{2n}}{\partial \tau}\right) - \delta q_{2n} + (q_{2n+1} + q_{2n-1}) + r_1 |q_{2n}|^2 q_{2n} = 0, \tag{8.25}$$

$$i\left(\frac{\partial q_{2n+1}}{\partial \zeta} - \frac{\partial q_{2n+1}}{\partial \tau}\right) + \delta q_{2n+1} - (q_{2n} + q_{2n+2}) - r_2 |q_{2n+1}|^2 q_{2n+1} = 0, \tag{8.26}$$

where $\delta = \Delta\beta L_c/2$ is the phase mismatch. Nonlinearity parameters are defined by the expressions

$$r_1 = \frac{2\pi\omega_0^2 \mu(\omega_0) A_0^2 \chi_{eff}^{(1)}}{c^2 \beta^{(1)} K_{21}\sqrt{K_{21}K_{12}}}, \quad r_2 = \frac{2\pi\omega_0^2 \mu(\omega_0) A_0^2 \chi_{eff}^{(2)}}{c^2 \beta^{(2)} K_{12}\sqrt{K_{21}K_{12}}}.$$

If we introduce the "block" variables $q_{2n} = A_j$, $q_{2n+1} = B_j$, this system of equations becomes

$$i\left(\frac{\partial}{\partial \zeta} + \frac{\partial}{\partial \tau}\right) A_j - \delta A_j + (B_j + B_{j-1}) + r_1 |A_j|^2 A_j = 0, \tag{8.27}$$

$$i\left(\frac{\partial}{\partial \zeta} - \frac{\partial}{\partial \tau}\right) B_j + \delta B_j - (A_j + A_{j+1}) - r_2 |B_j|^2 B_j = 0, \tag{8.28}$$

The linear waves in oppositely directional waveguides array are governed by these equations, where $r_1 = r_2 = 0$. It follows

$$i\left(\frac{\partial}{\partial\zeta}+\frac{\partial}{\partial\tau}\right)A_j-\delta A_j+(B_j+B_{j-1})=0, \tag{8.29}$$

$$i\left(\frac{\partial}{\partial\zeta}-\frac{\partial}{\partial\tau}\right)B_j+\delta B_j-(A_j+A_{j+1})=0, \tag{8.30}$$

To find the spectrum of the permissible waves for this waveguides array we can substitute the following Ansatz: $A_j = a_j \exp(-i\omega\tau + i\kappa\zeta + i\kappa_\perp j)$, $B_j = b_j \exp(-i\omega\tau + i\kappa\zeta + i\kappa_\perp j)$ in (8.29) and (8.30). The resulting linear system of algebraic equations has the nonzero solution only if the corresponding determinant is equal to zero. That leads to the dispersion relation

$$[\omega(\kappa,\kappa_\perp)-\delta]^2=\kappa^2+4\cos^2(\kappa_\perp/2)=0. \tag{8.31}$$

Thus the spectrum of the linear waves has the gap $\Delta\omega(\kappa_\perp) = 2|\cos(\kappa_\perp/2|$. Maximum of the gap correspond to $\kappa_\perp = 2\pi s$, where s is integer. That is the Bragg resonant condition for transverse waves. The lump like solitary waves in the oppositely directional nonlinear waveguides array would be expected.

8.3.2 Two Tunnel Coupled Waveguides

The oppositely directional nonlinear coupler corresponds to the arrangement consisting of only two coupled waveguides. This particular case of the general model (8.25)–(8.26) has been studied in [30–33, 42, 46]. Evolution of the electromagnetic solitary wave in the coupled waveguides is described by the equations

$$i\left(\frac{\partial}{\partial\zeta}+\frac{\partial}{\partial\tau}\right)q_1-\delta q_1+q_2+r_1|q_1|^2q_1=0, \tag{8.32}$$

$$i\left(\frac{\partial}{\partial\zeta}-\frac{\partial}{\partial\tau}\right)q_2+\delta q_2-q_1-r_2|q_1|^2q_1=0, \tag{8.33}$$

In the linear regime, $r_1 = r_2 = 0$, we can find solutions of the resulting equations in following form

$$q_{1,2}(\zeta,\tau)=(2\pi)^{-2}\int\limits_{-\infty}^{+\infty}\tilde{q}_{1,2}(\kappa,\nu)e^{-i\nu\tau+i\kappa\zeta}d\kappa d\nu.$$

The existence condition of this solution leads to the dispersion relation $\nu(\kappa) = \delta \pm \sqrt{1+\kappa^2}$. Thus the spectrum of the linear waves has the gap $\Delta\nu_g = 2$. This gap is a characteristic feature of a distributed mirror [43]. Hence, in the linear wave limit the oppositely directional coupler acts as a mirror. Formation of the gap in a uniform structure considered here is one of the unique properties of the oppositely directional coupler arising from introduction of the NIM into the nonlinear coupler.

If the real amplitudes and phases are introduced according to the formula $q_{1,2} = a_{1,2}\exp(i\varphi_{1,2})$ (8.32)–(8.33) can be reduced to following system of real equations

$$\left(\frac{\partial}{\partial\zeta}+\frac{\partial}{\partial\tau}\right)a_1 = a_2\sin\Phi, \quad \left(\frac{\partial}{\partial\zeta}-\frac{\partial}{\partial\tau}\right)a_2 = a_1\sin\Phi, \tag{8.34}$$

$$\left(\frac{\partial}{\partial\zeta}+\frac{\partial}{\partial\tau}\right)\varphi_1 = -\delta+\frac{a_2}{a_1}\cos\Phi + r_1a_1^2, \tag{8.35}$$

$$\left(\frac{\partial}{\partial\zeta}-\frac{\partial}{\partial\tau}\right)\varphi_2 = \delta-\frac{a_1}{a_2}\cos\Phi - r_2a_2^2, \tag{8.36}$$

where $\Phi = \varphi_1 - \varphi_2$. There is the conservation law

$$\frac{\partial}{\partial\tau}\left(a_1^2+a_2^2\right)+\frac{\partial}{\partial\zeta}\left(a_1^2-a_2^2\right)=0. \tag{8.37}$$

If the first term can be considered as total energy density, then the second term is the divergence of total flux density. In the case of solitary waves, for which the electromagnetic fields vanish at infinity, (8.37) leads to the modified Manley-Rowe relation

$$\frac{\partial}{\partial\zeta}\int_{-\infty}^{+\infty}\left(a_1^2-a_2^2\right)d\tau = 0.$$

To consider the solitary steady-state waves in the oppositely directional coupler we suppose that solutions of these equations depend only on single variable $\eta = (\zeta+\beta\tau)(1-\beta^2)^{-1/2}$, where β is parameter and $|\beta|<1$.

Let us define new variables $u_1 = \sqrt{1+\beta}a_1$ and $u_2 = \sqrt{1-\beta}a_2$. The equations (8.34) take the following form

$$u_{1,\eta} = u_2\sin\Phi, \quad u_{2,\eta} = u_1\sin\Phi, \tag{8.38}$$

The first integral of motion $u_1^2 - u_2^2 = C_1$ is evident from (8.38).

The (8.35) and (8.36) are reduced to following ones

$$\varphi_{1,\eta} = -\delta+\frac{u_2}{u_1}\cos\Phi+\vartheta_1u_1^2, \quad \varphi_{2,\eta} = \delta-\frac{u_1}{u_2}\cos\Phi-\vartheta_2u_2^2,$$

where

$$\vartheta_1 = \frac{r_1}{(1+\beta)}\sqrt{\frac{1-\beta}{1+\beta}}, \quad \vartheta_2 = \frac{r_2}{(1-\beta)}\sqrt{\frac{1+\beta}{1-\beta}}.$$

These equations are used to obtain the equation for Φ:

$$\Phi_{,\eta} = -2\delta + \left(\frac{u_1}{u_2} + \frac{u_2}{u_1}\right)\cos\Phi + \vartheta_1 u_1^2 + \vartheta_2 u_2^2. \tag{8.39}$$

This equation allows to find the second integral of motion

$$u_1 u_2 \cos\Phi + \frac{\vartheta_1 u_1^4 + \vartheta_2 u_2^4}{4} - \frac{\delta}{2}(u_1^2 + u_2^2) = C_2. \tag{8.40}$$

The values of C_1 and C_2 are determined by the boundary conditions at $\eta \to \pm\infty$. Here we consider a solitary wave with the amplitudes vanishing at infinity. That leads to $C_1 = C_2 = 0$, thus we have $u_1 = \varepsilon u_2$, $\varepsilon = \pm 1$. Solution of the system of equations (8.38) and (8.39) for boundary conditions under consideration was found in [31, 32].

If the synchronism condition is satisfied, $\delta = 0$, the real envelopes $a_{1,2}(\eta)$ and phases $\phi_{1,2}(\eta)$ are written

$$a_1^2(\eta) = \frac{4}{|\vartheta|(1+\beta)\cosh 2(\eta - \eta_c)}, \tag{8.41}$$

$$a_2^2(\eta) = \frac{4}{|\vartheta|(1-\beta)\cosh 2(\eta - \eta_c)}, \tag{8.42}$$

$$\phi_1(\eta) = \frac{3\vartheta_1 - \vartheta_2}{|\vartheta_1 + \vartheta_2|}\arctan e^{2(\eta-\eta_c)}, \tag{8.43}$$

$$\phi_2(\eta) = \frac{\vartheta_1 - 3\vartheta_2}{|\vartheta_1 + \vartheta_2|}\arctan e^{2(\eta-\eta_c)} - \pi/2, \tag{8.44}$$

where $\vartheta = \vartheta_1 + \vartheta_2$, and η_c is a new integration constant (position of gap soliton maximum). These solutions correspond with solitary steady-state wave propagation in both waveguides of the oppositely directional coupler.

In the general case there is the phase mismatch, i.e., $\delta \neq 0$. The expressions for real envelopes $a_{1,2}(\eta)$ and phases $\phi_{1,2}(\eta)$ are too cumbersome. For example,

$$(1+\beta)a_1^2(\eta) = (1-\beta)a_2^2(\eta) = \frac{4\Delta^2/|\theta|}{\cosh[2\Delta(\eta - \eta_c)] - \mathrm{sgn}(\theta)\delta(1-\beta^2)^{-1/2}},$$

where $\Delta^2 = 1 - \delta^2/(1-\beta^2)$. Since $\Delta^2 > 0$ it is evident the phase velocity mismatch is restricted by the values $\delta_\pm = \pm(1-\beta^2)^{1/2}$, else the solitary waves are unavailable.

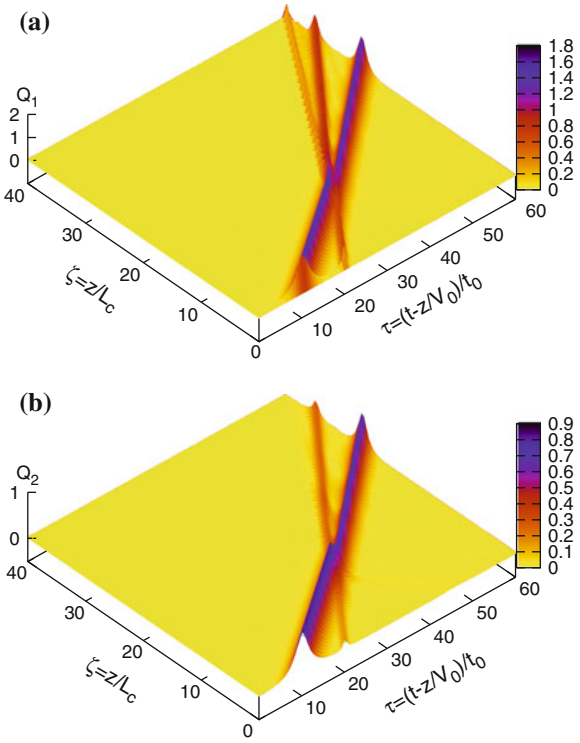

Fig. 8.9 Crossing collision between two solitary waves with $\beta = -0.5$ and $\beta = -0.9$. Panel **a** is for the solitary wave in the PRI waveguide; Panel **b** is for the solitary wave in the NRI waveguide

8.3.3 Interaction of the Gap Solitons in Oppositely Directional Coupler

In our opinion the system of equations (8.32)–(8.33) does not belong to the class of completely integrable equations. Hence the solution of these equations does not represent true soliton. However, we name them as gap solitons by analogy with gap solitons in nonlinear periodic structures [44, 45]. To investigate interactions between the gap solitons (8.41)–(8.44) the numerical simulation has been pursued in [32]. Due to the fact that soliton velocity is controlled by parameter β, the velocities of the pulses are different for different β. As a result, the faster pulse attains the slower pulse and collides with it. As Fig. 8.9 illustrate, the gap soliton sheds some amount of radiation after collision, also a weak radiating wave arises as a result of their interaction. The velocities and the amplitudes of the gap solitons after collision are slightly different from their corresponding values before the collision. Thus inelastic interaction takes place.

To demonstrate the robustness of the gap soliton the collision between two gap soliton with the same absolute values of the velocity $\beta = 0.7$ and $\beta = -0.7$.

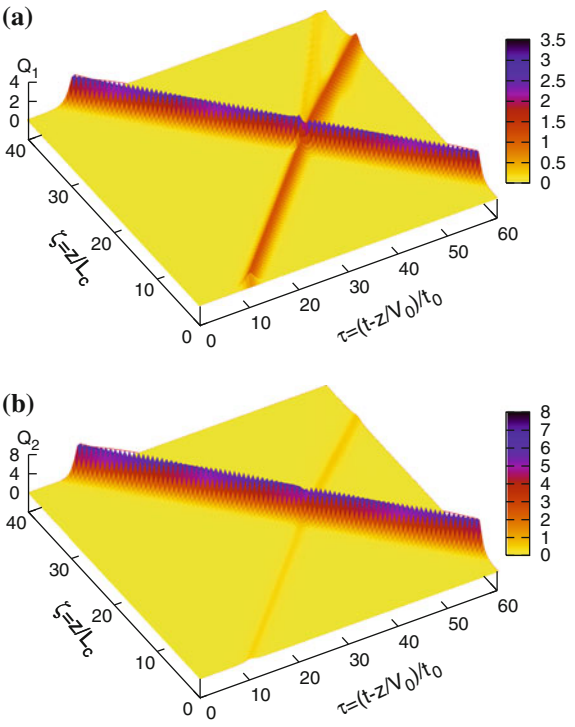

Fig. 8.10 Collision between two solitary waves with $\beta = 0.7$ and $\beta = -0.7$. Panel **a** is for the solitary wave in the PRI waveguide; Panel **b** is for the solitary wave in the NRI waveguide

Solitary waves in this case are propagating as Fig. 8.10 shows, a more energetic gap soliton with $\beta = 0.7$ remains unchanged after collision and the less energetic gap soliton with $\beta = -0.7$ drops some radiation, this results in change of its trajectory.

Thus, the collision of two steady state pulses with different velocities has shown significant robustness of powerful gap solitons. Small amplitude radiation appearing after collision attests that the small amplitude gap soliton eventually will disappear.

8.3.4 Influence of Dissipation on Threshold of Gap Soliton Formation

For the current state of fabrication technology the losses in the real NRI materials are considerable. The influence of the linear losses in the NRI waveguide on the existence of the solitary waves was studied in [32, 33]. The numerical simulation demonstrates that even small losses affect considerably the propagation properties of the solitary waves. By passing some distance the gap soliton transform into linear-like wave packet. This wave stops in the waveguide and changes direction of its propagation, i.e., the oppositely directional coupler now acts as a distributed mirror.

The gap soliton formation in an extended nonsymmetric (i.e., only an ordinary waveguide has nonlinear optical properties, $r_2 = 0,\ r_1 = r$) oppositely directional coupler was considered in [33]. It has been shown that a small amplitude electromagnetic pulse, introduced into one of the waveguides, is emitted in the opposite direction from the other waveguide. The coupler acts as a mirror. If the amplitude of the input pulse exceeds a certain threshold, then the pair of coupled pulses propagating in both waveguides is formed. Thus, the formation of a gap soliton in the oppositely directional coupler has a threshold character. The numerical simulation of the soliton formation from initially Gaussian envelope pulse $a(\zeta = 0, \tau) = a_0 \exp(-\tau^2)$ allows one to estimate dependence of the amplitude threshold a_{th} versus nonlinearity parameter $r : a_{th} = 2.1\, r^{-1/2}$.

In the case of the symmetric (i.e., both waveguide has the same nonlinear optical properties, $r_1 = r_2 = r$) oppositely directional coupler there is analytical approximate formula for the amplitude threshold [41]:

$$a_{th}^2 r = 4\sqrt{(\pi/2)^2 - 1} \approx 4.85.$$

It should be remarked that this expression provides the good estimation for numerical results of [33], even thought the nonlinear properties of couplers are different.

8.3.5 A Selection of Nonlinear Phenomena in Oppositely Directional Coupler

8.3.5.1 Modulation Instability

Modulation instability (MI) in nonlinear oppositely directed coupler was investigated in [46]. It was shown that the ratio of the forward- to backward-propagating wave power and the nonlinear parameters have a profound effect on MI. In the normal dispersion regime the threshold value of this forward/backward ratio and the input power threshold exist. MI occurs only for finite values of input power when the NRI waveguide is manufactured from self-defocusing nonlinear material and PRI waveguide is produced from self-focusing nonlinear material in the anomalous dispersion regime. It was found that increasing input power may suppress the MI, which is quite different from the MI in the conventional couplers. For the conventional one, the increase of input power generally promotes the occurrence of MI.

8.3.5.2 Spatial Discrete Solitons

Existence and properties of discrete solitons in arrays of alternating waveguides with positive and negative refractive indices was studied in [47]. The stationary (i.e.,

continuous wave) field distribution in the array $(A_j,\ B_j)$ has been described by the modified version of the (8.27) and (8.28)

$$iA_{j,\zeta} + \delta A_j + (B_j + B_{j-1}) + r_1|A_j|^2 A_j = 0, \tag{8.45}$$

$$iB_{j,\zeta} - \delta B_j - (A_j + A_{j+1}) - r_2|B_j|^2 B_j - i\gamma B_j = 0, \tag{8.46}$$

where γ is absorption index. In the case of $\gamma = 0$ spectrum of the linear waves has the gap.

It was supposed that a discrete soliton has the form $A_j(\zeta) = a_j \exp(i\kappa\zeta)$ and $B_j(\zeta) = b_j \exp(i\kappa\zeta)$ where a_j and b_j are real and vanish as $|j| \to \infty$. Furthermore, soliton propagates along waveguides without distortion.

Spectrum of the linear continues waves arises from (8.31)

$$\kappa^2 = \delta^2 - 4\cos^2(\kappa_\perp/2).$$

If $|\delta| > 2$, then the gap $\Delta\kappa = 2\sqrt{\delta^2 - 4}$ exists. As is shown in [47] the gap solitons exist for waveguides having nonlinearities of different types. When the nonlinearities of all waveguides are focusing, solitons exist if the propagation constant κ lies outside of the gap.

Numerical simulation [47] shown that there exist soliton families bifurcating from the gap edges of the linear spectrum. The field distribution in the oppositely directional nonlinear waveguides array reveals nonexponential decay and nonmonotonic dependence of the energy growth in the positive index waveguides on the absorption index.

8.3.5.3 Bistability

Bistability of an optical system results from the multi-valued dependence of the transmission (or refraction) coefficient on the input wave power. Transmission and reflection coefficients for the nonlinear oppositely directional coupler of a finite width in the case of continuum wave radiation was found [30]. It was demonstrated that the transmission (and reflection) coefficient is multivalued function of input power. It leads to hysteresis behavior of the transmission and reflection coefficients.

The transmission characteristics of the nonlinear oppositely directional coupler are very similar to those of the distributed feedback structures with an important fundamental difference that bistability in the coupler is facilitated by the effective feedback mechanism originating from the forbidden zone in a linear waves spectrum.

In [48, 49], the nonlinear transmission properties of oppositely directional coupler is considered. One waveguide was assigned to be of positive index material and the other waveguide of negative index material. Only one of the waveguides is considered to be nonlinear. The phase mismatch affect was taking into account. The effect of nonlinearity and mismatch on the multistable behavior for this coupler was studied.

8.4 Extremely Short Steady State Pulses

Commonly electromagnetic pulse propagation in resonant media is considered in the slowly varying envelope approximation. However, there are number of nonlinear optical phenomena taking place in the limit of extremely short pulses, when the slowly varying envelope approximation is not valid. For example, the spectrum of extremely short electromagnetic pulse can be covering the frequency range with both PRI and NRI features of the resonant material. In this case different frequency components of electromagnetic pulses can be localized in the different spectral regions.

8.4.1 The Model Formulation

In [35] the Maxwell-Duffing-Lorentz model has been used to account for simultaneous magnetic and electric resonances, with the magnetic susceptibility being linear, while the electric polarization being nonlinear. For simplicity, the transverse electromagnetic plane waves propagating along the z-axis with the electric field $\mathbf{E} = (E(z,t), 0, 0)$ and the magnetic field $\mathbf{B} = (0, B(z,t), 0)$ were considered. The Maxwell equations take the following scalar form:

$$E_{,z} + c^{-1}H_{,t} + 4\pi c^{-1}M_{,t} = 0, \quad H_{,z} + c^{-1}E_{,t} + 4\pi c^{-1}P_{,t} = 0, \tag{8.47}$$

where electric polarization P and magnetization M are governed by the equations

$$P_{,tt} + \omega_D^2 P + \kappa P^3 - \omega_p^2 E = 0, \tag{8.48}$$

$$M_{,tt} + \omega_T^2 M + \beta H_{,tt} = 0, \tag{8.49}$$

where κ is a constant of anharmonisity, ω_D and ω_T are the resonant frequency, which are intrinsic to model under consideration. Constant β is characterizing magnetization [34].

The system of equations (8.47), (8.48) and (8.49) can be represented in the normalized form

$$e_{,\tau} + h_{,\eta} + m_{,\tau} = 0, \quad h_{,\tau} + e_{,\eta} + q_{,\tau} = 0, \tag{8.50}$$

$$q_{,\tau\tau} + \omega_1^2 q + \gamma q^3 - e = 0, \quad m_{,\tau\tau} + \omega_2^2 m + \beta h_{,\tau\tau} = 0, \tag{8.51}$$

where $e = E/P_0$ and $h = H/P_0$ are normalized fields, $q = P/P_0$ and $m = M/P_0$ are normalized polarization and magnetization ($P_0 = \omega_p/\sqrt{\kappa}$ is the maximal achievable medium polarization), $\tau = t/\tau_0$ ($\tau_0 = 1/\omega_p$ is the characteristic time), $\eta = z/z_0$ ($z_0 = c\tau_0$ is the characteristic distance). The parameters of the model are $\gamma = \kappa/\left(|\kappa|\,\omega_p^2\right)$, $\omega_1 = \omega_D/\omega_p$, and $\omega_2 = \omega_T/\omega_p$.

A natural question arises is whether the system of equations (8.50) and (8.51) possesses any solitary-wave solutions.

8.4.2 Extremely Short Solitary Waves

If we assume that both an electric and magnetic fields and a polarization and magnetization are functions of the variable $\xi = \tau - \eta/V$, Then the (8.50) and (8.51) become a system of ordinary differential equation. Integrating of these equations under zero conditions for all fields, polarization and magnetization at $\xi \to \pm\infty$ yields the following expressions for h and e

$$h = a_1 m + a_2 q, \quad e = a_2 m + a_1 q,$$

where

$$a_1 = V^2 \left(1 - V^2\right)^{-1}, \quad a_2 = V \left(1 - V^2\right)^{-1}.$$

These formulae allow to obtain the following system of second order equations: for q and m

$$q_{,\xi\xi} + \left(\omega_1^2 - a_1\right) q - a_2 m + \gamma q^3 = 0,$$
$$\beta a_2 q_{,\xi\xi} + (1 + \beta a_1)\, m_{,\xi\xi} + \omega_2^2 m = 0.$$

This system of equations was base of investigation for qualitative properties of the solitary-wave solutions for original equations. The details are represented in [35].

The analytical solutions of the system of equations (8.50)–(8.51) have not been found. However, numerical simulations of the solitary waves evolution demonstrated existence of steady state solitary waves [35]. Only at certain velocities the steady state solitary waves exist.

Different types of solitary wave solutions are classified by the number of the electromagnetic field spikes that are referred to as humps. Figures 8.11 and 8.13 show the two examples of the multi-hump pulses.

The issue of stability can be addressed analytically by studying the linearization of the system of partial differential equations (8.50)–(8.51) about arbitrary steady state solitary wave solutions and analyzing the corresponding linear evolution operator. Analysis showed that this operator is skew-Hermitian in L_2 with the appropriate norm. Therefore the spectrum of the evolution operator is purely imaginary and the traveling wave solutions are neutrally linearly stable [51].

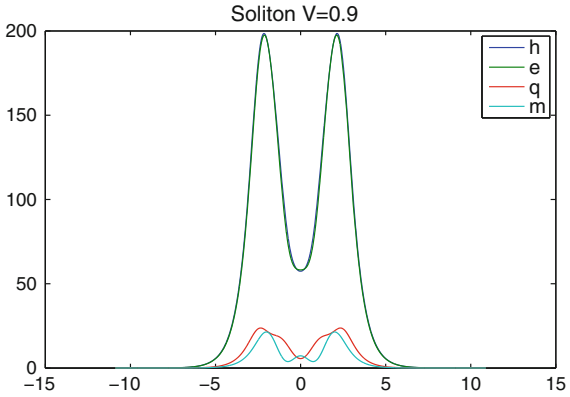

Fig. 8.11 The two-hump steady state solitary wave

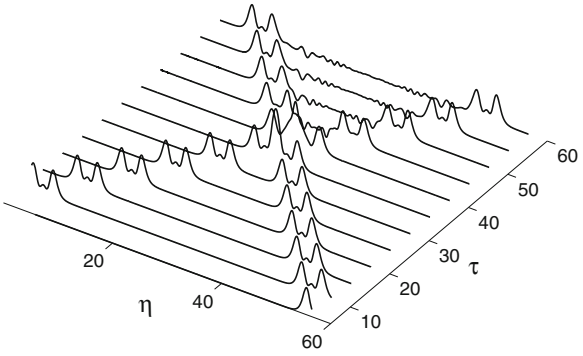

Fig. 8.12 Collision of the two-hump steady state solitary waves

8.4.3 Interaction of the Steady State Solitary Waves

The formation of the steady state solitary wave from arbitrary initial-boundary condition, stability of travelling waves under small perturbations and stability under strong perturbations due to wave collisions have been considered.

The numerical simulation have shown that both one-hump pulse and multi-hump (number of the hump is variety up to eight ones) pulses are stable. Furthermore, the collision of the steady state solitary waves doesn't perturb initial waves. Some examples of the two steady state solitary waves collisions are shown in Figs. 8.12 and 8.13.

These results allow us to take reference for the described steady state solitary waves as the new kind of quasi-solitons. The collision between these multi-hump pulses are not elastic, but multi-hump pulses are robust.

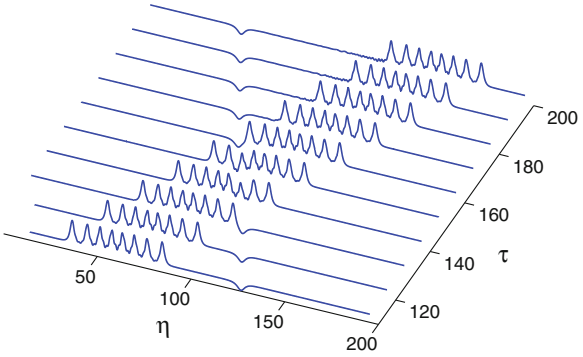

Fig. 8.13 Solitary wave collisions: an eight-hump soliton and a phase-inverted soliton with negative polarity

8.5 Conclusion

The unusual properties of negative refractive index materials reveal themselves most prominently when a wave passes through, or is localized near, an interface between such a material and a conventional dielectric. New wave propagation phenomena can also be expected when the refractive index of the same medium can be positive in one spectral region and negative in another. We are referring to these cases as positive-negative refractive index materials. As the significant examples of nonlinear phenomena in the positive-negative refractive index materials we consider the parametric interaction of the electromagnetic waves, the solitary waves propagating in the nonlinear oppositely directional coupler and the propagation of extremely short electromagnetic pulses in a homogeneous doubly-resonant medium.

Study on the second and third harmonic generation shows that there is some critical value of the mismatch Δ_{cr}. If $\Delta \leq \Delta_{cr}$ the transformation of the fundamental wave into harmonic wave goes monotonically. If $\Delta = \Delta_{cr}$ the conversion efficiency sharply drops up to some value. If $\Delta > \Delta_{cr}$ amplitudes of the interacting waves are varying periodically. In the case of conventional harmonic generation the critical value of mismatch is zero.

Efficiency of second harmonic amplification depends on the phase difference of the incident fundamental and second harmonic fields. If phase of the fundamental field $\arg E_1(0) = 0$ and $\Delta = 0$, then optimal conversion takes place when $\arg E_2(L) = -\pi/2$, which is consistent with SHG case. This is also true in presence of losses. The optimal angle is different from $-\pi/2$ when $\Delta \neq 0$. In this case the value of the optimal angle changes with Δ.

In linear regime the oppositely directional coupler acts as a mirror. The radiation entering one waveguide leaves the device through the other waveguide at the same end but in the opposite direction. However, if the input pulse power exceeds certain threshold, the steady state solitary wave can be appeared.

An investigation of ultra-short electromagnetic pulses in the homogeneous doubly-resonant medium in the framework of the total Maxwell-Duffing-Lorentz model results in revelation of the new kind of nonlinear waves. It is the one-parameter family of traveling-wave solutions with the structure of single or multiple humps. Solutions are parameterized by the velocity of propagation. The waves are found to be stable with respect to weak perturbations. Numerical simulations demonstrate that these multi-hump pulses collide in a nearly elastic fashion.

Acknowledgments We are indebted to P. Lushnikov for helpful discussion. A.I. Maimistov appreciates the support and hospitality of the Nonlinear Physics Center, the Australian National University. The research of A.I. Maimistov was partially supported by RFBR (grants No. 09-02-00701-a, 12-02-00561) and ARO-MURI award 50342-PH-MUR. I.R. Gabitov was partially supported by NSF grant DMS-0509589, FTP S&SPPIR, ARO-MURI award 50342-PH-MUR, and by Russian Ministry of Education and Science.

References

1. D.R. Smith, W.J. Padilla, D.C. Vier, S.C. Nemat-Nasser, S. Schultz, Composite medium with simultaneously negative permeability and permittivity. Phys. Rev. Lett. **84**, 4184–4187 (2000)
2. J.B. Pendry, Negative refraction makes a perfect lens. Phys. Rev. Lett. **85**, 3966–3969 (2000)
3. R.A. Shelby, D.R. Smith, S. Schultz, Experimental verification of a negative index of refraction. Sci. **292**, 77–79 (2001)
4. M.A. Bodea, G. Sbarcea, G.V. Naik, A. Boltasseva, T.A. Klar, J.D. Pedarnig, Negative permittivity of ZnO thin films prepared from aluminium and gallium doped ceramics via pulsed-laser deposition. Appl. Phys. A (2012). doi:10.1007/s00339-012-7198-6
5. G.V. Naik, J. Liu, A.V. Kildishev, V.M. Shalaev, A. Boltasseva, Demonstration of Al:ZnO as a plasmonic component of near-infrared metamaterials. Proc. Nat. Acad. Sci. **109**, 8834–8838 (2012)
6. G.V. Naik, J.L. Schroeder, X. Ni, A.V. Kildishev, T.D. Sands, A. Boltasseva, Titanium nitride as a plasmonic material for visible and near-infrared wavelengths. Opt. Mat. Express **2**, 478–489 (2012)
7. Chen K.-P., Drachev V. P., Liu Z., Kildishev A. V., Shalaev V. M., Improving Au nanoantenna resonance by annealing, in *Plasmonics and Metamaterials Topical Meeting 2008*, Rochester, NY, USA, 20–23 October 2008
8. W. Chen, K.-P. Chen, M.D. Thoreson, A.V. Kildishev, V.M. Shalaev, Toward ultra-thin, ultra-smooth and low-loss silver films through wetting and annealing. Appl. Phys. Lett. **97**, 211107 (2010)
9. S. Xiao, Vl.P. Drachev, Al.V. Kildishev, Xingjie Ni, U.K. Chettiar, H.-K. Yuan, Vl.M. Shalaev, Loss-free and active optical negative-index metamaterials. Nat. **466** (lett.) 735–738 (2010)
10. J.B. Pendry, Negative refraction. Contemp. Phys. **45**, 191–202 (2004)
11. S.A. Ramakrishna, Rep. Prog. Phys. **68**, 449–521 (2005)
12. V. Veselago, L. Braginsky, V. Shklover, Ch. Hafner, Negative refractive index materials. J. Comput. Theor. Nanosci. **3**, 189–218 (2006)
13. S.G. Rautian, Reflection and refraction at the boundary of a medium with negative group velocity. Phys. Usp. **51**, 981–988 (2008)
14. G.V. Eleftheriades, K.G. Balmain (eds.), *Negative-Refraction Metamaterials: Fundamental Principles and Applications* (Wiley, New York, 2005)
15. A.K. Sarychev, V.M. Shalaev, *Electrodynamics of Metamaterials* (World Scientific, Singapore, 2007)

16. W. Cai, V. Shalaev, *Optical Metamaterials: Fundamentals and Applications* (Springer, Heidelberg, 2009)
17. M.A. Noginov, V.A. Podolskiy (eds.), *Tutorials in Metamaterials* (Taylor and Francis Group, LLC/CRC Press, Boca Raton, 2012)
18. V.M. Agranovich, Y.R. Shen, R.H. Baughman, A.A. Zakhidov, Linear and nonlinear wave propagation in negative refraction metamaterials. Phys. Rev. B **69**, 165112 (2004)
19. A.I. Maimistov, I.R. Gabitov, Nonlinear optical effects in artificial materials. Eur. Phys. J. Special Topics **147**, 265–286 (2007)
20. I.V. Shadrivov, A.A. Zharov, Y.S. Kivshar, Second-harmonic generation in nonlinear left-handed metamaterials. J. Opt. Soc. Am er. **B23**, 529–534 (2006)
21. A.K. Popov, V.M. Shalaev, Negative-index metamaterials: second-harmonic generation, Manley-Row relations and parametric amplification. Appl. Phys. B **84**, 131–137 (2006)
22. A.K. Popov, V.V. Slabko, V.M. Shalaev, Second harmonic generation in left-handed metamaterials. Laser Phys. Lett. **3**, 293–297 (2006)
23. M.W. Klein, Ch. Enkrich, M. Wegener, S. Linden, Second-Harmonic eneration from Magnetic Metamaterials. Sci. **313**, 502–504 (2006)
24. W. Klein, M. Wegener, N. Feth, S. Linden, Experiments on second- and third-harmonic generation from magnetic metamaterials. Opt. Express **15**, 5238–5247 (2007)
25. N. Feth, S. Linden, M.W. Klein, M. Decker, F.B.P. Niesler, Y. Zeng, W. Hoyer, J. Liu, S.W. Koch, J.V. Moloney, M. Wegener, Second-harmonic generation from complementary split-ring resonators. Opt. Lett. **33**, 1975–1977 (2008)
26. F.B.P. Niesler, N. Feth, S. Linden, J. Niegemann, J. Gieseler, K. Busch, M. Wegener, Second-harmonic generation from split-ring resonators on a GaAs substrate. Opt. Lett. **34**, 1997–1999 (2009)
27. Kudyshev Zh., Gabitov I., Maimistov A.: The effect of phase mismatch on second harmonic generation in negative index materials. arxiv:1102.0538v1 [physics. optics]
28. S.O. Elyutin, A.I. Maimistov, I.R. Gabitov, On the third harmonic generation in a medium with negative pump wave refraction. JETP **111**, 157–169 (2010)
29. E.I. Ostroukhova, A.I. Maimistov, Third harmonic generation in the field of a backward pump wave. Opt. Spectrosc. **112**, 255–263 (2012)
30. N.M. Litchinitser, I.R. Gabitov, A.I. Maimistov, Optical bistability in a nonlinear optical coupler with a negative index channel. Phys. Rev. Lett. **99**, 113902 (2007)
31. A.I. Maimistov, I.R. Gabitov, N.M. Litchinitser, Solitary waves in a nonlinear oppositely directed coupler. Optics and Spectroscopy. **104**, 253–257 (2008)
32. E.V. Kazantseva, A.I. Maimistov, S.S. Ozhenko, Solitary electromagnetic wave propagation in the asymmetric oppositely directed coupler. Phys. Rev. A **80**, 43833 (2009)
33. M.S. Ryzhov, A.I. Maimistov, Gap soliton formation in a nonlinear antidirectional coupler. Quantum Electron. **42**, 1034–1038 (2012)
34. R.W. Ziolkowski, E. Hayman, Wave propagation in media having negative permittivity and permeability. Phys. Rev. E **64**, 056625 (2001)
35. Frenkel Y., Gabitov I., Maimistov A., Roytburd V.: Propagation of extremely short electromagnetic pulses in a doubly-resonant medium. arxiv:0812.4794 [nlin.PS]
36. A.I. Maimistov, I.R. Gabitov, E.V. Kazantseva, Quadratic Solitons in Media with Negative Refractive Index. Opt. Spectrosc. **102**, 90–97 (2007)
37. M. Scalora, G. D'Aguanno, M. Bloemer, M. Centini, D. de Ceglia, N. Mattiucci, Y.S. Kivshar, Dynamics of short pulses and phase matched second harmonic generation in negative index materials. Opt. Express **14**, 4746–4756 (2006)
38. V. Roppo, M. Centini, C. Sibilia, M. Bertolotti, D. de Ceglia, M. Scalora, N. Akozbek, M.J. Bloemer, J.W. Haus, O.G. Kosareva, V.P. Kandidov, Role of phase matching in pulsed second-harmonic generation: Walk-off and phase-locked twin pulses in negative-index media. Phys. Rev. A **76**, 033829 (2007)
39. V. Roppo, M. Centini, D. de Cegliac, M.A. Vicenti, J. Haus, N. Akozbek, J. Mark, M.J. Bloemer, M. Scalora, Anomalous momentum states, non-specular reflections, and negative refraction of phase-locked, second-harmonic pulses. Metamaterials **2**, 135–144 (2008)

40. V. Roppo, C. Ciraci, C. Cojocaru, M. Scalora, Second harmonic generation in a generic negative index medium. J. Opt. Soc. Amer. B **27**, 1671–1679 (2010)
41. Maimistov A.I., Kazantseva E.V., Desyatnikov A.S.: Linear and nonlinear properties of the antidirectional coupler, in Coherent optics and optical spectroscopy, Lect.notes, Kazan State University, Kazan, (2102), pp. 21–31. (in Russian)
42. N.A. Kudryashov, A.I. Maimistov, D.I. Sinelshchikov, General class of the traveling waves propagating in a nonlinear oppositely-directional coupler. Phys. Letts. **A376**, 3658–3663 (2012)
43. C. Elachi, P. Yeh, Periodic structures in integrated optics. J. Appl. Phys. **44**, 3146–3152 (1973)
44. D.L. Mills, S.E. Trullinger, Gap solitons in nonlinear periodic structures. Phys. Rev. B. **36**, 947–952 (1987)
45. G. Agrawal, Y.S. Kivshar, *Optical Solitons: From Fibers to Photonic Crystals* (Academic Press, Amsterdam, 2003)
46. X. Yuanjiang, W. Shuangchun, D. Xiaoyu, F. Dianyuan, Modulation instability in nonlinear oppositely directed coupler with a negative-index metamaterial channel. Phys. Rev. E **82**, 056605 (2010)
47. D.A. Zezyulin, V.V. Konotop, F.K. Abdullaev, Discrete solitons in arrays of positive and negative index waveguides. Opt. Lett. **37**, 3930–3932 (2012)
48. Zh Kudyshev, G. Venugopal, N.M. Litchinitser, Generalized analytical solutions for nonlinear positive-negative index couplers. Phys. Res. International **2012**, 945807 (2012)
49. G. Venugopal, Zh Kudyshev, N.M. Litchinitser, Asymmetric positive-negative index nonlinear waveguide couplers. IEEE J. Sel. Top. Quantum Electron. **18**, 753–756 (2012)
50. A.I. Maimistov, E.V. Kazantseva, A waveguide amplifier based on a counterdirectional coupler. Opt. Spectrosc. **112**, 264–270 (2012)
51. Frenkel Y. : A Numerical Study of Ultra-Short Pulse Propagation in Maxwell-Duffing Media, Ph.D. thesis, Rensselaer Polytechnic Institute, Troy, New York (2008)

Chapter 9
From 'Trapped Rainbow' Slow Light to Spatial Solitons

Allan D. Boardman, Kosmas L. Tsakmakidis, Rhiannon C. Mitchell-Thomas, Neil J. King, Yuri G. Rapoport and Ortwin Hess

9.1 Introduction

The metamaterial global revolution, stimulated by the pioneering work of Pendry [1], in the year 2000, raises all kinds of questions as to what they can be used for. This chapter addresses two globally recognised, important, desires. One concerns the deployment of metamaterials to slow down light. The other embraces the question of how nonlinearity, manifested as spatial solitons [2], can be controlled in a metamaterial environment. Both of these activities will have a very positive influence upon device design, especially in the optical domain.

Metamaterial (MM) investigations [3–5] and 'slow light' (SL) [6, 7] behaviour have, in the last decade, matured into two of the largest and most exciting realms of contemporary science, opening up a view of a wealth of useful applications. These include *sub*-diffraction-limited lenses, ultra-compact photonic devices and, very dramatically, invisibility cloaks. The theoretical demonstration [8] that two highly technologically important areas of research, such as metamaterials and slow

A.D. Boardman (✉) · N.J. King
Joule Physics Laboratory, Materials and Physics Research Centre, University of Salford, Greater Manchester M5 4WT, UK
e-mail: A.D.Boardman@salford.ac.uk

K.L. Tsakmakidis · O. Hess
The Blackett Laboratory, Department of Physics, South Kensington Campus, Imperial College London, London SW7 2AZ, UK

R.C. Mitchell-Thomas
School of Electronic Engineering and Computer Science, Queen Mary University of London, London E1 4NS, UK

Y.G. Rapoport
Faculty of physics, Taras Shevchenko National University,
Prospect Glushkov 6,
22, Kiev, Ukraine
e-mail: yuriy.rapoport@gmail.com

I.V. Shadrivov et al. (eds.), *Nonlinear, Tunable and Active Metamaterials*,
Springer Series in Materials Science 200, DOI 10.1007/978-3-319-08386-5_9

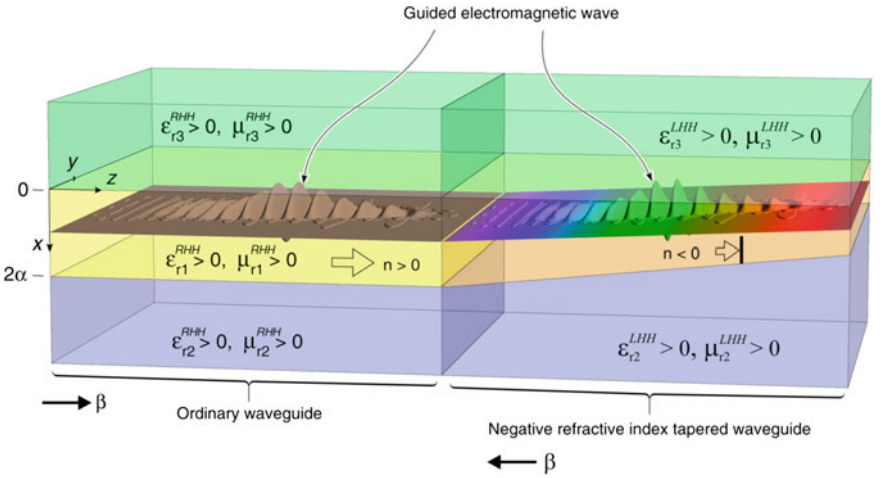

Fig. 9.1 The 'trapped rainbow' principle [8]. Owing to negative Goos-Hänchen shifts, light is slowed and eventually stopped in an adiabatically tapered negative-refractive-index waveguide—with each frequency 'stopping' at a different point in space—forming a 'trapped rainbow'

light, which were following separate/parallel tracks, could, in fact, be combined, exposed the potential of novel metamaterial-enabled slow-light structures. The latter can dramatically improve on existing slow-light designs and structures in terms of the degree to which light can be decelerated, as well as of performance, nanoscale functionality and efficiency; see Fig. 9.1. Indeed, some of the most successful slow-light designs at present, based on photonic-crystals (PhCs) [9], or coupled-resonator optical waveguides (CROWs) [10], can, so far, efficiently slow down light by a factor of around 50—otherwise, large group-velocity-dispersion and attenuation-dispersion occur, i.e. the guided light pulses broaden and the attainable bandwidth is severely restricted. Such a drawback directly imposes an upper limit on the degree to which one can shrink the area of the corresponding slow-light devices (compactness), as well as reducing the driving electrical power. Additionally, it has by now also been realised that such positive-index slow-light structures are, unfortunately, extremely sensitive to the presence of (even weak) fabrication disorder [11]—to the point that disorder on the scale of only 2–5 nm (at a wavelength of 1,550 nm) leads to group velocities that cannot, even in the presence of dispersion, be smaller than approximately $c/300$ [6, 12].

By contrast, it has been theoretically and experimentally established that metamaterials are highly insensitive to the presence of (even a high degree of) fabrication disorder [13, 14], since their properties arise from an averaged/effective response of their constituent 'meta-molecules', without necessarily requiring a 'perfect' lattice crystal—a situation which is similar to, e.g., crystalline or amorphous silicon, where the presence, or not, of a periodic atomic lattice does not, of course, preclude the attainment of an effective refractive index. This ability of metamaterial-

based heterostructures to dramatically decelerate, or even completely stop light, under realistic experimental conditions, has recently led to a series of experimental works [15, 16] for the observation of 'trapped rainbow' light-stopping in metamaterial waveguides. In the following sections we shall show, based on analytic theory and computational simulations, that negative-refraction (or negative-refractive-index) metamaterial-enabled slow-light structures enable efficient deceleration of light by factors of, at least, tens of thousands without suffering from the aforementioned group-velocity- and attenuation-dispersion limitations.

Moving on now from a discussion of how to control slow light in ***active*** metamaterials, to beam propagation in ***nonlinear*** metamaterial environments, it should first of all be acknowledged that the history of solitons [2, 17–20] is fascinating in its own right, and the theory of them is usually based upon a weakly guiding nonlinear foundation. This soliton family can be managed within an externally applied magnetooptic environment, so it is not surprising that it can also be managed by metamaterials. Very important members of the soliton family are called spatial solitons and are well-known in the literature as optical beams in which diffraction is balanced by the presence of self-focussing nonlinearity [2]. They will be discussed here in terms of how such beams change their behaviour when they are created within a metamaterial guiding system. It is pointed out that spatial solitons have a lot of application possibilities, especially when placed into the context of materials being used in a light-controlling-light environment that is suitable for the optical chips of the future. Metamaterials, being artificially controlled, open up a completely new range of devices so the possibility of additionally operating these devices through magnetooptic control is really exciting. This is largely because magnetooptics, developed over many years, now points to readily available materials, in nanostructured form, that can be easily embedded into plasmonic and photonic metamaterials. Indeed, sophisticated downstream magnetooptic devices are now entirely accessible. In addition, it is becoming clear that isotropic metamaterials, with loss-free frequency windows, are within reach through composites containing certain types of nanospheres, especially since it is possible to make such composites using magnetooptic spheres. New portals are emerging, implying new frontiers that need to be addressed in a lot more detail. Nonlinear systems are a vital part of this development. Hence, the interest in solitons, especially when coupled to tunability. The very special properties that emerge when dealing with negative index metamaterials may well be the way forward when addressing potentially devastating loss windows.

In hydrodynamics and electromagnetism, solitons [21] have been studied for a long time and have found particular importance in the optical domain, especially in connection with optical fibres [22]. It is, therefore, very important to investigate the extent to which new materials are capable of sustaining various types of solitons. Since any soliton is drawn from a very large family, it is necessary to restrict attention to particular members of this family and very important ones are bright spatial solitons. The balance mentioned earlier is actually between the chirps associated with beam diffraction and nonlinear self-focussing. This property is in contrast to temporal solitons that are pulses which rely upon balancing phase changes across their width and arise from material dispersion and nonlinearity. Both spatial solitons

and slow light trapping will now be discussed in detail, beginning with an account of what has become known as the "trapped rainbow".

9.2 The "Trapped-Rainbow" Principle: Light Stopping in Metamaterial and Plasmonic Waveguides

Slow-light nanoguides are expected to lead to substantial reductions in the size of and power consumption in photonic devices and systems. For instance, recent theoretical studies and computational simulations (see also below) suggest that dispersionless slow group velocities of light pulses in multilayer negative-refraction MM waveguides can dramatically increase the induced phase shifts in Mach-Zehnder modulators, to the point of reducing the length of the modulator's arms from a typical present-day value of a few mm down to only a few tens of microns (see, e.g., [23]). Similarly promising results can also be achieved for a number of other photonic components, such as switches, buffers, filters, dispersion compensators, and so forth. Furthermore, by deploying suitably designed all-semiconductor based [24, 25] (i.e. not metallic) metamaterial waveguides that include active/gain layers, we can engineer practical slow-light structures wherein the optical (dissipative) losses of the guided slow-light pulses are reduced by orders of magnitude—or completely eliminated—compared to their metallic counterparts; a further key requirement for any useful slow-light structure.

A variety of physical effects have recently been exploited in order to dramatically decelerate or 'store' light. These include electromagnetically induced transparency (EIT), coherent population oscillations (CPO), stimulated Brillouin scattering (SBS), photonic-crystal (PhC) line-defect waveguides and coupled-resonator optical waveguides (CROWs). However, (atomic) EIT uses ultracold or hot gases and not solid-state materials, CPO and SBS are very narrowband (typically, several kHz or MHz) owing to the narrow transparency window of the former and the narrow Brillouin gain bandwidth of the latter, while PhCs are prone to tiny fabrication imperfections (nm-scale disorder) [26, 27] that can considerably modify (shift) the photonic bandgaps. In an effort to provide an alternative that would allow to overcome the above intrinsic limitations of positive-index slow-light schemes, a fundamentally new approach has been proposed [8, 28, 29] that relies on the use of negative-electromagnetic-parameters (refractive index and/or permittivity) waveguides. In such waveguide the power-flow direction inside the negative-index/-permittivity regions is opposite to the one in the positive-index regions, resulting in a pronounced deceleration of the guided electromagnetic energy (see Fig. 9.2).

We now first describe the basic premises of (dispersionless) slow/stopped light in negative-constitutive-parameters metamaterial and plasmonic waveguides ('trapped rainbow' principle). We proceed by studying the waveguide dispersion equations in the presence of disorder and/or dissipative losses, and show that the zero-group- and zero-energy-velocity points are preserved; hence, a guided light pulse can still

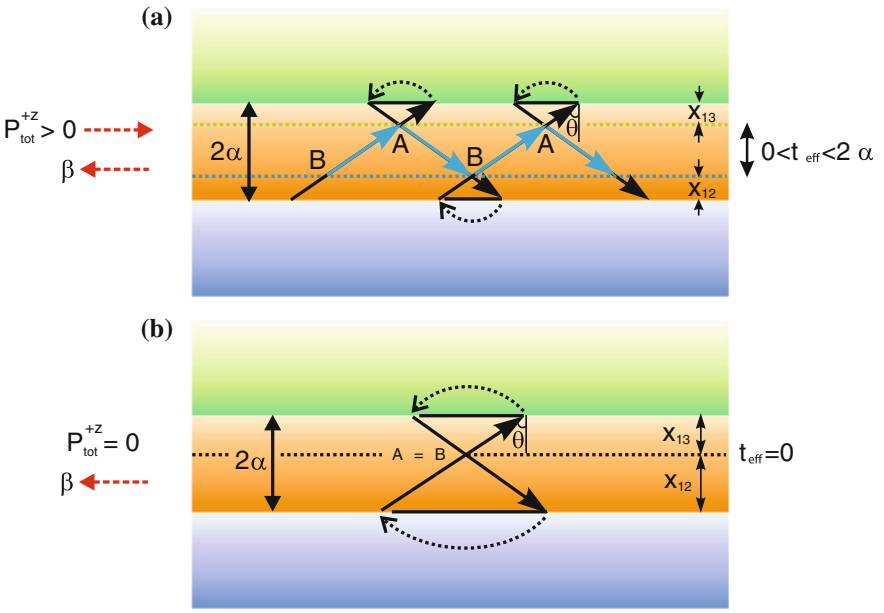

Fig. 9.2 Slow and stopped light in negative-refractive-index hetero-structures. **a** Slow zigzag ray propagation along a NRI hetero- structure. **b** Here, the ray returns exactly to its original point; the ray, thus, becomes permanently trapped (zero group velocity, $v_g = 0$) and an 'optical clepsydra' is formed. In both figures, β is the longitudinal propagation constant, P^{+z} the (total) time-averaged power flow, and t_{eff} the effective guide thickness

be dramatically decelerated and stopped inside these lossy structures. Finally, we show how the incorporation of thin layers made of an active/gain medium placed adjacently to the core of a negative-index metamaterial waveguide can lead to a complete elimination of the dissipative losses experienced by a guided, slow-light pulse.

The 'trapped rainbow' scheme uses efficiently excitable waveguide oscillatory modes and is remarkably simple, since the slowing of the guided modes is performed solely by adiabatic decrease of the core thickness. The scheme is, also, resilient to fabrication disorder/imperfections because it does not rely on the use of stringent conditions (such as a 'perfect' photonic-crystal lattice or attainment of ultralow temperatures, etc.) for decelerating and stopping light, but rather on the deployment of negative bulk/effective electromagnetic parameters (such as, e.g., negative refractive index or, simply, negative permittivity) that can readily be realised by even amorphous and highly disordered metamaterials [13, 14]. Furthermore, these metamaterial heterostructures can be designed in such a way that they exhibit zero group-velocity-dispersion *and* attenuation-dispersion, even in the 'stopped-light' regime [30]. Utilizing a non-resonant scheme, we are able to allow for *extremely large bandwidths over which the slowing* [31] *or stopping* [32] *of the incoming optical signals*

can be achieved, as well as for ultrashort device lengths. This approach also has the important advantage that it can facilitate very efficient butt-coupling, directly to a slow mode alone because: (i) It can support single-mode operation in the slow-light regime [29]; (ii) The characteristic impedance of the NRI waveguide can be appropriately adjusted by varying the core thickness [8]; and (iii) The spatial distribution of the slow mode closely matches that of a single-mode dielectric waveguide [8]. These conclusions have been drawn following exact manipulations of Maxwell's equations, without invoking paraxial, heuristic or other approximations.

It is interesting to point out that, in addition to metallic (metallodielectric) metamaterial or plasmonic slow-light structures, we can also deploy all-semiconductor based, negative-refraction, heterostructures to realise 'trapped rainbow' slowing or stopping of light. Such semiconductor-heterostructure designs have recently been experimentally shown [24, 25] to enable negative refraction at infrared wavelengths (8.4 μm to 13.3 μm), and (upon heavy doping) they can indeed be extended to the telecommunication—or even the ultraviolet [32]—regime. Owing to their negative-refraction property, these structures can facilitate slow-light propagation, and would be particularly well-suited for the compensation of optical losses by means of active semiconductor cladding layers, as well as for a variety of slow-light devices, such as, e.g., (ultra-compact) modulators [23].

9.2.1 Light Stopping in the Presence of Disorder and Plasmonic Losses

An important consideration in assessing the potential of metamaterial heterostructures for 'stopping' light pulses ($\upsilon_g = 0$) is the degree to which such a feat can be achieved in the presence of realistic (residual) losses and/or fabrication disorder. Already theoretical studies [8, 29, 33] have shown (see also Figs. 9.1 and 9.2) that very large light-decelerations can be achieved in metamaterial waveguides—even when dissipative (Ohmic) losses are present [34]. More recently, it has been ascertained [35] that complete 'stopping' of light inside negative-index metamaterial waveguides is also possible when decoherence mechanisms, such as dissipative losses, remain in the structure. This realisation stems from the fact that light pulses (i.e. not sinusoidal, single-frequency, waves) with a well-defined transverse envelope are, in the presence of losses, characterised by a *complex* frequency and a *real*wavenumber [34] (see also Fig. 9.3)—in contrast to sinusoidal waves, which are characterised by a complex wavevector when dissipative losses remain in the structure. This feature becomes even more prominent in the stopped-light regime, where (owing to the fact that light does not propagate any more) a consideration of spatial losses (complex wavenumber) lacks any appreciable physical meaning [22, 30], and one should instead consider temporal losses (complex frequency).

Our studies have revealed that a zero group velocity ($\mathrm{Re}\{\mathrm{d}\omega/\mathrm{d}\beta\} = 0$), i.e. complete adiabatic stopping of light pulses, can be achieved even when residual dissipa-

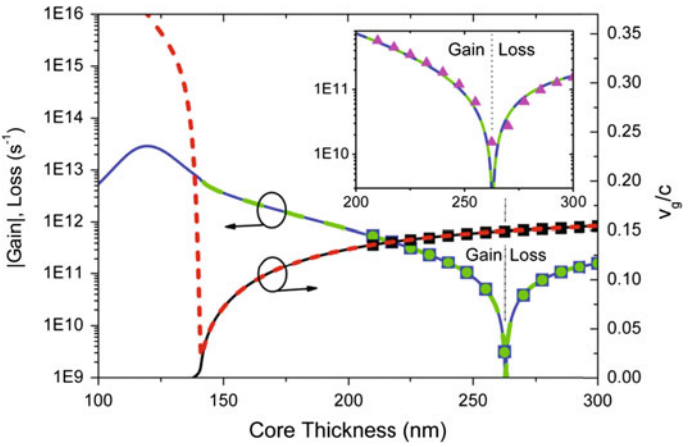

Fig. 9.3 Direct comparison between calculations based on finite-difference time-domain (FDTD, symbols) and the transfer-matrix method (TMM, lines) methods showing the dependence of the group velocity (υ_g) of the complex-ω solutions (*solid black*), the group velocity of the complex-k solutions (*red dashed line*), the imaginary part of the complex-ω solutions (*solid blue*) and the imaginary part of the complex-k solutions multiplied by υ_g (*green dashed*) on the thickness of the core waveguide [35]. The inset shows the rate of energy loss (or gain) for the whole wavepacket (*purple symbols*) with varying core thickness as calculated by the discrete Poynting's theorem within the FDTD method

tive losses (or gain) remain in the metamaterial waveguides. In Fig. 9.3 we examine how the spatial and temporal losses (or gain) experienced by, both, the central frequency of a pulse and the pulse as a whole (guided along the active slow-light metamaterial heterostructure of Fig. 9.4) vary with core thickness. The complex-ω solutions can be calculated with the finite-difference time-domain (FDTD) method by recording the spatial variation of the field amplitude along the central axis of the heterostructure at two different time points, and then dividing the spatial Fourier transforms of the two longitudinal spatial profiles. The rate of energy change for the whole wavepacket (total loss or gain) is calculated using the discrete Poynting's theorem integrated over a spatial region sufficiently wide to contain the pulse.

Figure 9.3 shows that for core thicknesses above 262 nm the central frequency of the pulse experiences loss. For smaller thicknesses, for which the amplitude of the field increases inside the gain region, we find that the gain supplied by the cladding strips overcompensates the loss induced by the core layer. At a core thickness of 262 nm the central frequency experiences neither gain nor loss, while the wavepacket as a whole experiences gain (inset in Fig. 9.3). In all cases we have verified that $\mathrm{Re}\{n_{eff}\} < 0$ (data not shown here). Overall, we find excellent agreement and consistency between five distinct sets of results: the spatial losses/gain (multiplied by the group velocity [22]) for the central frequency as calculated by the FDTD (green dots) and the transfer-matrix method (TMM) (green dashed line), the temporal losses/gain for the central frequency as calculated by the FDTD

(blue squares) and TMM (blue dashed line), and the temporal losses of the whole wavepacket as calculated by the FDTD method (triangular symbols in the inset of Fig. 9.3). This fact provides further evidence that loss-compensation is in principle possible in the slow-light NRI regime, including the light-stopping point at around 137 nm. Note that for core thicknesses smaller than around 140 nm the group velocity of the complex-k mode characteristically differs from that of the complex-ω mode (red dashed and black solid lines in Fig. 9.4). As with the case of SPPs in plasmonic films [34], the group velocity of the complex-k solutions exhibits a "back-bending", never becoming zero, while that associated with the complex-ω solutions may reduce to zero even in the presence of excessive gain (or losses).

Finally, it is to be noted that series of recent works [13, 14, 36] have conclusively shown that metamaterials can, when judiciously designed, be completely insensitive to even high degrees of fabrication disorder. This is simply because metamaterials owe their effective properties to an averaged electromagnetic response of their constituent meta-molecules, without necessarily requiring a 'perfect' lattice to achieve negative electromagnetic responses. Semiconductor-based metamaterial heterostructures are, also, expected to exhibit minimal sensitivity to fabrication disorder, since therein we do not make use of plasmonic meta-molecules, but planar semiconductor layers—one or more of which exhibit a negative electric permittivity below its plasma frequency. Current molecular beam epitaxy (MBE) facilities are indeed capable of growing high-quality semiconductor superlattices owing to mature, optimised growth-temperature, composition and doping-profile techniques.

9.2.2 From Loss-Compensation to Amplification by Cladding Gain

Recently it has been shown that metamaterial losses can be compensated on the materials level by gain [37]. Here we discuss how in a suitably designed metamaterial heterostructure, the losses that a slow-light pulse experiences can be completely removed macroscopically by using evanescent gain (stimulated emission). An example of such a structure is schematically illustrated in Fig. 9.4, where we note that two gain layers are placed adjacently to the negative-refractive-index core layer. Similar loss-compensation configurations have recently been shown to work remarkably well [37], to the point of even allowing for lasing [38] in hybrid plasmonic-dielectric configurations. It turns out that by properly adjusting the 'pump' laser intensity, the (negative) imaginary part of the refractive index of the gain medium can become equal (in magnitude) to the (positive) imaginary part of the effective refractive index of the metamaterial heterostructure, so that losses can be altogether eliminated.

Indeed, in Fig. 9.5 we are presenting numerical results (confirming the aforementioned conclusions) that were obtained using full-wave FDTD simulations and analytical TMM calculations of pulse propagation in the metamaterial waveguide structures of the type shown in Fig. 9.4. Four simulations were run, and in each sim-

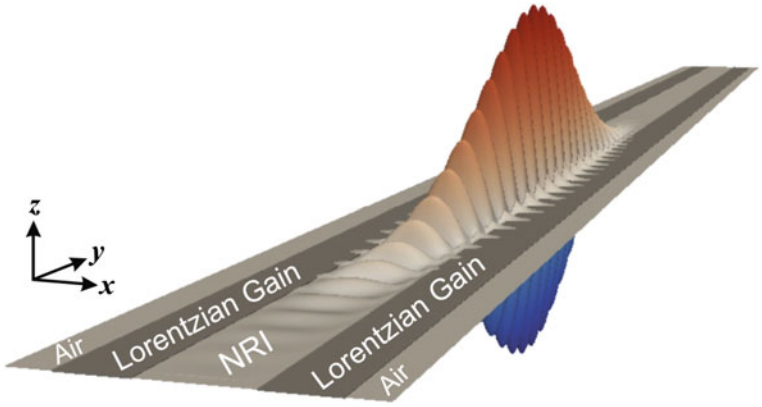

Fig. 9.4 Schematic illustration of the metamaterial-waveguide configuration for the (complete) compensation of the dissipative losses arising from the negative-index core layer

ulation an oscillatory mode pulse was injected into the waveguide. The simulations examined the effect on the pulse when: only gain is present (the metamaterial is modelled as being lossless); only losses are present (the gain material is removed); neither losses nor gain are present; and both gain and losses are present. A NRI material was used for the core layer, which had a width of $0.4\lambda_0$ (λ_0 being the free-space wavelength of the pulse's central frequency). The gain layers were positioned immediately adjacent to the core layer, and extended outwards into the cladding for a distance of $0.25\lambda_0$. The rest of the cladding (see Fig. 9.4) was assumed to be a non-dispersive material with a refractive index of 1 (air).

For simplicity, both the permittivity and permeability response of the NRI material are simulated using the same Drude model. Thus, the refractive index of the NRI material is given by: $n_D(\omega) = 1 - \omega_p^2/(\omega^2 + i\omega\Gamma_D)$, where $\omega_p = 2\pi \times 893.8 \times 10^{12}$ rad/s is the plasma frequency and $\Gamma_D = 0.27 \times 10^{12}\,\mathrm{s}^{-1}$ is the collision frequency. The frequency response of the permittivity of the gain layer obeys a Lorentzian dispersion: $\varepsilon(\omega) = \varepsilon_\infty + \Delta\varepsilon\omega_L^2/(\omega_L^2 - i2\delta\omega - \omega^2)$, with $\varepsilon_\infty = 1.001$, $\Delta\varepsilon = -0.0053$, $\omega_L = 2\pi \times 370 \times 10^{12}$ rad/s, and $\Gamma_L = 10^{14}\,\mathrm{s}^{-1}$, resulting in a line-shape that is similar to that produced by, e.g., an electronic transition in a quantum dot.

The effective refractive index of the waveguide is extracted from the simulation by recording over time the H_z-field amplitude of the pulse at two points along the waveguide's central axis. Using the Fourier transforms of these results, the change in phase and amplitude undergone by each frequency between the two points can be calculated, from where the real and imaginary parts of the effective refractive index can then be obtained. Exemplary plots of the so-extracted imaginary part of the effective index (related to the absorption coefficient $\alpha = 2\omega\mathrm{Im}\{n_{eff}\}/c$) of the guided light pulses are shown in Fig. 9.5. We note that when gain layers are placed adjacently to the negative-index core layer, the loss experienced by the guided light pulse is (at a frequency around 400 THz) completely removed (green squares in

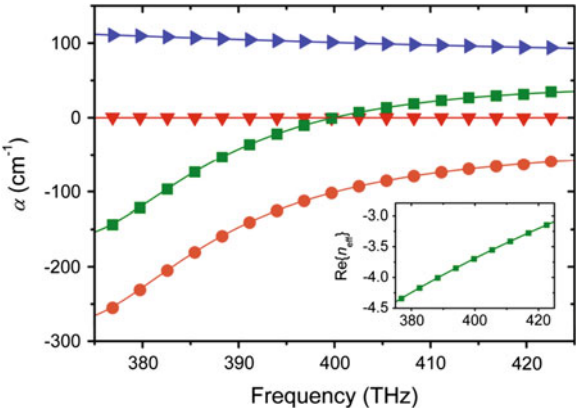

Fig. 9.5 Comparison between FDTD (symbols) and TMM (lines) calculations of the absorption coefficient α (spatial losses) versus frequency for the TM_2^b mode in the cases where the NRI core layer is: lossless (*red vertical triangles*); lossy (*blue horizontal triangles*); lossy and gain cladding layers are used (*green squares*); lossless and gain cladding layers are used (*orange circles*) [35]. The inset depicts the frequency dispersion of Re$\{n_{eff}\}$in all four cases

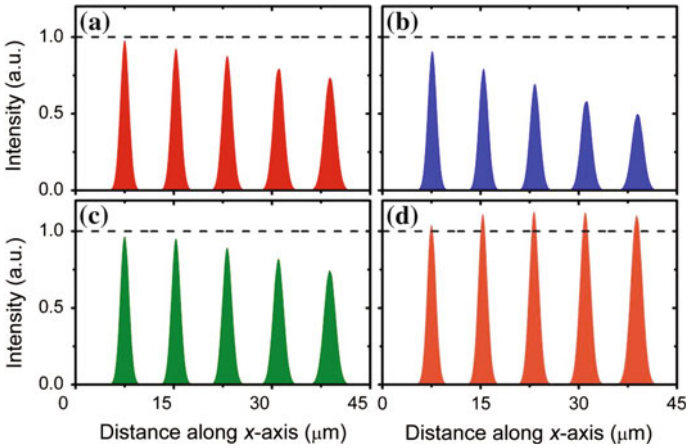

Fig. 9.6 Snapshots of slow-light pulse propagation along the central axis of the considered waveguides for the cases where use is made of: **a** neither loss nor gain **b** loss but no gain **c** both, loss and gain and **d** gain but no loss [28]. In all cases propagation is from *left* to *right*

Fig. 9.5). For lower frequencies, this slow-light, negative-phase-velocity pulse is amplified while propagating inside the negative-index waveguide. Further evidence for the removal of losses is shown in Fig. 9.6, from where it can be directly seen that the incorporation of gain layers completely restores the amplitude of the slow-light negative-phase-velocity pulse.

9.3 Spatial Solitons in Controlled Metamaterials

Spatial solitons are stable if they are solutions of what is known as the one-dimensional cubic nonlinear Schrödinger equation. Even though a beam of electromagnetic energy in a bulk medium has two transverse-dimensional degrees of freedom, perpendicular to its propagation direction, it can, in principle, balance diffraction with nonlinearity, but the balance is azimuthally unstable. It was shown, some time ago [39], that placing an electromagnetic beam in a planar waveguide produces stability in an elegant fashion and this is the basic model adopted here. Within a planar waveguide, a stable soliton can be created by permitting the beam to diffract in the plane of the guide so the role of any diffraction-management that is present, naturally, or artificially, will be important. In fact, for positive phase materials, diffraction-management has been investigated [40], already, for spatial solitons [39], especially through the utilization of waveguide arrays.

Spatial solitons will be discussed in detail, here, using the basic nonlinear cubic Schrödinger equation. The latter is usually an adequate, initial, model for the behaviour of such electromagnetic beams but it is often the case that important additions to this core equation have to be included. One well-known example is the appearance of non-paraxial terms, when the slowly varying amplitude approximation is, partially, relaxed. In this chapter, it will be shown that nonlinearly-induced diffraction is a vital addition [41, 42] to the nonlinear Schrödinger equation. It is a phenomenon that is not often discussed but it interesting that it can dominate over non-paraxiality and plays a really vital role as the beams become very narrow, preventing beam collapse at high powers. Even though the core nonlinear Schrödinger equation is modified to take into account other effects the solutions will still be referred to as 'solitons', as is common practice.

The study of solitons in a nonlinear negative metamaterial results in an elegant formulation of a generalised nonlinear Schrödinger equation in which it is emphasised that a lot of new possibilities can be anticipated. The metamaterial properties, therefore, appear now as an influence upon the nonlinearly-induced diffraction.

The fundamental derivation of the nonlinear Schrödinger equation, now to be presented, includes diffraction-management [43] and nonlinear diffraction. It will not include loss, however, because, as recent literature shows, it is possible to diminish the loss [44, 45] to a very *small quantitative* impact, whilst retaining all the qualitative double negative behaviour that is such an attractive feature of negative phase metamaterials.

9.3.1 The Schrödinger Equation Description of Propagating Beams

A spatial soliton that is established in a dielectric planar guide is stable because diffraction along the y-axis is frozen, and replaced by guiding. Figure 9.7 shows a

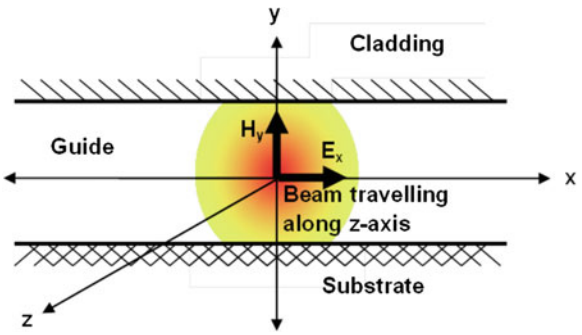

Fig. 9.7 Sketch of a TE-polarised electromagnetic beam trapped in a planar dielectric waveguide of infinite extent in the x-direction and in the absence of any magnetooptic influence. This is an illustration of a $(1+1)$ spatial soliton with diffraction in the x-direction and propagation in the z-direction. In this example the beam carries the electromagnetic field components (E_x, H_y)

typical example of stable electromagnetic beam in a planar waveguide, suffering diffraction only in the x-direction.

If **E** is the electric field vector of an electromagnetic beam travelling through a polarisable, normal, dielectric medium, like glass, for example, then, from Maxwell's equations,

$$\nabla^2\mathbf{E} - \nabla\left(\nabla\cdot\mathbf{E}\right) = \mu_0\frac{\partial^2\mathbf{D}}{\partial t^2} + \mu_0\frac{\partial^2\mathbf{P}^{NL}}{\partial t^2} \tag{9.1}$$

where **D** is the *linear* displacement vector, $\mathbf{P}^{NL}$ is the *nonlinear* electric polarisation of the dielectric, μ_0 is the permeability of free-space and the medium is assumed to be ***non-magnetic***. The standard assumption in the literature is to set $div\left(\mathbf{E}\right) = 0$, but this action will not be taken here because it will eliminate any nonlinear diffraction. As will be seen later on, eliminating such diffraction removes a very important metamaterial influence, whenever the latter material is deployed to diminish any linear diffraction.

In order to establish the basic principle of nonlinear diffraction, in a non-metamaterial dielectric, consider, the TE-polarised beam shown in Fig. 9.7 that has only an electric field component E_x, so there is no electric field component along the z-axis. Such beams can be monochromatic with an angular frequency $\omega = \omega_0$, defined through the transformations $\mathbf{E} \Rightarrow 1/2\{\mathbf{E}\left(\mathbf{r},\omega_0\right)e^{-i\omega_0 t} + c.c.\}$, $\mathbf{P}^{NL} \Rightarrow 1/2\{\mathbf{P}^{NL}\left(r,\omega_0\right)e^{-i\omega_0 t} + c.c.\}$, $\mathbf{D} \Rightarrow 1/2\{\mathbf{D}\left(\mathbf{r},\omega_0\right)e^{-i\omega_0 t} + c.c.\}$, where c.c. means the complex conjugate and **r** is the vector (x, y, z). The propagation of the beam is along the z-axis, and a weakly nonlinear guide, exhibiting the classic Kerr nonlinearity, is being used for which the modal field of the waveguide is both linear and stationary. It will determine an effective guide-width. This sort of nonlinearity is a safe assumption for the vast majority of optically nonlinear materials. Equation (9.1) has an x-component equal to

$$\frac{\partial^2 E_x}{\partial z^2} - \frac{\varepsilon(\omega_0)}{c^2} E_x = -\omega_0^2 \mu_0 P_x^{NL} - \frac{\partial^2 E_x}{\partial x^2} - \frac{1}{\varepsilon_0 \varepsilon(\omega_0)} \frac{\partial^2 P_x^{NL}}{\partial x^2} - \frac{1}{\varepsilon_0 \varepsilon(\omega_0)} \frac{\partial^2 P_z^{NL}}{\partial x \partial z} \tag{9.2}$$

In which $\varepsilon(\omega_0)$ is the dielectric, frequency-dependent, permittivity of the planar dielectric waveguide, ε_0 is the permittivity of free-space, c is the velocity of light in free-space and the magnetic permeability is $\mu(\omega_0) = 1$. Now, a conventional slowly-varying approximation can be introduced in the following way. All the variables in (9.2) can be defined as having a slow variation associated with propagation down the z-axis, a transverse x-dependence to take account of the diffraction, and a fast variation associated with the plane wave e^{ikz}, where k is a wave number, i.e. the variables can be transformed as follows $\left(E_x, P_x^{NL}, P_z^{NL}\right) \Rightarrow (E_x(x, z, \omega_0), P_x^{NL}(x, z, \omega_0), P_z^{NL}(x, z, \omega_0))e^{ikz}$, where the explicit dependence upon the x and z coordinates, and the frequency are shown here, for clarity, but will not be explicitly shown in the development below. Since the longitudinal field component E_z is an order of magnitude smaller than the transverse component E_x, only P_x^{NL} needs to be used, so in this 'scalar model' the x-component of the nonlinear polarisation has, for a Kerr medium, the standard form

$$P_x^{NL} = \frac{3}{4} \chi^{(3)} \varepsilon_0 |E_x|^2 E_x \tag{9.3}$$

where $\chi^{(3)}$ is the third-order nonlinear coefficient. Hence, the 'modified' nonlinear Schrödinger equation, in which the final term models nonlinear diffraction, is [46]

$$2ik\frac{\partial E_x}{\partial z} + \frac{\partial^2 E_x}{\partial x^2} + \frac{3\omega^2 \chi^{(3)}}{4c^2} |E_x|^2 E_x + \frac{\partial^2 E_x}{\partial z^2} + \frac{3\chi^{(3)}}{4\varepsilon(\omega_0)} \frac{\partial^2}{\partial x^2} \left(|E_x|^2 E_x\right) = 0 \tag{9.4}$$

In arriving at (9.4), the possibility of quintic nonlinearity has not been included, that only the role of the third-order nonlinear diffraction has been identified. This action is taken to demonstrate the form and appearance of the nonlinear diffraction term. Its effectiveness in competition with quintic nonlinearity, non-paraxiality and higher-order diffraction is such that it is a very competitive and dominant term when narrow beams are being propagated. Naturally, this dominance of such a third-order term can be quantitatively modified by the inclusion of quintic nonlinearity and higher-order diffraction in a straightforward way but this chapter will focus upon a choice of materials for which nonlinear diffraction can interact dramatically with a metamaterial environment.

What can be said at this stage is that if only the nonlinear diffraction appears in the modified nonlinear Schrödinger equation then its influence upon the control and formation of narrow beams will be strong, and this point will be checked in the simulations given below. For low power beams, the nonlinear diffraction is not going to compete with the main diffraction term. As the beams become narrower, the effect

of the $\frac{\partial^2}{\partial x^2}$ operator becomes stronger, and if the power in the beam becomes greater, then it should be expected that the nonlinear diffraction will begin to have an impact.

Up to now the discussion has centred upon electric nonlinearity, but metamaterials may also display a magnetic nonlinearity. This type of nonlinearity will cause div $(\mathbf{H}) \neq 0$, where $\mathbf{H}$ is the magnetic field carried by the propagating electromagnetic field. This creates a nonlinear diffraction contribution determined now by the nonlinear magnetic properties.

For an isotropic, double negative, metamaterial capable of sustaining both nonlinear electric and magnetic polarizations, the constitutive relations of the metamaterial are

$$\mathbf{D}(\mathbf{r}, \omega) = \varepsilon_0 \varepsilon(\omega) \mathbf{E}(\mathbf{r}, \omega) + \mathbf{P}_{NL}(\mathbf{r}, \omega) \tag{9.5}$$

$$\mathbf{B}(\mathbf{r}, \omega) = \mu_0 \mu(\omega) \mathbf{H}(\mathbf{r}, \omega) + \mu_0 \mathbf{M}_{NL}(\mathbf{r}, \omega) \tag{9.6}$$

where ω is an angular frequency, $\mu(\omega)$ and $\varepsilon(\omega)$ are, respectively, the frequency-dependent permeability and permittivity of the metamaterial, and the Fourier transforms $\mathbf{D}, \mathbf{B}, \mathbf{E}, \mathbf{H}, \mathbf{P}_{NL}, \mathbf{M}_{NL}$ are of the displacement vector, the magnetic flux density vector, the electric field, the magnetic field, the dielectric nonlinear polarization and the nonlinear magnetization. Any possible bianisotropy, anisotropy, or spatial dispersion, is neglected. All the nonlinearity is accounted for in the polarisations that are defined.

For spatial solitons, a monochromatic beam, with a frequency ω_0, can be launched into the kind of planar guide sketched in Fig. 9.7. Maxwell's equations then yield the following fundamental equations governing its behaviour

$$\nabla^2 \mathbf{E} - \nabla(\nabla \cdot \mathbf{E}) + k_0^2(\omega_0)\mathbf{E} + \frac{\omega_0^2}{c^2}\mu(\omega_0)\frac{\mathbf{P}_{NL}}{\varepsilon_0} + i\omega_0\mu_0\nabla \times \mathbf{M}_{NL} = 0 \tag{9.7}$$

$$\nabla^2 \mathbf{H} - \nabla(\nabla \cdot \mathbf{H}) + k_0^2(\omega_0)\mathbf{H} + \frac{\omega_0^2}{c^2}\varepsilon(\omega_0)\mathbf{M}_{NL} - i\omega_0\nabla \times \mathbf{P}_{NL} = 0 \tag{9.8}$$

where $k_0^2(\omega_0) = \frac{\omega_0^2}{c^2}\varepsilon(\omega_0)\mu(\omega_0)$.

Equations (9.7) and (9.8) appear to be coupled and, indeed, it has been asserted in the literature that they are, being a dramatic aspect arising from using a metamaterial. The short answer is that asserting that these equations are coupled is an incorrect conclusion. The point will now be addressed but, because the the nonlinear diffraction involves either $\nabla \cdot \mathbf{E}$, or $\nabla \cdot \mathbf{H}$, and neither term contributes to any coupling, of this kind, they will be dropped from the argument for the time being.

The notation can be simplified by adopting the definitions $k \equiv k_0(\omega_0), \varepsilon \equiv \varepsilon(\omega_0)$, $\mu \equiv \mu(\omega_0)$. Also, the development can be made more specific, at this stage, by considering a TE-polarized beam which is defined by the field vectors $\mathbf{E} = \hat{\mathbf{x}}E_x$ and $\mathbf{H} = \hat{\mathbf{y}}H_y$, where $\hat{\mathbf{x}}$ and $\hat{\mathbf{y}}$ are unit vectors. If the nonlinear polarizations are generated by Kerr-like responses of the metamaterial, either from the meta-atoms themselves, or the background medium suitably prepared with nonlinear inclusions,

then $P_{NL} = \varepsilon_0 \varepsilon_{NL}^{(3)} |E_x|^2 E_x$ and $M_{NL} = \mu_{NL}^{(3)} |H_y|^2 H_y$ where $\varepsilon_{NL}^{(3)}$ and $\mu_{NL}^{(3)}$ are, respectively, the electric and magnetic cubic nonlinearity coefficients. A Kerr assumption is not a serious restriction because a saturable medium can easily be modelled by adding quintic terms to enhance the $|E_x|^2$ and $|H_y|^2$ assumptions, or by using suitably descriptive functions.

The transverse Laplacian $\nabla_\perp^2 = \frac{\partial^2}{\partial x^2} + \frac{\partial^2}{\partial y^2}$, could now be simply introduced, in order to create more generality, but, more importantly, the fast spatial variation can be extracted, in the manner outlined earlier, by setting $E_x \Rightarrow E_x(x, z)e^{ikz}$, $H_y \Rightarrow H_y(x, z)e^{ikz}$, where k is a wave number. In this procedure, E_x and H_y are replaced by the slowly varying functions $E_x(x, z)$ and $H_y(x, z)$. The x-component of (9.7), after adopting a well-known vector identity, is

$$2ik\frac{\partial E_x}{\partial z} + \nabla_\perp^2 E_x + \frac{\omega_0^2}{c^2}\mu\varepsilon_{NL}^{(3)} |E_x|^2 E_x + i\omega_0\mu_0\mu_{NL}^{(3)}\left[|H_y|^2 \left(\nabla \times H_y\hat{\mathbf{y}}\right)\right]\cdot\hat{\mathbf{x}} + i\omega_0\mu_0\mu_{NL}^{(3)}\left[\nabla |H_y|^2 \times \left(H_y\hat{\mathbf{y}}\right)\right]\cdot\hat{\mathbf{x}} = 0 \tag{9.9}$$

Since the envelopes are slowly varying only the nonlinear term involving $\nabla \times (H_y\hat{\mathbf{y}}) = -i\omega\varepsilon_0\varepsilon(\omega_0)E_x\hat{\mathbf{x}}$ needs to be retained. It is interesting that the nonlinear Schrödinger equation also emerges from a multiple-scale analysis that retains all the third-order terms. These third-order terms are presented here. Other terms are of higher than third-order. The equations for the TE mode components of **E** and **H** are, therefore

$$2ik\frac{\partial E_x}{\partial z} + \nabla_\perp^2 E_x + \frac{\omega_0^2}{c^2}\left[\mu\varepsilon_{NL}^{(3)} |E_x|^2 + \varepsilon\mu_{NL}^{(3)} |H_y|^2\right] E_x = 0 \tag{9.10}$$

$$2ik\frac{\partial H_y}{\partial z} + \nabla_\perp^2 H_y + \frac{\omega_0^2}{c^2}\left[\mu\varepsilon_{NL}^{(3)} |E_x|^2 + \varepsilon\mu_{NL}^{(3)} |H_y|^2\right] H_y = 0 \tag{9.11}$$

The nonlinear coefficients $\varepsilon_{NL}^{(3)}$ and $\mu_{NL}^{(3)}$ can be positive, or negative, and a sign has not been attached to the wave number k.

As indicated earlier, whenever a multiple-scale method is used, each of the terms in (9.10) and (9.11) can be associated with a given order and all the higher-order corrections have been omitted. The $|H_y|^2$ term in (9.11), for example, is *not* of a single order. If $|H_y|^2$ is retained *explicitly* in (9.10) and $|E_x|^2$ *explicitly* in (9.11), and an assertion is made that the equations are coupled, it would be effectively including corrections from an order that has already been neglected. In other words, to assert that coupling of this kind takes place because we are dealing with a metamaterial is incorrect. In fact, the following simple relationship for a plane wave should be deployed

$$|H_y|^2 = \frac{\varepsilon_0 |\varepsilon|}{\mu_0 |\mu|} |E_x|^2 \tag{9.12}$$

Even if the modal fields of the guides, like the one displayed in Fig. 9.7, are explicitly included this will only result in a modification of the effective width of the guide and will still leave the reducibility implied by (9.12) in place. This point has been also recently acknowledged in a different discussion about slow temporal solitons, but without making contact with the original assertion of irreducibility. To the correct order, then, the basic equations for the slowly-varying electric and magnetic field components under discussion are, after restoring the non-paraxial terms and returning back to diffraction only along the x-axis,

$$2ik\frac{\partial E_x}{\partial z}+\frac{\partial^2 E_x}{\partial z^2}+\frac{\partial^2 E_x}{\partial x^2}+\frac{\omega_0^2}{c^2}\left[\mu\varepsilon_{NL}^{(3)}+\varepsilon\mu_{NL}^{(3)}\frac{\varepsilon_0\,|\varepsilon|}{\mu_0\,|\mu|}\right]|E_x|^2\,E_x=0 \quad (9.13)$$

$$2ik\frac{\partial H_y}{\partial z}+\frac{\partial^2 H_y}{\partial z^2}+\frac{\partial^2 H_y}{\partial x^2}+\frac{\omega_0^2}{c^2}\left[\mu\varepsilon_{NL}^{(3)}\frac{\mu_0\,|\mu|}{\varepsilon_0\,|\varepsilon|}+\varepsilon\mu_{NL}^{(3)}\right]|H_y|^2\,H_y=0 \quad (9.14)$$

These equations, include non-paraxiality, but are *not coupled* and can be used to model beam formation in a metamaterial. They can be readily generalized to arbitrary nonlinearities by introducing functions $f_1\left(|E_x|^2\right)$ and $f_2\left(|H_y|^2\right)$ to include the saturations associated with the dielectric and magnetic behaviour respectively. In their un-normalised form, (9.13) and (9.14) show that the nonlinear coefficients depend upon the choice of operating frequency and could change quite rapidly if a monochromatic beam is launched close to a resonance in the permittivity, or permeability. Equations (9.13) and (9.14) can now be modified by including higher-order diffraction and nonlinear diffraction and non-paraxiality. As shown in previous publications, however, nonlinear diffraction dominates over non-paraxiality, longitudinal field component (vector) effects and also over quintic nonlinearity. In the examples to be given below, therefore, the quintic nonlinear contributions to the electric or magnetic nonlinearity will be taken as negligible. The final form of the nonlinear Schrödinger equations to be used in the numerical simulations will always assume that narrow beam formation requires the dominance of nonlinear diffraction over non-paraxial terms, so the latter will be omitted from now on. Higher-order *linear* diffraction is retained at this stage, however, because diffraction-management is to be discussed later and it remains to be seen whether a managed reduction of the main linear diffraction, for example, will bring the higher-order diffraction into play, or not. The magnetooptic influence that will be used later on to control beam behaviour will exploit the Voigt effect and, as will be shown, it requires the use of an asymmetric waveguide structure *only* and TM modes. The specific nature of the term to be added to the nonlinear Schrödinger equation to account for the Voigt effect will be addressed in the next section but, at this point, the next set of equations recognises that the nonlinear diffraction of the TE-polarised beam equation depends upon the condition $\nabla\cdot\mathbf{E}\neq 0$ and that the TM-polarised beam equation depends upon the condition $\nabla\cdot\mathbf{H}\neq 0$. Hence, before the addition of the term that creates the magnetooptic Voigt influence, the final form of the modified nonlinear Schrödinger equation needed for TE-polarised beam simulations is

TE-polarised beams

$$i\frac{\partial E_x}{\partial z}+\frac{1}{2k}\frac{\partial^2 E_x}{\partial x^2}-\frac{1}{8k^3}\frac{\partial^4 E_x}{\partial x^4}+\frac{1}{2k}\frac{\omega_0^2}{c^2}\left[\mu\varepsilon_{NL}^{(3)}+\varepsilon\mu_{NL}^{(3)}\frac{\varepsilon_0|\varepsilon|}{\mu_0|\mu|}\right]|E_x|^2E_x$$
$$+\frac{1}{2\varepsilon k}\varepsilon_{NL}^{(3)}\frac{\partial^2}{\partial x^2}\left(|E_x|^2E_x\right)=0 \tag{9.15}$$

in which it can be seen that *only* the dielectric nonlinear polarisation can produce the nonlinear diffraction. Note, that for a double-negative metamaterial $\mu=-|\mu|$ and $\varepsilon=-|\varepsilon|$. For this type of metamaterial, backward waves would exist for which $k=-|k|$ and bright spatial solitons would only be possible for $N_{TE}=\left(|\mu|\,\varepsilon_{NL}^{(3)}+|\varepsilon|\,\mu_{NL}^{(3)}\frac{\varepsilon_0|\varepsilon|}{\mu_0|\mu|}\right)<0$. It is interesting, now, that a sufficient condition to make $N<0$ is to make $\varepsilon_{NL}^{(3)}<0$ and $\mu_{NL}^{(3)}<0$ but this is not a necessary condition and it is possible to have either $\varepsilon_{NL}^{(3)}>0$ or $\mu_{NL}^{(3)}>0$ depending on their magnitude, but not simultaneously. As a consequence, the coefficient in front of the nonlinear diffraction term can, in principle, be positive or negative.

For TM-polarised beams the final form of the nonlinear Schrödinger equation, in the absence of any magnetooptical effects, is

TM-polarised beams

$$i\frac{\partial H_x}{\partial z}+\frac{1}{2k}\frac{\partial^2 H_x}{\partial x^2}-\frac{1}{8k^3}\frac{\partial^4 H_x}{\partial x^4}+\frac{1}{2k}\frac{\omega_0^2}{c^2}\left[\varepsilon\mu_{NL}^{(3)}+\mu\varepsilon_{NL}^{(3)}\frac{\mu_0|\mu|}{\varepsilon_0|\varepsilon|}\right]|H_x|^2H_x$$
$$+\frac{1}{2\mu k}\mu_{NL}^{(3)}\frac{\partial^2}{\partial x^2}\left(|H_x|^2H_x\right)=0 \tag{9.16}$$

in which it can be seen that *only* the magnetic polarisation can produce the nonlinear diffraction and that the vector $\mathbf{H}=(H_x,\,0\,,\,0)$ has been adopted to characterise the TM beam. The same arguments concerning the signs of k, $\varepsilon_{NL}^{(3)}$ and $\mu_{NL}^{(3)}$ also apply to this equation, but in this case $N_{TM}=\left(|\varepsilon|\,\mu_{NL}^{(3)}+|\mu|\,\varepsilon_{NL}^{(3)}\frac{\mu_0|\mu|}{\varepsilon_0|\varepsilon|}\right)<0$.

Equations (9.15) and (9.16) model the propagation of bright spatial solitons in a double-negative metamaterial. For each polarisation, the fast spatial variation is a backward plane phase wave, with wave number $k=-|k|$. The energy flow is manifested as beam propagation, in the positive z direction, and the beam coordinates can be scaled by the transformations $z=|k|\,w^2Z$ and $x=wX$, in which w is the effective width of the beam. If no diffraction-management is anticipated at this stage, through which the lowest-order, *linear*, diffraction can be reduced, the higher-order diffraction term can be neglected. It will be reintroduced later. Proceeding on this basis, both the nonlinear Schrödinger equations, produced above, assume the same generic form

$$i\frac{\partial\psi}{\partial Z}-\frac{1}{2}\frac{\partial^2\psi}{\partial X^2}-|\psi|^2\psi-\kappa\frac{\partial^2}{\partial X^2}\left(|\psi|^2\psi\right)=0 \tag{9.17}$$

This is the complex conjugate of the standard modified nonlinear Schrödinger equation. Observing the roles played by the electric nonlinearity and the magnetic nonlinearity in bringing nonlinear diffraction into play for TE and TM polarised beams, respectively, it has been assumed that the nonlinear coefficient in the TE-polarised case is $\varepsilon_{NL}^{(3)} = -\left|\varepsilon_{NL}^{(3)}\right|$ and that $\mu_{NL}^{(3)}$ is negligible, whilst in the TM-polarised case, it has been assumed that the nonlinear coefficient is $\mu_{NL}^{(3)} = -\left|\mu_{NL}^{(3)}\right|$, with, $\varepsilon_{NL}^{(3)}$ set as negligible. The reasons, emphasised again, for these choices are because for TE beams the nonlinear diffraction is controlled by $\varepsilon_{NL}^{(3)}$ and for TM beams, it is controlled by $\mu_{NL}^{(3)}$. For both polarisations, $\kappa = \frac{1}{k^2 w^2}$, which for a particular metamaterial that can be varied by changing the operating frequency of the beams and/or the beam width. ψ has been normalised to the following:

$$\mathbf{TE}: \psi = \left(\sqrt{\frac{w^2\omega_0^2}{2c^2}\,|\mu|\left|\varepsilon_{NL}^{(3)}\right|}\right) E_x, \quad \mathbf{TM}: \psi = \left(\sqrt{\frac{w^2\omega_0^2}{2c^2}\,|\varepsilon|\left|\mu_{NL}^{(3)}\right|}\right) H_x. \tag{9.18}$$

Equation (9.17) can be used to show how the frequency bands offered up by a particular metamaterial can control the behavior of narrow beams and it can also be readily incorporated into a discussion of a special kind of diffraction-management to be defined below.

Given that applications for metamaterials will be very important within the visible optical range, and the existence of the highly developed downstream magnetooptics sector of the world of magnetism, a combination of homogeneous negative phase metamaterial and a magnetooptical material will be assessed here. This can be achieved using the magnetooptic Voigt configuration, as opposed to the Faraday effect, through the use of the kind of asymmetric waveguide structure shown in Fig. 9.8. For a symmetric structure, the Voigt configuration has no influence upon the guided waves and, even for an asymmetric guide, it is only the TM modes that are affected by the applied magnetic field. Spatial solitons must be TM-polarised, therefore, to engage in any magnetooptic control and for narrow beams it will be the nonlinear magnetic polarisation that determines the nonlinear diffraction.

9.3.2 Introduction of a Magnetooptic Environment

The magnetooptical influence manifests itself as a perturbation to the nonlinear Schrödinger equation is defined here as$v(x)\,H_x$, which is a term that can be simply added to the envelope equation. In order to justify this, first of all, consider the magnetooptic tensor describing the substrate, which has the form

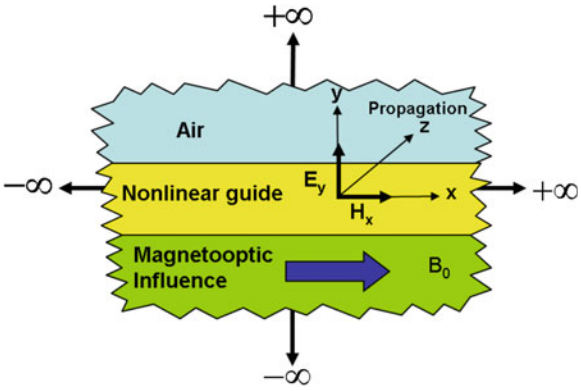

Fig. 9.8 An asymmetric planar waveguide structure with a magnetooptic substrate. Wave propagation is across the externally applied magnetic flux density $\mathbf{B}_0$, producing the Voigt effect

$$\varepsilon_{\mathbf{m}} = \begin{pmatrix} (n_m^2) & 0 & 0 \\ 0 & (n_m^2) & (-iQn_m^2) \\ 0 & (iQn_m^2) & (n_m^2) \end{pmatrix} = \begin{pmatrix} \varepsilon & 0 & 0 \\ 0 & \varepsilon & \varepsilon_{yz} \\ 0 & -\varepsilon_{yz} & \varepsilon \end{pmatrix} \tag{9.19}$$

where n_m is the refractive index of the substrate, and typically Q could be as small as $O(10^{-4})$. All of the diagonal elements are set equal to each other. This is not exactly true, but it is a common practical assumption, based upon the actual values of the physical parameters. In the bulk, the Voigt effect is of $O(Q^2)$ and is negligible [46], but it is an interesting possibility that a deliberately created asymmetric guide permits access to an O(Q) Voigt effect provided that TM-polarised spatial solitons are used. For polarised beams, using the tensor shown in (9.19), the magnetooptic perturbations to the Schrödinger equation are

$$\textbf{TE-polarisation} : i\frac{\partial E_x}{\partial z} = 0, \quad \textbf{TM-polarisation} : i\frac{\partial H_x}{\partial z} = -\frac{\omega}{c} n_m^2 Q H_x \tag{9.20}$$

where Q is now an *average* along the y-axis over the whole waveguide structure. It is very clear that such an integration along y would be zero if the structure in Fig. 9.8 was symmetric, with *both* the substrate and cladding being magnetooptic. This makes the point, very nicely, about now being able to access the Voigt effect to O(Q), as opposed to it being only accessible to $O(Q^2)$ in the bulk.

The right-hand side of the TM-polarised part of (9.20) can now be added to the general Schrödinger equation in order to account for any magnetooptic control. Using the transformations given above that put the nonlinear Schrödinger equation into dimensionless form means that the appropriate form of (9.20), for a TM-polarised beam is

$$i\frac{\partial \psi}{\partial Z} = -\frac{\omega_0}{c} |k| \, w^2 n_m^2 Q \psi = -v\psi \tag{9.21}$$

In which the dimensionless Z, introduced earlier, in terms of the beam width, is used. An important point to note here, however, is that if Q is a constant, it will do nothing but add an additional phase shift to the solitary wave solution of (9.17). This can be appreciated by redefining ψ to be ψe^{ivz} and then noticing that the derivative with respect to Z immediately eliminates the magnetooptic term from the Schrödinger equation. It is necessary, therefore, to make the magnetooptic parameter some function of the transverse coordinate, x, of the nonlinear guiding structure. Using the dimensionless coordinate X, where $\mathrm{x} = w\mathrm{X}$, and $= w$ is the beam width, an example, is to set the magnetooptic parameter to be the function $v(X) = v_{\max} sech\left(\frac{X}{X_0}\right)$, where it is anticipated that the magnetooptic parameter defined in (9.21) is the kind of function of X that has a maximum value $v_{\max}$, and then spreads over the X-axis under the control of a dimensionless half-width, X_0. The maximum value, $v_{\max}$, is associated with the saturation of the magnetization. In fact, it is necessary to adopt a spatial form that causes the magnetization to decline away, in both directions, from $X = 0$.

If the spatial soliton is imagined to be like a particle in a well, then the X-dependent magnetooptic term is in a position to influence the bright spatial soliton by creating deeper wells, or spatial barriers depending upon the direction the applied magnetic field assumes along the X-axis. A full scale, non-reciprocal effect should be expected with one sign of the applied magnetic field permitting bright spatial soliton formation, whilst the other sign can be expected to destroy any soliton creation.

9.3.3 Controlling the Beam Diffraction

Managing the dispersion, or diffraction, of electromagnetic waves in waveguide structures is a valuable tool in any downstream application. Indeed, dispersion-management is now a very important technique in optical fibre communications systems, and diffraction-management is an important feature of waveguide arrays [47]. A negative phase metamaterial [NPM] can be used to compensate any phase accumulation in normal positive phase medium [PPM], such as glass, for example. For beams this form of diffraction-management has been investigated for ring-cavities, for which it has been deployed in a manner that encourages impedance-matching [43, 48] in order to avoid unwanted reflections. It will also be assumed, here, for the simulations to be described later on, that the periodic system illustrated in Fig. 9.9, is also impedance-matched. From a practical device point of view this should be too difficult to achieve, especially when graded-indices are used. The positive phase accumulated in the PPM slabs could be compensated, completely, or partially, by negative phase accumulation in the NPM slabs. Given this type of propagation, the unit cell, of length L, shown in Fig. 9.9, can be used to develop an averaging process that will then lead to the final form of a dimensionless generic form the slowly-varying envelope equation, applicable to both TE and TM polarised beams and will model spatial solitons propagating under the linear diffraction-management environ-

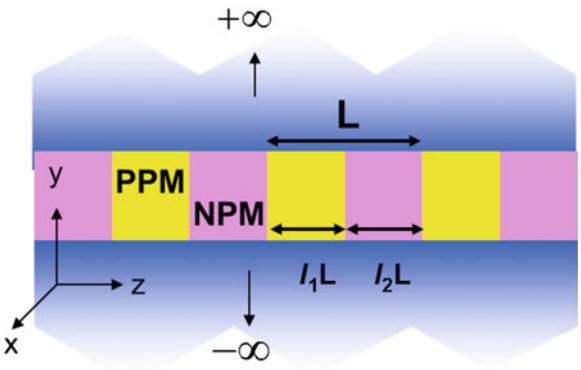

Fig. 9.9 A planar periodic waveguide structure constructed from alternating layers of positive phase media (PPM) and negative phase media (NPM). Propagation of the guided waves is along z and diffraction takes place along the X-axis

ments given below. If the first-order *linear* diffraction is to be reduced by this kind of management then, in principle, higher-order diffraction could take over so this possibility also needs to be quickly identified.

The unit cell, shown in Fig. 9.9, is divided up into the lengths, l_1L and l_2L, where l_1 and l_2 are simply fractions of L, i.e. $0 \leq l_{1,2} \leq 1$, containing a PPM and an NPM material, respectively. For a TE-polarised beam the forms of the nonlinear Schrödinger equations, in each part of the unit cell, are

PPM:

$$2i\frac{\partial E_x}{\partial z} + \frac{1}{k_1}\frac{\partial^2 E_x}{\partial x^2} + \frac{\omega^2}{c^2 k_1}\varepsilon^{(3)}_{NL1}\left|E_x\right|^2 E_x - \frac{1}{4k_1^3}\frac{\partial^4 E_x}{\partial x^4} + \frac{\varepsilon^{(3)}_{NL1}}{\varepsilon_1 k_1}\frac{\partial^2}{\partial x^2}\left(\left|E_x\right|^2 E_x\right) = 0 \tag{9.22}$$

NPM:

$$2i\frac{\partial E_x}{\partial z} - \frac{1}{|k_2|}\frac{\partial^2 E_x}{\partial x^2} - \frac{\omega_0^2}{c^2\,|k_2|}\left|N_{TE}\right|\left|E_x\right|^2 E_x + \frac{1}{4\left|k_2^3\right|}\frac{\partial^4 E_x}{\partial x^4} + \frac{\varepsilon^{(3)}_{NL2}}{|\varepsilon_2|\,|k_2|}\frac{\partial^2}{\partial x^2}\left(\left|E_x\right|^2 E_x\right) = 0 \tag{9.23}$$

where $N_{TE} = \left(|\mu|\,\varepsilon^{(3)}_{NL} + |\varepsilon|\,\mu^{(3)}_{NL}\frac{\varepsilon_0|\varepsilon|}{\mu_0|\mu|}\right)$ and, as defined earlier, the subscripts 1 and 2 are used to label the regions of the unit cell. For a TM polarised beam N_{TE} is simply substituted by N_{TM} but for this polarisation, the final term in (9.22) is absent since, in a PPM, there is no nonlinear magnetic polarisation. In the NPM, however, the TM-polarisation does permit a nonlinear diffraction term, for which

the coefficient is $\mu^{(3)}_{NL2}\Big/(|\mu_2|\,|k_2|)$. In order to be more general, *both* nonlinear diffraction and higher-order diffraction are included *for the time being*. Nevertheless, as discussed earlier, the nonlinear diffraction dominates over possible contributions from non-paraxiality and the role of quintic nonlinearity in any nonlinear saturation that prevents beam collapse. The average over the unit cell can be effected by considering the types of terms in the Schrödinger equations one at a time and adjusting the coefficients according to whether they refer to the PPM or the NPM part of the cell. In other words, the averages are going to be integrations with respect to z over L and it must be assumed that the unit cell is smaller in scale than a diffraction length measured as $k_1 w^2 \text{or} |k_2|\, w^2$, where w is the width of the spatial soliton. For TE-polarised beams, the outcomes for the averaging are, labelling each term in the nonlinear Schrödinger equation by its physical role:

Propagation

$$\frac{1}{L}\int_0^L \frac{\partial E_x}{\partial z}dz \approx \frac{\partial E_x}{\partial z} \tag{9.24}$$

Diffraction

$$\frac{1}{L}\int_0^L \frac{1}{k}\frac{\partial^2 E_x}{\partial x^2}dz \approx \frac{1}{k_1}\left(l_1 - \frac{k_1}{|k_2|}l_2\right)\frac{\partial^2 E_x}{\partial x^2} \tag{9.25}$$

Nonlinearity

$$\left(\left(\frac{\omega_0^2\varepsilon^{(3)}_{NL1}}{c^2 k_1}\right)\frac{1}{L}\int_0^{l_1 L} dz - \left(\frac{\omega_0^2}{c^2\,|k_2|}\right)\frac{1}{L}\int_{l_1 L}^{L}|N_{TE2}|\,dz\right)\left(|E_x|^2\,E_x\right)$$
$$\approx \frac{\omega_0^2}{c^2 k_1}\left(l_1\varepsilon^{(3)}_{NL1} - \frac{k_1}{|k_2|}l_2\,|N_{TE2}|\right)\left(|E_x|^2\,E_x\right) \tag{9.26}$$

Nonlinear diffraction

$$\frac{1}{L}\int_0^L \frac{\varepsilon^{(3)}_{NL}}{\varepsilon k}\frac{\partial^2}{\partial x^2}\left(|E_x|^2\,E_x\right) \approx \frac{1}{k_1}\left(l_1\frac{\varepsilon^{(3)}_{NL1}}{\varepsilon_1} + \frac{k_1}{|k_2|}l_2\frac{\varepsilon^{(3)}_{NL2}}{|\varepsilon_2|}\right)\frac{\partial^2}{\partial x^2}\left(|E_x|^2\,E_x\right) \tag{9.27}$$

Higher-order diffraction

$$\frac{1}{L}\int_0^L \frac{1}{4k^3}\frac{\partial^4 E_x}{\partial x^4} \approx \frac{1}{4k_1^3}\left(l_1 - l_2\frac{k_1^3}{|k_2^3|}\right)\frac{\partial^4 E_x}{\partial x^4} \tag{9.28}$$

Hence, the taking of a spatial average over the unit cell, shown in Fig. 9.3, leads to the dimensional equations

TE:

$$2ik_1\frac{\partial E_x}{\partial z}+D\frac{\partial^2 E_x}{\partial x^2}+\frac{\omega_0^2}{c^2}\left(l_1\varepsilon_{NL1}^{(3)}-\frac{k_1}{|k_2|}l_2\,|N_{TE2}|\right)|E_x|^2\,E_x-\frac{F}{4k_1^2}\frac{\partial^4 E_x}{\partial x^4}$$
$$+\left(l_1\frac{\varepsilon_{NL1}^{(3)}}{\varepsilon_1}+\frac{k_1}{|k_2|}l_2\frac{\varepsilon_{NL2}^{(3)}}{|\varepsilon_2|}\right)\frac{\partial^2}{\partial x^2}\left(|E_x|^2\,E_x\right)=0 \tag{9.29}$$

TM:

$$2ik_1\frac{\partial H_x}{\partial z}+D\frac{\partial^2 H_x}{\partial x^2}+\frac{\omega_0^2}{c^2}\left(l_1\varepsilon_{NL1}^{(3)}\frac{\mu_0\,|\mu|}{\varepsilon_0\,|\varepsilon|}-\frac{k_1}{|k_2|}l_2\,|N_{TM2}|\right)|H_x|^2\,H_x$$
$$-\frac{F}{4k_1^2}\frac{\partial^4 H_x}{\partial x^4}+\left(\frac{k_1}{|k_2|}l_2\frac{\mu_{NL2}^{(3)}}{|\mu_2|}\right)\frac{\partial^2}{\partial x^2}\left(|H_x|^2\,H_x\right)=0 \tag{9.30}$$

in which

$$D=l_1-\frac{\sqrt{\varepsilon_1\mu_1}}{\left|\sqrt{\varepsilon_2\mu_2}\right|}l_2\quad F=l_1-\left(\frac{\varepsilon_1\mu_1}{|\varepsilon_2\mu_2|}\right)^{\frac{3}{2}}l_2 \tag{9.31}$$

where ε_i, μ_i are the respective relative permittivities and permeabilities of the parts of the unit cell shown in Fig. 9.9a. The strategy for using this equation is to reduce the value of D, so that the linear diffraction can be minimised, thus permitting an influence from the nonlinear diffraction to appear. If the first-order diffraction is reduced in this way, however, it is possible in principle that the higher-order diffraction term, controlled by the parameter F, is not minimised.

Nevertheless, $\frac{k_1}{|k_2|}$ does not have to be unity, and higher-order linear diffraction can be changed by adjusting the structure. In fact, the kind of compensation to be discussed here, can be targeted at D or F. Indeed, for any choice of D it is possible to arrange for the ratio $\frac{k_1}{|k_2|}$ to make the contribution of higher-order linear diffraction negligible. This is a fascinating possibility that means that the reduction of D does not necessarily mean that higher-order diffraction has to be introduced. Because of this conclusion, *it will not be regarded as a critical contribution to the envelope equation* and the emphasis will be directed towards first-order diffraction-management. In addition, it should be noted that the non-paraxiality is also reduced as D tends to zero, but in any case, it is emphasised, once again, that nonlinear diffraction is going to be the dominant influence as beams become narrower and, as shown earlier, takes over the role of preventing beam collapse. Clearly if a nonlinear material is selected that has a large quintic contribution then the latter will compete with the nonlinear diffraction. The latter will still present a limit to beam narrowing, even if the small z-component of the electric field is restored to the argument, it only has a small impact on the role of the nonlinear diffraction. In summary, there are two broad scenarios. In

one, there is no diffraction-management but the nonlinear diffraction becomes a very important influence as the beams narrow. The second scenario involves manipulating D, to engage in some form of linear diffraction-management that can be arranged in a number of ways to make $D \rightarrow D(z)$ through the agency of a metamaterial.

As stated earlier, the scales $z = \left(kw^2\right) Z$ and $x = (w)\, X$ can be used, where w is actually an arbitrary unit but can be physically interpreted as the beam width. These steps towards dimensionless equations results in the following generic equation that describes both polarisations in terms of the useful dimensionless parameters D, which measures the control of the linear diffraction and κ, which measures the nonlinear diffraction

$$i\frac{\partial \psi}{\partial Z} + \frac{D}{2}\frac{\partial^2 \psi}{\partial X^2} + |\psi|^2 \psi + \kappa \frac{\partial^2}{\partial X^2}\left(|\psi|^2 \psi\right) = 0 \tag{9.32}$$

where

TE:

$$\psi = w\sqrt{G_1^{TE}}E_x, \quad G_1^{TE} = \frac{\omega_0^2}{c^2}\left(l_1 \varepsilon_{NL1}^{(3)} - \frac{k_1}{|k_2|} l_2 \left|N_{TE2}\right|\right),$$
$$G_2^{TE} = \left(l_1 \frac{\varepsilon_{NL1}^{(3)}}{\varepsilon_1} + \frac{k_1}{|k_2|} l_2 \frac{\varepsilon_{NL2}^{(3)}}{|\varepsilon_2|}\right); \tag{9.33}$$

TM:

$$\psi = w\sqrt{G_1^{TM}}H_x, \quad G_1^{TM} = \frac{\omega_0^2}{c^2}\left(l_1 \varepsilon_{NL1}^{(3)} \frac{\mu_0 |\mu|}{\varepsilon_0 |\varepsilon|} - \frac{k_1}{|k_2|} l_2 \left|N_{TM2}\right|\right),$$
$$G_2^{TM} = \left(\frac{k_1}{|k_2|} l_2 \frac{\mu_{NL2}^{(3)}}{|\mu_2|}\right); \tag{9.34}$$

and for each polarisation $\kappa_{TE} = \frac{G_2^{TE}}{w^2 G_1^{TE}}$ and $\kappa_{TM} = \frac{G_2^{TM}}{w^2 G_1^{TM}}$.

Equations (9.32)–(9.34) show that there are a number of possibilities for choosing the kind of metamaterial that will support bright spatial solitons. For TE beams, it will be assumed that the PPM is contributing the major part of the nonlinearity, to such an extent, that in practice, $\varepsilon_{NL2}^{(3)} = 0$ and $\mu_{NL2}^{(3)} = 0$ and, of course, $\mu_{NL1}^{(3)} = 0$. Without nonlinear diffraction, it is not necessary for TM beams to use only magnetic nonlinearity. However, if κ_{TM} is required, then it will be assumed that this applies to the case when the nonlinearity is located within the NPM, and that $\varepsilon_{NL2}^{(3)} = 0$, $\varepsilon_{NL1}^{(3)} = 0$ and $\mu_{NL2}^{(3)} \neq 0$. For the diffraction-managed cases to be presented below, therefore, κ_{TE} and κ_{TM} reduce to the simple forms

$$\kappa_{TE} = \frac{1}{k_1^2 w^2}, \quad \kappa_{TM} = \frac{1}{k_2^2 w^2} \tag{9.35}$$

9.3.4 Simulation Outcomes

Equation (9.32) is a generic equation that controls linear diffraction through D and the nonlinear diffraction through the frequency dependent parameter κ. Nonlinear diffraction will prevent beam collapse as the power carried by a spatial soliton increases and results in a limit on how narrow the beams can be. It is a process that dominates over non-paraxiality and even quintic nonlinearity, provided the latter is not too large. Nonlinear diffraction is still, nevertheless, a diffraction process so that as beams become narrow, and the power goes up, it will still have to compete with the linear diffraction, unless the latter is managed to be a small influence.

The soliton literature for metamaterials contains a number of examples involving classic cases of modulation instability, self-steepening, self-induced transparency, and dark solitons. The question of soliton control has been addressed, as have the properties of gap solitons [49]. The latter, however deals with quadratic nonlinear material that does not feature here, since all of the issues addressed involve only bright spatial solitons driven by third-order nonlinearity.

If there is no linear diffraction-management then the planar waveguide is filled with PPM and the nonlinear diffraction coefficient will be practically non-dispersive over an operational frequency range and can be taken as a constant. On the other hand, for an NPM planar guide the nonlinear diffraction coefficient is $\frac{c^2}{\omega_0^2 w^2 (\varepsilon(\omega_0)\mu(\omega_0))} \equiv \kappa$, where c is the velocity of light in vacuo and Drude models have been assigned to $\varepsilon(\omega_0)$ and $\mu(\omega_0)$. If the beam width is set to $w = m\lambda$, where λ is the free-space wavelength, and m is an integer then, for a typical ratio of ω_{pm}/ω_{pe}, where ω_{pm} and ω_{pe} are the effective plasma frequencies, it is seen in Fig. 9.10 that κ varies quite rapidly with frequency, and rises and falls with respect to the, practically

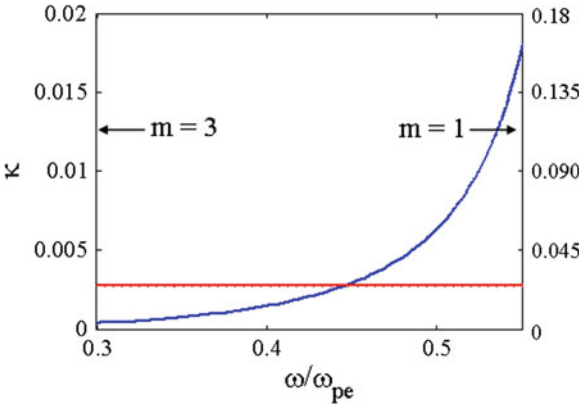

Fig. 9.10 Uses Drude models for permittivity and permeability. *Red* PPM and *blue* NPM. $\omega_{pm}/\omega_{pe} = 0.6$, $\kappa = \left(4\pi^2 m^2\right)^{-1}\left(1-\frac{1}{\Omega^2}\right)^{-1}\left(1-\frac{0.6}{\Omega^2}\right)^{-1}$, where $\Omega = \frac{\omega}{\omega_{pe}}$. *Left-hand* scale, $m = 3$, *right-hand* scale, $m = 1$. The data for the PPM curve is for typical glass with $\varepsilon \approx 2.25$

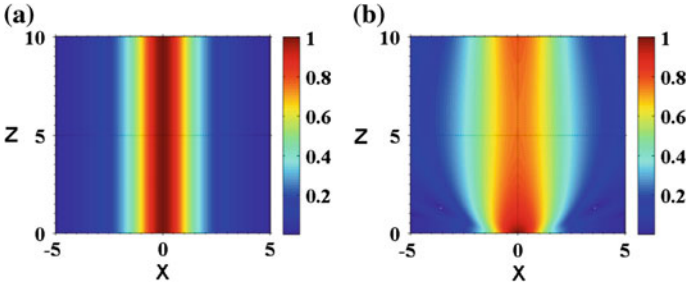

Fig. 9.11 Initial inputs: $sech(X)$, $m = 1$ **a** $\kappa = 0$ **b** $\kappa = 0.17$

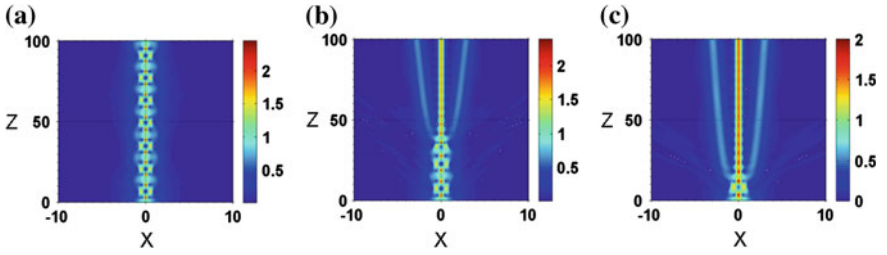

Fig. 9.12 D = 0.1. Inputs: $\psi = sech(X)$. **a** $\kappa = 0$ **b** $\kappa = 0.00168$ **c** $\kappa = 0.005$

dispersion-free PPM line, created for a substance like ordinary glass, for example. The example given in Fig. 9.3 shows that the nonlinear diffraction coefficient rises rapidly as the narrow beam regime is approached. Note that here the beam width is a function of the wavelength and, therefore, a function of frequency to ensure that a narrow beam is being considered. It should also be recalled that the type of nonlinearity changes as TE-polarised beams are exchanged with TM-polarised beams. In addition to the variation of κ with the beam width, Fig. 9.3b also shows a significant variation with operational frequency, especially as the resonance frequency is approached.

Figure 9.11 shows how strongly a typical metamaterial, such as the double negative one used here, can influence a typical waveguide structure. As an initial illustration, Fig. 9.11a, using arbitrary scales, since the envelope equation has been made dimensionless, shows, first of all, a standard first-order bright spatial soliton beam, without any diffraction-management [D = 1], magnetooptics or the influence of nonlinear diffraction. Figure 9.11b illustrates how to bring nonlinear diffraction into play for a D = 1 environment, a beam width of the order of a wavelength, and $\kappa = 0.17$. The beam intensity is lowered and some broadening occurs. It is not a necessary condition to reduce the beam width dramatically, to access greater nonlinear diffraction influence, because larger κ can be obtained with frequency tuning, because of the dispersive metamaterial properties.

Figure 9.12 reveals the outcomes of reducing linear diffraction to 10 %. If a first-order soliton is launched at Z = 0, then the act of decreasing the linear diffraction

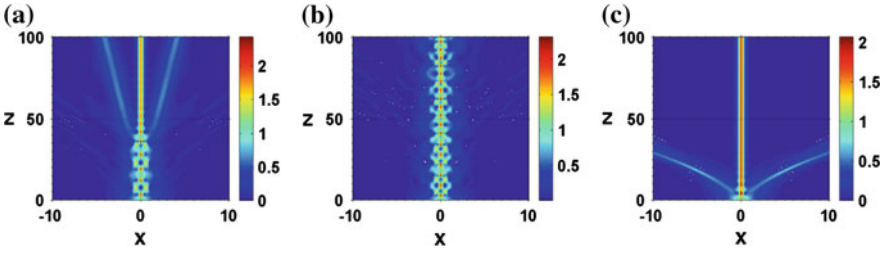

Fig. 9.13 D = 0.1, $\kappa = 0.00168$, $m = 3$, $v(X) = v_{\max} sech\left(\frac{X}{X_0}\right)$ Input: $\psi = sech(X)$, **a** $v(X) = 0$, **b** $v(X) > 0$, **c** $v(X) < 0$. $v_{\max} = \pm 1.8$

to 10 % means that there is now too much power available for the propagation of a first-order (N = 1) soliton. By analogy with optical fibre work, this act of diffraction reduction should lead to a breathing soliton, of order approximately $\sqrt{10}$. Figure 9.12a shows that this is exactly what happens, and a third-order breathing soliton is created. Nonlinear diffraction is introduced to achieve Fig. 9.12b. The outcome is that the nonlinear diffraction acts as a perturbation to split the breather. Three low-power, pseudo-solitons, are produced, where the power contained within each is not enough for it to retain its soliton status if it is entered into a normal, 100 % diffraction medium. It would then simply radiate. In Fig. 9.12c, a higher value of the nonlinear-diffraction coefficient is used to create a larger perturbation. As a consequence, the breather is split after approximately 15 Rayleigh propagation lengths.

Magnetooptic control is enabled through the function $v(X) = v_{\max} sech\left(\frac{X}{X_0}\right)$ and a straightforward addition to the nonlinear Schrödinger equation. $v_{\max}$ is proportional to Q, which is the magnetooptic saturation parameter introduced in (9.19). Typically [50], Q is the order of 10^{-4}–10^{-3}, and this means that for available magnetooptic materials, $v_{\max}$ would be in the range 0.6–6. An intermediate value $v_{\max} = \pm 1.8$ is used, where the $\pm$ indicates the direction of the applied magnetic field along $\pm X_{directions}$. Briefly, switching the field direction produces an impressive, non-reciprocal, behaviour. The physical explanation of this is that the applied magnetic field raises, or lowers, the effective potential well in which the bright spatial soliton [viewed for this purpose as a "particle"] is located. The same effects would appear in the behaviour of a narrow-beam as well, when nonlinear diffraction is in operation.

Figure 9.13 shows the degree of magnetooptic influence in diffraction-managed metamaterial structure, for which D = 0.1. The result of applying an external magnetic field effectively changes the depth of the potential well in which the soliton appears to find itself. It is emphasized that in order to achieve the well-known Voigt effect, the magnetic field must be directed along the x-direction, and the waveguide must be asymmetric. Figure 9.13a shows that the input has become a third-order breathing soliton, but it is soon perturbed by the nonlinear diffraction. The application of an applied magnetic field, Fig. 9.13b, however, deepens the "well" in which

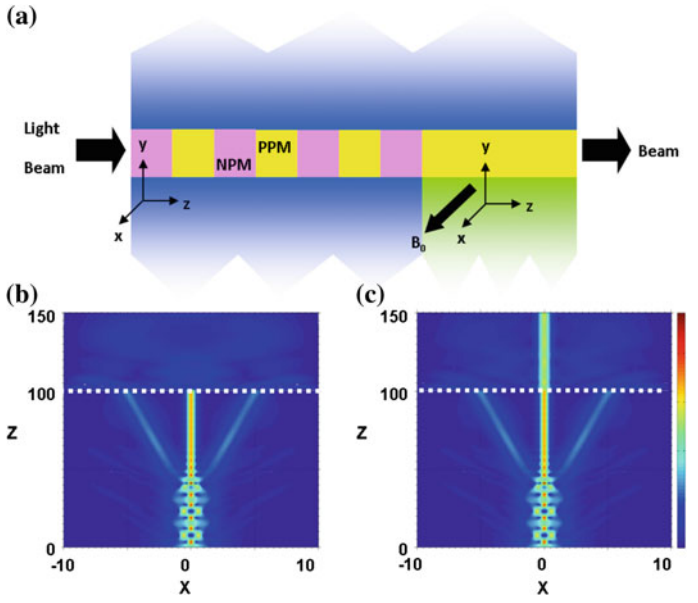

Fig. 9.14 $\psi = sech(X), \kappa = 0.00168$, D = 0.1 for $0 < Z < 100$, D = 1 for $Z > 100$. **a** Sketch of a diffraction-managed waveguide with a magnetooptic control end-section **b** $v_{max} = 0$, **c** $v_{max} = +1.8$

the spatial soliton finds itself. As a result, the third-order breathing soliton is fully captured. In Fig. 9.13c the magnetic field is completely reversed and this means that the floor of the well is "lifted", with the consequence that, not only can a breather not be formed, but a single narrow beam is created with excess energy being rapidly ejected to the left and to the right. All of this shows that the magnetooptics is a very important control mechanism, many interesting applications now appear on the horizon.

A device that could be very useful in data processing and other integrated optics applications, is sketched in Fig. 9.14. Suppose that a beam produced from the diffraction-management system does not contain enough power to sustain its shape when it is finally projected into a 100 % diffraction medium. Figure 9.14b, shows such a case, in which the first 100 Rayleigh lengths is a 10 % diffraction-managed medium, but then the linear diffraction is increased to 100 %. This causes the beam emerging from the diffraction-managed region to diffract away and become lost. Figure 9.14c shows that when this emerging beam is fired into a magnetooptic region it now captured in a deep well, and could be used in an application for further processing. It is assumed that the magnetooptic control region is the asymmetric waveguide configuration considered earlier on, and that, in a downstream application, some form of impedance matching can be put into place, in order to enable free transmission of the beam across all the boundaries.

9.4 Conclusions

Two globally important deployments of metamaterial control are investigated. One involves the slowing down of light and the other the behaviour of spatial solitons. Both will have a strong positive impact upon device design. It is shown that metamaterial waveguides with negative electromagnetic parameters (permittivity, permeability, refractive index) can enable complete stopping of light, under realistic, experimental, conditions [8, 15, 16]. This attribute is underpinned by the resilience of the deceleration mechanism in these structures to fabrication imperfections (e.g., disorder) and dissipative losses. By nature, these schemes invoke solid-state materials and, as such, are not subject to low-temperature or atomic coherence limitations. The NRI-based scheme, in particular, inherently allows for high in-coupling efficiencies, polarization-independent operation, and broadband function, since the deceleration of light does not rely on refractive index resonances. This versatile method for stopping photons opens the way to a multitude of hybrid, optoelectronic devices to be used in 'quantum information' processing, communication networks and signal processors, and conceivably heralds a new realm of combined metamaterials and slow light research.

The spatial soliton study also adds, immensely, to the promise of a range of new devices and anticipates the use of planar metamaterial waveguides in integrated optical circuits of the future. They will be nanostructured and function within visible to near infra-red frequency windows. It is here that magnetooptic controls can also be readily introduced. In the light of recent work addressing losses in metamaterials [44, 45, 50], loss has not been added into the nonlinear Schrödinger equation, but, as has been pointed out recently [51], practical soliton applications, using metamaterials, will not be impossible to achieve. There is a growing interest in soliton phenomena in metamaterials so the basic methodology for studying polarised soliton beams is presented in some detail and the novel idea that nonlinear diffraction is a major player is discussed extensively. The concepts are made relevant to homogeneous planar waveguides, containing stable spatial solitons, and these are then extended to investigate the role of a form of diffraction-management. To all of this can be added magnetooptic control that relies upon the famous Voigt, or Cotton-Mouton, effect that requires an asymmetric guiding structure. It is clear from the outset that a beautiful degree of magnetic control can be achieved and that metamaterial environments are going to be the foundation of very important and life-changing applications.

Finally, the work presented here on slow light offers a vast improvement on current devices and, similarly, the outcomes associated with spatial solitons offer high quality opportunities for beam control in the optical chips of the future, especially when modern metamaterials are mapped onto the results given here.

References

1. A.D. Boardman, J. Opt. **13**, 020401 (2011)
2. B.E.A. Saleh, M.C. Tech, *Fundamentals of Photonics* (John Wiley, New Jersey, 2007)
3. P. Markoš, C.M. Soukoulis, *Wave Propagation: From Electrons to Photonic Crystals and Left-Handed Materials* (Princeton University Press, Princeton, 2008)
4. V.M. Shalaev, A.K. Sarychev, *Electrodynamics of Metamaterials* (World Scientific Publishing, New Jersey, 2007)
5. N. Engheta, R.W. Ziolkowski (eds.), *Electromagnetic Metamaterials: Physics and Engineering Explorations* (Wiley-IEEE Press, New York, 2006)
6. J.B. Khurgin, R.S. Tucker (eds.), *Slow Light: Science and Applications* (Taylor & Francis, New York, 2009)
7. P.W. Milonni, *Fast Light, Slow Light and Left-Handed Light* (Taylor & Francis, New York, 2005)
8. K.L. Tsakmakidis, A.D. Boardman, O. Hess, 'Trapped rainbow' storage of light in metamaterials. Nature **450**, 397 (2007)
9. B. Corcoran et al., Green light emission in silicon through slow-light enhanced third- harmonic generation in photonic crystal waveguides. Nat. Photonics **3**, 206 (2009)
10. F. Xia et al., Ultracompact optical buffers on a silicon chip. Nat. Photonics **1**, 65 (2006)
11. A. Petrov et al., Backscattering and disorder limits in slow light photonic crystal waveguides. Opt. Express **17**, 8676 (2009)
12. D.P. Fussell et al., Influence of fabrication disorder on the optical properties of coupled- cavity photonic crystal waveguides. Phys. Rev. B **78**, 144201 (2008)
13. C. Helgert et al., Effective properties of amorphous metamaterials. Phys. Rev. B **79**, 233107 (2009)
14. N. Papasimakis et al., Coherent and incoherent metamaterials and order-disorder transitions. Phys. Rev. B **80**, 041102(R) (2010)
15. Q. Gan et al., Experimental verification of the rainbow trapping effect in adiabatic plasmonic gratings. Proc. Nat. Acad. Sci. **108**(13), 5169–5173 (2011)
16. V.N. Smolyaninova et al., Experimental observation of the trapped rainbow. Appl. Phys. Lett. **96**, 211121 (2009)
17. E. Infeld, G. Rowlands, *Nonlinear Waves, Solitons and Chaos* (Cambridge University Press, Cambridge, 1990)
18. A.D. Boardman, A.P. Sukhorukov, *Soliton-Driven Photonics* (Kluwer Academic Publishers, Dordecht, 2000)
19. G.P. Agrawal, *Nonlinear Fiber Optics*, 3rd edn. (Academic Press, San Diego, 2001)
20. S. Trillo, W. Torrellas, *Spatial Solitons* (Springer, Berlin, 2001)
21. M. Remoissenet, *Waves Called Solitons* (Springer, Berlin, 1996)
22. K.C. Huang et al., Nature of lossy Bloch states in polaritonic photonic crystals. Phys. Rev. B **69**, 195111 (2004)
23. J.-S. Li, Optical modulator based on negative refractive material. Opt. Laser Technol. **41**, 627 (2009)
24. A.J. Hoffman et al., Negative refraction in semiconductor metamaterials. Nat. Mater. **6**, 946–950 (2007)
25. A.J. Hoffman et al., Midinfrared semiconductor optical metamaterials. J. Appl. Phys. **105**, 122411 (2009)
26. Z.V. Vardeny, A. Nahata, Anderson localisation of slow light. Nat. Photonics **2**, 75 (2008)
27. S. Mookherjea et al., Localisation in silicon nanophotonic slow- waveguides. Nat. Photonics **2**, 90 (2008)
28. O. Hess, K.L. Tsakmakidis, Stopping light in metamaterials: The trapped rainbow. SPIE Newsroom (Nanotechnology) (2008). doi:10.1117/2.120086.1163
29. K.L. Tsakmakidis et al., Single-mode operation in the slow light regime using oscillatory waves in generalised left-handed heterostructures. Appl. Phys. Lett. **89**, 201103 (2006)

30. A. Karalis et al., Plasmonic dielectric systems for high-order dispersionless slow or stopped subwavelength light. Phys. Rev. Lett. **103**, 043906 (2009)
31. J.W. Dong, H.Z. Wang, Slow electromagnetic propagation with low group velocity dispersion in all-metamaterial based waveguide. Appl. Phys. Lett. **91**, 111909 (2007)
32. M.A. Vincenti et al., Semiconductor-based superlens for subwavelength resolution below the diffraction limit at extreme ultraviolet frequencies. J. Appl. Phys. **105**, 103103 (2009)
33. E.I. Kirby et al., FDTD analysis of slow light propagation in negative-refractive-index metamaterial waveguides. J. Opt. A: Pure Appl. Opt. **11**, 114027 (2009)
34. A. Archambault et al., Surface plasmon Fourier optics. Phys. Rev. B **79**, 195414 (2009)
35. E.I. Kirby, J.M. Hamm, T. Pickering, K.L. Tsakmakidis, O. Hess, Evanescent gain in "trapped rainbow" negative refractive index heterostructures. Phys. Rev. B **84**, 041103 (2011)
36. J.J. Cook et al., Ultralow-loss optical diamagnetism in silver nanoforests. J. Opt. A.: Pure Appl. Opt. **11**, 114026 (2009)
37. O. Hess et al., Active nanoplasmonic metamaterials. Nat. Mater. **11**, 573 (2012)
38. S. Wuestner et al., Plasmon lasers at deep subwavelength scale. Phys. Rev. B. **85**, 201406(R) (2012)
39. J.S. Aitchison, A.M. Weiner, Y. Silberberg, D.E. Leaird, M.K. Oliver, J.L. Jackel, P.W. Smith, Opt. Letters **15**, 471–473 (1990)
40. M. Ballav, A.R. Chowdhury, Prog. Electromagnetics Res. **63**, 33–50 (2006)
41. A.D. Boardman, K. Marinov, D.I. Pushkarov, A. Shivarova, Optical Quantum Electronics **32**, 49–62 (2000)
42. A.D. Boardman, K. Marinov, D.I. Pushkarov, A. Shivarova, Physical Rev. E **62**, 2871–2876 (2000)
43. P. Kockaert, P. Tassin, G. Van der Sande, I. Veretennicoff, M. Tlidi, Physical Rev. A **74**, 033822 (2006)
44. K.J. Webb, A. Ludwig, Physical Rev. B **78**, 153303 (2008)
45. P. Kinsler, M.W. McCall, Physical Rev. Letters **101**, 167401 (2008)
46. A.D. Boardman, R.C. Mitchell-Thomas, N.J. King, Y.G. Rapoport, Opt. Comm. **283**, 1585–1597 (2009)
47. T. Mizumoto, Y. Naito, IEEE Transactions Microw. Theory Techniques **30**, 922–925 (1982)
48. M.J. Ablowitz, Z.H. Musslimani, Physical Rev. Letters **87**, 254102 (2001)
49. P. Tassin, G. Van der Sande, N. Veretenov, P. Kockaert, I. Veretennicoff, M. Tlidi, Optics Express **14**, 9338–9343 (2006)
50. A.D. Boardman, Y.G. Rapoport, N. King, V.N. Malnev, J. Optical Society Am. B **24**, A53 (2007)
51. G. D'Aguanno, N. Mattiucci, M.J. Bloemer, J. Optical Society Am. B **25**, 1236 (2008)

Chapter 10
Nonlinear Optics with Backward Waves

Alexander K. Popov

Abstract Extraordinary properties of nonlinear optical propagation processes in double-domain positive/negative index metamaterials are reviewed. These processes enable coherent energy exchange between ordinary and backward electromagnetic waves, which allows huge increase of frequency-conversion efficiency at second harmonic generation, three-wave mixing and optical parametric amplification. Striking contrasts with properties of the counterparts in ordinary materials are outlined. Particularly, exotic features arise for amplification and generation of counter-propagating short pulses. Novel class of materials, which enable such processes through electromagnetic waves with negative group velocity, are proposed. The possibility to mimic such processes in readily available crystals that support elastic backward waves (optical phonons) is shown. The concepts of unique photonic devices such as data processing chips, tunable nonlinear-optical mirrors, filters, switches and sensors are discussed.

10.1 Introduction

Optical negative-index materials (NIMs) form a class of electromagnetic media that promise revolutionary breakthroughs in photonics. The possibilities of such breakthroughs originate from backwardness, the exotic property that electromagnetic waves (EMWs) acquire in NIMs. Unlike ordinary positive-index materials, the energy flow, **S**, and the wave-vector, **k**, become counter-directed in NIMs that determines their unique linear and nonlinear optical (NLO) propagation properties. The appearance of backward electromagnetic waves (BEMW) can be explained as follows. The direction of the wave-vector **k** with respect to the energy flow **S**

A.K. Popov (✉)
Birck Nanotechnology Center, Purdue University, West Lafayette, IN 47907, USA
e-mail: popov@purdue.edu

I.V. Shadrivov et al. (eds.), *Nonlinear, Tunable and Active Metamaterials*,
Springer Series in Materials Science 200, DOI 10.1007/978-3-319-08386-5_10

(Poynting vector) depends on the signs of electrical permittivity ε and magnetic permeability μ:

$$\mathbf{S} = (c/4\pi)[\mathbf{E} \times \mathbf{H}] = (c^2\mathbf{k}/4\pi\omega\varepsilon)H^2 = (c^2\mathbf{k}/4\pi\omega\mu)E^2.$$

If $\varepsilon < 0$ and $\mu < 0$, refractive index becomes negative, $n = -\sqrt{\mu\varepsilon}$, and vectors $\mathbf{S}$ and $\mathbf{k}$ become counter-directed, which is in striking contrast with the electrodynamics of ordinary, positive index (PI) media (PIM). Hence, magnetic response at optical frequencies, including magnetic nonlinear polarization, opens new avenues in electromagnetics and for its numerous revolutionary breakthrough applications. Such property does not exist in naturally occurring materials but becomes achievable in the plasmonic metamaterials. Extraordinary features of coherent NLO energy conversion processes in NIMs that stem from wave-mixing of ordinary and BEMW and the possibilities to apply them for compensating optical losses have been investigated in [1–11]. Essentially different properties of three-wave mixing (TWM) and four-wave mixing processes as opposite to second harmonic and third harmonic generation have been revealed in [1, 12–19]. Ultimately, it was shown that NLO propagation processes that involve backward waves (BWs) enable a great enhancement of energy-conversion rate at otherwise equal nonlinearities and intensities of input waves. Coherent NLO energy exchange between ordinary and BWs acquires particularly extraordinary properties in short pulse regime. A review can be found in [12, 13] and in the references therein. Outlined features have the potential of unprecedented applications, such as compensation of optical losses [2, 3] and remote optical sensing [20]. A family of unique photonic devices such as data processing chips, tunable NLO mirrors, filters, switches and sensors can be created making use of indicated unparallel processes.

Usually, NIMs are nanostructured metal-insulator composites with a special design of their building blocks at the nanoscale that enables negative optical magnetism. Metal component imposes strong absorption of optical radiation in NIMs, which presents a major obstacle towards their numerous prospective exciting applications. However, different approaches are possible to engineer the materials that can support coexistence and coherent NLO coupling of ordinary and BWs [21]. Two different classes of materials have been proposed: metamaterials with specially engineered spatial dispersion of the nanoscopic building blocks and crystals that support optical phonons with negative group velocity. Both do not rely on nanoresonators which provide negative optical magnetism and constitute current mainstream in fabricating NIMs. In the second case, the possibility to exploit ordinary crystals instead of plasmonic NLO metamaterials that are very challenging to engineer is demonstrated. It appears that extraordinary NLO frequency-conversion propagation processes attributed to NIMs can be mimicked in such fully dielectric materials. It is proved through numerical simulations that the detrimental effects of strong incoherent losses can be mitigated in the short-pulse regimes, which acquire exotic properties when ordinary EMWs and elastic BWs (optical phonons) are involved in the NLO coupling.

This chapter describes physical principles underlying the possibilities of greatly enhanced nonlinear-optical frequency-converting processes in negative-index metamaterials, their applications to tailoring transparency and reflectivity of such materials with control laser and novel approaches to engineering materials with negative phase velocity and to simulating some of the similar nonlinear optical processes in available crystals.

10.2 Huge Enhancement of Nonlinear Optical Energy Conversion, Reflectivity and Amplification Through Three-Wave Mixing of Ordinary and Backward Electromagnetic Waves

Most remarkable feature pertinent to NLO propagation processes in NIMs is appearance of huge, resonance type enhancement of the NLO coupling of EMWs. This section describes the physical principles underlying such extraordinary behavior and applications to all-optical tailoring of transparency and reflectivity of the metaslabs and to optical sensing.

10.2.1 "Geometrical" Resonances

Figure 10.1a depicts a slab of thickness L, strong control field E_3 at ω_3 and weak wave E_2 at ω_2, both are assumed as PI. Third, weak wave E_1 at ω_1 falls in the NI frequency domain and, therefore, possesses backward wave properties. The frequencies are related as $\omega_1 + \omega_2 = \omega_3$. The coupled waves experience strong dissipation represented by respective absorption indices $\alpha_{1,2}$. The slowly-varying effective amplitudes of the waves, $a_{e,m,j}$, (j $= \{1, 2\}$) and nonlinear coupling parameters, $g_{e,m}$, for the electric $\chi_{ej}^{(2)}$ and magnetic types of quadratic nonlinearity [14] $\chi_{mj}^{(2)}$ can be conveniently introduced as

$$\begin{aligned} a_{ej} &= \sqrt{|\varepsilon_j/k_j|}E_j, \quad g_e = \sqrt{|k_1k_2/\varepsilon_1\varepsilon_2|}2\pi\chi_{ej}^{(2)}E_3; \\ a_{mj} &= \sqrt{|\mu_j/k_j|}H_j, \quad g_m = \sqrt{|k_1k_2/\mu_1\mu_2|}2\pi\chi_{mj}^{(2)}H_3. \end{aligned}$$

The quantities $|a_j|^2$ are proportional to the photon numbers in the energy fluxes. Equation sets for the amplitudes a_j are identical for the both types of the nonlinearities:

$$da_1/dz = -iga_2^* \exp(i\Delta kz) + (\alpha_1/2)a_1, \tag{10.1}$$

$$da_2/dz = iga_1^* \exp(i\Delta kz) - (\alpha_2/2)a_2, \tag{10.2}$$

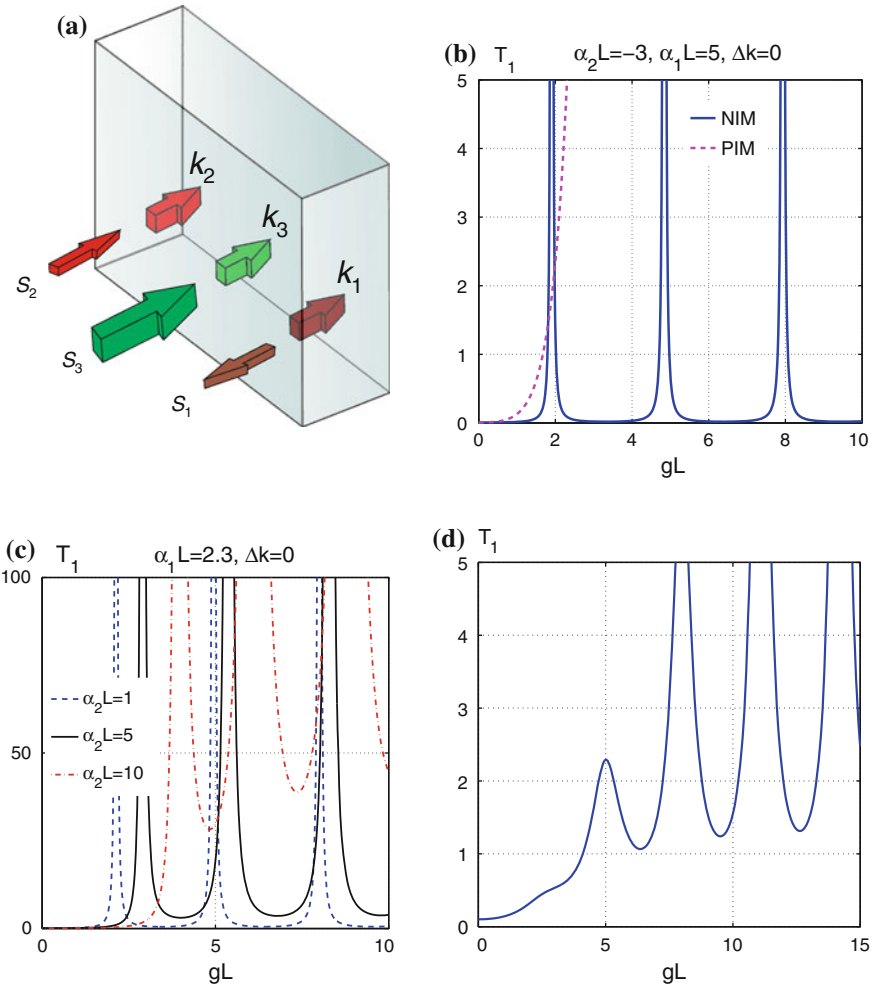

Fig. 10.1 Three-wave mixing and tailored transparency for negative-index signal. **a** Coupling geometry. $\mathbf{S_1}$—negative index signal, $\mathbf{S_3}$—positive-index control field, $\mathbf{S_2}$—positive-index idler. **b** *Solid* the dependence of the output signal $T_1(z = 0)$ on the slab thickness and on intensity of the control field (on factor gL). Here, the metamaterial is absorptive at the frequency of the signal and assumed amplifying for the idler, $\Delta k = 0$. *Dashed* the same dependence for the ordinary, PI media with the same other medium parameters. **c** Transmission $T_1(z = 0)$ of the signal at $\alpha_1 L = 2.3$ and different values of $\alpha_2 L$. $\Delta k L = 0$. **d** Effect of phase-mismatch on the output signal. $\alpha_1 L = 2.3$, $\alpha_2 L = 3$, $\Delta k L = \pi$. Diminished detrimental effect of phase mismatch on the transmission with the increase of intensity of the control field and/or the slab thickness is seen

where $\Delta k = k_3 - k_2 - k_1$. Here, the model is simplified. The equations account for absorption of the incident and reflected coupled fields, whereas depletion of the control field is neglected.

Three fundamental differences in (10.1) and (10.2) distinguish them from their counterpart in ordinary, PI materials. First, the sign with g in (10.1) is opposite to that in (10.2) because $\varepsilon_1 < 0$ and $\mu_1 < 0$. Second, the opposite sign appears with α_1 because the energy flow $\mathbf{S_1}$ is against the z-axis. Third, the boundary conditions for the incident and generated waves must be defined at the opposite sides of the sample ($z = 0$ and $z = L$) because the energy flows $\mathbf{S_1}$ and $\mathbf{S_2}$ are counter-directed. Consequently, the equations for a_1 and a_2 cease to be identical as they are in ordinary PI NLO materials. As will be shown below, this leads to dramatic changes in the solutions to the equations and in the general behavior of the generated wave.

10.2.1.1 Tailored Transparency and Compensating Optical Losses of Negative-Index Signal

If $a_1(z = L) = a_{1L}$, $a_2(z = 0) = 0$, the slab serves as optical parametric amplifier at ω_1. Transparency/amplification factor T_{10} is given by the equation

$$T_{10} = \left| \frac{a_1(0)}{a_{1L}} \right|^2 = \left| \frac{\exp\{-[(\alpha_1/2) - s]L\}}{\cos RL + (s/R)\sin RL} \right|^2. \tag{10.3}$$

It predicts the behavior, which is totally different from that in ordinary media. Most explicitly, it is seen at $\alpha_j = \Delta k = 0$. Then, the equation for transparency reduces to

$$T_{10} = 1/[\cos(gL)]^2, \tag{10.4}$$

where $R = \sqrt{g^2 - s^2}$, $s = [(\alpha_1 + \alpha_2)/4][-i\Delta k/2]$. The equation shows that the output signal experiences a sequence of *"geometrical" resonances* at $gL \to (2j + 1)\pi/2$, (j $= 0, 1, 2, \ldots$), as functions of the slab thickness L and of the intensity of the control field (factor g). Such behavior is in drastic contrast with that in an ordinary, PI medium, where, at $\alpha_j = \Delta k = 0$, the signal would grow *exponentially*

$$T_1 \propto \exp(2gL). \tag{10.5}$$

The possibility of such extraordinary resonances was pointed in textbook [22], and predicted for an exotic TWM phase-matching scheme, which has never been realized [23, 24]. All frequencies were suggested to fall in the positive-index domain, whereas one beam with far infrared wavelength was proposed to be directed opposite to others so that anomalous dispersion could be used for phase matching.

Crucial importance of the outlined geometrical resonances and striking difference of NLO propagation processes in the double domain NI/PI metamaterials compared with their counterparts in ordinary materials are illustrated in Fig. 10.1b–d. Besides the factor $g \propto \chi_m^{(2)} H_3$, the local NLO energy conversion rate for the signal is proportional to the amplitude of the idler (and vice versa) and depends on the phase mismatch Δk. Hence, the fact that the waves decay in opposite directions (absorption

indices $\alpha_{1,2}$) causes a specific, strong dependence of the entire propagation process and, consequently, of the transmission properties of the slab on the ratio of the signal and the idler decay rates. Such extraordinary resonance behavior, which occurs due to the backwardness of the light waves in NIMs, is explicitly seen when compared with the corresponding dependencies in ordinary, PI materials depicted in Fig. 10.1b (dashed line). Here, the centers amplifying the idler at ω_2 due to population inversion are assumed embedded in the slab. Basically, such induced transparency resonances are narrow, like those depicted in Fig. 10.1b and by the plot in Fig. 10.1c corresponding to $\alpha_2 L = 1$. This indicates that the sample remains opaque anywhere beyond the resonance values of the control field and of the sample thickness. Any sharp frequency dependence of nonlinear susceptibility or absorption indices translates into frequency *narrow-band* filtering.

The slab becomes *transparent* within the broad range of the slab thickness and the control field intensity if the transmission in all of the minimums is about or more than one. Figure 10.1c, d show the feasibility of achieving robust transparency and amplification in a NIM slab at the signal frequency through a wide range of the control field intensities and slab thicknesses by the appropriate adjustment of the absorption indices $\alpha_2 \geq \alpha_1$. Field amplitudes grow sharply near the resonances, which indicates the possibility of *cavity-less self-oscillations*. The distribution of the signal and the idler inside the slab would also dramatically change. Particularly, the simulations show that, unless optimized, the signal maximum inside the slab may appear much greater than its output value at $z = 0$ [1, 2, 4].

10.2.1.2 Tailored Reflectivity and Nonlinear Optical Metamirror

At $a_{1L} = 0$, $a_2(z = 0) = a_{20}$, the slab serves as an NLO mirror, which emits back the wave at ω_1. For the case of spatially homogeneous control field and real nonlinear susceptibility, the analytical solution to the (10.1, 10.2) can be found, and then the reflectivity, $r_1 = |a_1(0)/a_{20}^*|^2$, is given by the equation

$$r_1 = \left| \frac{(g/R) \sin RL}{\cos RL + (s/R) \sin RL} \right|^2 . \tag{10.6}$$

It is seen that the reflectivity also presents a set of "geometrical" resonances. For example, at $s = 0$, reflectivity is given by $r_{10} = tan^2(gL)$ and tends to infinity as $gL \to (2j + 1)\pi/2$, (j = 0, 1, 2, . . .), which indicates the possibility of mirrorless self-oscillations. Basically, the reflected wave has a different frequency, and the reflectivity may significantly exceed 100 %.

Ultimately, the simulations show the possibility to *tailor and switch the transparency and reflectivity* of the metachip over the wide range by changing intensity of the control field. Giant enhancement of the NLO coupling in the resonances indicates that strong absorption of the left-handed, negative-phase wave and of the idler can be turned into transparency, amplification and even into cavity-free self-oscillation.

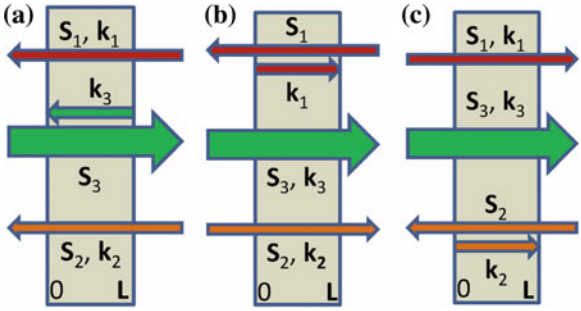

Fig. 10.2 Three different options of the proposed NLO sensors. **a** $\mathbf{S_{1,2}}$ and $\mathbf{k_{1,2}}$ are energy fluxes and wavevectors for the ordinary, positive index, signal and generated idler; $\mathbf{S_3}$ and $\mathbf{k_3}$—for the negative index control field. **b**, **c** Alternative prospective schemes. **b** The NLO sensor amplifies the signal $\mathbf{S_1}$ traveling agains the control beam ($n(\omega_1) < 0$) and frequency up-converts it to the beam $\mathbf{S_2}$ directed along the control one. **c** The NLO sensor shifts the frequency of the signal $\mathbf{S_1}$ traveling along the control field and sends it back in the direction against the control beam ($n(\omega_2) < 0$)

Self-oscillations would provide for the generation of *entangled counter-propagating* left-handed, $\hbar\omega_1$, and right-handed, $\hbar\omega_2$, photons without a cavity. Energy is taken from the control field. Here, distributed NLO feedback greatly increases the effective coupling length. It is similar to weakly amplifying medium placed inside a high-quality cavity which leads to lasing. The outlined features can be employed for design of ultracompact optical sensors, selective filters, amplifiers and oscillators generating beams of counter-propagating entangled photons.

10.2.2 Three Alternative Coupling Schemes: Three Sensing Options

This subsection describes application to all-optical sensing and the concepts of the prospective sensors. Figure 10.2 depicts three possible options for the phase matched NLO coupling of the ordinary and backward waves. Consider the example depicted in panel (a). Assume that the wave at ω_1 with the wave-vector $\mathbf{k_1}$ directed along the z-axis is a PI ($n_1 > 0$) signal. Usually it experiences strong absorption caused by metal inclusions. The medium is supposed to possess a quadratic nonlinearity $\chi^{(2)}$ and is illuminated by the strong higher frequency control field at ω_3, which falls into the NI domain. Due to the three-wave mixing (TWM) interaction, the control and the signal fields generate a difference-frequency idler at $\omega_2 = \omega_3 - \omega_1$, which is also assumed to be a PI wave ($n_2 > 0$). The idler, in cooperation with the control field, contributes back into the wave at ω_1 through the same type of TWM interaction and thus enables optical parametric amplification (OPA) at ω_1 by converting the energy of the control fields into the signal. In order to ensure effective energy conversion, the induced traveling wave of nonlinear polarization of the medium and the coupled

electromagnetic wave at the same frequency must be phase matched, i.e., must meet the requirement of $\Delta\mathbf{k} = \mathbf{k_3} - \mathbf{k_2} - \mathbf{k_1} = \mathbf{0}$. Hence, all phase velocities (wave vectors) must be co-directed. Since $n(\omega_3) < 0$, the control field is a BW, i.e., its energy flow $\mathbf{S_3} = (c/4\pi)[\mathbf{E_3} \times \mathbf{H_3}]$ appears directed against the z-axis. This allows to conveniently remotely interrogate the NLO microchip and to actuate frequency up-conversion and amplification of signal directed towards the remote detector by such a metamirror [11]. The signal can be, e.g., incoming far-infrared thermal radiation emitted by the object of interest, or signal that carries important spectral information about the chemical composition of the environment. The research challenge is that such unprecedented NLO coupling scheme leads to changes in the set of coupled nonlinear propagation equations and boundary conditions compared to the standard ones known from the literature. This, in turn, results in dramatic changes in their solutions and in multiparameter dependencies of the operational properties of the proposed sensor. Two other schemes depicted in Fig. 10.2b, c offer different advantages and operational properties for nonlinear-optical sensing [20].

10.3 Coherent Nonlinear Optical Coupling of Ordinary and Backward Electromagnetic Waves in Spatially Dispersive Metamaterials

This section describes exciting unparallel avenues for nonlinear electromagnetics which can be open by the metamaterials where formation of BWs becomes possible due to specific spatial dispersion of their structural elements. Basic idea is as follows. As outlined above, according to currently commonly adopted concept, negative refractive index and associated backwardness of optical waves require negative permeability and therefore magnetism at optical frequencies. However, a different approach is possible [25, 26]. In a loss-free isotropic medium, energy flux $\mathbf{S}$ is directed along the group velocity $\mathbf{v_g}$: $\mathbf{S} = \mathbf{v_g}U$, $\mathbf{v_g} = \mathrm{grad}_{\mathbf{k}}\omega(\mathbf{k})$. Here, U is energy density attributed to EMW. It is seen that the group velocity may become directed *against* the wavevector depending on sign of dispersion $\partial\omega/\partial k$. Basically, negative dispersion can appear in fully dielectric materials with particular dispersion of its structural elements. This opens an entirely novel research and application avenue. In the next subsection, we show the possibility to engineer such dispersive medium that supports coexistence of both ordinary and BEMWs. An example of enhanced coherent energy exchange between ordinary fundamental EMW and its BW second harmonic is considered in a lossless NLO slab [13] in Sect. 10.3.2.

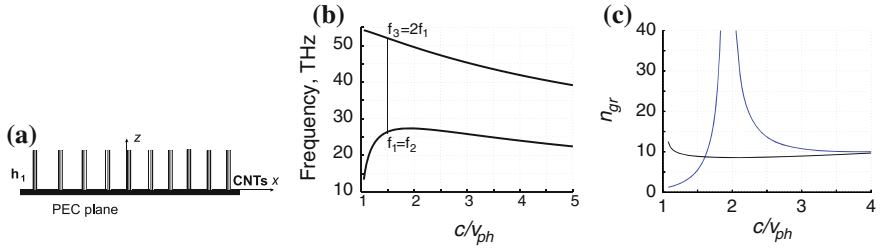

Fig. 10.3 **a** Geometry of free-standing CNTs. **b** Dispersion—the frequency versus slow-wave factor for the slab of CNTs with open ends. **c** Group delay factor versus the phase velocity slow-wave factor for the same modes as in panel (**b**). *Black (flat) curve* corresponds to the high-frequency mode, *blue curve* to the low-frequency mode. The tip of *blue curve* is cut. Its maximum corresponds to the stop-light regime

10.3.1 Carbon "Nanoforest" and Phase Matching of Ordinary Fundamental and Backward Second Harmonic Electromagnetic Waves

Appearance of BEM modes in nanoarrays and layered structures has been predicted recently in [27–29]. Obviously, many other options should have existed. Below, we propose such an option that seems promising in the context of nonlinear propagation and coherent energy conversion processes [21]. Namely, the possibility of conversion of ordinary EMW to the counter-propagating BEMW at its doubled frequency. Hence, such metaslab can be viewed as a frequency-doubling NLO metamirror [12, 16] that sends generated frequency towards the source of pump.

Figure 10.3a depicts a periodic array of carbon nanotubes (CNT) vertically standing on the surface of a perfect electric conductor (PEC) with the CNT ends open to air. As shown in [29], EM waves traveling through such CNT "nanoforest," along x or y directions, posses a hyperbolic dispersion and relatively low losses in the THz and mid-IR ranges. One of the most important consequences from the hyperbolic-type dispersion law is the possibility for propagation of both forward and backward EM waves. Consider EMW propagating along the x-axis. We also introduce group $n_{gr} = c/v_g$ and phase $n_{ph} = c/v_{ph}$ slow-wave factors. The latter one is refractive index. For the given case of surface waves propagating in the slab of CNTs with open ends, whose fields attenuate in air, the dispersion is given by [30]:

$$\tan(k_z h) = \sqrt{k_x^2 - k^2}/k_z. \tag{10.7}$$

Such a dependence can be understood from considering a planar waveguide formed by metal plate and air which is tampered by a CNT array. The array axis is orthogonal to the walls of the waveguide. Then, the propagation constant along

the waveguide is found as $k_\perp = \sqrt{\varepsilon_{zz}\left[k^2 - (m\pi/2h)^2\right]}$, where m is a positive integer, h is the height of the waveguide (CNT) and k is the wavenumber in free space [31]. If $\varepsilon_{zz} < 0$, BW propagation is allowed when $k < m\pi/2h$ and forbidden for $k > m\pi/2h$. The relation between the wavevector component k_x and wavenumber k is: $k_x^2 = [(k^2 - k_p^2)(k^2 - k_z^2)]/k^2$, where $k_z = m\pi/(2h)$, m is the integer determining a number of field variations along CNT, k_p is plasma wavevector. One can show that $\mathrm{d}k_\perp^2/\mathrm{d}k^2 < 0$, if $k_z/k > 1$ and $k_p/k > 1$.

Numerical analysis of (10.7) is depicted in Fig. 10.3b for the case of CNT radius $r = 0.82\,\mathrm{nm}$, the lattice period $d = 15\,\mathrm{nm}$ and EM modes with $m = 1$ and m=3. Slow-wave factor is proportional to the wave vector: $c/v_{ph} = k(\omega)/k_0$, where k_0 is the wave vector in the vacuum. The appearance of positive dispersion for small slow-wave factors is caused by interaction of BW in the CNT slab with the plane wave in air. Indeed, coexistence of the positive (ascending dependence) and negative (descending dependence) dispersion for different frequencies proves that such a metamaterial supports both ordinary and *backward* EMWs. It also proves that resonant plasmonic structures, like split-ring resonators, exhibiting negative ε and μ are *not* the necessary requirement for the realization of BW regime in the given mid-IR range. The possibility of considerably increased bandwidth of BEMW compared to most plasmonic MM made of nanoscopic resonators is seen that gives the ground to consider CNT arrays as a promising *perfect backward-wave metamaterial*. The slow-wave factor for both modes is shown in Fig. 10.3c. The magnitude of n_{gr} goes to infinity at $n_{ph} \approx 1.85$, which indicates the stop-light regime for the low-frequency mode. Particularly, Fig. 10.3b shows the possibility of *phase matching* of ordinary fundamental and backward second harmonic EMWs.

10.3.2 Coherent Energy Exchange Between Short Counter-Propagating Pulses of Fundamental Radiation and Its Second Harmonic

Here, we demonstrate unusual dependence of pulse shape and overall efficiency of SHG on the ratio of input fundamental pulse length and metamaterial slab thickness [13, 21]. This allows for shaping of the transmitted and generated counter-propagating pulses. Consider a frequency double-domain positive/negative index slab of thickness L that supports ordinary EMW at fundamental frequency (FF) and BEMW at SH frequency. To ensure phase matching, wavevectors of FF radiation and its SH must be co-directed and, hence, their energy fluxes - counter-directed. The slab operates as a *frequency up-converting nonlinear-optical mirror* with controllable reflectivity [1, 11]. The equations for amplitudes at FF, a_1, and of SH, a_2, can be written as

$$\frac{1}{v_1}\frac{\partial a_1}{\partial t} + \frac{\partial a_1}{\partial z} = -i2ga_1^* a_2 \exp(i\Delta kz) - \frac{\alpha_1}{2}a_1, \tag{10.8}$$

$$-\frac{1}{v_2}\frac{\partial a_2}{\partial t} + \frac{\partial a_2}{\partial z} = iga_1^2 \exp(-i\Delta kz) + \frac{\alpha_2}{2}a_2. \tag{10.9}$$

Here, $|a_{1,2}|^2$ are slowly varying amplitudes proportional to the instant photon numbers in the energy fluxes, $\alpha_{1,2}$ are absorption indices, $\Delta k = k_2 - 2k_1$ is phase mismatch, and v_i are the group velocities for the corresponding pulses. Note opposite signs in the equations and the requirement of the boundary conditions to be set at the opposite edges of the slab for the FF wave and SH. These lead to cardinal changes in the solutions to the equations as compared to those in the ordinary nonlinear optical material. We have chosen the input pulse shape as being close to a rectangular form

$$F(\tau) = 0.5\left(\tanh\frac{\tau_0 + 1 - \tau}{\delta\tau} - \tanh\frac{\tau_0 - \tau}{\delta\tau}\right), \tag{10.10}$$

where $\delta\tau$ is the duration of the front and tail, and τ_0 is the shift of the front relative to $t = 0$. All quantities are reduced by the pulse duration $\Delta\tau$. The magnitudes $\delta\tau = 0.01$ and $\tau_0 = 0.5$ have been selected for numerical simulations.

Unusual properties of BWSHG in NIMs in the pulsed regime stem from the fact that it occurs only inside the traveling pulse at FF. SHG begins on its leading edge, grows towards the back edge, and then exits the pulse with no further changes. Since the FF pulse propagates across the slab, the duration of the SH pulse is longer than the fundamental one. Depletion of the FF radiation along the pulse length and the conversion efficiency depend on its initial maximum intensity and phase matching. Ultimately, the overall properties of SHG, such as the pulse length, and the photon conversion efficiency, appear dependent on the ratio of the FF pulse and slab lengths. Such an extraordinary behavior is illustrated in Fig. 10.4a–d for an ultimate case of loss-free material. Here, d is the slab thickness reduced by the input pulse length, $d = L/v_1\Delta\tau$, g is proportional to product of nonlinear susceptibility $\chi^{(2)}$ and the input amplitude of the fundamental radiation. A rectangular shape of the input FF pulse $T_1 = |a_1(z)|^2/|a_{10}|^2$ is depicted at $z = 0$ when its leading front enters the medium. The results of numerical simulations for the output FF pulse, when its tail passes the slab's edge at $z = L$, as well as for the shape and conversion efficiency of the output SH pulse, $\eta_2 = |a_2(z)|^2/|a_{10}|^2$, when its tail passes the slab's edge at $z = 0$, are shown. For clarity, here, the medium is assumed loss-free, group velocities of the fundamental and SH pulses assumed equal, $\Delta k = 0$.

Panels (a) and (b) correspond to the fundamental pulse four time shorter than the slab thickness. Increase of the conversion efficiency with increase of the intensity of the input pulse is seen. It is followed by shortening of the SH pulse. The outlined properties satisfy the conservation law: the number of annihilated pairs of photons of FF radiation $(S_{10} - S_{1L})/2$ is equal to the number of output SH photons S_{20}. Panels (c) and (d) display corresponding changes for a longer input pulse with the length equal to the slab thickness. Here, larger conversion efficiency can be achieved at a lower input intensity compared with the preceding case because of the longer

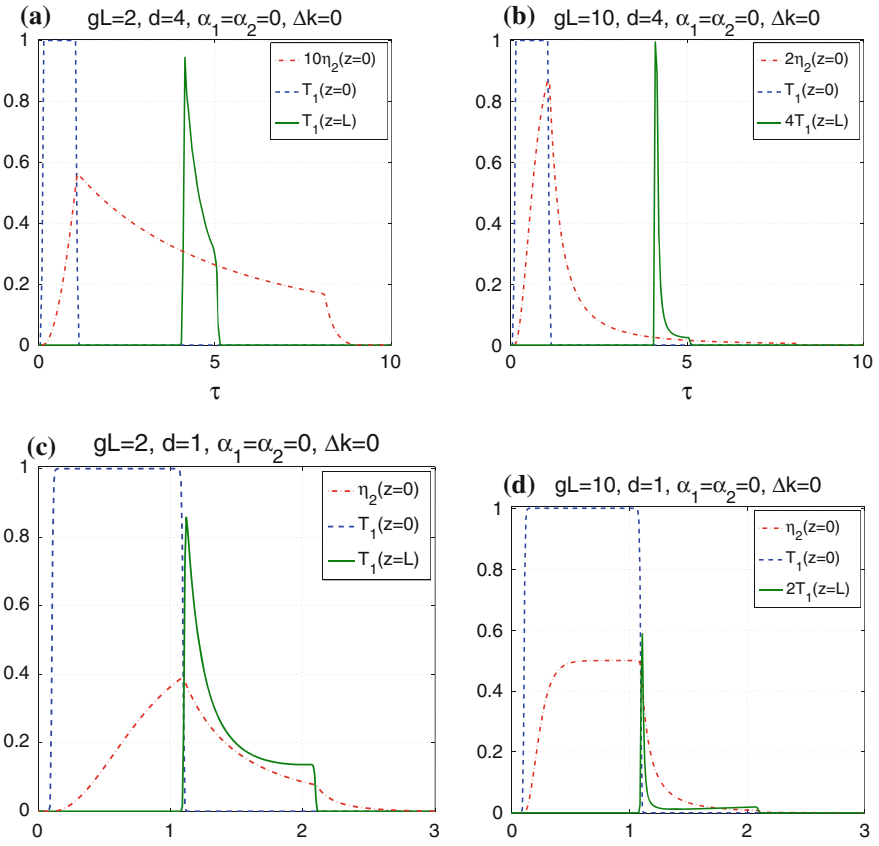

Fig. 10.4 Input, $T_1(z=0)$, and output, $T_1(z=L)$, pulses of fundamental and negative-index SH radiation, $\eta_2(z=0)$. **a** and **b**—short pulse: d = 4. **c** and **d**: longer pulse: d = 1. **b** and **d**—input power is 25 times larger than in (**a**) and (**c**). **a** Input pulse area (energy) $S_{10} = 0.9750$; output pulse areas (energy) $S_{1L} = 0.5031$, $S_{20} = 0.2392$. **b** Input pulse energy $S_{10} = 0.9750$; output pulse energy $S_{1L} = 0.0396$, $S_{20} = 0.4742$. **c** Input pulse energy $S_{10} = 0.9900$; output pulse energy $S_{1L} = 0.2516$, $S_{20} = 0.3692$. **d** Input pulse energy $S_{10} = 0.9900$; output pulse energy $S_{1L} = 0.0161$, $S_{20} = 0.4870$. Notations are defined in the text

conversion length. The changes in the SH pulse length and conversion efficiency with increase of input intensity appear less significant. Figure 10.4a–d display remarkable changes in the widths and shapes of counter-propagating pulses and corresponding possibilities to tailor their properties.

10.4 Mimicking Nonlinear Optics of Backward-Waves in Fully Dielectric Materials: Enhancing Coherent Energy Transfer Between Electromagnetic Waves in Ordinary Crystals by Coupling with Optical Phonons with Negative Phase Velocity

As described, NLO with backward *electromagnetic* waves enables a great enhancement of energy-conversion rate at the otherwise equal nonlinearities and intensities of input waves. Herein, we propose fundamentally different scheme of TWM of ordinary and BWs. It builds on the stimulated Raman scattering (SRS) where two ordinary EM waves excite backward elastic vibrational wave in a crystal, which results in TWM. The possibility of such BWs was predicted by L.I. Mandelstam in 1945 [32], who also had pointed out that negative refraction is a general property of the BWs. The idea underlying the proposed concept and its basic justification is described below. The goal is to show the possibility to replace the NI plasmonic composites, which are challenging to fabricate, with readily available ordinary crystals. Raman nonlinearities in some of such crystals have been already extensively studied. Thus the proposed approach allows to mimic the unparallel properties of coherent NLO energy exchange between the ordinary and BW. In [33], SRS on optical phonon was investigated in continuous wave regime. The possibility of distributed-feedback type resonance enhancement of amplification has been shown that stem from negative dispersion of elastic waves. The effect appeared similar to that in TWM of ordinary and BEMWs in NIMs, provided that special requirements are met. Yet, the required intensity of the fundamental field was found to be close to the optical breakdown threshold due to the high phonon damping rate. Here, we show that the indicated fundamental formidable obstacle can be removed by making use of *short pulses*, which opens the possibility to *mimic* TWM processes attributed to NIMs in readily available crystals. Besides that, we show that such mixing exhibits unparallel properties that allow for tailoring the shapes of the generated and transmitted pulses and for huge enhancement of the frequency conversion efficiency.

Typical dispersion curve $\omega(k)$ for optical phonons, which exist in crystals containing more than one atom per unit cell, is depicted in Fig. 10.5. The dispersion is negative in the range from zero to the boundary of the first Brillouin's zone. Hence, the group velocity of such phonons $\mathbf{v_v}$ is antiparallel with respect to its wave-vector $\mathbf{k}_v$. Such dispersion, which is determined by the spatial distribution of atoms at the nanoscale, can be approximated as [38] $\omega_v = \sqrt{\omega_0^2 - \beta k_v^2}$. Then, in the vicinity of $k_v = 0$, velocity v_v^{gr} is given by $v_v^{gr} = -\beta k_v/\omega_v = -\beta/v_v^{ph}$, where v_v^{ph} is the projection of the phase velocity of the vibrational wave on the z-axis and β is the dispersion parameter for the given crystal. Optical elastic vibrations can be excited by the light waves through the Raman scattering. The latter gives the ground to consider such a crystal as the analog of the medium with negative refractive index at the phonon frequency and to employ the processes of parametric interaction of three waves, two of which are ordinary EM waves and the third one is the backward wave of elastic

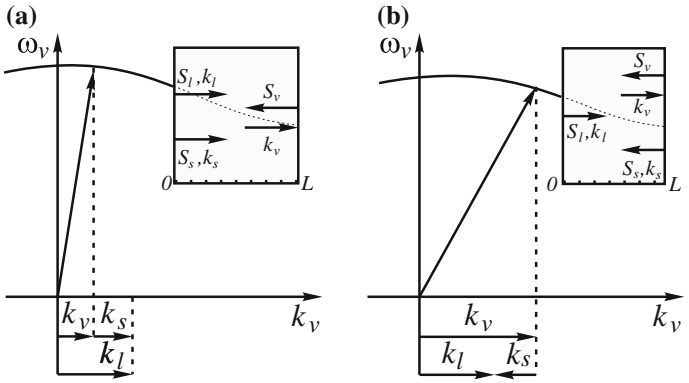

Fig. 10.5 Negative dispersion of optical phonons and two phase matching options for long- short-wave vibrations: **a**—co-propagating, **b**—counter-propagating fundamental (control) and Stokes (signal) waves. Insets: relative directions of the energy flows and the wave-vectors

vibrations. The coupled waves are described by the equations

$$E_{l,s} = (1/2)\mathscr{E}_{l,s}(z,t)e^{ik_{l,s}z - i\omega_{l,s}t} + c.c., \tag{10.11}$$

$$Q_v = (1/2)Q(z,t)e^{ik_v z - i\omega_v t} + c.c. \tag{10.12}$$

Here, $\mathscr{E}_{l,s}$, Q, $\omega_{l,s,v}$ and $k_{l,s,v}$ are the amplitudes, frequencies and wave-vectors of the fundamental, Stokes and vibrational waves; $Q_v(z,t) = \sqrt{\rho}x(z,t)$; x is displacement of the vibrating particles, ρ is the medium density and the requirements $\omega_l = \omega_s + \omega_v\,(k_v)$, $\mathbf{k}_l = \mathbf{k}_s + \mathbf{k}_v$ are supposed to be met. Partial differential equations for the slowly varying amplitudes in the approximation of the first order of Q in the polarization expansion are:

$$\frac{\partial \mathscr{E}_l}{\partial z} + \frac{1}{v_l}\frac{\partial \mathscr{E}_l}{\partial t} = i\frac{\pi\omega_l^2}{k_l c^2}N\frac{\partial \alpha}{\partial Q}\mathscr{E}_s Q \tag{10.13}$$

$$\frac{\partial \mathscr{E}_s}{\partial z} + \frac{1}{v_s}\frac{\partial \mathscr{E}_s}{\partial t} = i\frac{\pi\omega_s^2}{k_s c^2}N\frac{\partial \alpha}{\partial Q}\mathscr{E}_l Q^* \tag{10.14}$$

$$\frac{\partial Q}{\partial z} - \frac{1}{v_v}\frac{\partial Q}{\partial t} - \frac{Q}{v_v \tau_v} = -i\frac{1}{4\omega_v v_v}N\frac{\partial \alpha}{\partial Q}\mathscr{E}_l\mathscr{E}_s^*. \tag{10.15}$$

Here, $v_{l,s}$ and $-v_v$ are projections of the group velocities of the fundamental, Stokes and vibration waves on the z-axis, N is the number density of the vibrating molecules, α is the molecule polarizability, τ_v is phonon lifetime. Equations (10.13)–(10.15) are similar to those describing TWM of counter-propagating waves in NIMs for the phase-matching sch eme of co-propagating fundamental and Stokes waves, where vibration wave counter-directed to the Stokes wave, which is depicted in Fig. 10.5a. In the case of continuous waves and neglected depletion of the fundamental wave, resonance enhancement becomes possible, similar to that, depicted in Fig. 10.1.

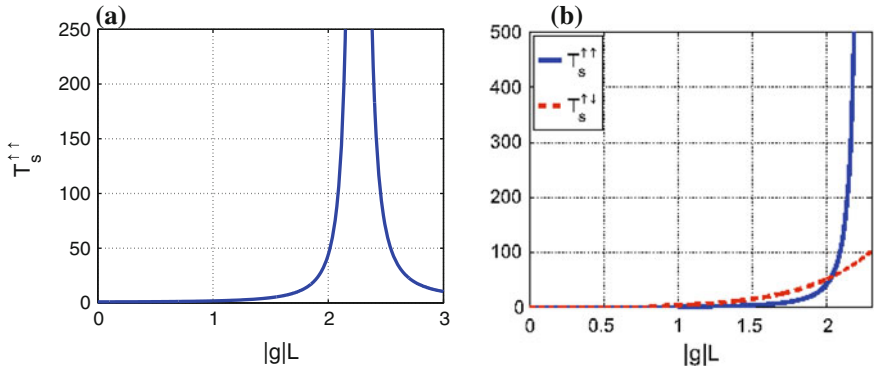

Fig. 10.6 **a** Transmission (amplification) of the Stokes wave $T_s^{\uparrow\uparrow}(z = L)$ versus intensity of the fundamental control field in the vicinity of first "geometrical" resonance (co-propagating E_l and E_s geometry, Fig. 10.5a). $g = \sqrt{g_v^* g_s}$, L is thickness of the slab. Such extraordinary resonance appears because of backwardness of the coupled vibration wave and opposite direction of propagation for the Stokes and phonon waves. **b** Comparison of the output intensities of the Stokes wave versus intensity of the control field for co- (*the blue, solid line*) and counter-propagating (*the red, dashed line*) fundamental (control) and signal (Stokes) waves (coupling geometries depicted in Fig. 10.5a, b respectively)

On the contrary, only standard exponential behavior is possible in the case of Fig. 10.5b. Corresponding transmission factors in the vicinity of first "geometrical" resonance are shown in Fig. 10.6. In the resonance, $T_s^{\uparrow\uparrow} \to \infty$, which is due to the approximation of constant control field. Conversion of the control field to the Stokes one and to excited molecule vibrations would lead to saturation of the control field which limits the maximum achievable amplification. Strong amplification in the maximums indicates the possibility of *unidirectional* amplification self-oscillations and thus creation of *mirrorless* optical parametrical Raman oscillator with unparalleled properties. Figure 10.6a, b indicate the possibility to *fit* the effective conversion length within the crystal of a given thickness and to *concentrate* the generated Stokes field nearby its output facet. Such atypical extraordinary behavior in readily available crystals may find exciting applications. However, the estimates have shown that intensity of the fundamental field which is to attain such extraordinary amplification appears close to the optical breakdown threshold [33]. It is because of fast phonon damping and corresponding high rate of energy conversion of the fundamental beam in heat.

Below, we show that such seemingly unavoidable obstacles can be overcome in short pulse regime. For the sake of simplicity, we consider model of a rectangular pulse of input fundamental radiation with the pulse duration $\tau_p \ll \tau_v$. A seeding Stokes wave is assumed a weak continuous wave. In the moving coordinate frame associated with this pulse and within its range, complex amplitudes of two other interacting fields become time independent. Then the analytical solution to the equations can be found for amplification corresponding to negligible depletion of the pump

due to the conversion. Numerical solution is found for the opposite case. Inside the crystal, the boundary conditions must be fulfilled not at the boundaries of the medium but at the boundaries of the fundamental pulse. The latter is correct for the period of time after the instant when the generated Stokes and vibration pulses reach the boundaries of the fundamental pulse. Such approximation becomes true after travelling a distance $l > L^{\max}$, where $L^{\max} = \max\{L^s, L^v\}$, $L^s = l_p v_l/|v_s - v_l|$ and $L^{s,v} = l_p v_l/(v_l + v_v)$, $l_p = \tau_p v_l$ is length of the fundamental pulse. Hereinafter, the waves are referred to as co-propagating if the Poynting vector of the Stokes wave is co-directed with that of fundamental wave (Fig. 10.5a), and as counter-propagating in the opposite case (Fig. 10.5b). Note, that v_s is negative for counter-propagating Stokes wave.

In the approximation of constant pump amplitude and in the coordinate frame locked to the pump pulse, equations for the generated Stokes and backward vibration waves inside the pulse take the form:

$$dQ/d\xi = -ig_v\mathscr{E}_s^* + QK_v/l_v, \quad d\mathscr{E}_s/d\xi = ig_s Q^*. \tag{10.16}$$

Here, $\xi = z - v_l^{gr}t$, $g_v = K_v N(d\alpha/dQ)\mathscr{E}_l/(4\omega_v v_v)$, $l_v = \tau_v v_v$ is the phonon mean free path, $K_v = v_v/(v_l + v_v)$, $g_s = K_s N(d\alpha/dQ)\mathscr{E}_l\pi\omega_s^2/(k_s c^2)$, $K_s = v_s/(v_s - v_l)$; $v_s, k_s > 0$ for co-propagating and $v_s, k_s < 0$ for counter-propagating beams. Since the Stokes frequency is less than that of the fundamental one, $v_s > v_l$ and $v_l \gg v_v$. Equation (10.16) are similar to those describing CW TWM [33] except the boundary conditions. They correctly describe possible huge amplification of the Stokes signal until relatively small part of the strong input laser beam is converted. For co-directed laser and Stokes waves, the boundary conditions are:

$$\mathscr{E}_s(\xi = 0) = \mathscr{E}_s^0, \quad Q(\xi = l_p) = 0. \tag{10.17}$$

In the opposite case, they are written as

$$\mathscr{E}_s(\xi = l_p) = \mathscr{E}_s^{l_p}, \quad Q(\xi = l_p) = 0. \tag{10.18}$$

The analysis of solution to (10.16) shows that, in the given approximation of neglected depletion of the fundamental wave, amplification of *co-directed* signal tends to infinity, when the pulse energy approaches the *resonance* value corresponding to $gl_p = \pi/2$, where $g = \sqrt{g_v^* g_s}$. This indicates the possibility of *huge enhancement* of the conversion efficiency. Respective intensity of the fundamental field $I_{\min}^p$ is given by the equation

$$I_{\min}^p = \frac{K_v}{K_s}\frac{cn_s\lambda_{s0}\omega_v}{16\pi^3 v_v\tau_v^2}\left|N\frac{\partial\alpha}{\partial Q}\right|^{-2}, \tag{10.19}$$

where, n_s is refractive index at ω_v and λ_{s0} is the wavelength in vacuum. From comparison with the corresponding value $I_{\min}$ for the CW regime [33], one concludes

$$\frac{I^p_{\min}}{I_{\min}} = \frac{K_v}{K_s} \approx \frac{v_v}{v_l}\frac{v_s - v_l}{v_s}. \tag{10.20}$$

For the crystal parameters, which are characteristic for calcite [34] and diamond [35–37], (10.20) yields $I^p_{\min}/I_{\min} \approx 10^{-11}$ and, hence, suggests a decreases of $I^p_{\min}$ down to $I^p_{\min} \sim 10^7$ W/cm^2. The latter is achievable with commercial femtosecond lasers and falls below the optical breakdown threshold for most transparent crystals.

Equation (10.20) displays two factors that determine substantial decrease of $I^p_{\min}$ in pulsed regime compared to that in CW one. First factor is the ratio of phonon to fundamental group velocity v_v/v_l, which is on the order of $\sim 10^{-8}$. This factor is attributed to the fact that phonons generated on the front edge of the laser pulse propagate in the opposite direction and, hence, exit very fast from the fundamental pulse zone, practically with the optical group velocity. Hence, effective phonon mean free pass becomes commensurable with the fundamental pulse length. This mitigates the detrimental effect of phonon damping. The second factor in (10.20) determines further decrease of $I^p_{\min}$ due to small optical dispersion in the transparency region of the crystals. Hence, Stokes pulse surpasses the fundamental one slowly, which significantly increases the effective NLO coupling length.

To investigate the regimes of significant energy conversion, a set of partial differential (10.13)–(10.15) was solved numerically in three steps: TWM in the vicinity of the entrance, inside and in the vicinity of the exit from the Raman slab. Simulations for the first and third intervals were made in the laboratory reference frame with the boundary conditions applied to the corresponding edges of the slab. The propagation process inside the slab was simulated in the moving frame of reference with the boundary conditions applied to the pulse edges. Such an approach allowed for significant reduction of the computation time because, for each given instant, the integration was required only through the space interval inside the fundamental pulse and not through the entire medium. Shape of the fundamental pulse was chosen nearly rectangular and symmetric with respect to its center

$$\mathscr{E}_l = \frac{1}{2}\mathscr{E}^0_l\{\tanh[(t_0 + t_p - t)/t_f] - \tanh[(t_0 - t)/t_f]\}.$$

The slope $t_f = 0.1$, the pulse duration at half-maximum $t_p = 1$ and its delay $t_0 = 0.6$ were scaled to the fundamental pulse width τ_p. The amplitude of input CW Stokes signal was chosen $\mathscr{E}^0_s = 10^{-5}\mathscr{E}^0_l$. Numerical investigations were done for the model with parameters typical for calcite [34] and diamond [35–37]: carrying wavelength $\lambda_l = 800$ nm, pulse duration $\tau_p = 60$ fs, $\omega_v = 1332\,\text{cm}^{-1}$, $\tau_v = 7\,ps$, $v_l = 1.228 \cdot 10^{10}$ cm/s, $v_s = 1.234 \cdot 10^{10}$ cm/s, $v_v = 100$ cm/s for co-propagating and $v_v = 2000$ cm/s for counter-propagating waves, $Nd\alpha/dQ = 3.78 \cdot 10^7\,(\text{g/cm})^{1/2}$, the crystal length L = 1 cm.

Figure 10.7a displays the output quantum conversion efficiency $\eta_q = (\omega_l/\omega_s) \cdot \int_t I_s(z,t)dt / \int_t I_l(z=0,t)dt$ versus input pulse intensity, both for co-propagating ($z = L$) and counter-propagating ($z = 0$) geometries. Many orders increase of

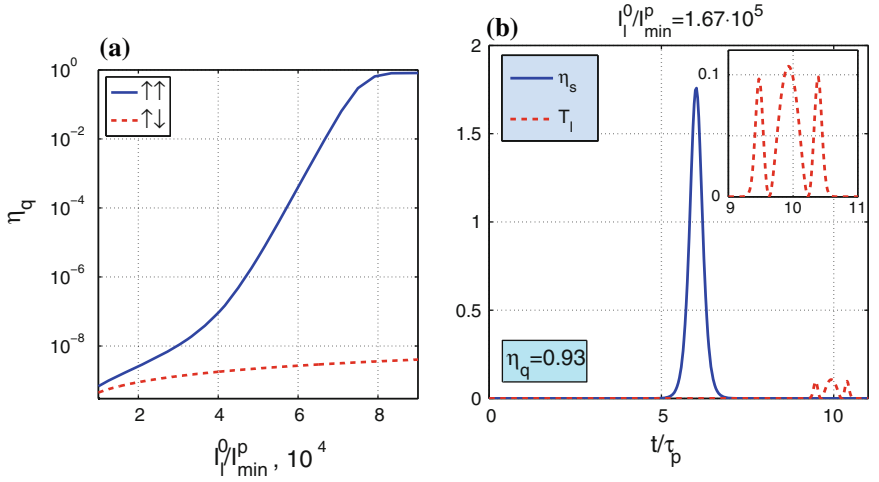

Fig. 10.7 **a** Conversion efficiency versus intensity of the input pump for co-propagating (*solid line*) and counter-propagating (*dash line*) geometries. **b** Output Stokes (*solid line*) and fundamental (*dash line*) pulses for co-propagating coupling

the conversion efficiency due to BW effect in the case of co-propagating waves is explicitly seen. Saturation at $I_l^0/I_{min}^p > 7 \cdot 10^4$ is due to depletion of fundamental radiation caused by conversion to Stokes radiation. Figure 10.7b displays a shortened Stokes output pulse that has surpassed the inhomogeneously depleted and broadened fundamental pulse (zoomed in the inset). The simulations also show that shapes of the output Stokes and fundamental pulses differ and vary significantly depending on the intensity of the input fundamental wave. Figure 10.8a depicts amplified output pulse $T_s = \left|\mathscr{E}_s(L,t)/\mathscr{E}_s^0\right|^2$ of Stokes radiation for relatively small depletion due to conversion of the fundamental beam. Here, shape of the fundamental pulse is unchanged. The shape of the amplified Stokes pulse is different and determined by the fact that $v_s > v_l$ and Stokes pulse has surpassed the fundamental one. In contrast, the quantum conversion becomes significant in Fig. 10.8b–d. Corresponding depletion of the output fundamental pulse and changes in its shape are explicitly seen. Note that in the case depicted in Fig. 10.8d, the output Stokes pulse significantly overtakes the pump pulse. In the latter case, major conversion occurred inside, far from the crystal edges, and then both pulses propagated without interaction. It is seen that output Stokes pulse narrows with the increase of energy of the fundamental pulse. Here, crystal length of 1 cm fits $L/l_p = 1357$ input pulse lengths. The threshold intensity $I_{min}^p = 6 \cdot 10^6\,\mathrm{W/cm^2}$ corresponds to 60 fs pulse of about 5 μJ energy focused to the spot of diameter D = 100 μm. Intensity of the seeding Stokes signal was chosen $I_s^0/I_l^0 = 10^{-10}$.

Note, that the described NLO propagation process is in a striking contrast with its positive group velocity counterparts [38, 39], including acoustic waves with energy

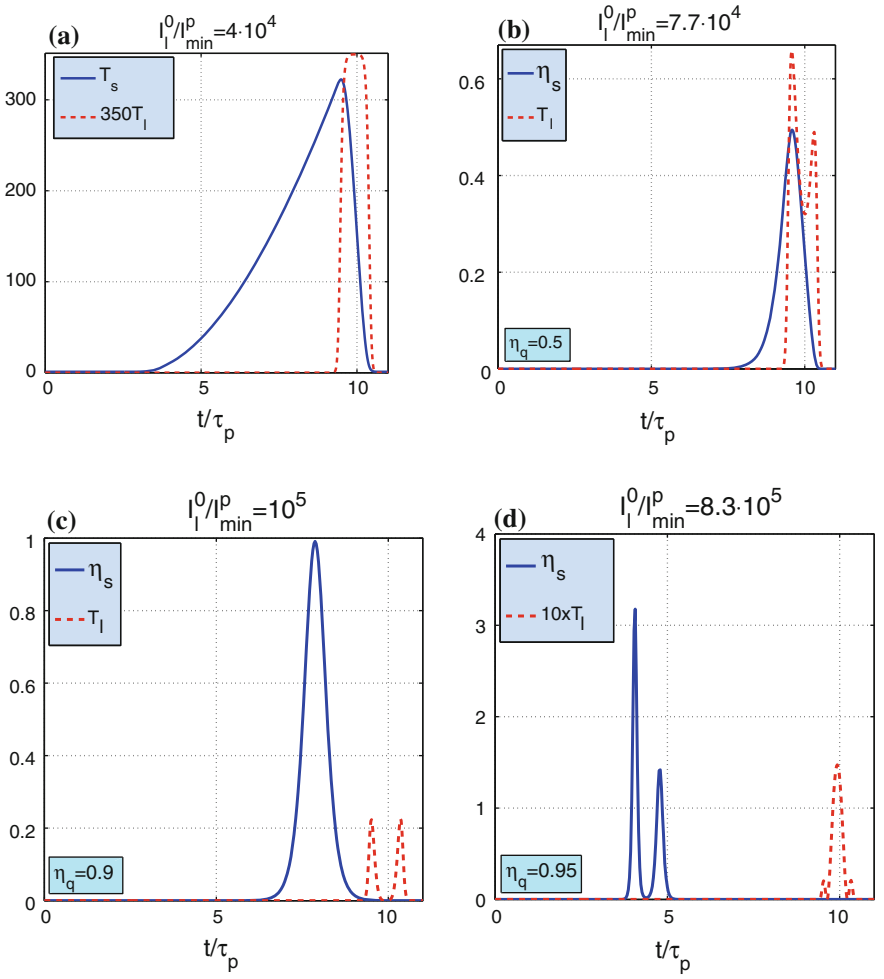

Fig. 10.8 Changes in the shapes of generated Stokes (*solid line*) and transmitted fundamental (*dash line*) output co-propagating pulses with the increase of energy of the input fundamental pulse. η_q is corresponding conversion efficiency. **a** small, **b–d** significant depletion of the fundamental pulse

fluxes directed against that of EM waves [40]. The proposed here concept is also different from the one earlier proposed in [23] and does not require periodic poling of quadratic nonlinear susceptibility of crystals at the nanoscale as proposed in [41] (and the references therein). The described possibility could supplement and extend the recent breakthrough in modeling NLO processes with BWs in the microwave range [42, 43].

10.5 Conclusions

Extraordinary nonlinear optical propagation processes in frequency double-domain materials with co- and counter-directed phase and group velocities are described. Exciting possibilities of manipulating light through controllable resonantly enhanced transparency, amplification, reflectivity and frequency conversion are shown. Unusual resonance dependence on the product of intensity of the fundamental (control) radiation, nonlinear susceptibility and the material slab thickness is demonstrated. Unparallel properties of frequency conversion and energy exchange between counter-propagating short pulses are described.

Two different classes of novel photonic materials are proposed: metamaterials with deliberately engineered spatial dispersion of its structural elements at the nanoscale and crystals that support optical phonons with negative phase velocity. Both options do not rely on crafting the nanoresonators that provide negative optical magnetism and thus constitute current mainstream in fabricating negative index metamaterials. Extraordinary properties of coherent frequency conversion processes in the proposed materials are numerically simulated both in continuous wave and in short pulse regimes.

As an example of dispersion engineering, a metamaterial made of standing carbon nanotubes is described which supports coexistence of ordinary fundamental and backward second harmonic electromagnetic waves that can be phase matched. Unparallel properties of such frequency-doubling metamirror operating in short-pulse regime appear in striking contrasts with second harmonic generation in ordinary materials.

The possibility to mimic plasmonic negative-index metamaterials with readily available Raman active crystals is described. In addition, such approach allows to circumvent the challenge of engineering of a strong fast quadratic NLO response by the plasmonic mesoatoms. Here, optical phonons, the elastic waves with negative group velocity, replace the negative index electromagnetic waves in the process of three-wave mixing through stimulated Raman scattering. The possibility to remove a severe detrimental factor imposed by fast phonon damping in short pulse regime is demonstrated. Consequently, significant decrease of the required minimum intensity of fundamental radiation, as compared with that in the continuous-wave regime, is predicted down to commercial lasers. Unparallel properties of the unidirectional short-pulse process are numerically simulated and the possibility of huge enhancement of quantum conversion efficiency as well as of tailoring the durations and the shapes of the generated and transmitted fundamental pulses is shown.

Further elaboration of the proposed paradigms offers the potential for creation of a family of unique photonic devices with advanced functional properties such as nonlinear-optical mirrors with frequency-dependent controllable reflectivity, unidirectional optical amplifiers, frequency narrow band filters, switches and cavity-free optical parametric oscillators, which can be exploited for optical sensing. There exist many dispersive materials and readily available Raman-active transparent crystals that support electromagnetic and elastic waves with negative group velocity and,

hence, hold promise to be exploited for the given purpose. Some of them may offer the opportunities for further optimization of unparallel operational characteristics of the proposed photonic devices.

Acknowledgments This work was supported in parts by the Air Force Office of Scientific Research (Grant FA9550-12-1-0298) and by the National Science Foundation (Grant ECCS-1346547). The author is grateful to V. Shalaev, V. Slabko, S. Myslivets, I. Nefedov and M. Shalaev for collaboration, inspiring discussions and help with numerical simulations concerning different parts of this work.

References

1. A.K. Popov, V.M. Shalaev, Negative-index metamaterials: second-harmonic generation, Manley Rowe relations and parametric amplification. Appl. Phys. B: Lasers Opt. **84**, 131–137 (2006)
2. A.K. Popov, V.M. Shalaev, Compensating losses in negative-index metamaterials by optical parametric amplification. Opt. Lett. **31**, 2169–2171 (2006)
3. A.K. Popov, S.A. Myslivets, T.F. George, V.M. Shalaev, Four-wave mixing, quantum control, and compensating losses in doped negative-index photonic metamaterials. Opt. Lett. **32**, 3044–3046 (2007)
4. A.K. Popov, S.A. Myslivets, Transformable broad-band transparency and amplification in negative-index films. Appl. Phys. Lett. **93**(19), 191117(3) (2008)
5. A.K. Popov, S.A. Myslivets, V.M. Shalaev, Resonant nonlinear optics of backward waves in negative-index metamaterials. Appl. Phys. B: Lasers Opt. **96**, 315–323 (2009)
6. A.K. Popov, S.A. Myslivets, V.M. Shalaev, Microscopic mirrorless negative-index optical parametric oscillator. Opt. Lett. **34**(8), 1165–1167 (2009)
7. A.K. Popov, S.A. Myslivets, V.M. Shalaev, Plasmonics: nonlinear optics, negative phase and transformable transparency (Invited Paper), ed. by S. Kawata, V. M. Shalaev, D. P. Tsai, in *P*lasmonics: Nanoimaging, Nanofabrication, and their Applications V, in Proc. SPIE **7395**, 73950Z–1(12) (2009). doi:10.1117/12.824836
8. A.K. Popov, S.A. Myslivets, V.M. Shalaev, Coherent nonlinear optics and quantum control in negative-index metamaterials. J. Opt. A: Pure Appl. Opt. **11**, 114028(13) (2009)
9. A.K. Popov, S.A. Myslivets, Numerical simulations of negative-index nanocomposites and backward-wave photonic microdevices, in *ICMS 2010: International Conference on Modeling and Simulation, Proceedings of WASET* **37**, International Science Index 4, No 1, pp. 1133–1147 (2010). http://waset.org/publications/12065
10. A. K. Popov, T. F. George, Computational studies of tailored negative-index metamaterials and microdevices, ed. by T. F. George, D. Jelski, R. R. Letfullin, G. Zhang, *Computational Studies of New Materials II: From Ultrafast Processes and Nanostructures to Optoelectronics, Energy Storage and Nanomedicine,* World Scientific, Singapore (2011)
11. A.K. Popov, S.A. Myslivets, Nonlinear-optical metamirror. Appl. Phys. A: Mater. Sci. Process. **103**, 725–729 (2011). doi:10.1007/s00339-010-6218-7
12. A. K. Popov, Nonlinear optics of backward waves and extraordinary features of plasmonic nonlinear-optical microdevices. Eur. Phys. J. D **58**, 263–274 (2010) (topical issue on Laser Dynamics and Nonlinear Photonics)
13. A.K. Popov, V.M. Shalaev, Merging nonlinear optics and negative-index metamaterials. Proc. SPIE **8093–06**, 1–27 (2011). doi:10.1117/12.824836
14. I.V. Shadrivov, A.A. Zharov, YuS Kivshar, Second-harmonic generation in nonlinear left-handed metamaterials. J. Opt. Soc. Am. B **23**, 529–534 (2006)
15. M. Scalora, G. D'Aguanno, M. Bloemer, M. Centini, N. Mattiucci, D. de Ceglia, YuS Kivshar, Dynamics of short pulses and phase matched second harmonic generation in negative index materials. Opt. Express **14**, 4746–4756 (2006)

16. A.K. Popov, V.V. Slabko, V.M. Shalaev, Second harmonic generation in left-handed metamaterials. Laser Phys. Lett. **3**, 293–296 (2006)
17. A.I. Maimistov, I.R. Gabitov, E.V. Kazantseva, Quadratic solitons in media with negative refractive index. Opt. Spectrosc. **102**, 90–97 (2007)
18. A.I. Maimistov, I.R. Gabitov, Nonlinear optical effects in artificial materials. Eur. Phys. J. Special Topics **147**, 265–286 (2007)
19. S.O. Elyutin, A.I. Maimistov, I.R. Gabitov, On the third harmonic generation in a medium with negative pump wave refraction. JETP **111**, 157–169 (2010)
20. A. K. Popov, Frequency-tunable nonlinear-optical negative-index metamirror for sensing applications, in Proc. SPIE **8034**, Photonic Microdevices/Microstructures for Sensing III, 80340L (2011), doi:10.1117/12.884127
21. A.K. Popov, M.I. Shalaev, S.A. Myslivets, V.V. Slabko, I.S. Nefedov, Enhancing coherent nonlinear-optical processes in nonmagnetic backward-wave materials. Appl. Phys. A: Mat. Sci. Process. **109**, 835–840 (2012)
22. A. Yariv, Quantum electronics, 2nd edn. (Wiley, New York, 1975), Ch. 18
23. S.E. Harris, Proposed backward wave oscillations in the infrared. Appl. Phys. Lett. **9**, 114–117 (1966)
24. K.I. Volyak, A.S. Gorshkov, Investigations of a reverse-wave parametric oscillator. Radiotekhnika i Elektronika (Radiotechnics and Electronics) **18**, 2075–2082 (1973)
25. V.M. Agranovich, Y.R. Shen, R.H. Baughman, A.A. Zakhidov, Linear and nonlinear wave propagation in negative refraction metamaterials. Phys.Rev. B **69**, 165112 (2004)
26. V. M. Agranovich, Yu. N. Gartstein, Spatial dispersion and negative refraction of light, Physics-Uspekhi (UFN) **176**, 1051–1068 (2006) (Also in Physics of Negative Refraction (Eds C.M. Krowne, Y. Zhang) (Springer, 2007)
27. I. Nefedov, S. Tretyakov, Ultrabroadband electromagnetically indefinite medium formed by aligned carbon nanotubes. Phys. Rev. B **84**, 113410–113414 (2011)
28. P. A. Belov, A. A. Orlov, A. V. Chebykin, Yu. S. Kivshar, Spatial dispersion in layered metamaterials, in *Proceedings of the International Conference on Electrodynamics of complex Materials for Advanced Technologies,* PLASMETA'11, September 21–26, Samarkand, Uzbekistan, pp. 30–31
29. I. S. Nefedov, Electromagnetic waves propagating in a periodic array of parallel metallic carbon nanotubes, Phys. Rev. B **82**, 155423(7) (2010)
30. I. S. Nefedov, S. A. Tretyakov, Effective medium model for two-dimensional periodic arrays of carbon nanotubes, in Photonics Nanostruct. Fundam. Appl. **9**, 374–380 (2011) (TaCoNa-Photonics 2010)
31. P.A. Belov, R. Marques, S.I. Maslovski, I.S. Nefedov, M. Silveirinha, C.R. Simovski, S.A. Tretyakov, Strong spatial dispersion in wire media in the very large wavelength limit. Phys. Rev. B **67**, 113103 (2003)
32. L.I. Mandelstam, Group velocity in a crystall lattice. ZhETF **15**, 475–478 (1945)
33. M.I. Shalaev, S.A. Myslivets, V.V. Slabko, A.K. Popov, Negative group velocity and three-wave mixing in dielectric crystals. Opt. Lett. **36**, 3861–3863 (2011)
34. R.R. Alfano, S.I. Shapiro, Optical phonon lifetime measured directly with picosecond pulses. Phys. Rev. Lett. **26**, 1247–1250 (1971)
35. V. S. Gorelik, *Contemporary problems of Raman spectroscopy*, Moscow, Nauka Publishing Co., 1978 (in Russian), pp. 28–47
36. E. Anastassakis, S. Iwasa, E. Burstein, Electric-field-induced infrared absorption in diamond. Phys. Rev. Lett. **17**, 1051–1054 (1966)
37. Y. Chen, J.D. Lee, Determining material constants in micromorphic theory through phonon dispersion relations. Int. J. Eng. Sci. **41**, 871–886 (2003)
38. Y.R. Shen, N. Bloembergen, Theory of stimulated brillouin and raman scattering. Phys. Rev. **137**, A1787–A1805 (1965)
39. R.W. Boyd, *Nonlinear Optics*, 3rd edn. (Academic Press, Amsterdam, 2008)
40. D.L. Bobroff, Coupled-modes analysis of the phonon-photon parametric backward-wave oscillator. J. Appl. Phys. **36**, 1760–1769 (1965)

41. J.B. Khurgin, Mirrorless magic. Nat. Photonics **1**, 446–448 (2007)
42. A. Rose, D. Huang, D.R. Smith, Controlling the second harmonic in a phase-matched negative-index metamaterial. Phys. Rev. Lett. **107**, 063902 (2011)
43. N.I. Zheludev, Y.S. Kivshar, From metamaterials to metadevices. Nat. Mater. **11**, 917–924 (2012)

Chapter 11
Tailoring Nonlinear Interactions in Metamaterials

Jinwei Zeng, Xi Wang, Mikhail I. Shalaev, Alexander N. Cartwright and Natalia M. Litchinitser

Abstract Recent progress in the field of metamaterials is likely to revolutionize both of the linear and nonlinear optics. The unique properties of metamaterials, including negative index of refraction, magnetism at optical frequencies, and anti-parallel phase and energy velocities were shown to fundamentally change many nonlinear light-matter interactions. In this chapter we discuss a number of unique nonlinear optical properties and novel applications such as backward phase-matched second-harmonic generation and four-wave mixing, entirely new classes of solitons such as plasmon polariton solitons and knotted solitons, reconfigurable nonlinear structures, including nonlinear cloaking devices, light concentrators, and light-tunable metamateria-based lenses, reflectors and beam-shapers.

11.1 Introduction

Metamaterials represent a group of synthetic materials where desirable material properties are engineered through the structure using meta-atoms. They have been the focus of significant research effort during the past decade that has resulted in the observation of a number of unique material properties that are not available in

J. Zeng (✉) · X. Wang · M.I. Shalaev · A.N. Cartwright · N.M. Litchinitser
University at Buffalo, The State University of New York, Buffalo, NY 14260, USA
e-mail: jzeng@buffalo.edu

X. Wang
e-mail: xw28@buffalo.edu

M.I. Shalaev
e-mail: mshalaev@buffalo.edu

A.N. Cartwright
e-mail: anc@buffalo.edu

N.M. Litchinitser
e-mail: natasha.litchinitser@gmail.com

I.V. Shadrivov et al. (eds.), *Nonlinear, Tunable and Active Metamaterials*,
Springer Series in Materials Science 200, DOI 10.1007/978-3-319-08386-5_11

naturally occurring materials [1, 2]. Much of the ability to realize these novel properties is due to the flexibility in design that is afforded by recent developments in nanofabrication. The impact of nanofabrication techniques on metamaterials research was clearly demonstrated through the first experimental realizations of negative index of refraction [3], a phenomena that was predicted over thirty years earlier by Veselago [4]. Moreover,there has been amazing progress in the development of optical metamaterials where a number of additional novel optical properties that do not occur in natural materials have been demonstrated. For example, the ability of a hyperlens to focus light beyond the diffraction limit has been explored by a number of groups [5–19] since they were first predicted by Narimanov [20]. Similarly, invisibility cloaking has received much attention since the initial demonstrations [21, 22]. In the context of nonlinear optics, the emergence of metamaterials necessitates the consideration of many, if not all, fundamental processes, including second harmonic generation (SHG), soliton propagation, four-wave mixing, modulation instability, and optical bistability to name a few [2, 23, 24]. The reason for this is that many of these nonlinear effects rely of phase matching conditions that turn out to be modified significantly in metamaterials, and especially in negative index materials (NIMs). Indeed, one of the most important and interesting properties of NIMs, is the opposite directionality of the Poynting vector and the wave vector, thus, enabling the backward phase matching mechanism. Backward phase matching in combination with the strong frequency dependency of these materials has been demonstrated to facilitate new regimes of SHG and parametric amplification. Before we discuss these properties, it is necessary to briefly review the key physics behind the nonlinear optical material response and resulting nonlinear light-matter interactions.

Any material can be considered as a collection of charged particles, electrons and ions. In conductors, when an external electric field is applied, positive and negative charges move in opposite directions. In dielectrics, the charged particles are bound together so that the charge cannot move freely under the influence of the externally applied field, instead they are displaced from their original positions and with respect to each other. This leads to the formation of induced dipole moments. In the regime of linear optics, the oscillation of an electron is proportional to the strength of the electric field of light. However the nonlinear response is related to the anharmonic motion of bound electrons in the presence of an electric field.

The position of an electron is governed by the oscillator equation:

$$eE = m\left(\frac{d^2x}{dt}\right) + 2\Gamma\left(\frac{dx}{dt}\right) + \Omega^2 x - \left(\xi^{(3)}x^2 + \xi^{(3)}x^3 + \cdots\right) \tag{11.1}$$

Here x is the displacement from the mean position, Ω is the resonance frequency, and Γ is the damping constant. The term from the right hand side represents the force on the electron due to applied field, which leads to the driven oscillations.

Considering just the harmonic term we can thereby get an equivalent equation for x as follows:

$$E\,(t) = E_0 \cos\,(\omega t)\; = \frac{1}{2}E_0[e^{-i\omega t} + e^{i\omega t}] \tag{11.2}$$

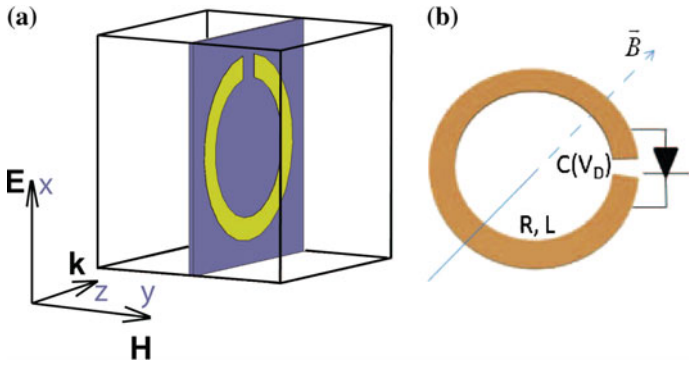

Fig. 11.1 Configuration of the unit cell (**a**). Equivalent effective circuit model (**b**) [26]

$$x = -\frac{eE}{2m}\frac{e^{-i\omega t}}{\Omega^2 - 2i\Gamma\omega - \omega^2} + c.c \tag{11.3}$$

If N is the number of electric dipoles per unit volume, the polarization induced in the medium is given by $P = -Nex$. Thus based on x, we can find the polarization P for this system as:

$$P = -\frac{\chi\varepsilon_0 E}{2}e^{-i\omega t} + c.c \tag{11.4}$$

where χ is the susceptibility.

The motion of charged particles in a dielectric medium is linear in a limited range of values of E. However, as the intensity increases, then the response becomes nonlinear, and this nonlinearity can be accounted for with the anharmonic terms in the oscillator equation [25]. The polarization P (or magnetization M) in such a case will be expressed based on anharmonic term as:

$$P = \varepsilon_0(\chi^{(1)}E + \chi^{(2)}E^2 + \chi^{(3)}E^3 + \cdots) \tag{11.5}$$

where $\chi^{(1)}$ represents a linear susceptibility and the higher order terms are the nonlinear susceptibilities of the medium.

Recently, an analytical description of a nonlinear metamaterial in terms of effective nonlinear susceptibilities based on a perturbative solution to the nonlinear oscillator model was proposed in [26, 27]. An application of this approach for a varactor-loaded split ring resonator (VLSRR) medium can be summarized as follows. Figure 11.1 shows the orientation of the VLSRR-based unit cell with respect to the incident field and its equivalent representation as an effective RLC-circuit. The response of the SRR can be expressed in terms of the charge across the capacitive gap, which is described by the following nonlinear oscillator equation:

$$\ddot{q} + \gamma \dot{q} + \omega_0^2 V_D(q) = -\omega_0^2 A \mu_0 \dot{H}_y \tag{11.6}$$

where $q(t)$ is the normalized charge, $V_D(q)$ is the voltage across the effective capacitance, ω_0 is linear resonant frequency of the unit cell, g is the damping factor, A is the area of the circuit, μ_0 is the permeability of vacuum, and $H_y(t)$ is the incident magnetic field.

The voltage V_D can be expanded in a Taylor series in terms of the normalized charge according to $V_D(q) = q + aq^2 + bq^3$, where the Taylor coefficients a and b depend on the particular mechanism of nonlinearity. The perturbation solution to (11.6) leads to the following expressions [26] for the linear and the second order effective susceptibilities

$$\chi_y^{(1)}(\omega) = \frac{F\omega^2}{D(\omega)} \tag{11.7}$$

$$\chi_{yyy}^{(2)}(\omega_r; \omega_n, \omega_m) = -ia \frac{\omega_0^4 (\omega_n + \omega_m) \omega_n \omega_m \mu_0 A F}{D(\omega_n) D(\omega_m) D(\omega_n + \omega_m)} \tag{11.8}$$

where $\omega_r \equiv \omega_n + \omega_m$, indices n and m take values between $\pm\Lambda$, and L is the total number of distinct waves incident on the medium. The denominator is defined as $D(\omega) \equiv \omega_0^2 - \omega^2 - i\gamma\omega$, $\mathrm{F} \equiv \omega_0^2 N A^2 C_0 \mu_0$ is the amplitude factor in the expression for the linear susceptibility, and the arguments of the nonlinear susceptibility are written in conventional notations signifying that the first term is the sum of the subsequent arguments.

Next, the microscopic equation of motion (11.6) for a single inclusion can be converted into the macroscopic one for the effective medium polarization that in combination with Maxwell's equations provides a complete description of the metamaterials. For a dilute medium, the magnetization can be written as $M(t) = Nm(t)$, where N is the volume density of moments, and $m(t)$ is the magnetic dipole moment of the effective circuit enclosing the effective area S. Then, the equation for the magnetization can be written as

$$\ddot{M}_y + \gamma \dot{M}_y + \omega_0^2 M_y = -F\ddot{H}_y - \alpha M_y \int M_y dt \tag{11.9}$$

where $\alpha \equiv \frac{2\omega_0^2 a}{NAC_0}$ and assuming only second order nonlinear response in the expansion of VD was included.

In general, it should be noted that $\chi^{(1)}$ in (11.5) is a tensor element, and the terms $\chi^{(2)}$ and $\chi^{(3)}$ are relatively small so the overall impact of these terms on the optical response of the material to light is insignificant. Thus, these terms were mostly ignored until the advent of ultrafast lasers that could produce optical pulses where the electric fields could be generated with sufficiently large intensity so that these terms become important. In fact, these terms have remarkable consequences in optical systems. $\chi^{(2)}$, the second order nonlinear susceptibility, only occurs in noncentrosymmetric crystals and gives rise to a number of nonlinear effects including

SHG, optical rectification, sum and difference frequency generation, and parametric amplification. $\chi^{(3)}$, the third order nonlinear susceptibility, gives rise to such phenomena as self-phase modulation, spatial solitons, cross phase modulation, optical phase conjugation, self-focusing through the optical Kerr effect, third harmonic generation and temporal solitons. Thus, remarkable optical properties have been demonstrated through nonlinear optics through the use of ultrafast pulsed lasers. Moreover, these nonlinear optical processes, once a subject of scientific curiosity, are prevalent in everyday devices such as solid state green and blue lasers, multiphoton microscopes, supercontinuum light sources used in metrology applications, and others.

However, to date, the observation of nonlinear optical processes in naturally occurring materials has relied on high intensity laser beams. There have been some attempts at tailoring the response in these materials by manipulating the structure of the material. For example, quasi-phase matching in SHG [28] used layered structures that effectively increased the interaction lengths by correcting the relative phase. In an analogous manner, nanostructured optical metamaterials have the potential to increase the nonlinear response by modifying the material structure to enhance the interaction between light and matter. Specifically, it may be possible to design structures that can trap and concentrate light to produce exceptionally large electric fields—even with relatively low intensity excitation. In fact, the promise of these materials for nonlinear optics has already begun to be realized [29].

Specifically, there have been a number of reports related to wave-mixing in metamaterials using the second order nonlinearity. Enhancement of second-harmonic generation has been demonstrated by several groups [30–35]. Husu et al. recently demonstrated that the second order nonlinear response can be tailored by controlling the interactions between metal nanoparticles [36]. Wegener's group used nonlinear optical spectroscopy to demonstrate that the fundamental split-ring resonance in split-rings serves as the nonlinear source [37]. In addition, novel propagation dynamics have also been realized. Second-harmonic generation in negative index metamaterials has been demonstrated to result in interesting propagation of the second-harmonic light back towards the source [38–42]. Smith's group has demonstrated a nonlinear-optical mirror in which the SHG in NIM is generated in the backward direction, i.e. toward the source [43]. In addition, there has been an interest in coherent optical amplification [44].

In addition to second-order nonlinearities, there has been continued interest in third-order nonlinearities. Four-wave mixing in left-handed materials has been investigated [45]. Soliton propagation in nonlinear and left-handed metamaterials has demonstrated new propagation dynamics [46–55]. Katko et al. have demonstrate phase conjugation using split-ring resonators [56]. Modulation instability in structures with a saturable nonlinearity has also been demonstrated [57, 58].

In this chapter, we will present an overview of recent efforts to exploit this ability to design metamaterials that can enhance the nonlinear optical response by either increasing the effective nonlinear coefficient of the material or by enhancing the field localization and thus increasing the field magnitude. We will demonstrate that the potential of metamaterials is beginning to be realized in nonlinear optical metamaterials that have increased the efficiencies of nonlinear processes and further enabled

their integration within optical devices systems. Specifically, in Sect. 11.2, we will consider a generalized theoretical approach to nonlinear wave mixing processes in metamaterials and pulse propagation in these structures. Sect. 11.3 will focus on nonlinear magnetic metamaterials. Finally, Sect. 11.4 will discuss solitons, bistability and modulational instability in nonlinear metamaterials.

11.2 Nonlinear Wave-Mixing and Pulse Propagation

The nonlinear properties of naturally existing conventional materials are limited by the properties of their constituent components—atoms and molecules. The rapidly growing field of metamaterials opens unprecedented opportunities to overcome those limitations. It was previously shown that the unique optical properties of metamaterials, such as magnetism at optical frequencies, negative index of refraction and its associated backward propagating waves, strong anisotropy, or chirality, enabled a number of new regimes of light-matter interaction in the linear optical regime. However, in recent years, it has become clear that nonlinear properties of metamaterials can be engineered as well, opening new perspectives for modern nonlinear optics and enabling devices with entirely novel functionalities [59].

The development of nonlinear metamaterials is likely to impact both nonlinear optics and metamaterials fields enabling entirely new phenomena [60]. In particular, novel optical properties facilitated by metamaterials field prompt us to reconsider many nonlinear light-matter interactions, including SHG [39, 41, 61, 62], parametrical amplification [63], ultra-short pulse dynamics [64–66] and soliton propagation [67]. From applications viewpoint, nonlinear metamaterials make possible the creation of dynamically-tunable materials, optical switches, filters, beam deflectors, focusing/defocusing reflectors, and reconfigurable structures with controlled transparency, refractive index and nonlinear response.

Conventionally, in natural materials nonlinear optical response depends on the intensity of electric field and is described only by nonlinear properties of dielectric permittivity while the nonlinear magnetic response is neglected. The metamaterials can "turn on" the interaction with magnetic component of the electromagnetic wave using carefully engineered linear and nonlinear components of magnetic permeability [68]. It was recently shown that metamaterials containing split-ring resonators (SRR) loaded with varactor possess nonlinear magnetic response and can be used as building-blocks for nonlinear metamaterials with light—controllable properties. This approach provides a range of new functionalities, such as focusing, defocusing, and deflection of light and most importantly, the possibility of controlling and manipulating the properties of materials with unprecedented speed, enabling new approaches to all-optical processing, tunable lenses and waveguides, and reconfigurable cloaking devices.

Nonlinear wave-mixing is one of the best studied nonlinear processes in metamaterials [39, 41, 61–63, 69–71]. In particular, many new regimes of nonlinear interactions were predicted in NIMs, including backward phase-matching, unconventional

Manley-Rowe relations, spatially-distributed nonlinear feedback and cavity-less optical parametrical oscillations. These unusual properties potentially enable such novel functionalities as quadratic nonlinear mirror and SHG-based lenses. Here we consider the SHG, as one of the most fundamental parametric nonlinear process. The material is assumed to possess a negative refractive index at the fundamental field (FF) frequency ω_1 and positive refractive index at second harmonic (SH) frequency $\omega_2 = 2\omega_1$. Electric fields of the FF and that of the SH waves are taken in the following form $\bar{E}_{1,2} = E_{1,2}\exp(ik_{1,2}z - i\omega_{1,2}t) + c.c.$, respectively. Following [72], comprehensive studies of the SHG process for continuous wave and pulse propagation, as well as the propagation of complex light beams such as optical vortices or solitons with transverse field distribution can be performed using the following model:

$$\nabla_{\perp}^2 E_1 + 2ik_1\frac{\partial E_1}{\partial z} + \frac{2ik_1}{v_1^g}\frac{\partial E_1}{\partial z} - \frac{1}{c^2}\left(\frac{\omega_1\mu_1\alpha_1^{'}}{2} + \gamma_1\alpha_1 + \frac{\gamma_1^{'}\omega_1\varepsilon_1}{2}\right)\frac{\partial^2 E_1}{\partial t^2} + \frac{8\pi\omega_1^2\mu_1\chi^{(2)}E_1^* E_2 e^{i\Delta kz}}{c^2} = 0, \tag{11.10}$$

$$\nabla_{\perp}^2 E_2 + 2ik_2\frac{\partial E_2}{\partial z} + \frac{2ik_2}{v_2^g}\frac{\partial E_2}{\partial z} - \frac{1}{c^2}\left(\frac{\omega_2\mu_2\alpha_2^{'}}{2} + \gamma_2\alpha_2 + \frac{\gamma_2^{'}\omega_2\varepsilon_2}{2}\right)\frac{\partial^2 E_2}{\partial t^2} + \frac{4\pi\omega_2^2\mu_2\chi^{(2)}E_1^2 e^{-i\Delta kz}}{c^2} = 0, \tag{11.11}$$

where $\nabla_{\perp}^2$ is the transverse Laplace operator; χ (11.2) is the effective second-order nonlinear susceptibility; $\alpha_{1,2} = \frac{\partial[\omega_{1,2}\varepsilon(\omega_{1,2})]}{\partial\omega}$; $\alpha_{1,2}^{'} = \frac{\partial^2[\omega_{1,2}\varepsilon(\omega_{1,2})]}{\partial\omega^2}$; $\gamma_{1,2} = \frac{\partial[\omega_{1,2}\mu(\omega_{1,2})]}{\partial\omega}$; $\gamma_{1,2}^{'} = \frac{\partial^2[\omega_{1,2}\mu(\omega_{1,2})]}{\partial\omega^2}$; $\varepsilon_{1,2}$ and $\mu_{1,2}$ are dielectric permittivity and magnetic permeability for fundamental and SH waves, respectively; $v_{1,2}^g$ are group velocities of pump and SH waves; $\Delta k = k_2 - 2k_1$ is phase mismatch; A is the speed of light in free space. Note that (11.6)–(11.7) describe SHG for both positive and negative index materials, but the signs for the wave vectors $k_{1,2}$, magnetic permeabilities $\mu_{1,2}$, dielectric permittivities $\varepsilon_{1,2}$ and group velocities $v_{1,2}^g$ should be chosen according to the phase-0 matching geometry and material properties at the corresponding frequency.

Here, for simplicity we consider the steady-state process with perfect phase-matching for a plane wave assuming that dispersion for permeability and permittivity are negligible. For the SHG process in NIM slab with a finite length L, decomposing the complex amplitudes into real amplitudes and phases as $E_{1,2} = \mathrm{E}_{1,2}e^{i\phi_{1,2}}$ and using the boundary conditions $\mathrm{E}_1(z=0) = \mathrm{E}_1^0$, $\mathrm{E}_2(z=L) = 0$ the solution can be written in the following form:

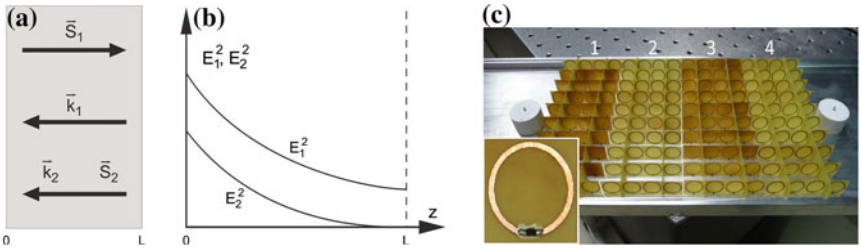

Fig. 11.2 The SHG process: phase-matching geometry (**a**). Fundamental field and second harmonic intensity distribution (**b**). Photo of experimental setup for observing SHG in NIM [43] (**c**)

$$\mathrm{E}_1(z) = \frac{C}{\cos\left[Cg\left(L-z\right)\right]} \tag{11.12}$$

$$\mathrm{E}_2(z) = C\tan\left[Cg\left(L-z\right)\right] \tag{11.13}$$

here $CgL = \cos^{-1}\left[C/\mathrm{E}_1^0\right]$, $g = \frac{4\pi\omega^2\mu_2}{c_2 k_2}\chi^{(2)}$.

Figure 11.2a illustrates the directions of wavevectors and Poyning vectors for the FF and SH in a metamaterials that possesses NIM characteristics at the FF frequency and PIM characteristics at the SH frequency. This is due to the backward phase-matching in a PIM-NIM system, signifying that the energy flows of FF and SH waves are counter-directional with respect to each other. Figure 11.2b shows the field distributions of the FF and SH waves. Importantly, the difference between energy flows is constant at each point of such metamaterial slab, while in conventional materials, the sum of the energy flows is unchanged with propagating distance. Furthermore, as it could be seen from (11.4), the intensity of the SHG is a function of the slab thickness such that long enough lossless metamaterials slab would act as 100 % nonlinear mirror.

Experimental realization of a propagating SHG at microwave wavelengths was demonstrated using the experimental setup shown in Fig. 11.2c [43]. The nonlinear metamaterial was realized using the varactor-loaded split-ring resonators placed in an aluminum waveguide. Second harmonic generation was studied in three configurations including reflected SH phase matching in a negative-index spectral range, transmitted SH quasi-phase matching, and simultaneous quasi-phase-matching of both the reflected and transmitted SH waves near a zero-index spectral range. Also, experimental measurements of three- and four-wave mixing phenomena in an artificially structured nonlinear magnetic metacrystal at microwave frequencies have been reported [73].

Observation of second and third harmonic generation at optical wavelengths was inspired by the theoretical work by Pendry, who predicted that SRRs would provide artificial magnetism up to optical frequencies [74]. Essentially, the light field can induce a circulating current in the ring leading to a large magnetic-dipole moment close to the magnetic-resonance frequency. In addition, it was predicted that meta-

materials composed of SRRs would enable enhanced nonlinear-optical effects due to the combination of resonance effects and local-field enhancements. First experiments on second- and third-harmonic generation at a surface of a nonlinear magnetic metamaterial composed of nanoscale gold split-ring resonators were performed by Wegener's group and demonstrated that much larger signals are detected when the magnetic-dipole resonances are excited, as compared with purely electric-dipole resonances [37, 75–78].

Until now we considered continuous wave effects in NIMs. However, several fascinating phenomena have been discovered by Scalora's group in the pulsed second-harmonic generation regime [64–66]. In particular, in agreement with previous reports, they predicted the presence of a double-peaked second harmonic signal in nonmetallic PIMs, which comprises a pulse that walks off and propagates at the group velocity expected at the second-harmonic frequency, and a second pulse that is "captured" and propagates under the pump pulse. The origin of the double-peaked structure was explained by a phase-locking mechanism that characterizes not only second-harmonic generation, but also $\chi^{(3)}$ processes and third-harmonic generation. The phase-locking occurs for arbitrarily small pump intensities, and therefore, in second harmonic generation a phase-matched component is always generated, even under conditions of material phase mismatch. However, if the material is phase matched, phase locking and phase matching are indistinguishable, and the conversion process becomes efficient. A similar phase-locking phenomenon was also predicted in NIMs. A spectral analysis of the pump and the generated signals reveals that the phase-locking phenomenon causes the forward moving, phase-locked second-harmonic pulse to experience the same negative index as the pump pulse, even though the index of refraction at the second-harmonic frequency is positive. Our analysis further shows that the reflected second-harmonic pulse generated at the interface and the forward-moving, phase-locked pulse appear to be part of the same pulse initially generated at the surface, part of which is immediately back-reflected, while the rest becomes trapped and dragged along by the pump pulse. These pulses thus constitute twin pulses generated at the interface, having the same negative wave vector, but propagating in opposite directions. These structures may provide an alternative to the experimental realization of nonlinear optical and plasmonic phenomena in bulk optical negative index materials which is particularly challenging due to absorption losses. In the case of phase-locking, the pump impresses its dispersive properties on its harmonics, which in turn experience no absorption as long as the material is somewhat transparent to the pump.

Another nonlinear wave mixing process, optical parametric amplification (OPA), becomes of significant importance in metamaterials. As is well-known, one of the main obstacles delaying practical applications of optical metamaterials is the significant losses prevalent in practical implementations. The losses originate from a number of sources, including the resonant nature of the metamaterial's magnetic response, intrinsic absorption of the metallic constitutive components, and losses from surface roughness. Therefore, developing efficient loss-compensating techniques is of paramount importance. One of the promising approaches to loss compensation is the technique based on a three-wave mixing process that takes place in nonlinear

media exhibiting second-order susceptibility and induces OPA. Optical parametric amplification refers to a process of amplification of a light signal through mixing with a pump light in a nonlinear material, in which the photon flux in the signal wave grows through coherent energy transfer from a higher frequency intense pump wave. A photon from an incident pump laser is divided into two separated photons: the stronger one of which is the signal, and the other is the idler. The pump field with different angular frequency and wavenumber will generate a difference signal and idler frequency. The OPA process requires both momentum and energy conservation. While most OPA devices to date have been realized in conventional PIMs, an OPA process in NIMs was predicted to have several advantages, including the possibility of optical parametric oscillations without a cavity, compactness and simplicity in both design and alignment. Just like in the case of the SHG process, the difference between PIM-based and NIM-based OPAs is that the wave vector and the Poynting vector are antiparallel, that is, in opposing directions. Thus, an OPA with counter-directed energy flows can be realized with all three waves having co-directed wave vectors. Therefore, if the pump and idler frequencies correspond to the PIM, and the signal wave frequency belongs to the NIM, the energy flow of the signal wave will be antiparallel to that of the pump and the idler, resulting in an effective feedback mechanism without any external mirrors or gratings. Such an OPA enables compensation of the metamaterial's absorption by the parametric amplification process and energy transfer to the strongly absorbing wave from the pump wave [62, 63].

In addition, properly engineered optical metamaterial structures can be used to realize strong localization of light and, as a result, the enhancement of nonlinear interactions. Various approaches to field localization and enhancement were investigated, including graded and near-zero refractive index metamaterials, periodic structures consisting of alternating layers of PIM and NIM [79–81]. For instance, D'Aguanno et al. predicted a possibility of significantly improved conversion efficiencies of SHG, owing to the presence of NIM layers [80]. Furthermore the efficiency stays relatively high even in the case of strongly absorbing structures.

11.3 Magnetic and Reconfigurable Metamaterials

One of the unique properties that became possible only with the emergence of metamaterials is magnetism at optical frequencies. Indeed, relative magnetic permeability that is equal to one in ordinary materials can be designed to be positive, negative or even zero at certain frequencies in metamaterials.

Nonlinear magnetic metamaterials in microwave frequency range were demonstrated by several methods. In one implementation, the characteristics of split-ring resonators have been altered by introducing nonlinear current-voltage device such as varactor diodes within the gap of the resonator in each unit cell, as shown in Fig. 11.2a [60]. Inside each double split-ring resonator, a varactor diode, which introduces nonlinear current-voltage dependence and results in nonlinear magnetic dipole moment, is added so the magnetic resonance is dependent on the input power.

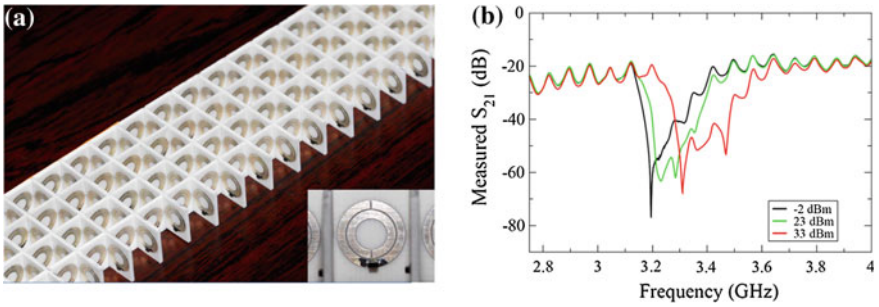

Fig. 11.3 Photograph of the nonlinear magnetic metamaterial created by a square lattice of SRRs with a varactor in each SRR (**a**); measured transmission parameter S21 under different input powers (**b**) [60]

The transmission of this metamaterial is measured under various input power. Figure 11.2b shows a significant power-dependent shift in such a structure.

Recently, several novel types of nonlinear metamaterials based on the geometric conformation changes have been proposed and demonstrated. In one implementation, the nonlinear metamaterial performance based on the interplay between electromagnetic attraction and elastic repulsion was proposed [77]. Figure 11.3 shows such magnetoelastic metamaterial, in which magnetic metamaterial is combined with an elastic medium. The metamaterial is compressed by the electromagnetic forces (F_I), which come from current attraction and are balanced by elastic forces (F_S). Both electromagnetic forces and elastic forces depend on the lattice distance b. In this case, the effective magnetization is changing along with the lattice distance and induced current (Fig. 11.4).

The overall structure is built from a lattice of resonant elements, such as split-ring resonators or capacitively-loaded rings. In response to electromagnetic waves with magnetic field H_0 along the axial direction, such a metamaterials shows resonant magnetic behavior. The currents induced in the resonators not only affect each other through mutual inductance, but also result in an attractive force between the resonators when the neighboring currents are in phase. So if the resonators are allowed to move along the axial direction, they will shift from their original positions. Their displacement results in changing their mutual impedance that in turn alters the current amplitudes, and interaction forces. The balance is kept with a restoring force, which originates from the elastic properties of the host medium. Measured magnetic resonance shift is shown in Fig. 11.5a, b [82].

Another implementation of a reconfigurable nonlinear magnetic metamaterial structure based on the geometric conformation changes was based on the interplay of electromagnetic forces, elastic forces and thermal expansions. Figure 11.5c shows a structure consisting of spirals forming the resonators with chiral properties. The origin of the nonlinearity in this case can be understood by noticing that the resonant frequency of the spiral resonator depends on the spiral pitch ξ as well as on the radius of the spiral r. Therefore, the resonance shifts when the spiral compresses in response

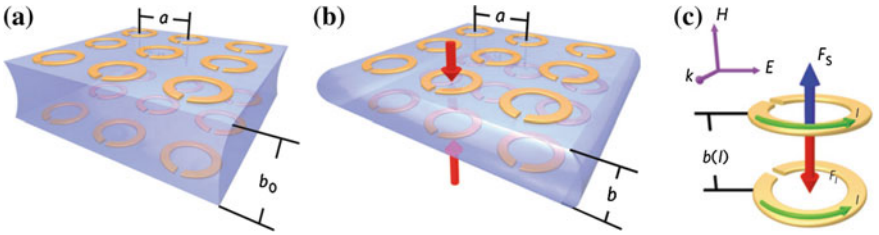

Fig. 11.4 An anisotropic magnetic metamaterial combined with an elastic medium: without the electromagnetic field applied (**a**); with the electromagnetic field applied (**b**); lattice dimensions a, b_0 and b are normalized to the resonator radius r_0; schematic of the forces acting on a ring within a metamaterial (**c**) [82]

to attraction between the turns as well as when a thermal expansion occurs due to heating. Both of the effects caused by the induced currents. As a result intensity-dependent phenomena are enabled, leading to nonlinear behavior, for example, in dependence of the induced magnetization on the incident magnetic field. Figure 11.5d shows experimentally measured and theoretically predicted a magnetic resonance shift as a function of input power [83].

Recently, a number of nonlinearly controlled devices were proposed, including nonlinear cloaking devices [84], reconfigurable nonlinear light concentrators [85], and light-tunable reflection, shaping, and focusing of electromagnetic waves in metamaterials [86], as shown in Fig. 11.3. Let's consider light tunable metamaterial shown in Fig. 11.3 in more detail. The microwave light-tunable metamaterials mirror consists of an array of broadside-coupled SRRs, such that each SRR contains a pair of varactors, one in each ring, and the biasing of the varactors is achieved by photodiodes. This device enables reconfigurable mirror or lenses in which switching between focusing or defocusing can be achieved by adjusting the light illumination profile. The advantages of this approach include fast and remote control of the device performance, a possibility of extension to higher dimensions, and a possibility of realization of such devices at higher frequencies, at least up to terahertz range.

In summary, nonlinear magnetic metamaterials in microwave and optical wavelength are discussed. The electrical parameters and geometric conformation can be modified to generate a nonlinear magnetic response in microwave. Kerr-type medium was studied in optical magnetic metamaterials, where SHG/THG can be also generated at magnetic resonance (Figs. 11.6, 11.7).

11.4 Optical Solitons, Bistability and Modulation Instability

Soliton or a solitary wave is a remarkable nonlinear phenomenon that relies on the balance of nonlinear and dispersive (or diffractive) effects and was observed in optics, quantum mechanics, particle physics and many other fields. In optics, the term

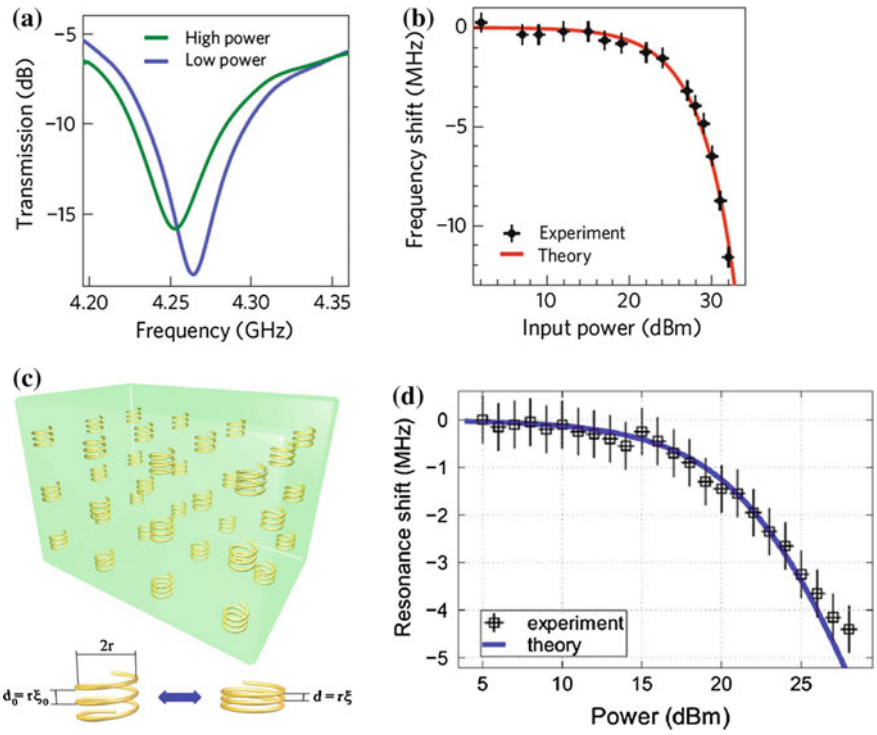

Fig. 11.5 Experimental observation of the magnetoelastic nonlinearity: measured transmission spectra at low and high power (**a**); experimental and theoretical results of the resonance frequency vs. incident power (**b**) [85]; schematic of magnetic metamaterial composed of spirals resonators (**c**); the frequency shift as a function of input power, including a comparison between the theory and experiment (**d**) [83]

soliton refers to a localized pulse or beam that travels without changing its shape. Metamaterials provide a new environment for soliton-like phenomena. There have been a lot of theoretical and recently experimental studies of soliton propagation in various metamaterials systems [87–100]. Here we consider only several examples of such phenomena. For instance, Liu et al. considered subwavelength discrete solitons in nonlinear metamaterials consisting of nanoscale periodic metal and nonlinear dielectric slabs as shown in Fig. 11.3a [87–89]. The subwavelength surface plasmon polariton solitons in these structures result from a balance between tunneling of surface plasmon modes and nonlinear self-trapping. An interplay between periodicity, nonlinearity, and surface plasmon polaritons leads to substantially different soliton dynamics as compared to that in conventional uniform nonlinear media and nonlinear dielectric waveguide arrays. Figure 11.3b, c show the propagation in linear and nonlinear metal-dielectric multilayers, respectively. At low intensities, surface plasmon polaritons tunnel between neighboring slabs, resulting in linear diffraction of the initial wave packet. At higher intensity,the wave packet maintains its original

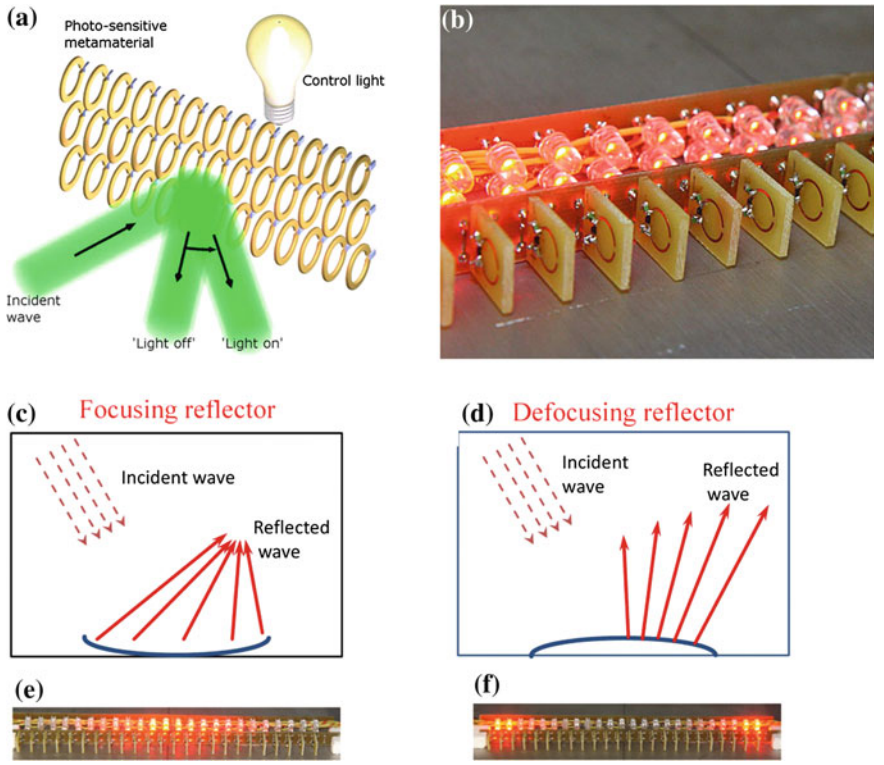

Fig. 11.6 Light-tunable metamaterials that reflects incident electromagnetic wave at different angles depending on the control light illumination using an array of LEDs (**a**); image of the microwave light-tunable metamaterials mirror made of an array of broadside-coupled SRRs (each SRR containing a pair of varactors, one in each ring, and the biasing of the varactors is achieved by photodiodes). The schematics of focusing (**c**) and defocusing (**d**) reflector and their corresponding performance, (**e**) and (**f**), respectively [68]

shape during propagation. Figure 11.3c clearly demonstrates the self-focusing effect and the formation of the lattice solitons.

One of the remarkable examples of entirely new class of solitons that can be supported in metamaterials was recently predicted by Rosanov et al. [90]. Nonlinear magnetic metamaterials comprised of a lattice of weakly coupled split-ring resonators driven by an external electromagnetic field were predicted to support so-called knotted solitons, which are stable self-localized dissipative structures in the form of closed knotted chains. Such knotted structures have been discovered in many branches of science, from biology to statistical mechanics and multi-component superconductors. In nonlinear fields, knotted solitons were introduced by Faddeev and Niemi [91, 92] as knotted lines without self-crossings embedded into a three-dimensional space. The existence of knot solitons as stationary solutions of non-linear models was confirmed in numerical experiments [93].

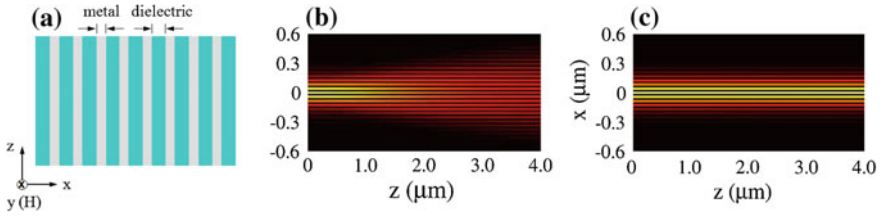

Fig. 11.7 Schematic of metal-dielectric multilayers (**a**), linear (**b**) and nonlinear (**c**) propagation of the mode over 4 μm distance in lossless metal-dielectric multilayers [55]

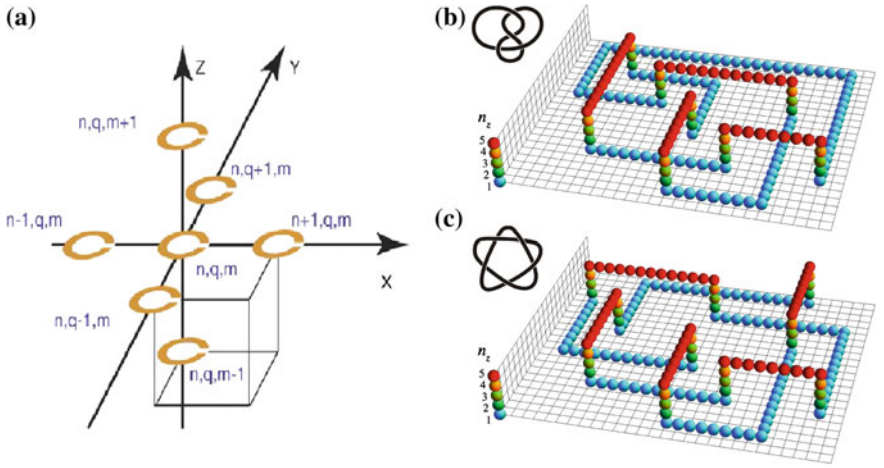

Fig. 11.8 Three-dimensional geometry of a cubic lattice of split-ring-resonators (**a**); the examples of higher-order knotted solitons with 4 and 5 crossings: figure-eight (**b**), and cinquefoil (**c**) knots [90, 94]

A nonlinear magnetic metamaterial comprised of a cubic lattice of weakly coupled SRRs (Fig. 11.4a) was previously shown to exhibit a variety of nonlinear dissipative phenomena, including bistability and modulational instability, and one-dimensional dissipative solitons [94, 95]. The possibility of building rather complex stable knotted solitons in such system is illustrated in Fig. 11.4b, c.

In summary, solitons, bistability and modulation instability, well-understood phenomenal nonlinear optics, were predicted to reveal themselves in entirely new way in nonlinear metamaterials. These new features are expected to be observed with the continued development of metamaterials and lead to a new plethora of novel applications (Fig. 11.8).

References

1. N.M. Litchinitser, V.M. Shalaev, Metamaterials: transforming theory into reality. J. Opt. Soc. Am. B **26**, B161–B169 (2009)
2. N.I. Zheludev, Y.S. Kivshar, From metamaterials to metadevices. Nat. Mater. **11**, 917–924 (2012)
3. R.A. Shelby, D.R. Smith, S. Schultz, Experimental verification of a negative index of refraction. Science **292**, 77–79 (2001)
4. V.G. Veselago, The electrodynamics of substances with simultaneously negative values of ε and μ. Sov. Phys. Usp. **10**, 509–514 (1967)
5. Y.T. Wang et al., Gain-assisted hybrid-superlens hyperlens for nano imaging. Opt. Express **20**, 22953–22960 (2012)
6. C.L. Cortes et al., Quantum nanophotonics using hyperbolic metamaterials, J. Opt. **14**, 063001(15) (2012)
7. H. Benisty, F. Goudail, Dark-field hyperlens exploiting a planar fan of tips. J. Opt. Soc. Am. B **29**, 2595–2602 (2012)
8. A. Andryieuski, A.V. Lavrinenko, D.N. Chigrin, Graphene hyperlens for terahertz radiation, Phys. Rev. B **86**, 121108(R)(5) (2012)
9. W.B. Zhang, H.S. Chen, H.O. Moser, Subwavelength imaging in a cylindrical hyperlens based on S-string resonators. Appl. Phys. Lett. **98**, 073501(3) (2011)
10. X.J. Ni et al., Loss-compensated and active hyperbolic metamaterials. Opt. Express **19**, 25242–25254 (2011)
11. Q.Q. Meng et al., Deep subwavelength focusing of light by a trumpet hyperlens. J. Opt. **13**, 075102(4) (2011)
12. D.D. Li et al., Two-dimensional subwavelength imaging from a hemispherical hyperlens. Appl. Opt. **50**, G86–G90 (2011)
13. J. Rho et al., Spherical hyperlens for two-dimensional sub-diffractional imaging at visible frequencies. Nat. Commun. 1148(5) (2010)
14. Y. Xiong, Z.W. Liu, X. Zhang, A simple design of flat hyperlens for lithography and imaging with half-pitch resolution down to 20 nm. Appl. Phys. Lett. **94**(20), 3 (2009)
15. E.J. Smith et al., System investigation of a rolled-up metamaterial optical hyperlens structure. Appl. Phys. Lett. **95**, 083104(3) (2009) (Erratum: Appl. Phys. Lett. **96**, 019902(2) (2010))
16. A.V. Kildishev et al., Materializing a binary hyperlens design, Appl. Phys. Lett. **94**, 071102(3) (2009)
17. Z.W. Liu et al., Far-field optical hyperlens magnifying sub-diffraction-limited objects. Science **315**, 1686–1686 (2007)
18. H. Lee et al., Development of optical hyperlens for imaging below the diffraction limit. Optics Express **15**, 15886–15891 (2007)
19. Z. Jacob, L.V. Alekseyev, E. Narimanov, Semiclassical theory of the hyperlens. J. Opt. Soc. Am. A **24**, A54–A61 (2007)
20. Z. Jacob, L.V. Alekseyev, E. Narimanov, Optical hyperlens: Far-field imaging beyond the diffraction limit. Opt. Express **14**, 8247–8256 (2006)
21. D. Schurig et al., Metamaterial electromagnetic cloak at microwave frequencies. Science **314**, 977–980 (2006)
22. J.B. Pendry, D. Schurig, D.R. Smith, Controlling electromagnetic fields. Science **312**, 1780–1782 (2006)
23. N.M. Litchinitser, V.M. Shalaev, Metamaterials loss as a route to transparency. Nat. Photonics **3**, 75–76 (2009)
24. C.M. Soukoulis, M. Wegener, Past achievements and future challenges in the development of three-dimensional photonic metamaterials. Nat. Photonics **5**, 523–530 (2011)
25. R.W. Boyd, *Nonlinear optics*, 2nd edn. (Academic Press: San Diego, CA, 2003)
26. E. Poutrina, D. Huang, D.R. Smith, Analysis of nonlinear electromagnetic metamaterials. New J. Phys. **12**, 093010 (2010)

27. E. Poutrina, D. Huang, Y. Urzhumov, D.R. Smith, Nonlinear oscillator metamaterial model: numerical and experimental verification. Opt. Express **19**, 8312–8319 (2011)
28. P.A. Franken, J.F. Ward, Optical harmonics and nonlinear phenomena. Rev. Mod. Phys. **35**, 23–39 (1963)
29. N.M. Litchinitser, V.M. Shalaev, Photonic metamaterials. Laser Phys. Lett. **5**, 411–420 (2008)
30. T. Kanazawa et al., Enhancement of second harmonic generation in a doubly resonant metamaterial. Appl. Phys. Lett. **99**, 024101(3) (2011)
31. Z.Y. Wang et al., Second-harmonic generation and spectrum modulation by an active nonlinear metamaterial. Appl. Phys. Lett. **94**, 134102(3) (2009)
32. N.I. Zheludev, V.I. Emel'yanov, Phase matched second harmonic generation from nanostructured metallic surfaces. J. Optics A **6**, 26–28 (2004)
33. H. Merbold, A. Bitzer, T. Feurer, Second harmonic generation based on strong field enhancement in nanostructured THz materials. Opt. Express **19**, 7262–7273 (2011)
34. W.L. Schaich, Second harmonic generation by periodically-structured metal surfaces. Phys. Rev. B **78**, 8 (2008)
35. M.W. Klein et al., Second-harmonic generation from magnetic metamaterials. Science **313**, 502–504 (2006)
36. H. Husu et al., Metamaterials with Tailored Nonlinear Optical Response. Nano Lett. **12**, 673–677 (2012)
37. F.B.P. Niesler et al., Second-harmonic optical spectroscopy on split-ring-resonator arrays. Opt. Lett. **36**, 1533–1535 (2011)
38. L. Chen, C.H. Liang, X.J. Dang, Second-harmonic generation in nonlinear left-handed metamaterials. Acta Phys. Sinica **56**, 6398–6402 (2007)
39. V. Roppo et al., Second harmonic generation in a generic negative index medium. J. Opt. Soc. Am. B **27**, 1671–1679 (2010)
40. I.V. Shadrivov, A.A. Zharov, Y.S. Kivshar, Second-harmonic generation in nonlinear left-handed metamaterials. J. Opt. Soc. Am. B **23**(3), 529–534 (2006)
41. A.K. Popov, V.V. Slabko, V.M. Shalaev, Second harmonic generation in left-handed metamaterials. Laser Phys. Lett. **3**, 293–297 (2006)
42. D. de Ceglia et al., Enhancement and inhibition of second-harmonic generation and absorption in a negative index cavity. Op. Lett. **32**, 265–267 (2007)
43. A. Rose, D. Huang, D.R. Smith, Controlling the second harmonic in a phase-matched negative-index metamaterials, Phys. Rev. Lett. **107**, 063902(4) (2011)
44. I.R. Gabitov, B. Kennedy, A.I. Maimistov, Coherent amplification of optical pulses in Metamaterials. IEEE J. Sel. Topics Quantum Electron. **16**, 401–409 (2010)
45. S.M. Gao, S.L. He, Four-wave mixing in left-handed materials. J. Nonlinear Optical Phys. Mater. **16**, 485–496 (2007)
46. I.V. Shadrivov, Y.S. Kivshar, Spatial solitons in nonlinear left-handed metamaterials. J. Opt. a-Pure Appl. Optics **7**, S68–S72 (2005)
47. A.B. Kozyrev, D.W. van der Weide, Nonlinear left-handed transmission line metamaterials. J. Physics D **41**, 173001(10) (2008)
48. X.Y. Dai et al., Frequency characteristics of the dark and bright surface solitons at a nonlinear metamaterial interface. Opt. Commun. **283**, 1607–1612 (2010)
49. N.A. Zharova, I.V. Shadrivov, A.A. Zharov, Nonlinear transmission and spatiotemporal solitons in metamaterials with negative refraction. Opt. Express **13**, 1291–1298 (2005)
50. W.N. Cui et al., Self-induced gap solitons in nonlinear magnetic metamaterials, Phys. Rev. E **80**, 036608(5) (2009)
51. M. Scalora et al., Gap solitons in a nonlinear quadratic negative-index cavity. Phys. Rev. E **75**(6), 066606 (2007)
52. N.N. Rosanov et al., Knotted solitons in nonlinear magnetic metamaterials, Phys. Rev. Lett. **108**, 133902(4) (2012)
53. M. Marklund et al., Solitons and decoherence in left-handed metamaterials. Phys. Lett. A **341**, 231–234 (2005)

54. R. Noskov, P. Belov, Y. Kivshar, Oscillons, solitons, and domain walls in arrays of nonlinear plasmonic nanoparticles, Scientific Rep. **2**, 873(8) (**2**01**2**)
55. Y.M. Liu et al., Subwavelength discrete solitons in nonlinear metamaterials, Phys. Rev. Lett. **99**, 153901(4) (2007)
56. A.R. Katko et al., Phase Conjugation and negative refraction using nonlinear active metamaterials, Phys. Rev. Lett. **105**, 123905(4) (2010)
57. Y.J. Xiang et al., Modulation instability in metamaterials with saturable nonlinearity. J. Opt. Soc. Am. B **28**(4), 908–916 (2011)
58. Y.J. Xiang et al., Modulation instability induced by nonlinear dispersion in nonlinear metamaterials. J. Opt. Soc. Am. B **24**(12), 3058–3063 (2007)
59. A.I. Maimistov, I.R. Gabitov, Nonlinear optical effects in artificial materials. European Physical J. Special Topics **147**, 265–286 (2007)
60. I.V. Shadrivov et al., Nonlinear magnetic metamaterials. Opt. Exp. **16**, 20266 (2008)
61. I.V. Shadrivov et al., Second-harmonic generation in nonlinear left-handed metamaterials. J. Opt. Soc. Am. B **23**, 529–534 (2006)
62. A.K. Popov, V.M. Shalaev, Negative-index metamaterials: second-harmonic generation, Manley-Rowe relations and parametric amplification. Appl. Phys. B **84**, 131–137 (2006)
63. A.K. Popov, V.M. Shalaev, Compensating losses in negative-index metamaterials by optical parametric amplification. Opt. Lett. **31**, 2169–2171 (2006)
64. V. Roppo et al., Anomalous momentum states, non-specular reflections, and negative refraction of phase-locked, second-harmonic pulses Metamaterials'2008 Congress 2, pp. 135–144
65. M. Scalora et al., Dynamics of short pulses and phase matched second harmonic generation in negative index materials. Opt. Express **14**, 4746–4756 (2006)
66. V. Roppo et al., Role of phase matching in pulsed second-harmonic generation: Walk-off and phase-locked twin pulses in negative-index media. Phys. Rev. A **76**, 033829 (2007)
67. P.Y.P. Chena, B.A. Malomed, Single- and multi-peak solitons in two-component models of metamaterials and photonic crystals. Opt. Comm. **283**, 1598–1606 (2010)
68. I.V. Shadrivov et al., Metamaterials controlled with light. Phys. Rev. Lett. **109**, 083902 (2012)
69. A.K. Popov et al., Four-wave mixing, quantum control, and compensating losses in doped negative-index photonic metamaterials. Opt. Lett. **32**, 3044–3046 (2007)
70. S. Gao, S. He, Four-wave mixing in left-handed materials. J. Nonlinear Optic. Phys. Mat. **16**, 485 (2007)
71. A. Rose et al., Controlling the second harmonic in a phase-matched negative-Index metamaterial. Phys. Rev. Lett. **107**, 063902 (2011)
72. M. Scalora et al., Generalized nonlinear Schrodinger equation for dispersive susceptibility and permeability: application to negative index materials, Phys. Rev. Lett. **95**, pp. 013902–013904 (2005); (Erratum: Phys. Rev. Lett. **95**, 239902(E) (2005))
73. D. Huang et al., Wave mixing in nonlinear magnetic metacrystal Appl. Phys. Lett. **98**, 204102 (2011)
74. J.B. Pendry et al., Magnetism from conductors and enhanced nonlinear phenomena. IEEE Trans. Microw. Theory Tech. **47**, 2075–2084 (1999)
75. M.W. Klein et al., Second-harmonic generation from magnetic metamaterials. Science **313**, 502 (2006)
76. M.W. Klein et al., Experiments on second- and third-harmonic generation from magnetic metamaterials. Opt. Express **15**, 5238–5247 (2007)
77. N. Feth et al., Second-harmonic generation from complementary split-ring resonatorsOpt. Lett. **33**, 1975–1977 (2008)
78. F.B.P. Niesler et al., Second-harmonic generation from split-ring resonators on a GaAs substrate. Opt. Lett. **34**, 1997–1999 (2009)
79. D. de Ceglia et al., Enhancement and inhibition of second-harmonic generation and absorption in a negative index cavity. Opt. Lett. **32**, 265–267 (2007)
80. G. D'Aguanno et al., Second-harmonic generation at angular incidence in a negative-positive index photonic band-gap structure. Phys. Rev. E **74**, 026608 (2006)

81. M. Scalora et al., Gap solitons in a nonlinear quadratic negative-index cavity. Phys. Rev. E **75**, 066606 (2007)
82. M. Lapine, Magnetoelastic metamaterials. Nat. Mater. **11**, 33012 (2012)
83. M. Lapine et al., Metamaterials with conformational nonlinearity. Scientific Rep. **1**, 138 (2011)
84. N.A. Zharova et al., Nonlinear control of invisibility cloaking. Opt. Express **20**, 14954–14959 (2012)
85. A. Pandey, N.M. Litchinitser, Nonlinear light concentrators. Opt. Lett. **37**, 5238–5240 (2012)
86. I.V. Shadrivov et al., Metamaterials Controlled with Light, Phys. Rev. Lett. **109**, 083902(4) (2012)
87. E. Feigenbaum, M. Orenstein, Plasmon-Solitons. Opt. Lett. **32**, 674–676 (2007)
88. N. Zharova et al., Nonlinear transmission and spatiotemporal solitons in metamaterials with negative refraction. Opt. Express **13**, 1291 (2005)
89. Y. Liu et al., Subwavelength discrete solitons in nonlinear metamaterials. Phys. Rev. Lett. **99**, 153901 (2007)
90. N.N. Rosanov et al., Knotted solitons in nonlinear magnetic metamaterials. Phys. Rev. Lett. **108**, 133902 (2012)
91. L.D. Faddeev, A.J. Niemi, Stable knot-like structures in classical field theory. Nature **387**, 58 (1997)
92. L.D. Faddeev, A.J. Niemi, Magnetic geometry and the confinement of electrically conducting plasmas. Phys. Rev. Lett. **85**, 3416 (2000)
93. R.A. Battye, P.M. Sutcliffe, Knots as stable soliton solutions in a three-dimensional classical field theory. Phys. Rev. Lett. **81**, 4798–4801 (1998)
94. I.V. Shadrivov et al., Nonlinear magnetoinductive waves and domain walls in composite metamaterials. Photon. Nanostr. Fundam. Appl. **4**, 69 (2006)
95. N.N. Rosanov et al., Discrete dissipative localized modes in nonlinear magnetic metamaterials,". Opt. Express **19**, 26500–26506 (2011)
96. R. Hegde, H. Winful, Optical bistability in periodic nonlinear structures containing left handed materials. Microw. Opt. Technol. Lett. **46**, 6 (2006)
97. N.M. Litchinitser et al., Optical bistability in a nonlinear optical coupler with a negative index channel. Phys. Rev. Lett. **99**, 113902 (2007)
98. G. Venugopal et al., Asymmetric positive-negative index nonlinear waveguide couplers. IEEE J. Sel. Opt. Quantum Electron. **18**, 2 (2012)
99. J. Peng et al., Modulation instability in dissipative soliton fiber lasers and its application on cavity net dispersion measurement. IEEE J. Lightwave Technol. **30**, 2707–2712 (2012)
100. Y. Xiang et al., Modulation instability induced by nonlinear dispersion in nonlinear metamaterials. J. Opt. Soc. Am. B **24**, 3058–3063 (2007)

Chapter 12
Metamaterials Tunable with Liquid Crystals

Maxim V. Gorkunov, Andrey E. Miroshnichenko and Yuri S. Kivshar

Abstract One of the efficient approaches to create tunable metamaterials is to infiltrate them with nematic liquid crystals taking advantages of a variety of tuning strategies employing temperature, external voltage, magnetic field, and power tunability of the parameters of liquid crystals. After infiltration, a hybrid metamaterial composite possesses tunable electromagnetic properties, which can be efficiently controlled by external fields and electromagnetic irradiation. In this chapter, we review different designs of liquid-crystal-infiltrated metamaterial structures for a new generation of tunable microwave, THz, and optical metadevices combining the advantages of metamaterials with the flexibility and large nonlinear response of liquid crystals.

12.1 Introduction

The great advantage of metamaterials is the possibility to control and design their electromagnetic properties by adjusting the assembly process. Upon the final arrangement, however, the metamaterial structures are robust and their response cannot be easily altered by external physical factors (e.g., irradiation or electric/magnetic fields). Prospects of tuning, spatially modulating or even switching on and off the

M.V. Gorkunov (✉)
A.V. Shubnikov Institute of Crystallography,
Russian Academy of Sciences, Moscow 119333, Russia
e-mail: gorkunov@crys.ras.ru

A.E. Miroshnichenko · Y.S. Kivshar
Nonlinear Physics Centre, Research School of Physics and Engineering,
Australian National University, Canberra, ACT 0200, Australia
e-mail: Andrey.Miroshnichenko@anu.edu.au

Y.S. Kivshar
e-mail: Yuri.Kivshar@anu.edu.au

I.V. Shadrivov et al. (eds.), *Nonlinear, Tunable and Active Metamaterials*,
Springer Series in Materials Science 200, DOI 10.1007/978-3-319-08386-5_12

functional metamaterial properties are extremely advantageous for photonic applications, near-field microscopy and imaging. Many important applications of photonic structures require also all-optical tunability provided by a nonlinear change of the optical response.

Liquid crystals (LCs) combine properties of crystalline solids and fluids in many unique and unexpected ways, giving rise to an increasingly broad range of technological and biomedical applications. LCs can be found in different phases, featuring different properties and order degrees, depending on their chemical composition and such external conditions as temperature, pressure, magnetic and electric fields. One of the most common phases of LCs is the so-called *nematic* phase, where the molecules exhibit a uniaxial orientational and no positional order. The average molecular orientation can be effectively described by a *director* pointing along the preferred orientation of molecules in the neighborhood of a certain point. In the absence of external fields or illumination, the director's spatial distribution is determined by the boundary conditions, i.e., the anchoring of the LC molecules at the interfaces. Importantly, LC molecules respond to applied electric and magnetic fields and sufficient illumination by changing their average orientation and thus modifying the director distribution and optical characteristics of the material. A general feature of the both voltage-driven and all-optical reordering of LCs is their strong dependence on the LC-cell geometry, positioning of the electrodes, the director field distribution, polarization and intensity of the incident light, etc.

A very natural way of attaining the metamaterial tunability is to combine the advantages of solid metal-dielectric structures with the flexibility of LC media. Generally, the feasibility of such approach is affirmed by several basic preconditions: (i) unusual properties of metal-dielectric structures are characterized by strong frequency dispersion and relatively small properly placed modifications of the structure may result in a substantial change of its response at a given signal frequency; (ii) optical properties of LCs can be easily switched by moderate temperature or electric fields, and by optical or UV irradiation; (iii) metal constituents of metamaterial structures can be readily used as electrodes, and they also significantly enhance the local electromagnetic fields. Another attractive opportunity is the possibility of self-assembly of metallic nanoparticles immersed into liquid crystals, which alignment can be further tuned by external fields. While in materials occurring in nature a sizable optical nonlinearity requires ultra-high light intensities and external voltages, the significant field concentration and subwavelength confinement in plasmonic and metamaterial structures allows achieving tunable linear or strongly nonlinear LC response with much more moderate powers.

Liquid crystals allow for unique realization of tunability of metamaterials by a variety of approaches: changing the temperature, applying external voltage or magnetic field, and also all-optically by employing strong nonlinear response. Importantly, these approaches are useful for microwave, THz and optical metamaterials and important 'proof of concept' first results have been obtained recently in all those frequency ranges.

In this chapter, we review the recent advances in the field of tunable and reconfigurable LC-metamaterials. In Sect. 12.2, we discuss a particular example of electrically

tunable wire metamaterial, where we describe all key mechanisms of liquid-crystal-induced tunability. Section 12.3 summarizes successful experimental realizations of liquid-crystal-tunability of microwave and THz metamaterials. Nanoscale-patterned metamaterials with tunable optical response are considered in the final Sect. 12.4.

12.2 Liquid-Crystal Tunability of Metamaterials

Liquid crystals are used in many practical devices which affect our lives, from simple displays for watches and calculators to fast colour displays for mobile phones, computer monitors and TVs. The industrial growth of diverse applications of liquid crystals is based on their remarkable electrical sensitivity. The vast experience accumulated in synthesis, processing and manipulation of LC substances has been primarily aimed at the LC display applications in the flat electro-optic cell geometry. Nevertheless, there are many gaps in the understanding of how liquid crystals behave in complex non-standard (e.g. metamaterial) environments. Thus, the development of hybrid LC-metamaterials has required to bridge these gaps and develop full understanding of LCs the behavior under new conditions.

To illustrate how the nematic LC behaves within a metamaterial and provides it with tunability, we analyze in this Section variation of the plasma frequency of wire-grid metamaterial as has been proposed in [1]. Applying voltage to the wire-grid structure immersed into a nematic LC induces the reorientation of the LC above a certain threshold. This rather simple metamaterial geometry allows semi-analytical description and provides a clear physical picture. Notably, the effect is present and qualitatively similar in a wide frequency range from microwaves to visible.

Regular arrays of parallel wires with subwavelength periodicity exhibit plasma-like permittivity for electromagnetic waves traveling normally to the wires and polarized along them (xy-plane of incidence and z-polarization of electric field in Fig. 12.1). The relevant component of the effective permittivity equals

$$\varepsilon_{zz}(\omega) = \varepsilon_{zz}^{(h)}(\omega) - \frac{\Omega^2}{\omega^2}, \tag{12.1}$$

where $\varepsilon_{zz}^{(h)}$ is the zz-component of the permittivity tensor of host medium surrounding the wires, while the characteristic frequency Ω is determined by the wire material, its diameter d and the lattice period a.

Since the wire grid permittivity (12.1) changes its sign at the so-called plasma-frequency $\omega_0 = \Omega/(\varepsilon_{zz}^{(h)})^{1/2}$, the grid on its own is transparent at frequencies higher than ω_0 and reflecting at lower frequencies.

The presence of $\varepsilon_{zz}^{(h)}$ in (12.1) suggests an easy way of tuning the metamaterial by varying the host medium permittivity. Nematic LCs provide a natural opportunity to realize this.

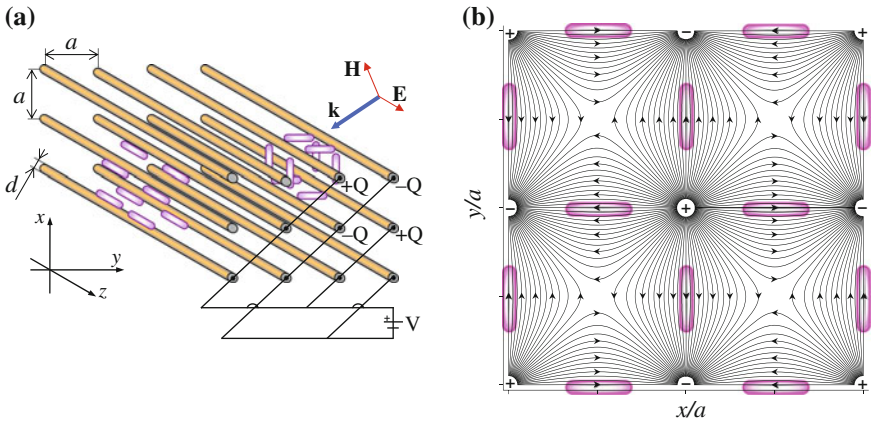

Fig. 12.1 Wire-grid metamaterial immersed into nematic LC: **a** LC-molecules oriented along wires (*left*) and across the wires (*right*). Note: the size of LC molecules is extremely exaggerated. **b** Field lines of alternatingly charged wires (for wire diameter set to 0.1 of the lattice period) with superimposed LC molecules orientations

Nematic LCs exhibit anisotropic tensorial permittivity, which axes follow the orientation of the nematic director **n**:

$$\varepsilon_{ij}^{(h)}(\omega) = \varepsilon_{\perp}(\omega)\,\delta_{ij} + \varepsilon_a(\omega)\,n_i n_j. \tag{12.2}$$

On appropriately prepared surfaces, elongated LC molecules typically tend to orient along them. The corresponding LC alignment by this so-called surface anchoring at the wires is shown in Fig. 12.1a on the left. Applying voltage across the neighboring wires, one can load the wires with charges of different signs, which give rise to static electric field in the xy-plane. The latter reorients the LC molecules perpendicularly to the wires as shown in Fig. 12.1a on the right. As a result, $\varepsilon_{zz}^{(h)}$ switches from $(\varepsilon_{\perp} + \varepsilon_a)$ to $\varepsilon_{\perp}$ shifting ω_0 relatively by

$$\frac{\Delta\omega_0}{\omega_0} \simeq \frac{\varepsilon_a}{2\varepsilon_{\perp}}. \tag{12.3}$$

The dielectric anisotropy of LC is known to be at least of the order of several dozens of percent for both microwaves and light [5, 6]. Therefore, the proposed design provides a possibility of shifting the plasma-frequency by 10–20 %.

A single wire stretched along the line $x = 0$, $y = 0$ and loaded with the charge Q per unit length produces the electric field potential $\varphi_1(\rho) = -Q/(2\pi\varepsilon_0\varepsilon_{\mathrm{st}})$ $\log(2\rho/d)$, where $\rho = \sqrt{x^2 + y^2}$, $\varepsilon_{\mathrm{st}} = \varepsilon_{\perp}(0)$ is the static permittivity of the LC, and the zero of the potential is assigned to the wire surface. In the infinite 2D lattice of alternatingly charged wires, the total potential outside of the wires is

$$\varphi(\mathbf{r}) = \sum_{n,m=-\infty}^{n,m=\infty} (-1)^{n+m} \varphi_1(\rho_{nm}), \tag{12.4}$$

where $\rho_{nm} = \sqrt{(x - na)^2 + (y - ma)^2}$ and the coordinate origin lies on the axis of a positively charged wire. Typical calculated electric field pattern is shown in Fig. 12.1b.

Analyzing the effect of the electric field on the nematic LC one can start with totally neglecting the LC elasticity, when the anisotropic molecules align along the field lines. The director $\mathbf{n}$ then lies strictly in the xy-plane and the switching is perfect (see Fig. 12.1b). The finite elasticity of LC disturbs this ideal picture and the bending pattern of the director differs from the field lines pattern. However, this is of minor importance for the component $\varepsilon_{zz}^{(h)}$ involved in (12.1) since the director still stays in the xy-plane.

To ensure the LC orientation along the wires when the voltage is switched off, the anchoring of LC molecules at the wires must be strong. When the voltage is switched on, the surface anchoring still forces the adjacent molecules to point along the z-axis and the director has to rotate by an angle of $\pi/2$ within a transient layer. Efficient switching occurs when this layer is thin compared to the scale of the structure (lattice constant), i.e., the limit of strong electric field and thin transient layer is practically important. In this limit, we can neglect the contributions from other wires to the field near a wire surface. In the cylindrical coordinates, the only present ρ-component of the electric field equals $E_\rho(\rho) = \frac{Q}{2\pi\varepsilon_0\varepsilon_{\rm st}}\rho^{-1}$ while the nematic director has two components $n_\rho(\rho)$ and $n_z(\rho)$. At the wire surface $n_\rho(d/2) = 0$. The free energy of the LC can be presented as the sum $F = F_K + F_E$ of the elastic deformation energy and the dielectric energy [5], where the latter reads

$$F_E = -\pi\varepsilon_0\varepsilon_a^{\rm st} \int_{d/2}^{R} \rho\, d\rho\, (E_\rho n_\rho)^2. \tag{12.5}$$

Here the upper limit R is large enough to assure $n_z(R) = 0$ and can be extended to infinity. The simplest form of the LC elastic energy is given by the so-called one constant approximation:

$$F_K = \frac{K}{2} \int dV \left[(\nabla \cdot \mathbf{n})^2 + (\nabla \times \mathbf{n})^2 \right]. \tag{12.6}$$

Introducing the director polar angle θ as $n_\rho = \sin\theta$, $n_z = \cos\theta$ we obtain the compact form of the total energy

$$F = \pi K \int_{d/2}^{\infty} \rho\, d\rho \left[(\theta')^2 + (1 - v^2)\frac{\sin^2\theta}{\rho^2} \right], \tag{12.7}$$

where the parameter $v^2 = V^2 c_1^2 \varepsilon_a^{\rm st}/(4\pi^2 K \varepsilon_0)$ characterizes relative contribution of the voltage-driven term, where c_1 is the capacitance per pair of wires in vacuum per length.

Minimizing the functional (12.7) yields the differential equation for $\theta(\rho)$:

$$\theta'' + \frac{1}{\rho}\,\theta' + (v^2 - 1)\frac{\sin 2\theta}{2\rho^2} = 0 \tag{12.8}$$

with the boundary conditions $\theta(d/2) = 0$ and $\theta(\infty) = \pi/2$. For $v^2 > 1$ the exact solution reads:

$$\theta(\rho) = \frac{\pi}{2} - 2\arctan\left[(d/2\rho)^{\sqrt{v^2-1}}\right]. \tag{12.9}$$

The spatial variation of the zz-component of dielectric tensor (12.2), is controlled by the factor $n_z^2(\rho) = \cos^2\theta(\rho)$. For $v^2 \gtrsim 2$ the layer thickness becomes comparable with the wire diameter. For estimates, we take a nematic LC elastic modulus $K \simeq 10^{-11}$N, static permittivity $\varepsilon_{\rm st} \simeq 10$ and static dielectric anisotropy $\varepsilon_a^{\rm st} \simeq 1$. We also set the wire diameter to be ten times smaller than the lattice constant, which yields $c_1 \simeq 10^{-11}$F/m. Then appropriate voltage is estimated as

$$V = \frac{2\pi}{c_1}\sqrt{\frac{2K\varepsilon_0}{\varepsilon_a^{\rm st}}} \simeq 8.4\,\text{V}. \tag{12.10}$$

Remarkably, this moderate voltage is independent of the scale of the grid and is equally appropriate for the estimates of switching of microwave and optical wire-grid metamaterial.

12.3 Tunable Microwave and THz Metamaterials

Although for many decades the research on LCs has been primarily focused on visible and near-infrared frequency ranges, LCs have been known to possess low losses and reasonably high dielectric anisotropy at lower THz and microwave frequencies. Their straightforward implementation for microwave manipulation by analogy with optics, however, requires fabrication of planar LC-cells of thickness larger than the operational wavelength, i.e., up to several millimeters and even more. Within the conventional technological approach to align LC by specially treated surfaces, there exists a rather strict limit on the LC thickness that cannot be extended to more than few hundred microns, and already then the LC switching slows down drastically and becomes unreliable [8]. Therefore, from the 1990s the moderate progress in LCs for microwaves was restricted to designs employing small volumes of LCs, such as LC-filled resonator cavities [9] or more complex stack-layered structures composed of many thin LC layers [10].

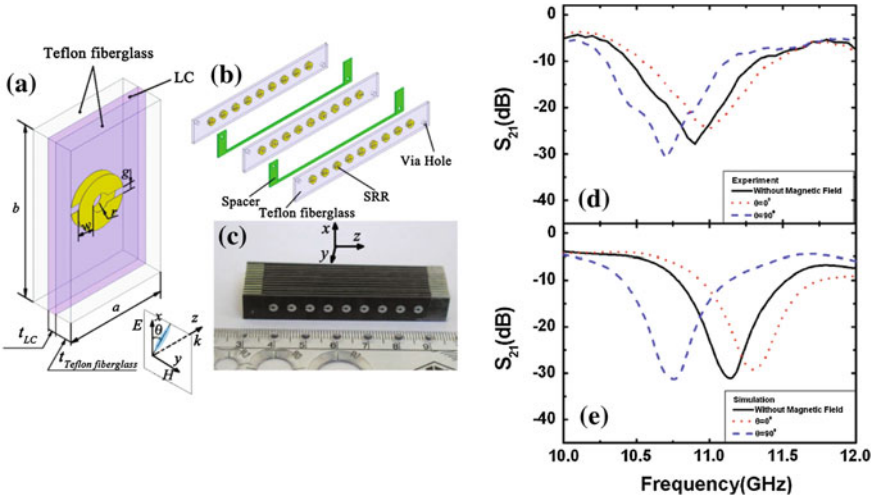

Fig. 12.2 Magnetically tunable broadside coupled SRR metamaterial based on anisotropic LC [12]: **a** Schematic diagrams of basic unit cell and the reorientation of LC molecule, **b** schematic diagram of the assembly process, **c** photograph of the SRR sample, **d** experimental demonstration of the magnetically tunable transmittance, **e** calculated tunable transmittance. See [12] for further details

In the past decade, the emergence of metamaterials (or, more generally, subwavelength structures with metallic components) has demonstrated the vast prospects of controlling wave propagation by structures of deeply subwavelength scale and thickness. This opened new prospects for LCs in the microwave range and from the middle of 2000s new designs involving subwavelength metal structures have started to emerge [6, 7].

Naturally, a direct immersion of multilayered microwave metamaterial into LC environment requires large volumes of LC to be controlled. A straightforward scaling up of the optical geometries is accompanied by the necessity to use rather high external power to achieve a noticeable effect. Indeed, since the electric field amplitudes necessary for LC reorientation are typically of the order of several Volts per micron, for a microwave metamaterial sample of the size of several centimeters this can easily sum up to the voltage drop of several kV. Only upon such voltages, the LC reorientation appears to be sufficient to cause a noticeable variation of the metamaterial electromagnetic properties. As has been shown in [11], where such an approach was used for realigning the LC-environment of a conventional microwave metamaterial made of millimeter-sized split rings, the corresponding shift of the metamaterial 10 GHz resonance by up to 200 MHz is feasible. One may expect, however, that the characteristic switching times in such geometry exceed by orders of magnitude those required for microwave device applications.

Alternatively, one can employ dc magnetic fields, which have been known to produce sufficient orientation of the LC-director in comparably large volumes. In this

approach, the amount of efficiently controlled LC is limited only by the technological capabilities of creating a volume with sufficiently strong homogeneous magnetic field. It is due to the very small anisotropy of the LC magnetic susceptibility, however, that one has to use rather extreme magnetic fields of 1 kG and more in order to orient a conventional LC properly, and the practical value remains diminished by the necessity to use strong magnets. Having said that, one still acknowledges the role of such designs in demonstrating the general value of LC-metamaterial systems as a tool for microwave manipulation.

It is the magnetic reorientation of LC molecules that has allowed the authors of [12] to demonstrate that realigning the LC environment of a metamaterial made of mm-sized split rings one can indeed produce noticeable changes to the microwave transmittance (see Fig. 12.2). Although the observed tuning of the transmittance was somehow weaker than predicted by modeling, the distinct shift of the sharp transmittance dip related to the magnetic resonance of the metamaterial has confirmed the feasibility of the promising phenomenon and some of its valuable details. Quite naturally, the LC in the absence of magnetic field appeared to be not in a fully ordered state. Applying magnetic field along and perpendicular to the metamaterial split ring elements has aligned the LC director macroscopically and the resonance shift from the initial position at 10.9–11 and 10.7 GHz respectively has been clearly seen. The same effect has been obtained later on with a microwave metamaterial made of omega-shaped elements [13]. Such an element shape gave rise to a definite negative index pass band of the metamaterial, which has been successfully tuned by about 0.5 GHz when dc magnetic field of 0.5 kG along and perpendicular to the metamaterial planes has been applied. Notably, here also a strong dependence of the phase retardation of the microwave signal on the LC orientation has been reported. At frequencies close to the lower edge of the pass band, the LC environment has been able to tune the output signal phase by up to 180°.

More prospective from the practical point of view type of LC-metamaterial arrangement for microwaves comprises a pair of planar patterned metal planes separated by a relatively thin (hundreds of microns) inter-layer of nematic LC. The reduced LC thickness here critically decreases the driving voltage to several tens of Volts and the tuning response time to the sub-second range. The role of patterned metal layers in this case is to provide distinct frequency dispersion of the transmittance due to intrinsic resonances and narrow pass-bands as well as to deliver the driving voltage across the LC layer.

A simple realization of this strategy has been reported in 2007 [14] where the sub-THz transmittance of a pair of frequency-selective surfaces (arrays of rectangular slots in copper planes as shown in Fig. 12.3a has been continuously tuned via reorientation of 130 μm thin nematic LC inter-layer (see Fig. 12.3b, c). The transmittance spectrum of such patterned planes possesses a rather sharp Rayleigh-Wood diffraction grating anomaly for 45° obliquely incident TM wave. By applying a moderate bias voltage of 10 V (5 kHz with triangular pulse shape) across the LC inter-layer the authors have been able to move continuously the spectral anomaly around 130 GHz by about 3 % as illustrated by Fig. 12.3d. The physical mechanism of this becomes clear when one notices that the spectral position of the diffraction

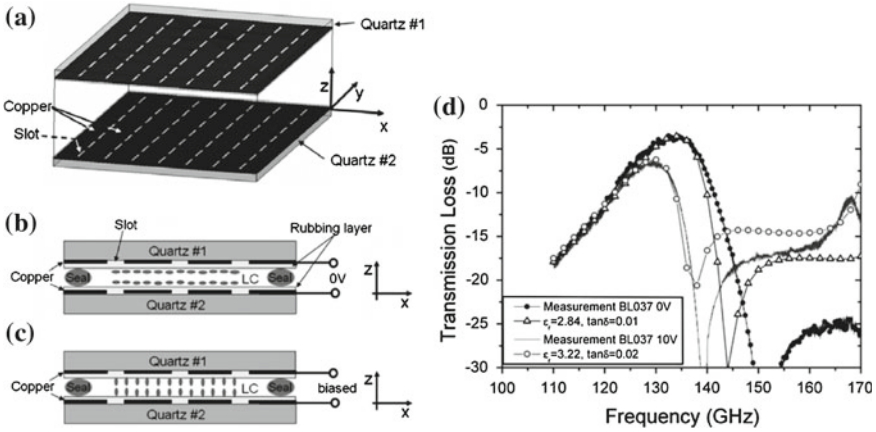

Fig. 12.3 Electrically tunable microwave frequency selective surface [14]: **a** Schematic plot of dual layer tunable frequency selective surface, **b** LC orientation in the unbiased state, **c** LC orientation upon external voltage, **d** measured and predicted tunable spectral response. See [14]

anomaly is fully determined by the frequency at which a certain order of diffraction disappears (transforms from propagating into evanescent wave). For a grating clad with a dielectric, this diffraction cut off condition directly depends on the wavelength of radiation in the dielectric, or, more precisely, on the refractive index of waves traveling parallel to the grating plane. Voltage applied across the LC causes rotation of its main dielectric axes, which modifies the relevant refractive index and continuously shifts the diffraction anomaly.

As has been demonstrated in [15], this geometry can be employed also at lower frequencies around 10 GHz. In order to achieve a noticeable tunability, one has to employ here thicker LC layers (up to half a millimeter). This increases the necessary driving voltage to 60 V, which provides a 340 MHz shift of the pass-band although the relative changes in the transmission spectrum are still weaker than those reported for the 130 GHz structure [14]. At the same time, the effect of the LC reorientation on the transmitted wave phase shift by about 30° is quite remarkable. The origin of such a high sensitivity is the very sharp frequency dispersion of the phase around the resonant spectral anomalies of the slot grating. Therefore, in prospective one can employ such metamaterial-LC structures in tunable microwave phase shifters.

More efficient tuning at frequencies around 10 GHz has been achieved by employing more complex patterning of metal planes. Thus two surfaces with rectangular metal patches being brought close enough arrange effectively a layer of the short wire-pair metamaterial with a pronounced sharp magnetic resonance. Filling the complimenter void between the planes with a nematic LC and controlling its alignment by the voltage applied to the patches across the LC the authors of [16] have been able to tune the resonant frequency by up to 5 % . Remarkably, here the sharpness of the resonance enables a substantial variation of the transmitted energy by up to an order of magnitude in the vicinity of the resonance. The variation of the transmitted

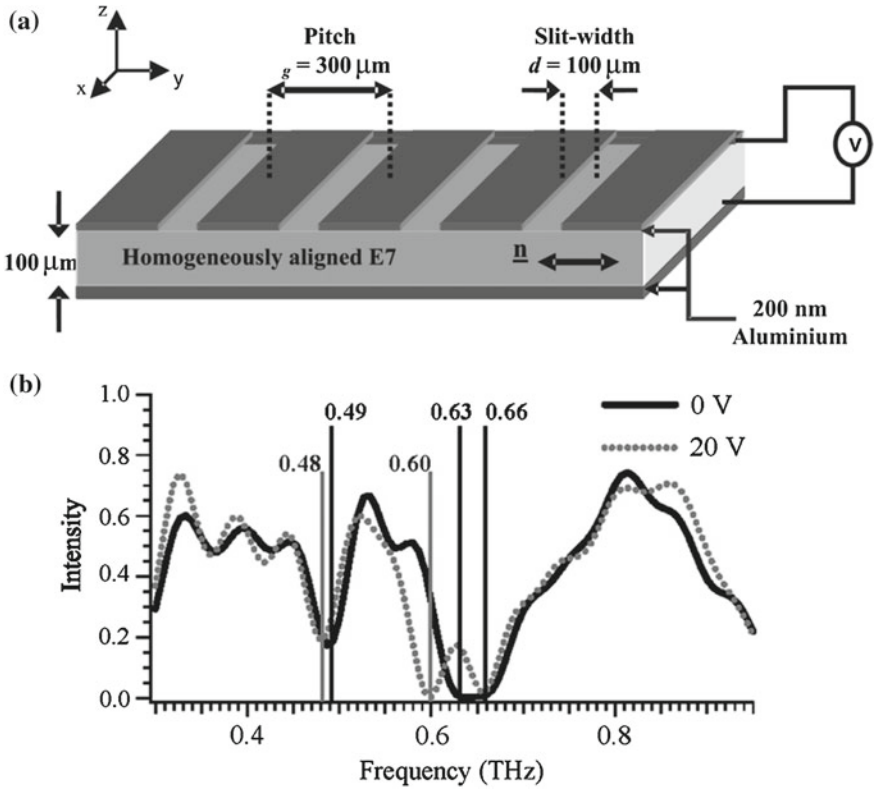

Fig. 12.4 Grating structure with electrically tunable resonant absorption of THz radiation [17]: **a** Schematic of the structure filled with homogeneously aligned E7 nematic LC, **b** measured reflected intensity (arbitrary units) versus frequency for a THz pulse polarized perpendicular to the slits with 0 and 20 V peak-to-peak voltage at frequency of 10 kHz applied. See [17] for further details

wave phase shift can be made here as high as 90° with the voltage around 100 V applied. Quite notable also is the low response time of 300 ms reported in [16] for the 0.6 mm thick LC inter-layer.

By replacing one of the patterned metal planes with a metal mirror one can naturally obtain very similar effects for microwaves in the reflection geometry. Thus the feasibility of LC-assisted switching of reflectivity of a subwavelength metal grating at frequencies from 100 GHz to 3 THz has been demonstrated experimentally [17]. In this work a 200 nm thin 300 μm-periodic 1D grating was placed at 100 μm above a metal mirror while the space between the grating and the mirror was filled with homogeneously aligned nematic LC (See Fig. 12.4a). Such a structure on its own possesses pronounced reflectivity resonances related to the formation of standing waves in the cavities effectively formed by the grating stripes and the mirror plane. Applying voltage across the LC layer, causes the LC reorientation sufficient to produce a noticeable modification of the reflectivity spectrum. At certain sub-THz

frequencies a substantial drop of the reflectivity from about 30 % to almost zero has been observed, while at other frequencies a moderate 5–10 % variation of reflectivity close to unity has been reported. The bias voltage of 20 V was sufficient here to achieve such an efficient switching (See Fig. 12.4b).

In order to decrease further the size and driving voltage, more complex reflecting structures are to be used. As shown in [18], it is not really necessary to create a full LC inter-layer between the patterned metal and the mirror planes. It appears that the substantial part of this volume underneath the metal strips of the pattern can be filled with a solid transparent dielectric (e.q. a polymer), and the tuning can take place only due to reorientation of the nematic LC filling the structural gaps of the scale of tens of microns. This has allowed increasing the tuning sensitivity and enabled switching of the reflectivity by voltages of just few Volts, i.e., common for optical LC cells. The absorption resonance has been continuously shifted down from 2.62 to 2.5 THz, which, due to the sharpness of the resonance, appeared to be enough to decrease the absorbance from 0.85 to 0.55 % at the 2.62 THz frequency.

To summarize, the concept of LC-assisted tunability has opened wide prospects for designing tunable and adjustable metamaterials and has resulted in new types of various devices for microwave and THz applications: tunable phase shifters and modulators, adjustable absorbers and mirrors, etc. While the simple scaling of optical geometries can provide noticeable switching, the large amount of LC to be controlled increases the necessary driving powers substantially, decreases the reliability and slows down the switching. At the same time, specific arrangements comprising two parallel patterned metal planes or a single patterned plane above a mirror are able to provide efficient and fast control of the microwave and THz wave propagation.

12.4 Tunable Optical Metamaterials

The reorientation of nematic molecules, responsible, e.g., for modulation of the refractive index, can be induced by the electric field of a laser beam, similar to the externally applied voltage, as in the majority of current applications. The optical feedback provided by the variation of the refractive index beyond the transition results in the so-called *giant optical nonlinear response*. The strength of the nonlinear response depends on the degree of the reorientation. It is known that such orientational nonlinearity is several orders of magnitudes stronger than conventional Kerr-type nonlinearity [19]. Local variation of the molecular orientation results in changes to polarization of light, as it passes through the reoriented liquid crystal beyond the transition.

Realization of the liquid-crystal tunability of metamaterials in the near infrared and optical regime is a hard task, however, thermal and UV-irradiation-induced tunability of optical metamaterials have been were performed experimentally [20, 21]. In the former case, the magnetic response wavelength of the metamaterial was effectively tuned through control of the ambient temperature, changing the refractive index of liquid crystal via phase transitions. By increasing the ambient temperature

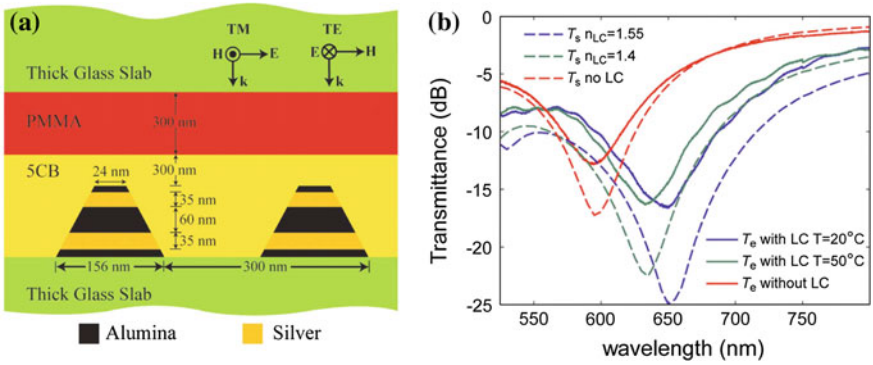

Fig. 12.5 **a** The cross-sectional schematic of arrays of coupled nanostrips. **b** Demonstration of a thermally tunable magnetic response in a metamaterial. Solid lines show the experimental data, and dashed lines represent simulated results without LCs (*blue lines*), with LCs on top at 20 °C (*black lines*) and at 50 °C (*red lines*)

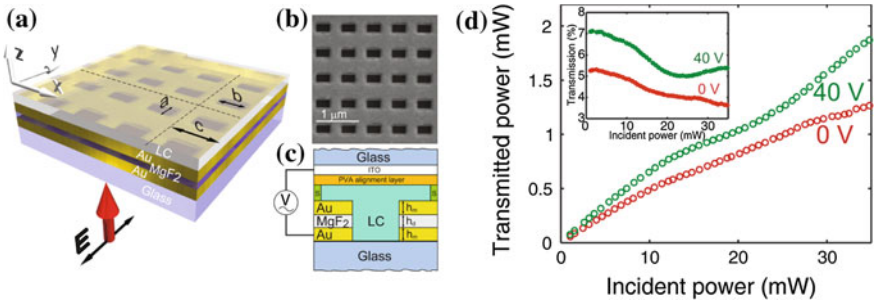

Fig. 12.6 **a** Schematic of the LC infiltrated fishnet metamaterial. **b** Scanning electron microscope image (*top view*) of the fabricated fishnet metamaterials. **c** Side view of the LC cell: S is 100 μm thick plastic spacers. Parameters for the fabricated Au-MgF_2-Au fishnet are $h_d = h_m = 50$, $a = 190$, $b = 350$, and $c = 600$ nm. **d** Measured transmission at 1550 nm versus input power for two bias voltages 0 and 40 V. *Dashed curve*—linear dependence. Inset: Normalized transmission versus incident laser power

from 20 to 50°C, the magnetic response wavelength was shown to shift from 650 to 632 nm (see Fig. 12.5). As the phase transition of liquid crystals can affect the refractive index over the whole optical wavelength spectrum and even into the microwave range, it is therefore possible to tune the magnetic response of metamaterials through the whole optical range [22, 23].

All-optical control of fishnet metamaterials infiltrated with liquid crystals was studied experimentally only recently [24]. In their experiments, the authors fabricate fishnet structure using gold and MgF_2 as metal and dielectric layers deposited on a glass substrate (see Fig. 12.6a). For nanostructuring of the metal-dielectric layers, they use focused ion beam milling, fabricating a typical fishnet structure as shown in the scanning electron microscope in Fig. 12.6b. This sample is then infiltrated with

E7 nematic LC (from Merck) making sure that the LC completely fills the holes of the fishnet. The presence of the LC inside the structure is verified by transmission measurements where the shift of the hole mode manifesting the infiltration is observed. Furthermore, bias electric field can be applied between the top ITO electrode and the gold film for electrical control of the LC molecular alignment (see Fig. 12.6c).

In order to test the dependence of the optical transmission on light intensity, they illuminate the infiltrated structures from the substrate side by a laser beam at a telecom wavelength of 1550 nm. If the fishnet structure is placed into the laser beam, a substantial drop in the transmission is observed with increasing of the incident laser power. As the power is increased, the transmission is reduced by approximately 30 % (see Fig. 12.6d). Minovich et al [24] also observed that the transmission drop is strongly dependent on the application of a bias electric field, indicating again strong molecular reorientation of the liquid crystals inside the holes of the fishnet structure. This interplay between the optical and the bias electric field induced liquid crystal reorientation demonstrates an important mechanism of electrically controlled optical non-linearity in metamaterials.

Another interesting study was focused on the optical response of a metamaterial surface created by a lattice of split-ring resonators (SRRs) covered with a nematic liquid crystal [25]. The LC-metamaterial cell is shown in Fig. 12.7 and consist of an array of gold SRRs with a lattice spacing of 300 nm on a glass substrate covered with 5 nm of Indium-Tin-Oxide (ITO) fabricated by a standard electron-beam lithography (EBL) process. The lateral dimensions of the individual SRR meta-atoms are $l_x \approx 138$ nm, $l_y \approx 124$ nm and the line width is $w \approx 45$ nm. The SRR thickness is 25 nm. The transparent conductive ITO layer prevents charge accumulation during EBL and also serves as one of the two electrodes needed to apply the electric potential to the LC cell. The second ITO-covered glass substrate serves as the top electrode of the LC cell. To allow for a defined pre-alignment of the LC at the top electrode we additionally spin-coat a 200 nm-thin layer of polyvinyl alcohol (PVA) on top of the ITO layer and mechanically brush the PVA to obtain a preferred direction for LC pre-alignment (yellow arrow in Fig. 12.7a). No LC pre-alignment layer has been used on the metasurface. Finally, the LC cell is assembled by placing a 31 μm-thick spacer between the metamaterial substrate and the second PVA-coated electrode. After infiltration with the liquid crystal E7 from Merck at T = 90 °C, the LC cell is mounted in a home-built white-light transmittance setup and connected to an adjustable function generator that provides a sinusoidal AC voltage with 1 kHz frequency.

Figure 12.7b shows experimental rests for the x-polarized incident light with and without bias voltage V. In this configuration the electric resonance at $\lambda_{e0} \approx 900$ nm is excited in the "OFF" state. When changing from "OFF" to "ON" a clear change in the transmittance spectrum occurs and the magnetic resonances at $\lambda_{m1} \approx 800$ nm and $\lambda_{m2} \approx 600$ nm are observed. By changing the voltage from "ON" to "OFF" the original spectrum is restored. Remarkably, the dynamical switching between the electric and magnetic resonances of the SRR metamaterial is be achieved on a

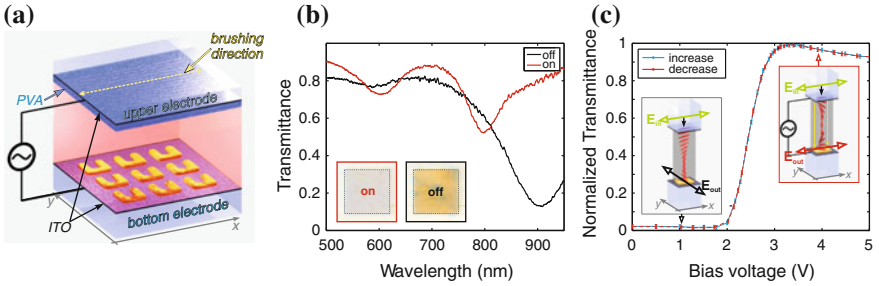

Fig. 12.7 **a** Artistic view of the LC cell. The SRR metamaterial is processed on top of the bottom electrode while the upper electrode is covered with an alignment layer of mechanically brushed PVA. An AC power supply is connected to the conductive ITO films (plotted in *dark gray*). **b** Experimental transmittance spectra of the LC cell with no voltage applied (*OFF state, black*) and for V = 6 V ("ON" state, *red*). Insets: CCD images of the metamaterial area in the OFF and ON state. **c** Threshold behavior of the switching process for increasing (*blue*) and consecutive decreasing (*red*) voltages. The left inset depicts the (helical) LC distribution in the "OFF" state, the right inset shows the situation in the ON state (no helical distribution). The incident and output light polarizations are indicated as *green* and *red/black arrows*, respectively

millisecond timescale. This effect is a result of the reorientation of LC molecules in the presence of a bias electric field.

Opposite effect is observed for y-polarized incident light. In this configuration, the emerging light is x-polarized in the "OFF" state, and no transmittance is observed in y-polarization, while in the "ON" state the full spectrum is detected. The voltage dependent transmittance is then averaged over the whole spectral range. Clearly, the switching process for increasing (blue line) and decreasing (red dashed line) values of the applied voltage reproducibly takes place in the voltage range of 2–3 V showing no hysteresis (see Fig. 12.7c). Above V = 5 V the transmittance saturates, hence, for this case the LC molecules are completely reoriented by the electric field.

These results have important implications for LC tuning of optical metamaterials since those experiments crucially rely on the ability to reorient the LC molecules within the near-fields of the metallic structure in the negative-index spectral range. Moreover, this scheme opens up new opportunities for fast switching between electric and magnetic metasurfaces, which also allows for dynamic control of light reflection.

When more than one particle is immersed in the LC the particles interact with each other via a unique type of interaction that arises from the anisotropic orientational elasticity of LCs [26, 27]. Depending on the interactions between the particles, colloidal structures can be dramatically modified and modulated by applying an additional external field [28, 29]. In multi-particle structures the orientational elasticity of liquid crystals gives rise to long-range anisotropic interactions between particles with both repulsive and attractive components. Altering the shapes of particles can lead to remarkable changes in the symmetry of their elastic interactions [30]. This concept was suggested for the creation of *reconfigurable optical metamaterials*, for example by aggregation-free elastic self-alignment of gold nanorods dispersed in liq-

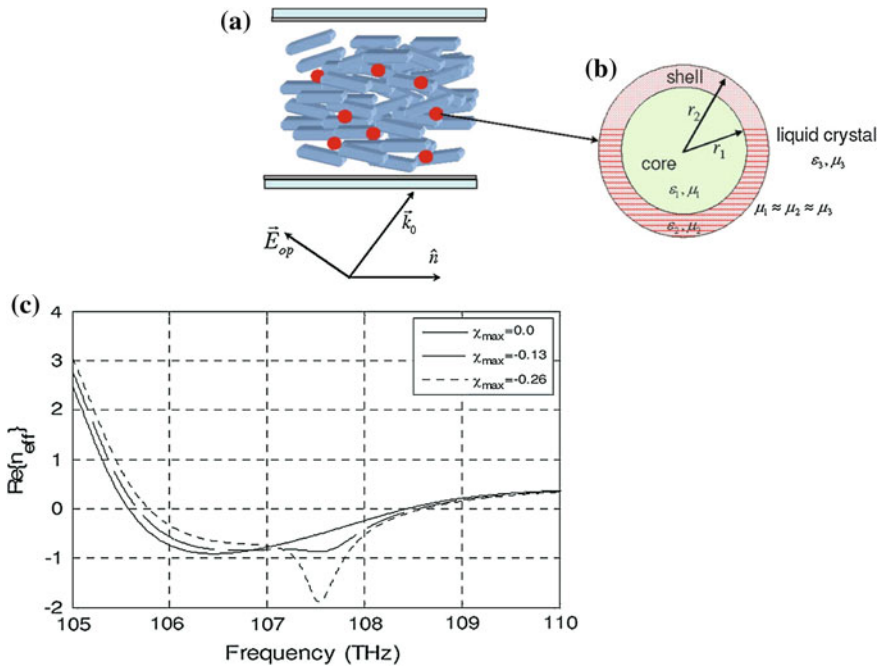

Fig. 12.8 **a** Schematic depiction of a linearly polarized light incident as an extraordinary wave on a planar aligned nematic liquid crystal containing core- shell nanoparticles. Figure on *right-hand side* shows an exploded view of the core-shell nanospheres. **b** Real and **c** imaginary parts of the refractive index of nano-dispersed dye-doped nematic liquid crystals showing enhanced negative index behavior and a lowered loss (smaller imaginary refractive index)

uid crystals [31]. These recent developments in the robust control over positioning, orientation and assembly of colloidal particles of various forms permit new types of structured composite materials to be created [32, 33].

In particular, recently it was suggested to use the special case of core-shell nanoparticles immersed in dye-doped nematic liquid crystals that could also provide with optical gain [34]. There are several dyes that provide sufficient optical gain which have been used in laser generations in nematic and cholesteric liquid crystalline media. Thus, they maybe effectively use to suppress the metamaterials' loss, while achieving the desired tunable birefringence. Figure 12.8 shows the real and imaginary part of the effective refractive index of the core-shell nanoparticles embedded into dye-doped nematic LCs for three representative values of the imaginary part of the susceptibility of dye molecules transition at the resonant frequency $\chi_{max} = 0, -0.13,$ and -0.26. It clearly demonstrates that one could maintain negative refractive index $Re[n_{eff}]$ while reducing the loss $Im[n_{eff}]$ considerably. It is also interesting to note that the real part of the refractive index $Re[n_{eff}]$ could also be decreased even further with the incorporation of the gain medium (for $\chi_{max} = -0.26$). This also allows to achieve relatively fast sub-microsecond response of LCs [35].

One of the most promising applications of tunable optical metamaterials is a light-driven reconfigurable near perfect plasmonic absorber. Recently, there were suggested two design based on LC-coated arrays of asymmetric nanodisks [36] and metamaterial cells [37]. In the former case, nanodisks of different sizes were employed in certain arrangement allowing for near perfect absorption of incident electromagnetic waves. It was demonstrated that optically induced changes in the dielectric constant of the adjacent LC layer can be used as an effective mechanism to tune the absorption bands of an asymmetric gold nanodisk array with a tunable range of 25 nm [36]. In the second case the ability to modify the absorption of the specifically designed optical metamaterial by 30 % at 2.62 THz was experimentally demonstrated, as well as tunability of the resonant absorption over 4 % in bandwidth [37].

Acknowledgments M.V.G. acknowledges a support from the Russian Foundation for Basic Research (project No. 13-02-12151 ofi_m), A.E.M. and Y.S.K. acknowledge a support from the Australian Research Council. The authors are very grateful for useful collaboration with many colleagues including especially M. Osipov, D. Neshev, I. Shadrivov, M. Lapine, A. Minovich, and M. Decker.

References

1. M.V. Gorkunov, M.A. Osipov, J. Appl. Phys. **103**, 036101 (2008)
2. J.B. Pendry, A.J. Holden, W.J. Stewart, I. Youngs, Phys. Rev. Lett. **76**, 4773 (1996)
3. P.A. Belov, R. Marques, S.I. Maslovski, I.S. Nefedov, M. Silveirinha, C.R. Simovski, S.A. Tretyakov, Phys. Rev. B **67**, 113103 (2003)
4. M.G. Silveirinha, Phys. Rev. E **73**, 046612 (2006)
5. W.H. de Jeu, *Physical Properties of Liquid Crystalline Materials* (Gordon and Breach, London, 1980)
6. J.R. Sambles, R. Kelly, F. Yang, Phil. Trans. R. Soc. A **364**, 2733 (2006)
7. T.S. Kasirga, Y. Nuri Ertas, M. Bayindir, Appl. Phys. Lett. **95**, 214102 (2009)
8. M. Tanaka, T. Nose, S. Sato, Jpn. J. Appl. Phys. **39**, 6393 (2000)
9. K.C. Lim, J.D. Margerum, A.M. Lackner, Appl. Phys. Lett. **62**, 1065 (1993)
10. M. Tanaka, S. Sato, Jpn. J. Appl. Phys. **40**, L1123 (2001)
11. Q. Zhao, L. Kang, B. Du, B. Li, J. Zhou, H. Tang, X. Liang, B. Zhang, Appl. Phys. Lett. **90**, 011112 (2007)
12. F. Zhang, Q. Zhao, L. Kang, D.P. Gaillot, Z. Zhao, J. Zhou, D. Lippens, Appl. Phys. Lett. **92**, 193104 (2008)
13. F. Zhang, L. Kang, Q. Zhao, J. Zhou, X. Zhao, D. Lippens, Opt. Exp. **17**, 4360 (2009)
14. W. Hu, R. Dickie, R. Cahill, H. Gamble, Y. Ismail, V. Fusco, D. Linton, N. Grant, S. Rea, IEEE Microw. Wirel. Compon. Lett. **17**, 667 (2007)
15. F. Zhang, W. Zhang, Q. Zhao, J. Sun, K. Qiu, J. Zhou, D. Lippens, Opt. Exp. **19**, 1563 (2011)
16. F. Zhang, Q. Zhao, W. Zhang, J. Sun, J. Zhou, D. Lippens, Appl. Phys. Lett. **97**, 134103 (2010)
17. S.A. Jewell, E. Hendry, J.R. Sambles, Mol. Cryst. Liq. Cryst. **494**, 320 (2008)
18. D. Shrekenhamer, W. Chen, W.J. Padilla, arXiv:1206.4214v1 (2012)
19. N.V. Tabiryan, A.V. Sukhov, B.Ya. Zeldovich, Mol. Cryst. Liq. Cryst. **136**, 1 (1986)
20. S. Xiao, U.K. Chettiar, A.V. Kildishev, V. Drachev, I.C. Khoo, V.M. Shalaev, Appl. Phys. Lett. **95**, 033115 (2009)
21. B. Kang, J.H. Woo, E. Choi, H.-H. Lee, E.S. Kim, J. Kim, T.-J. Hwang, Y.-S. Park, D.H. Kim, J.W. Wu, Opt. Exp. **18**, 16492 (2010)

22. D.H. Werner, D.-H. Kwon, I.-C. Khoo, A.V. Kildishev, V.M. Shalaev, Opt. Express **15**, 3342 (2007)
23. X. Wang, D.-H. Kwon, D.H. Werner, I.-C. Khoo, A.V. Kildishev, V.M. Shalaev, Appl. Phys. Lett. **91**, 143122 (2007)
24. A. Minovich, J. Farnell, D.N. Neshev, I. McKerracher, F. Karouta, J. Tian, D.A. Powell, I.V. Shadrivov, H. Hoe Tan, C. Jagadish, Yu.S. Kivshar, Appl. Phys. Lett. **100**, 121113 (2012)
25. M. Decker, C. Kremers, A. Minovich, I. Staude, A.E. Miroshnichenko, D. Chigrin, D.N. Neshev, C. Jagadish, Y.S. Kivshar, Opt. Express **21**, 8879 (2013)
26. I. Musevic, M. Skarabot, U. Tkalec, M. Ravnik, S. Zumer, Science **313**, 954 (2006)
27. O.D. Lavrentovich, Proc. Natl. Academy Sci. **108**, 5143 (2011)
28. A.B. Golovin, O.D. Lavrentovich, Appl. Phys. Lett. **95**, 254104 (2009)
29. M.V. Gorkunov, M.A. Osipov, Soft Matter **7**, 4348 (2011)
30. C. Lapointe, T. Mason, I.I. Smalyukh, Science **326**, 1083 (2009)
31. S. Khatua, W.-S. Chang, P. Swanglap, J. Olson, S. Link, Nano Lett. **11**, 3797 (2011)
32. R. Pratibha, K. Park, I.I. Smalyukh, W. Park, Opt. Express **17**, 19459 (2009)
33. Q. Liu, Y. Cui, D. Gardner, X. Li, S. He, I.I. Smalyukh, Nano Lett. **10**, 1347 (2010)
34. I.C. Khoo, A. Diaz, M.V. Stinger, J. Huang, Y. Ma, IEEE L. Selected Topics Quantum Electron. **16**, 410 (2010)
35. I.-C. Khoo, J. Liou, M.V. Stinger, S. Zhao, Mol. Crys. Liq. Crys. **543**, 151 (2011)
36. Y. Zhao, Q. Hao, Y. Ma, M. Lu, B. Zhang, M. Lapsley, I.C. Khoo, T.J. Huang, Appl. Phys. Lett. **100**, 053119 (2012)
37. D. Shrekenhamer, W.-C. Chen, W.J. Padilla, Phys. Rev. Lett. **110**, 177403 (2013)

Chapter 13
Superconducting Quantum Metamaterials

Alexandre M. Zagoskin

Abstract Quantum metamaterials is a concept bridging the fields of conventional metamaterials and quantum processing in solid state. These are artificial media comprised of quantum coherent, specifically designed unit elements (e.g., qubits), such that the quantum state of these elements can be externally controlled, and that the system maintains quantum coherence on the characteristic times and scales of electromagnetic signal propagation through it. This chapter focuses on quantum metamaterials based on superconducting qubits, which—due to the developments in theory and experimental and fabrication techniques over the last decade—currently provide the most feasible implementation of the concept.

13.1 Introduction

The term "quantum metamaterial" was first introduced as a logical extension of a conventional metamaterial in [1, 2], independently and in somewhat different contexts. In [1] it was applied to the plasmonic properties of a stack of 2D layers, each of them thin enough for the motion of electrons in the normal direction to be completely quantized. Therefore "the wavelike nature of matter" had to be taken into account at a single-electron level, but the question of quantum coherence in the system did not arise. On the contrary, in [2] the requirement that their system comprised of artificial atoms (qubits) maintains quantum coherence on the time scale of the electromagnetic pulse propagation across it was made explicit, along with the direct control of the quantum state of at least some qubits, for the reason that it was the *coherent quantum dynamics* of qubits, that determined the "optical" properties of the system. Currently the term "quantum metamaterial" is being used in both senses (see, e.g., [3–8]).

A.M. Zagoskin (✉)
Loughborough University, Loughborough LE11 3TU, UK
e-mail: a.zagoskin@lboro.ac.uk

I.V. Shadrivov et al. (eds.), *Nonlinear, Tunable and Active Metamaterials*,
Springer Series in Materials Science 200, DOI 10.1007/978-3-319-08386-5_13

We will here follow the more restrictive usage and call quantum metamaterials only such artificial optical (in the broad sense) media that [6]

(i) are comprised of quantum coherent unit elements with desired (engineered) parameters;
(ii) have quantum states of these elements that can be directly controlled; and
(iii) have a structure that can maintain global coherence for the duration of time, exceeding the traversal time of a relevant electromagnetic signal.

(The requirement that the size of a unit cell of the system be much less—in practice at least twice less—than the wavelength of the relevant electromagnetic signal, is implied in the definition of a quantum metamaterial as a "medium".) It is the totality of (i)–(iii) (in short: controlled macroscopic quantum coherence) that makes a quantum metamaterial a qualitatively different system, with a number of unusual properties and applications.

A conventional metamaterial can be described by effective macroscopic parameters, such as the refractive index. From the microscopic point of view, these parameters are functions of the appropriately averaged quantum states of individual building blocks. In a quantum metamaterial, these states can be directly controlled and maintain phase coherence on the relevant spatial and temporal scale. This allows, e.g., to put a quantum metamaterial into a superposition of states with different refractive indices. The observation of such *quantum birefringence* would be a direct look at a Schrödinger's cat. One could thus invert the classic double-slit experiment: instead of scattering a quantum particle off a classical screen we would scatter a classical electromagnetic wave packet off a screen, where the slits are in a superposition of "open" and "closed" states. This kind of experiments would be useful for a direct investigation of the quantum-classical transition. There will be as well interesting opportunities for new technologies (e.g., bifocal superlens [4], quantum phase-sensitive antennas [9]).

So far, these tantalizing possibilities largely remain the matter of theoretical predictions. Nevertheless, there is good circumstantial evidence in support of these predictions. The progress achieved over the last decade in the development of superconducting qubits for the purpose of quantum computing (see, e.g., [10, 11]) led to the realization of quite large (in excess of a hundred units) qubit arrays with at least partial quantum coherence and quantum state control [12]. A series of experiments with a superconducting qubit placed in a transmission line [13–16], motivated by the proposal for a 1D quantum metamaterial [2, 24], confirmed that such an artificial atom interacts with the electromagnetic wave in a quantitative agreement with theory. We are therefore confident that the experimental realization of a superconducting quantum metamaterial will be achieved in the near future.

13.2 Superconducting Quantum Circuits

Before proceeding, we will briefly recapitulate here the physics of superconducting quantum circuits and their mathematical description.[1]

The key component of such circuits is a Josephson junction [17], which is the only known nonlinear *and* nondissipative electrical circuit element. Josephson junctions are formed by two superconductors separated by a "weak link", which suppresses the probability amplitude for an electron to pass between them (e.g., a tunneling barrier, a constriction, a region with suppressed superconductivity).

The nondissipative, equilibrium superconducting current *(supercurrent)* is carried by the Bose-condensate of Cooper pairs of electrons. This condensate is characterized by the superconducting order parameter,

$$\Delta(\mathbf{r}, t) \equiv |\Delta(\mathbf{r}, t)| \exp[i\phi(\mathbf{r}, t)], \tag{13.1}$$

where the square of the amplitude, $|\Delta|^2$, is proportional to the average density of electrons in the condensate, n_s, and the superconducting phase ϕ is relate to the *superfluid velocity*, $\mathbf{v}_s$, and the supercurrent density, $\mathbf{j}_s$, via (m_e is the electron mass)

$$\mathbf{v}_s = \frac{\hbar}{2m_e}\nabla\phi; \quad \mathbf{j}_s = n_s e\mathbf{v}_s. \tag{13.2}$$

The qubits are operated at much lower temperatures ($\sim$10–50 mK) than the critical temperature of superconductors routinely used for fabricating qubits (Al and Nb), $\sim$1 K and $\sim$10 K respectively. This is done in order to suppress the effects of decoherence due to thermal fluctuations.

In a Josephson junction, due to the weakness of the link, the order parameter can be taken as constant in either superconductor, and the supercurrent *(Josephson current)* is determined by the superconducting phase difference between them:

$$I_J = I_c \sin(\phi_1 - \phi_2). \tag{13.3}$$

Here I_c is the critical current, determined by the properties of the superconductors and of the weak link (it will thus depend on, e.g., temperature and the magnetic field).[2] (13.3) describes the *dc Josephson effect*: the equilibrium (i.e., zero-voltage), nondissipative current flow through the weak link between two superconductors. If the current through the junction is made to exceed its critical value, I_c, then in addition to the Josephson current there appears the *quasiparticle current*, I_{qp}. This is a usual, nonequilibrium current, accompanied by the voltage drop and dissipation. To a good approximation, it can be expressed through the resistance R_N of the Josephson junction in normal state (i.e., above the critical temperature T_c of superconducting phase transition):

[1] For a more detailed presentation see [10] and references therein.

[2] The sine in (13.3) is characteristic for a tunneling junction. Generally, it can be replaced by a different odd function, depending on the properties of the weak link [17].

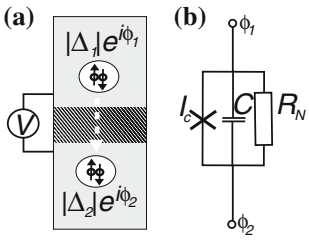

Fig. 13.1 A tunneling Josephson junction (**a**) and its RSJ (resistively shunted junction) model (**b**)

$$I_{qp} = V/R_N, \tag{13.4}$$

leading to the widely used RSJ (resistively shunted junction) model of the Josephson junction (Fig. 13.1). The voltage on the Josephson junction is related to the superconducting phase difference across it via

$$V = \frac{\hbar}{2e}\frac{d(\phi_1 - \phi_2)}{dt} \tag{13.5}$$

(the *ac Josephson effect*).

Together, the fundamental relations (13.3) and (13.5) and a good approximation (13.4) allow to describe all the properties of a Josephson junction we will be needing in the following.

Note that as a circuit element, a Josephson junction can be considered a tunable nonlinear inductance. Indeed, from (13.5) and the definition of inductance, $V = L\dot{I}/c$, we see, that[3]

$$L_J(\phi) = \frac{c^2 V(\phi)}{\dot{I}(\phi)} = \frac{\hbar c^2}{2eI_c \cos\phi}. \tag{13.6}$$

The equilibrium current can be obtained directly by differentiating the appropriate thermodynamic potential by the corresponding state variable,

$$I_J = c\frac{\partial U}{\partial \Phi}, \tag{13.7}$$

where the variable $\Phi = \Phi_0(\phi/2\pi)$ has the dimensionality of the magnetic flux, and $\Phi_0 = hc/2e$ is the superconducting magnetic flux quantum. The Josephson energy is then

$$U = \frac{1}{c}\int d\Phi\, I_J = -\frac{I_c\Phi_0}{2\pi c}\cos\phi \equiv -E_J\cos\phi \equiv -E_J\cos\left(2\pi\frac{\Phi}{\Phi_0}\right). \tag{13.8}$$

If the junction is current-biased, i.e., if a constant supercurrent I_b flows through it, then (13.8) must be modified,

[3] We will be using the Gaussian units throughout, as more convenient for our formalism.

$$U(\phi; I_b) = -E_J \cos\phi - I_b \Phi \equiv -\frac{I_c \Phi_0}{2\pi c} \cos\phi - \frac{I_b \Phi_0}{2\pi c} \phi, \tag{13.9}$$

to yield the equilibrium value $I_J(\phi) = I_b$ (when $\partial U/\partial\phi = 0$).

Adding to $U(\phi; I_b)$ the electrostatic energy of the Josephson junction with capacitance C,

$$K(V) = \frac{CV^2}{2} = \frac{C}{2}\left(\frac{\hbar}{2e}\right)^2 \left(\frac{d\phi}{dt}\right)^2, \tag{13.10}$$

which looks like a kinetic energy term, if ϕ were a coordinate, we find the energy of the system

$$E(\phi, \dot{\phi}; I_b) = \frac{C}{2}\left(\frac{\hbar}{2e}\right)^2 \dot{\phi}^2 + U(\phi; I_b). \tag{13.11}$$

It is formally equivalent to the energy of a particle in a washboard potential. We can now consider one of the local minima of $U(\phi; I_b)$, approximate it by a cubic potential and quantize the system (as in [18], Sect. 38). The ground and first excited states of this nonlinear oscillator can be used as the two states of a qubit (so called *phase qubit*; see, e.g., [10]). We will postpone this operation in favour of first presenting the standard approach, which allows to deal with an arbitrary circuit in both classical and quantum case.

An electric circuit can always be represented by an equivalent lumped-element circuit, to which then the Lagrange formalism can be directly applied (see, e.g., [19]), followed by switching to the Hamiltonian picture and canonical quantization [20, 21]. As coordinates we choose the "node fluxes" (or proportional to them "node phases"), which are related to the voltages at the given circuit nodes by the relations formally equivalent to (13.5):

$$\Phi_j(t) \equiv \Phi_0 \frac{\phi_j(t)}{2\pi} = c \int^t dt'\, V_j(t')\, dt'. \tag{13.12}$$

In case that the corresponding part of the circuit happens to be superconducting, the phase $\phi_j(t)$ is the superconducting phase. Otherwise it is just a formal dimensionless variable.

The current between the nodes j and k is determined from

$$\frac{d}{dt} I_{jk}(t) = -\frac{c(V_j - V_k)}{L_{jk}}, \tag{13.13}$$

if they are connected by an inductor, and from

$$I_{jk}(t) = C_{jk} \frac{d(V_j - V_k)}{dt}, \tag{13.14}$$

if they are connected by a capacitor.[4] Comparing these equations with (13.12), we see that, respectively,

$$I_{jk} = \frac{c(\Phi_j - \Phi_k)}{L_{jk}} \quad \text{or} \quad I_{jk} = \frac{C_{jk}(\ddot{\Phi}_j - \ddot{\Phi}_k)}{c}. \tag{13.15}$$

The corresponding "potential" and "kinetic" energies[5] are

$$\mathscr{U}_{jk} = \frac{L_{jk} I_{jk}^2}{2c^2} = \frac{(\Phi_j - \Phi_k)^2}{2L_{jk}}; \tag{13.16}$$

$$\mathscr{T}_{jk} = \frac{C_{jk}(V_j - V_k)^2}{2} = \frac{C_{jk}(\dot{\Phi}_j - \dot{\Phi}_k)^2}{2}, \tag{13.17}$$

and the Lagrangian of the system

$$\mathscr{L} = \sum_{jk} \left[\mathscr{T}_{jk} - \mathscr{U}_{jk} \right]. \tag{13.18}$$

The external fluxes $\tilde{\Phi}$ through the closed loops formed by inductors are taken into account by replacing for one of these inductors its contribution (13.16) to the Lagrangian by

$$\tilde{\mathscr{U}}_{jk} = \frac{(\Phi_j - \Phi_k + \tilde{\Phi})^2}{2L_{jk}}. \tag{13.19}$$

The external bias currents, $\tilde{I}$, and gate voltages, $\tilde{V}$, are included by adding to the corresponding nodes' contributions the terms

$$\frac{\Phi_j \tilde{I}}{c} \quad \text{and} \quad \frac{C_j(\dot{\Phi}_j - c\tilde{V})^2}{2c^2}. \tag{13.20}$$

Finally, a Josephson junction connecting two nodes will contribute to the Lagrangian the term

$$\frac{C_{J,jk}(\dot{\Phi}_j - \dot{\Phi}_k)^2}{2c^2} + E_{J,jk} \cos\left[2\pi \frac{\Phi_j - \Phi_k}{\Phi_0} \right]. \tag{13.21}$$

The behaviour of a circuit in the classical limit is described by the Lagrange equations,

$$\frac{d}{dt} \frac{\partial \mathscr{L}}{\partial \dot{\Phi}_j} - \frac{\partial \mathscr{L}}{\partial \Phi} = 0. \tag{13.22}$$

[4] The circuits we will be dealing with here do not contain resistive elements. In a general case, they can be taken care of through the so called dissipative function (see [10] and references therein).

[5] The distinction is here purely notional—if instead of node fluxes, which are essentially *currents*, as follows from (13.15), we chose as coordinates the node *charges*, proportional to the voltages V_j, the roles would have been reversed.

Its quantization is straightforward. First we introduce the canonical momenta and the Hamiltonian function,

$$\Pi_j = \frac{\partial \mathscr{L}}{\partial \dot{\Phi}}, \quad \mathscr{H}(\Phi, \Pi) = \sum_j \Pi_j \dot{\Phi}_j - \mathscr{L}(\Phi, \dot{\Phi}), \tag{13.23}$$

and then replace Φ_j and Π_j with operators such that $[\hat{\Phi}_j, \hat{\Pi}_k] = i\hbar\delta_{jk}$. It is convenient to express these directly through Bose creation/annihilation operators:

$$\hat{\Phi}_j = \frac{a_j + a_j^\dagger}{2}\Lambda, \quad \hat{\Pi}_j = \frac{a_j - a_j^\dagger}{i\Lambda}, \quad [a_j, a_k^\dagger] = \delta_{jk}, \tag{13.24}$$

where Λ is a real constant.

Let us apply the formalism to the biased Josephson junction. We find

$$\mathscr{L} = \frac{C\dot{\Phi}^2}{2c^2} + E_J \cos\left[2\pi\frac{\Phi}{\Phi_0}\right] + \frac{I_b\Phi}{c}, \tag{13.25}$$

the canonical momentum is $\Pi = C\dot{\Phi}/c^2 \equiv (\hbar/2e)Q$, where $Q = CV$ is the charge on the junction, and the Hamiltonian function

$$\mathscr{H} = \frac{c^2\Pi^2}{2C} - E_J \cos\left[2\pi\frac{\Phi}{\Phi_0}\right] - \frac{I_b\Phi}{c}, \tag{13.26}$$

which, of course, coincides with the expression (13.11). Neglecting the anharmonicity, we find near a local minimum

$$\hat{H} = \hbar\omega_J(a^\dagger a + 1/2), \tag{13.27}$$

where the bias-dependent Josephson plasma frequency

$$\omega_J = \left[\frac{E_J}{C(\hbar/2e)^2}\right]^{1/2}\left[1 - \left(\frac{I_b}{I_c}\right)^2\right]^{1/4}. \tag{13.28}$$

The potential barrier ΔU, which separates the local minimum from the continuum, is

$$\Delta U = \frac{2}{3}E_J\frac{\left[1 - \left(\frac{I_b}{I_c}\right)^2\right]^{3/2}}{(I_b/I_c)^2}, \tag{13.29}$$

and the anharmonicity, $\kappa = (\omega_{01} - \omega_{12})/\omega_{01}$, is of order $0.1\cdot(\hbar\omega_J/\Delta U)$. It is usually strong enough to allow us to work only in the subspace spanned by the ground and

first excited state of this system (i.e., using it as a qubit). In a typical phase qubit [22] $\hbar\omega_J/\Delta U \approx 0.25$, the anharmonicity $\kappa \approx 0.03$, and $\omega_J/2\pi \approx 9\,\mathrm{GHz}$.

Sometimes it is convenient to quantize only some of the Φ_j's, namely, those describing the qubits. This may be the case when a (quasi) classical electromagnetic wave propagates through the system. Then we can instead of fully switching to the Hamiltonian picture (13.23) perform only partial Legendre transform, with respect to the variables later to be quantized [10]. In this way we obtain the *Routh function*,

$$\mathscr{R}(\Phi_j, \Pi_j; \Phi_k, \dot{\Psi}_k) = \sum_j \Pi_j \dot{\Phi}_j - \mathscr{L}(\Phi_j, \dot{\Phi}_j; \Phi_k, \dot{\Phi}_k), \tag{13.30}$$

which satisfies the Lagrangian equations for the set $\{\Phi_k, \dot{\Phi}_k\}$ and the Hamiltonian ones for $\{\Phi_k, \Pi_k\}$. After quantization, the latter become the Heisenberg equations of motion for the operators $\{\hat{\Phi}_k, \hat{\Pi}_k\}$, while of the former we take the expectation value over the quantum state of the system:

$$\left\langle \psi \left| \frac{d}{dt} \frac{\partial \hat{\mathscr{R}}}{\partial \dot{\Phi}_j} \right| \psi \right\rangle - \left\langle \psi \left| \frac{\partial \hat{\mathscr{R}}}{\partial \Phi_j} \right| \psi \right\rangle = 0; \tag{13.31}$$

$$i\hbar \frac{d}{dt} \hat{\Pi}_k = [\hat{\Pi}_k, \hat{\mathscr{R}}]; \quad i\hbar \frac{d}{dt} \hat{\Phi}_k = [\hat{\Phi}_k, \hat{\mathscr{R}}]. \tag{13.32}$$

13.3 1D Quantum Metamaterials

The simplest example of a superconducting quantum metamaterial is a 1D array of qubits placed along a transmission line (Fig. 13.2). The transmission line is modelled by a lumped-element circuit, with the unit self-inductance ΔL and capacitance ΔC (assuming for simplicity that they are all the same). In the absence of qubits, the phase velocity in the line is

$$s = \Omega\, d, \quad \Omega = \frac{c}{\sqrt{\Delta L\, \Delta C}}, \tag{13.33}$$

where d is the length of a unit section.

13.3.1 Flux Qubit Quantum Metamaterial

Consider first the case of flux qubits. A *flux qubit* is a superconducting loop (typically about 10 μm across) interrupted by three or more Josephson junctions and threaded

by an external magnetic flux close to $\Phi_0/2$ [10, 23]. Its ground and excited state are close to $(|0\rangle + |1\rangle)/\sqrt{2}$ and $(|0\rangle - |1\rangle)/\sqrt{2}$ respectively, where $|0\rangle(|1\rangle)$ is the state with the superconducting current flowing (counter)clockwise around the loop. The operator of magnetic flux produced by the flux qubit number m in the adjacent section of the line is

$$\hat{\tilde{\Phi}}_m = \frac{1}{c} M_m \hat{J}_m, \tag{13.34}$$

where M_m is the mutual inductance, and $\hat{J}_m$ is the circulating current operator. This operator is eventually expressed in terms of the nodal flux operators in the superconducting loop, but for most cases it is sufficient to write it as a constant times the Pauli matrix, $\hat{J}_m = J_m \sigma_m^z$, thus explicitly making use of the standard "spin-1/2" approximate description of a qubit.

Introducing the node fluxes Φ_m as shown in Fig. 13.2b and using the formalism of the previous section, we obtain (13.31) in the form

$$\ddot{\Phi}_m - \Omega^2(\Phi_{m+1} - 2\Phi_m + \Phi_{m-1}) = \Omega^2 \frac{M}{c} \left\langle \psi \left| \hat{J}_m - \hat{J}_{m-1} \right| \psi \right\rangle. \tag{13.35}$$

The matrix element on the right hand side, of course, does not depend on whether we will use the Heisenberg or the Schrödinger representation. Its time evolution will be determined by the Hamiltonian of the flux qubits. In the absence of direct qubit-qubit coupling it can be written as

$$\hat{H}_m = -\frac{1}{2}\left[\epsilon_m \sigma_m^z + \Delta_m \sigma_m^x\right] + \frac{M J_m}{\Delta L}(\Phi_m - \Phi_{m-1})\sigma_m^z. \tag{13.36}$$

Here the bias ϵ_m and the tunneling splitiing Δ_m are the parameters, which characterize the mth flux qubit.

Now we can make certain simplifications. Assume that the quantum state of the system of qubits is factorized, i.e., that at any moment (in Schrödinger representation)

$$|\psi(t)\rangle = \cdots \otimes |\psi_{m-1}(t)\rangle \otimes |\psi_m(t)\rangle \otimes |\psi_{m+1}(t)\rangle \otimes \ldots \tag{13.37}$$

Then the quantum state of the system can be described by a position-dependent "wave function" $\Psi(x) = a(x)|0\rangle + b(x)|1\rangle$, not unlike the "macroscopic wave function" of a superconductor. Here $x = md$ is the coordinate of the mth unit cell, and $|0\rangle, |1\rangle$ are the eigenstates of the operator σ^z. The difference equation (13.35) now reduces to a partial differential equation

$$\ddot{\Phi}(x,t) - s^2 \frac{\partial^2}{\partial x^2}\Phi(x,t) = s\Omega \frac{M}{c}\frac{\partial}{\partial x}\left\langle \Psi(x) \left| \hat{J}(x) \right| \Psi(x) \right\rangle. \tag{13.38}$$

This approximation is justified as long as the wavelength of the electromagnetic signal in the system greatly exceeds the unit size d (of order of the qubit size).

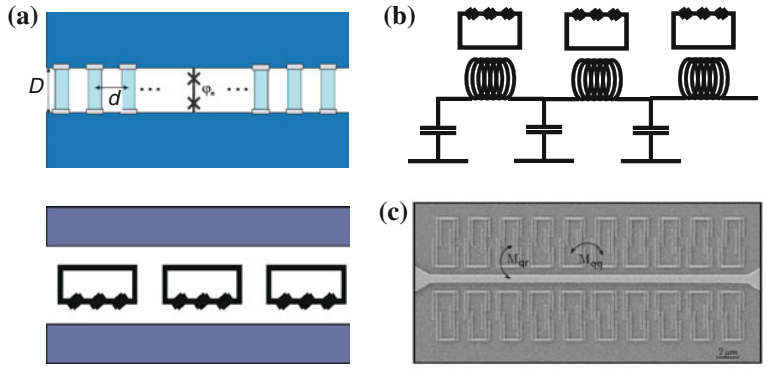

Fig. 13.2 One-dimensional quantum metamaterial: a set of qubits in a transmission line. **a** Charge (*top*) and flux (*bottom*) qubits (after [2, 24]). **b** The lumped-element circuit for a flux-qubit-based 1D quantum metamaterial. **c** An experimental prototype of a flux-qubit-based 1D quantum metamaterial (courtesy of E. Il'ichev, IPHT-Jena) [25]

Solving (13.36) and (13.38) will determine the propagation of a (quasi)classical electromagnetic wave through the 1D quantum metamaterial.[6]

In the first experimental investigation of a quantum metamaterial prototype comprising 20 flux qubits in a microwave resonator [25] their collective coupling to the electromagnetic field was clearly seen in the appearance of disctinct collective modes, despite the expected relatively large dispersion of the parameters of individual flux qubits. This shows that the behaviour of quantum metamaterials is relatively insensitive to the imperfections of unit elements, and post factum justifies our current assumption of identical qubits as the first approximation.

13.3.2 Charge Qubit Quantum Metamaterial

Now consider a 1D quantum metamaterial comprising a chain of *charge qubits* inside a superconducting transmission line (Fig. 13.2a). These are superconducting islands of so small capacitance, that the states differing by a single Cooper pair have distinguishable electrostatic energies [10, 26]. In a similar fashion we can derive [2]

$$\frac{\partial^2}{\partial\tau^2}\alpha(\xi,\tau) - \beta^2\frac{\partial^2}{\partial\xi^2}\alpha(\xi,\tau) + \langle\Psi(\xi,\tau)|\cos\phi(\xi,\tau)|\Psi(\xi,\tau)\rangle = 0. \quad (13.39)$$

[6] The approximation of a factorized wave function, (13.37), is quite a drastic simplification, since it excludes such macroscopic quantum superposition states as $(\cdots\otimes|0\rangle\otimes|0\rangle\otimes|0\rangle\otimes\ldots)\pm(\cdots\otimes|1\rangle\otimes|1\rangle\otimes|1\rangle\otimes\ldots)$. Such GHz-like states are necessary for the realization of, e.g., quantum birefringence. Nevertheless even factorized states should give rise to interesting quantum effects [2], while both their theoretical treatment and experimental realization are significantly simpler.

Here ξ is a dimensionless position along the line; $\tau = \omega_J t$ is the dimensionless time; $\omega_J = [eI_c/\hbar C]^{1/2}$ is the Josephson plasma frequency for either of the Josephson junctions of the charge qubit; $E_J = I_c\Phi_0/2\pi c$; $\alpha(\xi, \tau)$ is the dimensionless vector potential of the electromagnetic field in the line:

$$\alpha(\xi = m) = 2\pi \frac{DA_z(\xi = m)}{\Phi_0} \tag{13.40}$$

(in our approximation the vector potential A_z is constant inside each $(d \times D)$-unit cell); and the parameter $\beta = (\Phi_0/2\pi)[8\pi d D E_J]^{-1/2}$ is the dimensionless phase velocity of signal in the line (the number of unit cells travelled by the wave during a period of oscillations). The superconducting phase on the qubit island at the point ξ at the time τ is $\phi(\xi, \tau)$.

For a typical charge qubit in a strip-line resonator [27] (an arrangement close to the one we are considering) the Josephson energy $E_J/h \sim 6\,\text{GHz}$, much greater than the qubit decoherence rate, $\sim$5 MHz, and the resonator leakage rate, $\sim$0.5 MHz. This justifies our neglecting the decoherence and dissipation in the system. Moreover, for the unit cell size $d \times D \sim 100\,\mu\text{m}^2$, the parameter $\beta \sim 30 \gg 1$, which validates the treatment of quantum metamaterials as effective optical media (in the microwave range) in (13.38) and (13.39).

The dimensionless Hamiltonian the charge qubit at the point ξ in the limit of a weak classical electromagnetic field propagating in the line, $|\alpha| \ll 1$, is given by [2, 10]

$$\hat{H}(\xi) = -\frac{\partial^2}{\partial\phi(\xi)^2} + \alpha(\xi)^2 \cos[\phi(\xi)]. \tag{13.41}$$

This is the Hamiltonian of an anharmonic oscillator with the field-modulated potential, as one could expect from our discussion in Sect. 13.2. Now we can solve (13.39) and (13.41) perturbatively. Expanding the "wave function"

$$|\Psi(\xi, \tau)\rangle = C_g(\xi, \tau)e^{i\epsilon\tau/2}|g_\xi\rangle + C_e(\xi, \tau)e^{-i\epsilon\tau/2}|e_\xi\rangle, \tag{13.42}$$

where ϵ is the interlevel distance (in units of $\hbar\omega_J$) between the ground and excited states of the qubit at the point ξ, $|g_\xi\rangle$ and $|e_\xi\rangle$, we find in the lowest approximation [2]:

$$\frac{\partial^2}{\partial\tau^2}\alpha^{(0)} - \frac{\partial^2}{\partial\xi^2}\alpha^{(0)} + V^{(0)}\alpha^{(0)} = 0. \tag{13.43}$$

The coefficient $V^{(0)}$ is determined by the initial quantum state of the qubits:

$$V^{(0)}(\xi, \tau) = |C_g^{(0)}(\xi)|^2 V_{gg}(\xi, \tau) + |C_e^{(0)}(\xi)|^2 V_{ee}(\xi, \tau) + \left[C_g^{(0)}(\xi)C_e^{(0)*}(\xi)e^{i\epsilon\tau}V_{ge}(\xi, \tau) + \text{Hermitian conjugate}\right]; \tag{13.44}$$

$$V_{eg}(\xi, \tau) \equiv \langle e_\xi|\cos\phi(\xi, \tau)|g_\xi\rangle \text{ etc.} \tag{13.45}$$

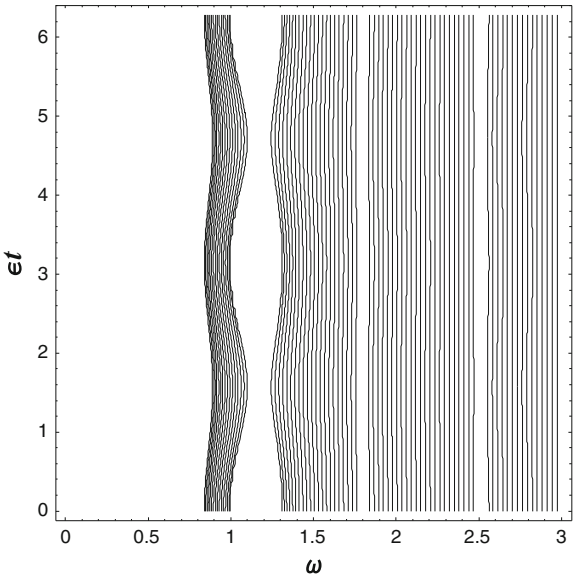

Fig. 13.3 "Breathing" quantum photonic crystal: time-dependent bandgap structure in a 1D quantum metamaterial with the spatially periodic qubit quantum state: $|\Psi_A\rangle = |g\rangle, |\Psi_B\rangle = (|g\rangle + |g\rangle)/\sqrt{2}$. Reprinted with permission from Rakhmanov et al. [2]. (C) 2008 American Physical Society

Therefore the dispersion law following from (13.43) depends on the initial state of the qubits. For example, if the qubits are initially in the ground (excited) state or in their symmetric superposition, we find

$$k_g(\omega) = \frac{1}{\beta}\sqrt{\omega^2 - V_{gg}};\quad k_e(\omega) = \frac{1}{\beta}\sqrt{\omega^2 - V_{ee}};$$
$$k_s(\omega) = \frac{1}{\beta}\sqrt{\omega^2 - \{V_{ee} + V_{gg} + 2|V_{eg}|\cos[\epsilon(\tau - \tau_0)]\}/4}. \tag{13.46}$$

In the latter case we see that the dispersion law undergoes quantum beats with the frequency $\epsilon\omega_J$.

If the initial quantum state of the system is spatially periodic (e.g., with $|\Psi(\xi)\rangle$ equal either $|\Psi_A\rangle$ or $|\Psi_B\rangle$), then bandgaps will open in its transmission spectrum, as in a conventional photonic crystal. If this state is a quantum superposition, like in (13.46), we will obtain a "breathing" photonic crystal (see Fig. 13.3).

13.3.3 Tuneable, Quantum Birefringent and Ambidextrous Quantum Metamaterials

Another interesting possibility is provided by the fact that a biased Josephson junction can function both as a tunable inductance (13.6) and a (phase) qubit (13.11) and

(13.29). Consider a standard ("right-handed") transmission line and the "left-handed" one (Fig. 13.4) (the meaning will become clear in a moment). Using the standard formalism, it is straightforward to obtain for the node fluxes the equations of motion

$$\ddot{\Phi}_n - \Omega^2(\Phi_{n+1} + \Phi_{n-1} - 2\Phi_n) = 0 \quad \text{and} \quad \Phi_n - \frac{1}{\Omega^2}(\ddot{\Phi}_{n+1} + \ddot{\Phi}_{n-1} - 2\ddot{\Phi}_n) = 0, \tag{13.47}$$

respectively. Substituting here $\Phi_n(t) = F\exp[ikdn - i\omega t]$, we find the dispersion relations

$$\omega_{(R)}(k) = 2\Omega\left|\sin\left(\frac{kd}{2}\right)\right| \quad \text{and} \quad \omega_{(L)}(k) = \Omega\left|2\sin\left(\frac{kd}{2}\right)\right|^{-1}. \tag{13.48}$$

Now we see that our "right-" and "left-handed" labels were justified: in the latter case the group velocity is negative, i.e., antiparallel to the wave vector, as it should be in a left-handed medium [28].

If replace all inductors and capacitors by the Josephson junctions (which can be treated as a nonlinear inductance in parallel with a capacitance, see Fig. 13.1b), we obtain the dispersion relation ([10], Chap. 6)

$$\omega^2(k) = \frac{2L_x^{-1}(1-\cos kd) + L_y^{-1}}{2(C_x/c^2)(1-\cos kd) + C_y/c^2}, \tag{13.49}$$

which interpolates between those of (13.48). If $(L_y/L_x) < (C_x/C_y)$, the system will be left-handed, otherwise right-handed. By tuning the "horizontal" and "vertical" Josephson junctions we could thus switch our transmission line between these two regimes at will.[7]

A more interesting possibility follows from the fact that such a biased Josephson junction can be placed in a superposition of its ground and excited states [10, 22]. The expectation value of the superconducting phase drop across it is different [6],

$$\langle\phi\rangle_e - \langle\phi\rangle_g = \frac{I_b}{2I_c}\left[\frac{2e^2}{CE_J}\right]^{1/2}, \tag{13.50}$$

producing different effective inductances (13.6), and therefore different dispersion relations, (13.49). If we place our set of qubits in a GHz-type macroscopic quantum superposition state, $|ggggg...\rangle + |eeeee...\rangle$, then the system will be *quantum birefringent*, i.e., it will be in a superposition of states with different optical properties. Choosing the parameters of the junctions in such a way that switching between the ground and excited states of the "horizontal" and "vertical" sets of qubits would shift it from right-handed to left-handed dispersion law, we obtain the *ambidextrous*

[7] A tunable classical transmission-line metamaterial was considered in [29], while a tunable classical *left-handed* transmission-line metamaterial was recently realized on experiment [30]. Both designs incorporate Josephson junctions.

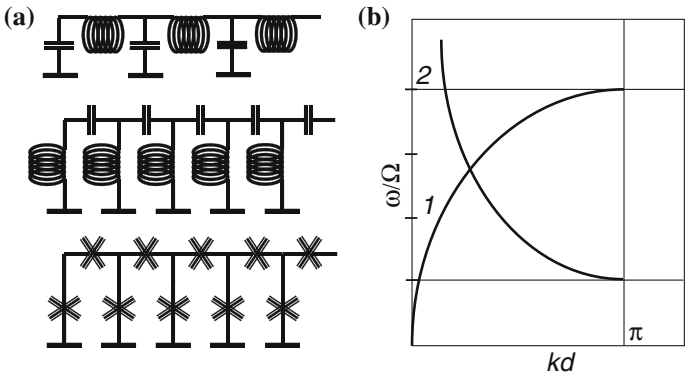

Fig. 13.4 Ambidextrous quantum metamaterial. **a** *Right*- and *left-handed* and ambidextrous transmission lines. **b** Schematic *right*- and *left-handed* dispersion relations

quantum metamaterial. If the corresponding shifts in the effective inductances are respectively $L_x^{-1} \to L_x^{-1} + \delta L_x^{-1}$, $L_y^{-1} \to L_y^{-1} + \delta L_y^{-1}$, then a wave with the wave vector k_c, such that [10]

$$2(1 - \cos k_c d)\delta L_x^{-1} = -L_y^{-1}, \tag{13.51}$$

could be made to propagate in both right- and left-handed way simultaneously.

13.3.4 Initializing a Quantum Photonic Crystal

Controlling the quantum state of each qubit in a quantum metamaterial (item (ii) on our list of Sect. 13.1) could be difficult task: each additional circuit makes it harder to insulate the system from the environment and to keep it at the required 10–50 mK, and it may increase the noise level by itself. Fortunately, there can be a way around this requirement, allowing us to limit the amount of access by what is actually needed to realize a particular property of a quantum metamaterial.

A simple example is a spatially periodic modulation of the absolute value of qubits' quantum state in a 1D quantum metamaterial, which can be achieved without a direct local access to the qubits [31]. Instead, it is enough to send two properly shaped electromagnetic pulses through the system in the opposite directions: their interference produces the desired spatial pattern.

To see how it works, consider a finite section of a quantum metamaterial inserted in a transmission line (Fig. 13.5). The case considered is the same as in Sect. 13.3.2, the charge-qubit based quantum metamaterial, but the results can be applied to the general case, mutatis mutandis. For the dimensionless field amplitude we obtain, similar to (13.39),

$$\frac{\partial^2}{\partial\tau^2}\alpha(\xi,\tau)-\beta^2\frac{\partial^2}{\partial\xi^2}\alpha(\xi,\tau)+\langle\Psi(\xi,\tau)|\cos\phi(\xi,\tau)|\Psi(\xi,\tau)\rangle\alpha(\xi,\tau)=0 \quad (13.52)$$

inside the metamaterial and

$$\frac{\partial^2}{\partial\tau^2}\alpha(\xi,\tau)-\tilde{\beta}^2\frac{\partial^2}{\partial\xi^2}\alpha(\xi,\tau)=0 \quad (13.53)$$

in the transmission line without qubits. The difference between the signal propagation speed in these two sections, β and $\tilde{\beta}$, can be eliminated by choosing different parameters for the "active" and "passive" parts of the transmission line.

As before, we assume that the wave function of the system is factorized and the electromagnetic field in the system is weak. We will solve the equations for the field (13.52) and (13.53) and for the "metamaterial wave function" (13.42),

$$i\frac{\partial}{\partial\tau}C_a=\alpha^2(\xi,\tau)\sum_b d_{ab}C_b e^{i(\omega_a-\omega_b)\tau}, \quad \{a,b\}=\{g,e\}, \quad (13.54)$$

perturbatively in the resonance approximation ($\omega=\epsilon/2$). We find

$$\alpha^{(1)}(\xi,\tau)=e^{-\left[(\xi-\omega\tau/k)^2\right]}(Ae^{i(k\xi-\omega\tau)}+c.c); \quad (13.55)$$

$$\alpha^{(2)}(\xi,\tau)=e^{-\left[(\xi+\omega\tau/k)^2\right]}(Ae^{i(k\xi-\omega\tau+\zeta_0)}+c.c) \quad (13.56)$$

for the "priming pulses" incident from the left and from the right. If the qubits were initially in their ground state, $C_g(\xi,0)=1$, $C_e(\xi,0)=0$, then

$$|C_e(\xi,\tau)|=\frac{|\Omega_R(\xi)|\sin\left[\tau(|\Omega_R(\xi)|^2+(1/4)\gamma(\xi)^2)^{1/2}\right]}{(|\Omega_R(\xi)|^2+(1/4)\gamma(\xi)^2)^{1/2}}. \quad (13.57)$$

Here

$$\gamma(\xi)=\Delta+4A^2(d_{gg}-d_{ee})\left[\cos(2k\xi+\zeta_0)+1\right], \quad (13.58)$$

$\Delta=2\omega-\epsilon$ is the detuning from the resonance, and $\Omega_R(\xi)$ is the local Rabi frequency:

$$|\Omega_R(\xi)|=2d_{ge}A^2\left[\cos(2k\xi+\zeta_0)+1\right]. \quad (13.59)$$

The periodic modulation of $|C_e(\xi)|$ was thus achieved without separately addressing the quantum state of each qubit. This approach can be useful in simplifying the design for certain quantum metamaterial prototypes (e.g., shown in Fig. 13.2c).

The results of numerical simulations, which confirm this conclusion, are shown in Fig. 13.5b. Here, instead of (13.52) and (13.53), we solved directly the difference equations (similar to (13.35), which reduce to the former in the continuous limit [31].

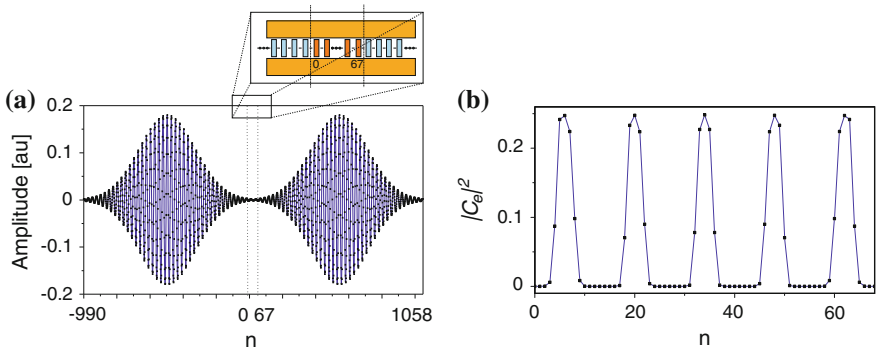

Fig. 13.5 Forming a spatially periodic pattern in a 1D quantum metamaterial. **a** The initial amplitudes (in arb. units) of the "priming" pulses in the transmission line to the *right* and to the *left* of the quantum metamaterial section, as a function of the site number. The quantum metamaterial (see inset) occupies the position in the middle, indicated by the *parallel dotted lines*. In the simulations, the length of the metamaterial section is $68d$, and the total length of the system $\tilde{L} = 2048\,\mathrm{d}$. The pulse parameters are $\tilde{\beta} = \beta$, $\omega = \epsilon/2$, $\Delta = 0.18\epsilon$, $kd = 2\pi/25$; the pulse width $l = 240\,\mathrm{d}$, and amplitude $A = 0.18\,\mathrm{a.u.}$ The matrix elements $d_{gg} = 0.4\epsilon$, $d_{ee} = 3.6\epsilon$, and $d_{ge} = 0.2\epsilon$. **b** Periodically modulated average population of the excited levels of qubits after passing of the priming pulses. After Shvetsov et al. [31] with permission

13.4 Initial Data: Single Superconducting Artificial Atom in a Transmission Line

While the first superconducting metamaterials prototypes are already being tested, the detailed experimental data are currently available for a simpler, "proof-of-principle" system. It comprises of a single "artificial atom" placed in a 1D transmission line; the role of this atom was played by either a flux qubit (Fig. 13.6) [13–15] or a so called transmon (another type of superconducting qubit) [16].

Since there is only one qubit in the transmission line, and its size ($\sim 10\,\mu\mathrm{m}$) is negligible compared to the signal wavelength (millimeters), we can somewhat simplify our approach. Following [13], we place the qubit at the origin and write the telegraph equations for the current and voltage in the transmission line for $x \neq 0$ as

$$\begin{cases} \dfrac{\partial V(x,t)}{\partial x} = \dfrac{\tilde{L}}{c^2}\dfrac{\partial I(x,t)}{\partial t} \\ \dfrac{\partial I(x,t)}{\partial t} = \tilde{C}\dfrac{\partial V(x,t)}{\partial t}, \end{cases} \tag{13.60}$$

where $\tilde{L}, \tilde{C}$ are the inductance and capacitance per unit length of the transmission line. The qubit's influence is incorporated through matching the solutions at $x = 0$. Namely,

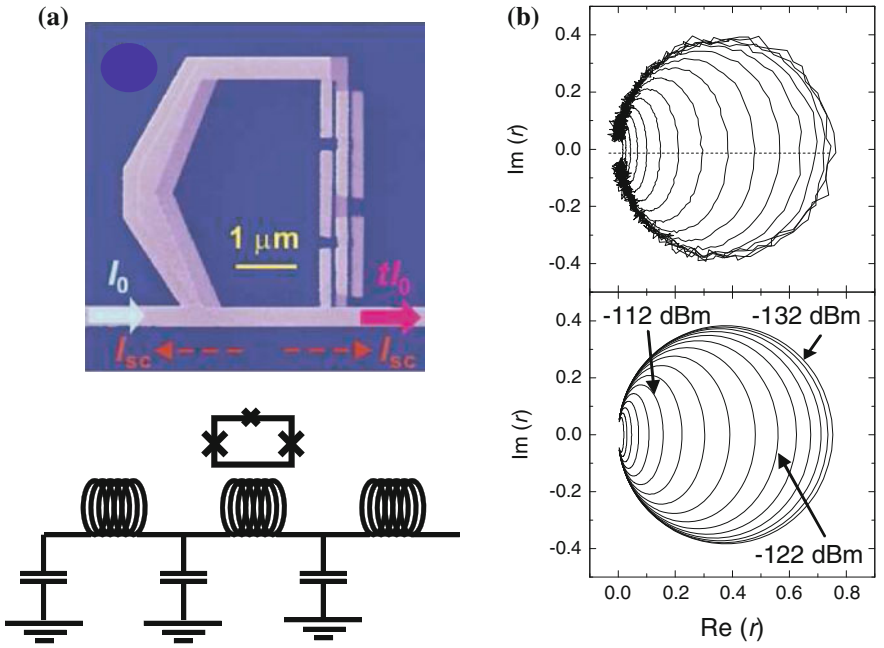

Fig. 13.6 **a** A flux qubit coupled to a transmission line. **b** Reflection amplitude: experimental data (*top*) and theory (13.68) (*bottom*). Different *curves* correspond to the driving power changing from −132 to −102 dBm in steps of 2 dBm. From Astafiev et al. [13], with permission from AAAS

$$\begin{cases} V(+0,t) = V(-0,t) - \frac{M}{c}\frac{\partial}{\partial t}\langle \hat{J}_q(t)\rangle \\ I(+0,t) = I(-0,t). \end{cases} \tag{13.61}$$

These equations simply account for the voltage drop due to the time-dependent magnetic flux, induced in the line by the qubit current operator $\hat{J}_q$. Looking for the stationary solution, we introduce the transition and reflection amplitudes, $\mathtt{t}$ and $\mathtt{t}$, and write the current in the line and the expectation value of the qubit current as

$$I(x<0,t) = \mathrm{Re}\left[I_0 e^{ikx-i\omega t} - \mathtt{r} I_0 e^{-ikx-i\omega t}\right]; \tag{13.62}$$

$$I(x>0,t) = \mathrm{Re}\left[\mathtt{t} I_0 e^{ikx-i\omega t}\right]; \tag{13.63}$$

$$\langle \hat{J}_q(t)\rangle \equiv \mathrm{Re}[\overline{J_{q,\omega}}]\cos\omega t + \mathrm{Im}[\overline{J_{q,\omega}}]\sin\omega t. \tag{13.64}$$

Then we find from (13.60) and (13.61)

$$\mathtt{t} + \mathtt{r} = 1; \quad \mathtt{r} = \frac{i\omega M \overline{J_{q,\omega}}}{2c^2 Z I_0}, \tag{13.65}$$

where $Z = [\tilde{L}/\tilde{C}c^2]^{1/2}$ is the impedance of the transmission line.

The stationary value of the average qubit current, $\langle \hat{J}_q(t) \rangle$, is found by solving the master equation for the qubit density matrix in the presence of the relaxation and dephasing rates, Γ_1 and Γ_2 (see, e.g., [10], Chap. 6). Let us tune the qubit to its degeneracy point, so that its Hamiltonian in the energy basis is

$$\hat{H} = -\frac{\hbar\Delta}{2}\sigma^z - \frac{MI_pI_0}{c^2}\sigma^x \cos\omega t \equiv -\frac{\hbar\Delta}{2}\sigma^z - \hbar\eta\sigma^x \cos\omega t, \tag{13.66}$$

where I_p is the supercurrent amplitude in the qubit loop. Then in the rotating wave approximation we find

$$\langle \hat{J}_q(t) \rangle = \frac{I_p\eta/\Gamma_2}{1 + \eta^2/\Gamma_1\Gamma_2 + (\omega-\Delta)^2/\Gamma_2^2} \left[\frac{\omega - \Delta}{\Gamma_2} \cos\omega t - \sin\omega t \right] \tag{13.67}$$

and, finally [13] (see Fig. 13.6b),

$$\mathtt{r} = \frac{\Gamma_1}{2\Gamma_2} \frac{1 + i(\omega-\Delta)/\Gamma_2}{1 + (\omega-\Delta)^2/\Gamma_2^2 + \eta^2/\Gamma_1\Gamma_2}. \tag{13.68}$$

The experimental data are remarkably well described by (13.68). Note that a naïve "self-consistent" solution, i.e., with the incident current, $I_0(x = 0)$, replaced in the expression for η by $\mathtt{t}I_0$, is in a complete disagreement with the experiment. This is to be expected, since the qubit in this situation does behave as a single point-like quantum scatterer.

A qubit in transmission line demonstrates such standard quantum-optical effects as the *Mollow triplet* [13]—the appearance in the spectrum of scattered light of the side peaks at frequencies $\omega \pm \Omega_R$, where Ω_R is the Rabi frequency of the atom's dipole moment in the field of the scattered wave (see, e.g., [32], Chap. 10). Its advantage over natural atoms is in its huge dipole moment and therefore coupling strength, as well as the greater field concentration in 1D line compared to the 3D space. The coupling strength, g/ω, is 3×10^{-7} for a 3D cavity QED in the optical and 10^{-7} in the microwave range, while it is 5×10^{-3} for a charge qubit in 1D line, 0.012 for a flux qubit, and 0.022 for a transmon (all microwave; see [10], Table 4.1, and references therein). This provides additional opportunities for using the devices based on such artificial atoms, e.g., as efficient quantum switches—even with a small number of qubits. To be more precise, for such an application one needs to use the three, not two, lowest energy levels of a superconducting qubit (i.e., operate it as a "qutrit"). Illuminating the device with a control signal at a frequency ω_{12} and with the amplitude η_c (cf. 13.66) allows to control the transmission amplitude of the weak

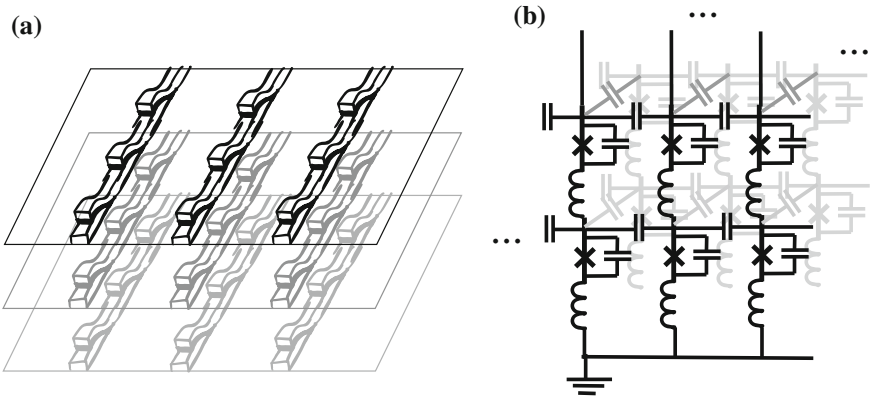

Fig. 13.7 A possible realization of a 2D and 3D superconducting quantum metamaterial based on phase qubits (**a**) and its lumped-element scheme (**b**). After [6] with permission

probe signal at a frequency ω_{01}:

$$\mathtt{t}(\eta_c) = 1 - \frac{\Gamma_{10}}{2\gamma_{10} + \eta_c^2/2\gamma_{20}}. \tag{13.69}$$

Here γ_{jk} are the dephasing rates, and Γ_{jk} the relaxation rates between the corresponding levels (the ground state being $|0\rangle$) [15]. In the experiments with a flux qubit the extinction of the probe signal by changing the amplitude of the control signal was 96 % [15], while for two different transmon qubit samples it was 90 and 99.6 % respectively [16].

13.5 Further Perspectives

A 1D superconducting quantum metamaterial based around a transmission line is the closest, but not the only realization of such a system. Another, and possibly more flexible, design disposes of the transmission lines (Fig. 13.7). The metamaterial would be formed of 1D chains of current-biased Josephson junctions (acting as phase qubits), capacitively coupled to each other. 2D layers of such chains could be used to form a 3D quantum metamaterial.

As in the 1D case, a periodic pattern of the qubit state would form a photonic crystal with state-dependent bandgaps. Putting such a device with properly chosen parameters in a GHz-type state, $|gggg...\rangle + |eeee...\rangle$, would realize a macroscopic "screen" with the slits in a superposition of "open" and "closed" states, and thus provide the means for inverting the standard double-slit experiment—a different way of investigating the quantum-classical transition.

Another possible use of a 2D or 3D quantum metamaterial is as a quantum-limited sensor array. Consider the situation, when a weak remote signal must be resolved against a local noise at the same frequency. This can be done by sensing the wave front of the signal: the signal arriving at different elements of the sensor array will have fixed phase differences, while the local noises will be spatially uncorrelated. The simplest example of this approach is the coincidence counter. Nevertheless if the signal is so weak that on average only a single photon at a time reaches the sensor, the scheme seems to be in jeopardy: a photon can only be detected once!

Nevertheless, it was suggested that a combination of a quantum metamaterial sensor and its quantum non-demolition readout allows to sidestep this obstacle [9]. The idea of the approach is to pass the incoming photon through the quantum coherent set of qubits, and then to measure their total magnetic moment (or a related variable). The photon itself will not be absorbed by any of the qubits, but the interaction with its electromagnetic field will produce coherent phase shifts in their quantum states, and therefore to the readout. The effects of noise, due to their being local, would instead tend to cancel each other, with the naïve expectation of $\sim\sqrt{N}$ gain in the signal-to-noise ratio as the number of qubits in the array is increased. A convenient method of quantum non-demolition readout of a system of qubits—so called *impedance measurement technique*, IMT [10, 33]—is based on inductively coupling the qubits to a high-quality LC curcuit (tank circuit) and measuring the response of the tank to a weak resonant signal. It turns out to be sensitive enough to observe the shift in the resonance frequency of the tank, induced by the quantum state-dependent magnetic flux produced by the qubits.

To be more specific, let us consider a quantum metamaterial array comprised of N qubits, which are all coupled to two LC circuits: the one (A) represents the input mode, and the other (B) the readout (Fig. 13.8). The system is described by the Hamiltonian

$$H = H_a + V_a + H_{qb} + V_b + H_b + H_{\text{noise}}, \tag{13.70}$$

where

$$H_a = \omega_a(a^\dagger a + 1/2) + f(t)(a^\dagger + a) \tag{13.71}$$

describes the input circuit, excited by the incoming field;

$$H_{qb} = \left(-\frac{1}{2}\right)\sum_{j=1}^{N}\left(\Delta_j\sigma_j^x + \varepsilon_j\sigma_j^z\right) \tag{13.72}$$

is the Hamiltonian of the qubits;

$$H_b = \omega_b(b^\dagger b + 1/2) + h(t)(b^\dagger + b) \tag{13.73}$$

is the Hamiltonian of the output circuit with the probing field, used for a quantum non-demolition readout;

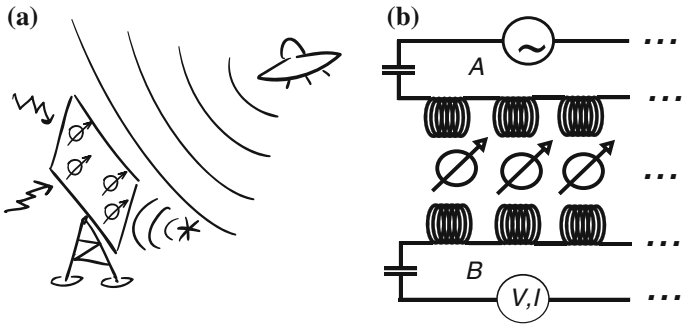

Fig. 13.8 Observing a single photon's wave front. **a** A quantum metamaterial sensor array undergoes a spatially phase coherent quantum evolution due to the interaction with a photon. Local noise effects are spatially uncorrelated. **b** Schematic for the photon detector system. Photons are incident on to the quantum metamaterial sensor array, which is comprised of N qubits. The quantum metamaterial array is also coupled to the readout tank circuit in order to perform quantum non-demolition measurement of its collective variable. From [9] with permission

$$V_a = \sum_j g_j^a (a^\dagger + a)\sigma_j^x, \quad V_b = \sum_j g_j^b (b^\dagger + b)\sigma_j^x \tag{13.74}$$

describe the coupling between the quantum metamaterial array and the input and output circuits; and finally,

$$H_{\text{noise}} = \sum_j \left(\xi_j(t)\sigma_j^x + \eta_j(t)\sigma_j^z\right) \tag{13.75}$$

takes care of the ambient noise sources, $\langle \xi_j(t)\xi_k(t')\rangle \propto \delta_{jk}$; $\langle \xi_j(t)\delta\eta_k(t')\rangle = 0$.

In order to minimize chances that the signal photon will be absorbed by one of the qubits and lost for our scheme, we will use the dispersive regime, i.e., when the mismatch between the qubits' and incoming photon's resonant frequencies, $\delta\Omega_j = |\omega_a - \sqrt{\Delta_j^2 + \epsilon_j^2}| \gg g_j^a$. This allows us to use the Schrieffer-Wolff transformation: if $\Delta = 0$, the interaction term V_a in (13.70) is reduced to [10, 34]

$$\tilde{V}_a = \left(\sum_j \frac{(g_j^a)^2}{\delta\Omega_j}\sigma_j^z\right) a^\dagger a. \tag{13.76}$$

Now the effect of the input field on the detector qubits is the additional phase gain proportional to the number of incoming photons, which can be read out using a quantum non-demolition technique.

In addition to (13.76) we also obtain the effective coupling between qubits through the vacuum mode of the oscillator, which in case of identical qubits and coupling parameters is

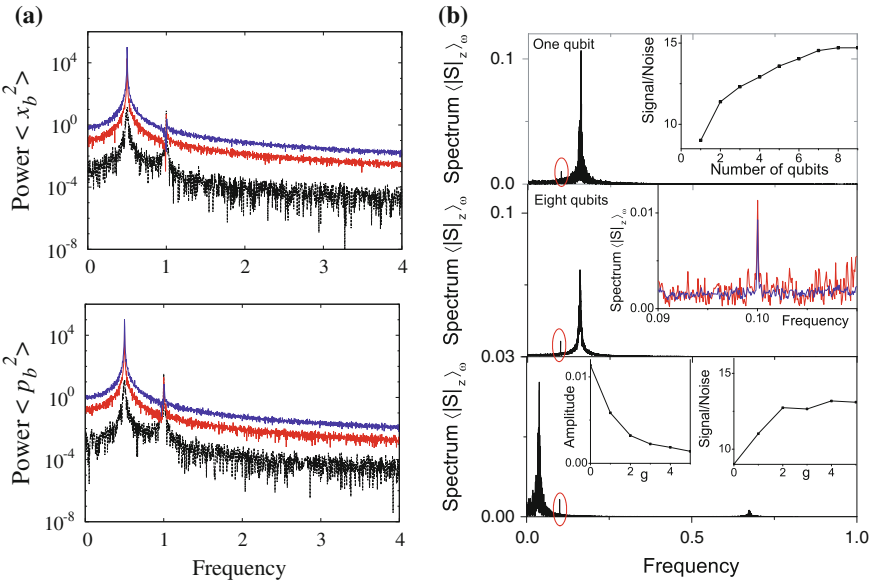

Fig. 13.9 Numerical calculations for a quantum sensor array. **a** Simulated readout power spectra for a tank circuit coupled to two noisy qubits in the presence of zero (*bottom curve*), one (*middle*) and five (*top curve*) signal photons. The panels show the power spectra for the readout field's position $\langle x_b^2 \rangle_\omega$ and momentum $\langle p_b^2 \rangle_\omega$ quadratures for the case where $\omega_a/\epsilon = \omega_b/\epsilon = 0.5$. **b** (*Top panel*) Spectral density of total detector "spin" S_z in a qubit in the presence of noise and drive. The signal due to drive is a small thin peak on the left of the resonant noise response. Inset: Signal to noise ratio as the function of number of qubits. (*Center panel*) Same in case of 8 qubits. Inset: A close up of the signal-induced feature. The noise is suppressed in case of 8 qubits (*blue*) compared to the case of a single qubit (*red*). (*Bottom panel*) The spectral density of S_z in case of two coupled qubits. Note that the significant shift of the resonant frequency of the system (position of the noise-induced feature). Inset: Signal response amplitude (*left*) and signal to noise ratio (*right*) as functions of the coupling strength. From [9] with permission

$$\tilde{H}_{\text{eff}} = \frac{(g^a)^2}{2\delta\Omega} \sum_{jk} \sigma_j^x \sigma_k^x. \tag{13.77}$$

If $N \gg 1$, this term can be approximated by an effective tunneling term for each qubit, $\Delta_{\text{eff}}(t)\sigma_j^x = \langle \sum_k \sigma_k^x \rangle \sigma_j^x$.

Exciting the input circuit with a resonant field, $f(t) = f_e(t) \exp[-i\omega_a t] + c.c.$, with slow real envelope function $f_e(t)$, we can write for its wave function

$$i\frac{d}{dt}|\psi_a(t)\rangle \approx f_e(t)(a + a^\dagger)|\psi_a(t)\rangle, \tag{13.78}$$

and

$$|\psi_a(t)\rangle \approx e^{-i\left[\int_0^t dt' f_e(t')\right](a+a^\dagger)} |\psi_a(0)\rangle. \tag{13.79}$$

This is a coherent state with the average number of photons

$$\langle a^\dagger a\rangle_t \approx \langle\psi_a(t)|a^\dagger a|\psi_a(t)\rangle \approx \langle\alpha(t)|a^\dagger a|\alpha(t)\rangle = |\alpha(t)|^2 = \left[\int_0^t dt' f_e(t')\right]^2. \tag{13.80}$$

Replacing H_a and V_a in the Hamiltonian (13.70) with

$$h(t) = \left(\sum_j \frac{(g_j^a)^2}{\delta\Omega_j}\sigma_j^z\right)|\alpha(t)|^2 \equiv \left(\sum_j \gamma_j\sigma_j^z\right)|\alpha(t)|^2, \tag{13.81}$$

and solving for the expectation value of the total magnetic moment of the qubit array, $S^z(t) = \langle\sum_{j=1}^N \sigma_j^z(t)\rangle$, (if initialized in an eigenstate of σ^x at $t = 0$) the plausible expression

$$S^z(t) \equiv \sum_{j=1}^N s_j^z(t) \approx -2\gamma\Delta_{\text{eff}} s^x(0) N\left[\int_0^t\int_0^{t'} |\alpha(t'')|^2 dt'dt'' + \int_0^t\int_0^{t'} \frac{1}{N}\sum_{j=1}^N \eta_j(t'')dt'dt''\right], \tag{13.82}$$

which indeed predicts the standard $\sim\sqrt{N}$-suppression of the noise compared to the coherent signal.

These heuristic considerations are supported by more solid numerical calculations presented in Fig. 13.9. They were obtained using (a) quantum state diffusion formalism [35] and (b) master equation for the density matrix. As we see, the signal is expected to be discernible even at a single-photon level, and increasing the number of qubits and introducing coupling between them (i.e., making the system more rigid and less responsiove to local fluctuations) increases the signal-to-noise ratio. It remains to be seen whether these expectations are carried out by experiments.

Whatever promise of novel technological applications the quantum metamaterials may hold, one should not lose from sight the main prize: the possibility of using quantum metamaterials to investigate the limits of applicability of quantum mechanics. There is no accepted theoretical limit on how big a physical system can become before it can no longer maintain quantum coherence. Moreover, the experimental results in the field of solid state quantum computing so far encourage the belief that such a limit may not exist at all, and the system may remain coherent as long as its interactions with the environment are kept under control. A quantum metamaterial is by definition a quantum coherent, controllable, scalable, macroscopic system

designed to interact with the electromagnetic signal, and would be therefore a natural testing ground for investigating the quantum-classical transition (and literally "watching a Shrödinger's cat jump").

Acknowledgments I am greatly indebted to O. Astafiev, M. Everitt, E. Il'ichev, F. Nori, A.L. Rakhmanov, J.H. Samson, S. Saveliev and R.D. Wilson for their inspiring collaboration in developing this field and for many illuminating discussions. This work was supported by a grant from John Templeton Foundation.

References

1. J. Plumridge et al., Solid State Comm. **146**, 406 (2008)
2. A. Rakhmanov et al., Phys. Rev. B **77**, 144507 (2008)
3. N.I. Zheludev, Science **328**, 582 (2010)
4. J.Q. Quach et al., Opt. Express **19**, 11018 (2011)
5. D. Felbacq, M. Antezza, SPIE Newsroom 2012, doi:10.1117/2.1201206.004296
6. A.M. Zagoskin, J. Opt. **14**, 114011 (2012)
7. V. Savinov et al., Sci. Rep. **2**, 450 (2012)
8. N.I. Zheludev, Y.S. Kivshar, Nat. Mater. **11**, 917 (2012)
9. A.M. Zagoskin et al., arXiv:1211.4182 (2012); extended version: A.M. Zagoskin et al., Sci. Rep. 3, 3464 (2013)
10. A.M. Zagoskin, *Quantum Engineering: Theory and Design of Quantum Coherent Structures*. (Cambridge University Press, Cambridge, 2011)
11. G. Wendin, V.S. Shumeiko, in *Superconducting quantum circuits, qubits and computing*, ed. by M. Rieth, W. Schommers. Handbook of Theoretical and Computational Nanotechnology, vol. 3 (American Scientific Publishers, Los Angeles, 2005)
12. M.W. Johnson et al., Nature **473**, 194 (2011)
13. O. Astafiev et al., Science **327**, 840 (2010)
14. O. Astafiev et al., Phys. Rev. Lett. **104**, 183603 (2010)
15. A.A. Abdumalikov et al., Phys. Rev. Lett. **104**, 193601 (2010)
16. I.-C. Hoi et al., Phys. Rev. Lett. **107**, 073601 (2011)
17. A. Barone, G. Paterno, *Physics and Applications of the Josephson Effect* (Wiley, New York, 1982)
18. L.D. Landau, E.M. Lifshitz, *Quantum Mechanics (Non-relativistic Theory)*, 3rd edn. (Butterworth-Hrinemann, Oxford, 2003)
19. D.A. Wells, *Schaum's Outline of Theory and Problems of Lagrangian Dynamics* (McGraw-Hill, New York, 1967)
20. M.H. Devoret, in *Les Houches Session LXIII, 1995*, eds. S. Reynaud, E. Giacobino, J. Zinn-Justin. Quantum Fluctuations in Electrical Circuits (Elsevier Science B.V., Amsterdam, 1997)
21. G. Burkard, Theory of solid state quantum information processing. In: Handbook of Theoretical and Computational Nanotechnology, vol. 2, eds. M. Rieth, W. Schommers (American Scientific Publishers, Los Angeles, 2005)
22. J. Martinis et al., Phys. Rev. Lett. **89**, 117901 (2002)
23. J.E. Mooij et al., Science **285**, 1036 (1999)
24. A.M. Zagoskin et al., phys. stat. solidi B **246**, 955 (2009)
25. P. Macha et al., arXiv:1309.5268 (2013)
26. Y. Nakamura, Y.A. Pashkin, J.S. Tsai, Nature **398**, 786 (1999)
27. J. Gambetta et al., Phys. Rev. A **74**, 042318 (2006)
28. B.E.A. Saleh, M.C. Teich, *Fundamentals of Photonics*, 2nd edn. (Wiley, New York, 2007)
29. C. Hutter et al., Phys. Rev. B **83**, 014511 (2011)

30. E. A. Ovchinnikova et al., arXiv:1309.7557 (2013)
31. A. Shvetsov et al., Phys. Rev. B **87**, 235410 (2013)
32. M.O. Scully, M.S. Zubairy, *Quantum Optics* (Cambridge University Press, Cambridge, 1997)
33. Y.S. Greenberg et al., Phys. Rev. B **66**, 214525 (2002)
34. A. Blais et al., Phys. Rev. B **69**, 062320 (2004)
35. I. Percival, *Quantum State Diffusion* (Cambridge University Press, Cambridge, 2008)

Chapter 14
Nonlinear Localization in Metamaterials

Nikos Lazarides and George P. Tsironis

Abstract Metamaterials, i.e., artificially structured ("synthetic") media comprising weakly coupled discrete elements, exhibit extraordinary properties and they hold a great promise for novel applications including Super-Resolution imaging, cloaking, hyperlensing, and optical transformation. Nonlinearity adds a new degree of freedom for metamaterial design that allows for tunability and multistability, properties that may offer altogether new functionalities and electromagnetic characteristics. The combination of discreteness and nonlinearity may lead to intrinsic localization of the type of discrete breather in metallic, SQUID-Based, and $\mathscr{P}\mathscr{T}$-symmetric metamaterials. We review recent results demonstrating the generic appearance of breather excitations in these systems resulting from power-balance between intrinsic losses and input power, either by proper initialization or by purely dynamical procedures. Breather properties peculiar to each particular system are identified and discussed. Recent progress in the fabrication of Low-Loss, active and superconducting metamaterials, makes the experimental observation of breathers in principle possible with the proposed dynamical procedures. Recent experimental results on dynamical phenomena due to intrinsic nonlinearities in SQUID metamaterials are briefly summarized.

N. Lazarides (✉) · G.P. Tsironis
Crete Center for Quantum Complexity and Nanotechnology, Department of Physics,
University of Crete, P.O. Box 2208, 71003 Heraklion, Greece

N. Lazarides · G.P. Tsironis
Institute of Electronic Structure and Laser,Foundation for Research and Technology-Hellas,
P.O. Box 1527, 71110 Heraklion, Greece
e-mail: nl@physics.uoc.gr

G.P. Tsironis
Department of Physics, School of Science and Technology, Nazarbayev University,
53 Kabanbay Batyr Ave., Astana 010000, Kazakhstan
e-mail: gts@physics.uoc.gr

I.V. Shadrivov et al. (eds.), *Nonlinear, Tunable and Active Metamaterials*,
Springer Series in Materials Science 200, DOI 10.1007/978-3-319-08386-5_14

14.1 Introduction

Advances in theory and nanofabrication techniques have opened new unprecedented opportunities for researchers to create artificially structured media with extraordinary properties that rely on particular geometric arrangements. A well-known paradigm is that of *metamaterials* that provide access to all quadrants of the real Permittivity-permeability plane, exhibiting negative refraction index, optical magnetism, and other fascinating properties [1–4]. Their unique properties are particularly well suited for novel devices like hyperlenses [5] and optical cloaks of invisibility [6], while they may form a material base for other functional devices with tuning and switching capabilities [7, 8]. The key element for the construction of metamaterials has customarily been the split-ring resonator (SRR), a subwavelength resonant "particle" which is effectively a kind of an artificial "magnetic atom" [9]. A periodic arrangement of SRRs in space forms a *magnetic metamaterial* that exhibits high frequency magnetism and negative permeability [10]. In several applications, real-time tunability of the effective parameters of a metamaterial is a desired property, that can be achieved by nonlinearity [11–13].

Metamaterials comprising metallic elements suffer from high losses at frequencies close to those in their operating region, that place a strict limit on their performance and hamper their use in devices. The quest for loss compensation is currently following two different pathways: a "passive" one, where the metallic elements are replaced by superconducting ones [14], and an "active" one, where appropriate constituents are added to metallic metamaterials that provide gain through external energy sources. The latter has been recently recognized as a very promising technique for compensating losses [15]. *Superconducting metamaterials* exhibit both significantly reduced losses and intrinsic nonlinearities due to the extreme sensitivity of the superconducting state to externally applied fields [16–20]. The fabrication of superconducting SRRs with narrow slits filled with a dielectric oxide brings the Josephson effect into play [21]. For a thin enough dielectric barrier a Josephson junction (JJ) is formed, and the currents in the ring are then determined by the Josephson relations [21]. The Josephson element thus turns the superconducting ring into an rf SQUID (Superconducting QUantum Interference Device) [22, 23], a long known device in the Josephson community. The replacement of metallic and/or superconducting SRRs with rf SQUIDs, suggested a few years ago [24, 25], results in (SQUID-Based) metamaterials with both reduced losses and yet another source of nonlinearity due to the Josephson element. The feasibility of constructing SQUID metamaterials has been recently demonstrated, and their tunability and dynamic multistability properties were explored [26–29].

Nonlinear metallic metamaterials can be constructed by appropriate combinations of highly conducting SRRs with nonlinear electronic components; several types of diodes have been successfully employed for this purpose [11–13]. In order to construct nonlinear and *active metamaterials*, however, Gain-Providing electronic components such as tunnel (Esaki) diodes [30], have to be employed. The latter feature a negative resistance part in their current-voltage characteristics, and therefore can

provide both gain and nonlinearity in an otherwise conventional metamaterial. Tunnel diodes may also be employed for the construction of $\mathscr{P}\mathscr{T}$–symmetric metamaterials, that rely on balanced gain and loss, in a way similar to that used in electronic circuits [31]. $\mathscr{P}\mathscr{T}$–symmetric systems do not obey separately the parity ($\mathscr{P}$) and time ($\mathscr{T}$) symmetries, but instead they do exhibit a combined $\mathscr{P}\mathscr{T}$ symmetry. The notions of $\mathscr{P}\mathscr{T}$–symmetric systems originate for Non-Hermitian quantum mechanics [32], but they have been recently extended to dynamical lattices, particularly in optics [33, 34]. Spontaneous $\mathscr{P}\mathscr{T}$–symmetry breaking and power oscillations have been actually observed recently in a $\mathscr{P}\mathscr{T}$ coupled optical system [35]. Following these ideas, a $\mathscr{P}\mathscr{T}$ metamaterial with elements having alternatingly gain and equal amount of loss has been suggested [36, 37].

Conventional (metallic), SQUID-Based, and $\mathscr{P}\mathscr{T}$-metamaterials share a number of common features. They can all be constructed by discrete elements which are weakly coupled through magnetic and/or electric forces [38–41], while in most cases the inter-element coupling may be limited to nearest-neighbors. SQUIDs are coupled magnetically; also, for particular mutual orientations of the SRR slits in conventional metamaterials, either active or not, the magnetic coupling is dominant. These *magnetoinductive* systems support a new kind of waves with frequencies in a relatively narrow band of the optical type. In the presence of nonlinearity, intrinsic localization in the form of discrete breathers (DBs) may occur generically by purely deterministic dynamics. DBs are spatially localized and Time-Periodic excitations whose properties have been extensively explored in the past [42]; rigorous mathematical proofs of existence have been given for both energy conserved and dissipative lattices [43, 44]. Moreover, they have been observed in a variety of physical systems including superconducting ones [45, 46]. Dissipative DBs, in particular, may exist as a result of a power balance between input power and internal loss [47]. The input power comes either from an applied alternating magnetic field or, in the case of $\mathscr{P}\mathscr{T}$ metamaterials, from an external source through the gain mechanism. Although the existence of dissipative DBs has been numerically demonstrated in both metallic SRR-Based [48–52] and SQUID-Based metamaterials [25, 53, 54], their experimental observation is still lacking. In metallic metamaterials, losses constitute a major problem that prevents breather formation; DB frequencies lie outside but close to the linear frequency bands where high losses destroy Self-Focusing. However, DBs could be in principle observed in SQUID-Based metamaterials, or in metamaterials where losses have been compensated by a gain mechanism. In $\mathscr{P}\mathscr{T}$ metamaterials with alternating gain and loss, the net loss can become in principle very low. Then, novel Gain-Driven DBs, whose existence has been also demonstrated numerically [36, 37], could be also observed.

The present chapter focuses on the generation of stable or at least Long-Lived DBs in Dissipative-Driven metallic and SQUID-Based metamaterials, and novel Gain-Driven DBs in $\mathscr{P}\mathscr{T}$ metamaterials that rely on balanced gain and loss. For the sake of clarity in presentation we present only One-Dimensional (1D) DBs, since their temporal and spatial dependences are visible in a single figure. However, calculations with the corresponding Two-Dimensional (2D) models reveal that these DBs are not destroyed by dimensionality, and moreover they may exist in the case of moderate

Fig. 14.1 Schematic view of a one-dimensional array of split-rings in (*upper*) the planar geometry; (*lower*) the axial geometry. The magnetic field is perpendicular to the planes of the rings

anisotropy in the coupling coefficients [25, 49]. In Sects. 14.2 and 14.3, the discrete model equations and dissipative DBs for metallic metamaterials and SQUID-Based metamaterials, respectively, are presented along with the corresponding frequency dispersions of the linearized systems. Furthermore, recent experimental results on SQUID metamaterials [26–29, 55] are briefly reviewd in a separate subsection of Sect. 14.3. In Sect. 14.4, the model equations for a $\mathscr{PT}$ metamaterial with alternatingly gain and loss are presented in 1D, along with the corresponding frequency dispersion. In this case, a condition for the metamaterial being in the exact $\mathscr{PT}$ phase is also obtained. Gain-Driven DBs by either proper initialization or a purely dynamical mechanism are presented as well. In Sect. 14.5 we conclude with a brief summary of the findings.

14.2 Metalic SRR-Based Metamaterial

Consider a periodic arrangement of N nonlinear, identical, metallic SRRs in 1D (Fig. 14.1), in two distinct configurations depending on the mutual orientation of the SRRs in the array; the planar and the axial. Assuming that an SRR can be regarded as a resistive-inductive-capacitive (RLC) oscillator featuring an Ohmic resistance R, self-inductance L, and capacitance C, its state can be described by the charge Q in its capacitor and the current I induced by an alternating magnetic field with appropriate polarization. Assuming that the mutual orientations of the SRR slits are such that the magnetic interaction dominates over the electric one, the latter can be neglected. The magnetic coupling strength λ can be quantified as the ratio of the mutual inductance M between neighboring SRRs and the self-inductance of a single SRR, L, i.e., $\lambda = M/L$. Note that λ is negative (positive) between SRRs in the planar (axial) configuration. The most common configurations in 2D (not shown) are the planar, where all SRR loops are in the same plane, or the planar-axial configuration where the SRRs have the planar configuration in one direction while they have the axial configuration in the other direction [49, 51]. In 2D metamaterials on a square lattice there are two coupling coefficients $\lambda_x = M_x/L$ and $\lambda_y = M_y/L$, for coupling along the x- and y-direction, respectively, with M_x and M_y being the corresponding

mutual inductances. The (normalized) dynamic equations for the state variables of each SRR in a 2D metamaterial read [48, 56]

$$\ddot{q}_{n,m} + \lambda_x \left(\ddot{q}_{n-1,m} + \ddot{q}_{n+1,m}\right) + \lambda_y \left(\ddot{q}_{n,m-1} + \ddot{q}_{n,m+1}\right) + \gamma\, \dot{q}_{n,m} + f(q_{n,m}) = \varepsilon(\tau), \tag{14.1}$$

where $q_{n,m}$ is the charge in the capacitor of the $(n.m)$-th SRR, τ is the normalized temporal variable, $\varepsilon(\tau) = \varepsilon_0 \sin(\Omega\tau)$ is the induced electromotive force, and $\gamma = RC_\ell\omega_\ell$ is the loss coefficient, with C_ℓ and $\omega_\ell = 1/\sqrt{LC_\ell}$ being the linear capacitance and resonance frequency, respectively, and Ω is the normalized driving frequency. The overdots denote differentiation with respect to τ, while the induced current in the (n, m)-th SRR, $i_{n,m}$, is $i_{n,m} = dq_{n,m}/d\tau \equiv \dot{q}_{n,m}$. The function $f(q_{n,m})$ that provides the on-site nonlinearity, that may result from filling the SRR slits with a Kerr-type dielectric [57] or by mounting a diode into each SRR slit [58], is approximated by $f(q_{n,m}) \simeq q_{n,m} - \chi q_{n,m}^3$, where χ is a nonlinearity coefficient. The natural variables can be recovered from the normalized ones through the relations $t = \tau/\omega_\ell, \omega = \omega_\ell\Omega$, $Q_{n,m} = Q_c q_{n,m}$, $\mathscr{E} = U_c\varepsilon$, $I_{n,m} = I_c i_{n,m}$, with $I_c = U_c\omega_\ell C_\ell$, $Q_c = C_\ell U_c$ and U_c a characteristic voltage. The frequency spectrum of linear excitations is obtained by substitution of $q_{n,m} = A\cos(\kappa_x n + \kappa_y m - \Omega\tau)$ into (14.1) where we also set $\chi = 0$ and $\varepsilon_0 = 0$. We thus obtain

$$\Omega_\kappa = [1 + 2\,\lambda_x\,\cos(\kappa_x) + 2\,\lambda_y\,\cos(\kappa_y)]^{-1/2}, \tag{14.2}$$

where $\kappa = (\kappa_x, \kappa_y)$ is the normalized wavevector in 2D.

Equation (14.1) support dissipative DBs for relatively low losses, that can be generated with standard algorithms [47, 59]. The Key-Point here is the identification of two different, simultaneously stable solutions of a single SRR oscillator. Let us denote the high (low) amplitude solution with q_h (q_ℓ). Then, a trivial dissipative DB can be constructed by fixing the amplitude of a particular SRR oscillator of the metamaterial to q_h while the amplitude of all the others is fixed to q_ℓ. The corresponding currents $dq_{n,m}/d\tau \equiv i_{n,m}$, are all set to zero. Using this trivial DB configuration as initial condition, the dynamic equations are integrated while the coupling coefficients are switched on adiabatically. It turns out that the trivial DB can be continued to nonzero couplings leading to dissipative DB formation [48, 49, 51, 52]. The spatiotemporal evolution of a typical, single-site dissipative DB in 1D is shown in Fig. 14.2 during approximately two periods of oscillation. Both the central DB site and the background are oscillating with different amplitudes but same frequency $\Omega_b = 2\pi/T_b$, equal to that of the driver ($\Omega_b = \Omega$). Importantly, high and low amplitude current oscillations occur in anti-phase, which indicates differences in response to the applied field that modify locally the magnetization [48]. Depending on the frequency, DBs modify not only the magnitude but also the nature of the metamaterial response from paramagnetic to diamagnetic or even extreme diamagnetic, the latter corresponding to negative magnetic permeability μ. Different types of DBs can be constructed using appropriate trivial breathers as initial conditions. A dissipative DB

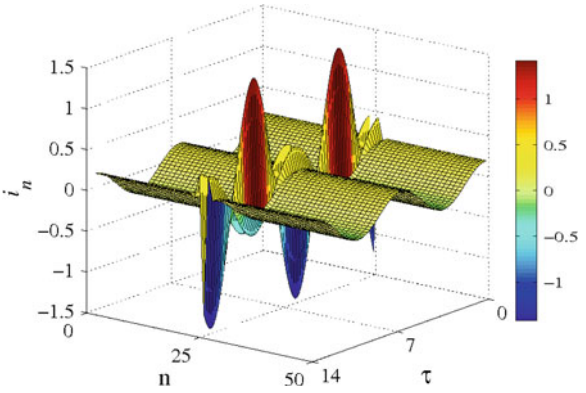

Fig. 14.2 Spatiotemporal evolution of a single-site, dissipative current breather, for $T_b = 6.82$, $\lambda = -0.02$, $\gamma = 0.01$, $\varepsilon_0 = 0.04$, $\chi = 0.16$, and $N = 50$. Both the background and the central breather site are oscillating with frequency $\Omega_b = 2\pi/T_b$. The phase-difference of high and low current oscillations is almost π

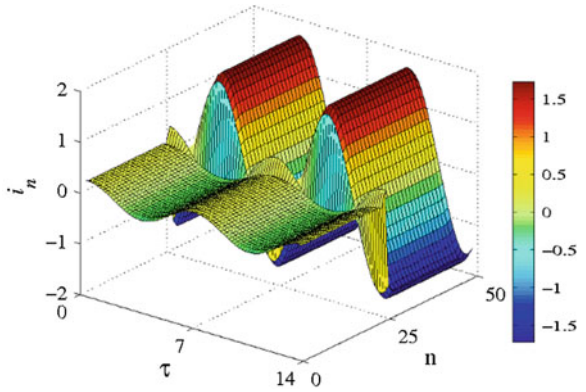

Fig. 14.3 Spatiotemporal evolution of a domain-wall dissipative breather for $T_b = 6.82$, $\lambda = -0.02$, $\gamma = 0.01$, $\varepsilon_0 = 0.04$, $\chi = 0.16$, and $N = 50$. This peculiar type of breather separates regions of the metamaterial with different magnetizations

in the form of an oscillating domain-wall that separates regions of a 1D metamaterial with different magnetizations, is illustrated in Fig. 14.3. Dissipative DBs may also be generated spontaneously in magnetic metamaterials with a binary configuration [60–62], through a purely dynamical proccess that relies on the developement of modulational instability by a frequency-chirped driving field. This procedure is particularly well suited for DB generation in experimental situations, and has been applied successfully in micromechanical cantilever oscillator arrays [63].

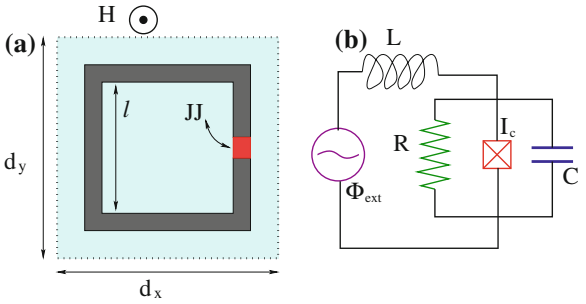

Fig. 14.4 **a** Schematic drawing of the unit cell of a SQUID metamaterial with one SQUID per cell. The applied magnetic field $\mathbf{H}(t)$ is perpendicular to the SQUID plane. **b** The equivalent circuit model for an rf SQUID driven by a flux source Φ_{ext}

14.3 rf SQUID Metamaterial

14.3.1 Dynamic Equations and Dissipative Breathers

A SQUID metamaterial may be formed as a conventional one, where the metallic elements are replaced by rf SQUIDs [24, 25]. The simplest rf SQUID, shown schematically in Fig. 14.4a, consists of a superconducting path interrupted by a single JJ; it constitutes the direct superconducting analogue of a nonlinear metallic SRR, that plays the role of the 'magnetic atom' in SQUID-Based metamaterials. For a realistic description of a SQUID, the Resistively and Capacitively Shunted Junction (RCSJ) model for the JJ is adopted [22, 23]. According to this model, the real JJ results from shunting the ideal JJ, with critical current I_c, with a resistance R and a capacitance C. The equivalent lumped circuit model for an rf SQUID in a magnetic field results from a series connection of the real JJ with an inductance L and a flux source Φ_{ext} (Fig. 14.4b). The dynamic equation for a single SQUID is then obtained by direct application of Kirkhhoff laws. SQUID metamaterials in 1D and 2D may be formed by repetition of the unit cell shown in Fig. 14.4a [64]. Nonlinearity and discreteness, combined with weak coupling between neighboring SQUIDs may lead in breather generation in this system as well [25, 53, 54]. The relevant dynamical variables in SQUID metamaterials are the magnetic fluxes, $\phi_{n,m}$, threading the SQUIDs, whose temporal evolution is described by the (normalized) equations

$$\ddot{\phi}_{n,m} + \gamma\dot{\phi}_{n,m} + \phi_{n,m} + \beta\,\sin(2\pi\phi_{n,m}) - \lambda_x(\phi_{n-1,m} + \phi_{n+1,m}) - \lambda_y(\phi_{n,m-1} + \phi_{n,m+1}) = \phi_{eff}\,, \tag{14.3}$$

where $\lambda_x = M_x/L$ and $\lambda_y = M_y/L$ are the magnetic coupling coefficients between neighboring SQUIDs in the x- and y- direction, respectively, with M_x and M_y being the mutual inductances (negative in the planar geometry). The overdots

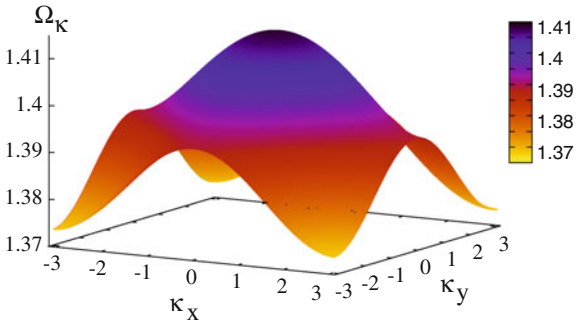

Fig. 14.5 The frequency dispersion Ω_κ plotted as a function of κ_x and κ_y for a two-dimensional SQUID metamaterial with $\lambda_x = \lambda_y = -0.014$ and $\beta = 0.15$. The band extends from $\Omega_{min} = 1.374$ to $\Omega_{min} = 1.414$

denote differentiation with respect to the normalized time τ, $\beta = LI_c/\Phi_0 = \beta_L/(2\pi)$ is the SQUID parameter, and $\gamma = \sqrt{L/C}\,/R$ is the loss coefficient of each individual SQUID, with Φ_0 being the magnetic flux quantum. The rf SQUID exhibits strong resonant response to an alternating magnetic field at a particular frequency $\omega_{SQ} = \omega_{LC}\sqrt{1+\beta_L}$, with $\omega_{LC} = 1/\sqrt{LC}$ being its corresponding inductive-capacitive frequency. In (14.3), the fluxes are normalized to Φ_0, while τ is normalized to ω_{LC}^{-1}. The term on the right-hand-side of (14.3) is the *effective* external flux $\phi_{eff} = [1 - 2(\lambda_x + \lambda_y)]\phi_{ext}$, where $\phi_{ext} = \phi_{dc} + \phi_{ac}\cos(\Omega\tau)$ is the flux due to the spacially uniform, applied magnetic field. The latter may have both constant (dc) and alternating (ac) terms, resulting from a constant and an alternating magnetic field with normalized frequency Ω, respectively.

By linearization of the free (i.e., $\gamma = 0$, $\phi_{ext} = 0$) (14.3) and substitution of the trial solution $\phi_{n,m} = A\,\exp[i(\kappa_x n + \kappa_y m - \Omega_\kappa \tau)]$, we obtain

$$\Omega_\kappa = \sqrt{1 + \beta_L - 2(\lambda_x\,\cos\kappa_x + \lambda_y\,\cos\kappa_y)}, \tag{14.4}$$

where Ω_κ is the eigenfrequency at wavevector $\kappa = (\kappa_x, \kappa_y)$, which components are normalized to the center-to-center distance between neighboring SQUIDs in the x- and y-direction, respectively. Equation (14.4) provides the frequency dispersion of magnetoinductive flux-waves whose typical form is shown in Fig. 14.5 [25], that is very similar to that of metallic metamaterials in 2D [65]. In the absence of losses ($\gamma = 0$) and ac flux $\phi_{ac} = 0$, (14.3) can be obtained from the Hamiltonian

$$\frac{H}{E_J} = \sum_{n,m}\left\{\frac{\pi}{\beta}\dot{\phi}_{n,m}^2 + u_{n,m}\right\} - \frac{2\pi}{\beta}\sum_{n,m}\left\{\lambda_x(\phi_{n,m} - \phi_{dc})(\phi_{n-1,m} - \phi_{dc})\right.$$
$$\left. + \lambda_y(\phi_{n,m} - \phi_{dc})(\phi_{n,m-1} - \phi_{dc})\right\}, \tag{14.5}$$

where $E_j = I_c \Phi_0/(2\pi)$ is the Josephson energy, and

$$u_{n,m} = \frac{\pi}{\beta}(\phi_{n,m} - \phi_{dc})^2 - \cos(2\pi\phi_{n,m}), \tag{14.6}$$

is the on-site potential. The Flux-Balance relation for the 2D SQUID metamaterial, expressed in the same order of approximation as the dynamic equations, reads $\phi^{loc}_{n,m} = \phi_{eff} + \beta\, i_{n,m}$, where $\phi^{loc}_{n,m} = \phi_{n,m} - \lambda_x(\phi_{n-1,m} + \phi_{n+1,m}) - \lambda_x(\phi_{n,m-1} + \phi_{n,m+1})$ and $i_{n,m}$ is the local flux and the current (normalized to I_c), respectively, at the lattice site (n, m).

For generating dissipative DBs in SQUID metamaterials we use two approaches; first, we employ the same algorithm as in the previous Section, and second, by introducing weak disorder in the SQUID parameter β. Estimates for the coupling strength between SQUIDs, obtained from available data [64] give $|\lambda_{x,y}| \simeq 0.014$, which is consistent with a weak coupling approximation. This value is also consistent with the corresponding ones obtained for metallic metamaterials. However, we sometimes use higher values of the coupling coefficients in order to demonstrate that breather generation is not just a marginal effect. The SQUID potential $u_{n,m}$ given in (14.6) allows for the generation of several breather types.

The number and the location of minima of $u_{n,m}$ can be controlled either by the parameter β or in Real-Time by a dc applied flux ϕ_{dc}. While for $\beta_L < 1$ there is only one minimum, multiple minima appear for $\beta_L > 1$ with their number increasing with further increasing β_L. The dc flux, on the other hand, may both create new minima and move their positions to different flux values. For example, for $\phi_{dc} = 0.5$ ($\beta_L < 1$) the potential takes the form of a symmetric Double-Well. Then, the construction of trivial DBs is a rather obvious task; one may choose flux states with high and low flux amplitude corresponding to the minima of the potential. Then, one of the SQUIDs is set to the high amplitude state and the other ones to the low amplitude state. A typical DB of this type is shown in Fig. 14.6; it cannot appear in metallic metamaterials, for which the on-site potential has a single minimum. The temporal evolution of the DB diverges significantly from a sinusoidal, due to strong nonlinearities even at low powers; this is another peculiarity resulting from the form of $u_{n,m}$. In this case, all SQUIDs oscillate almost in phase, while they differ only in their current oscillation amplitude.

The strong nonlinearity in the SQUIDs manifests itself also with the existence of several simultaneously stable solutions. The multistability of SQUID states implies multistability for possible DB configurations; indeed, by combination of two or more simultaneously stable single SQUID states for the construction of 'trivial breathers', we may generate simultaneously stable DBs [25]. Typical DBs of this type look like that in Fig. 14.7, which exhibits features similar to those of the DBs in metallic metamaterials (see e.g. Fig. 14.2), and change locally the nature of the magnetic response in SQUID metamaterials. In most cases the DB frequency equals to that of the driver. However, there is also the possibility for multiperiodic DBs to appear, whose period T_b is an integer multiple of that of the driver $T = 2\pi/\Omega$. A period-3 dissipative DB, with $T_b = 3T$, is shown in Fig. 14.8 [25]. Poincaré diagrams for the trajectories of

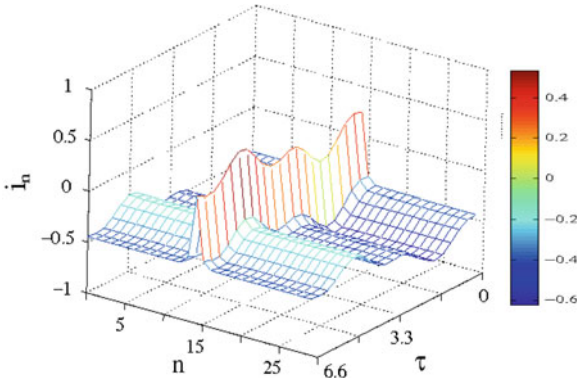

Fig. 14.6 Spatiotemporal evolution of a single-site dissipative breather during one period of oscillation, for a SQUID metamaterial with $\beta = 1.27$, $\gamma = 0.001$, $N = 30$, $\lambda = -0.1$, and $T_b = 6.6$, $\phi_{dc} = 0.5$, and $\phi_{ac} = 0.2$. Note the phase-coherence and the non-sinusoidal time-dependence of the oscillations

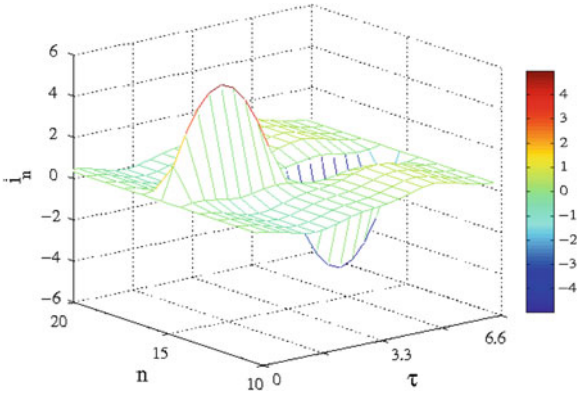

Fig. 14.7 Spatiotemporal evolution of single-site dissipative breather during one period of oscillation, for a SQUID metamaterial with $\beta = 1.27$, $\gamma = 0.001$, $N = 30$, $\lambda = 0.1$, and $T_b = 6.6$, $\phi_{dc} = 0$, and $\phi_{ac} = 0.6$

the central DB site against those for the sites in the background (not shown) confirm the observed multiperiodicity. Although we have presented mostly single-site and "bright" DBs, multi-site as well as 'dark' DBs can be also generated by appropriate choice of a trivial breather [49, 52, 54]. The linear stability of dissipative DBs can be addressed through the eigenvalues of the Floquet matrix (Floquet multipliers). A dissipative DB is linearly stable when all its Floquet multipliers lie on a circle of radius $R_e = \exp(-\gamma T_b/2)$ in the complex plane [47]. The breathers presented here are all linearly stable. Moreover, they were let to evolve for long times t ($> 10^5\ T_b$) without any observable change in their shapes.

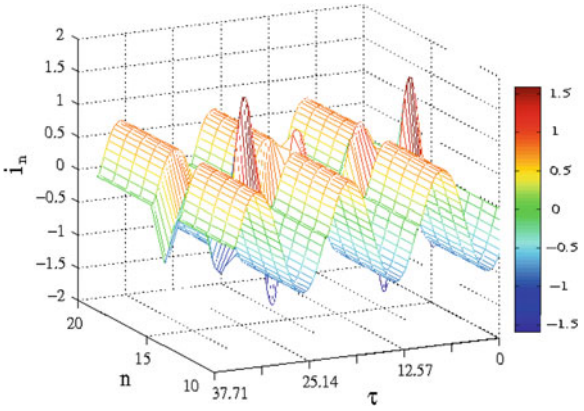

Fig. 14.8 Spatiotemporal evolution of a dissipative, period-3 breather during three driver periods, for a SQUID metamaterial with $N = 30, \phi_{dc} = 0, \phi_{ac} = 1.2, \gamma = 0.001, \beta = 1.27$, and $T_b = 12.57$

The algorithm used above requires initialization of the system with a 'trivial breather' configuration, which may not be always convenient in experimental situations. However, in SQUID metamaterials spontaneous DB generation is facilitated by the existence of weak disorder due to limited accuracy during fabrication. In a particular realization of an rf SQUID metamaterial, the elements cannot be completely identical but the values of their parameters fluctuate around a mean. The critical current I_c of the JJs seems to be more sensitive to misperfections in fabrication, since it depends exponentially on the thickness of the insulating dielectric. Then, fluctuations of I_c result in fluctuating β. We have performed numerical calculations for a SQUID metamaterial in 1D with β allowed to vary randomly within $\pm 1\,\%$ around its mean value. Then, by integrating (14.3) for a number different configurations of disorder, we obtained in most cases spontaneously generated dissipative DBs. For this approach to work, it is required that the coupling between SQUIDs is very weak. Typical results for the spatiotemporal evolution of spontaneously generated DBs in disordered SQUID metamaterials are shown in Fig. 14.9, where the instantaneous voltage $v_n = d\phi_n/dt$ is plotted on the $n - \tau$ plane. The left and right panels correspond to two different configurations of disorder, while all the other parameters are fixed. The number of generated DBs is different for the two different configurations (one and three, respectively), with the DB central sites located at different positions. In the left panel, the period of voltage oscillation in the central DB sites is twice that of the driver, so that it is actually a period-2 breather.

14.3.2 Recent Experimental Results on SQUID Metamaterials

SQUIDs are extremely sensitive to applied magnetic fields, either dc or ac (i.e., rf); a dc field, in particular, is capable of tuning the SQUID resonance periodically over a wide frequency band [26, 27, 29, 66]. Those resonance shifts due to an applied dc

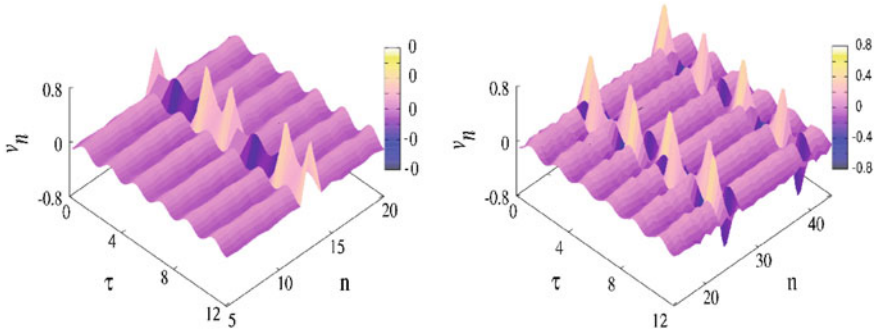

Fig. 14.9 Spatiotemporal evolution of dissipative breathers excited spontaneously in weakly disordered rf SQUID metamaterials in 1D during six periods. The voltage amplitude in the Josephson junction of the nth SQUID $v_n = d\phi/d\tau$ is plotted on the $\tau - n$ plane for $\phi_{dc} = 0$, $\phi_{ac} = 0.03$, $\beta = 1.27$, $\gamma = 0.001$, $\lambda = -0.0014$, $\omega = 3.11$, and $N = 50$. The *left* and *right* panels correspond to different configurations of disorder

and/or ac field may also reproduced numerically from the SQUID model equation [25, 54]. The remarkable property of wide-band tunability is tranfered to the SQUID metamaterial as a whole; thus, in a SQUID metamaterial, the linear flux-wave band (14.4) can be tuned over a wide frequency range by an applied dc field. Recent experiments on quasi-2D and 2D SQUID metamaterials constructed from low critical temperature superconductors (e.g. Niobium, Nb) clearly reveal the tunability of the linear band by measuring the frequency dependent, complex microwave transmission $|S_{21}|(\omega)$ as a function of the dc applied flux [27–29]. The shifts turn out to be periodic with the dc flux, while their period equals to one flux quantum Φ_0. With a transmission line model for the SQUID metamaterial, effective electromagnetic parameters such as the effective magnetic permeability μ_{eff} were retrieved from the measured data, both as a function of the frequency and the applied dc flux. Remarkably, the real part of μ_{eff} becomes negative in particular frequency intervals that may vary as a function of the dc flux [27]. Note that in these experiments, special care should be taken for the minimization of stray fields that may otherwise spoil the tunability patterns [28]. These fields may arise due to magnetic components of the measurement setup as well as Abrikosov vortices that are trapped in the superconducting film. Moreover, tunability with temperature for both single SQUIDs and SQUID metamaterials has been demonstrated [29]. The rf SQUID meta-atoms exhibit, however, an unusual response to temperature variations; the resonance frequency can either increase or decrease, depending on the dc flux applied to it. The rf power may also tune the resonance frequency of rf SQUIDs [29]. In this case, the strength of the resonant response varies with the rf power, while it remains constant with temperature tuning. Tuning with the rf power can also either increase or decrease the resonance frequency, depending on the applied dc flux.

Although the remarkable tunability properties of SQUID metamaterials described above are due to the Josephson nonlinearity, the excitation powers were low enough

for treating the Josephson junction as a quasi-linear inductive element. With increasing power, however, SQUID metamaterials start to exhibit more complex behavior that has also been explored experimentally [55]. A manifestation of that behavior is the dynamic multistability which occurs in SQUID metamaterials that consist of non-hysteretic ($\beta_L < 1$), single junction rf SQUIDs, at intermediate power levels [26]. The observed multistability, which has been also investigated numerically [67], is a purely dynamical phenomenon that is not related to the multistability known from hysteretic SQUIDs. For a particular choice of parameters, the multistability is manifested with a small number of simultaneously stable states, each of which corresponds to a different value of magnetic flux susceptibility χ_ϕ. As a result, depending on the current state of the metamaterial, it can be either almost magnetically transparent, or in a state of significantly reduced transmission. For a SQUID metamaterial in this regime, the magnitude of the transmission $|S_{21}|$ as a function of the input power exhibits large loops of hysteresis; a typical example is illustrated in figure 3 of [55], where nanosecond-long microwave pulses have been used to excite a 1D SQUID metamaterial in different branches of the hysteresis loop. The switching process, unlike other switchable metamaterial implementations, takes advantage of the intrinsic nonlinearities due to the Josephson element in each rf SQUID, which makes each of them a very fast-switching meta-atom.

14.4 $\mathscr{PT}$-Symmetric Metamaterial

Consider a 1D array of dimers, each comprising two nonlinear SRRs; one with loss and the other with equal amount of gain. The dimers can be arranged in the array either with all the SRRs being equidistant (Fig. 14.10, upper panel), or with the distance between them being modulated according to a binary pattern (Fig. 14.10, lower panel). Due to balanced gain and loss in each dimer, these configurations obey

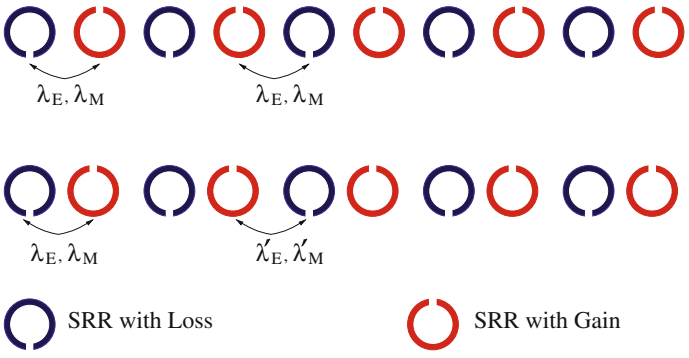

Fig. 14.10 Schematic of a $\mathscr{PT}$ metamaterial. *Upper panel* all the SRRs are equidistant. *Lower panel* the separation between SRRs is modulated according to a binary pattern ($\mathscr{PT}$ dimer chain)

a combined $\mathscr{P}\mathscr{T}$-symmetry. Building $\mathscr{P}\mathscr{T}$-symmetric metamaterials may provide a way to overcome losses and moreover to reveal new extraordinary properties. These systems undergo spontaneous symmetry breaking from the exact $\mathscr{P}\mathscr{T}$ phase, where all eigenfrequencies are real, to the broken $\mathscr{P}\mathscr{T}$ phase, where at least one pair of eigenfrequencies are complex, with the variation of a control (gain/loss) parameter. For low values of the gain/loss parameter, $\mathscr{P}\mathscr{T}$-symmetric systems are usually in the exact phase; however, when that parameter exceeds a critical value, the system goes into the broken phase. For linear $\mathscr{P}\mathscr{T}$-symmetric systems, stable solutions exist only in the exact phase.

In the equivalent circuit model picture [41, 48, 56, 60, 68], extended for the $\mathscr{P}\mathscr{T}$ dimer chain, the dynamics of the charge q_n in the capacitor of the nth SRR is governed by

$$\begin{aligned}\lambda'_M\ddot{q}_{2n} + \ddot{q}_{2n+1} + \lambda_M\ddot{q}_{2n+2} + \lambda'_E q_{2n} + q_{2n+1} + \lambda_E q_{2n+2} + \gamma\dot{q}_{2n+1} \\ + \alpha q_{2n+1}^2 + \beta q_{2n+1}^3 = \varepsilon_0 \sin(\Omega\tau) \qquad (14.7)\\ \lambda_M\ddot{q}_{2n-1} + \ddot{q}_{2n} + \lambda'_M\ddot{q}_{2n+1} + \lambda_E q_{2n-1} + q_{2n} + \lambda'_E q_{2n+1} - \gamma\dot{q}_{2n} \\ + alphaq_{2n}^2 + \beta q_{2n}^3 = \varepsilon_0 \sin(\Omega\tau), \qquad (14.8)\end{aligned}$$

where λ_M, λ'_M and λ_E, λ'_E are the magnetic and electric interaction coefficients, respectively, between nearest neighbors, α and β are nonlinear coefficients, γ is the gain/loss coefficient ($\gamma > 0$), ε_0 is the amplitude of the external driving voltage, while Ω and τ are the driving frequency and temporal variable, respectively, normalized to $\omega_0 = 1/\sqrt{LC_0}$ and ω_0^{-1}, with C_0 being the linear capacitance. The total number of SRRs is an even integer N, so that there are $N/2$ $\mathscr{P}\mathscr{T}$ symmetric dimers. In the following, we consider that the relative orientation of the SRRs in the chain is such that the magnetic coupling dominates, while the electric coupling can be neglected ($\lambda_E = \lambda'_E = 0$) [39].

In the linear regime, without external driving, we set $\alpha = \beta = 0$ and $\varepsilon_0 = 0$ in (14.7) and (14.8). We keep however the gain/loss terms that are proportional to $\pm\gamma$ and provide $\mathscr{P}\mathscr{T}$-symmetry. We then substitute $q_{2n} = A\exp[i(2n\kappa - \Omega_\kappa\tau)]$ and $q_{2n+1} = B\exp[i((2n+1)\kappa - \Omega_\kappa\tau)]$, where κ is the normalized wavevector, and request nontrivial solutions for the resulting stationary problem. We thus obtain the frequency dispersion

$$\Omega_\kappa^2 = \frac{2 - \gamma^2 \pm \sqrt{\gamma^4 - 2\gamma^2 + (\lambda_M - \lambda'_M)^2 + \mu_\kappa\mu'_\kappa}}{2(1 - (\lambda_M - \lambda'_M)^2 - \mu_\kappa\mu'_\kappa)}, \qquad (14.9)$$

where $\mu_\kappa = 2\lambda_M\cos(\kappa)$, $\mu'_\kappa = 2\lambda'_M\cos(\kappa)$. The condition for having real Ω_κ for any κ in the earlier equation then reads

$$\cos^2(\kappa) \geq \frac{\gamma^2(2-\gamma^2) - (\lambda_M - \lambda'_M)^2}{4\lambda_M\lambda'_M}, \qquad (14.10)$$

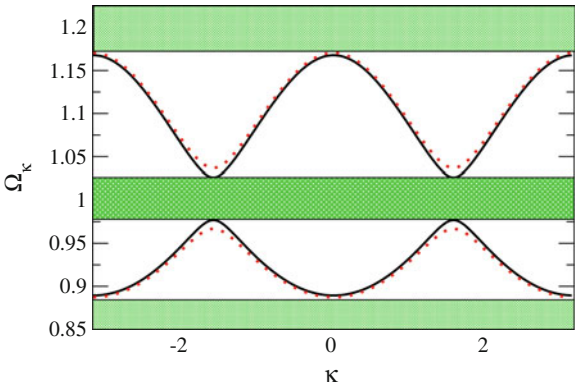

Fig. 14.11 Frequency bands for a $\mathscr{P}\mathscr{T}$-symmetric dimer chain with balanced gain and loss for $\lambda_M = -0.17$, $\lambda'_M = -0.10$, and $\gamma = 0.05$ (*black solid curves*); $\gamma = 0$ (*red dotted curves*). The forbidden frequency regions are indicated in *green*(*dark*) color. Note that the gain/loss coefficient γ has a minor effect on the dispersion curves

From (14.10) it is easy to see that for $\lambda_M = \lambda'_M$, corresponding to the equidistant SRR configuration, the condition for real Ω_κ for all κ cannot be satisfied for any positive value of the gain/loss coefficient γ. This result implies that a large $\mathscr{P}\mathscr{T}$-symmetric SRR array cannot be in the exact phase and therefore stable, stationary solutions cannot exist. To the contrary, for $\lambda_M \neq \lambda'_M$, i.e., for a $\mathscr{P}\mathscr{T}$ dimer chain, the condition (14.10) is satisfied for all κ's for $\gamma \leq \gamma_c \simeq |\lambda_M - \lambda'_M|$, ($\gamma^4 \simeq 0$). In the exact phase ($\gamma < \gamma_c$), the $\mathscr{P}\mathscr{T}$-symmetric dimer array has a gapped spectrum with two frequency bands (Fig. 14.11).

Equations (14.7) and (14.8), implemented with the boundary conditions $q_0(\tau) = q_{N+1}(\tau) = 0$, are integrated numerically with $q_m(0) = (-1)^{m-1}\mathrm{sech}(m/2)$, $\dot{q}_m(0) = 0$, and $\varepsilon_0 = 0$. The nonlinear coefficients are fixed to $\alpha = -0.4$ and $\beta = 0.08$, values that are typical for a diode [68], while γ is chosen so that the $\mathscr{P}\mathscr{T}$ metamaterial is well into the exact phase. The coupling coefficients are chosen relatively large in comparison with the values reported in the literature. However, breathers appear generically even for much lower coupling values. In order to prevent instabilities that would result in divergence of the energy at particular sites in finite time scales, we embbed the $\mathscr{P}\mathscr{T}$-symmetric dimer chain into a lossy dimer chain. In practice, we consider a longer dimer chain with total number of SRRs $N + 2N_\ell$; then we replace the gain with equivalent amount of loss at exactly N_ℓ SRRs at each end of the extended chain. That helps the excess energy to go smoothly away during the long transient phase of integration, living behind stable (or at least very long-lived, for more than $\sim 10^8$ time units) DBs [36, 37]. Typical energy density, E_n, plots in the $n - \tau$ plane are shown in Fig. 14.12. A large amount of the total energy $E_{tot} = \sum_n E_n$ is concentrated into two neighboring sites (SRRs) that belong to the same dimer. Thus, the fundamental breather excitation in the $\mathscr{P}\mathscr{T}$ metamaterial is actually a two-site DB, and not a single-site DB like those presented in the previous

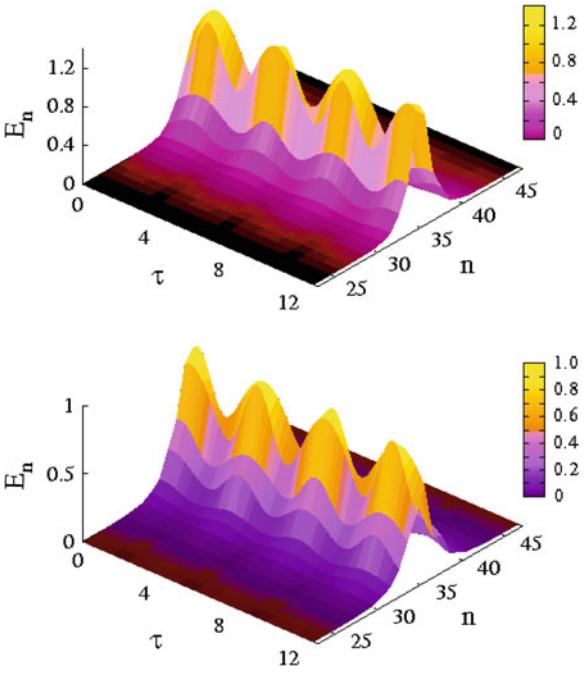

Fig. 14.12 Spatiotemporal evolution of the energy density E_n on the $n - \tau$ plane during two periods of oscillation for a $\mathscr{P}\mathscr{T}$ metamaterial with $N = 70$, $N_\ell = 10$, $\gamma = 0.002$, $\lambda'_M = -0.10$, $\lambda_E = \lambda'_E = 0$, and (*upper*) $\lambda_M = -0.17$; (*lower*) $\lambda_M = -0.21$. Energy localization at two neighboring sites, one with gain and one with loss, is clearly observed

Sections. The energy densities also exhibit regular oscillations, as it is expected for $\mathscr{P}\mathscr{T}$-symmetric systems. Inspection of the corresponding instantaneous current profiles (Fig. 14.13) i_n as a function of n, reveal that these DBs are neither symmetric nor antisymmetric at the single SRR level.

For a gapped linear spectrum, large amplitude linear modes become unstable in the presence of driving and nonlinearity. If the curvature of the dispersion curve in the region of such a mode is positive and the lattice potential is soft, large amplitude modes become unstable with respect to formation of DBs in the gap below the linear spectrum [63]. For the parameters in Fig. 14.11, the bottom of the lower band is located at $\Omega_0 = 2\pi/T_0 \simeq 0.887$, where the curvature is positive. Moreover, the SRRs are subjected to soft on-site potentials for the selected values of α and β. Then, DBs can be generated spontaneously by a frequency chirped alternating driver; after the driver is turned off, the breathers are driven solely by gain. A similar procedure has been applied succesfuly to lossy nonlinear metamaterials with a binary structure [60–62]. Gain-driven DBs that are spontaneously generated by a frequency chirped driver can be visualized on an energy density map on the $n - \tau$ plane (Fig. 14.14). We use the following procedure:

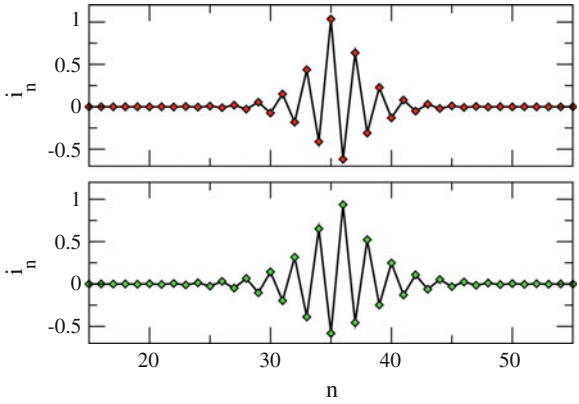

Fig. 14.13 Gain-driven, current breather profiles i_n as a function of n at maximum amplitude, for the breathers shown in Fig. 14.12. These profiles are neither symmetric nor antisymmetric at the single SRR level

- At time $\tau = 0$, we start integrating (14.7) and (14.8) with zero initial state without external driving for 500 $T_0 \simeq 3500$ time units (t.u.), to allow for significant development of large amplitude modes.
- At time $\tau \simeq 3{,}500$ t.u. (point A on Fig. 14.14), the driver is switched-on with low-amplitude and frequency slightly above Ω_0 ($1.01\ \Omega_0 \simeq 0.894$). The frequency is then chirped downwards with time to induce instability for the next 10,600 t.u. ($\sim 1{,}500\ T_0$), until it is well below Ω_0 ($0.997\ \Omega_0 \simeq 0.882$). During that phase, a large number of excitations are generated that move and strongly interact to each other, eventually merging into a small number of high amplitude multi-breathers.
- At time $\tau \simeq 14{,}100$ t.u. (point B on Fig. 14.14), the driver is switched off and the DBs are solely driven by the gain (gain-driven phase). They continue to interact to each other until they reach an apparently stationary state. The high density horizontal segments between points B and C in Fig. 14.14 present precisely those stationary gain-driven (multi-)breathers generated through the dynamics.
- At time $\tau \sim 85{,}150$ t.u. (point C on Fig. 14.14), the gain is replaced by equal amount of loss, and the breathers die out rapidly.

The above procedure is very sensitive to parameter variations of the external fields; the number of DBs as well as their locations in the lattice may change with slight parameter variation (Fig. 14.14). The DBs formed during the chirping phase continue to interact with each other for longer times, showing a tendency to merge together into wide multi-site structures that occupy an even number of sites. The frequency Ω_b of these DBs lies slightly below the lower band of the linear spectrum. Gain-driven DBs may still be generated by the above procedure when there is a slight imbalance between gain and loss [37]. The gain/loss imbalance is manifested either as a decay or growth of the total energy, in a timescale that depends on the amount of imbalance. When loss exceeds gain, a multibreather gradually looses its energy, since its excited sites at its end-points fall the one after the other in a low

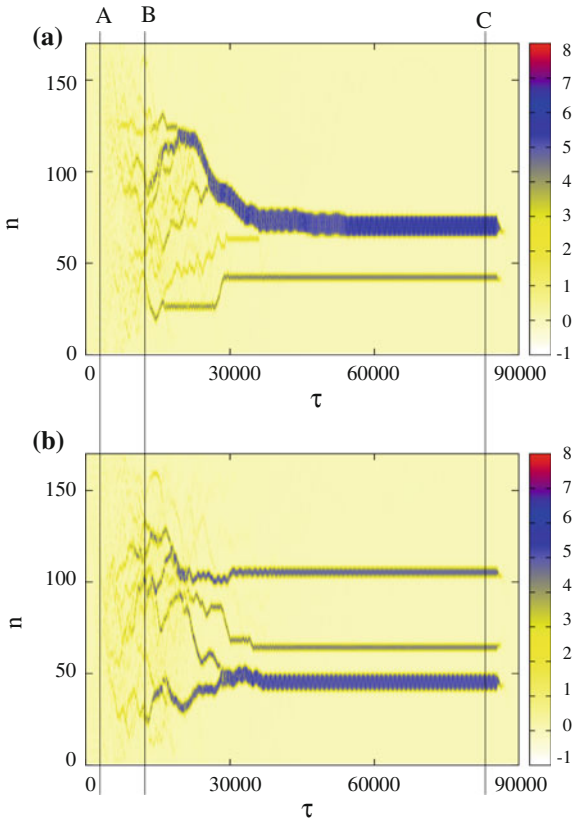

Fig. 14.14 The energy density, E_n, mapped on the $n-\tau$ plane for a $\mathscr{P}\mathscr{T}$ metamaterial (*dimer chain*) with $N = 170, N_\ell = 10, \Omega_0 = 0.887, \gamma = 0.002, \lambda_M = -0.17, \lambda'_M = -0.10\,(\lambda_E = \lambda'_E = 0)$, and **a** $\varepsilon_0 = 0.085$; **b** $\varepsilon_0 = 0.095$. The vertical lines separate different stages in the chirping procedure. Between the points B and C, the breathers indicated by the *blue-green*(*dark*) horizontal segments are solely driven by the gain. They show a clear tendency to merge together forming wide multi-site structures

amplitude state. In the opposite case, where gain exceeds loss, a multibreather slowly gains energy and becomes wider. Thus, in a realistic experimental situation where gain/loss balance is only approximate, it would be still possible for breathers to be observed at relatively short Time-Scales.

14.5 Summary

Breather excitations appear generically in nonlinear metallic, SQUID-Based, and $\mathscr{P}\mathscr{T}$ metamaterials in the presence of dissipation that is always present in practice. These *dissipative breathers* can be accurately constructed either by using standard

algorithms that require a proper initialization of the system or by dynamic effects that are more suitable in real experimental situations. Low losses, a prerequisite for DB observation, can be achieved either by inserting electronic elements that provide gain, or by replacing the metallic SRRs with superconducting ones. In conventional, metallic metamaterials and $\mathscr{P}\mathscr{T}$ metamaterials, which expose their unusual properties when driven by an alternating field, DB generation by frequency chirping seems to be a convenient approach well suited for experiments. Also, as it is demonstrated for SQUID-Based metamaterials, weak disorder may trigger localization leading to breather formation through self-focusing. Dissipative breathers are certainly closer to reality than their energy-conserving counterparts (i.e., Hamiltonian breathers) and result from a Power-Balance of intrinsic losses and input power. The latter may either come from an externally applied alternating field, as in the case of metallic and SQUID-Based metamaterials, or by a particular gain mechanism, as in the case of the proposed $\mathscr{P}\mathscr{T}$ metamaterials [36, 37]. Dissipative DBs are very robust since they correspond to attractors of the "motion" in a high-dimensional phase space, and relatively weak perturbations disappear in short time-scales. Moreover, they exhibit features not seen in Hamiltonian DBs; e.g., current oscillations appear in all the elements of a metamaterial in a dissipative breather configuration. High and low current oscillations are almost in anti-phase and, as a result, the magnetization of the metamaterial is locally modified [48, 49]. Breathers exhibiting in-phase oscillations may be however generated in SQUID metamaterials for which the on-site potential has multiple minima. Fundamental dissipative DBs in metallic and SQUID metamaterials are single-sited that however cannot exist in $\mathscr{P}\mathscr{T}$ metamaterials, due to the $\mathscr{P}\mathscr{T}$ symmetry. In the latter, the fundamental breather occupies at least two sites, i.e., a dimer, which is $\mathscr{P}\mathscr{T}$-symmetric by itself. Although experimental observations of DBs in metamaterials are still lacking, the advances in fabrication of active and superconducting metamaterials may provide structures with significantly reduced losses. Then, breather observation would be in principle possible with the dynamic approaches presented above. Note that the field of SQUID metamaterials has been recently explode and their complex behavior due to intrinsic nonlinearities is currently explored. Purely dynamic phenomena observed in experiments are briefly discussed in Sect. 14.3.2.

Acknowledgments This work was partially supported by the European Union's Seventh Framework Programme (FP7-REGPOT-2012-2013-1) under grant agreement no 316165, and by the Thales Projects ANEMOS and MACOMSYS, cofinanced by the European Union (European Social Fund ESF) and Greek national funds through the Operational Program "Education and Lifelong Learning" of the National Strategic Reference Framework (NSRF) Research Funding Program: THALES. Investing in knowledge society through the European Social Fund.

References

1. V.M. Shalaev, Nat. Photonics **1**, 41 (2007)
2. C.M. Soukoulis, S. Linden, M. Wegener, Science **315**, 47 (2007)

3. C.M. Soukoulis, M. Wegener, Nat. Photonics **5**, 523 (2011)
4. N.I. Zheludev, Y.S. Kivshar, Nat. Mater. **11**, 917 (2012)
5. J.B. Pendry, Phys. Rev. Lett. **85**, 3966 (2000)
6. D. Schurig, J.J. Mock, B.J. Justice, S.A. Cummer, J.B. Pendry, A.F. Starr, D.R. Smith, Science **314**, 977 (2006)
7. N.I. Zheludev, Science **328**, 582 (2010)
8. N.I. Zheludev, Opt. Photonics News **22**, 31 (2011)
9. J.G. Caputo, I. Gabitov, A.I. Maimistov, Phys. Rev. B **85**, 205446 (2012)
10. S. Linden, C. Enkrich, G. Dolling, M.W. Klein, J. Zhou, T. Koschny, C.M. Soukoulis, S. Burger, F. Schmidt, M. Wegener, IEEE J. Selec. Top. Quant. Electron. **12**, 1097 (2006)
11. D.A. Powell, I.V. Shadrivov, Y.S. Kivshar, M.V. Gorkunov, Appl. Phys. Lett. **91**, 144107 (2007)
12. I.V. Shadrivov, A.B. Kozyrev, D.W. van der Weide, Y.S. Kivshar, Appl. Phys. Lett. **93**, 161903 (2008)
13. B. Wang, J. Zhou, T. Koschny, C.M. Soukoulis, Opt. Express **16**, 16058 (2008)
14. S.M. Anlage, J. Opt. **13**, 024001 (2011)
15. A.D. Boardman, V.V. Grimalsky, Y.S. Kivshar, S.V. Koshevaya, M. Lapine, N.M. Litchinitser, V.N. Malnev, M. Noginov, Y.G. Rapoport, V.M. Shalaev, Laser Photonics Rev. **5**(2), 287 (2010)
16. M.C. Ricci, N. Orloff, S.M. Anlage, Appl. Phys. Lett. **87**, 034102 (2005)
17. M.C. Ricci, H. Xu, R. Prozorov, A.P. Zhuravel, A.V. Ustinov, S.M. Anlage, IEEE Trans. Appl. Supercond. **17**, 918 (2007)
18. J. Gu, R. Singh, Z. Tian, W. Cao, Q. Xing, M.X. He, J.W. Zhang, J. Han, H. Chen, W. Zhang, Appl. Phys. Lett. **97**, 071102 (2010)
19. V.A. Fedotov, A. Tsiatmas, J.H. Shi, R. Buckingham, P. de Groot, Y. Chen, S. Wang, N.I. Zheludev, Opt. Express **18**, 9015 (2010)
20. H.T. Chen, H. Yang, R. Singh, J.F. OHara, A.K. Azad, A. Stuart, S.A. Trugman, Q.X. Jia, A.J. Taylor, Phys. Rev. Lett. **105**, 247402 (2010)
21. B. Josephson, Phys. Lett. A **1**, 251 (1962)
22. A. Barone, G. Patternó, *Physics Applications of the Josephson Effect* (Wiley, New York, 1982)
23. K.K. Likharev, *Dynamics of Josephson Junctions and Circuits* (Gordon and Breach, Philadelphia, 1986)
24. N. Lazarides, G.P. Tsironis, Appl. Phys. Lett. **16**, 163501 (2007)
25. N. Lazarides, G.P. Tsironis, M. Eleftheriou, Nonlinear Phenom. Complex Syst. **11**, 250 (2008)
26. P. Jung, S. Butz, S.V. Shitov, A.V. Ustinov, Appl. Phys. Lett. **102**, 062601 (2013)
27. S. Butz, P. Jung, L.V. Filippenko, V.P. Koshelets, A.V. Ustinov, Opt. Express **29**(19), 22540 (2013)
28. S. Butz, P. Jung, L.V. Filippenko, V.P. Koshelets, A.V. Ustinov, Supercond. Sci. Technol. **26**, 094003 (2013)
29. M. Trepanier, D. Zhang, O. Mukhanov, S.M. Anlage, Phys. Rev. X 3, 041029 (2013)
30. L. Esaki, Phys. Rep. **109**, 603 (1958)
31. J. Schindler, A. Li, M.C. Zheng, F.M. Ellis, T. Kottos, Phys. Rev. A **84**, 040101(R) (2011)
32. D.W. Hook, Ann. Phys. (Berlin) **524**(6–7), A106 (2012)
33. R. El-Ganainy, K.G. Makris, D.N. Christodoulides, Z.H. Musslimani, Opt. Lett. **32**, 2632 (2007)
34. K.G. Makris, R. El-Ganainy, D.N. Christodoulides, Z.H. Musslimani, Phys. Rev. Lett. **100**, 103904 (2008)
35. C.E. Rüter, K.G. Makris, R. El-Ganainy, D.N. Christodoulides, M.Segev, D. Kip, Nat. Phys. **6**, 192–195 (2010)
36. N. Lazarides, G.P. Tsironis, Phys. Rev. Lett. **110**, 053901 (2013)
37. G.P. Tsironis, N. Lazarides, Appl. Phys. A **115**, 449 (2014)
38. O. Sydoruk, A. Radkovskaya, O. Zhuromskyy, E. Shamonina, M. Shamonin, C. Stevens, G. Faulkner, D. Edwards, L. Solymar, Phys. Rev. B **73**, 224406 (2006)
39. F. Hesmer, E. Tatartschuk, O. Zhuromskyy, A.A. Radkovskaya, M. Shamonin, T. Hao, C.J. Stevens, G. Faulkner, D.J. Edwardds, E. Shamonina, Phys. Stat. Sol. (b) **244**, 1170 (2007)
40. I. Sersić, M. Frimmer, E. Verhagen, A.F. Koenderink, Phys. Rev. Lett. **103**, 213902 (2009)

41. N.N. Rosanov, N.V. Vysotina, A.N. Shatsev, I.V. Shadrivov, D.A. Powell, Y.S. Kivshar, Opt. Express **19**, 26500 (2011)
42. S. Flach, A.V. Gorbach, Phys. Rep. **467**, 1 (2008)
43. R.S. MacKay, S. Aubry, Nonlinearity **7**, 1623 (1994)
44. S. Aubry, Physica D **103**, 201 (1997)
45. P. Binder, D. Abraimov, A.V. Ustinov, S. Flach, Y. Zolotaryuk, Phys. Rev. Lett. **84**(4), 745 (2000)
46. E. Trías, J.J. Mazo, T.P. Orlando, Phys. Rev. Lett. **84**, 741 (2000)
47. J.L. Marín, F. Falo, P.J. Martínez, L.M. Floría, Phys. Rev. E **63**, 066603 (2001)
48. N. Lazarides, M. Eleftheriou, G.P. Tsironis, Phys. Rev. Lett. **97**, 157406 (2006)
49. M. Eleftheriou, N. Lazarides, G.P. Tsironis, Phys. Rev. E **77**, 036608 (2008)
50. N. Lazarides, G.P. Tsironis, Y.S. Kivshar, Phys. Rev. E **77**(6), 065601(R) (2008)
51. M. Eleftheriou, N. Lazarides, G.P. Tsironis, Y.S. Kivshar, Phys. Rev. E **80**, 017601 (2009)
52. G.P. Tsironis, N. Lazarides, M. Eleftheriou, Springer Ser. Opti. **150**, 273 (2010)
53. G.P. Tsironis, N. Lazarides, M. Eleftheriou, PIERS Online **5**, 26 (2009)
54. N. Lazarides, G.P. Tsironis, Proc. SPIE **8423**, 84231K (2012)
55. P. Jung, S. Butz, M. Marthaler, M.V. Fistul, J. Leppäkangas, V.P. Koshelets, A.V. Ustinov, Nat. Commun. **5**, 3730 (2014)
56. I.V. Shadrivov, A.A. Zharov, N.A. Zharova, Y.S. Kivshar, Photonics Nanostruct. Fundam. Appl. **4**, 69 (2006)
57. A.A. Zharov, I.V. Shadrivov, Y.S. Kivshar, Phys. Rev. Lett. **91**, 037401 (2003)
58. M. Lapine, M. Gorkunov, K.H. Ringhofer, Phys. Rev. E **67**, 065601 (2003)
59. P.J. Martínez, M. Meister, L.M. Floria, F. Falo, Chaos **13**, 610 (2003)
60. M.I. Molina, N. Lazarides, G.P. Tsironis, Phys. Rev. E **80**, 046605 (2009)
61. N. Lazarides, M.I. Molina, G.P. Tsironis, Acta Phys. Pol. A **116**(4), 635 (2009)
62. N. Lazarides, G.P. Tsironis, Phys. Lett. A **374**, 2179 (2010)
63. M. Sato, B.E. Hubbard, A.J. Sievers, B. Ilic, D.A. Czaplewski, H.G. Graighead, Phys. Rev. Lett. **90**, 044102 (2003)
64. J.R. Kirtley, C.C. Tsuei, Ariando, H.J.H. Smilde, H. Hilgenkamp, Phys. Rev. B **72**, 214521 (2005)
65. E. Shamonina, V.A. Kalinin, K.H. Ringhofer, L. Solymar, J. Appl. Phys. **92**, 6252 (2002)
66. S. Poletto, F. Chiarello, M.G. Castellano, J. Lisenfeld, A. Lukashenko, P. Carelli, A.V. Ustinov, Phys. Scr. **T137**, 014011 (2009)
67. N. Lazarides, G.P. Tsironis, Supercond. Sci. Technol. **26**, 084006 (2013)
68. N. Lazarides, V. Paltoglou, G.P. Tsironis, Int. J. Bifurc. Chaos **21**, 2147 (2011)

Chapter 15
Field Enhancement with Classical Electromagnetically Induced Transparency

Philippe Tassin, Thomas Koschny and Costas M. Soukoulis

Abstract A key challenge in the design of tunable and nonlinear metamaterials is creating large local electromagnetic fields to enhance the nonlinear interaction. An attractive way to achieve local field enhancement is the use of metamaterials with dark resonators, i.e., with meta-atoms that do not directly couple to the external field. Such metamaterials exhibit a scattering response that is similar to what is observed for electromagnetically induced transparency (EIT): they combine large group delay with low absorption at the same frequency. Classical EIT metamaterials are interesting for nonlinear metamaterials because of the large field enhancement due to the lack of radiation loss in the dark element and for tunable metamaterials because of the high sensitivity of the resonance to the environment or a control signal. We discuss the design and modeling of EIT metamaterials and some early work on their applications to media with nonlinear/tunable response.

15.1 Introduction

Electromagnetically induced transparency (EIT) is originally a quantum-mechanical effect that renders an otherwise opaque medium transparent in a narrow transmission window with low absorption [1]. It occurs in certain three-level atomic systems—e.g., alkali metal vapors, doped solid-state materials, or quantum-dot-based systems—where destructive interference between two radiative transitions creates a dark dressed superposition state with no electric dipole moment [2–4]. In the simplest case, these atomic systems have two ground states and one common excited state (as in Fig. 15.1a), and transitions between the two ground states are forbidden. A laser beam (the probe) couples one of the ground states to the excited state, resulting in a typical Lorentzian absorption spectrum. When a second beam

P. Tassin (✉)
Department of Applied Physics, Chalmers University, SE-412 96 Göteborg, Sweden

T. Koschny · C.M. Soukoulis
Ames Laboratory—U.S. DOE, Iowa State University, Ames, IA 50011, USA

T. Koschny · C.M. Soukoulis
Department of Physics and Astronomy, Iowa State University, Ames, IA 50011, USA

I.V. Shadrivov et al. (eds.), *Nonlinear, Tunable and Active Metamaterials*,
Springer Series in Materials Science 200, DOI 10.1007/978-3-319-08386-5_15

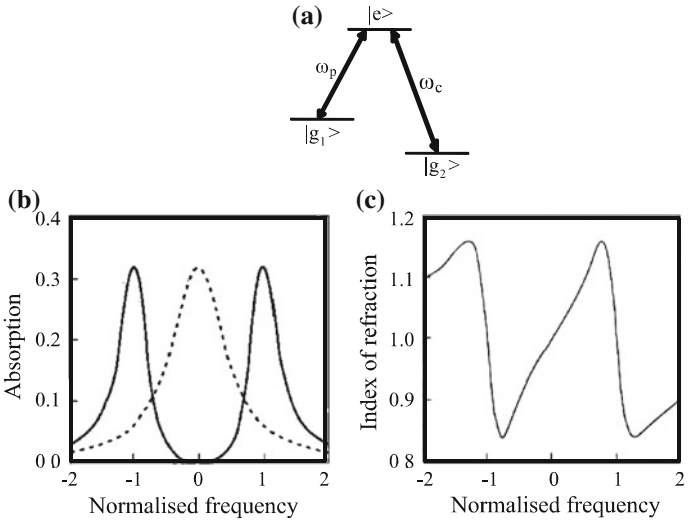

Fig. 15.1 **a** Energy diagram of atomic EIT media **b** Absorption spectrum of an EIT medium showing the transparency window (*dashed*) inside the Lorentzian background (*solid*) **c** Index of refraction of an EIT medium showing steep dispersion at the same frequency of the absorption minimum (From [2])

couples the other ground state to the excited state, a peculiar phenomenon is observed: destructive interference between both excitation pathways results in vanishing probability for the atomic system to be found in the excited state. The material decouples from the external field of the probe beam and behaves at this frequency almost like vacuum. The result is an incision (the transmission window) in the Lorentzian absorption spectrum of the probe, as shown in Fig. 15.1b. At the same frequency, there is very strong normal dispersion (Fig. 15.1c), which can lead to a remarkable increase in the group delay of the sample.

Quantum-mechanical EIT has the potential for dramatic slowdown of light to a group velocity of about 17 m/s [5] and even for the storage of light [6, 7]. However, the rather short coherence time of the dark superposition state necessitates complicated experimental handling, often requiring cryogenic temperatures and/or strong magnetic fields. However, it was realized recently that the characteristic features of EIT—simultaneously low absorption and strong dispersion—can also be realized in purely classical systems such as coupled mechanical or electrical resonators [8], i.e., no quantum-mechanical superposition states are necessary. Although the physics of such classical EIT systems is very different from the quantum-mechanical EIT in atomic systems, the underlying idea is similar—there are two resonances that interfere destructively in a narrow transmission band causing decoupling from the external field. Many classical analogues have since been demonstrated in optical microresonators [9] or coupled acoustic resonators [10].

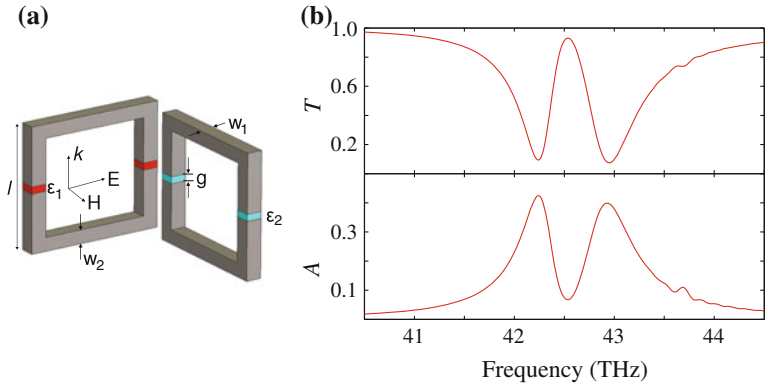

Fig. 15.2 **a** Metamaterial implementing the classical analogue of electromagnetically induced transparency using two coupled split-ring resonators. **b** Transmission and absorption spectra (Adapted from [11])

A few years ago, three groups of scientists independently proposed to create meta-atoms consisting of coupled electrical or plasmonic resonators to achieve effective metamaterials with an EIT response [11–13].[1] A very illustrative example is the meta-atom in Fig. 15.2a, which consists of two perpendicular split-ring resonators. An incident plane electromagnetic wave, propagating from bottom to top, can couple to the leftmost split-ring resonator, which has the magnetic dipole of its magnetic resonance parallel to the magnetic field. This resonator is commonly called the radiative or the bright resonator. However, the wave cannot couple directly to the other split ring, which has the magnetic dipole oriented perpendicularly—designated as the dark resonator. Of course, there is a capacitive (and inductive) interaction between the two split-ring elements, so when the magnetic dipole mode of the first ring is excited, energy will be exchanged between the two rings through the quasistatic interaction. The transmittance and absorbance of the resulting metamaterial are shown in Fig. 15.2b. One can observe the characteristic features of EIT: a transmission window with low absorption and strong dispersion. Note that the capacitive interaction can be straightforwardly altered by changing the distance between the two split rings. There is also no need for a pump beam to achieve the interaction between the two resonators as opposed to the quantum-mechanical version. In the past few years, classical EIT metamaterials have been demonstrated experimentally by many scientists around the world.[2]

[1] Some authors have described this phenomenon as a classical analogue of Fano resonances rather than electromagnetically induced transparency. The difference originates in whether the radiative resonator is considered a single resonance (it is indeed a single electromagnetic resonance) or a continuum of resonances (the electromagnetic resonance is broadened by dissipative loss or radiation loss). It is merely a matter of terminology.

[2] See, for example, [11–23].

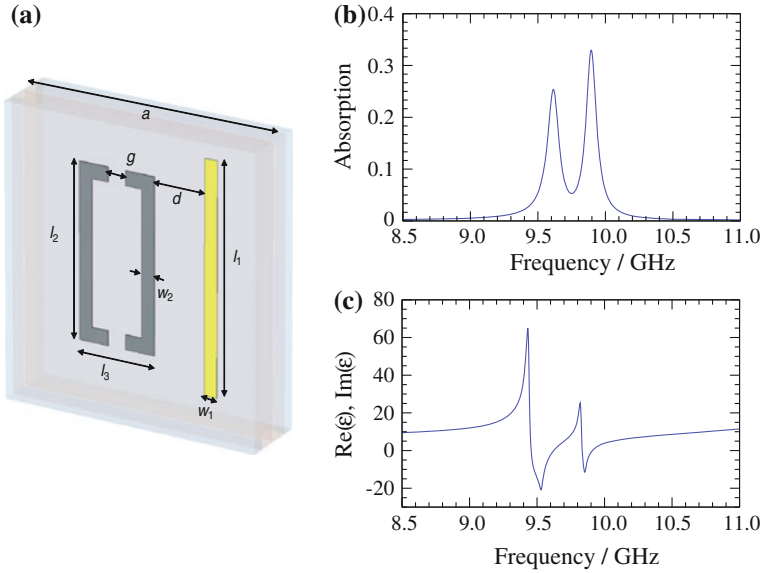

Fig. 15.3 **a** A planar EIT metamaterial. **b** Absorption spectrum showing the transmission window with low absorption. **c** Effective permittivity of the EIT metamaterial showing the strong dispersion (From [14])

15.2 Design of EIT Metamaterials

The double split-ring meta-atom discussed above is very instructive in explaining the physics, but its three-dimensional geometry makes it impractical for fabrication. Planar metamaterials are indeed often preferred since they are much easier to make than three-dimensional structures, e.g., with lithographic techniques. Figure 15.3a shows an example of a planar EIT metamaterial. The meta-atom contains a double-gap split-ring resonator and a cut wire. The incident wave propagates normal to the substrate and with the electric field polarized along the cut wire, so it can directly couple to the electric dipole resonance of the cut wire. The two-gap split-ring resonator is designed to have a magnetic resonance at the same frequency, but since it has a symmetry plane parallel with the electric field, the incident field cannot directly couple to it. The magnetic dipole resonance of the split ring is thus the dark resonance. Figure 15.3b plots the absorption spectrum. At $f = 9.75\,\text{GHz}$, we observe the transmission window with minimal absorption. In Fig. 15.3c, we observe strong dispersion in the effective permittivity of the metamaterial (this metamaterial has a group delay that is 100 times larger than in vacuum). It is instructive to look at the electric currents in the wire and the ring, because they confirm the physics of destructive interference in the electric dipole moment. Figure 15.4a shows the electric current distribution at an absorption peak, i.e., away from the dark resonance frequency. We observe that the electric current flows predominantly in the cut wire.

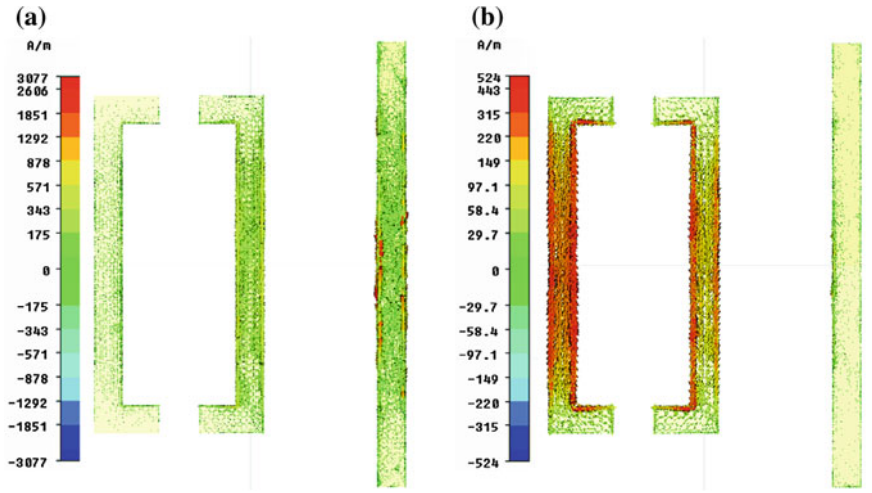

Fig. 15.4 Current distribution in the EIT metamaterial depicted in Fig. 15.3a, **a** at the absorption peak, **b** at the transparency frequency (From [14])

At the EIT frequency, a large current is flowing in the split-ring resonator, i.e., the dark resonator is strongly excited, while there is almost no current in the wire. This is because the current directly induced by the external field in the wire cancels the current induced by the interaction with the split-ring resonator. As a consequence, the material decouples from the external field at this point and the effective permittivity is close to unity (like vacuum). The result is the excitation of a mode with very small electric dipole moment—hence the large transmission.

An important aspect of classical electromagnetically induced transparency is the quality factor of the dark resonator. In Sect. 15.3, we will see that EIT can only be achieved if the quality factor of the dark resonator is much larger than the quality factor of the radiative resonator. Special care must therefore be taken in the design of the dark resonator to reduce energy loss as much as possible. In general, there are two mechanisms that contribute to the finite quality factor of the dark resonator:

- Dissipative loss; and
- Radiation loss.

Radiation loss occurs because the meta-atoms act as small antennae that reradiate electromagnetic waves. For the radiative resonator, this is desired, since its radiated fields combine to form the transmitted and reflected waves of the metamaterial. We do not need radiation loss in the dark resonator, of course, but reradiation by the split-ring resonator of Fig. 15.3a into a mode that is orthogonal to the incident wave can still happen. The quality factor of the dark resonator can be increased by reducing the radiation loss. This is achieved in the metamaterial pictured in Fig. 15.5a. The unit cell contains a double planar split-ring resonator symmetrically located around a metal wire. Similar as above, the cut wire has an electrical dipole moment

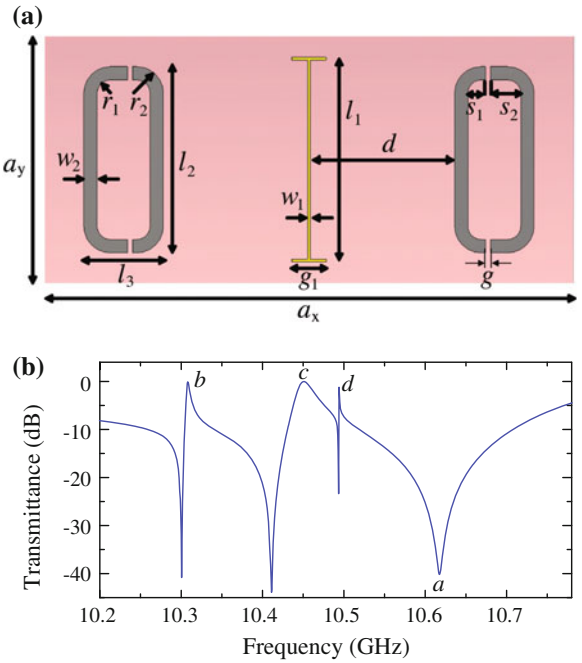

Fig. 15.5 **a** Meta-atom with a dark element that has no dipole moment to reduce radiation loss. **b** Transmittance spectrum of this EIT metamaterial (From [24])

providing for the radiative resonator. The transmitted waves (Fig. 15.5b) indicate that this metamaterial does not have just one, but three dark modes.

The current distributions at the maximum-transmission frequencies illustrate what is happening. In Fig 15.6a, displaying the current distribution at $f = 10.62\,\text{GHz}$ (the feature labeled a in Fig. 15.5b), there is a large current density in the wire only; this is the radiative electric dipole resonance of the wire. At the EIT feature at $f = 10.30\,\text{GHz}$ (b in Fig. 15.5b), we see large currents in the split rings and only a small current in the wire commensurate with a dark mode excitation (Fig. 15.6b). The current distribution reveals that this dark mode is one of the hybridizations of the electric dipole resonances of the split-ring resonators. We see that the currents in the two different split rings flow in opposite directions. The EIT feature at $f = 10.41\,\text{GHz}$ (c in Fig. 15.5b) has the main currents circling around the split rings—one in a clockwise direction, the other in a counterclockwise direction (Fig. 15.6c); this is the symmetric hybridization of the magnetic dipole resonances of the split-ring resonators. At the frequencies of the EIT feature at $f = 10.49\,\text{GHz}$ (d in Fig. 15.5b), the current density is again circling the split-ring resonators, but now in the same direction for both split rings (Fig. 15.6d). This is the antisymmetric hybridization of the magnetic dipole resonances of the split-ring resonators.

The resonances in Figs. 15.6b, c are especially attractive, because they eliminate the electric (magnetic) dipole moment—i.e., they are quadrupole modes.

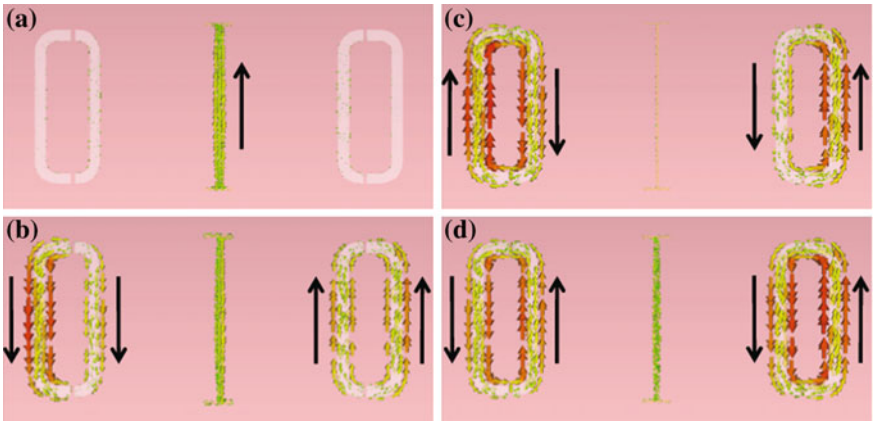

Fig. 15.6 Current distributions in an EIT metamaterial with a dark resonator with vanishing dipole radiation. The labels **a**–**d** correspond to the spectral features marked with the same label in Fig. 15.5b (From [24])

This eliminates any dipole radiation from the dark resonator, increasing its quality factor. In other words, a good geometrical design of the dark resonator can improve EIT metamaterials significantly. It is important to note that the dark "resonator" does not need to be a distinct physical structure, but can rather be just another electromagnetic eigenmode of the meta-atom. The electric quadrupole mode has another advantage here: when the wire is placed exactly in the symmetry plane of the double ring structure, there is no interaction between the dark and bright resonators. This enables us to create very small coupling strength by moving the wire slightly away from the symmetry plane.

At microwave frequencies, a very effective way to address dissipative loss in the dark resonator is to fabricate it out of a superconductor and using high-quality substrates [24]. This strategy was actually used in the metamaterial depicted in Fig. 15.5a, where the wire is made from a superconducting niobium (Nb) film. When cooled down sufficiently below the critical temperature, Nb has a resistivity that is five orders of magnitude smaller than the resistivity of silver at room temperature (at 10 GHz). With the use of a superconductor, we have achieved group delays of 300 ns in the X band from a subwavelength-thin metamaterial (see group delay measurements in Fig. 15.7). For this 250 μm-thick metamaterial, the measured delay corresponds to a group velocity of roughly 1000 m/s—or slowdown of light by a factor of 250,000—and may find application as compact delay lines in microwave photonics. The delay-bandwidth product (DBP) of the metamaterial pictured in Fig. 15.5a is 0.3, which approaches the DBPs in resonant cavities (DBP $\approx$ 1), but is still smaller than media containing atomic vapors (DBP $\approx$ 10) and some photonic crystal waveguides (DBP $\approx$ 100), but we should keep in mind that the latter systems are much longer than a single wavelength.

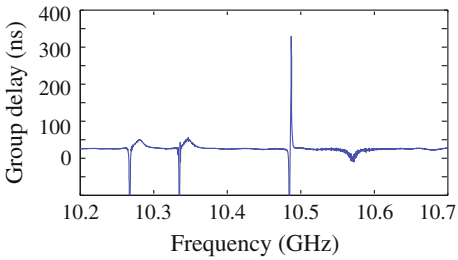

Fig. 15.7 Experimentally measured group delay of an EIT metamaterial with a dark resonator made from the superconductor niobium to minimize dissipative loss (From [24])

15.3 A Simple Model for EIT Metamaterials

To further our understanding of EIT metamaterials and to aid in their design, it is desirable to have a simple model describing their main properties.

15.3.1 The Two-Oscillator Model

The simplest model to describe classical EIT systems is a set of two coupled mass-spring oscillators or two RLC circuits coupled by a shunt capacitor (see Fig. 15.8)—i.e., two coupled harmonic oscillators with a linear interaction term:

$$\begin{aligned} \omega_r^{-2}\ddot{p}(t) + \gamma_r\omega_r^{-1}\dot{p}(t) + p(t) &= f(t) - \kappa q(t), \\ \omega_d^{-2}\ddot{q}(t) + \gamma_d\omega_d^{-1}\dot{q}(t) + q(t) &= -\kappa p(t). \end{aligned} \tag{15.1}$$

The radiative resonator with resonance frequency ω_r and damping factor γ_r is described by the excitation $p(t)$ and is driven by the external force $f(t)$. The dark resonator with resonance frequency ω_d and damping factor γ_d is described by the excitation $q(t)$. Both resonators are linearly coupled with coupling strength κ. The individual oscillators are electromagnetic resonators or electromagnetic resonances of the meta-atoms.

The equations of model (15.1) reflect the essential ingredients of EIT systems: they contain two coupled resonances that are asymmetrically driven by the external force. They can be solved in the frequency domain to obtain:

$$\begin{aligned} p(\omega) &= \frac{D_d(\omega)f(\omega)}{D_d(\omega)D_r(\omega) - \kappa^2}, \\ q(\omega) &= \frac{\kappa f(\omega)}{D_d(\omega)D_r(\omega) - \kappa^2}, \end{aligned} \tag{15.2}$$

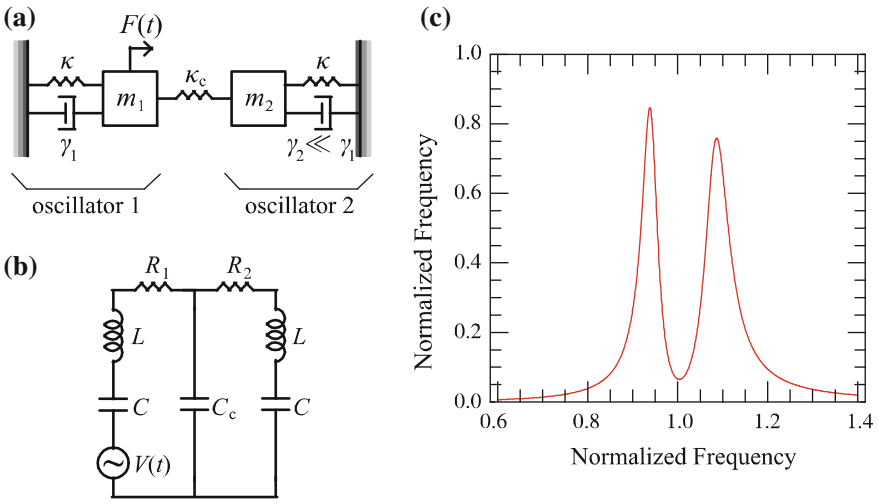

Fig. 15.8 Two-oscillator models **a** Mechanical analogue **b** Electrical circuit analogue **c** Absorbed power spectrum in a system of two linearly coupled harmonic oscillators

where $D_r(\omega) = 1 - (\omega/\omega_r)^2 - i\gamma_r(\omega/\omega_r)$ and $D_d = 1 - (\omega/\omega_d)^2 - i\gamma_d(\omega/\omega_d)$.

The dissipated power per unit cell, shown in Fig. 15.8c and obtained from

$$Q = \frac{1}{2} Re\,[f \cdot \dot{p}] = \frac{\omega^2}{2}\left(\gamma_r\,|p(\omega)|^2 + \gamma_d\,|q(\omega)|^2\right), \tag{15.3}$$

has a Lorentzian shape with a sharp incision at the resonance frequency if $\omega_r \approx \omega_d$, $\gamma_d \ll \gamma_r$ (i.e., the quality factor of the dark resonator must be larger than the quality factor of the radiative resonator), and $\gamma_d\,\gamma_r \ll \kappa^2 \ll 1$. Based on the two-resonator model, we can derive a few rules of thumb by expanding (15.3) in the vicinity of the EIT resonance frequency. These rules of thumb are depicted in Fig. 15.9. It is important to note that the bandwidth of the EIT resonance is related to the coupling strength κ, and not to the quality factor as would be the case for a simple Lorentzian resonance.

Even though the two-resonator model can qualitatively describe the absorption of classical EIT analogues, it fails to model the scattering parameters of metamaterials exhibiting a classical EIT response, i.e., there is no information about the transmission and reflection spectra. This is especially troublesome since it makes it impossible to determine the group delay, quite an essential parameter for slow-light media.

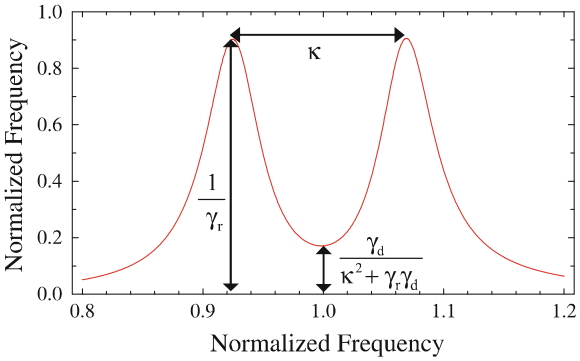

Fig. 15.9 Rules of thumb for the bandwidth of the transmission window and the absorption minimum of the EIT spectrum

15.3.2 The Radiating Two-Oscillator Model

To obtain a model that rigorously describes both the microscopic and the macroscopic response in terms of the radiated field (i.e., the incident, reflected, and transmitted waves), we have to include the actual coupling of the bright resonator to the external world [25]. Most of the EIT metamaterials fabricated to date are essentially single-layer structures rather than bulk media. Hence, their effective response can be described by an electric current sheet with surface conductivity σ_{se}. The scattering parameters of an electric current sheet are

$$R = -\frac{\zeta\sigma_{se}}{2+\zeta\sigma_{se}},$$
$$T = \frac{2}{2+\zeta\sigma_{se}}, \tag{15.4}$$

where ζ is the wave impedance of the external waves. Equations (15.4) serve as the *world model*, i.e., they describe the interaction of the medium with the external electromagnetic field. The local microscopic behavior of the EIT medium can still be described by the two-resonator model as given by (15.1).

In order to complete the radiating two-oscillator model, we have to find a connection between the external behavior of the system (the surface field $E_s = R\,E_{in} = (1+T)E_{in}$) and the surface conductivity (σ_s) and the microscopic behavior (the excitations p and q and the driving force f). First, we observe that each of the constituent meta-atoms contributes a dipole moment p to the metamaterial and, if there are n_s atoms per unit of surface area, the average polarization current thus equals

$$\langle j_s(t)\rangle = n_s\dot{p}(t) \Rightarrow \langle j_s(\omega)\rangle = -i\omega n_s p(\omega). \tag{15.5}$$

The dark resonator does not contribute to the surface current since it has no dipole moment commensurate with the external field. Secondly, we need to find a connection between the surface field E_s, which drives the dipole oscillation in the world model, and the driving force f in the microscopic model, i.e., we seek the proportionality constant C in $f(t) = CE_s$. (Note that the surface field E_s is different from the incident field because of the scattering from the meta-atoms.) This can be done by recalling that for our linear meta-atom the average dipole moment must be proportional to the electric field at the surface:

$$n_s p(\omega) = \varepsilon_0 \chi_{se}(\omega) E_s(\omega), \tag{15.6}$$

where χ_{se} is the surface susceptibility. In the static limit, this yields

$$\varepsilon_0 \chi_{se}^{(static)} E_s(0) = n_s p(0) = n_s \left(1 - \kappa^2\right)^{-1} f(0) \approx n_s f(0), \tag{15.7}$$

where we used the fact that $\kappa^2 \ll 1$ under EIT conditions. Using (15.5, 15.6 and 15.7), we can now determine the surface conductivity:

$$\sigma_{se} \approx \varepsilon_0 \chi_{se}^{(static)} \frac{-i\omega p(\omega)}{f(\omega)} = \frac{-i\omega\beta D_d(\omega)}{D_d(\omega) D_r(\omega) - \kappa^2}, \tag{15.8}$$

where $\beta \equiv \varepsilon_0 \chi_{se}^{(static)}$. Once we have determined the surface conductivity, we can calculate the scattering parameters from (15.4) and other derived quantities, in particular the absorbance and the group delay:

$$\begin{aligned} A &= 1 - |T|^2 - |R|^2 = |T|^2 \, Re\left(\zeta \sigma_{se}\right), \\ \tau_g &= Im\left(\frac{d \ln T}{d\omega}\right) = -\frac{1}{2} Im\left(T \frac{d\zeta\sigma_{se}}{d\omega}\right). \end{aligned} \tag{15.9}$$

In Fig. 15.10 we compare results of the radiating two-oscillator model with experimental data for a copper-on-alumina EIT metamaterial that takes advantages of the quadrupole dark mode described in Sect. 15.2. The model describes the experimental results very well. It is a very useful tool to decide what parameters need to be changed in order to achieve a certain dispersion and absorption spectrum. For example, in Fig. 15.10, we see that larger coupling strength results in an EIT resonance with larger bandwidth, in agreement with the rule of thumb derived in Sect. 15.3.1.

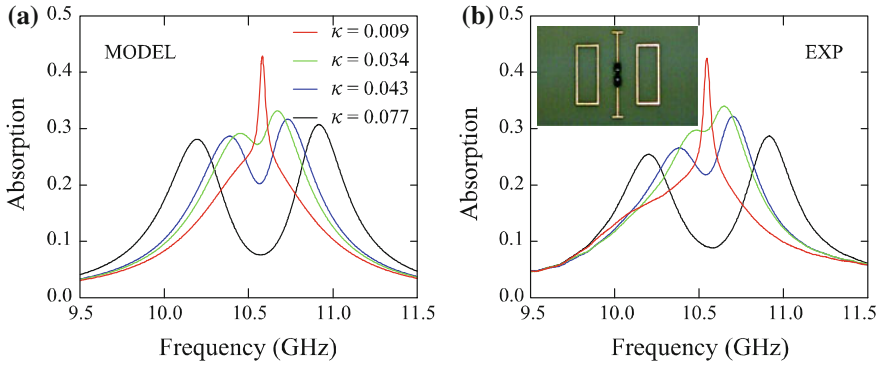

Fig. 15.10 Comparison between absorption spectra obtained from **a** the radiating two-oscillator model and **b** from experimental results of an EIT metamaterial for several values of the coupling strength (From [25])

15.4 Electromagnetically Induced Absorption

One of the spectra in Fig. 15.10 ($\kappa = 0.009$) has a curious feature—it has an absorption peak instead of an absorption dip at the EIT resonance frequency. It can therefore be considered as the classical analogue of electromagnetically induced *absorption* (EIA) first studied by Akulshin, Barreiro and Lezama in atomic systems [26]. This classical analogue was recently predicted and observed by several groups [22, 25, 27]. Let us use the radiating two-oscillator model to study this phenomenon in more detail.

In Fig. 15.11a, we show how the absorption, transmission, and group delay spectra evolve if we decrease the dissipative loss factor γ_r of the radiative resonator. There is still a frequency window with high transmission, but the incision in the absorption spectrum becomes smaller and finally disappears. This does not mean, however, that the dark resonance has disappeared, as we can clearly see from the enhanced group delay. Rather, the background absorption of the radiative resonance is decreased, but the radiative resonance is still sufficiently broadened by radiation damping, while the excitation of the dark resonance is barely changed. At a certain point, the absorption reduction in the radiative resonator due to the destructive interference mechanism is exactly cancelled by the absorption in the dark resonator. When we further decrease the dissipative loss of the radiative resonator, the absorption spectrum turns into a very shallow and weak background with a narrow peak at the resonance frequency ω_d. The transition between EIT and EIA can also be observed when we increase the dissipative loss of the dark resonator [see Fig. 15.11b]. When γ_d is increased, the radiative resonance remains unaltered, but the absorption in the center of the transparency window goes up. Eventually, the loss in the dark resonator overcomes the loss reduction due to the destructive interference in the radiative resonator. Finally, EIA can also be achieved by decreasing the coupling strength κ. Weaker coupling creates

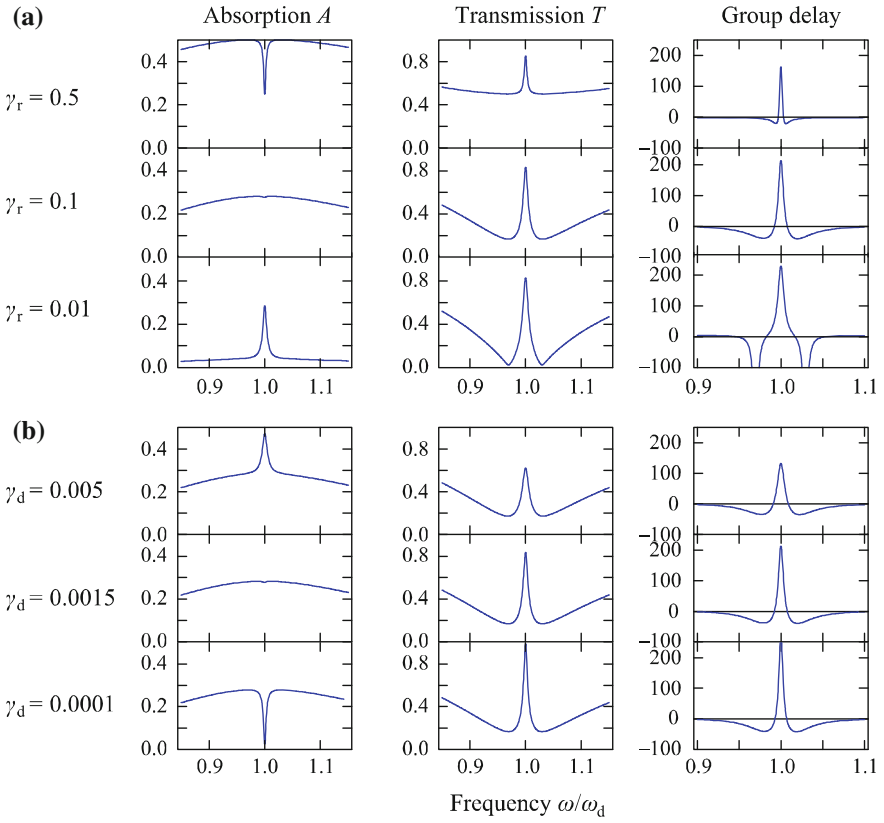

Fig. 15.11 Study of the radiating two-oscillator model and appearance of electromagnetically induced absorption when **a** the dissipative loss of the bright resonance is decreased **b** the dissipative loss of the dark resonance is increased (From [25])

a narrower transparency window with larger excitation in the dark resonator. This in turn increases the absorption at the resonance frequency, resulting in EIA when the dissipation in the dark resonance overcomes the loss reduction in the radiative resonance.

We believe the classical analogue of electromagnetically induced absorption may be interesting for applications in spectroscopy and sensing, since it produces a spectral feature with a narrow bandwidth. The width of the peak is reduced by the lack of radiation damping in the dark resonator and the additional narrowing due to the coupling mechanism. Note that the EIA effect could only be described by the radiating two-oscillator model, since the bare two-resonator model lacks radiative broadening of the radiative resonator. Alternatively, electromagnetically induced absorption can be achieved by introducing a retardation-induced phase shift in the interaction

between the dark and bright resonators [27] or by coupling both the dark and bright resonator to the external wave but with different phase advance [22].

15.5 EIT Metamaterials for Nonlinear and Tunable Operation

15.5.1 At Microwave Frequencies

As we have discussed above, large fields (see, for example, Fig. 15.4b) can be generated at the EIT frequency. The large field enhancement can be taken advantage of for nonlinear and tunable metamaterials by introducing a nonlinear medium in the vicinity of the dark resonator. One possibility is fabricating the dark resonator out of a superconducting material. The meta-atom shown in Fig. 15.12a is the same as the one discussed in Sect. 15.2, but now we have deliberately introduced very sharp corners in the split-ring resonators [28]. At low input power ($P < 10\,\mathrm{dBm}$), the EIT metamaterial works as usual and we observe the resonance with high transmittance and large group delay (see Fig. 15.12b). However, if we increase the power of the incident beam, we observe that the EIT transmission window disappears, i.e., we can switch the transmission window through the input beam without need for an external signal. The disappearance of the EIT window is related to local field hotspots at the corners of the split rings, which we observe in numerical simulations and local field measurements (Fig. 15.12c). The localized spots of highly enhanced current density can reach the critical current density of the superconductor. In that state, there is magnetic flux generated by the microwave currents that enters the Nb film and causes dissipation. As the critical state extends further into the material (see measured current distributions in Fig. 15.12d), the dissipation leads to thermal runaway and eventually to quenching of the superconductivity at 22 dBm. This in turn leads to a decrease in the resonator's quality factor and switching off of the EIT features.

15.5.2 At Terahertz Frequencies

The idea of damping the dark resonance was subsequently transposed to the terahertz domain by Jianqiang Gu et al. [29]. They created an EIT metamaterial made from an aluminium double SRR (dark resonance) and an aluminium cut wire (bright resonance), deposited on undoped silicon islands. Due to much smaller radiation loss in the magnetic quadrupole resonance in the double SRR (see also Sect. 15.2), sufficient contrast in quality factor is achieved to enable the EIT phenomenon. This is reflected in the transmission peak at 0.74 THz (Fig. 15.13, top row).

To decrease the quality factor of the dark resonance, an optical pump beam is used to illuminate the Si islands under the SRRs. The pump excites photocarriers in the silicon, creating a resistive path for the carriers participating in the SRR res-

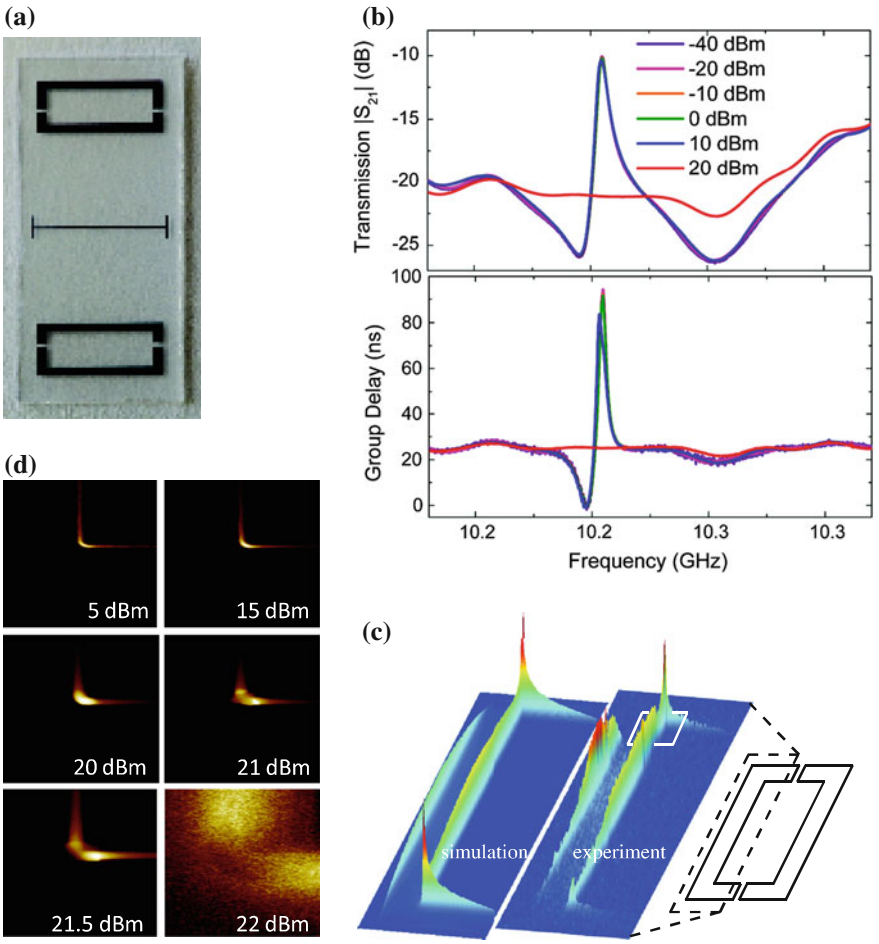

Fig. 15.12 **a** EIT metamaterial with nonlinear response. **b** Transmittance and group delay spectra as a function of input power. **c** Field hotspots at the corners of the split-ring resonators. **d** Thermal runaway and quenching of the superconducting state (From [28])

onance. The result is a gradual disappearance of the EIT spectral feature when the power of the pump beam is increased from 0 to 1350 mW. The structure is thus a tunable metamaterial with the optical pump beam as the external control signal. The control of the quality factor can also be exercised through thermal heating of the semiconductor [30].

All these examples amount essentially to changing the quality factor of the dark resonance to take advantage of strong field enhancement in the dark resonator of the EIT metamaterial.

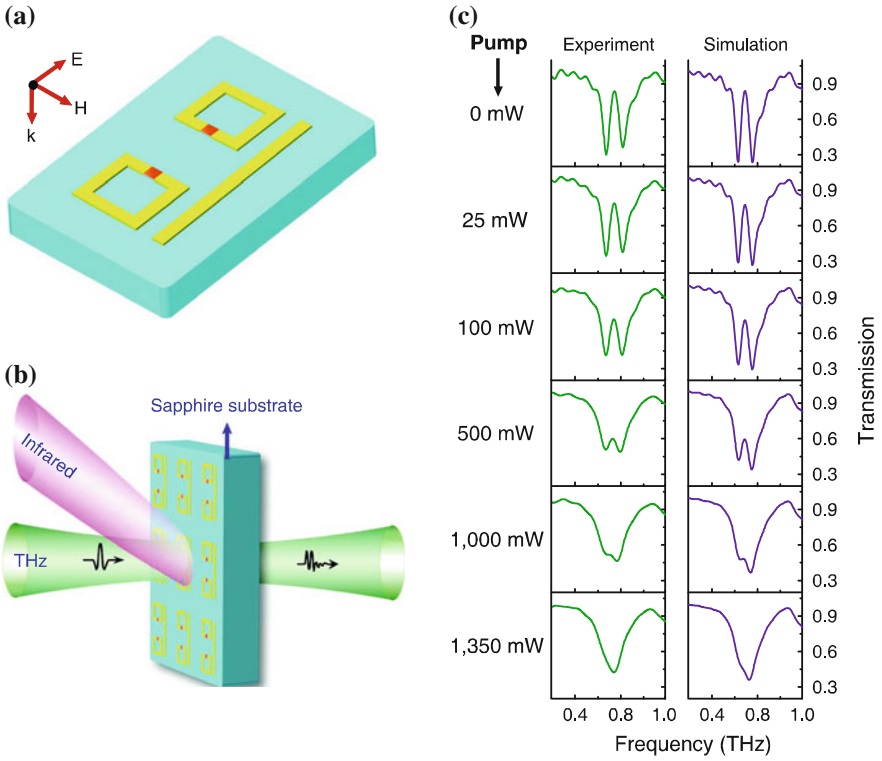

Fig. 15.13 **a** An EIT metamaterial with tunable response. **b** Schematic showing the optical pump beam as external control signal. **c** Transmission spectra showing the gradual destruction of the EIT response when the optical pump power is increased (From [29])

References

1. S.E. Harris, J.E. Field, A. Imamoglu, Nonlinear optical processes using electromagnetically induced transparency. Phys. Rev. Lett. **64**, 1107–1110 (1990)
2. S.E. Harris, Electromagnetically induced transparency. Phys. Today **50**, 36–42 (1997)
3. P. Mandel, Electromagnetically induced transparency. Hyperfine Interact. **135**, 223–231 (2001)
4. M. Fleischhauer, A. Imamoglu, J.P. Marangos, Electro-magnetically induced transparency: optics in coherent media. Rev. Mod. Phys. **77**, 633–673 (2005)
5. L.V. Hau, S.E. Harris, Z. Dutton, C.H. Benroozi, Light speed reduction to 17 metres per second in an ultracold atomic gas. Nature **397**, 594–598 (1999)
6. M. Fleischhauer, M.D. Lukin, Dark-state polaritons in electro-magnetically induced transparency. Phys. Rev. Lett. **84**, 5094–5097 (2000)
7. C. Liu, Z. Dutton, C.H. Behroozi, L.V. Hau, Observation of coherent optical information storage in an atomic medium using halted light pulses. Nature **409**, 490–493 (2001)
8. C.L. Garrido-Alzar, M.A.G. Martinez, P. Nussensveig, Classical analog of electromagnetically induced transparency. Am. J. Phys. **70**, 37–41 (2002)
9. Q. Xu, S. Sandhu, M.L. Povinelli, J. Shakya, S. Fan, M. Lipson, Phys. Rev. Lett. **96**, 123901 (2006)

10. F. Liu, M. Ke, A. Zhang, W. Wen, J. Shi, Z. Liu, P. Sheng, Acoustic analog of electromagnetically induced transparency in periodic arrays of square rods. Phys. Rev. E **82**, 026601 (2010)
11. P. Tassin, L. Zhang, T. Koschny, E.N. Economou, C.M. Soukoulis, Low-loss metamaterials based on classical electromagnetically induced transparency. Phys. Rev. Lett. **102**, 053901 (2009)
12. S. Zhang, D.A. Genov, Y. Wang, M. Liu, X. Zhang, Plasmon-induced transparency in metamaterials. Phys. Rev. Lett. **101**, 047401 (2008)
13. N. Papasimakis, V.A. Fedotov, N.I. Zheludev, S.L. Prosvirnin, Metamaterial analog of electromagnetically induced transparency. Phys. Rev. Lett. **101**, 253903 (2008)
14. P. Tassin, L. Zhang, T. Koschny, E.N. Economou, C.M. Soukoulis, Planar designs for electromagnetically induced transparency in metamaterials. Opt. Express **17**, 5595–5606 (2009)
15. N. Liu, L. Langguth, T. Weiss, J. Kastel, M. Fleischhauer, T. Pfau, H. Giessen, Plasmonic analogue of electromagnetically induced transparency at the drude damping limit. Nat. Mater. **8**, 758–762 (2009)
16. N. Liu, T. Weiss, M. Mesch, L. Langguth, U. Eigenthaler, M. Hirscher, C. Sonnichsen, H. Giessen, Planar metamaterial analogue of electromagnetically induced transparency for plasmonic sensing. Nano Lett. **10**, 1103–1107 (2010)
17. R. Singh, C. Rockstuhl, F. Lederer, W. Zhang, Coupling between a dark and a bright eigenmode in a terahertz metamaterial. Phys. Rev. B **79**, 085111 (2009)
18. L. Zhang, P. Tassin, T. Koschny, C. Kurter, S.M. Anlage, C.M. Soukoulis, Large group delay in a microwave metamaterial analog of electromagnetically induced transparency. Appl. Phys. Lett. **97**, 241904 (2010)
19. K.L. Tsakmakidis, M.S. Wartak, J.J.H. Cook, J.M. Hamm, O. Hess, Negative-permeability electromagnetically induced transparent and magnetically active metamaterials. Phys. Rev. B **81**, 195128 (2010)
20. J. Zhang, S. Xiao, C. Jeppesen, A. Kristensen, N.A. Mortensen, Electromagnetically induced transparency in metamaterials at near-infrared frequency. Opt. Express **18**, 17187–17192 (2010)
21. K. Ooi, T. Okada, K. Tanaka, Mimicking electromagnetically induced transparency by spoof surface plasmons. Phys. Rev. B **84**, 115405 (2011)
22. L. Verslegers, Z. Yu, Z. Ruan, P.B. Catrysse, S. Fan, From electromagnetically induced transparency to superscattering with a single structure: a coupled-mode theory for doubly resonant structures. Phys. Rev. Lett. **108**, 083902 (2012)
23. N. Papasimakis, Y.H. Fu, V.A. Fedotov, S.L. Prosvirnin, D.P. Tsai, N.I. Zheludev, Metamaterial with polarization and direction insensitive resonant transmission response mimicking electromagnetically induced transparency. Appl. Phys. Lett. **94**, 211902 (2009)
24. C. Kurter, P. Tassin, L. Zhang, T. Koschny, A.P. Zhuravel, A.V. Ustinov, S.M. Anlage, C.M. Soukoulis, Classical analogue of electromagnetically induced transparency with a metal-superconductor hybrid metamaterial. Phys. Rev. Lett. **107**, 043901 (2011)
25. P. Tassin, L. Zhang, R. Zhao, A. Jain, T. Koschny, C.M. Soukoulis, Phys. Rev. Lett. **109**, 187401 (2012)
26. A.M. Akulshin, S. Barreiro, A. Lezama, Electromagnetically induced absorption and transparency due to resonant two-field excitation of quasidegenerate levels in Rb vapor. Phys. Rev. A **57**, 2996–3002 (1998)
27. R. Taubert, M. Hentschel, J. Kastel, H. Giessen, Classical analog of electromagnetically induced absorption in plasmonics. Nano Lett. **12**, 1367–1371 (2012)
28. C. Kurter, P. Tassin, A.P. Zhuravel, L. Zhang, T. Koschny, A.V. Ustinov, C.M. Soukoulis, S.M. Anlage, Switching nonlinearity in a superconductor-enhanced metamaterial. Appl. Phys. Lett. **100**, 121906 (2012)
29. J. Gu, R. Singh, X. Liu, X. Zhang, Y. Ma, S. Zhang, S.A. Maier, Z. Tian, A.K. Azad, H.-T. Chen, A.J. Taylor, J. Han, W. Zhang, Active control of electromagnetically induced transparency analogue in terahertz metamaterials. Nat. Commun. **3**, 1151 (2012)
30. Q. Bai, C. Liu, J. Chen, C. Cheng, M. Kang, H.-T. Wang, Tunable slow light in semiconductor metamaterial in a broad terahertz regime. J. Appl. Phys. **107**, 093104 (2010)

Index

I.V. Shadrivov et al. (eds.), *Nonlinear, Tunable and Active Metamaterials*,
Springer Series in Materials Science 200, DOI 10.1007/978-3-319-08386-5